TECHNOLOGICAL UNIVERSITY (MANDALAY)

ENGINEERING, SCIENCE & EDUCATIONAL JOURNAL

ESEJ

ISBN: 978-99986-0-248-9

ENGINEERING, SCIENCE AND EDUCATIONAL JOURNAL

VOLUME 1, AUGUST 2024

Organized by

TECHNOLOGICAL UNIVERSITY (MANDALAY)

ISBN: 978-99986-0-247-2

pdf ISBN: 978-99986-0-248-9

CDROM ISBN: 978-99986-0-249-6

TECHNOLOGICAL UNIVERSITY (MANDALAY)

ENGINEERING, SCIENCE AND EDUCATIONAL JOURNAL

VOLUME 1, AUGUST 2024

TECHNOLOGICAL UNIVERSITY (MANDALAY)

ENGINEERING, SCIENCE AND EDUCATIONAL JOURNAL

VOLUME 1, AUGUST 2024

REVIEWERS

Architecture

Dr. Thet Oo, Professor, Mandalay Technological University

Dr. Zin Zin Moe, Professor, Naypyidaw Technological University

Daw Thae Su San, Assistant Lecturer, Technological University (Mandalay)

Chemical Engineering

Dr. Ni Lwin Aye, Professor, Technological University (Mandalay)

Dr. May Myat Khine, Professor, West Yangon Technological University

Dr. Swe Zin Win, Professor, Technological University (Thanlyin)

Civil Engineering

Dr. Nwe Nwe Win, Professor, Technological University (Mandalay)

Dr. Kyaw Naing Soe, Professor, Technological University (Mandalay)

Daw San San Myint, Associate Professor, Technological University (Mandalay)

Electrical Power Engineering

Dr. Aung Myo Naing, Professor, Technological University (Hmawbi)

Daw Moe Moe, Associate Professor, Technological University (Mandalay)

Daw Thet Thet Aung, Lecturer, Technological University (Mandalay)

Electronic Engineering

Dr. Pa Pa Winn San, Professor, Technological University (Mandalay)

Dr. Nyan Phyo Aung, Professor, Technological University (Mandalay)

Dr. Yin Hnin Thet Htun, Associate Professor, Technological University (Mandalay)

Engineering Chemistry

Dr. Hla Thidar Aung, Professor, Technological University (Mandalay)

Dr. Khin Khin Win Aung, Professor, Technological University (Hmawbi)

Dr. Cherry Than, Associate Professor, Technological University (Mandalay)

Engineering Mathematics

Dr. Khin Saw Myint, Pro Rector, Technological University (Thanlyin)

Dr. Hla Hla Myint, Professor, Technological University (Mandalay)

Dr. Aye Thanda Lwin, Associate Professor, Technological University (Mandalay)

Engineering Physics

Dr. Khaing Khaing Thinn, Professor, Technological University (Mandalay)

Dr. Nwe Ni Hlaing, Professor, Magway University

Daw Aye Mar Khin, Associate Professor, Technological University (Mandalay)

English

U Aung Kyaw Myint, Professor, Technological University (Kyaukse)

Daw Zin Mar Hnin, Associate Professor, Technological University (Mandalay)

Daw Khaing Mi Mi Htun, Lecturer, Technological University (Mandalay)

Information Technology Engineering

Dr. Khin Myo Chit, Professor, Technological University (Mandalay)

Dr. Cho Me Me Maung, Professor, Technological University (Mandalay)

Dr. Phyo Thu Zar Tun, Professor, Mandalay Technological University

Mechanical Engineering

Dr. Aye Mya Thandar, Professor, Technological University (Mandalay)

Dr. Swe Swe Maw, Professor, Technological University (Mandalay)

Dr. Aung Ko Win, Professor, Technological University (Toungoo)

Mechatronics Engineering

Dr. Wut Yi Win, Professor, Mandalay Technological University

Daw Ei Wai Phyo, Associate Professor, Technological University (Mandalay)

Dr. Myint Htun Naing, Tutor, Technological University (Mandalay)

Mining Engineering

Dr. Aung Myo, Professor, Technological University (Mandalay)

Dr. Win Min Latt, Professor, Technological University (Taunggyi)

Myanmar

Dr. Aye Aye Htun, Professor, Technological University (Mandalay)

Dr. Aye Aye Than, Professor, University of Computer Studies (Mandalay)

Daw Thidar Hnin, Associate Professor, Technological University (Mandalay)

Petroleum Engineering

U Ye Tun, Demonstrator, Technological University (Mandalay)

TECHNOLOGICAL UNIVERSITY (MANDALAY)

ENGINEERING, SCIENCE AND EDUCATIONAL JOURNAL

VOLUME 1, AUGUST 2024

CONTENTS

Civil Engineering

Electrical Power Engineering

Electronic Engineering

Engineering Chemistry

Engineering Physics

English

Information Technology Engineering

Mechanical Engineering

Mechatronics Engineering

Myanmar

Petroleum Engineering

Investigation on Influenced Factors for Car Ownership Motivations among Undergraduate Students

Khin Hnin Swe[1], Kyaw Naing Soe[2]

[1]*Department of Civil Engineering and Technological University (Mandalay)*

[2]*Department of Civil Engineering and Technological University (Mandalay)*

Email: [1]khinhninswe154@gmail.com, [2]mknsoe@gmail.com

***Abstract*— Car ownership levels are increasing rapidly in South-East Asian developing countries leading to unsustainable developments. This study aims to realize undergraduate students' motivations to purchase cars after they graduate and employ. The main foci of this research are undergraduate students where it is expected that their current attitudes and habits will influence their travel behavior after they graduate and obtain a job. This study used paper surveys to ask students about their attitudes towards car and attitudes towards public transportation, social norms, their socio-demographic situations, current transportation patterns and the intention to own a car in the future. This study conducted a descriptive analysis of the survey data focusing on explaining intentions to own a car in the future. Although current private car usage of students was found to be about 26.4%, it can be surprisely seen that car purchase intentions of student's rate at about 92% which means most of the students have inner desire to buy their own car. The younger students have more desire to purchase cars in the future. In past car usage, it can be seen that the students who do not grew up with car has intentions to purchase cars than the students grew up with car. In attitude towards car, symbolic affective, independence and comfort are the important factors of car ownership motivations among undergraduate students. In the norming effects, parents' expectation and parents' influence are the important factor of car ownership motivations among undergraduate students.**

Keywords*— attitude towards car, car purchase intentions, car ownership motivations, present and past car usage, social norms, undergraduate students

I. Introduction

Transport is one of the most important aspects in the day-to-day life of the people, as their activities cannot be fulfilled without moving. Moreover, transportation plays a vital role in economic growth, developing urban environment and globalization. Therefore, a good planning of transport is essential to make effective and sustainable transport systems. To found a successful transportation system for a country, public transportation has to retain the main modal share among other commuting modes. Car ownership levels are rising rapidly in many developing countries. Increasing income levels allow particular citizens of the major cities to purchase more and modern vehicles. So, to estimate future car use trends, it is necessary to understand car ownership decisions of younger people. It is critical to understand whether their current attitudes, habits and expectations have influence on their travel behavior after they graduate and obtain a job. And then, understanding car use trends and underlying factors is important for deriving policy measures to reduce traffic congestion and other environmental side effects, such as air and noise pollution, accidents and land-use developments trends. The factors of attitudes towards car and social norms are the important factors to explain car ownership trends.

II. Questionnaire Design

A. *Dependent Variable*

In this paper, intentions to buy a car in the future (next 10 years)used as dependent variable, which was measured on a 7-point Likert scale (very unlikely – very likely)

B. *Explanatory Variables*

Explanatory variables are socio-demographic characteristics, current transportation patterns, attitudes/perceptions and social norms

III. Methodology

This paper use primary data to analyze the factors such as socio-demographic characteristics, car ownership, use & intentions (past, present, future), attitudes, perceptions and Social norms.

A. *Data Collection Method*

All data were collected by using paper survey (Random sampling method) from two Universities of Mandalay. Average number of students in Technological University Mandalay (TUM) and Mandalay Technological University (MTU) are about 2000 and 1000. Students of these universities contain locals and who come from many regions from Myanmar.

B. Sample Size Computation

This paper was carried out by questionnaire survey and the total student numbers in two universities are about 3000 so that the number of samples, which is enough to give the overview of the study area, is needed to be concerned. As indicated in the following Table I, to reduce the margin of error to half, for instance, from 4 to 2, the sample size determination has been increased considerably, from 500 to 2000. As the sample size is inversely proportional to margin of error [4].

I. Margin of Error Percentages for Certain Surveys Sample Sizes

Survey Sample Size	Margin of Error Percent

2,000	2
1,500	3
1000	3
900	3
800	3
700	4
600	4
500	4
400	5
300	6
200	7
100	10
50	14

There are many formulas used for calculating sample size. One of the most common formulas used is Yamane's formula: as shown in (1)

The sample size equation is

$$n=\frac{N}{1+N\,E^2} \qquad (1)$$

Where
n = sample size,
N = population size,
E = margin of error, the total maximum number of students is roundabout 3000 students margin of error will be 4%.

Calculation:

$$n=\frac{(3000)}{(1+3000\times 0.04^2)}=517.24$$

IV. Results and Discussions

The following sections describe the analyzed results of student car ownership motivations by socio-demographic characteristics, car ownership, use & intentions (past, present, future), attitudes, perceptions and social norms.

A. Car Ownership, Use and Intentions of Respondents (Past, Present & Future)

In this paper, a large number of students almost hundred percent have intentions to buy a car in the future. Although current private car usage of students was found to be about 26.4%, it can be surprisely seen that car purchase intentions of student's rate at about 92% which means most of the students have inner desire to buy their own car as shown in Table II.

II. Car Ownership, Use and Intentions of Respondents (Past, Presenr & Future)

Variables (Number of Observations)	
Past	**Percentage**
Grew up with car (%)	40
Present: Ownership and Transportation Pattern	**Percentage**
Car user (%)	30
Car user & owner (%)	3.4
Car user and non-owner (%)	26.4
Driving License (%)	37
Mode of Commuting	**Percentage**
Car (%)	14
Taxi (%)	2
Motorcycle (%)	64
Bicycle (%)	1
Ferry (%)	3
Walk (%)	16
Future: Purchase Intentions(how likely are you to buy a car within the next 10 years)	**Percentage**
%have Intention	92
Very Likely	46.8
Likely	38
Somewhat Likely	7.6
%Undecided	4
%have no Intention	4
Somewhat Unlikely	1.8
Unlikely	1.2
Very Unlikely	0.6

B. Socio-demographic Characteristics of Respondents in Mandalay

A large number of students live with friends and live in dormitory within the university and near the university. The students in gender split have 44 % male and 56 % female. The average age of students is 20.62. And then; the students' average family income and average personal income are 16.64 lakhs and 1.28 lakhs as shown in Table III. It is higher the income will be greater the intentions.

III. Socio-Demographic Characteristics of Respondents in Mandalay

Variables (Number of Observations)	
Socio-Demographic Characteristics	
Living Arrangement	**Percentage**
Living alone (%)	9.4
Living with family (%)	41
Living with friends (%)	47.6
Others (%)	2
Dwelling Unit	**Percentage**
Dormitory (%)	66
Apartment (%)	7
Others (%)	27
Gender	**Percentage**
Gender spilt(% male)	44
Gender spilt(% female)	56
Age, Distance, Income	**Mean**
Average age	20.62
Average commuting distance(km)	9.29
Average personal income(lakhs)	1.28
Average family income(Lakhs)	16.64

C. Attitudes toward Car and Public Transportation and Norming Effects

In attitude towards car, symbolic affective, independence and comfort are the important factors of car ownership motivations among undergraduate students because a large number of students agree in these

statements. Symbolic affective has agreement over 80% and questions such as independence and comfort have agreement over 80% and over 90 % except “cars are fun to have” which has agreement 75%.A large number of students do not have negative aspects with respect to attitude towards car except “cars are expensive to own and maintain” and “cars are giving arrogant impression” as shown in Table IV. In attitude towards ferry, there are many weaknesses in safety, reliability and have less convenience and needed to improve a lot in order to maximize usage of public transport in the future as shown in Table V. In subjective social norms, the students think that owning a car is a right thing. In injunctive norms and personal norms, parent’s expectation and parent’s influence is higher than others as shown in Table VII.

IV. Attitude Towards Car

Attitude Towards Car	Disagree %	Undecided %	Agree %
Symbolic Affective			
Cars allow to express oneself from others.	15.2	4	80.8
Cars are cool.	10.8	8	81.2
Cars are trendy	2.8	1	96.2
Arrogant Prestige			
Cars are giving arrogant impression	42.6	4.4	53
Cars allow to distinguish oneself from others.	52	7	41
Cars are expensive to own and maintain.	3.8	1.2	95
Cars are disturbing one’s neighborhood.	82.4	4	13.6
Cars bring prestige	29	6.8	64.2
Independence			
Cars are convenient.	5	2	93
Cars help one to save time for travel	7.8	1.4	90.8
Cars allow one to ravel anytime.	13.6	2	84.4
Cars allow one to be independent.	8.2	3.2	88.6
Comfort			
Cars allow one to ravel safely.	4.2	1.6	94.2
Cars are comfortable.	6.6	3	90.4
Cars allow one to pick up or see off others	2.8	2	95.2
Cars are fun to have	12.4	12.4	75.2
Social Orderliness			
Cars allow one to care for others	15.2	9.4	75.4
Cars are environmentally friendly.	38.6	18.4	43

V. Attitude Towards Public Transportation

Attitude Towards (Ferry)	Disagree (%)	Undecided (%)	Agree (%)
Safety-Reliability(PT)			
Ferry drivers drive carelessly.	37.4	9.4	53.2
I feel unsafe using ferry service.	45.4	14.4	40.2
Ferry is not punctual.	40.2	13.4	46.4
Convenience(PT)			
Ferry is clean enough to make me want to ride along.	54.6	17.2	28.2
Ferry service covers the city area well.	67.6	9	23.4

VI. Descriptive Norms

Descriptive Norms	YES	%	NO	%
Did you grow up with a car	202	40.4	298	59.6
Does your Friends or partner have a car?	322	64.4	178	35.6
Do your siblings have a car?	176	35.2	324	64.8
Do most people in your neighborhood have cars?	419	83.8	81	16.2

VII. Subjective Norms, Injunctive Norms and Personal Norms

Social Norms	Disagree (%)	Undecided (%)	Agree (%)
Subjective Social Norms			
It is no smarter to have a car.	47.2	6	46.8
I feel that there is social pressure to have a car.	40.2	7.2	52.6
Transport modes other than car are looked down.	73.4	3.6	23
Majority of people think that having a car is the right thing to do.	2.6	1.8	95.6
Injunctive Norms			
Intention to buy a car in the future	3.6	4	92.4
Expectation of parents	7	8.6	84.4
Expectation of Friends/partner	9.2	13.4	77.4
Expectation of siblings	10.4	10.6	79
Expectation of neighbors	18.2	26.6	55.2
Personal Norms			
Importance of parents' expectation	18.2	7	74.8
Importance of Friends/partner's expectation	34.2	7	58.8
Importance of siblings' expectation	28.2	6.8	65
Importance of neighbors' expectation	75.6	9.6	14.8

D.Distribution of Car Purchase Intentions Based on Age

In this paper, the younger students have more desire to purchase a car in the future after they graduate and employ as shown in Fig.1.

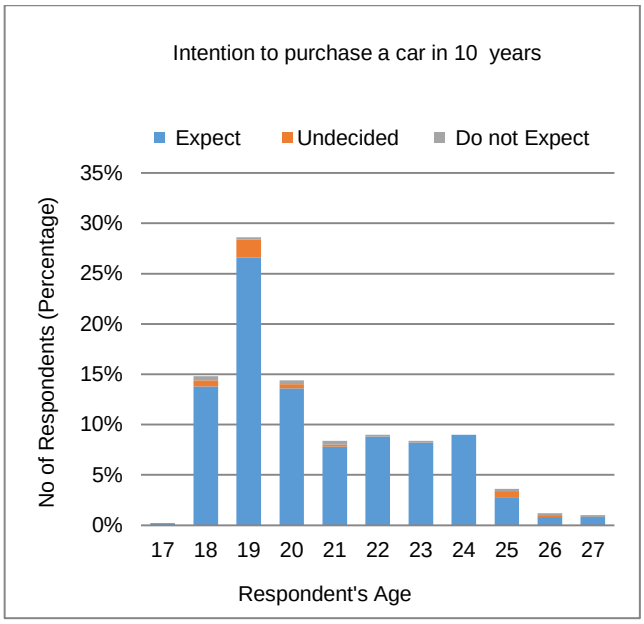

Fig.1. Distribution of Car Purchase Intention Based on Age

E.Distribution between Car Usage History and Car Purchase Intentions

Students who do not grow up with car strongly expect to buy a car (55%) than those who grew up with car (37%) as shown in Fig. 2. However, most students expect to purchase a car when they make their money and there are slight percentages who do not expect to buy.

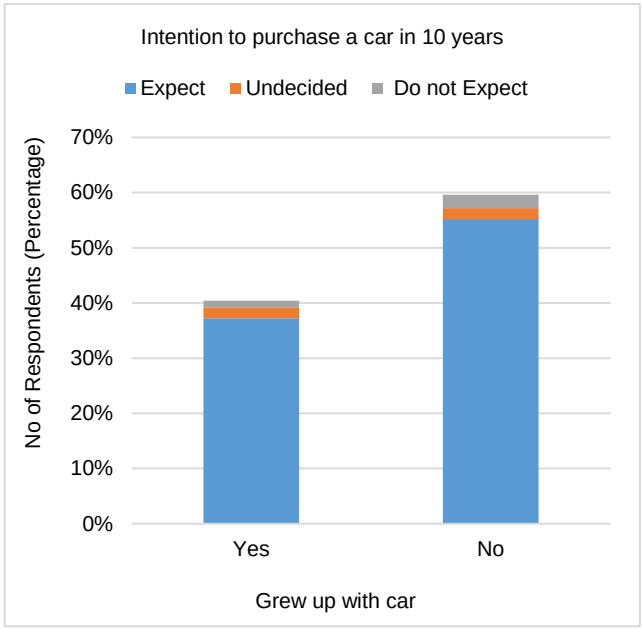

Fig. 2. Distribution between Car Usage History and Car Purchase Intentions

F. Distribution of Current Travelling Behavior and Car Purchase Intentions

Students who currently use private car, motorcycle and walking expect to purchase car more than other travel mode choice groups as shown in Fig. 3. Actually, all groups who use different types of travel mode expect to purchase car in the high percentage. There are tiny percentages who do not expect to buy a car in the future.

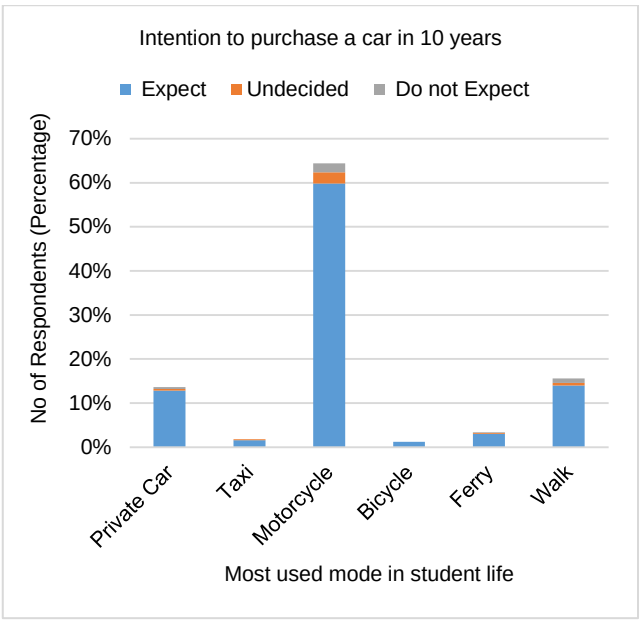

Fig. 3. Distribution of Current Travelling Behavior and Car Purchase Intentions

V. Conclusion

This study aims to realize undergraduate students' motivations to purchase cars after they graduate and employ. In this study, it can be seen that the younger students have more desire to purchase a car in the future. In present car usage, although current private car usage of university students was found to be about 26.4%, it can be surprisely seen that car purchase intentions of student's rate at about 92% which means most of the students have inner desire to buy their own car.

Past car usage and past non-car usage of university students was found to be 40.4% and 59.6%, it can be seen that non-car usage of students has intentions to buy a car than past car usage students. Then, between the travel mode choice and car purchase intentions, Students who currently use private car, motorcycle and walking have intentions to purchase car more than other travel mode choice groups. In socio-demographic variables, students 'family income has relations with car purchase decisions that it is higher the income will be greater car purchase decisions. In attitude towards car, the factors such as symbolic affective, independence and comfort are the important factors of car ownership motivations among undergraduate students.

In the norming effects, four types of norms were examined including descriptive norms, subjective social norms, injunctive norms and personal norms. In subjective social norms, personal thoughts or view on using private cars were asked and over 95% of students think that owning a car is a right thing. Other people thoughts or expectation on each student were asked in injunctive social norms' sections. In this section, parent's expectation is higher than other's expectation so that car purchase intentions are stronger relation with parent's expectation. In personal norms section, it was studied how other people expectation effects on their decisions. In this section, parent's influence is higher than other's influence so that car purchase intentions are also stronger relation with parent's influence. So, parents' expectation and parents'

influence are the important factors of car ownership motivations among undergraduate students.

It was seen that causality between car ownership and arrogant prestige is not clear, it might still conclude that this factor could be used to deter especially young students from buying cars.

ACKNOWLEDGMENT

The author would like to express her heartfelt gratitude to Dr. Su Yin Win, Pro Rector, Technological University (Mandalay), for her invaluable directions, managements and helps. The author would like to express her heartfelt gratitude to Dr. Hnit Thit Shein, Pro Rector, Technological University (Mandalay), for her kind help and invaluable permission. The author is deeply indebted to Dr. Nwe Nwe Win, Professor and Head, Department of Civil Engineering, Technological University (Mandalay), for her guidance, advice and invaluable encouragement. The author wishes to extend grateful thanks to her supervisor, Dr. Kyaw Naing Soe, Professor, Department of Civil Engineering, Technological University (Mandalay), for his patient guidance, supervision and encouragement during long period of this study. The author specially thanks to all her teachers from Department of Civil Engineering for their supports and encouragement. Finally, the author would like to show deeply grateful thanks to her family, especially her parents, for their supports and encouragement to attain her destination. The author thanks to all her classmates for their understanding, sharing the knowledge through the course, and to all others who have helped towards the successful completion of this study.

REFERENCES

[1] Juan de Dios Ortizar,Luis G. Willumsen. Modelling Transport,4th Edition,2011

[2] Belgiawan, Prawira Fajarindra; Schmocker, Jan-Dirk; AbouZeid, Maya;Walker,Joan;Lee,Tzu-hang;Ettema,DickF.;Fujii,Satoshi:Car ownership motivations among undergraduate students in China, Indonesia,Japan,Lebanon, Netherlands, Taiwan, and USA (available online),2014.

[3] Prawira F.Belgiawan,Jan-Dark Schmocker and Satoshi Fujii: Understanding Car Ownership Motivations among Indonesian Students. Department of Urban Management, Kyoto University, Japan.

[4] http://www.questionpro.com/blog/ margin-of-error

Comparative Study on Structural Responses of Eight Storey Reinforced Concrete Building without and with Isolation System by Using Recycle Rubber

Latt Latt Win[1], Nwe Nwe Win[2]

[1]*Department of Civil Engineering, Technological University (Mandalay)*
[2]*Department of Civil Engineering, Technological University (Mandalay)*

Email: [1]lattlatwin@gmail.com, [2]nwenwewin.ce@gmail.com

Abstract **– This paper presents comparative study on the structural responses of eight-storeyed hotel reinforced concrete building without and with isolation system in Mandalay. The proposed building is irregular shape reinforced concrete building and its length and width are 115ft and 115ft respectively. Total height of the building is 89ft above ground level. Gravity and lateral Loadings are considered according to American Society of Civil Engineering (ASCE 7-05), spectrum acceleration and local wind speed are taken from Myanmar National Building Code (MNBC-2020). The superstructure is analyzed with response spectrum analysis. All structural members are designed based on American Concrete Instituted (ACI 318-14) code. In this study, the recycle rubbers are used as major components of lead rubber bearings. The require experimental tests are conducted to get recycle rubber properties in Rubber Research Development Centre at Yangon. Circular shape lead rubber bearing (LRB) type isolator is used in this study and designed with International Building Code (IBC 2000). The isolation system is installed at the base of each column between superstructure and plinth beam of the proposed building. The material properties and the size of the structural members are the same in both fixed base building and isolated base building. Structural responses of the proposed building without and with isolation system are compared. According the analysis results, storey drift, storey shear and storey acceleration of isolated base building are lower than that of fixed base building and storey stiffness and structural periods of isolated base building are greater than that of fixed base building. So isolated base building has significant high capacity during earthquake than that of fixed base building.**

Keywords— lead rubber bearing, recycle rubbers, reinforced concrete building, response spectrum analysis, structural responses

I. INTRODUCTION

In recent year, developing country like Myanmar, the population is increasing day by day. Most of people from rural areas are migrating to cities due to increase in job opportunities and to increase their living standard. Thus, the cities become crowded and densely populated. Therefore, high-rise buildings are needed to be constructed and essential in the future. There are many natural hazard all over the world. Myanmar is one of the most seismically active regions in the world. Therefore, the seismic isolation technique is conducted for the whole of Myanmar and for Mandalay as well since it is located adjacent to the most active fault in Myanmar, the Sagging Fault. There will be land congestion, necessitating the construction of high-rise building that must be seismically safe to reduce damage from natural disasters. The primary objective of earthquake resistant design is to create a structure that has adequate strength and ductility to ensure the safety of its occupants. Therefore, application of isolator is very popular in today which reduce the vibrations induced by lateral load such as strong wind and earthquake [4]. The objective of base isolation system is to reduce the seismic demand and force on structures, produced at a low cost and easily available materials (recycle rubber).

There are various types of seismic isolation system. The most common use types of isolation systems are

- Elastomeric Bearing System and
- Sliding Bearing System

Elastomeric isolators contain low and high damping rubber bearing and lead rubber bearing.

Sliding bearings contain the following bearing types:

- rigid sliding bearing System
- elastic sliding bearing System [2].

Lead rubber bearings are used in this study because they provide a flexible and effective way to mitigate the damaging effects of seismic forces. These bearings consist of a lead core surrounded by rubber layers. The lead core allows for lateral movement, while the rubber layers provide damping, absorbing and dissipating seismic energy [1]. When subjected to low lateral loads such as minor earthquake the lead-rubber bearing is stiff both lateral and vertical directions [1]. The advantages of the lead-rubber bearing are that protect the structural integrity of a building, minimizing the need for costly repairs or reconstruction after an earthquake.

II. CASE STUDY

A. Data for Proposed Building

The proposed building is irregular shape reinforced concrete structure. Plan and 3D view of proposed building are shown in Fig.1 and Fig.2. Data for the proposed building is as follows;

Type of structure	= eight-storeyed R.C building
Type of occupancy	= hotel
Occupancy Category	= II
Shape of building	= irregular shape
Structure length	= 115 ft
Structure width	= 115 ft
Typical story height	= 10 ft
Overall height	= 89 ft
Number of stair and lift	= 2

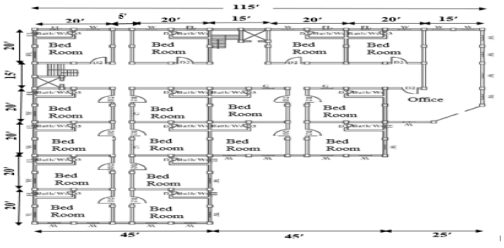

Fig. 1. Ground floor plan of the proposed building.

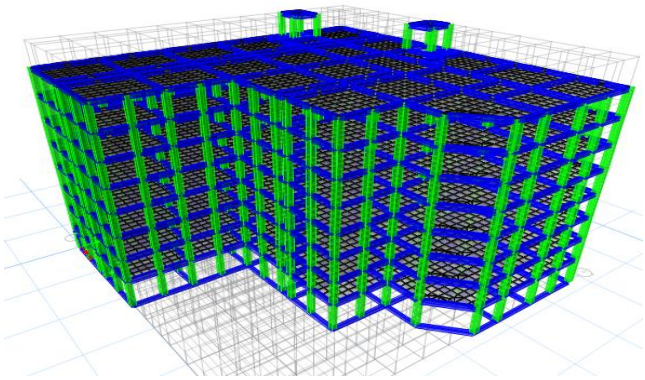

Fig. 2. 3D View of the proposed building.

B. Material Properties of the Structure

Materials Properties used for reinforced concrete structure are as follow.

Weight per unit volume of concrete, ω_c = 150 pcf
Compressive strength of concrete, f'_c = 3 ksi
Bending reinforcement; yield stress, f_y = 40 ksi
Shear reinforcement; yield stress, f_{ys} = 40 ksi
Modulus of elasticity, E_c = 3122 ksi

C. Loading Consideration

Gravity load such as dead loads, live loads and lateral load such as wind load and earthquake load are considered. Dead load consists of the weight of all materials and fixed equipment incorporated into the building. Floor finishing, partitions are considered as superimposed dead loads. Loading considering are applied according to ASCE 7-05.

For dead load,
Unit weight of concrete = 150 pcf
9" thick brick wall = 100 psf
4.5" thick brick wall = 55 psf
Finishing weight = 10 psf
Super imposed dead load = 20 psf
Weight of lift = 2 ton

For live load,
Bed room = 40 psf
Dining room, gym and spa and hall = 100 psf
Live load on roof = 20 psf
Live load on stair case = 100 psf
Live load on landing = 100 psf
Weight of water = 62.4 pcf

For wind load,
Exposure type = C
Wind speed = 80 mph
Wind importance factor = 1
Windward coefficient = 0.8
Leeward coefficient = 0.5

For earthquake load,
Spectral response acceleration S_s = 1.2
Spectral response acceleration S_1 = 0.7
Response Modification Coefficient, R = 8
System over strength factor, Ω_0 = 3
Framing system = SMRF
Seismic important factor I = 1
Deflection amplitude factor C_d = 5.5
Building period coefficient, C_t = 0.016

III. Dynamic Analysis and Design of Fixed Base Building

Eight-storeyed reinforced concrete building with fixed base is analyzed with response spectrum analysis by using ETABS (2018) software. After analyzing is completed, the structure is designed using ACI 318-14. Beam and column sections of the proposed building are shown in Table I and Table II respectively. The structural stabilities of fixed base building are checked based on ASCE 7-05 shown in Table III.

I. Table Beam Design Section of the Proposed Building

Beam Types	Size (in × in)
B_1	10 × 15
B_2	12 × 18
B_3	12 × 20
B_4	12 × 22
B_5	12 × 24
B_6	14 × 24
B_7	14 × 26
B_8	16 × 24
B_9	16 × 26

II. Table Column Design Section of the Proposed Building

Type	Storey Level	Size (in × in)	Type	Storey Level	Size (in × in)
C_1	GF to1F	20 × 20	C_6	GF to 1F	30 × 30
	1F to 3F	18 × 18		1F to 2F	28 × 28
	3F to 5F	16 × 16		2F to 4F	26 × 26
	5F to 7F	14 × 14		4F to 7F	22 × 22
	7F to RF	12 × 12		7F to RF	12 × 12
C_2	GF to1F	20 × 20	C_7	GF to 1F	26 × 26
	1F to 5F	16 × 16		1F to 3F	20 × 20
	5F to 7F	14 × 14		3F to 4F	18 × 18
	7F to RF	12 × 12		4F to RF	14 × 14
C_3	GF to 1F	18 × 18	C_8	GF to1F	20 × 20
	1F to 3F	16 × 16		1F to 4F	18 × 18
	3F to 7F	14 × 14		4F to 6F	16 × 16
	7F to TRF	12 × 12		6F to RF	14 × 14
C_4	GF to 4F	16 ×16	C_9	GF to 4F	18 × 18
	4F to 7F	14 × 14		4F to 6F	16 × 16
	7F to RF	12 × 12		6F to RF	14 × 14
C_5	GF to 7F	14 × 14	C_{10}	GF to 5F	16 × 16
	7Fto TRF	12 × 12		5F to RF	14 × 14

III. Table Stability Checking for Fixed Base Building

Checking	Fixed Base Building		Limit
	X direction	Y direction	
Stroey Drift	1.378	1.464	< 2.88
Sliding	3.2	3.05	> 1.5
Overturning moment	9.24	6.12	> 1.5
Torsional Irregularity	1.19	1.02	< 1.2
P-Δ Effect	0.0041	0.0051	< 0.1

According to Table III, structural stability checks are within allowable limits. Therefore, the structure is stable in dynamic condition.

IV. Test Result for Recycle Rubber

The recycle rubbers are used as major components of lead rubber bearings. The benefits of using recycled rubber isolators include ease of handling, simple shear stiffness adjustments, by changing its number of rubber layers and being eco-friendly compare to other commercially available base isolators. To know the properties of the scrap tyre rubber, the required experimental tests are performed in Rubber Research Development Centre at Yangon. The type of recycle rubber is bridge stone (Japan) rubber. In the calculation of shear modulus of recycle rubber, the poison ratio for recycle rubber is used 0.5 as natural rubber. The properties of recycle rubber are shown in Table IV.

IV. Table The Properties of Recycle Rubber

Hardness IRHD	Young's Modulus E (kip/ft^2)	Shear Modulus G (kip/ft^2)	Elongation at Break (%)
60	91.896	30.632	385

VI. Classifications of Isolator Group

The reaction values of gravity load from the analysis are divided into four groups. In this study, lead core rubber bearing (LRB) is used as isolation device with the range of reactions and these are shown in Table V. The maximum support reaction of each group is used to design the base isolator. The isolator dimension and analysis properties are calculated according to IBC-2000. The isolation system is installed at the base of each column between superstructure and plinth beam of the proposed building. The location of the isolator is shown in Fig. 3.

V. Table Range of Reaction for Isolator Group

Isolator Group	Reaction Range (kips)	Symbols	No. of Isolators
1	96-160	●	33
2	161-190	▲	31
3	191-220	▼	33
4	221-278	★	13

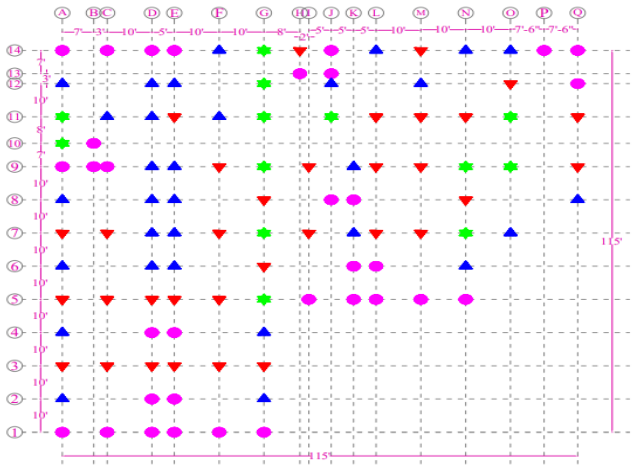

Fig. 3. Location of isolator.

VI. Table Dimension of Bearing

Group	Group 1	Group 2	Group 3	Group 4
d (in)	16	18	20	22
H (in)	29	26	24	23
t (in)	0.25	0.28	0.312	0.343
N (no)	64	57	52	47
Ns (no)	63	56	51	46
t_s (in)	0.249	0.136	0.114	0.111
d_p (in)	3.5	3.5	3.5	3.5

Where,

d = diameter of bearing (in)
H = total height of bearing (in)
t = thickness of individual layer (in)
N = number of rubber layers (nos)
Ns = number of steel plate (nos)
t_s = thickness of steel plate (in)
d_p = diameter of lead core (in)

VII. Table Analysis Properties of Bearing for Etabs Input Data

Group	Group1	Group 2	Group 3	Group 4
K_{eff} (kip/in)	2.242	2.663	3.083	3.882
K_e (kip/in)	15.379	18.262	21.147	26.625
K_v (kip/in)	2332.714	2952.34	3644.9	4410.29
F_y (kip)	8.826	10.48	12.135	15.279
ξ_{eff}	0.19	0.19	0.19	0.19

Where,

K_{eff} = Effective horizontal stiffness (kip/in)
K_e = Initial stiffness of bearing (kip/in)
K_v = Vertical stiffness of bearing layer (kip/in)
ξ_{eff} = Effective damping ratio

VIII. Stability Check for Dynamic Analysis of Isolated Base Building

After the dynamic analysis of isolated base building by using response spectrum method, the structural stability checkings are done according to ASCE 7-05. The results for stability checking of the proposed building are shown in Table VIII. The proposed buildings are satisfied within the limitation under the dynamic analysis.

VIII. Table Stability Checking for Isolated Base Building

Checking	Isolated Base Building		Limit
	X Direction	Y Direction	
Stroey Drift	1.04	1.17	< 2.88
Sliding	8.83	7.73	> 1.5
Overturning moment	29.416	27.936	> 1.5
Torsional Irregularity	0.983	1.011	< 1.2
P-Δ Effect	0.0079	0.0079	< 0.1

IX. Comparison of Structural Responses for Fixed Base and Isolated Base Buildings

The comparison of structural responses such as storey drift, storey shear, storey acceleration, storey stiffness and structural periods of X and Y direction for fixed base and isolated base buildings are graphically represented in figures 4 to 12.

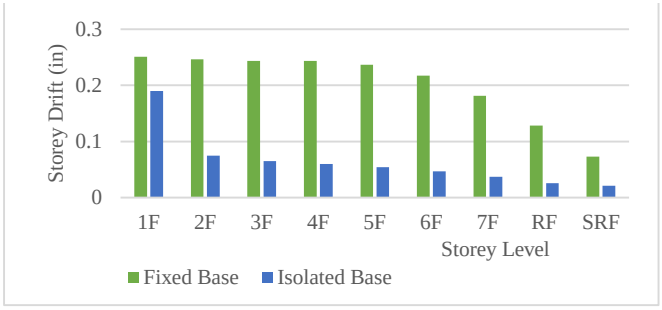

Fig. 4. Comparison of storey drift in X direction.

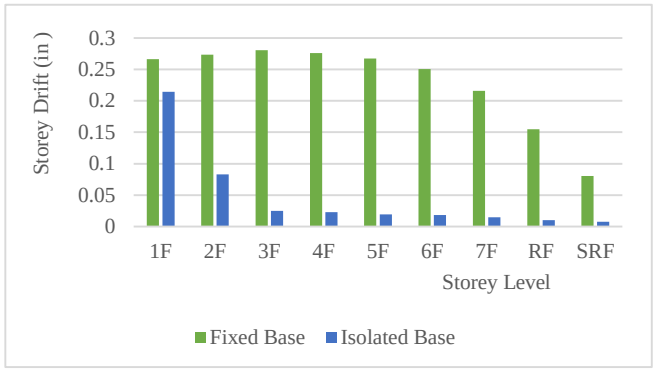

Fig.5. Comparison of storey drift in Y direction.

From Fig 4 and 5, the storey drift in isolated base building at the top floor is about 79.75% and 93.6% lower than that of the fixed base in X direction and Y direction.

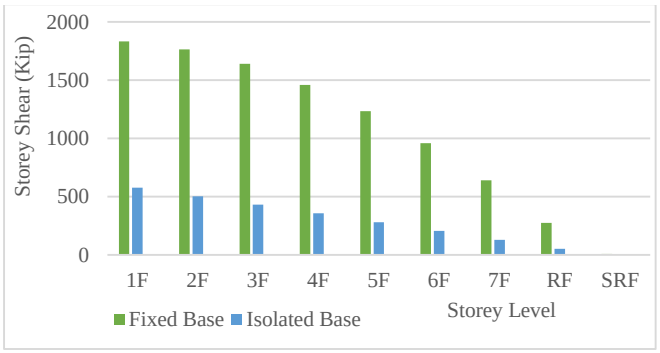

Fig.6. Comparison of storey shear in X direction.

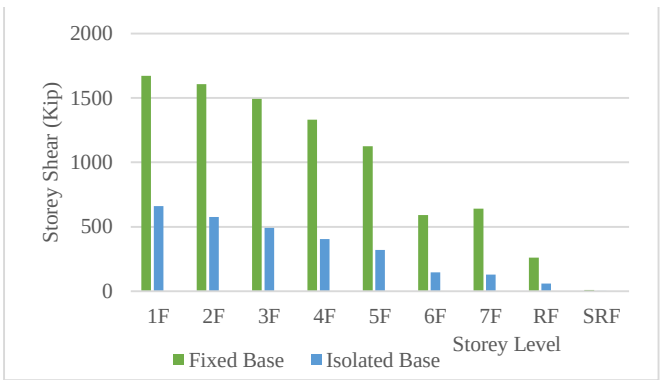

Fig.7. Comparison of storey shear in Y direction.

From Fig 6 and 7, the storey shear in isolated base building at the first floor is about 68.46% and 60.41% lower than that of the fixed base in X direction and Y direction.

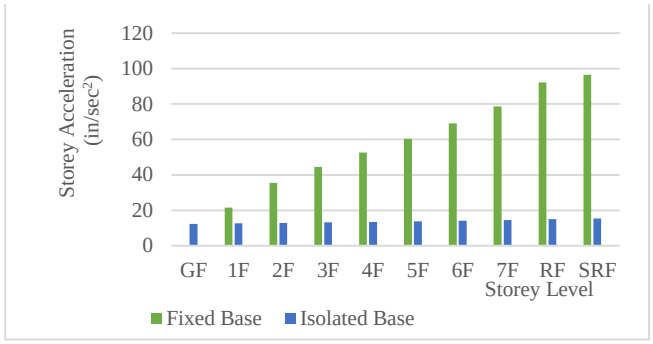

Fig.8. Comparison of storey acceleration in X direction.

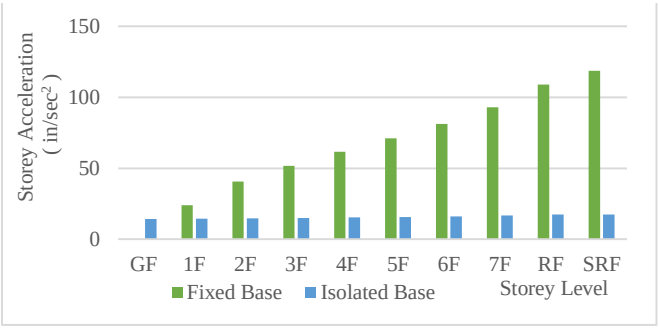

Fig.9. Comparison of storey acceleration in Y direction.

From Fig 8 and 9, the storey acceleration in isolated base building at the roof floor is about 83.68% and 84.08% lower than that of the fixed base in X direction and Y direction. The storey acceleration of fixed base building is zero at ground floor but appear at the isolated base building due to isolation system.

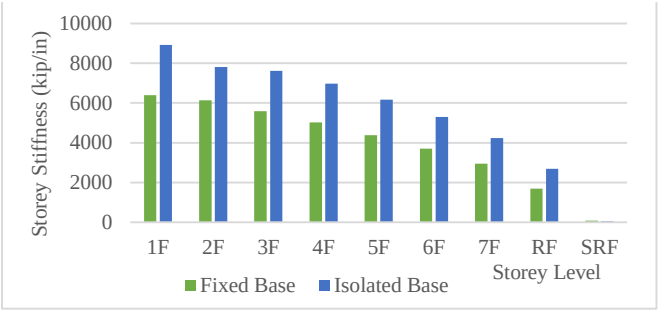

Fig.10. Comparison of storey stiffness in X direction.

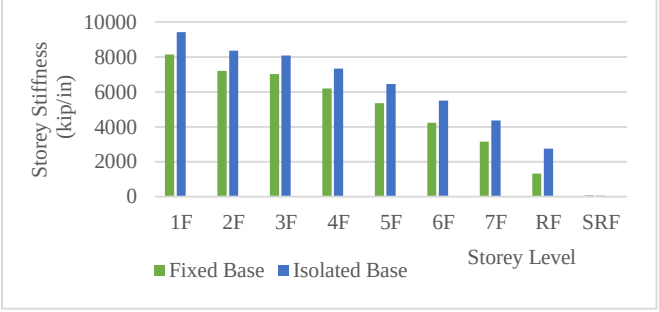

Fig.11. Comparison of storey stiffness in Y direction.

From Fig 10 and 11, the storey stiffness in isolated base building at the roof floor is about 52.15% and 37.24%

greater than that of the fixed base in X direction and Y direction respectively.

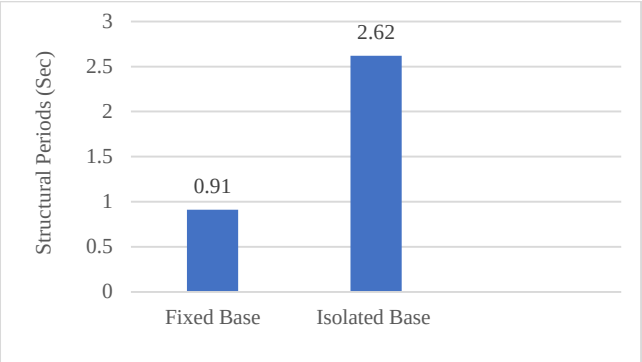

Fig.12. Comparison of structural periods for fixed base and isolated base buildings.

From this comparison, the structural period at isolated base building is increased about 2.5 times of fixed base building. The isolated base building has greater structural periods than the fixed base building. So isolated base building occurs more lengthen the period of the structure than fixed base building.

XI. Conclusions

The proposed building is eight-storeyed irregular shape R.C building. The type of occupancy is hotel and it is situated in Mandalay. Firstly, the proposed building is analyzed and designed for fixed base by response spectrum analysis. After this structural analysis is done, the stability of the superstructure is checked in accordance with ASCE 7-05. The unfactored gravity load from the analysis is used to design rubber bearing by the guide line of international building code IBC 2000. According to the range of loads, the isolators are divided into four groups. In this study, lead core rubber bearing (LRB) is used as isolation device. The response spectrum analysis was used to evaluate structural response of fixed base and isolated base such as storey drift, storey shear, storey acceleration, storey stiffness and structural period due to earthquake in X and Y direction. The following conclusions can be drawn after analyzing the results of eight storeys reinforced concrete building without and with isolation system.

(1) The storey drift, storey shear and storey acceleration of isolated building are significantly reduce than the fixed base building.
(2) The structural period of isolated base building is increases 65% than that of fixed base building.
(3) The storey stiffness of isolated base building is increased than that those of fixed base building.
(4) Therefore, lead rubber bearings with recycle rubber are found significantly effective in mitigating and preventing seismic responses of the proposed building.
(5) From the overall results of this study show that lead core rubber bearing (LRB) isolators with recycle rubber are suitable to use as affordable cost and have sufficient strength earthquake excitation.

Acknowledgment

The author would like to express her heartfelt gratitude to Dr. Su Yin Win, Acting-rector, Technological University (Mandalay), for her invaluable directions, managements and helps. The author is very grateful to Dr. Hnit Thit Shein, Pro-rector, Technological University (Mandalay), for her kind support and invaluable permission. The author is deeply indebted to Dr. Nwe Nwe Win, Professor and Head, Department of Civil Engineering, Technological University (Mandalay), for her suggestions, supervision and guidance throughout the preparation of this study. The author wishes to express especially appreciative to Daw San San Myint, Associate Professor, Department of Civil Engineering, Technological University (Mandalay), for her expert recommendations, comments and special interest to be perfect this study. The author heartfelt thanks to all her teachers from Department of Civil Engineering for their supports and encouragement.

References

[1] Robinson, W.H. "*Lead Rubber Hysteretic Bearings Suitable for Protecting Structure During Earthquakes, Earthquakes Energy Structural Dynamic"*, 10. (1982)593-604.
[2] Farzad Naeim and James M. Kelly. "*Design of Seismic Isolated Structures. From Theory to Practice"*, (1999).
[3] Illinois. "*international Building Code"*, International Code Council, IBC Country Club Hills, (2000).
[4] Ilkay URGU M. "*Design of Seismic Isolated Structure"* Middle East Technological University, (2006).
[5] American Society of Civil Engineers – Code 7: "*Minimum Design Loads for Buildings and Other Structures". (2005)*, 21 June (2011)
[6] American Concrete Institute (ACI) "*Building Code Requirements for Structural Concrete*," (ACI 318-14)".
[7] Myanmar Engineering Council. "*Myanmar National Building Code*", (2020).

Investigation on Factors Influencing to Motorcycle Accidents in Mandalay

May Sapae Phyoe[1], War War Myint[2]

[1]*Department of Civil Engineering, Technological University (Mandalay)*
[2]*Department of Civil Engineering, Technological University (Mandalay)*

Email: [1]mspp855@gmail.com, [2]wwmyint.mm@gmail.com

***Abstract*— Motorcycle accidents in Mandalay become a significant public safety concern due to the increasing reliance on motorbikes as the primary mode of transportation. This study aims to determine the factors that influence the severity of motorcycle crashes (slight, severe and fatal) by examining the variables, in which road geometries, collision types, human errors, and general characteristics. The qualitative method is used to find important predictors of accident severity. In this study, the road traffic crash records in Mandalay are obtained from the Mandalay Police Station between 2017 and 2019. The results show that drivers are more likely to increase in fatal injuries, and younger people are more likely to decrease severity injuries, especially in fatal outcomes. Age-specific safety programs should be developed to address the impact of age groups on accident severity. The environmental factors, such as time of day and weather, are also crucial. Promoting safe riding practices, enforcing speed limits, implementing traffic regulations, and addressing collision types like head-on, right-angle, and rear-end crashes can help reduce accident severity. Continuous monitoring and evaluation of implemented measures are crucial for ensuring their effectiveness and making necessary adjustments to enhance road safety standards.**

Keywords*— *factor affecting, motorcycle accidents, qualitative method, road traffic crashes , severity injuries

I. INTRODUCTION

Traffic accidents are a significant cause of human and economic losses in both developed and developing countries. The WHO predicts that road traffic accidents will become the 7th leading cause of death by 2030, with 1.25 million deaths and 20-50 million injuries annually [1].

In Myanmar, the number of road accident-related deaths has increased since 2013, with 1.2 million deaths and 50 million injuries annually[1]. Motorcycles are mostly used in upper region of Myanmar, especially in Mandalay. The number of motorcycles in Mandalay has been increasing year by year. By 2023, there are about 1,241,376 motorcycles registered in the city. Over the past five years, there has been a gradually increase the number of motorcycles, accounting from 1,135,099 in 2017 [2]. Increasing the number of motorcycles on the roads is one of the main reasons why there are more accidents happening in Mandalay. Motorcyclists may be the primary cause of accidents due to lack of crash protection, while regular car passengers are protected by belts, air bags, and covers [3].

Therefore, the injuries and fatalities of vehicle riders and passengers are increasing, and this becomes a major problem. It is important to prevent fatalities and injuries in Mandalay because the rate of death by vehicles accident is higher than by other rate of death. The analysis of motorcycle accidents is necessary and useful in several ways. The objective of this study is to provide the policy implication in reducing motorcycle accidents and the better understanding the factors that cause to motorcycle accidents.

II. METHODOLOGY

A. Data Collection and Description

The traffic crash records between 2017 and 2019 are collected from the Mandalay's Police Station. Microsoft Excel is used to identify the causes of motorcycle accidents, eliminate the irrelevant variables, and clean the data.

In this study, the dependent variables include the levels of accident severity, in which slight injury, severe injury, and fatality. Based on the previous studies [4, 5, 6], the independent variables are divided into five groups: general characteristics, human errors, road geometries, collision types and counterparts. The severity of an accident can be affected by a number of factors, including gender, age, time, day type, and seasonal effects. For instance, weather-related factors may increase the chance of accidents and younger riders may be more prone to risk-taking behavior. Table I describes the dependent and independent variables in this study.

I. DESCRIBES THE DEPENDENT AND INDEPENDENT VARIABLES IN THIS STUDY

Explanatory Variables	**Nature of Variables**
Accident severity ⊡ Slight injury ⊡ Severe injury ⊡ Fatality	Dependent
General characteristics ⊡ Gender ⊡ Age ⊡ Time ⊡ Day types ⊡ Seasonal effects (Summer, Winter and Rainy)	Independent
Human errors ⊡ Helmet use ⊡ Speedy ⊡ Careless driver ⊡ Against traffic flow ⊡ Other human errors	Independent
Road geometry ⊡ Straight ⊡ Curve ⊡ T Junction ⊡ X Junction(cross-junction)	Independent
Collision types ⊡ Head on ⊡ Rear end ⊡ Side swipe ⊡ Right angle ⊡ Other collision types	Independent
Counterparts ⊡ Motorcycle ⊡ Other vehicles ⊡ Fell alone ⊡ Bicycle ⊡ Fixed object ⊡ Pedestrian	Independent

B. Data Process

This study examines secondary data from accident reports in Mandalay. The data-collecting method involves accessing reported accidents, which are often in paper-based format, and then filtering and classifying the information in the Microsoft Excel for the purpose of analysis.

C. Data Analysis

This study uses the qualitative method to determine the factors that influence the severity of motorcycle accidents (slight, severe and fatal injury) by examining the variables, in which road geometries, collision types, human errors, and general characteristics. The results will enhance knowledge about motorcycle accidents and enable the formulation of focused interventions aimed at reducing their negative effects. Table II presents the proportion of contributing factors for each severity levels.

II. THE PROPORTION OF MOTORCYCLE ACCIDENTS WITH SEVERITY INJURIES FROM 2017 TO 2019

Explanatory Variables		Severity Level (%)			
		Slight	*Severe*	*Fatal*	*Total*
User	Driver	36	17	47	100
	Victim	21	51	28	100
Age of Driver	less 18	54	29	17	100
	between 18 and 40	37	14	49	100
	between 40 and 65	31	22	47	100
	above 65	0	25	75	100
Age of Victim	less 18	47	47	6	100
	between 18 and 40	24	52	24	100
	between 40 and 65	14	48	38	100
	above 65	0	67	33	100
Gender of Driver	Male	36	16	48	100
	Female	40	23	38	100
Gender of Victim	Male	21	50	29	100
	Female	21	53	26	100
Helmet Usage	Wearing	50	30	20	100
	Not Wearing	24	29	46	100
Human Errors	Speedy	21	21	58	100
	Careless Driver	42	38	20	100
	Against Traffic flow	20	25	55	100
	Other	46	38	15	100
Time	Day	33	33	34	100
	Night	29	27	45	100
Day Types	Weekday	29	32	40	100
	Weekend	36	23	41	100
Seasonal Effects	Winter	24	27	49	100
	Summer	32	29	38	100
	Rainy	34	31	35	100
Road Geometry	Straight	28	25	47	100
	Curve	22	25	53	100
	X Junction	38	38	24	100
	T Junction	31	50	19	100
Collision Types	Head On	21	28	50	100
	Right Angle	40	35	25	100
	Side Swip	38	25	38	100
	Rear End	35	23	42	100
	Other	43	14	43	100
Counterparts	With Motorcycle	45	37	18	100
	With Other Motor Vehicle	20	36	44	100
	Falling Alone	9	19	72	100
	With Fixed Object	8	14	78	100
	With Bicycle	50	20	30	100
	With Pedestrian	46	31	23	100

III. RESULTS AND DISCUSSIONS

A. General Characteristics

The general characteristics include significant background information about the users involved in the accident as well as the overall issue. A number of factors can influence the severity of an accident, including user, gender, age, time of day, type of day, and seasonal influences.

1) User: The motorcycle accident severity categorized by the role of users involved (driver or victim) is shown in Fig .1.

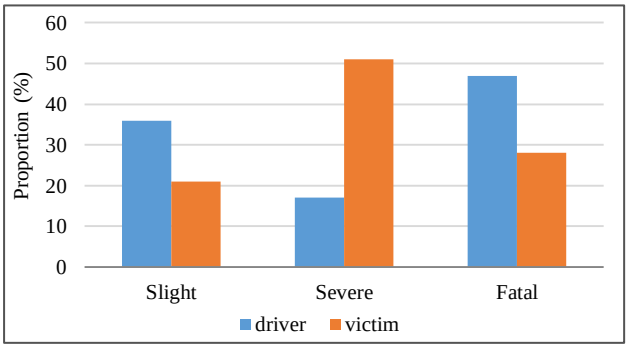

Fig. 1. The proportion of user categorized by injury severity.

In Fig .1, drivers showed a higher percentage of slight and fatal injuries compared to victims, while victims (pillion passengers including other side drivers) had a higher percentage of severe injuries compared to drivers. The results showed that drivers are more likely to increase in fatal injuries than victims. Drivers may be more likely to suffer fatal injuries since they are sitting in front of the motorcycle, which may fully hit the driver rather than the victims in the accident.

2) Age of Driver: The proportion of motorcycle accident severity by age interval among drivers is presented in Fig .2.

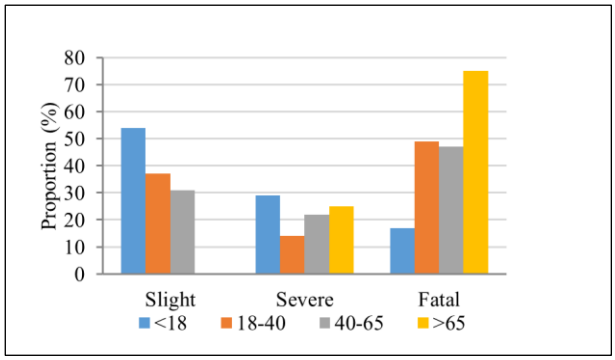

Fig. 2. The proportion of driver age intervals categorized by injury severity.

The Fig. 2 showed that drivers under 18 years old and the age group of 18 to 40 displayed a higher percentage of slight injuries, indicating a lower risk of severe and fatal injuries. On the other hand, drivers over 65 years old experienced an increase in fatality rate compared to others, showing the vulnerability of older drivers to fatal outcomes despite a lower percentage of slight injuries. Therefore, the data indicate that the younger people are more likely to decrease the severity injuries especially in fatal outcomes, compared to older age.

3) Age of Victim: The proportion of motorcycle accident severity by age interval among victims is shown in Fig. 3.

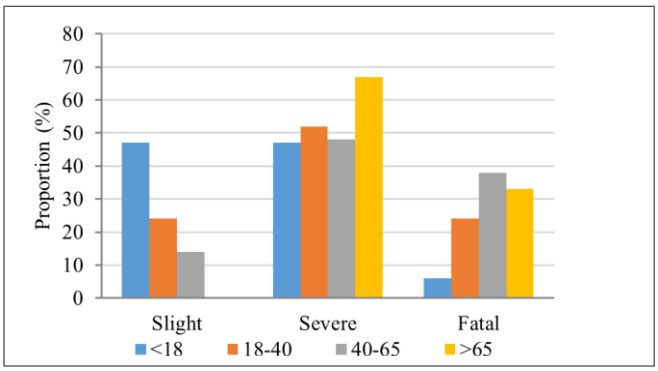

Fig. 3. The proportion of victim age intervals categorized by injury severity.

According to Fig. 3, victims under 18 years old displayed a lower severe and higher slight injuries, indicating a moderate risk of injuries, as well as age above 65 years old experienced in higher serve injuries. Moreover, victims aged 18 to 40 showed a higher percentage of severe injuries, suggesting a high risk of injuries compared to slight injuries. Similar trend with the drivers, the data indicate that the younger people are more likely to decrease the severity injuries especially in fatal outcomes, compared to older age.

4) *Gender of Driver*: The proportion of motorcycle accident severity by gender among drivers is shown in Fig. 4.

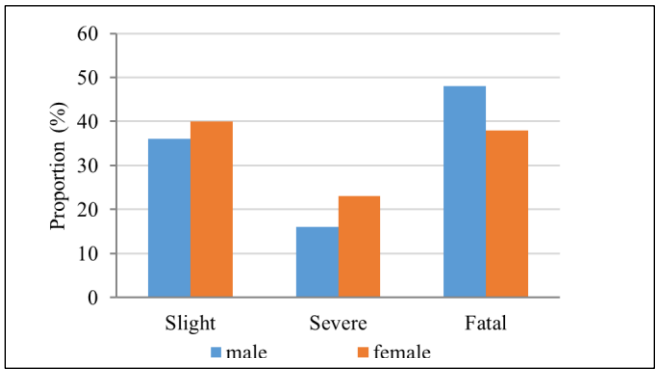

Fig. 4. The proportion of gender of driver categorized by injury severity.

According to Fig. 4, female drivers showed a higher percentage of slight and severe injuries. However, male drivers faced a higher fatality rate than female drivers. This means that male drivers are more likely to increase the risk of fatal outcomes compared to females.

5) *Gender of Victim:* The proportion of motorcycle accident severity by gender among victims is illustrated in Fig. 5.

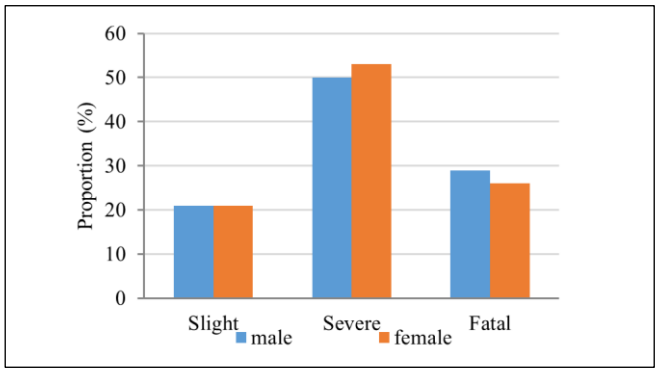

Fig. 5. The proportion of gender of victim categorized by injury severity.

According to Fig. 5, the severity injuries of victim (pillion passengers including other side drivers) occurred similar percentages of severity injuries between male and female victims, however, notable increased emerge in severe outcomes for both male and female victims. These findings suggest gender-specific factors influencing injury severity, indicating the importance of targeted measures to address vulnerabilities and mitigate risks effectively for both male and female victims.

6) *Time:* The proportion of time categorized by injury severity is presented in Fig. 6.

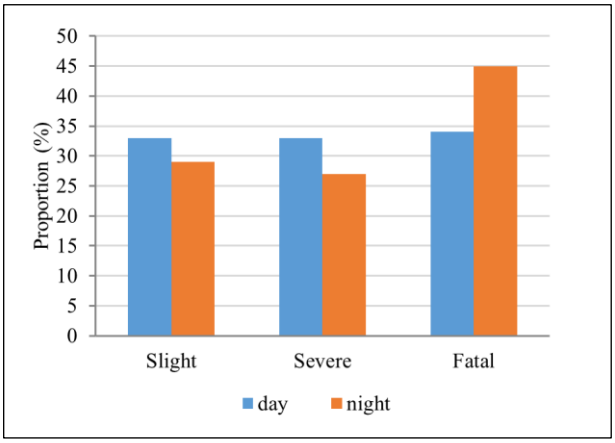

Fig. 6. The proportion of time categorized by injury severity.

The Fig. 6, illustrated that the percentage of motorcycle accident severity, categorized by the time of day (day and night). Day time accidents found a relatively balanced distribution across severity levels, with slight, severe, and fatal injuries. This suggests a more uniform risk distribution throughout the day. On the other hand, night time accidents showed a higher fatality rate, indicating a significant risk of fatality compared to slight injuries. Moreover, fatal injuries were more experienced at night, suggesting an increased risk of critical harm during night time hours.

7) *Day Type:* The proportion of day types categorized by injury severity is shown in Fig. 7.

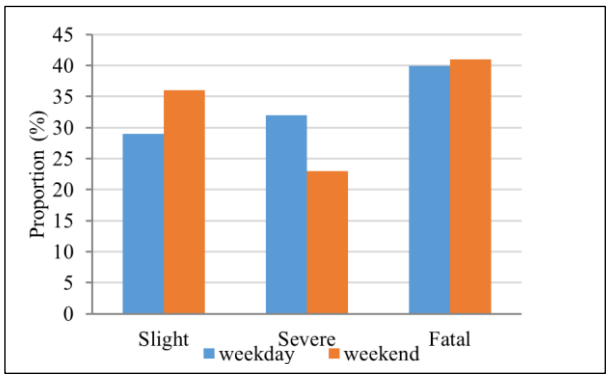

Fig. 7. The proportion of day types categorized by injury severity.

According to Fig. 7, weekends showed a higher percentage of fatal injuries, indicating a greater likelihood of critical harm compared to weekdays. Interestingly, both weekdays and weekends show similar rate for fatal injuries, indicating that the accidents are not highly depended on the day of the week. However, weekdays displayed a higher percentage of severe injuries, suggesting a relatively higher risk of severity injuries compared to weekends. The results indicate that the days of the week are not significantly difference in fatal outcomes of this study.

8) Seasonal Effects: The proportion of seasonal accidents categorized by injury severity is illustrated in Fig. 8.

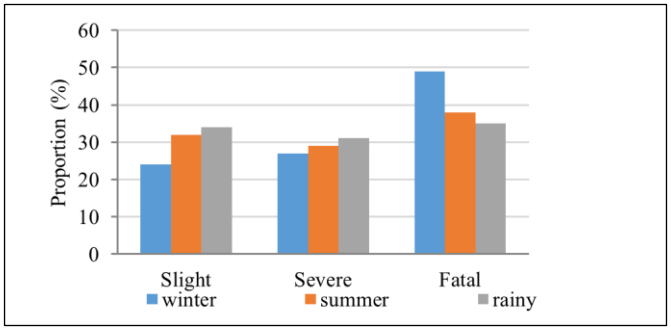

Fig. 8. The proportion of seasonal accidents categorized by injury severity.

In Fig. 8, winter months showed a higher fatality rate, suggesting an increased risk of fatal outcomes despite a comparable percentage of slight injuries. Meanwhile, summer months displayed a higher fatality rate, indicating a significant risk of fatality compared to slight injuries. Hence, rainy seasons presented an interesting contrast, with a lower fatality rate and a higher percentage of slight injuries, indicating a lower risk of severe harm despite adverse weather conditions. The findings show that winter months are more likely to increase fatal injuries compared to other.

B. Human Errors

Human errors, like speeding or impaired riding, helmet usage heighten the severity of motorcycle accidents. The proportion of motorcycle accident severity categorized by helmet usage (wearing or not wearing) is presented in Fig. 9.

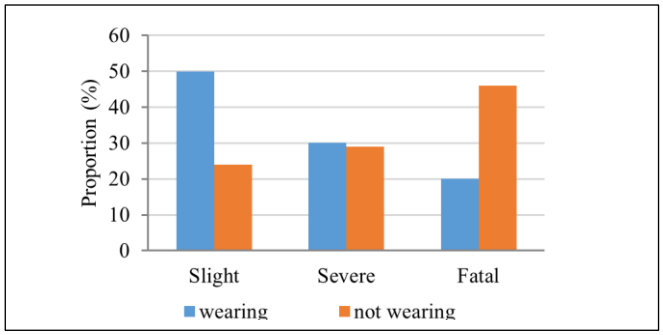

Fig. 9. The proportion of helmet use categorized by injury severity.

According to Fig. 9, users wearing helmets occurred a higher percentage of slight injuries, indicating a reduced risk of severe injuries compared to those not wearing helmets. On the other hand, users not wearing helmets faced a notably higher fatality rate, showing the critical role of helmets play in reducing the risk of fatality in accidents. These findings emphasize the importance of helmet use in preventing severe injuries and saving lives. Additionally, the proportion of human errors categorized by injury severity is shown in Fig. 10.

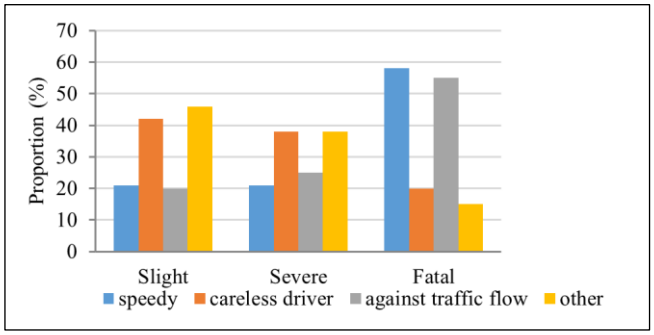

Fig 10. The proportion of human errors categorized by injury severity.

The Fig. 10, showed that speeding drivers exhibited a high fatality rate, indicating a significant risk of fatality compared to slight injuries. Conversely, careless drivers and "other" types of human errors had a higher percentage of severe injuries, suggesting a greater likelihood of critical harm resulting from their behavior. Similarly, drivers going against traffic flow experienced a high fatality rate. These findings show the critical role of addressing human errors and promoting safer driving practices to mitigate injury severity and save lives.

C. Road Geometries

Proper road planning and maintenance are essential for reducing the severity of motorcycle accidents. For instance, curve, X junction, and T junction heighten the risk of crashes. The proportion of road geometry categories by injury severity is illustrated in Fig. 11.

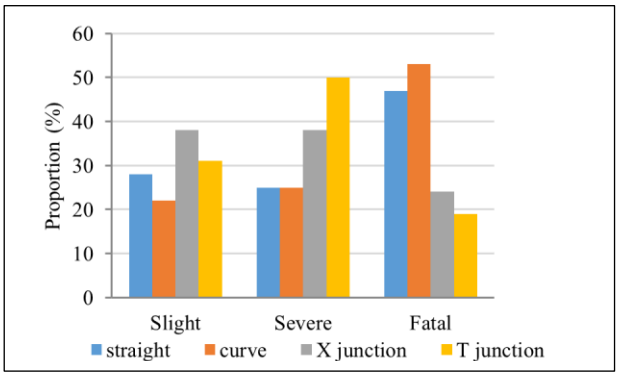

Fig. 11. The proportion of road geometry categories by injury severity

According to Fig. 11, straight and curve road showed a higher fatality rate, indicating a significant risk of fatality compared to slight injuries. However, X junction and T junction had notably decrease in the fatal injuries compared to slight injuries, indicating the lower risks. Moreover, X junctions and T junctions experienced with a higher percentage of severe injuries, indicating a heightened risk of critical harm compared to other types of intersections. These findings show the importance of considering road geometry in designing safer infrastructure and implementing measures to reduce injury severity and enhance road safety.

D. Collision Types

Motorcycle collision types have a major impact on how seriously people are injured. To effectively implement targeted safety measures like better road design, traffic management strategies, and rider education programs, it is essential to understand the dynamics of various collision types. The proportion of collision types categorized by injury severity is shown in Fig. 12.

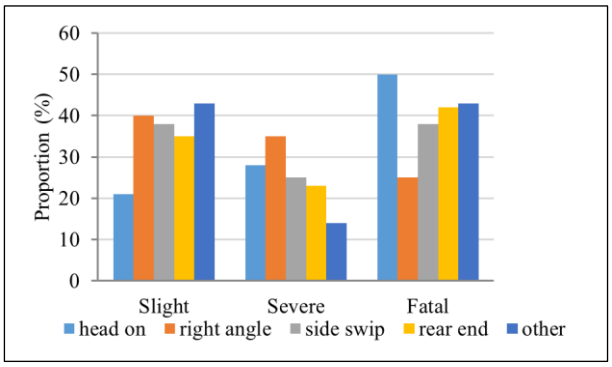

Fig. 12. The proportion of collision types categorized by injury severity.

The Fig. 12, illustrated that head-on collisions showed a remarkably high fatality rate, indicating a substantial risk of fatality compared to slight injuries. Right-angle collisions demonstrated a different pattern, with a lower percentage of fatal injuries, suggesting a relatively lower risk of fatal injuries. Side-swipe accidents presented an interesting scenario, with a comparable distribution of slight injuries and fatalities, indicating a significant risk of fatal outcomes.

Moreover, rear-end collisions displayed a similar trend, with a high fatality rate, despite a slightly lower percentage of head on injuries. Other collision types exhibited a notably high fatality rate but had a higher proportion of slight injuries, indicating a reduced risk of fatality but also significant reduced for severe injuries. The findings indicate that head-on collisions are significantly increased in the severity level, with the fatality rate jumping highest levels in this study. Moreover, the fatality rates across most types of accidents, except for side-swip collisions which still low the fatal type of accident, highly increased compared to other.

E. Counterparts

Understanding motorcycle accident severity requires analyzing causes, or incidents by way of occurrences. These consist of crashes involving a single vehicle, collisions with other vehicles, and collisions with fixed objects. For motorcycle riders, each opponent poses a different risk of injury. Accidents with one vehicle, which are frequently brought on by variables like losing control or unsafe driving, may cause serious injuries from crashes with objects or the ground. There are additional risks associated with collisions with other vehicles, such as the possibility of multiple impacts and further injuries. It may reduce the severity of motorcycle accident injuries by implementing targeted measures and identifying common patterns by researching their relationships. Fig. 13 shows the proportion of the manner of motorcycle accidents occurrence categorized by injury severity.

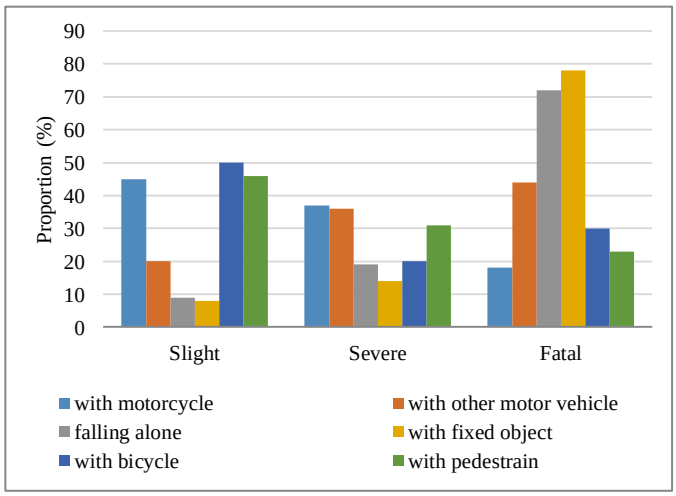

Fig. 13. The proportion of the manner of motorcycle accidents occurrence categorized by injury severity.

According to Fig. 13, accidents with motorcycles showed a relatively low of fatal injuries, while accidents with bicycle experienced with higher percentage of slight and severe injuries. Interestingly, falling alone results in lower slight injuries, with a remarkably high fatality rate, suggesting a high vulnerability to fatal outcomes in such incidents. Accidents experienced with fixed objects also display a higher level of fatality rate compared to other type of occurrences, indicating a substantial risk of fatal outcomes despite a lower percentage of severe injuries.

These results demonstrate how accident severity changes over time and emphasize the value of focused measures to reduce risks and improve safety for all users of the road. Moreover, accidents with fixed objects and falling alone had notably impacted the fatal injuries compared to other types of accidents in this study.

IV. Conclusion

The study investigates the factors that influence the severity of motorcycle accidents in Mandalay City. The qualitative method is used to find out the important predictors of accident severity. In this study, the traffic crash records between 2017 and 2019 are analysed.

The results showed that drivers are more likely to increase in fatal injuries than other users. For both driver and victims, the older people are more likely to increase in fatal outcomes compared to younger age groups. In addition to time of the day and environmental factors are also crucial. Additionally, driving with high speed and driving against traffic flow play a significant role in motorcycle accident severity in this study. The collision types, such as head-on, right-angle, and rear-end crashes, also cause a higher risk of fatalities. Hence, accidents with fixed objects showed a highest percentage of fatality injuries compared to other type of occurrences in this study.

In conclusion, this study highlights the importance of considering various factors in determining the severity of motorcycle accidents in Mandalay City. By addressing these factors, the severity of motorcycle accidents might be reduced by promoting safer driving practices.

Acknowledgment

The author is deeply gratitude to Dr. Nwe Nwe Win, Professor and Head, Department of Civil Engineering, for her guidance and advice. The author would like to express grateful thanks to her supervisor Dr. War War Myint, Professor, Department of Civil Engineering and to all her teachers from Civil Department, Technological University (Mandalay). The author's special thanks are sent to her parents for their guidance from childhood till now.

References

[1] World Health Organization, "World Health Organization. 2015. 'Global Status Report on Road Safety,'" *Injury prevention*, 2015.

[2] Road Transport Administration Department (RTAD), "Number of registered vechicles in Mandalay City from 2017 to 2023.," 2023.

[3] M. Abdel-Aty, "Analysis of driver injury severity levels at multiple locations using ordered probit models," *J Safety Res*, vol. 34, no. 5, pp. 597–603, 2003, doi: 10.1016/j.jsr.2003.05.009.

[4] N. Wady Aung and N. Tun, "Analysis of Factors Affecting Motorcyclists' Crash Severity in Mandalay City," 2017.

[5] S. M. Rifaat, R. Tay, and A. De Barros, "Severity of motorcycle crashes in Calgary," *Accid Anal Prev*, vol. 49, pp. 44–49, Nov. 2012, doi: 10.1016/j.aap.2011.02.025.

[6] S. Baral and K. Kanitpong, "Factors Affecting the Severity of Motorcycles Accidents and Casualties in Thailand by Using Probit and Logit Model," 2015.

Prediction of Basic Design Wind Speed and Development of Preliminary Wind Distribution Map for Magway Region

Moe Thandar Aye[1], San San Myint[2]

[1]*Department of Civil Engineering, Technological University (Mandalay)*

[2]*Department of Civil Engineering, Technological University (Mandalay)*

Email: [1]moethandaraye1992@gmail.com, [2]sansanmyint.mit73@gmail.com

***Abstract*—This paper illustrates to predict the basic wind speed and develop the preliminary wind distribution maps for Magway Region. In this study, the design wind speed is estimated for Magway, Minbu, Chauk, Aunglan, Pakkoku, Sinphyukyun, Taungdwingyi, Gangaw and Pauk by using the annual maximum hourly wind speed data for the period (2003 to 2022) from the Department of Meteorology and Hydrology of Magway Region. These recorded wind speed data is converted to ten minutes gust wind speed and three seconds gust wind speed at standard reference height of ten meters (33 ft). The gust wind for the study area is computed using Gust factor and ESDU methods (according to WMO guidelines) and Statistical Approach. Extreme wind speeds are estimated by using Type I extreme value Gumbel distribution. Gumbel distribution parameters are estimated with five methods such as MOM, MLM, MLS, OSA and PWM by using Python program. And then Anderson-Darling (AD), Kolmogorov-Smirnov (KS), Chi-square tests and diagnostic test involving Root Mean Square Error (RMSE) are used to diagnosed which methods is fitted for each study station. The fittest parameter estimation method for Gumbel distribution is used to evaluate design wind speeds for different return periods. The estimated extreme wind speed (W_T) + (SE) values are proposed as basic design wind speed for design purposes of the structures in Magway Region by using the Python Programming. After that, the results obtained from study stations for each returned period are used to develop basic design wind speed maps of Magway Region. The wind map is produced by using ArcMap in ArcGIS program (ARCGIS 10.6.1).**

***Keywords*—Basic Design Wind Speed, Wind Map, Gumbel Distribution, Python Program, ARCGIS Software**

I. Introduction

Wind speed is an atmospheric variable affected by several factors, such as geometric shapes, roughness, and ground surface elevations. For structural design, the wind speed can be converted into wind load that is simply considered as one of the lateral loadings [3]. In the field of structural engineering, it includes strong winds, which may cause discomfort, as well as extreme winds, such as in a tornado, hurricane or heavy storm, which may cause widespread destruction. With the structures becoming tall and slender, the effect of wind on these structures is becoming critical. The design wind speed serves the primary purposes of choosing the appropriate basic wind speed for the design of buildings and structures. Assessment of wind speed in a region can expediently be carried out by probabilistic modeling of historic Wind Speed Data (WSD) using an appropriate extreme value distribution. The distribution of wind speed is important in determining serviceability of buildings [2]. Typically, the design service life of building is round 50 years or more. ArcGIS is the tool that satisfies the need to finish the contour map, because of the ability to calculate and interpolate the data all over the entire map. ArcGIS from ESRI (Environmental System Research Institute) is used to issue the output as a map. Engineers can use GIS to collect and evaluate geographic data. Digital geographic maps can then be used to showcase the data in layered visuals. It overlays on top of geographic maps, allowing engineers and others to make more educated decisions. In analysis maps, historical data, future growth plans, industrial concerns, and other data can be merged. It can also help in predicting natural disasters.

II. Methodology

A. Wind Speed Calculations for Converting Ten Meters (33 ft) Height

In this study, the design wind speed is estimated for Magway, Minbu, Chauk, Aunglan, Pakkoku, Sinphyukyun, Taungdwingyi, Gangaw and Pauk in Magway Region. The annual maximum hourly wind speed data recorded for the period 2003 to 2022 is used to derive the series of ten minutes gust wind speed and three seconds gust wind speed using WMO guideline; and to estimate the extreme wind speed for different return periods adopting Gumbel distribution (using MOM, MLM, MLS, OSA and PWM). These recorded data are converted to ten minutes and three seconds gust wind speeds at hub height to standard reference height of ten meters (33ft) by considering roughness length for open terrain shown in Tables I to III.

Table I. Converted Annual Maximum Ten Minutes Gust Wind Speeds at Standard Height for All Stations (From Period 2003 To 2019)

Year	Maximum Ten Minutes Gust Wind Speed at Standard Height (m/s)								
	Magway	Minbu	Chauk	Aunglan	Pakokku	Sinphyu-kyun	Taung dwingyi	Gangaw	Pauk
2003	19.7	2.4	4.0	2.4	11.7	1.9	3.1	2.3	6.3
2004	22.9	2.4	5.6	2.3	7.9	2.5	3.1	3.1	2.3
2005	19.7	3.1	4.0	2.3	11.7	2.5	4.0	3.1	4.0
2006	16.4	2.3	8.7	4.7	7.9	2.5	2.3	3.1	4.1
2007	22.9	2.3	3.1	5.6	11.7	2.5	2.3	3.1	4.7
2008	13.1	3.1	4.0	3.1	7.9	2.3	2.3	6.3	4.0
2009	13.1	2.3	4.0	3.1	11.7	3.2	3.1	2.3	4.0
2010	16.4	2.3	4.7	5.6	19.7	2.6	2.3	5.3	4.0
2011	16.4	3.1	4.4	5.6	23.6	3.2	15.6	4.0	4.0
2012	15.1	3.1	5.9	4.0	11.7	3.4	23.6	2.6	3.1
2013	10.6	3.1	14.4	5.6	11.7	3.5	19.7	6.6	6.3
2014	15.7	5.3	7.0	3.3	6.3	3.1	19.7	5.9	7.0
2015	10.6	5.7	7.0	29	7.0	3.7	5.7	6.6	4.7
2016	6.3	8.5	5.6	31	9.1	3.7	11.7	3.2	4.7
2017	4.7	19.7	6.3	8.8	4.0	3.1	13.6	6.5	7.0
2018	5.6	8.5	6.5	9.4	4.0	3.2	25.7	4.3	11.7
2019	4.0	5.6	5.1	16.3	4.5	5.6	12.6	4.3	4.0

Table II. CONVERTED ANNUAL MAXIMUM TEN MINUTES GUST WIND SPEEDS AT STANDARD HEIGHT FOR ALL STATIONS (FROM PERIOD 2020 TO 2022)

2020	13.3	5.1	3.1	13.2	5.6	3.2	12.2	4.1	2.3
2021	4.0	5.1	3.1	5.1	1.6	2.8	5.3	4.4	2.3
2022	3.1	6.5	3.1	5.1	3.2	4.3	10.3	3.2	4.0

Table III. CONVERTED ANNUAL MAXIMUM THREE SECONDS GUST WIND SPEEDS AT STANDARD HEIGHT FOR ALL STATIONS

Year	Maximum Three Seconds Gust Wind Speed at Standard Height (m/s)								
	Magway	Minbu	Chauk	Aunglan	Pakokku	Sinphyu kyun	Taung dwingyi	Gangaw	Pauk
2003	28.3	3.4	5.7	3.4	16.9	2.7	4.4	3.4	9.1
2004	33.0	3.4	8.0	3.4	11.4	3.6	4.4	4.4	3.4
2005	28.3	4.4	5.7	3.4	16.9	3.6	5.7	4.4	5.7
2006	23.7	3.4	12.5	6.8	11.4	3.6	3.4	4.4	5.9
2007	33.0	3.4	4.4	8.0	16.9	3.6	3.4	4.4	6.8
2008	18.8	4.4	5.7	4.4	11.4	3.4	3.4	9.1	5.7
2009	19.0	3.4	5.7	4.4	16.9	4.7	4.4	3.4	5.7
2010	23.7	3.4	6.8	8.0	28.3	3.8	3.4	7.6	5.7
2011	23.7	4.4	6.3	8.0	34.0	4.7	22.6	5.7	5.7
2012	21.8	4.4	8.4	5.7	16.9	4.9	34.0	3.8	4.4
2013	15.2	4.4	20.7	8.0	16.9	5.1	28.3	9.5	9.1
2014	22.6	7.6	10.1	4.7	9.1	4.4	28.3	8.5	10.1
2015	15.2	15.2	8.4	41.8	10.3	5.3	22.6	9.5	6.8
2016	9.1	9.1	12.3	44.6	13.3	5.3	16.9	4.7	6.8
2017	6.7	28.3	9.1	12.7	5.7	4.4	19.7	9.3	10.1
2018	8.0	12.3	9.3	13.5	5.7	4.7	37.0	6.1	16.9
2019	5.7	8.0	7.4	23.5	6.6	8.0	18.2	6.1	5.7
2020	19.2	7.4	4.4	19.0	8.0	4.7	17.5	5.9	3.4
2021	5.7	7.4	4.4	7.4	2.3	4.0	7.6	6.3	3.4
2022	4.4	9.3	4.4	7.4	4.7	6.1	14.8	4.7	5.7

B. Analysis Based on GoF Test

For the assessment on checking the adequacy of the selected parameter's estimation methods of Gumbel distribution to the recorded wind speed data, GoF test statistics of Anderson-Darling (AD) test, Kolmogorov Smirnov (KS) test and Chi-Square test are used. The test statistics values are computed using equations (1), (2) and (3) by Python Program and given in Tables IV to IX. In this study, 95% confidence level is considered for all statistics tests [2].

$$AD = (-N) - \frac{1}{N}\sum_{i=1}^{N}\left\{(2i-1)\ln\left(Z_{(i)}\right) + (2N+1-2i)\ln\left(1-Z_{(i)}\right)\right\} \quad (1)$$

$$KS = \max_{i=1}^{N}\left(F_e\left(W_i\right) - F_D\left(W_i\right)\right) \quad (2)$$

where, $Z_{(i)} = F(W_i)$, for i = 1,2,3,…..,N and $W_1<W_2<\ldots<W_N$. F is the cumulative distribution function (CDF) of the specified distribution. W_i are the ordered data. where, $F_e\left(W_i\right) = \frac{i-0.44}{N+0.12}$ is the empirical CDF of W_i. If the computed values of GoF tests statistics given by the method are less than that of theoretical values at the desired significance level, then the method is accepted to be adequate for determination of parameters of Gumbel distribution for modeling wind speed data [2].

$$\chi^2 = \sum\frac{\left(O_i - E_i\right)^2}{E_i} \quad (3)$$

where, $E_i = n \times \Delta P_i$

P_i = probability interval

ΔP_i = the value of difference between probability interval

O_i = number of frequency

Table IV. COMPUTED PROGRAM RESULTS OF AD TEST STASTICS FOR TEN MINUTES GUST WIND SPEED

Region	Test Statistics of AD for Ten Minutes Gust Wind Speed				
	MOM	MLM	MLS	OSA	PWM
Magway	1.154	1.254	0.792	**4.366**	0.868
Minbu	1.472	1.349	1.845	**3.613**	1.283
Chauk	0.577	0.585	0.791	**5.813**	0.486
Aunglan	1.652	1.782	1.878	2.289	1.614
Pakokku	0.361	1.479	0.399	**3.769**	0.365
Sinphyukyun	0.391	1.666	0.454	**7.691**	0.383
Taungdwingyi	1.124	0.902	0.858	**3.174**	0.938
Gangaw	1.332	1.327	**3.786**	**6.833**	1.477
Pauk	**4.225**	**4.875**	**4.420**	**7.310**	**4.358**

Table V. COMPUTED PROGRAM RESULTS OF AD TEST STASTICS FOR THREE SECONDS GUST WIND SPEED

Region	Test Statistics of AD for Three Seconds Gust Wind Speed				
	MOM	MLM	MLS	OSA	PWM
Magway	1.162	1.333	0.790	**4.364**	0.872
Minbu	1.475	1.411	1.845	**3.613**	1.280
Chauk	0.577	0.785	0.79	**5.813**	0.488
Aunglan	1.652	1.835	1.878	2.289	1.614
Pakokku	0.361	1.703	0.399	**3.770**	0.365
Sinphyukyun	0.384	0.496	0.439	**7.719**	0.379
Taungdwingyi	1.173	1.047	0.944	**3.371**	1.057
Gangaw	0.611	**12.003**	0.507	**6.582**	0.542
Pauk	0.814	1.23	0.958	**6.048**	0.786

From Tables IV and V, it can be seen that the computed values of AD statistics results given for four estimator methods except OSA of Gumbel distribution are less than the theoretical values ($AD_{0.05}$ = 2.492, n >10) for all stations except Pauk and Gangaw both in ten minutes and three seconds gust wind speeds. All estimator methods for Pauk station, and MLS and OSA estimator methods for Gangaw station are not fitted to be adequate for determination of parameters of Gumbel distribution for modeling ten minutes gust wind speed and also MLM for Gangaw station is not fitted for determination of parameters of Gumbel distribution for three seconds gust wind speed.

Table VI. COMPUTED PROGRAM RESULTS OF KS TEST STASTICS FOR TEN MINUTES GUST WIND SPEED

Region	Test Statistics of KS for Ten Minutes Gust Wind Speed				
	MOM	MLM	MLS	OSA	PWM
Magway	0.143	0.195	0.114	0.125	0.123
Minbu	0.169	0.25	0.142	0.086	0.223
Chauk	0.101	0.121	0.122	0.118	0.097
Aunglan	0.248	0.301	0.235	0.147	0.278
Pakokku	0.135	0.290	0.150	0.128	0.140
Sinphyukyun	0.087	0.081	0.104	0.153	0.088
Taungdwingyi	0.180	0.168	0.158	0.051	0.171
Gangaw	**0.381**	**0.390**	**0.470**	0.244	**0.426**
Pauk	**0.772**	**0.799**	**0.556**	**0.336**	**0.771**

Table VII. COMPUTED PROGRAM RESULTS OF KS TEST STASTICS FOR THREE SECONDS GUST WIND SPEED

Region	Test Statistics of KS for Three Seconds Gust Wind Speed				
	MOM	MLM	MLS	OSA	PWM
Magway	0.144	0.202	0.114	0.125	0.123
Minbu	0.169	0.249	0.142	0.086	0.223
Chauk	0.101	0.138	0.122	0.118	0.097
Aunglan	0.248	**0.304**	0.235	0.147	0.278
Pakokku	0.135	**0.305**	0.150	0.128	0.140
Sinphyukyun	0.087	0.089	0.107	0.153	0.092
Taungdwingyi	0.181	0.17	0.153	0.07	0.172
Gangaw	0.158	**0.646**	0.137	0.161	0.149
Pauk	0.159	0.231	0.165	0.124	0.166

From Tables VI and VlI, the computed values of KS test statistic given by all five methods are less than the critical

values ($KS_{0.05,20}$ = 0.301) for all stations at the confidence level of 95% in both ten minutes and three seconds gust wind speed. KS test statistic in all estimator methods for Pauk and in Gangaw except OSA are greater than that of theoretical values at the desired significance level in ten minutes gust wind speed. In Aunglan, Pakokku and Gangaw stations MLM don't fit for determination of parameters of Gumbel distribution in three seconds gust wind speed.

Table VIII. COMPUTED PROGRAM RESULTS OF CHI-SQUARE TEST STASTICS FOR TEN MINUTES GUST WIND SPEED

Region	Test Statistics of Chi-square for Ten Minutes Gust Wind Speed				
	MOM	**MLM**	**MLS**	**OSA**	**PWM**
Magway	**9.547**	**17.181**	**10.58**	**20.675**	**10.296**
Minbu	5.989	4.484	7.085	7.55	4.955
Chauk	3.922	3.592	4.368	8.914	3.6
Aunglan	**12.397**	**10.412**	**14.332**	**12.041**	**10.763**
Pakokku	8.11	**13.018**	8.782	**14.23**	8.133
Sinphyukyun	1.198	0.793	1.303	5.294	1.179
Taungdwingyi	**11.622**	**14.984**	**13.082**	**17.406**	**12.582**
Gangaw	2.207	2.285	1.820	7.183	2.943
Pauk	3.244	3.205	6.896	7.68	3.471

Table IX. COMPUTED PROGRAM RESULTS OF CHI-SQUARE TEST STASTICS FOR THREE SECONDS GUST WIND SPEED

Region	Test Statistics of Chi-square for Three Seconds Gust Wind Speed				
	MOM	**MLM**	**MLS**	**OSA**	**PWM**
Magway	**13.763**	**25.339**	**15.254**	**29.796**	**14.842**
Minbu	8.629	6.763	**10.206**	**10.880**	7.137
Chauk	5.65	5.736	6.296	**12.844**	5.199
Aunglan	**17.869**	**15.584**	**20.654**	**17.353**	**15.509**
Pakokku	**11.686**	**19.941**	**12.65**	**20.503**	**11.713**
Sinphyukyun	1.725	1.476	1.88	7.666	1.714
Taungdwingyi	**16.75**	**21.823**	**18.558**	**24.654**	**17.505**
Gangaw	0.611	**21.823**	3.513	**10.353**	3.365
Pauk	4.675	5.413	5.192	**11.247**	**11.713**

According to the above results, the computed values of Chi-square test given by all five estimator methods of Gumbel distribution are less than the theoretical value ($\chi^2_{0.05} = 9.488$) for all stations at the confidence level of 95%, except Magway, Aunglan and Taungdwingyi stations in ten minutes and three seconds gust wind speeds and Pakokku station in later gust wind speed these values are more than the theoretical value. Moreover, the computed values of MLM for Gangaw, MLS for Minbu, OSA for Minbu, Chauk, Gangaw and Pauk, and PWM for Pauk stations are also more than the theoretical value in three seconds gust wind speed. If the computed values of GoF tests statistics given by the method are less than that of theoretical values at the desired significance level, then the method is fitted for determination of parameters of Gumbel distribution for modeling wind speed.

C. Analysis Based on Diagnostic Test

RMSE is the diagnostic test and it values are computed using equation (4) for five estimator methods of Gumbel distribution by Python Program. Computed values for all stations are shown in Table X for ten minutes gust wind speed and Table XI for three seconds gust wind speed.

$$RMSE = \left[\frac{1}{N} \sum_{i=1}^{N} \left(W_i - W_i^* \right)^2 \right]^{1/2} \quad (4)$$

where, W_i and W_i^* are the recorded and estimated wind speed i^{th} observation given by Gumbel distribution. N is numbers of data. The method provided minimum RMSE is considered as the most suitable method for estimation of design wind speed [2].

Table X. COMPUTED PROGRAM RESULTS OF RMSE VALUES FOR TEN MINUTES GUST WIND SPEED

Region	RMSE values for Ten Minutes Gust Wind Speed (m/s)				
	MOM	**MLM**	**MLS**	**OSA**	**PWM**
Magway	**5.606**	6.497	5.843	13.236	5.761
Minbu	3.013	**2.427**	3.396	4.826	2.583
Chauk	2.03	**1.825**	2.173	5.811	1.891
Aunglan	6.30	**5.351**	6.974	7.741	5.612
Pakokku	4.401	4.884	4.58	9.062	**4.361**
Sinphyukyun	0.650	**0.631**	0.675	3.431	0.636
Taungdwingyi	**6.636**	6.944	6.936	11.757	6.774
Gangaw	1.431	1.438	**1.218**	4.931	1.559
Pauk	1.897	**1.791**	3.239	5.428	1.894

Table XI. COMPUTED PROGRAM RESULTS OF RMSE VALUES FOR THREE SECONDS GUST WIND SPEED

Region	RMSE Values for Three Seconds Gust Wind Speed (m/s)				
	MOM	**MLM**	**MLS**	**OSA**	**PWM**
Magway	**8.081**	9.445	8.425	19.079	8.307
Minbu	4.34	**3.576**	4.894	6.955	3.719
Chauk	2.924	**2.691**	3.131	8.376	2.729
Aunglan	9.08	**7.795**	10.05	11.156	8.087
Pakokku	6.346	7.22	6.601	13.059	**6.282**
Sinphyukyun	0.945	**0.912**	0.98	4.982	0.926
Taungdwingyi	**9.308**	9.79	9.803	16.74	9.456
Gangaw	**1.764**	3.113	1.855	6.787	1.805
Pauk	2.454	2.386	2.611	7.356	**2.315**

From Table X, it can be seen that the Root Mean Square Error (RMSE) values given by MOM for Magway and Taungdwingyi, MLM for Minbu, Chauk, Aunglan, Sinphyukyun and Pauk, MLS for Gangaw and PWM for Pakokku are minimum while modeling wind speed for ten minutes gust wind speed. And then, from Table XI, it is noted that the Root Mean Square Error (RMSE) values given by MOM for Magway, Taungdwingyi and Gangaw, MLM for Minbu, Chauk, Aunglan, Sinphyukyun, and PWM for Pakokku and Pauk are minimum while modeling wind speed for three seconds gust wind speed.

D. Estimation of Extreme Wind Speed with Standard Error using Python Programming

In this paper, the Python program is developed and used to estimate the value of Standard Error (SE) and the extreme wind speed (W_T) for Magway, Minbu, Chauk, Aunglan, Pakokku, Sinphyukyun, Taungdwingyi, Gangaw and Pauk in Magway Region for 50-year, 500-year and 1000-year return periods. The values of Standard Error (SE) and the extreme wind speed (W_T) of the converted ten minutes and three seconds gust wind speeds for different return periods adopting Gumbel distribution using corresponding best fitted estimator method are computed by using equations (5), (6), (7) and (8). The estimated extreme wind speeds computed by Gumbel distribution are used for estimation of design wind speed using MOM in Magway and Taungdwingyi, MLM in Minbu, Chauk, Aunglan, Sinphyukyun and Pauk, MLS in Gangaw and PWM in Pakokku for ten minutes gust wind speed. And then, MOM in Magway, Taungdwingyi and Gangaw, MLM in Minbu, Chauk, Aunglan, Sinphyukyun and PWM in Pakokku and Pauk for three seconds gust wind speed.

The SE for MOM, MLM, MLS and PWM methods can be obtained from,

$$SE = \frac{\beta}{\sqrt{N}} \left(A + BY_T + CY_T^2 \right)^{0.5} \quad (5)$$

The coefficients used in computation of SE by MOM, MLM, MLS and PWM are given in Table XII.

Table XII. COEFFICIENTS USED IN COMPUTATION OF SE BY MOM, MLM, MLS AND PWM [1]

Parameter Estimation Method	Coefficients used in computation of SE		
	A	B	C
MOM and MLS	1.1589	0.1919	1.1
PWM	1.1128	0.4574	0.8046
MLM	1.1087	0.514	0.6079

The SE of the estimated wind speed by OSA can be obtained from,

$$SE = \left(r^{*} W_n + r' W_{n'} \right)^{1/2} \quad (6)$$

where $r^{*} = \left(\frac{1}{k}\right)\left(\frac{kn}{N}\right)^2$ and $r' = \left(\frac{n'}{N}\right)^2$. W_n and $W_{n'}$ are defined by the general form as:

$$W_n = \left(A_n Y_G^2 + B_n Y_G + C_n \right) \beta^2 \quad (7)$$

The values of A_n, B_n and C_n used in computing the SE for OSA are given in Table XIII (AERB safety guide) [1].

Table XIII. VARIANCE DETERMINATORS FOR W_n [1]

n	A_n	B_n	C_n
2	0.71186	-0.1286	0.65955
3	0.34472	0.04954	0.40286
4	0.22528	0.06938	0.29346
5	0.16665	0.06798	0.2314
6	0.13196	0.06275	0.19117

E. Development of Design Wind Speed Map

In this paper, the geographic information system (GIS) (10.6.1) software is used to produce the wind map. ArcGIS is the tool that satisfies the need to finish this contour map because of the ability to calculate and interpolate the data all over the entire map. ArcGIS from ESRI (Environmental System Research Institute) is used to issue the output as a map. The design wind speed maps with different return periods for study area are developed by adopting the ArcMap software.

III. RESULTS AND DISCUSSIONS

In this paper, after checking the various parameters estimation methods such as MOM, MLM, MLS, OSA and PWM with Goodness of Fit (GoF) tests involving Anderson-Darling (AD), Kolmogorov-Smirnov (KS) and Chi-square tests, the adequacy of fitting the parameter estimation methods for Gumbel distribution to the recorded data of study stations are obtained. And then, diagnostic test of Root Mean Square Error (RMSE) is adopted for the selection of a suitable method for determination of parameters of Gumbel distribution for modeling wind speed data. The method which gives the minimum RMSE values is established for evaluating the design wind speed. The fittest parameter estimation method for Gumbel distribution is used to evaluate design wind speeds for different return periods. Then, the Standard Error (SE) of the estimated wind speeds using MOM, MLM, MLS, OSA and PWM methods are also computed. The estimated extreme wind speed (W_T) + (SE) values by using Python Program are proposed as basic design wind speed for design purposes of the structures and buildings for study area. And then, the design wind speeds for 50-year, 500-year and 1000-year return periods are presented in Fig. 1 to 4 for ten minutes gust wind speed and three seconds gust wind speed respectively. The coordinates of latitude, longitude and design wind speed of various return periods for all study stations are shown in Table XIV to XVI for ten minutes gust wind speed and Table XVII to XIX for three seconds gust wind speed.

Table XIV. ESTIMATED TEN MINUTES DESIGN WIND SPEED WITH SE FOR ALL STATIONS (50 YEAR RETURN PERIOD)

Stations	North Latitude	East Longitude	Estimated Ten Minutes Design Wind Speed for 50 Year Return Period (mph)			
			W_T	SE	W_T+SE (m/s)	W_T+SE (mph)
Magway	20.1544°	94.9455°	29.2	4.8	34.0	76
Minbu	20.1714°	94.8702°	12.8	2.3	15.1	33.6
Chauk	20.9006°	94.8261°	11.8	1.8	13.6	30.5
Aunglan	19.3603°	95.2188°	26.6	5.2	31.8	71.3
Pakokku	21.3394°	95.0703°	23.3	4.1	27.4	61.2
Sinphyukyun	20.6635°	94.6941°	4.3	0.4	4.7	10.5
Taungdwingyi	20.001°	95.5460°	30.5	5.8	36.3	81.3
Gangaw	22.1757°	94.1347°	7.6	0.9	8.5	19.0
Pauk	21.4542°	94.4826°	10.5	1.6	12.1	27.0

Table XV. ESTIMATED TEN MINUTES DESIGN WIND SPEED WITH SE FOR ALL STATIONS (500 YEAR RETURN PERIOD)

Stations	North Latitude	East Longitude	Estimated Ten Minutes Design Wind Speed for 500 Year Return Period (mph)			
			W_T	SE	W_T+SE (m/s)	W_T+SE (mph)
Magway	20.1544°	94.9455°	40.7	7.4	48.1	107.6
Minbu	20.1714°	94.8702°	18.2	3.5	21.7	48.5
Chauk	20.9006°	94.8261°	16.2	2.8	19.0	42.4
Aunglan	19.3603°	95.2188°	39.2	8.1	47.3	105.7
Pakokku	21.3394°	95.0703°	33.1	6.3	39.4	89.6
Sinphyukyun	20.6635°	94.6941°	5.3	0.6	5.9	13.2
Taungdwingyi	20.001°	95.5460°	44.5	9.1	53.6	119.8
Gangaw	22.1757°	94.1347°	9.8	1.4	11.2	22.6
Pauk	21.4542°	94.4826°	14.3	2.5	16.8	37.6

Table XVI. ESTIMATED TEN MINUTES DESIGN WIND SPEED WITH SE FOR ALL STATIONS (1000 YEAR RETURN PERIOD)

Stations	North Latitude	East Longitude	Estimated Ten Minutes Design Wind Speed for 1000 Year Return Period (mph)			
			W_T	SE	W_T+SE (m/s)	W_T+SE (mph)
Magway	20.1544°	94.9455°	44.1	8.2	52.3	117.0
Minbu	20.1714°	94.8702°	19.8	3.9	22.7	52.9
Chauk	20.9006°	94.8261°	17.5	3.1	20.6	45.9
Aunglan	19.3603°	95.2188°	42.9	9.0	51.9	116.1
Pakokku	21.3394°	95.0703°	36.0	7.0	43.0	96.4
Sinphyukyun	20.6635°	94.6941°	5.5	0.7	6.2	13.9
Taungdwingyi	20.001°	95.5460°	48.7	10.0	58.7	131.4
Gangaw	22.1757°	94.1347°	10.4	1.6	12.0	26.8
Pauk	21.4542°	94.4826°	0.7	15.5	16.2	36.2

Table XVII. ESTIMATED THREE SECONDS DESIGN WIND SPEED WITH SE FOR ALL STATIONS (50 YEAR RETURN PERIOD)

Stations	North Latitude	East Longitude	Estimated Three Seconds Design Wind Speed for 50 Year Return Period (mph)			
			W_T	SE	W_T+SE (m/s)	W_T+SE (mph)
Magway	20.1544°	94.9455°	42.1	6.9	49.0	109.6
Minbu	20.1714°	94.8702°	19.1	3.4	22.5	50.3
Chauk	20.9006°	94.8261°	18.3	2.9	21.2	47.3
Aunglan	19.3603°	95.2188°	39.6	7.8	47.5	106.2
Pakokku	21.3394°	95.0703°	33.6	5.9	39.5	88.3
Sinphyukyun	20.6635°	94.6941°	7.0	0.7	7.7	17.3
Taungdwingyi	20.001°	95.5460°	44.0	8.4	52.4	117.2
Gangaw	22.1757°	94.1347°	11.6	1.6	13.2	29.5
Pauk	21.4542°	94.4826°	14.4	2.2	16.6	36.9

XVIII. ESTIMATED THREE SECONDS DESIGN WIND SPEED WITH SE FOR ALL STATIONS (500 YEAR RETURN PERIOD)

Stations	North Latitude	East Longitude	Estimated Three Seconds Design Wind Speed for 500 Year Return Period (mph)			
			W_T	SE	W_T+SE (m/s)	W_T+SE (mph)
Magway	20.1544°	94.9455°	58.6	10.7	69.3	155.1
Minbu	20.1714°	94.8702°	27.2	5.8	33.0	72.7
Chauk	20.9006°	94.8261°	25.2	4.5	29.7	66.3
Aunglan	19.3603°	95.2188°	58.4	12.1	70.5	157.7
Pakokku	21.3394°	95.0703°	47.7	9.1	56.8	127.0
Sinphyukyun	20.6635°	94.6941°	8.8	1.2	10.0	22.2
Taungdwingyi	20.001°	95.5460°	64.1	13.1	77.2	172.7
Gangaw	22.1757°	94.1347°	15.4	2.5	17.9	40.0
Pauk	21.4542°	94.4826°	19.6	3.4	23.0	51.3

XIX. ESTIMATED THREE SECONDS DESIGN WIND SPEED WITH SE FOR ALL STATIONS (1000 YEAR RETURN PERIOD)

Stations	North Latitude	East Longitude	Estimated Three Seconds Design Wind Speed for 1000Year Return Period (mph)			
			W_T	SE	W_T+SE (m/s)	W_T+SE (mph)
Magway	20.1544°	94.9455°	63.6	11.9	75.5	168.8
Minbu	20.1714°	94.8702°	29.7	5.8	35.5	79.4
Chauk	20.9006°	94.8261°	27.2	5.0	32.2	72.0
Aunglan	19.3603°	95.2188°	64.0	13.4	77.4	173.2
Pakokku	21.3394°	95.0703°	51.9	10.1	62.0	138.6
Sinphyukyun	20.6635°	94.6941°	9.3	1.3	10.6	23.6
Taungdwingyi	20.001°	95.5460°	70.2	14.5	84.7	189.3
Gangaw	22.1757°	94.1347°	16.6	2.8	19.4	43.2
Pauk	21.4542°	94.4826°	21.1	3.7	24.8	55.6

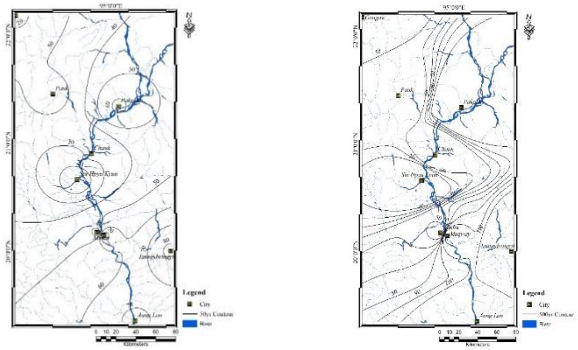

Fig.1. Contour maps of ten minutes design wind speed (mph) for 50-year and 500-year return periods

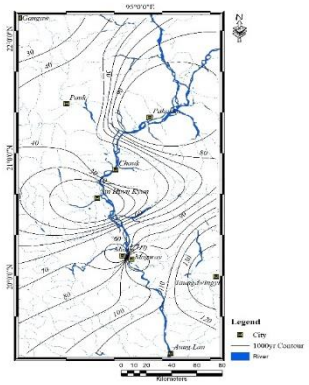

Fig.2. Contour map of ten minutes design wind speed (mph) for 1000-year return period

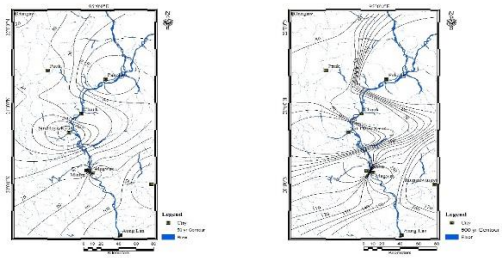

Fig.3. Contour maps of three seconds design wind speed (mph) for 50-year and 500-year return periods

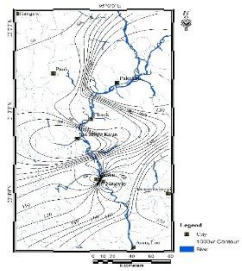

Fig.4. Contour map of three seconds design wind speed (mph) for 1000-year return period

From the above contour maps, it can be seen that the design wind speeds in the south-east part of the Magway Region are higher than those of other areas for both ten minutes and three seconds gust wind speeds.

IV. CONCLUSION

From this study, it can be concluded that the structural engineer can be reliable to use design wind speed in structural designs and can analyze the effects of wind in the natural and the built environment and be able to study the possible damage, inconvenience or benefits which may result from wind. And also concluded that the design wind speeds in south-east part of the Magway region are higher than those of other areas for both ten minutes and three seconds gust wind speeds according to wind map. Finally, this study provides the preliminary wind distribution map with different return periods for Magway region and would be useful for designer to estimate the effects of wind load on building and structures.

ACKNOWLEDGMENT

The author is deeply gratitude to Dr. Nwe Nwe Win , Professor and Head, Department of Civil Engineering, for her guidance and advice. The author would like to express grateful thanks to her supervisor Daw San San Myint, Associate Professor, Department of Civil Engineering and to all her teachers from Civil Department, Technological University (Mandalay). The author's special thanks are sent to her parents for their guidance from childhood till now.

REFERENCES

[1] Atomic Energy Regulatory Board (AERB), "*Extreme values of meteorological parameters – AERB Safety Guide No. NF/SG/S-3*", 2008.

[2] N.Vivekanandan, "*Comparison of design wind speed estimates using Gumbel distribution and IS 875 approach*", Journal of Research in Architecture and Civil Engineering (ISTP-JRAC), vol.1, no.1, January 2013.

[3] Chanthorn Lin, "*Determination of basic wind speed for the design of buildings in Cambodia*",Paper of IOP Conference Series:Earth and Environmental Science,2023.

Statistics Analysis of Travel-Activity Patterns of People at Mandalay City

Phyu Lay Wai[1] , War War Myint[2]
[1]*Department of Civil Engineering and Technological University (Mandalay)*
[2]*Department of Civil Engineering and Technological University (Mandalay)*

Email: [1]phyulaywai04@gmail.com, [2]wwmyint.mm@gmail.com

***Abstract* — In today's fast-paced world, the development of practical activity-based travel demand models for urban areas is crucial for effective planning and management. This study focuses on understanding the travel-activity patterns of residents in Mandalay city, aiming to provide a robust basis for travel demand modeling. The research analyzed various travel characteristics, including trip rates, travel modes, and activity duration and allocation. The study found that the average trip rate in Mandalay is approximately 5.0 trips per day. Through multiple regression model, it identified key predictors of trip rates, such as gender, household size, and monthly income. These insights into the travel behavior of Mandalay residents are instrumental for enhancing the accuracy and effectiveness of travel demand models, facilitating better urban planning and policy-making.**

Keywords—Activity-Based Travel Demand Models, Travel-Activity Patterns, Mandalay City, Trip Rates, Multiple Regression Model

I. INTRODUCTION

Transportation plays as an important role in the development of the country, especially, in economy. Nowadays, the developed and developing countries face many traffic problems such as traffic accidents and traffic congestion, etc. Especially, the disadvantages of traffic problems can be significantly visible in urban areas, where have offices, hospitals, schools, universities and shopping centers. As a reason, people who lives, works, studies and takes treatments in these places have the higher rates of making travels and the multiple usages of the city's traffic. And then, these people also produce complex daily travel schedules that cause many traffic problems. In order to solve and reduce these traffic problems, an accurate planning is originally essential before making the traffic design and the road. Improper management and planning of transportation facilities affected by other external and environmental conditions could cause heavy traffic congestion, which cause delay in the activities of people especially in an urban setting. Therefore, transportation demand analysis is one of the most efficient parts in transportation engineering and planning. However, a better understanding that how people organize and schedule their activities can give more solid basis for travel demand modeling. In activity-based travel demand analysis, the travel demand that occurs in the current is needed to be collected to forecast for the future. So, travel demand forecasting should be considered in the urban areas.

II. ACTIVITY-BASED TRAVEL DEMAND MODELING

Daily patterns of travelers are affecting their travel patterns which are one important aspect of transportation planning and travel demand forecasting. This aspect is normally analyzed through the conventional 4-step travel demand model. The model has four sub-models which are the trip generation, distribution, modal split, and traffic assignment. However, the models are entirely trip-based. This means that the models are based on the estimation of trip productions and attractions; then, simple tours are modeled until the trip assignment stage [1].

A. Trip Rates and Average Trip Rates

Trip rates refer to the intensity of travel due to the development and trip generation refers to the trips which enter and leave the particular development. The average trip rate is a number which the sum of the trips are divided by how many numbers are being averaged. Trip rates and average trip rates are defined in terms of the number of trips within the specific floor area and for a particular time period (for example peak hour or daily or weekly). The selection of a trip rate is important in estimating the travel generation of a site [2].

B. Trip Frequency

Frequency measures the number of times occurred in a specific amount of time. For example, if someone visits the store twice a week, her shopping frequency is 2 visits per week. Frequency can be used to measure the rate of any action. These frequencies even occur multiple times per second, times per minute, times per hour, times per day, times per week and so on [3]. And then, frequencies are measured in the related units.

C. *Four-Step Travel Demand Model Analysis*

After calculating sample size by Taro Yamani formula sampling method, the number of respondents is determined as 400 numbers. The surveys mainly focused on the purpose of trips, the number of person-trip in each zone is calculated on the land use, population and socio-economic activity. Production trips are generally performed from the households of each zone. In order to estimate the production trips, the numbers of households of each zone in the study area are required. The regression equation for production model is based on household characteristics of the study area. Factor affecting trip productions are socioeconomic factors, locational factors and public transport accessibility. Socioeconomic factors are household income, vehicle ownership, number of workers, number of family size and so on. Locational factors depend on land use characteristics. Public transport accessibility is based on the accessibility of the public transport system and its efficiency. In this study, survey data results are used as a main source of analysis for predicting the number of trips in the study area. Many other types of surveys are home interview survey, road-side

interview survey, public transport survey, online survey, commercial vehicles survey and registration number survey, etc. [4].

D. Computation the Number of Sample Size

The determination of sample size is a very important issue as too large samples may waste time, resources and money. It can be determined in the Taro Yamani formula. In this formula, the number of population is needed. Sampling of error is usually accepted at 5% or 0.05 by Taro Yamani formula. According to the data from the Ministry of Immigration and Population, the current population of Mandalay is 1875619. The number of sample size is determined as below:

$$N = 1875619$$
$$e = 0.05 \text{ or } 5\%$$
$$n = \text{number of sample size}$$
$$n = \frac{N}{1+N(e)^2} \quad (1)$$
$$= \frac{1875619}{1+1875619(0.05)^2}$$
$$= 399.91 \sim 400$$

III. Results And Discussion

A. Average Trips Rate of a Traveller

After data collection, the total number of respondents are 400 and the total number of trip rates is 2008 trips per day. The average trip rate of a traveler is determined as below:

$$\text{Number of trips} = 2008 \text{ trips per day}$$
$$\text{Number of respondents} = 400 \text{ numbers}$$
$$\text{Average Daily Trips} = \frac{\text{Total Trips}}{\text{Number of Respondents}} \quad (2)$$
$$= \frac{2008}{400}$$
$$= 5.02 \text{ trips}$$

I. Number of Trips and Corresponding Number of Travelers

Number of trips per day	Number of Respondents	Percent (%)
Between 1 to 2	29	7.2%
Between 3 to 4	123	30.7%
Between 5 to 6	163	40.8%
Between 7 to 8	85	21.3%
Total	400	100.00

Table I. shows that the traveler's average daily trips are at least 1 trip and the most is 8 trips. In detail, only 29 (7.2%) of the respondents averaged 1 to 2 trips per day, 123 (30.8%) averaged 3 to 4 trips per day, 163 (40.8%) averaged 5 to 6 trips per day, 85 (21.3%) averaged 7 to8 trips per day.

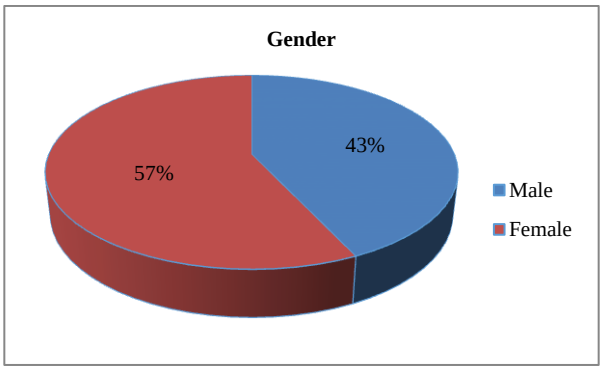

Fig. 1. Gender distribution of Respondents.

The Fig. 1 illustrates the gender breakdown among the respondents, with 172 individuals (43%) identified as male and 228 individuals (57%) identified as female. This data highlights a higher proportion of female respondents compared to male respondents, indicating a notable gender composition within the surveyed group.

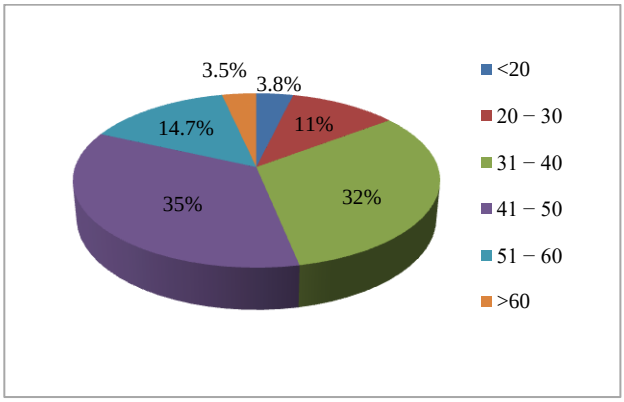

Fig. 2. Age distribution of respondents.

This Fig. 2 presents the age demographics of the surveyed residents, divided into six distinct age groups. The breakdown is as follows: 15 respondents (3.8%) are under 20 years old, 44 respondents (11%) are between 20 and 30 years old, 128 respondents (32%) fall within the 31 to 40 years age range, 140 respondents (35%) are aged between 41 and 50 years, 59 respondents (14.7%) are between 51 and 60 years old, and 14 respondents (3.5%) are over 60 years old. This distribution highlights the predominance of middle-aged residents in the sample, with the largest groups being those aged 31 to 50 years.

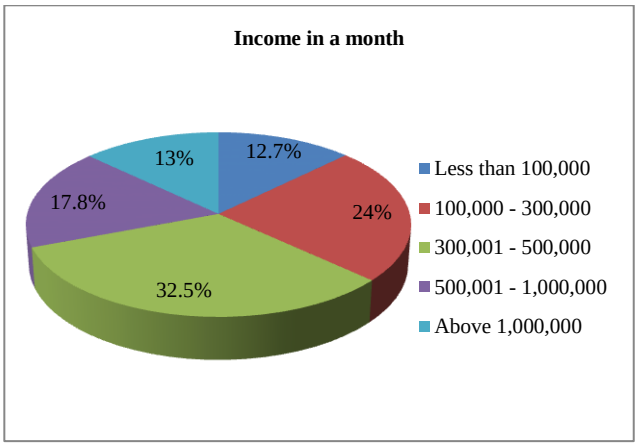

Fig. 3. Monthly income distribution of respondents.

This Fig. 3 illustrates the monthly income levels of respondents, categorized into five income brackets. Specifically, 51 respondents (12.7%) earn less than 100,000 MMK per month, 96 respondents (24%) have a monthly income between 100,000 and 300,000 MMK, 130 respondents (32.5%) fall within the 300,001 to 500,000 MMK range, 71 respondents (17.8%) earn between 500,001 and 1,000,000 MMK, and 52 respondents (13%) have a monthly income exceeding 1,000,000 MMK. This distribution reveals that the largest proportion of respondents is in the 300,001 to 500,000 MMK income bracket, indicating a significant diversity in income levels among the surveyed group.

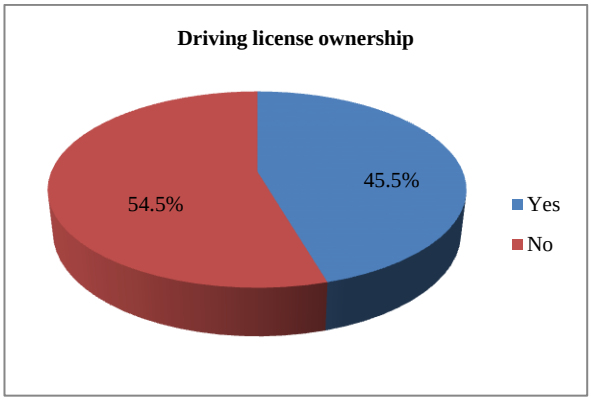

Fig. 4. Driving license status of respondents.

The Fig. 4 displays the distribution of driving license acquisition among the respondents. Out of the total, 182 individuals (45.5%) have acquired a driving license, while 218 individuals (54.5%) have not. This indicates that a majority of the respondents do not possess a driving license, with a significant proportion yet to obtain one.

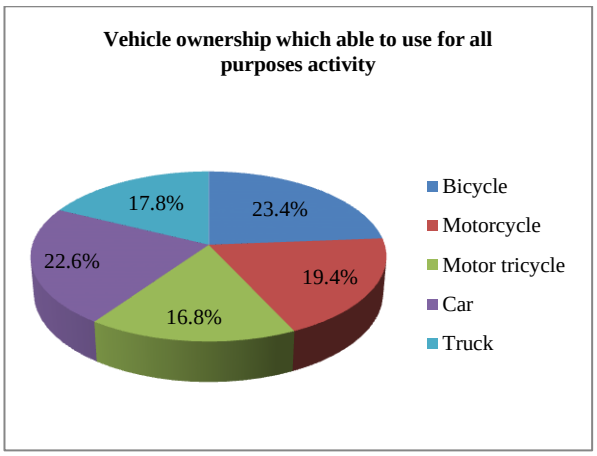

Fig. 5. Modes of transportation used by respondents.

The Fig. 5 illustrates the primary modes of transportation for various daily activities among respondents. Specifically, 95 respondents (23.4%) use bicycles for all-purpose activities, 77 respondents (19.4%) rely on motorcycles, 67 respondents (16.8%) utilize motor tricycles, 90 respondents (22.6%) prefer cars, and 71 respondents (17.8%) use trucks. This distribution highlights a diverse range of transportation choices, with bicycles and cars being the most common modes of transport among the group.

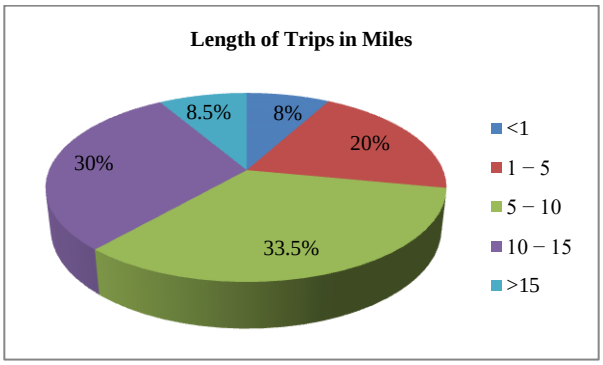

Fig. 6. Distance traveled by respondents for all activities.

This Fig. 6 categorizes the distances traveled by respondents into five groups. The breakdown is as follows: 32 respondents (8%) travel less than 1 mile, 80 respondents (20%) travel between 1 to 5 miles, 134 respondents (33.5%) travel between 5 to 10 miles, 120 respondents (30%) travel between 10 to 15 miles, and 34 respondents (8.5%) travel more than 15 miles. This distribution indicates that the majority of respondents travel distances ranging from 5 to 15 miles for their activities.

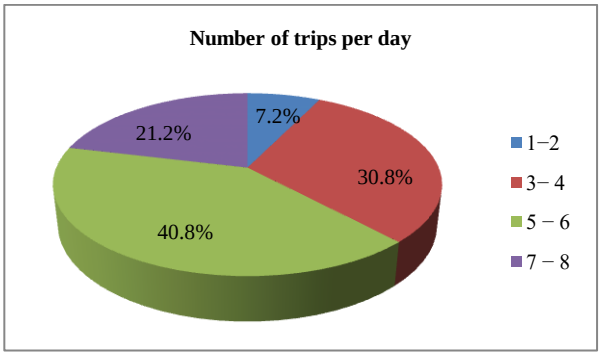

Fig. 7. Daily trip frequency of respondents.

This Fig. 7 categorizes the number of daily trips made by respondents into four groups. Specifically, 29 respondents (7.2%) make 1 to 2 trips per day, 123 respondents (30.8%) make 3 to 4 trips, 163 respondents (40.8%) make 5 to 6 trips, and 85 respondents (21.2%) make 7 to 8 trips daily. The data shows that the most common trip frequency among respondents is 5 to 6 trips per day, followed by 3 to 4 trips, indicating a high level of daily travel activity.

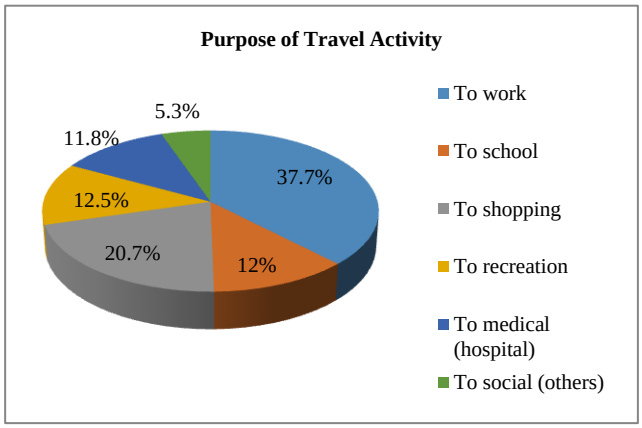

Fig. 8. Purpose of travel activity of respondents.

The Fig. 8 shows the distribution of travel purposes among respondents. It categorizes travel into six main purposes: 151 respondents (37.7%) travel to work, 48 respondents (12.0%) travel to school, 83 respondents (20.7%) travel for shopping, 50 respondents (12.5%) travel for recreation or leisure, 47 respondents (11.8%) travel to hospitals, and 21 respondents (5.3%) travel for social and organizational activities. The data highlights that commuting to work is the most common travel purpose, followed by shopping, reflecting the key motivations for daily travel among the surveyed group.

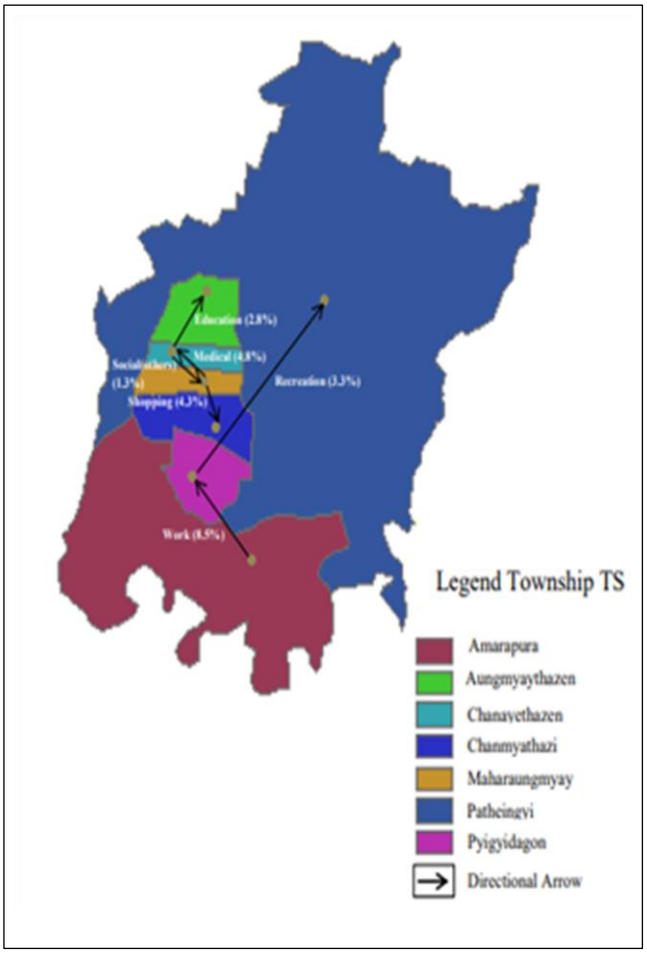

Fig. 9. Travel activities pattern of respondents at Mandalay City.

The Fig. 9 shows the results are as follows: a maximum of 34 people, which represents 8.5%, travel from Amarapura to Pyigyidagon for work-related purposes. From Chanayethazan to Aungmyaythazan, up to 11 people (2.8%) make the journey to Aungmyaythazan for educational activities. For shopping, the highest number of travelers, 17 people (4.3%), move from Aungmyaythazan to Chanmyathazi. When it comes to recreational activities, a maximum of 13 people (3.3%) commute from Pyigyidagon to Patheingyi. Additionally, for health-related reasons, as many as 19 individuals (4.8%) go from Mahaaungmyay to Chanayethazan. Lastly, the maximum number of people traveling for social activities, 5 people (1.3%), go from Chanayethazan to Mahaaungmyay.

B. Results for Statistical Model of Trip rates

The trip rates depending on the traveler's characteristics are analyzed by multiple regression model [5]. The result of the model parameter estimation is shown in Table II.

II. RESULTS OF THE MODEL PARAMETER ESTIMATION

Trip Rates	Coefficient	t	Sig
Gender	-0.184	-3.664	0.000**
Age	0.088	1.750	0.081
Marital status	0.012	0.227	0.821
Households' member	0.150	2.830	0.005**
Education level	-0.056	-1.119	0.264
Job Status	0.001	0.018	0.985
Monthly income	0.175	3.509	0.001**
Driving license ownership	0.025	-0.507	0.612
Vehicle ownership	0.071	1.426	0.155
Travel distance	-0.001	-0.021	0.984
Travel time	-0.067	-1.364	0.173
Travel cost	0.009	0.179	0.858
Comfort	0.085	1.670	0.096
Accessibility	-0.065	-1.325	0.186
Safety	-0.061	-1.234	0.218
Security	-0.038	-0.775	0.439
Privacy	0.065	1.319	0.188
Prestige	-0.025	-0.515	0.607
Reliability	0.022	0.448	0.655
Constant	1.520	0.924	0.356

From Table II, when analyzing the relationship between trip rate and gender of respondents, a coefficient value of -0.184 indicates that, on average, for every one-unit increase in the Gender variable (e.g., from male to female or vice versa), the predicted value of the dependent variable decreases by 0.184 units. In this study, a t-value of -3.664 suggests that the relationship between Gender and respondents' trip rate is statistically significant. A significance level of 0.00 (or very close to 0) typically means that the relationship is statistically significant. When examining the relationship between household members of respondents and their trip rate, a coefficient value of 0.150 indicates that, for every one-unit increase in household member, the predicted value of the dependent variable (trip rate) increases by 0.150 units. In this case, a t- value of 2.83 suggests that the relationship between household members and trip rate is statistically significant. When studying the relationship between monthly income and respondents' trip rate, a coefficient value of 0.175 means that, the predicted value of the dependent variable (trip rate) will increase by 0.175 for every one-unit increase in monthly income level of respondents. A significant level of 0.001 typically means that the relationship between monthly income and trip rate is statistically significant.

IV. CONCLUSIONS

This study aims at understanding the current transportation demand of the people at Mandalay City by the use of activity-based travel demand model. The activities of the people and their travel characteristics are analyzed in terms of trip rates, travel modes and activity. Firstly, the questionnaire form is designed. The questionnaire form includes the people's characteristics such as gender, age, monthly allowance, education, travel mode choices, driver's license ownership and vehicle ownership. And then, the sample size is determined by the Taro Yamani formula. The questionnaire forms are distributed to the 420 people. Since the samples from 20 people were incomplete, only the complete samples from 400 people were used to determine the average daily trip rate of the travelers. The results show the relationship between the trip rates and the people's characteristics. Female travelers are more likely to make a trip compared to male ones. People between the ages of 31 and 50 travel the most as compared to other age groups. The higher the monthly allowance of the travelers, the more likely travel. And then, in vehicle usage, the most travel is by motorcycle. And then, travelers who own driver's license and vehicle are more likely to travel than who do not own. Moreover, the trip rates depending on the people's characteristics are analyzed by using multiple regression model. The results show the relationship between the trip rates and the people's characteristics. In there, gender, household's member and monthly income are statistically significant at 99% level. Therefore, gender, household's member and monthly income are important in predicting trip rates. The results are found from the analysis of the people activity-travel patterns survey. The results estimate the number of trips people make from their activities, which is related to the determination of travel demand. Hence, the results of this study are helpful for future demand modeling.

ACKNOWLEDGMENT

The author deeply thanks to Dr. Nwe Nwe Win, Professor and Head of the Department of Civil Engineering at Technological University (Mandalay), for all her valuable advice. The author would like to express her deepest gratitude to her supervisor, Dr. War War Myint, Professor, Department of Civil Engineering, Technological University (Mandalay), for her patient guidance, supervision and encouragement during long period of this study. The author specially thanks to all her teachers from Department of Civil Engineering for their supports and encouragement. Finally, the author would like to show deeply grateful thanks to her family, especially her parents, for their supports and encouragement to attain her destination. The author thanks to all her classmates for their understanding, sharing the knowledge through the course, and to all others who have helped towards the successful completion of this study.

REFERENCES

[1] Fred L. Mannering: "Principles of Highway Engineering and Traffic Analysis", 5th Ed., J Wiley and Sons, 2013.

[2] Fred L. Mannering: "*Principles of Highway Engineering and Traffic Analysis"*, 4th Ed., J Wiley and Sons, 2009.

[3] Moshe Ben-Akiva, "Transportation Systems Analysis: Demand and Economics", Massachusetts Institute of Technology, USA, 2008.

[4] Bowman J.L, Ben-Akiva M.E: "*Activity-Based Disaggregate Travel Demand System with Activity Schedules"*, Transportation Research Part A, 35, 1-28, 2000.

[5] Taro Yamane: "*Statistics, An Introductory Analysis"*, 2nd Ed., New York, Harper and Row, 1967.

Evaluating the Role of Demographics in Domestic Air Travel Preferences in Myanmar

Shoon Pyae Pyae[1], Kyaw Naing Soe[2]

[1]*Department of Civil Engineering, Technological University (Mandalay)*
[2]*Department of Civil Engineering, Technological University (Mandalay)*

Email: [1] shoonpyaepyae.moc@gmail.com, [2]mknsoe@gmail.com

***Abstract*— This study examines the relationship between air travel demand and demographic factors among domestic travelers in Myanmar. Utilizing a questionnaire-based survey with 500 participants, the research analyzes various demographic variables such as age, gender, income, education, and profession. Descriptive statistics reveal that the majority of air travelers are male, aged 35 to 44, hold college degrees, and are primarily employed in the private sector or government. The findings highlight that business, education, and recreation are the main purposes for air travel. The study provides insights into travel patterns and preferences, offering valuable information for transportation planning and policy-making.**

Keywords*— *Air travel demand, demographic factors, domestic flights, travel patterns.

I. INTRODUCTION

Over the last few decades, civil aviation sector demand has continued to grow. With the ever increasing demand of aircrafts and freight liners especially in the civil market, the manufacturing sector is pursuing the development of innovative next generation platforms to achieve cost effectiveness, travel comfort and delivery targets. The social dimension points into the direction that, demand patterns for aircrafts are different between the world regions. But, in fact, the demand patterns are strongly affected by economic and demographic factors and it is difficult to identify social factors that play a relevant role. Myanmar has three active international airports and 30 domestic airports, catering to 28 foreign airlines and nine domestic carriers. The aviation sector is supervised by the Department of Civil Aviation (DCA), a division of the Ministry of Transport and Communications (MOTC) responsible for civil aviation administration and air navigation services.

Air transport contributes to the sustainable economic development of the country, by facilitating tourism and trade. The COVID-19 pandemic and the consequent travel restrictions have had an unprecedented impact on the air travel market. In addition, domestic instability also affects air travel demand. Therefore, the Myanmar Department of Civil Aviation is trying to develop and strengthen the safe, secure, efficient, sustainable and environmentally-friendly air transport industry in its jurisdiction, and integrate it with the international air transport environment in order to fulfill the requirements of the public. Hence, the analysis of air travel demand stands as a critical and efficient component of transportation engineering and planning. [1] The four-step travel demand model is essential for modeling air travel demand. These trip-based models do not consider people's activities. Understanding how people organize and schedule activities is crucial for accurate travel demand modeling. Current travel demand data collection is necessary for forecasting future air travel demand, which should be considered for all residential areas in Myanmar. [2]

II. METHODOLOGY

This study focused on analyzing the impact of demographic factors of travelers on air travel demand. Initially, a literature review is conducted to pinpoint issues and requirements in transportation planning, focusing on travel demand modeling approaches. The questionnaire form is created for conducting surveys through questionnaires. Concerning to fulfill the objectives of this study, the quantitative method is based on primary data. The survey period is from 28th, April and 4th, May 2024. The survey questionnaire had multiple choice questions, and (yes=2 or no=1) questions. Then, the data completeness is verified. Travel patterns are gathered from questionnaire forms based on individuals' characteristics, income, and travel modes using simple random sampling. Additionally, the data is analyzed descriptive method using SPSS Software and Microsoft Excel.

A. Survey Design

A questionnaire form has been created to gather the necessary data. The survey covers various aspects such as the air traveler's characteristics like gender, age, income, education, and profession status. It also includes information about the type of transport, duration of air transport, frequencies for domestic trips used air transport, travel mode choices such as bicycle, motorcycle, or private car, and vehicle ownership.

B. Sample Size Determination

The determination of the sample size is crucial as excessively large samples can waste time, resources, and money. Cochran's formula is usually used in a situation where the population size is too large (or infinite) or unknown. A confidence level of 95% is usually used when dealing with human population.
The formula is represented as follow:

$$n = \frac{Z^2 p(1-p)}{e^2} \quad (1)$$

Where:

- n = sample size
- *Z* = Z-score which depends on the confidence level chosen by the researcher. The Z-score for a confidence level of 95% = 1.96.
- *p* = the estimated proportion of an attribute that is present in the population (0.5).

e = margin of error or confidence interval (5%, 0.05).

$$n = \frac{(1.96)^2\, 0.5(1-0.5)}{(0.05)^2}$$

$$n = \frac{(3.8416 \times 0.5 \times 0.5)}{(0.0025)}$$

$$n = \frac{0.9604}{0.0025}$$

$$n = 384.16$$

C. Data Collection

The survey collected 500 samples to represent the population using domestic air transport services. The data collection process is conducted using an online questionnaire form. To obtain reliable responses, a total of 500 participants were included in this survey.

III. Descriptive Analysis

The collected data for this survey is analyzed through statistical software and used Microsoft Excel for descriptive analysis. Initially, a descriptive analysis is presented in Fig.1. These are included gender, age, education, occupation, monthly income, and car ownership.

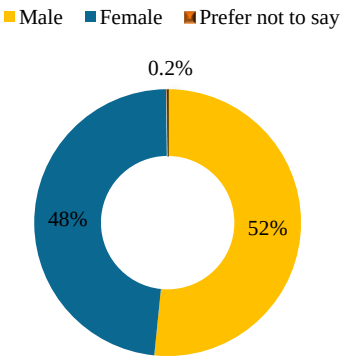

Fig. 1. Gender of travelers.

As shown in Fig.1, 258 (52%) are male, 241 (48%) are female and 1 (0.2%) are answered "Prefer not to say" respondents. The results show that male travellers are more than female travellers in this study.

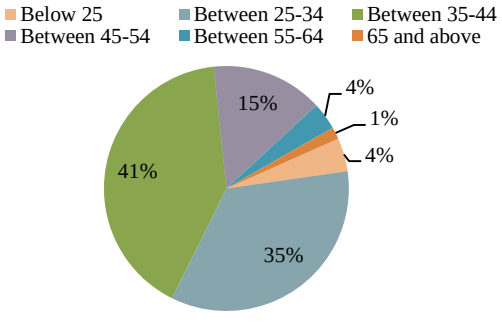

Fig .2. Age of travelers.

Out of 500 respondents, the age group of respondents is categorized into six groups. 22(4%) of respondents are below 25 years old, 173(35%) of respondents are between 25 to 34 years old, 205(41%) of respondents are between 35 to 44 years old, 74(15%) of respondents are between 45 to 54 years old, 18(4%) of respondents are between 55 to 64 years old and 8 (1%) are 65 and above years old. Among them, most of the respondents are the age between 35 to 44 years old.

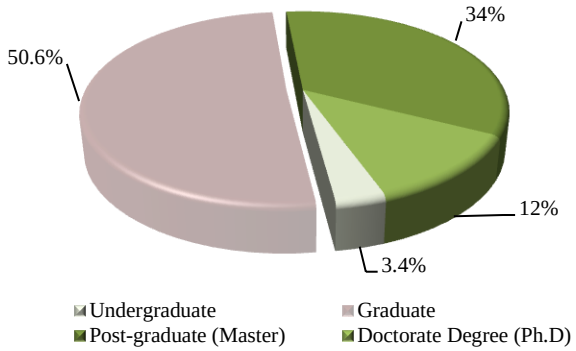

Fig. 3. Educational level of travelers.

Regarding education level, there are categorized into four groups including undergraduate, graduate, post-graduate (Master) and doctoral degrees (Ph.D). There are 17 (3.4%) of respondents are undergraduate level, 253 (50.6%) of respondents are graduate, 170(34.0%) are master degree holders, and 60 (12.0%) of respondents are Ph.D level.

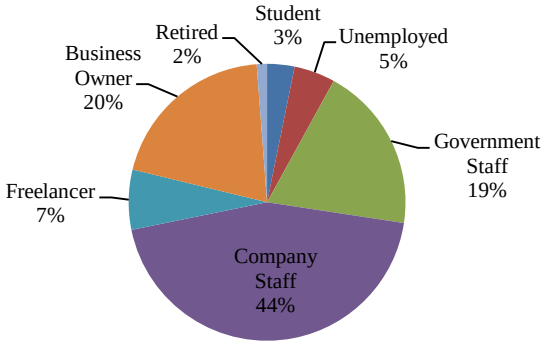

Fig. 4. Profession of travellers

According to the survey data, when studying the professional occupations of the respondents, there are 16(3%) are students, 24(5%) are unemployed, 97(19%) are government staff, 222(44%) are company staff, 35(7%) are freelancer, 100(20%) are business owner and 6(2%) are retired. The data clearly indicates that the majority of respondents were company staff.

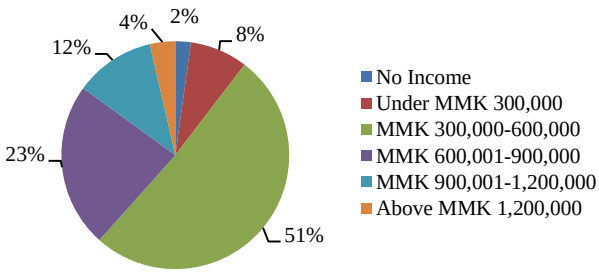

Fig. 5. Monthly personal income of traveler.

Regarding the personal monthly income of respondents, the survey findings are as follows: the majority of respondents (256, 51%) earn between 300,000

to 600,000 MMK. Additionally, 117 (23%) earn between 600,001 to 900,000 MMK, 57 (12%) earn between 900,001 to 1,200,000 MMK, 41 (8%) earn less than 300,000 MMK, and 18 (4%) earn more than 1,200,000 MMK. Furthermore, 11 respondents (2%) answered that they have no income. Notably, it is observed that most of the travelers have a high income level.

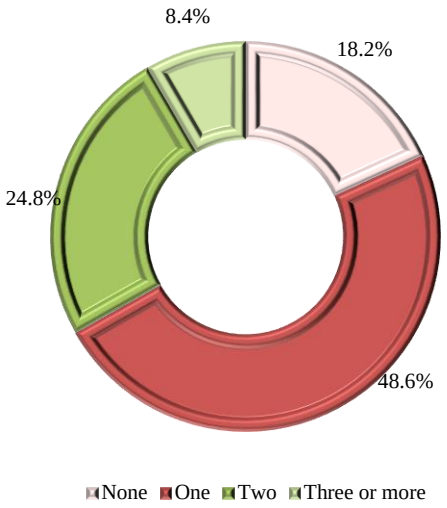

Fig. 6. Number of cars owned of respondents.

Moreover, the survey results indicate that a significant proportion of respondents owned a single car (48.6%), while 24.8% owned two cars, 8.4% owned three or more cars, and 18.2% did not own any cars.

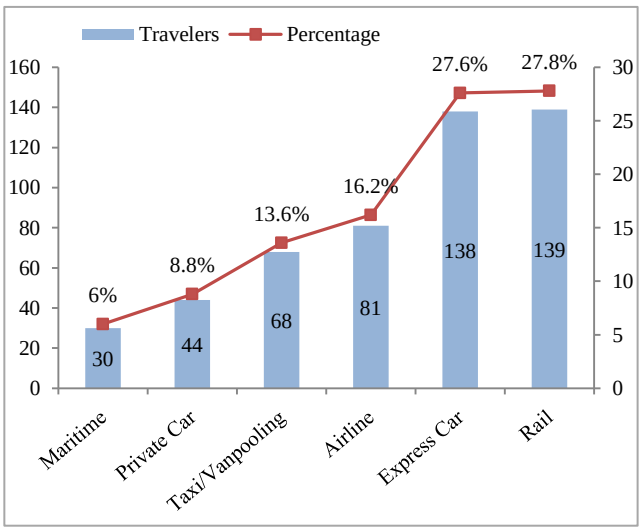

Fig. 7. Mode of transportation for domestic traveling.

When studying the transport mode for travel, it is found that most of the respondents (139, 27.8%) use the rail transport, and secondly, one third of respondents (138, 27.6%) use Express cars for domestic travel. In addition, the use of air transport is the third highest (81, 16.2%) for domestic travel.

IV. Results And Discussions

A. Air Travel Characteristics of Travelers

Table I. is illustrated travel times, travel modes, departure location, arrival location, departure time, arrival time, optimal season for air travel and duration of trips by airplane.

I. Travel Behaviors of Respondents

No	Description		Respondent	Percent
1	What is the departure airport location of your usual trips?	Bagan-Nyaung U	20	4.0
		Heho	70	14.0
		Kawthaung	4	0.8
		Kyaing Tong	18	3.6
		Mandalay	129	25.8
		Myitkyina	19	3.8
		Nay Pyi Taw	76	15.2
		Sittwe	21	4.2
		Tachileik	6	1.2
		Thandwe	46	9.2
		Yangon	91	18.2
	Total		**500**	**100**
2	What is the arrival airport location of your usual trip?	Bagan-Nyaung U	71	14.2
		Heho	58	11.6
		Kawthaung	9	1.8
		Kyaing Tong	41	8.2
		Mandalay	52	10.4
		Myitkyina	29	5.8
		Nay Pyi Taw	54	10.8
		Sittwe	32	6.4
		Tachileik	25	5.0
		Thandwe	65	13.0
		Yangon	64	12.8
	Total		**500**	**100**
3	What is the departure time of trips made by airplane?	Early Morning (Before 6 AM)	73	14.6
		Morning (6 AM -12 PM)	177	35.4
		Afternoon (12:01 PM-6 PM)	143	28.6
		Evening (6:00 PM – 12 AM)	90	18.0
		Late Night (After 12 AM)	17	3.4
	Total		**500**	**100**
4	What is the arrival time of trips made by airplane?	Early Morning(Before 6 AM)	44	8.8
		Morning (6 AM -12 PM)	65	13.0
		Afternoon (12:01 PM-6 PM)	125	25.0
		Evening (6:01 PM – 12 AM)	208	41.6
		Late Night (After 12 AM)	58	11.6
	Total		**500**	**100**
5	Type of available transport when you commute from your home to airport.	Walking	1	0.2
		Bicycle	28	5.6
		Mortorcycle	73	14.6
		Taxi	137	27.4
		Private Car	54	10.8
		Bus	154	30.8
		Ride-sharing (eg. Uber, Grab)	34	6.8
		Public Van	19	3.8
	Total		**500**	**100**

In the survey data, the majority of travelers depart from Mandalay (129, 25.8%) and Yangon (91, 18.2%), Nay Pyi Taw (76, 15.2%), and Heho (70, 14.0%) airports. Most of their arrival locations are Bagan-Nyaung U (71, 14.2%), Thandwe (65, 13.0%), Yangon (64, 12.8%), Heho (58, 11.6%), Nay Pyi Taw (54, 10.8%), and Mandalay (52, 10.4%). When traveling from home to the airport, most travelers typically use buses (154, 30.8%) or taxis (137, 27.4%).

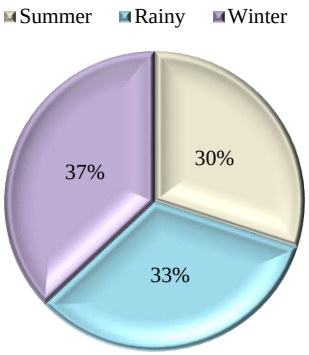

Fig. 8. Travel season.

It is also observed that most of the respondents depart from their place of origin throughout the morning (6 AM

to 12 PM) and afternoon (12 PM to 6 PM). Most frequently, the responders reach their destination in the afternoon (12:01 PM to 6 PM) or evening (6:01 PM to 12 AM).

184 (37.0%) respondents enjoy travel by airlines during the winter season, 165(33.0%) enjoy travel during the rainy season and 151(30.0%) enjoy travel during the summer season.

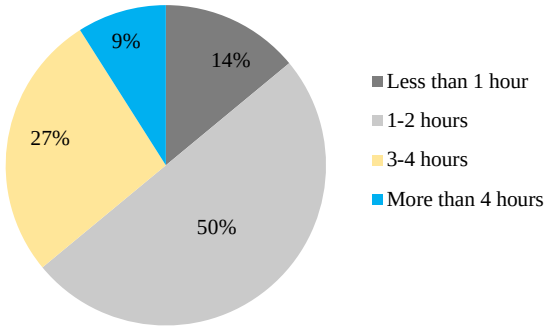

Fig. 9. Tavel time.

According to this study, travel time for 50% of respondents by flight are between 1 to 2 hours, 27% are 3 to 4 hours, 14% are less than one hour and only 9% are more than 4 hours to arrives their destination.

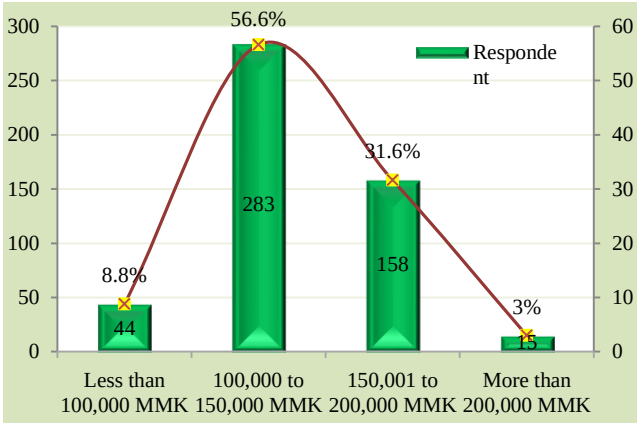

Fig. 10. Cost of travel by airplane.

When asking the question about the travel cost by flight, most of respondents (283, 56.6%) answered the cost between 100,000 to 150,000 MMK, 31.6% (158) are between 150,000 to 200,000 MMK, 8.8%(44) are less than 100,000 MMK and only 3%(15) are more than 200,000 MMK.

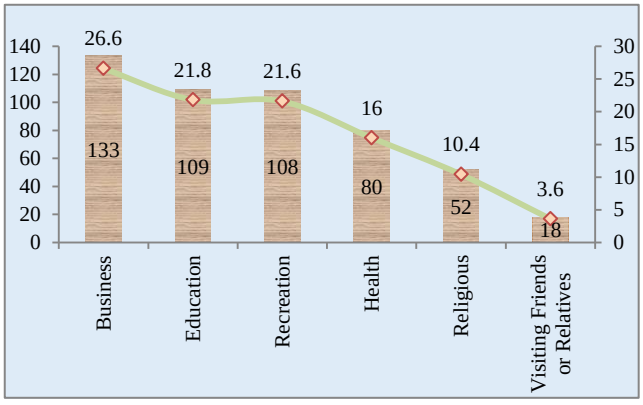

Fig. 11. Purpose of travel by air transport.

The above Fig.11 illustrates the purposes of air travel. According to survey data, 109(21.8%) travelers journey for education, 80(16.0%) for health, 133(26.6%) for business, 52(10.4%) for religious reasons, 108(21.6%) for recreation, and 18(3.6%) for visiting friends or relatives. It is evident that the majority of respondents use air travel for business purposes.

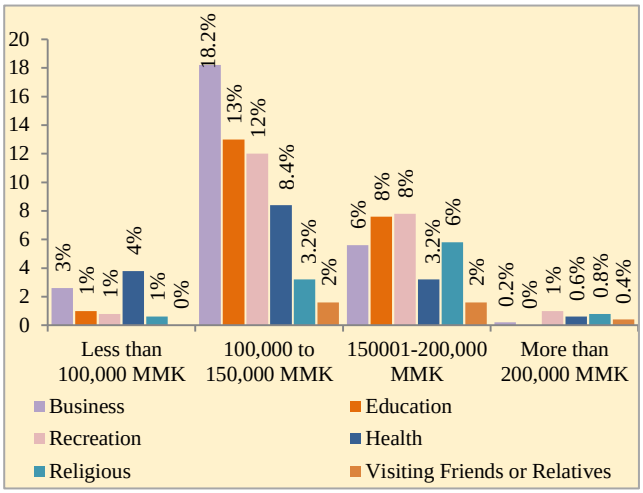

Fig. 12. Cost of travel by travelers' purpose.

The above figure shows that most of the travelers are traveling for business, education, recreation and health with travel cost between 100,000 to 150,000 MMK.

V. Conclusion

This study attempts to examine the relationship between air travel demand and demographic factors of travelers in Myanmar. The data are collected 500 sample respondents who have the travelling experience by domestic flights.

The research findings indicate that male travelers predominantly choose airlines for domestic journeys. The majorities of these travelers are aged 35 to 44, hold college degrees, and are employed in the private sector, government, or as business owners. Their monthly incomes typically range from 300,000 to 900,000 MMK. They often travel for business, education, and recreation.

Acknowledgment

The author is grateful to Dr. Nwe Nwe Win, Professor and Head of Department of Civil Engineering, Technological University (Mandalay) for her invaluable guidance and advice. The author expresses her sincere thanks to her supervisor, Dr. Kyaw Naing Soe, Professor, Department of Civil Engineering, Technological University (Mandalay) for supporting necessary suggestions and effective directions. The author recognizes and expresses gratitude for her supervisor's assistance to complete this work throughout the whole length of this research. The author would like to express special thanks each and every teacher in the Civil Engineering Department at Technological University (Mandalay). Finally, the author wishes to deeply thank her parents for all of their support, patient and encouragement throughout the years.

REFERENCES

[1] Htoo, Ni Lar Myint, and Daw Win Moe Moe Kyaw. "Tourism development and effects of covid-19 on tourism in Myanmar." International Journal Of Tourism 2, no. 1 (2023).

[2] Addepalli, Sri, Gerardo Pagalday, Konstantinos Salonitis, and Rajkumar Roy. "Socio-economic and demographic factors that contribute to the growth of the civil aviation industry." Procedia Manufacturing 19 (2018).

Investigation on Seismic Risk of Existing Building in Sagaing

Su Myat Naing[1], Nwe Nwe Win[2]

[1]*Department of Civil Engineering, Technological University (Mandalay)*
[2]*Department of Civil Engineering, Technological University (Mandalay)*

Email: [1]dawsumyatnaing.sgg@gmail.com, [2]nwenwewin.ce@gmail.com

***Abstract*— This study presents an investigation of seismic risk of three-storey reinforced concrete existing building. The existing building is being constructed in Sagaing (0.2 sec spectral acceleration of 1.8 and 1sec spectral acceleration of 1.2) at a basic wind speed of 80 mph. This building is being used as the main building of the Technological University (Sagaing) and all loadings on the structure are considered according to the American Society of Civil Engineers (ASCE 7-10). The required wind and earthquake data are used from the Myanmar National Building Code (MNBC 2020). Firstly, visual inspection of this building is done to find out the existing condition of the structural dimensions with measure tapes and material strength with rebound hammer test. Then the structure is initially analyzed and designed with nonlinear time history analysis. Stability checks are also done ASCE 7-10. From the results, it is found that the stability checking results are exceed the limitation. Non-linear static analysis (pushover) is carried out with gravity plus earthquake load by using a displacement coefficient method to investigate on seismic risk of the existing building.**

***Keywords*— existing building, pushover analysis, rebound hammer, seismic, stability checking, time history**

I. Introduction

An earthquake is a natural phenomenon characterized by the shaking of the Earth's surface. It occurs when there is a sudden release of energy that has been stored within the Earth's crust. This energy release seismic waves, which are vibrations that propagate through the Earth. One type of seismic wave is called the S wave, which moves in a sideways motion and is responsible for the shaking felt during an earthquake. The intensity and characteristics of an earthquake can vary depending on the specific seismic activities happening in a particular region. These activities include the movement of tectonic plates, volcanic eruptions, and other geological processes. Understanding these factors is crucial for assessing earthquake risks and implementing appropriate safety measures to protect lives and infrastructure. During an earthquake, the stored energy accumulated within the earth's crust is suddenly released, leading to the rapid movement and displacement of rock masses along fault lines. Earthquakes are one of the most destructive natural hazards that cause huge amount of loss of life and property [1].

Technological University (Sagaing) is a prominent educational institution located in Sagaing, Myanmar. The area of Technological University (Sagaing) is 86.98 acres wide, Kyaut Sitt Quarter on the Mandalay-Monywa highway. The main building of the Technological University Sagaing is a significant landmark in the city. In this university campus, the RC main building is a large and impressive structure that houses various departments, convocation hall, library, classrooms, laboratories, and administrative offices. It has frequently experienced earthquakes with various intensities. So, there is a requirement to check whether the structure's safe or not and what the performance level is. There are several methods to evaluate the structural performance of an existing building, including visual inspection, non-destructive testing, structural analysis, historical data analysis, and expert opinion. The evaluation of seismic risk of an existing building is a critical undertaking to ensure the safety and structural integrity of the facility. The structural assessment of the existing building is carried out through a ground field survey such as measure tapes and rebound hammer to gather data on the structural member sizes and compressive strength. The collected data is then used in an initial structural analysis and design check through dynamic analysis to evaluate the building's stability under Design Basic Earthquake (DBE) and Maximum Considered Earthquake (MCE). Non-linear static analysis (pushover) is carried out with gravity plus earthquake load by using displacement coefficient method to evaluate the performance levels of this building.

II. Objectives of the Study

The main objectives of this research are:

1. To analysis and design of existing three-storeyed reinforced concrete building at Technological University (Sagaing)
2. To investigate the seismic risks such as failure structural members and the structural performance levels of the existing building

III. Structural Configuration of Existing Building

The foundation depth of existing building is 8 ft. It is located in seismic zone V. The followings are the existing dimensional information for the building. Figure 1 is presented main building of Technological University (Sagaing).

Length of structure	= 396 ft
Width of structure	= 288 ft
Overall height of structure above ground level	= 74ft-4in
Typical storeyed height	= 14 ft
Total number of columns	= 1281
Total number of beams	= 2146
Shape of the structure	= Rectangular shaped
Structural type	= University
Location	= Sagaing

Fig.1. Main Building of Technological University (Sagaing)

IV. Data Collection of the Existing Building

The current state of the building has been assessed through an initial visual inspection, as well as data collection using rebound hammer tests and surveys conducted with measuring tapes to determine the structural layout and dimensions of its components. This preliminary evaluation methodology has been employed as part of this research to gather information on the building's condition and characteristics. The following equation (1) is used to calculate the size of the required sample for rebound hammer test,

$$n = \frac{z^2 p\,(1-p)}{e^2} \quad (1)$$

n = required sample size
z = level of confidence 1.95
(95% confidence level)
e = margin error (5%)
p = estimated proportion of the population (95%)

A total of 70 column locations, 71 beam locations, and 69 slab locations were selected for material strength testing using the rebound hammer method. The structural member sizes of the existing building under assessment by measure tape are described in Table I.

I. Data collection of Existing Building

Structural Details	Ground Floor	First Floor	Second Floor	Roof Floor	Remark
Building dimension (ft × ft)	396 × 288	396 × 288	396 × 288	396 × 288	By surveying
Column size (in ×in)	12×12 15×15 18×18 15×24 18×24	12×12 15×15 18×18 15×24 18×24	12×12 15×15 18×18 15×24 18×24	12×12 15×15 18×18 15×24 18×24	By surveying
Beam size (in × in)	12×12 12×15 12×20	12×12 12×15 12×18 12×20	12×12 12×15 12×18 12×20	12×12 12×15 12×18 12×20	By surveying

The selection of sample locations for testing concrete strength is based on areas with damage, cracks and exterior corners. The average concrete strength of samples taken from selected columns, beams and slabs, and the mean value is considered as the design material strength for the columns beams and slabs. The compressive strength of columns and beams is used 3000 psi for existing building. The minimum compressive strength of slabs values 2000 psi for slabs are used as the design material strength for the entire building during the design check. Fig.2. to Fig.4. show the existing structural damage of highlight in some places. The existing condition of the building visually shows the requirement of structural strengthening.

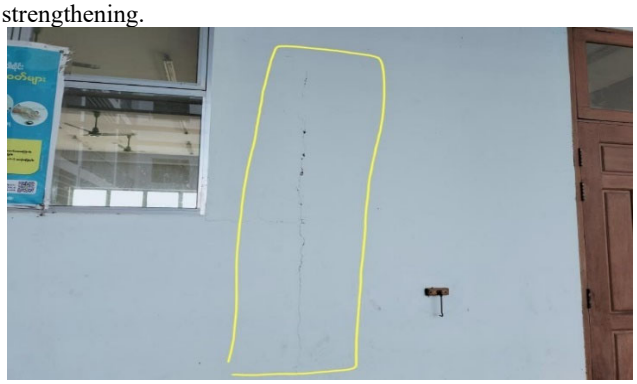

Fig. 2. Wall Cracks in Ground Floor

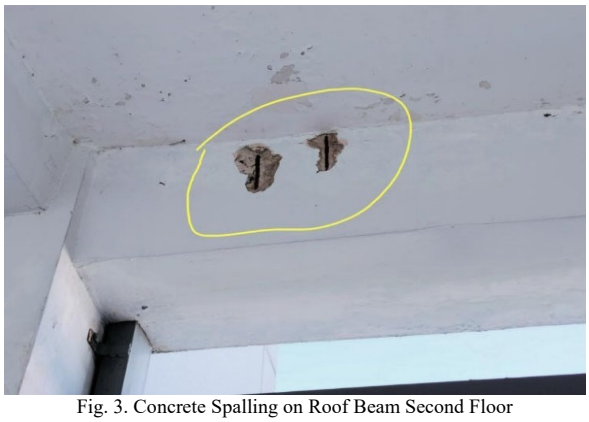

Fig. 3. Concrete Spalling on Roof Beam Second Floor

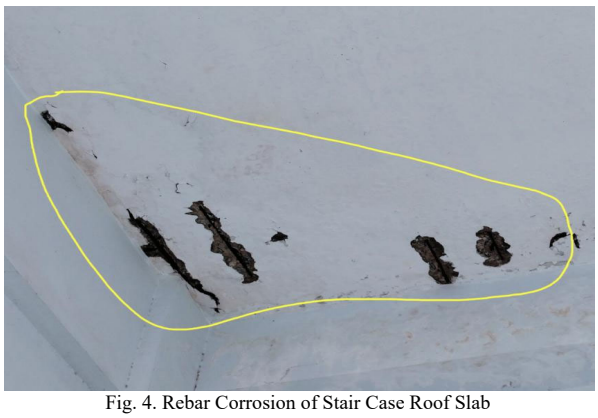

Fig. 4. Rebar Corrosion of Stair Case Roof Slab

V. Modelling of the Existing Building

The main building is rectangular-shaped reinforced concrete building located in Sagaing. The plan view and 3D view are shown in Fig.5. and Fig.6., respectively.

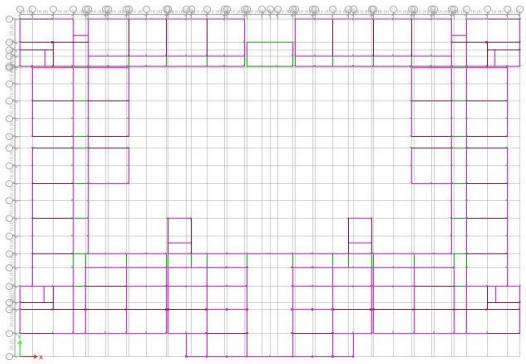

Fig. 5. Plan View of the Existing Building

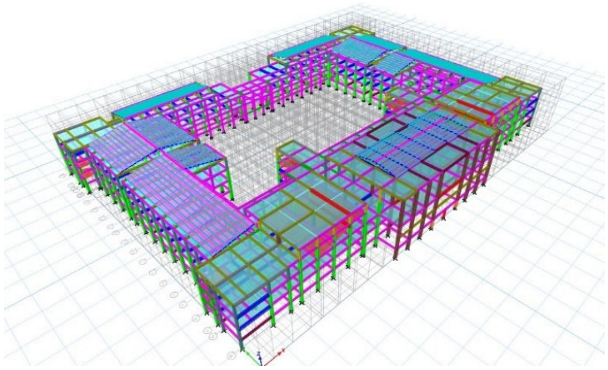

Fig. 6. 3D View of the Existing Main Building

VI. Data Analysis of the Existing Building

After surveying and testing the strength of the structure, the whole building consists of 2122 number of beams and 1352 number of columns. The existing building is analyzed by nonlinear time history without changing the actual member size of the building and structural stability is carried. Ground motions data has been selected from PEER (The Pacific Engineering Earthquake Center) ground motion database by using approximate parameters. This ground motion is properly matched to MNBC -2020 code specified design elastic response spectrum DBE and MCE levels. The ground motion record data is shown in Table II.

II. Selected and Scaled Earthquake Ground Motion Record Data

Record Sequence Number	Earthquake Name	Year	Station Name	Magnitude
22	El Alamo	1956	El Centro Array #9	6.8

Spectral acceleration at short and 1 sec period for DBE and MCE levels according to MNBC 2020 are as follow,
Design spectral acceleration at short period, S_{DS}= 1.2
Design spectral acceleration at 1 sec period, S_{D1}=1.2
Maximum spectral acceleration at short period, S_{MS}=1.8
Maximum spectral acceleration at 1 sec period, S_{M1}=1.8

III. Stability Checking Of the Existing Building (DBE)

Stability Checking	X-Direction	Y-Direction	Limit	Remark
Story Drift	20.2	13.67	≤ 2.48	Not Ok
P-Delta Effect	0.604	16.589	≤ 0 .1	Not Ok
Torsional Irregularity	1.456	0.999	≤ 1.2	Not Ok
Overturning Moment	15.971	0.557	≥ 1.5	Not Ok
Sliding	0.742	0.659	< 1.5	Not Ok

IV. Stability Checking of the Existing Building (MCE)

Stability Checking	X-Direction	Y-Direction	Limit	Remark
Story Drift	30.3	21.16	≤ 2.48	Not Ok
P-Delta Effect	0.604	0.416	≤ 0.1	Not Ok
Torsional Irregularity	1.873	1.432	≤ 1.2	Not Ok
Overturning Moment	4.664	0.463	≥ 1.5	Not Ok
Sliding	0.514	0.659	< 1.5	Not Ok

According to Table III and Table IV, all of the stability checking is not satisfied within the limitations. A total structural member of 427 beams and 57 columns are failed on the existing building at MCE level. Most of the failure structural members are found in ground floor. In First floor and second floor, only interior column and beam locations are failed. At most 4 columns and 20 beams are failed at roof floor level. So, the existing three-storeyed RC building needs to be retrofitted to improve its stability.

VII. Pushover Analysis of the Existing Building

Nonlinear static (pushover) analysis is conducted to assess the performance levels and safety of the existing three-storeyed RC building. This type of analysis allows for the identification of potential weaknesses, assessment of the building's overall stability, and determination of structural characteristics to improve its safety and structural integrity. Displacement control analysis method, 2 percent of total structure heights 12.55 in is used for displacement control value subjected to roof level at joint 66.

A. Structural Performance Levels

Performance level in seismic engineering refers to the anticipated behavior of a building during a design earthquake, based on the extent of damage to both structural and non-structural components. There are five distinct levels of global structural response that are determined through pushover analysis:

- Operational (O) level,
- Immediate Occupancy (IO) level,
- Life Safety (LS) level,
- Collapse Prevention (CP) level,
- Collapsed (C) level.

Hinge locations are assigned 5 percent from the length of columns and beams end. The deformed shape and pushover curve for PushX and PushY of the existing building results shown in Fig. 7 to Fig. 10.

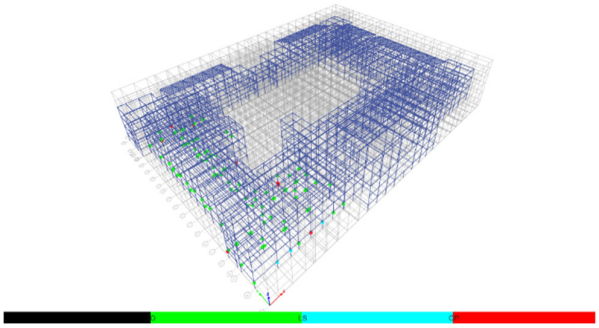

Fig. 7. Deformed Shaped for PushX

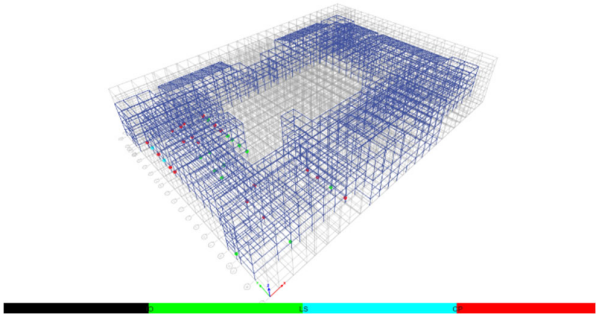

Fig. 8. Deformed shape for PushY

V. Base Shear vs Monitored Displacement for Push X

Time Steps	Displace-ment (in)	Base Force (kip)	A-IO	IO-LS	LS-CP	> CP	Total Hinges
0	0.000	0.0	6806	0	0	0	6806
1	1.255	1995.0	6806	0	0	0	6806
2	1.550	2463.7	6806	0	0	0	6806
3	2.821	4470.3	6806	0	0	0	6806
4	4.087	6179.5	6801	1	0	4	6806
5	5.454	7845.5	6775	24	1	6	6806
6	5.798	8252.5	6748	49	3	6	6806
7	5.798	8244.5	6747	50	2	7	6806
8	6.171	8685.6	6707	88	4	7	6806
9	6.171	8675.1	6705	90	4	7	6806
10	6.260	8782.4	6699	96	3	8	6806

The above Table V shows the existing structure in Push X has demonstrated its performance level across steps 1 to 10. From steps 4, the structure is deemed to be at the immediate occupancy (IO) level, indicating that it can be occupied and used safely. As the analysis progresses to step 4, the structure transitions to a state between IO and life safety (LS) levels, suggesting a slight decrease in performance but still within acceptable limits. By steps 4 and 10, the structure surpasses the collapse prevention (CP) level, indicating significant damage and plastic hinge formation in both columns.

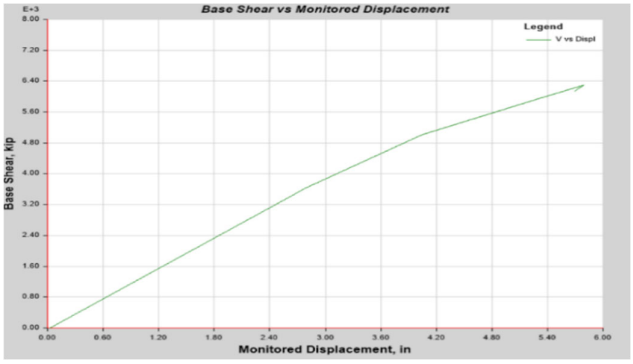

Fig. 9. Pushover curve for PushX

The slope of the pushover curve is gradually changed with the increase of the lateral displacement of proposed building. This is due to the progressive formation of plastic hinges in columns throughout the structure. The pushover curve reaches a maximum which corresponds to failure of the building. The damage level starts at a displacement of 4.087 in and ends at a displacement of 6.26 in.

VI. BASE SHEAR VS MONITORED DISPLACEMENT FOR PUSH Y

Time Steps	Displace-ment (in)	Base Force (kip)	A-IO	IO-LS	LS-CP	> CP	Total Hinges
0	0.026	0.0	6806	0	0	0	6806
1	1.281	1649.5	6806	0	0	0	6806
2	2.536	3299.0	6806	0	0	0	6806
3	2.779	3617.9	6806	0	0	0	6806
4	4.049	5008.6	6804	0	0	2	6806
5	5.343	5975.1	6780	9	1	16	6806
6	5.793	6291.9	6772	15	1	18	6806
7	5.692	6140.8	6772	13	2	19	6806

The performance level of the existing structure in Push Y reach step 1 to 7 are shown in Table VI. In step 4 to 7 the structure reaches beyond the CP level. Plastic hinges are formed throughout columns.

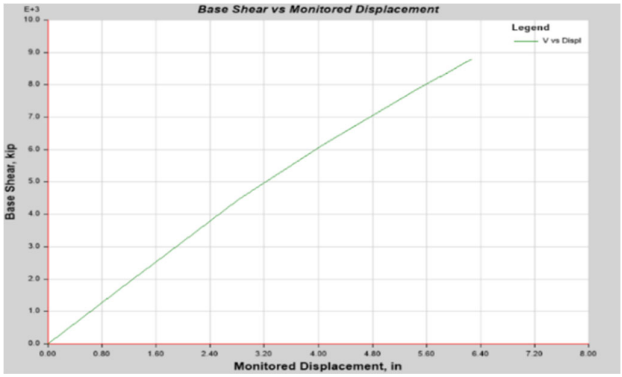

Fig. 10. Pushover curve for PushY

The slope of the pushover curve is gradually changed with the increase of the lateral displacement of proposed building. This is due to the progressive formation of plastic hinges in beams and columns throughout the structure. The pushover curve reaches a maximum which corresponds to failure of the building. The damage level starts at a displacement of 4.049 in and ends at a displacement of 5.692 in.

VIII. CONCLUSION

In this study, the existing building is a three-storeyed reinforced concrete main building, which is situated in the Technological University (Sagaing). The existing building is constructed by using older design concepts that mostly emphasized gravity loads only and the design code. The existing condition of the building visually shows the requirement of structural strengthening for minor repairs. The require local wind speed and earthquake data are taken from the MNBC 2020 which are used to analyse the existing building by non-linear time history analysis. The results were indicated that the structure is not stable in the event of a severe earthquake, leading to the need for seismic strengthening.

Pushover (nonlinear static) analysis is carried out to investigate the performance levels of the existing building. The roof displacements at joint 66 is considered to evaluate the performance levels of proposed building. Lateral displacement of the building is considered in both X-direction and Y-direction to evaluate the performance by calculating the roof displacement. By the studying of plastic hinge mechanism of structure, the structural performance levels and the first failed parts of the structures can be known. It is found that, plastic hinge formations are occurred at near the joint 66. So, it can be concluded that-

- According to the results of stability checking in dynamic analysis, the existing building was not efficient for lateral loads.
- By studying the plastic hinge mechanism of structure, the structural performance levels of existing building is beyond collapse prevention.
- In push X, 99.8% of the frame remains at the IO level, requiring minor retrofitting for continued safety, while the remaining 0.2% necessitates major repairs to maintain structural integrity reaches beyond the CP level.
- Push Y shows 99.7% of the frame is at IO level and needs to be retrofitted in minor repairs. 0.3% of the frame needs to maintain in a major repair.

As a result, the building's performance levels are beyond collapse prevention. Some falling debris hazards may have occurred because of substantial structural and nonstructural damage. So, the building needs to be strengthened by appropriate method.

ACKNOWLEDGMENTS

The author would like to express her heartfelt gratitude to Dr. Su Yin Win, Acting-Rector, and Dr. Hnit Thit Shein, Pro-Rector, Technological University (Mandalay).

The author is deeply indebted and wishes to extend grateful thanks to her supervisor, Dr. Nwe Nwe Win, Professor and Head, Department of Civil Engineering,

Technological University (Mandalay), for her guidance, advice, invaluable encouragement and supervision throughout the preparation of this research.

The author thanks to all her teachers from Department of Civil Engineering for their supports, advice, helpful comments and special interests.

REFERENCES

[1] Myanmar Engineering Council, Myanmar National Building Code, (2020).

[2] Seismic evaluation and retrofitting of an existing building in Athens using pushover analysis by Angelos Lazaris, (2019).

[3] Seismic Evaluation and Strengthening of the Exising Building by Dr. Durgesh C. Rai, (2005).

[4] American Concrete Institute Committee,"*Building Code Requirements for Structural Concrete (ACI 318-14)"*. U.S.A. American Concrete Institute, (2014).

[5] American Society of Civil Engineering, "*Minimum Design Loading for Buildings and Other Structures"*, USA,(2010).

[6] Federal Emergency Management Agency (FEMA 356) Pre standard and Commentary for the Seismic Rehabilitation of Buildings.

[7] Statics Formulas and Problems by Dietmar Gross- Wolfgang Ehlers Peter Wriggers, Jorg Schroder Ralf Muller.

Comparative Study on Performance Assessment of Asymmetrical Buildings

Su Yin Min Thwe[1], Nwe Nwe Win[2]

[1]*Technological University (Mandalay), Department of Civil Engineering*

[2] *Technological University (Mandalay), Department of Civil Engineering*

Email: [1]chawsu.cs.1997@gmail.com, [2]nwenwewin.ce@gmail.com

***Abstract*— This paper represents the comparative study on the performance assessment of asymmetrical buildings. Buildings are designed to resist earthquake forces and to minimize the structural damage. However, despite these design efforts, buildings can still have structural and non-structural damages and pose risks to building's occupants when an earthquake occur. Therefore performance assessment is required to know the amount of damage a structure may experience due to earthquake and determine the probable consequences of that damage such as repair cost, repair time and the number of injuries. In this study, two asymmetrical buildings, L and S shaped reinforced concrete buildings are used to compare their performances. Both structures are designed according to ACI 318-14 when the buildings are subjected to design basic earthquake (DBE) and maximum considered earthquake (MCE) level events in Mandalay. The story drift ratio and story acceleration obtained from nonlinear time history analysis is used to assess the seismic performance of the structure. The level of damage that a building experiences in an earthquake depends on the intensity of ground motion. Therefore the intensity based performance assessment is conducted for both buildings. The performance assessment calculation tool (PACT) is used for the performance assessment of the buildings. The performances are measured by means of repair cost, repair times and the number of injuries. Also, the performance results are compared for L and S shaped buildings. According to the performance assessment data, S shaped building is found to be a better performance than L shaped building.**

Keywords—Asymmetrical, fragility component, intensity based performance, PACT, story drift ratio.

I. INTRODUCTION

The seismic resistance buildings are designed according to prescriptive criteria contained within the building code. The code based design could achieve the goal of preventing loss of life or life threatening injuries to building occupants but they do not provide the designers with a means to determine if other performances would be achieved. In many cases, buildings designed to older codes may not perform adequately under modern seismic demands which can lead to structural upgrades and retrofits to enhance future performance and safety. Preventing losses before they happen is the effective way of reducing the impact of disasters [1]. One of the promising way to reduce the damages from an earthquake or similar disaster is to assess the performance of the building. The performance assessment of buildings allows building's owners or regulators to understand the risk of life, occupancy, and economic loss that may occur as a result of future earthquake. Assessing economic implications of post-earthquake damage involves estimating repair cost, downtime and potential loss of revenue. Buildings with better seismic performance typically have lower repair costs and shorter downtime. In some cases, the damage may be too costly to repair, leaving demolishing as the only option.

The Federal Emergency Management Agency (FEMA) developed the Performance Assessment Calculation Tool (PACT) software to assess the performance of the building. The performance measures in PACT software are related to the amount of damage the building may experience and the consequences of that damage including: potential casualties; loss of use or occupancy; and repair time and reconstruction costs [2]. PACT provides a user friendly platform for scenario-based, intensity-based, and time-based loss calculations. It can accommodate results obtained from nonlinear time history analyses as well as simplified analyses.

The performance assessment of buildings is critical for minimizing the number of injuries by ensuring structural integrity and safety. It helps identify the potential issues before an earthquake happen, thereby reducing repair costs and preventing costly emergency interventions. Furthermore prior assessments enable quicker repairs and restorations. According to previous seismic study, it is found that most of the structure failure occurs in irregular and asymmetrical buildings. Despite the previous proof of failure in system, asymmetric in plan is unavoidable in practical. Therefore, asymmetrical L and S shaped buildings are chosen to make performance assessments. And their performances are compared to know which building is more safety and economically beneficial for the building's occupants.

II. BUILDING INFORMATION

The propose buildings are L and S shaped twenty storeyed reinforced concrete residential buildings.

A. Material Properties

The same material properties were used for both structures.

The material properties are as follows:

- Concrete compression strength =4000psi
- Reinforcing yield stress = 60000psi
- Modulus of elasticity = 3605 ksi
- Weight per unit volume of concrete =150 pcf
- Poisson's ratio = 0.2

B. Structural Member Sizes

The same structural member sizes were used for both structures.

The structural member sizes are as follows:

- Column up to 6^{th} storey = 30in x 30in

- Column between 6th - 11th storey = 24in x 24in
- Column between 11th -16th storey = 18in x 18in
- Column between 16th – 21st storey = 15in x 15in
- Beam up to 11th storey = 18in x 24in
- Ground Beam = 12in x 18in
- Floor Beam = 12in x 18in
- Secondary beam = 12in x 15in
- Slab = 4 in
- Shear wall = 8in

C. Architectural Plan

The proposed L shape building has an area of 7110 square feet and S shape building has an area of 9480 square feet. The overall height of both structures is 240 feet. Architectural plan of the buildings are shown in Fig. 1 and Fig. 2.

Fig. 1. L shaped plan

Fig. 2. S shaped plan

III. Performance Assessment Process

For the performance assessment of the proposed structures, the models are built in PACT software by putting building characteristic, building population and fragility components. Then the assessment method is selected and input the seismic response data from nonlinear time history analysis.

A. Building Characteristic

The first step of building performance model is to input the building information including the date cost multiplier and region cost multiplier to adjust provided component repair cost to appropriate present value since the repair cost function is based on region of Northern California in 2011. According to the consumer price index (CPI) data provided by the U.S. Department of Labor and Bureau of Labor Statistic, the CPI value of Northern California in 2011 is 230% and 295% in 2022 [3]. The yield cost 28% is obtained by using relative change formula on these two CPI values. Therefore the date cost multiplier is taken as 1.28 for both L and S shaped structures. For the region cost multiplier, the yield cost is calculated by using relative change formula on CPI of Myanmar and Northern California. According to Trading Economic website, the consumer price index of Myanmar is 196% and the consumer price index of Northern California is 295% [4]. The calculated yield cost is (-34%) and the region cost multiplier is taken as 0.66 for both Land S shaped buildings. The necessary input factors are as follow;

Height factor for Floor 1-4 = 1.00
Height factor for Floor 5-10 = 1.08
Height factor for Floor 11-21 = 1.16
Hazard Factor =1
Occupancy Factor = 1.2

The aforementioned factors are taken according to PACT implementation guidelines

B. Building Population

Population model is defined to assess injury rate. The population model includes hourly distribution of people per 1000 square feet for week days or weekend and can be adjusted to include further variation by month. The program provided population model corresponded to multi-unit residential occupancy is used for this study. The peak number of occupants per 1000 square feet is taken as 5. The same population model is used for both L and S shaped buildings.

C. Fragility Component and Performance Group

The fragility components for multi-unit residential occupancy are selected from provided components in PACT. The normative quantity estimation tool which is an exele spread sheet provided by FEMA P-58, is used to determine the type and quantity of components for multi-unit residential building. The floor area of each building and type of occupancy are put into the exele spread sheet so the link in the exele sheet can identify the type and quantity of components. After setting the type and quantity of components in PACT, the fragility curves are developed for each component. The storydrift ratio and story acceleration data are used as demand parameters to build fragility curves. The selected components have fragility curves that have already defined in PACT. Also, the consequances repair function have already defined in PACT. PACT organizes the selected fragility components and forms the performance group for each floor. The selected fragility components and the quantities for this study are shown in Table I.

I. SELECTED FRAGILITY COMPONENTS AND QUANTITIES FOR THE PROPOSED BUILDINGS ABLE TYPE STYLES

Category	Fragility Component	Quantity Unit per One Component in PACT	Quantity Input into PACT	
			L shape	S shape
Wall Partition	Gypsum with metal studs, Full Height	100LF	2.20	2.80
Wall Finishes	Gypsum + Wallpaper, Full Height	100LF	4.40	5.80
	Gypsum + Ceramic Tile, Full Height	100LF	3.90	5.20
Floor Finishes	Raised access floor, seismically rated	100SF	4.70	6.20
Ceiling	Suspended Ceiling, Area (A): A < 250	250SF	22.60	30.1
Plumbing	Domestic Water Piping, Cold Water Piping (Dia> 2.5 inches), Piping Fragility	1000LF	0.80	1
	Domestic Water Piping, Cold Water Piping (Dia> 2.5 inches), Bracing Fragility	1000LF	0.80	1
	Domestic Water Piping, Hot Water Piping (Dia> 2.5 inches), Piping Fragility	1000LF	0.21	0.28
	Domestic Water Piping, Hot Water Piping (Dia> 2.5 inches), Bracing Fragility	1000LF	0.21	0.28
	Sanitary Waste Piping ,Cast Iron and spigot couplings (Dia> 2.5 inches), Piping Fragility	1000LF	0.86	1.15
	Sanitary Waste Piping ,Cast Iron and spigot couplings (Dia> 2.5 inches), Bracing Fragility	1000LF	0.86	1.15
Fire Protection	Fire Sprinkler Water Piping - Horizontal Mains and Branches	1000LF	1.60	2.1
	Fire Sprinkler Drop Standard Threaded Steel	100EA	0.90	1.1
Elevator	Traction Elevator	1EA	3.00	4.00

Where, LF is Linear feet, SF is square feet and EA is each. Since the proposed buildings has twenty floors, the same components and quantities are used for every floor of the buildings.

D. Selected Assessment Method And Inputting Demand Value

Among the assessment method available in PACT, "Intensity-based Assessment" is chosen for this study. The intensity-based assessment evaluates the probable performance of a building when it is subjected to specified earthquake shaking intensity. The performance of proposed buildings is determined under two seismic events: DBE (Design Basic Earthquake) and MCE (Maximum Considered Earthquake). The demand parameters such as story drift ratio and story acceleration data obtained from nonlinear time history analysis are used as input data into PACT.

IV. PERFORMANCE ASSESSMENT RESULTS OF THE PROPOSED BUILDINGS

After building the performance model and putting the demand value such as story drift ratios and story accelerations, the seismic performance of the proposed buildings are calculated. According to PACT guidelines, the mean value that has the probability of 50% is taken as the performance results. As the results of the assessments, the PACT provides the damage (repair) cost, repair time and the number of injuries; the consequences due to DBE and MCE level event in Mandalay.

A. Damage Cost Of The Proposed Building

The X-axis shows the damage costs in thousand dollars and the Y-axis shows the probability of repair cost. The estimated medium repair cost which has 50% probability is taken as the performance results. The repair cost for the L and S shaped buildings at DBE and MCE level seismic events are shown from Fig. 3 to Fig. 6.

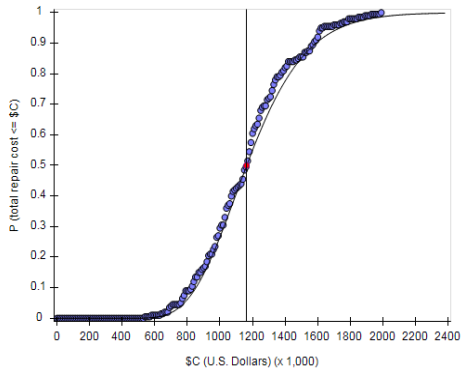

Fig. 3. Repair Cost for L Shaped Building under DBE Level

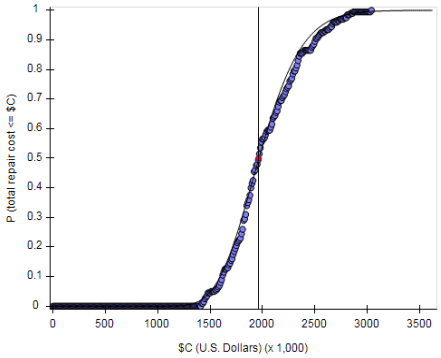

Fig. 4. Repair Cost for L Shaped Building under MCE Level

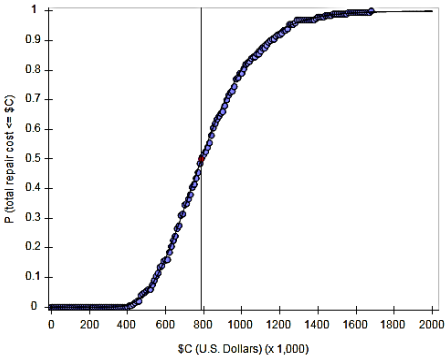

Fig. 5. Repair Cost for S Shaped Building under DBE Level

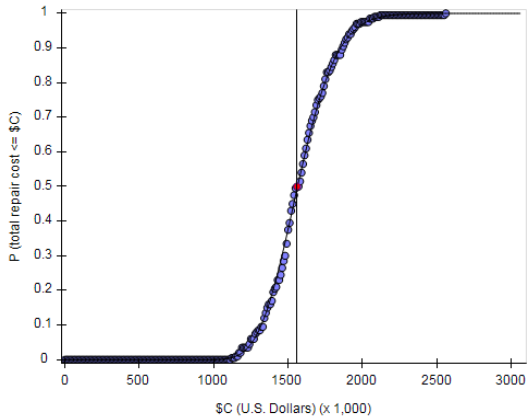

Fig. 6. Repair Cost for S Shaped Building under MCE Level

According to Fig. 3 and Fig. 4, damage cost of L shape building at DBE and MCE levels are $1.16 million and $1.96 million. The damage cost of S shaped building shown in Fig 5 and Fig.6 are $0.79 million and $1.56 million when the building is subjected to DBE and MCE level events.

B. Repair Time of the Proposed Buildings

The X-axis shows the repair times in Days and Y-axis shows the probability of repair time. The mean repair time is taken as the performance results. The repair time for the L and S shaped buildings at DBE and MCE level seismic events are shown from Fig. 7 to Fig. 10.

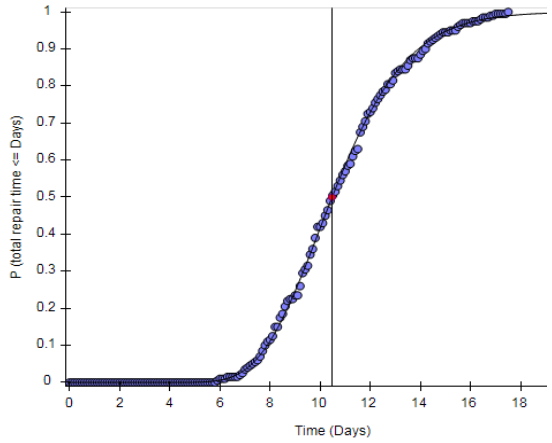

Fig. 7. Repair Time for L Shaped Building under DBE Level

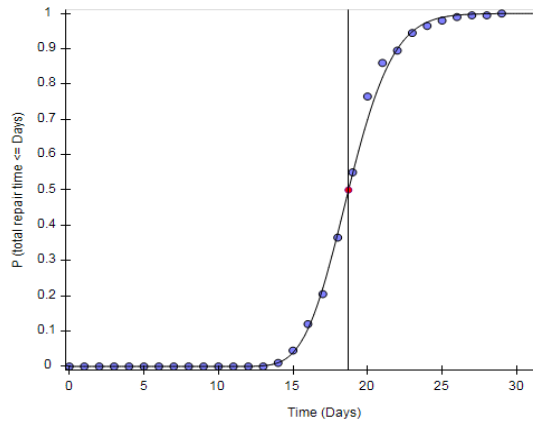

Fig. 8. Repair Time for L Shaped Building under MCE Level

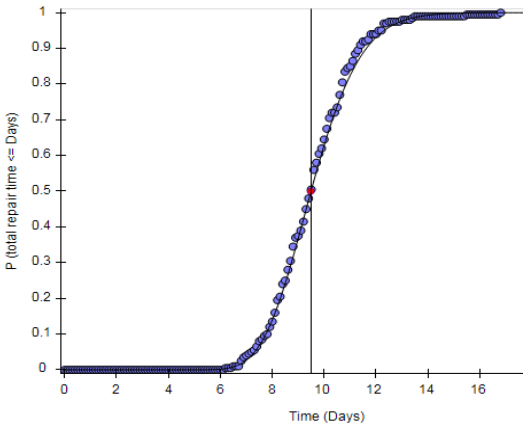

Fig. 9. Repair Time for S Shaped Building under DBE Level

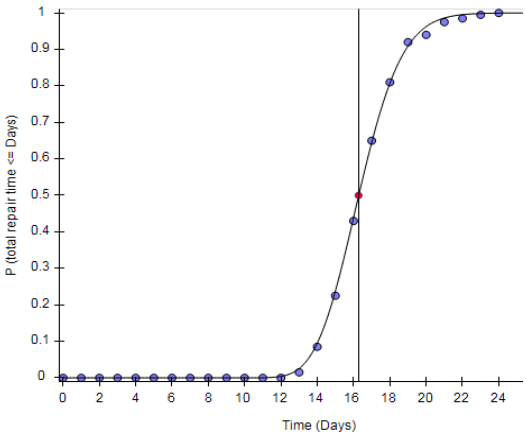

Fig. 10. Repair Time for S Shaped Building under MCE Level

The repair time for L shaped building under DBE and MCE level events are 10.47 days and 18.72 days. For S shaped building, the repair time are 9.2 days under DBE level and 16.3 days under MCE level.

C. Number of Injuries for the Proposed Building

The X-axis shows the number of injuries and Y-axis shows the probability of injuries. The number of injuries with 50% probability are shown in the results. The number of injuries of the proposed buildings due to DBE and MCE levels are shown from Fig. 11 to Fig. 14.

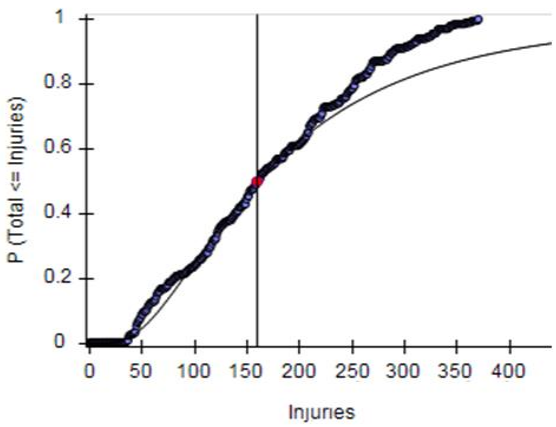

Fig. 11. Number of Injuries of L Shaped Building under DBE Level

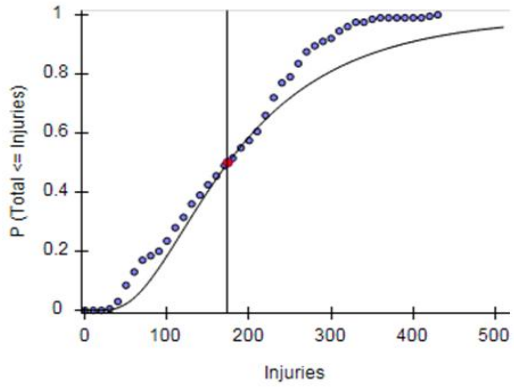

Fig. 12. Number of Injuries of L Shaped Building under MCE Level

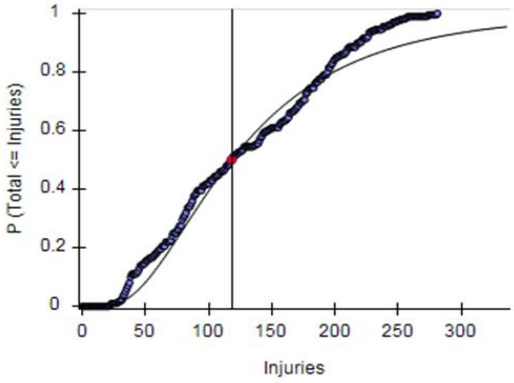

Fig. 13. Number of Injuries of S Shaped Building under DBE Level

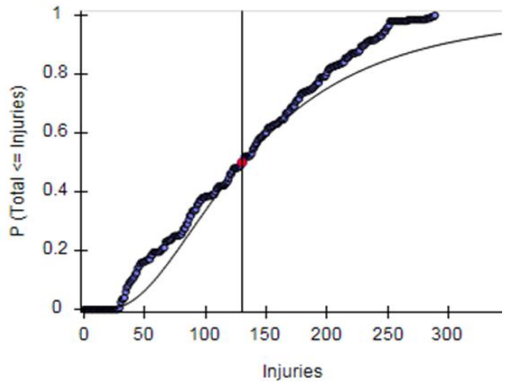

Fig. 14. Number of Injuries of S Shaped Building under MCE Level

In DBE level seismic event, the numbers of injuries of L and S shaped buildings are 159 and 118. In MCE level seismic event, the number of injuries of L and S shape buildings are 174 and 130.

V. Comparison of Seismic Performance Results

To evaluate the better performance of the proposed asymmetrical buildings, seismic performance results are compared in Table II.

II. Comparison of Performance Assessment Results of Proposed Buildings

Shape	Repair Cost ($ Million)		Repair Time (Days)		Number of Injury (Person)	
	DBE	MCE	DBE	MCE	DBE	MCE
L	1.16	1.96	10.47	18.72	159	174
S	0.79	1.56	9.2	16.3	118	130

In DBE level seismic event, it is found that the repair cost of L shaped building is $0.37 million larger than S shaped building as well as $0.4 million larger than S shaped building in MCE level seismic events. So the repair cost of L shaped building is 47% and 26% larger than S shape building in DBE and MCE level. For the repair time, L shaped building need 1.27 more days and 2.42 more days than S shaped building at DBE and MCE seismic events. It is found that the repair cost of L shaped building is 14% and 15% larger than S shaped building. It is found that, in L shape building, 41 and 44 more person will get injuries than in S shape building when subjected to DBE and MCE level seismic events. The number of injuries in L shape building when subjected to DBE and MCE level is 35% and 34% larger than S shape building.

It is found that L shaped building has more repair cost, repair time and number of injures than S shaped building when subjected to DBE and MCE level seismic events. Therefore S shaped building has better performance than L shaped building.

VI. Conclusion

In this study, the seismic performance of L and S shaped buildings are assessed by using PACT software and the results are compared to know the better performance building. According to the assessment data, L shaped building has more damage cost, repair time and number of injuries than S shaped building. Although, S shaped building has larger area and there are more occupants in the buildings than the L shaped building, it is found that more occupants get injury in L shaped building. And the repair costs and time are higher in L Shaped building. Therefore, L shaped building is less economically beneficial for the owners or occupants than S shaped building. According to the performance assessment data of this study, S shape building is found to be a better performance building than L shaped building.

Acknowledgment

First of all, the author would like to thank Dr. Su Yin Win, Acting-rector and Dr. Hnit Thit Shein, Pro-rector of Technological University (Mandalay), for permission to submit this paper. The author would also like to thank Dr. Nwe Nwe Win, Professor and Head, Department of Civil Engineering, Technological University (Mandalay), for her interest and guidance. The author would like to express thanks to all the teachers from the department of Civil Engineering, Technological University (Mandalay), for their effective suggestions and assistance in completing this paper.

References

[1] The Federal Emergency Management Agency, FEMA P-58-1, "*Seismic Performance Assessment of Buildings*", Vol-1, 2nd edition, (2018).

[2] The Federal Emergency Management Agency, FEMA P-58-2, "*Seismic Performance Assessment of Buildings*", Vol-2, 2nd edition, (2018).

[3] US Bureau of Labor Statistics (gov.), "Consumer Price Index" Internet: https://www.bls.gov/CPI.

[4] Trading Economics, "Myanmar Consumer Price Index" Internet: https://tradingeconomics.com. Jul 16, 2023.

Study on The Effects of Infill Wall in The Structural Responses of The Proposed Building

Than Toe Htay[1], Nwe Nwe Win[2]

[1]*Department of Civil Engineering, Technological University (Mandalay)*

[2]*Department of Civil Engineering, Technological University (Mandalay)*

Email: [1]mgthantoehtay123@mail.com, [2]nwenwewin.ce@mail.com

***Abstract* –This study is to comprehensively investigate and analyze the influence of infill walls on the structural responses and seismic behavior of the proposed buildings, with a focus on understanding how the presence of infill walls impacts the overall stability, load distribution, and responses of the structure to seismic forces, in order to provide the buildings with infill walls. The infill walls are placed at the lift core and outer periphery of the building. The width of infill walls is calculated according to the American Concrete Institute, ACI 530-11 by using the equivalent diagonal strut method. All loadings are considered according to American Society of Civil Engineering, ASCE 7-10 and local wind speed and spectral accelerations are based on the guidelines of the Myanmar National Building Code, MNBC 2020. The proposed building is analyzed with response spectrum analysis in ETABS 2016 software. The structural members are designed according to ACI 318-14. The structural responses of the proposed buildings without and with infill walls are compared with storey drift, storey displacement, storey shear and storey stiffness. In this study, it is cleared that structural responses of the proposed building with infill wall at the outer periphery are better than proposed building without and with infill walls at the lift core.**

Keywords— equivalent strut width, infill walls, reinforced concrete building, response spectrum analysis, structural response.

I. Introduction

In highly populated areas, available land area getting scarce. Developers are focusing on high rise building to keep up, the demand for development, business, housing and economic growth. Many cities with skylines featuring high rise buildings to be the landmark of modernization and advancement. In reinforced concrete buildings, the seismic response of structural displacement can be decreased by providing the infill walls as non-structural element [1]. So, the presence of masonry infill walls in reinforced concrete buildings has substantial impact on their seismic response. The development of infill wall in reinforced concrete building has a major effect of structures during moderate to severe earthquakes. This is mainly because of increase in stiffness provided by the infill walls which may either beneficial to the overall structural response [2]. It has been observed that different locations of infills contribute to the lateral stiffness and strength of the frames. A building should be constructed earthquake resistant building during and after earthquake. For this reason, the structure must be certain to sustain structural stability by providing the infill walls in different locations such as the outer periphery and lift core walls. The main purpose of this research is to assess the seismic response of the proposed building under the influence of without and with infill walls at various locations.

II. Data Preperation for The Proposed Building

The proposed building is fifteen-storeyed Y-shaped reinforced concrete building which is situated in Mandalay. The proposed building is composed of infill walls which are provided at lift core and outer periphery. The building is analyzed and designed by using ETABS software. The structure is designed to resist gravitational and lateral forces. The gravity and lateral loads are taken from the ASCE 7-10. The proposed building is analyzed with response spectrum analysis. The proposed building is designed according ACI 318-14.

A. Structural Information

The proposed building is a fifteen-storeyed Y-shaped reinforced concrete building that is considered to use as a multipurpose building which is located in Mandalay. The proposed building is composed of special moment resisting frame. The dimensions of main building are 46 ft and 190 ft in global axis and branches are 76 ft and 37 ft respectively. As a multipurpose building, different functional usages are included in each floor level. The perspective view of the proposed building is described in Fig. 1.

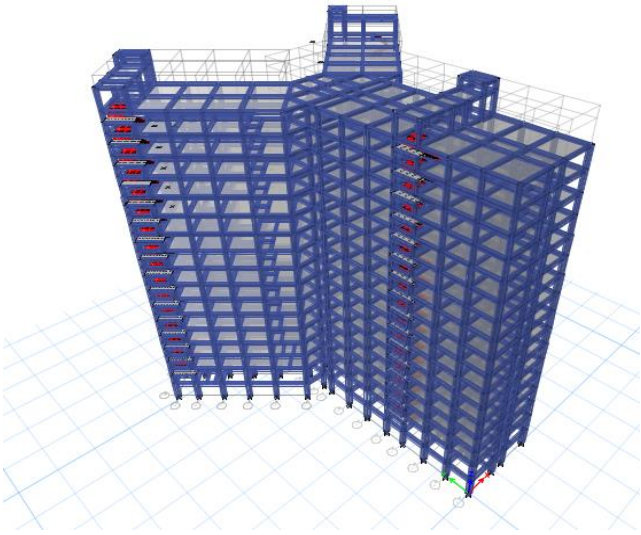

Fig. 1. Perspective view of the proposed building

B. Material Specifications of the Structure

The seismic efficiency of the structures depends on not only their configurations but also their material properties. The properties of clay bricks are taken from ACI 530-11. Material properties used for reinforced concrete structure and infill wall materials are as follows:

Concrete cylinder strength ($f'c$) = 4 ksi

Minimum yield stress (f_y)	= 50 ksi
Types of infill material	= clay brick
Unit weight of clay brick	= 100 lb/in^3
Compressive strength of clay brick	= 1900 lb/in^2
Modulus of Elasticity of clay brick	= 1710000 lb/in^2

II. Structure Model Description of The Proposed Building

The proposed building is situated in Mandalay, highest seismic intensity. The investigation of the impact for infill walls on a building structure, three model cases are considered in this study. The proposed building is composed of without and with infill walls which are placed at various locations are shown in Fig. 2 to Fig. 4. They are

- Model 1 : Without infill walls
- Model 2 : Infill walls at lift core
- Model 3 : Infill walls at outer periphery.

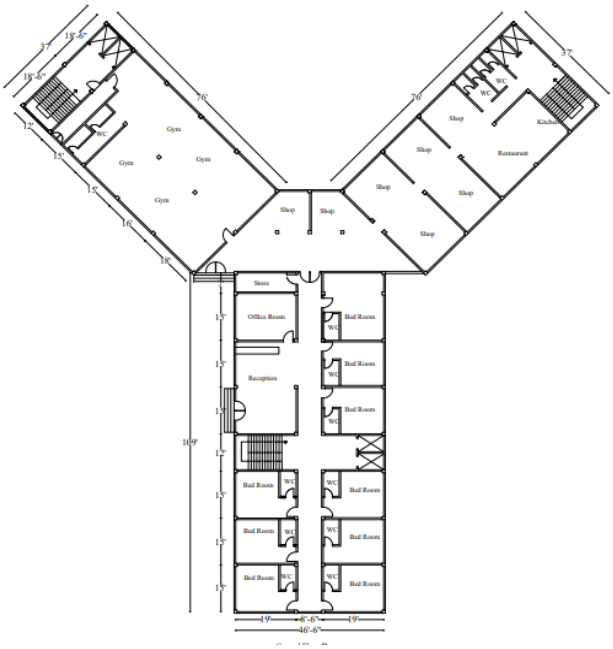

Fig. 2. Without infill wall of the proposed building

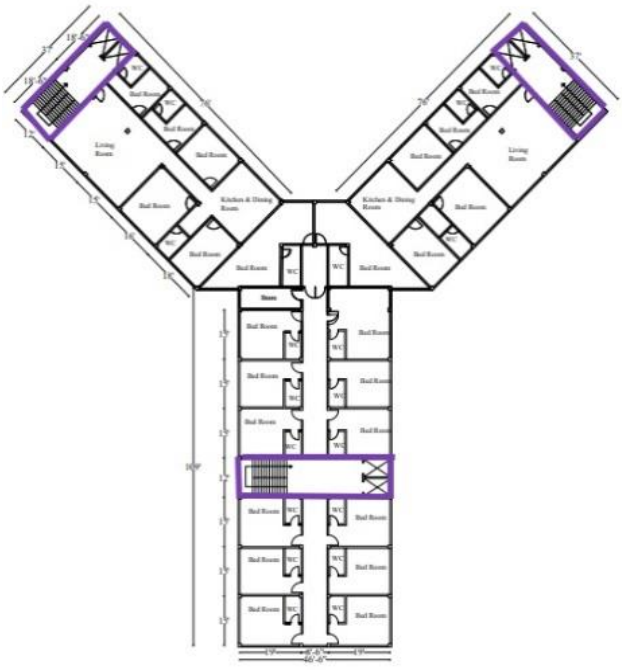

Fig. 3. Infill walls at lift core of the proposed building

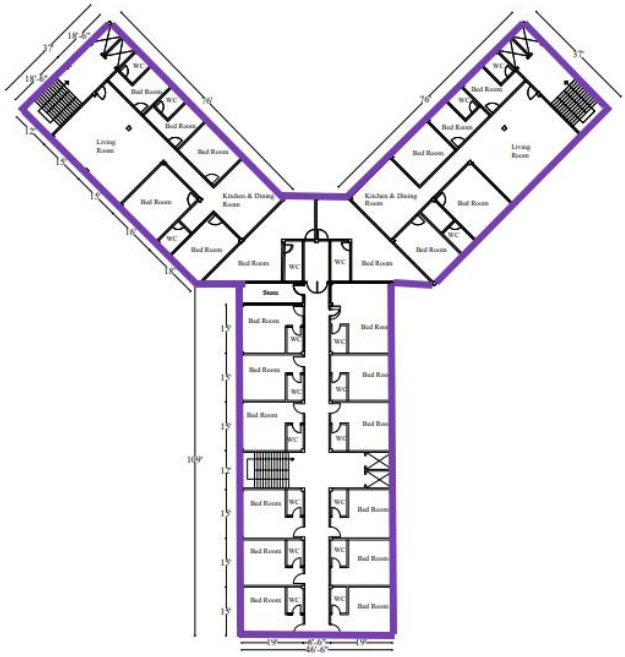

Fig. 4. Infill walls at outer periphery of the proposed building

III. Modelling of Equivalent Diagonal Strut

The inclusion of infill wall in reinforced concrete structures has changed the structural behavior of the building. There are two common types of analysis model for masonry infill. They are macro modeling, which uses an equivalent diagonal strut and micro modeling, which each infill panel is analyzed by finite elements. For this study, modelling of infill is done by macro modelling. Equivalent diagonal strut widths are calculated according to the Federal Emergency Management Agency, FEMA 356. Fig. 5 shows the key parameter for modelling of infill as an equivalent diagonal strut. The sample calculation of infill wall's width between GF and 1F for beam size 22 in × 26 in and column size 30 in × 30 in are illustrated.

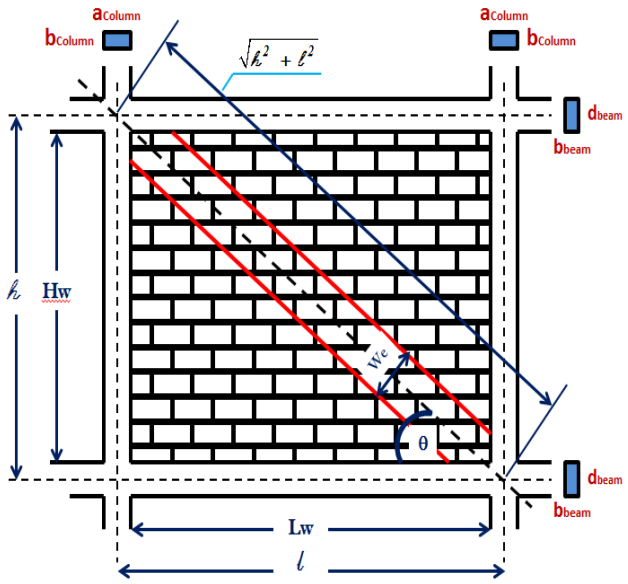

Fig. 5. Key parameter for modelling infill as an equivalent diagonal strut

f'_m = 1900 lb/in^2

E_{me} = 900 f'_m
= 900 × 1900
= 1710000 lb/in^2

t_{inf} = 4.5 in

h_{col} = 13ft ×12

$= 156$ in

$h_{inf} = h_{col}$ – beam depth
$= 156 - 26$
$= 130$ in

$I_{col} = \frac{bd^3}{12}$

$= 67500$ in^4

L_{inf} = span length – column width
$= (19 \times 12) - 30$
$= 198$ in

$r_{inf} = \sqrt{h_{inf}^2 + L_{inf}^2}$

$= \sqrt{130^2 + 198^2}$

$= 236.863$ in

$\theta = \tan^{-1} \frac{h_{inf}}{L_{inf}}$

$= \tan^{-1} \frac{130}{198}$

$= 33.288$ degree

$\lambda_1 = \left[\frac{E_{me} t_{inf} \sin 2\theta}{4 E_{fe} I_{col} h_{inf}} \right]^{1/4}$

$= 0.01828$

a = diagonal strut width
$= 0.175 (\lambda_1 h_{col})^{-0.4} r_{inf}$
$= 27$in

IV. Analysis and Design of The Proposed Building Without And With Infill Walls

The proposed buildings are analyzed with response spectrum analysis. Used as the same materials and structural member sections for without and with infill walls of the proposed buildings. There are fourteen numbers of different design beam cross-sections and four types of columns sections are obtained from analysis and design process which are summarized in Table I and Table II.

I. Table Beam Sections of The Proposed Buildings

Beam Types	Section (in x in)
B1	24 × 24
B2	24 × 28
B3	22 × 28
B4	22 × 26
B5	20 × 26
B6	20 × 24
B7	18 × 24
B8	18 × 22
B9	18 × 20
B10	16 × 22
B11	16 × 20
B12	14 × 20
B13	14 × 18
B14	12 × 14

II Table Column Sections of the Proposed Buildings

Column Type	Story Level	Size (in x in)
C1	Base to 5F	30 × 30
	6F to 9F	28 × 28
	10F to 11F	26 × 26
	12F to SRF	20 × 20
C2	Base	28 × 28
	GF	26 × 26
	1F to 3F	24 × 24
	4F to 8F	22 × 22
	9F to RF	20 × 20
C3	Base	26 × 26
	GF to 3F	24 × 24
	4F to 9F	22 × 22
	10F to SRF	20 × 20
C4	Base to 3F	24 × 24
	4F to 9F	22 × 22
	10F to SRF	20 × 20

V. Stability Checking of the Proposed Buildings

The stability checking of the proposed buildings are carried out with ASCE 7-10 but sliding check is based on UBC-97. The stability checking of X and Y directions of the proposed buildings are summarized in Table III and Table IV.

III. Table Stability Checking of the Proposed Building In X Direction

Stability Check	Model 1	Model 2	Model 3	Limit
Overturning	2.415	2.531	2.261	> 1.5
Sliding	3.589	3.769	3.348	> 1.5
Storey Drift	1.048344	1.0012	0.491502	< 2.64
P-Δ Effect	0.0105	0.0130	0.0052	≤ 0.1
Torsional	1.16571	1.06006	1.14857	< 1.2

IV. Table Stability Checking of The Proposed Building In Y Direction

Stability Check	Model 1	Model 2	Model 3	Limit
Overturning	13.978	13.135	9.536	> 1.5
Sliding	4.733	4.415	3.115	> 1.5
Storey Drift	0.56265	0.7013	0.266442	< 2.64
P-Δ Effect	0.0077	0.0092	0.0027	≤ 0.1
Torsional	1.01435	1.00103	1.00171	< 1.2

According to the above Table III and Table IV, the stability checking of the proposed buildings are within the specified limitation. And so, these structures are stable.

VI. Comparative Structural Response For the Proposed Buildings Without and With Infill Walls

The total number of 501 infill walls are placed at the lift core of the proposed building (model 2) and 869 infill walls are installed at the outer periphery of the proposed building (model 3). The structural responses are compared with storey drift, storey displacement, storey shear, and storey stiffness without and with infill walls in X and Y directions are shown in Fig. 6 to Fig. 10. Model (1), (2) and (3) expressed as in blue, orange and grey color in each figure.

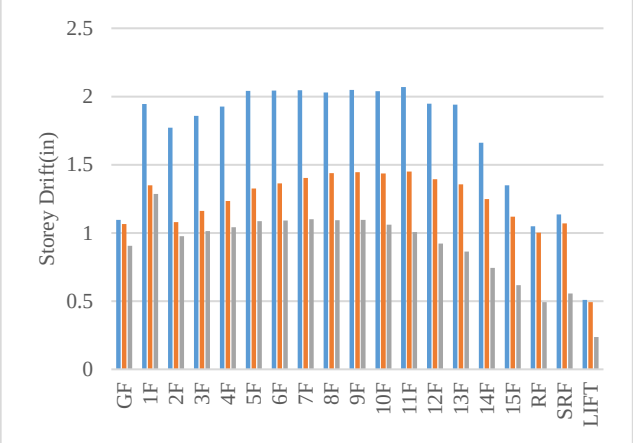

Fig. 6. Storey Drift of the Proposed Buildings in X Direction

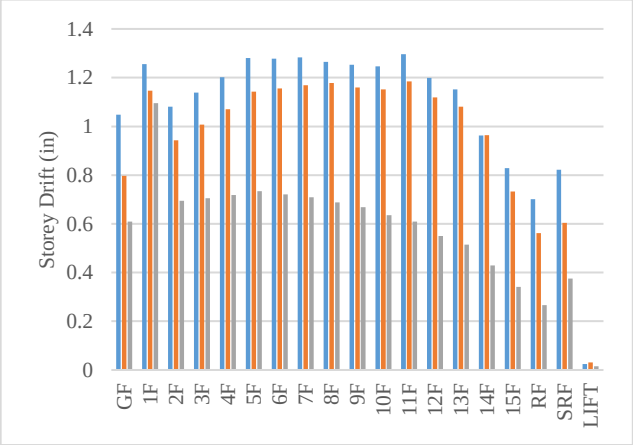

Fig. 7. Storey Drift of the Proposed Buildings in Y Direction

The results of storey drift in X and Y directions for three models are illustrated in Fig. 6 and Fig. 7. The average storey drift of model 2 and model 3 are reduced about 30% and 33% more than model 1 in Y direction. The values of storey drift are also reduced 9% and 13% more than model 1 in Y direction respectively.

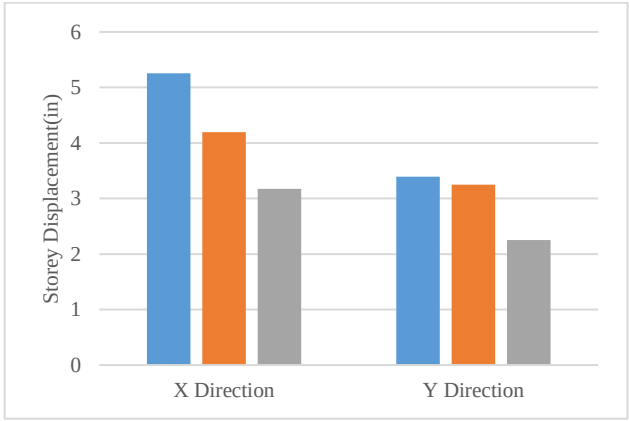

Fig. 8. Storey Displacement of the Proposed Buildings

The above Fig. 8 shows the comparison of storey displacement for the proposed building in X and Y directions. The maximum storey displacements are 5.253 in and 3.395 in in both X and Y direction and the minimum storey displacements are 3.174 in and 2.254 in in both directions occur at the roof level. In model 2, the displacements are decreased about 20% and 4.312% in both directions compared to the model 1. All of these models, storey displacement of the building with outer periphery infill walls (model 3) is nearly 50% decreased in both directions.

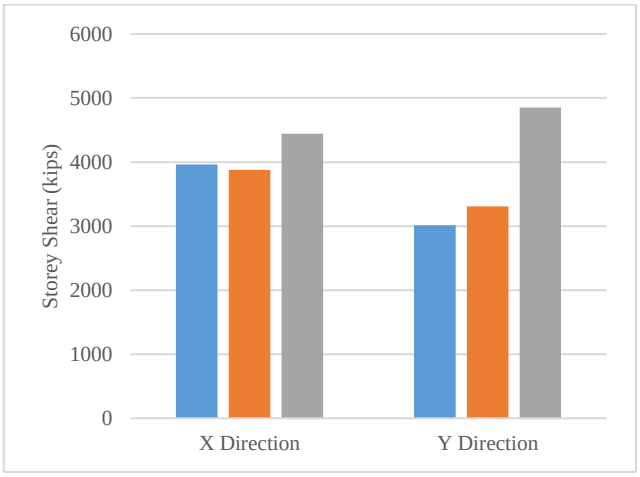

Fig. 9. Storey Shear of the Proposed Buildings

The results of storey shear for proposed building are presented as Fig. 9. The storey shear is greatest at ground floor level. The largest storey shears are occurred at model 3 which are 4443.207 kips and 4851.825 kips in both directions. The storey shear of model 2 is reduced about 2% in X direction but storey shear is increased 10% more than model 1 in Y direction. The storey shear of model 3 is also increased about 12% and 61% more than model 1 in both X and Y directions respectively.

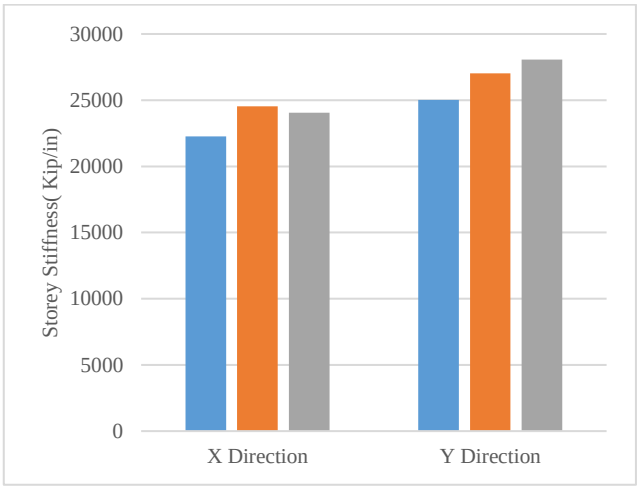

Fig. 10. Storey Siffness of the Proposed Buildings

The storey stiffness for three models is shown as Fig. 10. The minimum storey stiffness is occurred at model 1 which are 22267.283 kip/in and 25028.414 kip/in in both X and Y directions. The stiffness of model 2 is increased 1.12% and 1.1% in both directions than that of model 1. The stiffness of model 3 is increased 1.08% and 1.15% in both directions than model 1.

VII. Conclusion

It has been researched that the infill walls have been changed the structural responses because the infills acting as a bracing in the structure. The non-structural masonry

infill walls are significantly affected on the storey drift, storey displacement, storey shear, but storey stiffness is slightly increased in the structure, leading to increase in seismic resistant of the high-rise multipurposed building. It can be concluded that,

- Storey drift and storey displacement of model 3 (infill walls at the outer periphery) is significantly reduced more than other models in this research.
- Storey stiffness of the model 2 and model 3 are slightly increased than model 1 in both directions.
- Depending on the locations of infill wall of the building, base shear of the proposed building (model 3) is largest due to the presence of infill wall at outer periphery of the proposed building.
- All of these models, placing the infill walls at outer periphery of the proposed building (model 3) is the best suitable location for the proposed building.

ACKNOWLEDGMENT

The author expresses gratitude to Dr. Nwe Nwe Win, Professor and Head of the Department of Civil Engineering at Technological University (Mandalay), for her valuable supervision and careful instruction during this research.

REFERENCES

[1] ASTM C90 Standard Specification for Loadbearing Concrete Masonry Units.

[2] Building Code Requirements for Masonry Structures (ACI 530-11), (2011)

[3] Myanmar Engineering Council, Myanmar National Building Code, (2020).

[4] *"Building Code Requirements for Structural Concrete (ACI 318-14)",* American Concrete Institute, (2014).

[5] "*Minimum Design Loading for Buildings and Other Structures"*, American Society of Civil Engineering, (2010).

Experimental Investigation of Workability and Strength of Mortar with Saw Dust Ash as a Partial Replacement of Cement

Thuzar Win[1], San San Myint[2]

[1]*Department of Civil Engineering and Technological University (Mandalay)*
[2]*Department of Civil Engineering and Technological University (Mandalay)*

Email: [1]thuzarthuzarwin77@gmail.com, [2]sansanmyint.mit73@gmail.com

***Abstract*—Myanmar is a country that is undergoing development. In the modern era, engineers utilize efficient techniques to create the optimal construction material and construct high-quality structures. It is a fascinating fact that over 70% of the world's population resides in a concrete structure. Considering the current climate condition and the issue of global warming, it is crucial for construction and other industries to undergo a green revolution. Reducing the amount of cement used in concrete can have a positive impact on both carbon emissions and the environment. Using industrial waste like Saw Dust Ash (SDA) as a partial replacement for cement is a method employed to create Green cement mortar. Thus, the research aims to achieve eco-friendly construction materials by partially replacing energy-consuming cement with reusable materials like (SDA). This paper utilizes local materials. The Crown cement and saw dust are obtained from the timber industry in the Mandalay region, where they are burned at uncontrolled temperatures. At the Irrigation Training Centre in Patheingyi, the physical properties which are Fineness, Normal consistency, Specific gravity, Soundness and Setting time of local materials are thoroughly tested using the ASTM procedure. The cement replacement percentages of Saw Dust Ash (SDA) used in this paper is 3%, 5%, and 7% by weight of cement. The compressive strength of mortar for all different percentages of SDA with the ASTM-specified w/c and various w/c are tested. And then, the tensile strength of mortar with various percentages of SDA is tested according to ASTM procedure. For both compressive and tensile strengths of mortar, 5% of SDA substituted for cement yields the highest strength.**

Keywords—SDA, ASTM, carbon foot print, environmental pollution, Green cement mortar

I. INTRODUCTION

Portland cement has been around for more than 150 years and is practically a household word. Nowadays, many construction materials are produced and so the construction work should be done with low cost material. Concrete is a man-made (artificial) stone. Furthermore, due to its compressive strength, water resistance, and ease of shaping and placement, concrete is one of the most extensively utilized building materials. It calls for a lot of sophisticated building materials and processes. The most important component of a concrete mix is cement. Admixtures are frequently employed for specific purposes in concrete, even though cement plays a significant role in the mixture. Admixtures are used because they have the potential to provide significant economic and physical benefits. Admixture usage can save expenses on things like labor costs. The present uses of saw dust include filling ditches with sand and fuel for home cooking, both of which are considered environmental nuisances. After all, since cement is the most expensive component of mortar, using SDA in part substitution of cement should eventually result in lower manufacturing costs for concrete. One byproduct of the lumber business is saw dust. Sawmills situated in almost every major township across the nation create it by sawing timber into boards.

II. SAW DUST ASH

The majority of materials used as filler in concrete and mortar are saw dust ash. A byproduct of wood working operations like sawing, milling, drilling, and routing is saw dust, often known as wood dust. The process of sawing wood into planks at sawmills around the nation generates saw dust. Saw dust is currently used for sand filling and as fuel for residential cooking. Saw dust ash is created by burning saw dust, and it can be used in place of some cement. Saw dust ash is shown in Fig. 1.

Fig. 1. Saw dust ash

III. METHODOLOGY

The methodology used in this research is presented in the following flow chart shown in Fig. 2.

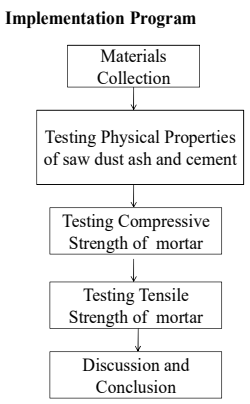

Fig. 2. Methodology for this research

IV. Chemical Composition Of Crown Cement And Saw Dust Ash

The chemical composition of Crown cement is obtained from Crown Cement Company. The chemical analysis of SDA is conducted in the laboratory of Chemistry Department, Monywa University. Result of Chemical Composition of Crown Cement and Saw Dust Ash are shown in Table I.

Table I. Test Result On Chemical Composition Of Crown Cement And Saw Dust Ash

Chemical Constituents	Crown Cement (%)	Approximate Composition Limits of Portland Cement (%)	SDA (%)
Silicon Dioxide (SiO_2)	20.40	17 – 25	87.383
Aluminum Oxide (Al_2O_3)	5.12	3-8	-
Ferric Oxide (Fe_2O_3)	3.11	0.5-6.0	1.262
Calcium Oxide (CaO)	62.38	60-67	6.546
Magnesium Oxide (MgO)	3.54	0.1-4.0	-
Sulphur Trioxide (SO_3)	2.34	1-3	0.656
Others	1.59	1.0	4.153
Ignition Loss	1.52	2.0	-
Total	100	100	100

V. Tests On Physical Properties Of Cement And Saw Dust Ash

Tests on physical properties of cement and saw dust ash is performed by following the American Standard of Testing Material (ASTM) procedure. Local materials used in this paper are Crown cement and saw dust is obtained from the timber industry of Mandalay region and saw dust ash is obtained by burning with uncontrolled temperature. Fineness, Normal consistency, Specific gravity, Soundness and Setting time are tested with cement only and cement with various percentage of Saw Dust Ash (SDA).

VI. Flow Table Test Of Mortar

Flow table test is firstly performed for the workability of cement mortar. So, water-cement ratio is determined by using the flow table test according to ASTM C1437.The flow table tests of mortar are performed to obtain a flow of 110 ± 5%. Result of flow value of mortar with various percentage of SDA is shown in Table II and illustrated in Fig. 3. The percentage of flow is calculated from the following formula.

$$\text{Percentage of Flow} = \frac{D - D_{mould}}{D_{mould}} \times 100 \quad (1)$$

Where,

D = average of four readings in millimeters

D_{mould} = the original inside base diameter in millimeters

Table II. Test Result On Flow Value Of Mortar

Mortar Mixture	Test No.	W/C Ratio	Flow Value (mm)
0%(SDA)	3	0.70	106
3%(SDA)	3	0.72	108.67
5%(SDA)	3	0.74	110.33
7%(SDA)	3	0.76	112

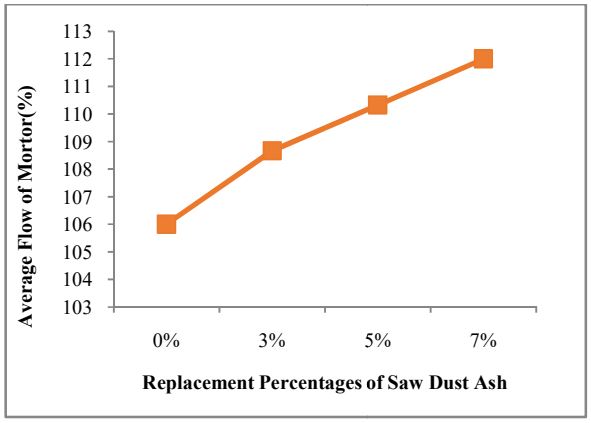

Fig. 3. Flow value of mortar with saw dust ash

According to the above test results, it is found that, the flow value increase when increase in amount of cement replacement material SDA is added.

VII. Compressive Strength Of Mortar

The purpose of this test is to ascertain, in accordance with ASTM C109, the compressive strength of mortar made of cement and sand (1:2.75). In this research, compressive strength is tested under two different w/c. ASTM standard water cement ratio is used 0.485 and according to flow table test water cement ratio are used 0.7, 0.72, 0.74 and 0.76 respectively. The sand used for mortar is conforming to the requirements for sieve No.20-30 standard sand. Fig. 4 shows the specimen for the mortar's compressive strength test, which is carried out three, seven, and twenty-eight days after curing. Test results for the compressive strength of mortar using the water cement ratio recommended by ASTM and the flow table test are displayed in Tables III and IV and are depicted in Figs. 5, 6 respectively.

Fig. 4. Specimen for compressive strength of mortar

Table III. Test Result On Compressive Strength Of Mortar With Flow Table Test w/c Ratio

Mortar Mixture	W/C Ratio	No. of Specimen	Compressive Strength (MPa)		
			3days	*7days*	*28days*
0% (SDA)	0.70	3	7.14	8.59	14.04
3% (SDA)	0.72	3	7.22	8.80	11.03
5% (SDA)	0.74	3	7.56	9.02	11.39
7% (SDA)	0.76	3	5.75	6.49	10.29

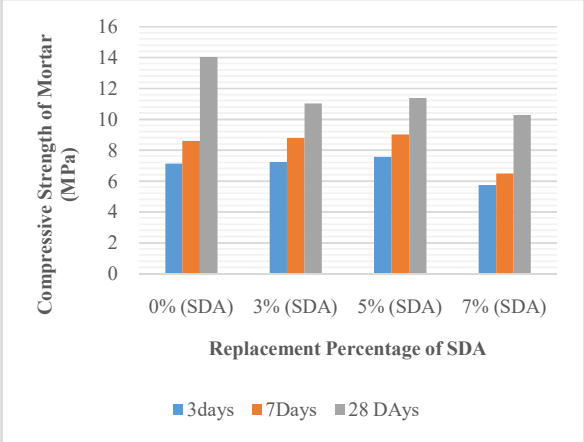

Fig. 5. Compressive strength of mortar for various % of saw dust ash with flow table test w/c

Table IV. Test Result On Compressive Strength Of Mortar With Astm Specified w/c

Mortar Mixture	W/C Ratio	No. of Specimen	Compressive Strength (MPa)		
			3 days	*7 days*	*28 days*
0%(SDA)	0.485	3	19.02	22.18	27.93
3%(SDA)	0.485	3	19.45	21.66	28.04
5%(SDA)	0.485	3	22.49	23.85	28.92
7%(SDA)	0.485	3	19.23	21.11	25.36

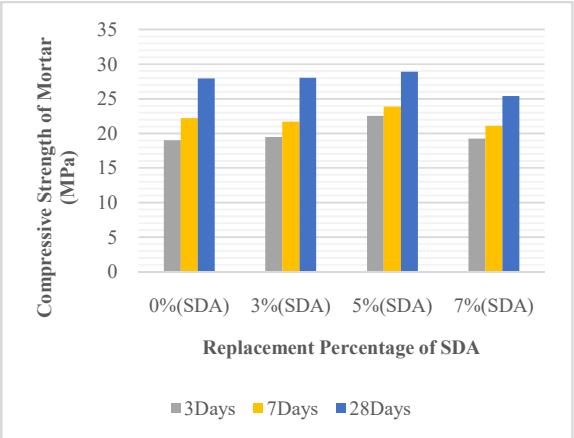

Fig. 6. Compressive strength of mortar for various % of saw dust ash with ASTM specified w/c

The compressive strength of mortar for all different percentages of SDA with the ASTM-specified w/c ratio is greater than that of the flow table test w/c ratio at 3, 7, and 28 curing days, according to the test findings on the compressive strength of mortar for Tables III and IV. Research indicates that a mortar's compressive strength decreases with increasing workability. Furthermore, at the 7-day and 28-day curing ages, the compressive strengths of mortar containing 3% SDA were lower than those of mortar containing cement alone. However, for all curing days, the compressive strength of mortar containing 5% saw dust ash in place of cement is higher than that of mortar containing cement alone. For this reason, it is determined that 5% is the ideal replacement percentage of saw dust ash for this study.

VIII. Tensile Strength Of Mortar

In accordance with ASTM C307, the tensile strength of mortar is evaluated using a mix proportion of 1:3 with cement and sand. The following equation 2 calculates the proportion of water. The water-to-cement ratios utilized for test specimens to determine the tensile strength of mortar are 0.450, 0.453, 0.459, and 0.457 at 0%, 3%, 5%, and 7% of saw dust ash as cement replacement material. Fig. 7 displays a specimen of mortar's tensile strength, and Table V and Fig. 8 illustrate the test results for mortar's tensile strength using saw dust ash.

$$Y = \frac{2}{3}\frac{P}{[N+1]+K} \qquad (2)$$

Where, Y = water required for the sand mortar, %
P = water required for neat cement paste of normal consistency, %
N = number of parts of sand to one of cement by weight
K = a constant which for the standard sand has the value of 6.5

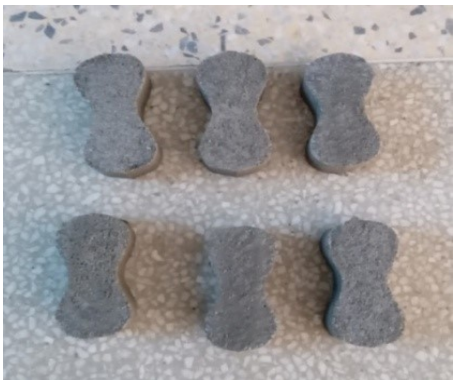

Fig. 7. Specimens for tensile strength of mortar

Table V. Test Result On Tensile Strength Of Mortar

Mortar Mixture	No. of Specimen	Tensile Strength (MPa)		
		3 days	*7 days*	*28 days*
0%(SDA)	3	1.51	2.09	2.21
3%(SDA)	3	1.77	2.16	2.75
5%(SDA)	3	2.13	2.25	2.96
7%(SDA)	3	2.08	2.19	2.69

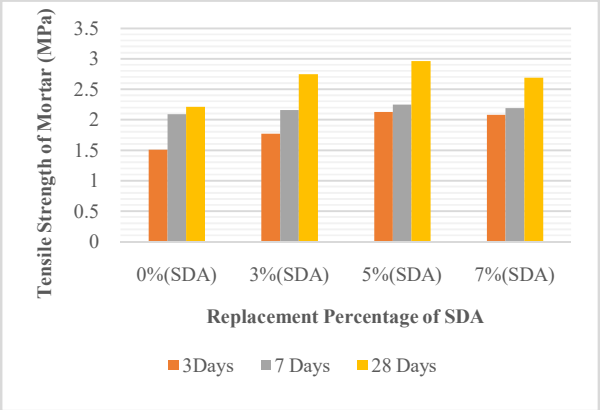

Fig. 8. Tensile strength of mortar with saw dust ash

The test findings showed that the mortar's tensile strength progressively rose as SDA grew up to 5% and decreased at 7% of SDA at three, seven, and twenty-eight days, respectively. According to this study, mortar that replaces saw dust ash with cement has a stronger tensile strength than mortar that only uses crown cement. Therefore, mortar can be made using 5% saw dust ash instead of cement.

IX. Conclusions

The compressive strength of mortar samples that have been left uncured for 3, 7, and 28 days is evaluated, with varying amounts of saw dust ash substituted for cement. The proportion of SDA mixture used to replace cement is 3%, 5%, and 7%. According to this study, the mortar's compressive strength decreases with increasing workability. For both compressive and tensile strengths, 5% of SDA substituted for cement yields the highest strength at every curing day. Thus, the ideal amount of cement to substitute in the mortar is 5%.

Acknowledgment

The author is grateful to her supervisor, Daw San San Myint, Associate Professor, Department of Civil Engineering, Technological University (Mandalay), from the bottom of her heart for her generosity, support in carrying out this research, close supervision, priceless counsel, direction, and outstanding cooperation.

References

[1] A.M. Neville. J.J. Brook. Second Edition, *Concrete Technology*, *English Language Book Society*, (2010).

[2] NYI, H. N.: *Properties of Concrete and Steel Design Concepts in Concrete Engineering, (1992).*

[3] John Wiley &sons, Inc., Hoboken, New Jersey: *Advanced Concrete Technology.*

[4] A.A. Raheem. Research Paper (2016), *Saw Dust Ash as Partial Replacement for Cement in Mortar and Concrete*.

[5] International Journal for Modern Trends in Science and Technology, 9(04):368-373, 2023 IJMTST, ISSN: 2455-3778, Volume 9, issue 04 html

[6] International Journal of scientific & Engineering Research, Volume 6, Issue 2015, ISSN 2229-5518

[7] Wang, Qiang, Peiyu Yan, and Guidong Mi "*Effect of Blended Steel Slage" GBFS mineral admixture on hydration and strength of cement, Construction and Building Materials,* 2012.

[8] Christopher Fapohunda, Bolatito Akinbile, Akintoye Oyelade,*"A Review of the Properties Structural Characteristics and Application Potentials of Concrete Containing Wood Waste as Partial Replacement of one of its Constituent Material*," YBL Journal of Built Environment, 2018.

[9] Chai Jaturapitakkul, Jatuphon Tangpagasit, Sawang Songmue, Krawood Kiattikomol,"*Filler Effect of fine Particle Sand on the Compressive strength of mortar*," International Journal of Minerals, Metallurgy and Materials, 2011.

[10] Divine Ingabire, Sanjeet Kumar, "*Enhancement of Engineering Properties of Black cotton Soil Using rice husk and sawdust ash*," E3S Web of Conferences, 2023.

[11] Dr. Bharadwaj Nanda and Prof. A. Nayak Department of Civil Engineering

[12] Cook. D.J "*Cement Replacement Materials",* (1990)

Analysis of Road Accident and Proposed Suitable Countermeasures for Naypyitaw-Mandalay Expressway

Yan Naung[1], War War Myint[2]
[1]*Department of Civil Engineering and Technological University (Mandalay)*
[2] *Department of Civil Engineering and Technological University (Mandalay)*
[1]yannaungmin@gmail.com, [2]wwmyint.mm @gmail.com

***Abstract*— This paper aims to reduce the rate of road accidents as well as the severity of injuries and to propose road safety countermeasures for Naypyitaw-Mandalay Expressway. All the required data used in this study was the data which collected by the Department of Highway, Ministry of Construction (MOC). This research study reviews the accident record for 7 years during the period of the year 2017 to 2023. After accident causes data are transposed from the data forms into the Microsoft Excel programme and analyzed, the data are shown by the use of Descriptive Analysis. Moreover, black spot locations are identified with three methods and the site investigations are done practically. After all the investigations, the proper countermeasures are proposed to decrease the severity casualties and the road safety improvement for Naypyitaw-Mandalay Expressway.**

Keywords*— *accidents, black spot locations, road safety, severity level, investigations, descriptive analysis

I. Introduction

In Myanmar, Naypyitaw-Mandalay Expressway is one of the infrastructure development projects of Government in the country. Naypyitaw-Mandalay Expressway construction period is from 2007 to 2010 and was opened in December, 2010. Until now, the life time of Naypyitaw-Mandalay Expressway is over 13 years. Although the design had created to be eight lanes in which it included medium-divided part, the only four lanes are being constructed. Therefore, the width of expressway could be extended in future to be eight lanes [4].

According to the latest WHO data published in 2017, Road Traffic Accidents Deaths in Myanmar reached 10,527 or 2.67% of total deaths. The age-adjusted Death Rate is 20.10 per 100,000 of population which ranks 80 in Myanmar [3]. Moreover, Recent road safety statistics are alarming in Myanmar since the number of road accidents are increasing year by year.

Road traffic accidents can be defined as "An accident that occurred on a way or street open to public traffic; resulted in one or more persons being killed or injured, and at least one moving vehicle was involved." An accident is an event occurring suddenly, unexpectedly and incidentally under unforeseen circumstances. It can be seen that road safety is the main problem in the developing countries. According to the limitation of accident data, there are five characteristics of motor vehicle crashes. There are day-type, week-type, weather conditions, manner of occurrence and the age of drivers.

In this study, the author aims to investigate the accidents that happened at Naypyitaw-Mandalay Expressway within three periods. These periods are divided into three distinct segments. The first period, spanning from 2017 to 2019, represents "Before COVID-19". Subsequently, the period from 2020 to 2021 is examined "During COVID-19." Finally, examining the year from 2022 to 2023 represents "Post COVID-19". The main objective of this study is to reduce both the rate of accidents as well as the severity of injuries. The specific objectives are to examine the contribution factor affecting the severity of accident, identify the blackspot location, to check the site location and to propose possible improvement of countermeasure.

II. Data Preparation of Proposed Expressway

A. Selection of the Study Location

Yangon-Mandalay expressway is 366/6 miles and lane width is about 12.5 ft and 4 lane median divided highway. Median width is 30 ft and shoulder is 3 ft wide along the expressway. Study area is located in Naypyitaw-Mandalay Expressway (220 to 366/3=166/6 miles) as shown in Fig. 1 [4].

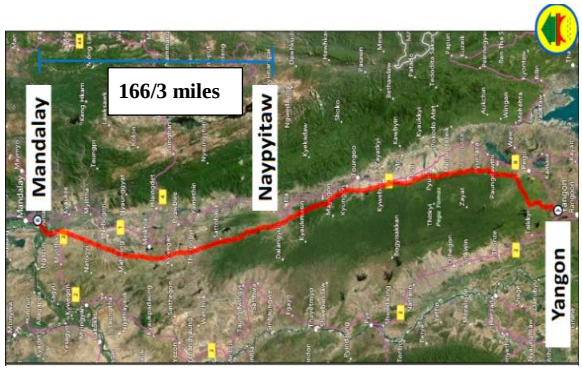

Fig. 1. Case study area of Naypyitaw-Mandalay Expressway

B. Methodology

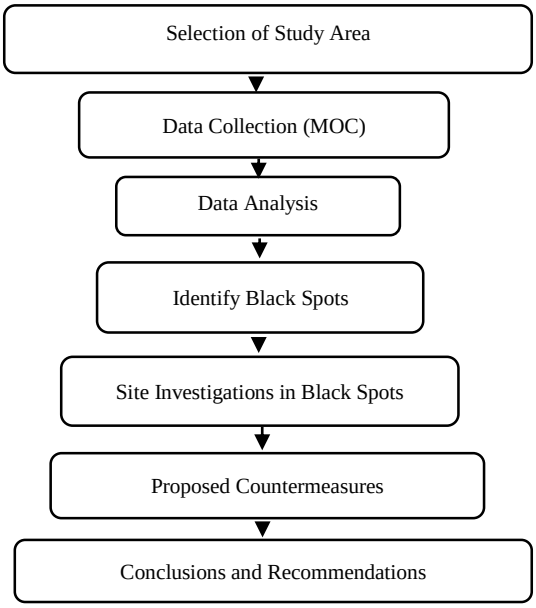

Fig. 2. Flow chart of methodology framework

The dependent variables are the crash severity levels, and the independent variables are the factors affecting the crash severity such as human characteristics, environmental characteristics, roadway characteristics, collision types, the opponent involved, and the location of the accident.

For identification of black spot areas, property damage accidents (PDO), injury accidents, fatality accidents, and total accidents are considered in the calculation of identification methods.

Due to limitations of traffic and accident case data, only three methods are used for this research. They are;

1. Accident Frequency Method
2. Accident Point Weightage method and
3. Poisson-Gamma Generalized Linear Model

The black spot locations are taken every 3 miles. After the black spot locations are compared by the above three methods, the first 10 locations at each method have been counted as sample data in this study. The frequency method ranks locations by the total number of accidents in each road section. The location with the highest number of accidents is ranked first, followed by the location with the second highest number of accidents, and so on [2].

In the Accident Point Weightage formula, the accidents are divided into three groups. They are fatal accidents, injury accidents, and property damage-only accidents. All types of accidents had their corresponding coefficients which for fatal, it was multiplied by 6.0, for serious injury multiplied by 3.0, and for property damage only, it was multiplied by 0.2[1].

$$APW=F\ (6) + I\ (3) + PDO\ (0.2) \quad (1)$$

Where, F = number of fatal accidents, I = number of injury accidents and PDO = number of property damage only accidents.

In Poisson-Gamma Generalized Linear Model, the accidents are also divided into three groups. All types of accidents had their corresponding coefficients which for fatal, was multiplied by 5.0, and serious injury, multiplied by 3.0.

$$P = X + 3Y + 5Z \quad (2)$$

Where, P = priority value, X= total number of Property Damage Only accidents, Y= total number of injury accidents and Z= total number of fatal accidents [5].

III. Data Descriptions

Vehicle crash database that occurred in Naypyitaw-Mandalay Expressway from 2017 to 2023 are obtained from the Ministry of Construction.

A. Data Analysis

According to the data obtained from the Ministry of Construction, there are 906 cases, which are all motor-vehicle involved accidents from 2017 to 2023 of traffic crash records. There is no doubt that the obtained data cannot be used directly into analysis; therefore screening and cleaning data is primary process. Screening process focused on only vehicle accidents happening in Naypyitaw-Mandalay Expressway.

The data of Fatal, Injuries, PDO and No. of Accident for Before Covid (2017-2019), During Covid (2020-2021) and Post Covid (2022-2023) occurring in Naypyitaw-Mandalay Expressway are shown in Table I, II and III.

I. Data of Fatal, Injuries, PDO and Accidents For Before Covid-19

No	Year	Fatal		Injuries		PDO	No. of accident	AADT
		Male	*Female*	*Male*	*Female*			
1	2017	41	10	176	150	85	214	23513
2	2018	29	28	193	176	61	172	27578
3	2019	25	13	171	135	68	184	28003

In this expressway, it had 214 accidents in 2017, 172 accidents in 2018 and 184 accidents in 2019. When comparing the three years of Before Covid-19, the most cases in AADT is the year 2019.

II. Data of Fatal, Injuries, PDO and Accidents For During Covid-19

No	Year	Fatal		Injuries		PDO	No. of accident	AADT
		Male	*Female*	*Male*	*Female*			
1	2020	20	10	108	75	57	139	19473
2	2021	25	6	69	37	24	87	13265

Table II represents to count the accident cases for During Covid-19. In this duration, it had139 accidents in 2020 and 87 accidents in 2021.

III. Data of Fatal, Injuries, PDO and Accidents For Post Covid-19

No	Year	Fatal		Injuries		PDO	No. of accident	AADT
		Male	*Female*	*Male*	*Female*			
1	2022	19	2	70	36	9	56	19119
2	2023	20	6	49	73	12	54	21255

The caused accidents 56 and 54 is in 2022 and in 2023. This numbers of cases show the less ones than other two durations.

The above motor vehicles involved accidents can be shown as the figures which describe the more proper way to express the data into information. Data of Fatal, Injuries, No. of Accident, PDO and AADT Before Covid (2017-2019), During Covid (2020-2021), Post Covid (2022-2023) are shown in Fig. 3, 4 and 5.

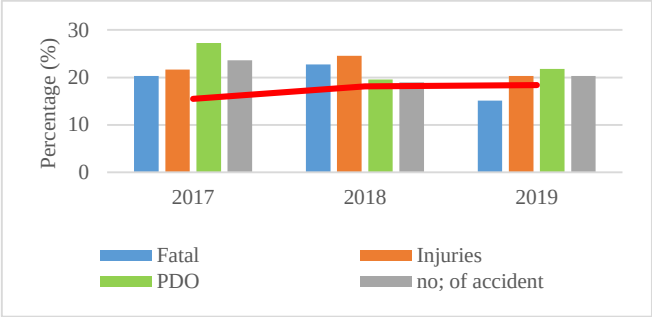

Fig. 3. Data of fatal, injuries, no. of accident, PDO and AADT Before Covid (2017-2019)

It can be seen that even though the number of cars increased, the accident rate in fatal did not rise. But, according to the comparison of the three-year Before Covid period, it can also be seen that the accident rate in injuries in 2018 was higher than other two years.

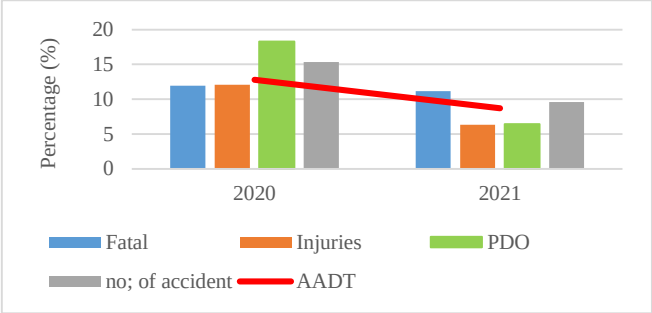

Fig. 4. Data of fatal, injuries, no. of accident, PDO and AADT During Covid (2020-2021)

It can be known that the AADT for the two-year During Covid period decreased significantly. When analysing the reason of why, the four-case data in 2021 were less than the data in 2020. Among them, the data of PDO was very remarkable. For the next one, the numbers of accidents were noticeable in decreasing the causes.

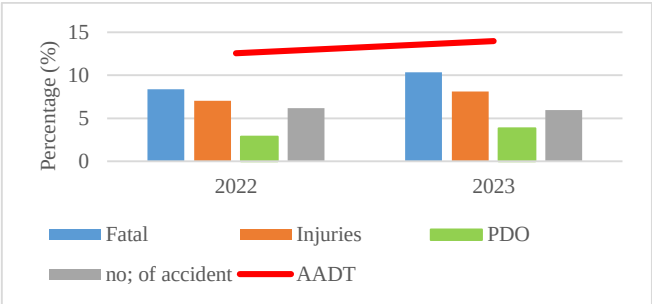

Fig. 5. Data of fatal, injuries, no. of accident, PDO and AADT Before Covid-19 (2022-2023)

Moreover, this Fig. 5 showed the severity levels, numbers of accidents and AADT caused during Post Covid-19. When comparing the two post-covid years, the numbers of accidents are nearly the same. But, the rest three of severity levels of 2023 are more than ones of 2022.

As the conclusion of analysing the data, the rate of fatal, the rate of accident and the rate of PDO in Before Covid-19 is higher for the rest of the durations. The number of cars has decreased slightly and the rate of fatal, the rate of accident and the rate of PDO has also decreased during Covid and Post Covid. But the accident rates are still existing. So, human characteristics, environmental characteristics, crash characteristics, roadway characteristics and vehicle characteristics are the explanatory variables used in predicting crash severity levels.

B. Descriptive Analysis

These four categories are considered as the significant input variables for the independent variables such as human characteristics, environmental characteristics, crash characteristics, and roadway characteristics.

Manners of occurrences and driver age are considered for the human characteristics. The possible input variables for the manner of occurrence are over speed, tyre deficiencies, driver sleepy, slipping, machinery failure, overtaking, collision with vehicle, collision with cycle, collision with pedestrians, collision with animals and collision with fixed objects.

Manners of occurrence for Before Covid, During Covid and Post Covid in Naypyitaw-Mandalay Expressway are shown in Fig. 6, 7 and 8.

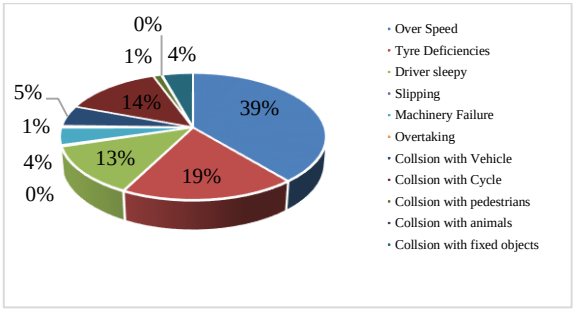

Fig. 6. Causes of accident for Before COVID-19(2017-2019)

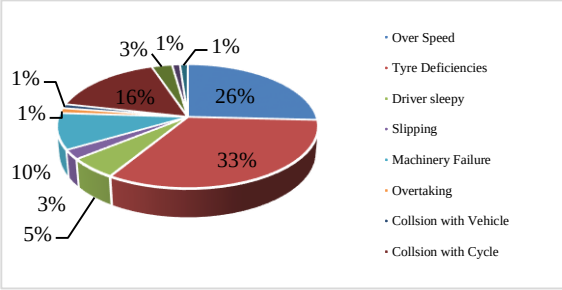

Fig. 7. Causes of accident for During COVID-19 (2020-2021)

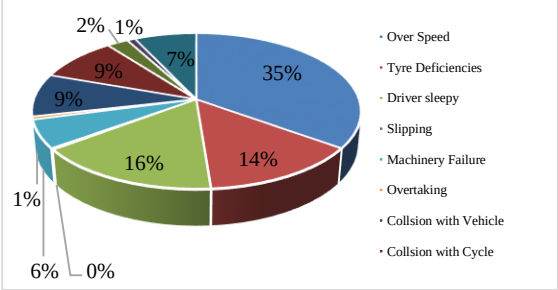

Fig. 8. Causes of accident for Post COVID-19 (2022-2023)

According to Fig. 6, 7, and 8, it can be concluded that the over speed, tyre deficiencies, driver sleepy and collision with cycle are the main causes of accident rate.

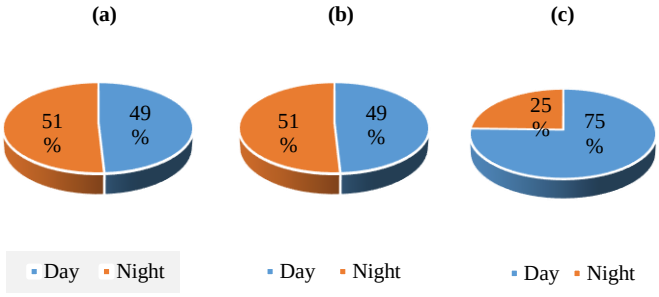

Fig. 9. Accident involvement in time

The most common accident involvement in time rate is the same in Fig (a) and Fig. (b). Remarkably, the percentage of crashes in day time (6 a.m to 6 p.m) is higher than night time (6 p.m to 6 a.m) in Post COVID-19 Fig. (c).

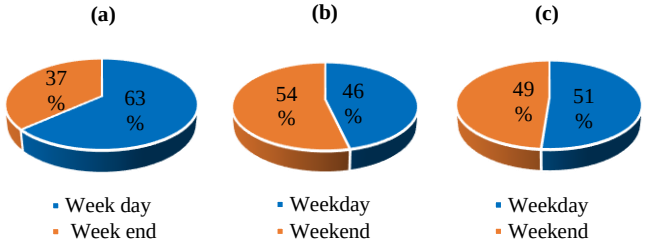

Fig.10 Accident involvement by weekdays and weekends

The percentage of crashes occurring on weekdays is more than that of crashes occurring on weekends in Fig. (a). The Fig. (b) and Fig. (c) are nearly the same.

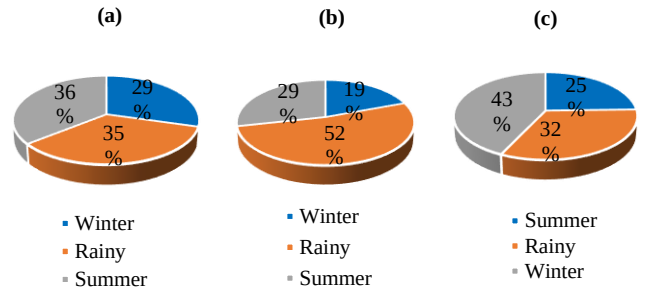

Fig.11 Accident involvement by seasons

Fig. 11 shows the importance of weather condition in consideration the analysis of motor vehicle crashes.

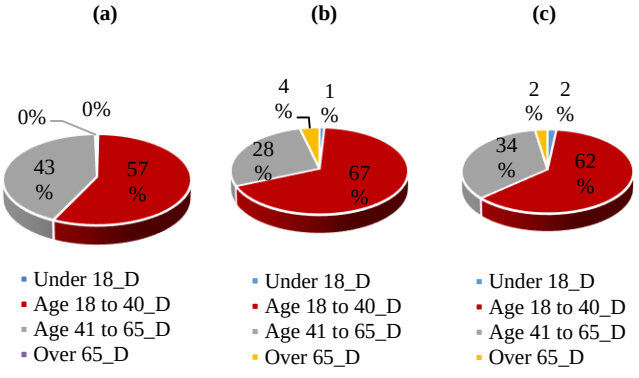

Fig.12 Accident involvement by driver age

As shown in Fig. 12, it describes the percentage of accident in different age grouped by injury severity level.It can be concluded that, the group with the highest accident rate is between the ages of 18 and 40. The second group with the highest accident rate is between the ages of 41 and 65.

IV. Identification of Black Spot Location

This study attempts to determine the black spot locations in Naypyitaw-Mandalay Expressway. The road section length chosen in each road section divided into 3 miles. Identification of black spot was done by three methods. The first one is the accident point weightage method. The second one is the frequency method and the last one is the poisson gamma generalized linear model method. Among these three methods, accident point weightage is the main method and the other two methods are used only for checking the accident point weightage method. This method is widely used in world wide. The ranking of accidents in every mile was determined by the Accident Point Weightage formula. The following Table IV shows the most hazardous locations by Accident Point Weightage method from high hazardous to low hazardous rank.

IV. Identification of Black Spot Locations By Accident Weightage Method

Miles	*F*	*I*	*PDO*	*APW*	*Rank*
229	19	89	2	381.4	1
227	11	48	2	210.4	2
329	7	32	1	138	3
280	3	34	2	120.4	4
230	3	33	0	117	5
286	3	31	2	111.4	6
284	2	29	3	99.6	7
271	4	24	1	96.2	8
242	1	28	15	93	9
243	1	27	1	87.2	10

In Table IV, it shows that the most hazardous locations by Poisson-Gamma Generalized Linear Model method from high hazardous to low hazardous rank.

V. Identification of Black Spot Locations By Poisson-Gamma Method

Miles	*F*	*I*	*PDO*	*P*	*Rank*
229	19	89	2	364	1
227	11	48	2	201	2
329	7	32	1	132	3
280	3	34	2	119	4
286	3	31	2	110	5
230	3	30	0	114	6
242	1	28	15	104	7
284	2	29	3	100	8
271	4	24	1	93	9
243	1	27	1	87	10

The frequency method ranks locations by the total number of accidents in each road section. The location with the highest number of accidents is ranked as first, followed by the location with the second highest number of accidents, and so on. This method is only for checking APW method. Frequency method

is eighty percent same as the APW method as shown in Table VI.

VI. IDENTIFICATION OF BLACK SPOT LOCATIONS BY POISSON-GAMMA METHOD

Miles	*F*	*I*	*PDO*	*Total*	*Rank*
229	19	89	2	110	1
227	11	48	2	61	2
242	1	28	15	44	3
329	7	32	1	40	4
280	3	34	2	39	5
286	3	31	2	36	6
230	3	33	0	36	7
284	2	29	3	34	8
271	4	24	1	29	9
243	1	27	1	29	10

Table VII shows the comparison of three methods of black spots. In 229 miles, poisson gamma generalized linear model and frequency method are the same in ranking number 1. Poisson gamma generalized linear mode, accident weightage method, and frequency method are second ranking in 227 miles.

VII. COMPARISON OF THREE METHOD

Mile	*APW*	*PGGLM*	*FM*
229	1	1	
227	2	2	2
242	9	7	3
329	3	3	4
280	4	4	5
286	6	5	6
230	5	6	6
284	7	8	7
271	8	9	8
243	10	10	8
203			9
317			10

The black spot location map is shown in Fig. 13. After identification of black spot with three methods, where the most common accident rate is mile 229. Moreover, site investigations are also considered in this study.

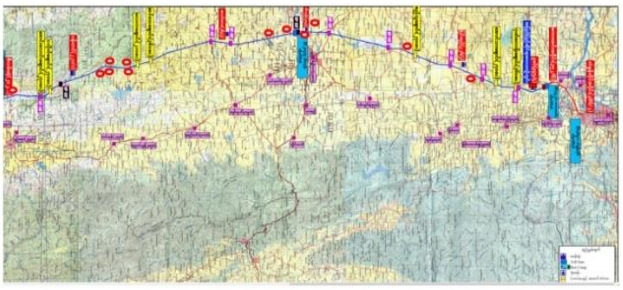

Fig.13 Black spot location map

VIII. INVESTIGATION AND ROAD SAFETY COUNTERMEASURES IN BLACK SPOT LOCATION

There are many factors affecting the road traffic accidents in black spot locations of Naypyitaw-Mandalay Expressway. Site investigations and proposed road safety measures in black spot locations are shown in Table VIII.

VIII. INVESTIGATION AND ROAD SAFETY COUNTERMEASURES IN BLACK SPOT LOCATIONS

Mile	Possible causes of road accidents	Road safety measures	Location
229(228/0) F=19 I=89 PDO=2	- Discontinuous/ Damaged Guard rail - No reflector on the Guard rail - Poor road marking	- To provide Guard rail - To provide reflector on the Guard rail - To provide road marking	
227/1 F=11 I=48 PDO=2	- Improper U turn - No reflector on the Guard rail - No pavement marking	- To provide close U turn and law enforcement - To provide reflector on the Guard rail - To provide road marking	
241/7 F=1 I=28 PDO=15	- Discontinuous/ Damaged Guard rail made by villager - Village near expressway - Poor pavement marking	- To provide Guard rail - To provide the fence near village - To provide proper road marking	
329 F=7 I=32 PDO=1	- Poor pavement marking - No warning sign	- To provide road marking - To provide proper road sign and rumble strips	
280/3 F=3 I=34 PDO=2	- Illegel U turn - Poor pavement markings	- To provide fence near village, proper road sign and law enforcement - To provide road markings	
286 F=3 I=31 PDO=2	- Cycle driving on the expressway - Weak law enforcement - Poor pavement marking	- To punish the indiscipline road user - To provide proper road marking	
230/1 F=3 I=33 PDO=0	- Prohibited Vehicle (Motorcycle) - Poor pavement marking	- To provide effective law enforcement - To provide road marking	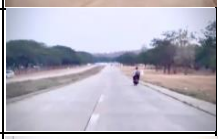
284 F=2 I=29 PDO=3	- Damaged Curb/ Inadequate Curb Maintenance - Poor pavement marking	- To provide adequate Curb Maintenance - To provide road marking	
271 F=4 I=24 PDO=1	- Illegel U turn - Prohibited Vehicle (Motorcycle) - Weak road marking	- To provide proper warning sign and law enforcement - To provide road marking	
243/6 F=1 I=27 PDO=1	- Illegel U turn - Poor warning sign	- To provide fence and law enforcement -To provide proper warning sign	

IX. CONCLUSION

This study investigated the black spot locations through Naypyitaw-Mandalay Expressway. Then, it analysed the cases of incidents, which happened at three durations to find out the way how to counteract for reducing the numbers of accidents. After examining the manners of occurrences of accidents, the safety of Naypyitaw-Mandalay Expressway can be provided by countermeasures. The highest occurrences have to be considered again; over speed, tyre deficiencies and driver sleepy for the various time and circumstances and for different driver age group. According to investigation, to prohibit the over speed, to provide proper warning sign and law enforcement needs to act as countermeasures. Moreover, by improving striping or signing along horizontal curves, drivers are more aware of the road's curvature and are more likely to slow down to a speed that matches the curve's perceived severity. Since tyre-related issues are the crucial ones, the law which punishes the indiscipline expressway users must act out. That is because the most drivers do not consider the tire maintenance, including air pressure and monitoring tire expiration before using the expressway. Furthermore, drivers who feel drowsy should pull over into a well-lit area, and make regular stops or switch drivers every 100 miles or 2 hours. Since drivers are most likely to feel drowsy between 1-4 p.m. and 2-6 a.m., if possible, avoid driving during these times. When these conditions are familiar with drivers, they will follow the measures of driving. After examining all the contribution factor affecting the severity of accident by identifying the black spot locations through Naypyitaw-Mandalay Expressway, this study takes the main objectives out as proper countermeasures, and the author hopes that this study supports to reduce both the rate of accidents as well as the severity of injuries. Moreover, it helps the authorized persons and traffic engineers to know which factors contribute more to the crash severity and the road safety plan to reduce accidents, occurring suddenly, unexpectedly, and incidentally under unforeseen circumstances in Naypyitaw-Mandalay Expressway.

ACKNOWLEDGMENTS

As the very first, the author would like to heartfully show his gratitude to Pro-rector Dr. Su Yin Win for her guidance and supportives. Then, his special thank goes to the HOD Dr. Nwe Nwe Win, Department of Civil Engineering, who is kindly giving helpness to do the study. After that, the author would like to express his deepest gratitude to his Supervisor, Dr. War War Myint, Professor, Department of Civil Engineering, Technological University (Mandalay), for her kindness, encouragement to fulfill of this research, close supervision, invaluable advice, guidance and excellent co-operation.

REFERENCES

[1] De Oña, J., Mujalli, R. O., and Calvo, F. J. *Analysis of Traffic Accident Injury Severity on Spanish Rural Highways Using Bayesian Networks.* Journal of Accident Analysis and Prevention 43 (1), 402-411, 2011.

[2] Yakar, F. *Identification of accident-prone road sections by using relative frequency method. Promet-Traffic&Transportation*, *27*(6), 539-547, 2015.

[3] World Health Organization: Life Expectancy in Myanmar 2017, <https:www.worldlifeexpectancy.com>, 2017.

[4] Ministry of Construction: Total Number of Injury and Fatality Accidents along Yangon-Mandalay Expressway, Departmental Report, 2024.

[5] Sitthiprapha, S. Factors Affecting Motorvehicle Accident Severity in Thailand, Master Thesis, Transportation Engineering, Asian Institute of Technology Thailand, 2011.

Design and Implementation of Solar Street Light System

Hnin Thet Aung[1], Myat Myat Moe[2], Moe Moe[3]

[1]*Department of Electrical Power Engineering, Technological University (Mandalay)*

[2]*Department of Electrical Power Engineering, Technological University (Mandalay)*

[3]*Department of Electrical Power Engineering, Technological University (Mandalay)*

Email: [1]hninthetaung1983@gmail.com, [2]myatmyatmoe88@gmail.com, [3]ms.dawmoemoe @gmail.com

***Abstract*— In Myanmar, various power sources such as biomass, solar, wind, and water. Among these power source, solar energy is being particularly advantageous due to its equator location. Sunlight is a significant source of electricity, and solar electricity is generated using solar panels or photovoltaic cells. The solar street light uses solar electricity, powered by a battery, a solar charger controller, lighting sensor control (LDR), and a PV solar panel. It is an alternative to traditional street lighting, with LEDs offering lower energy costs and a more efficient design. This system includes a battery backup system. This paper presents the design and implementation of solar street light system in Technological University (Mandalay). This research was built by using solar module, LEDs, light dependent resistor (LDR), charge controller and battery. The results indicate that the solar power streetlight efficiently generates electricity directly from sunlight at a low cost, without producing emissions, noise, or vibrations. Consequently, the performance of the proposed system has been assessed based on power consumption.**

Keywords*— solar energy, sunlight, solar street light, battery, LEDs, energy cost, battery backup system

I. Introduction

The study of light has been essential for the development of solar power systems. These systems utilize sunlight through photovoltaic cells. Sunlight is absorbed by the solar photovoltaic cells, which convert it into electrical energy. This electrical energy is then stored in batteries and used to power CFL or LED lights. The solar street light uses solar electricity, powered by a battery, a solar charger controller, lighting sensor control (LDR), and a PV solar panel. It is an alternative to traditional street lighting, with LEDs offering lower energy costs and a more efficient design. This system includes a battery backup system [7]. This paper presents the design and implementation of street light using solar power in Technological University (Mandalay). Solar street lights are beneficial in that the day to day running and maintenance costs are reduced, save energy, environment friendly and convenient to install. Solar lights are made up of five main components: the solar photovoltaic (PV) panel, battery, charge controller, light poles and the light fixture.

When sunlight is available, a solar panel captures it and generates electrical energy, which can be used immediately or stored in a battery. Utilizing the world's best LED chips ensures reliable performance for the lights, offering high luminous efficiency, minimal light degradation, energy savings, environmental protection, and a lifespan of 50,000 hours. The design of high-power LED street light circuits take into account battery life, operating voltage, electronic component performance, power efficiency and power factor [3].

Solar street lights have several advantages. They reduce the costs of daily operation and maintenance, save energy, are environmentally friendly, and are easy to install. These lights work by using mono-crystalline and poly-crystalline solar panels to convert sunlight into electricity, which is then stored in batteries without needing maintenance. They are equipped with a control system to prevent the batteries from overcharging or discharging excessively. Automatic street lights don't required manual switching on and off. They have sensor that detect the surrounding light levels [7]. When it gets dark enough, the streetlights turn on automatically, and when there's enough light from other sources, they switch off. Solar street light with sensor is powered by solar energy. This system is used Light Sensor (LDR) or Light Dependent Resistor. As the light intensity on the surface of the Light Dependent Resistor (LDR) increases, its resistance decreases, leading to an increase in conductivity. Conversely, when the light intensity on the LDR surface decreases, its resistance increases, resulting in reduced conductivity. This relationship allows LDRs to effectively respond to varying light conditions, making them useful in a variety of light-sensing applications. The proposed site was chosen Technological University (Mandalay), Patheingyi Township, Mandalay Division. The main purpose of stand- alone solar street light system is to supply electricity for proposed road. Main entrance road (Adipati Road) is two lane road and 191m (627ft) long. Each lane has a width of 7m (22ft) including side walk platform for pedestrians. In this journal, Light sensor (LDR) and control circuit of solar street light are explain. The results of this system, comparison for cost and estimation of solar street light and conventional street light are expressed completely [7].

II. Components Of Solar Street Light System

The solar street light system consists of five components. There are the following;

- Solar panel
- LEDs
- Charge controller
- Battery
- Light pole

The five components of solar street light system are showed the following block diagram. These components are described the short to the point in this journal. Now, the block diagram of solar street system is as following:

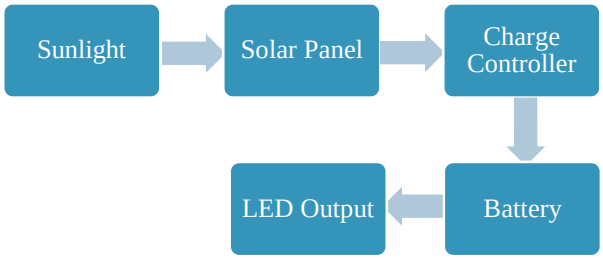

Fig. 1. Block Diagram of Solar Street Light System

III. Light Dependent Resistor (LDR)

The photoconductive cell, also known as Light Dependent Resistor (LDR), improves its conductivity as illumination increases, resulting in decreased resistance. However, a photoresistive cell has a long response time, often taking several seconds to adjust to changes in light intensity. Light Dependent Resistors (LDR) are used as lighting control devices in most of solar street lighting system, which are cheap light sensors. A Light Dependent Resistor (LDR) also known as a photoresistor, is a device whose resistivity varies based on the incident electromagnetic radiation. This sensor's resistance decreases when exposed to light. The resistance of the LDR changes according to the intensity of light falling on it as light intensity increases, the resistance decreases and conductivity increases. Conversely, when light intensity decreases, the resistance increases and conductivity decreases [2].

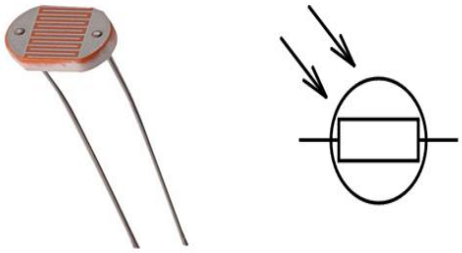

Fig. 2. (a) Light Dependent Resistor (b) Symbol of LDR

A. Battery

Solar electric systems generate power only when sunlight is available. To use this energy later, such as at night or during periods of low sunlight, some form of electrical energy storage is needed. Batteries are the most common storage solution in solar electric systems. They store electricity generated by solar panels during the day and supply energy to fixtures at night. The lifetime and capacity of the battery are crucial, as they impact the backup duration of the light. For solar street lighting, batteries should have a slow discharge rate and a long discharge time. The quality of the battery directly affects the performance of the street lights There are many battery types which can be used in solar lights. Below are the widely used rechargeable batteries for solar lights [8].

- Lead–acid battery,
- Lithium ion battery or Li-ion and
- Lithium ion battery phosphate or LiFePO4

This system is used Lithium ion battery phosphate or LiFePO4.

Fig. 3. LiFePO4 Battery

B. Solar Panel

The solar PV system is powered by numerous crystalline or thin film PV modules. These modules consist of interconnected PV cells made from light-sensitive semiconductor materials. These materials utilize photons to dislodge electrons, generating an electric current. There are two main types of technology used for PV cells: crystalline silicon, which accounts for the majority of PV cell production as shown in Figure 4, and thin film, which is newer and increasingly popular [5]. The three general types of silicon photovoltaic cells are:

- single or monocrystalline silicon,
- poly or multicrystalline silicon, and
- amorphous silicon (thin film silicon "a-Si").

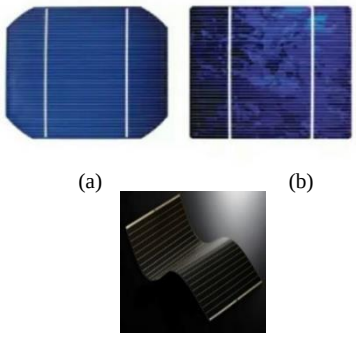

(a) (b)

(c)

Fig. 4. (a) Monocrystalline Silicon and (b) Polycrystalline Silicon

(c) Amorphous Silicon or Thin Film Silicon

I. Module Efficiency

Solar module	Efficiency	Lifetime	Price	Power/ Area
Monocrystal line-	10 - 13%	25 years 90% rated power 30 years 80% rated power typical	high	high
Polycrystalli ne-	9 - 13%	10 years 90% rated power 25 years 80% rated power typical	mode rate	moder ate
Amorphous-	6 - 8%	10 years	low	low

The monocrystalline is high efficiency, performance and higher cost. The polycrystalline is low efficiency and lower costs. The amorphous or thin-film is lower efficiency, portable and flexible.

C. Charge Controller

The rate at which electric current is injected into or removed from batteries is managed by a charge controller, sometimes referred to as a charge regulator. It guards

against overvoltage and overcharging, which both shorten battery life and present safety hazards. To prolong battery life, it may also prevent total draining (also known as “deep discharging”) of a battery or carry out controlled discharges, contingent on the battery technology. There are two types of solar charge controller:

- Pulse Width Modulation (PWM) and
- Maximum Power Point Tracking (MPPT)

The solar street light system is used PWM charge controller [1].

(a) PWM Type (b) MPPT Type

Fig. 5. Charge Controller

D. Types of Street Lighting Lamp

The most commonly used lamps are described briefly as follow;

- Incandescent lamps
- Reflector Lamps
- Gas Discharge Lamps
- LED

Modern solar street lights typically employ LEDs as their illumination source because they can produce far more lumens with less energy usage. High-power white LEDs are currently the illumination source of choice for the majority of solar street light installations. restricted to lighting items with LED bases only. Light should be produced in the visible portion of the spectrum. LEDs emit visible and, to a lesser extent, ultraviolet light. A power LED's useful operating lifetime is incredibly lengthy; in fact, it frequently outlasts the product in which it is included [4].

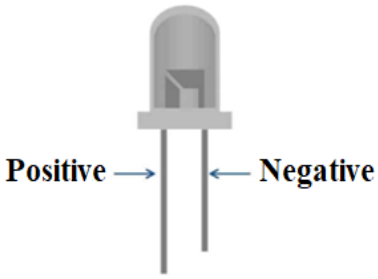

Fig. 6. Light Emitting Diode (LED)

E. Solar Street Light Control Circuit

Street lights ought to be turned "OFF" when there is enough daylight and "ON" as soon as evening darkness arrives. A circuit for automatic switching is depicted in the following diagram. Relay switch NO (Normally Open) is attached to it. Because T1 and T2 are two transistors in a bistable state, when one is "ON," the other is "OFF." When the LDR receives enough intense solar light during the day, its resistance lowers, creating a route for the incoming current [6].

The base-emitter junction becomes forward-biased as a result of the current entering T1’s base. Thus, the coil is not receiving any current. The LED won’t get any current because the relay switch is open. The LED won’t shine as a result. The resistance of the LDR increases as a solar light intensity drops. Transistor T1 will thus be “OFF” during the night, meaning that no current will flow through the LDR [6].

A portion of the circuit current pass through transistor T2 and the coil, rendering it “ON”. The relay switch is drawn to the coil by the magnetic flux created when current flows through it, connecting it to the normally closed (NC) state. Consequently, the LED illuminates.

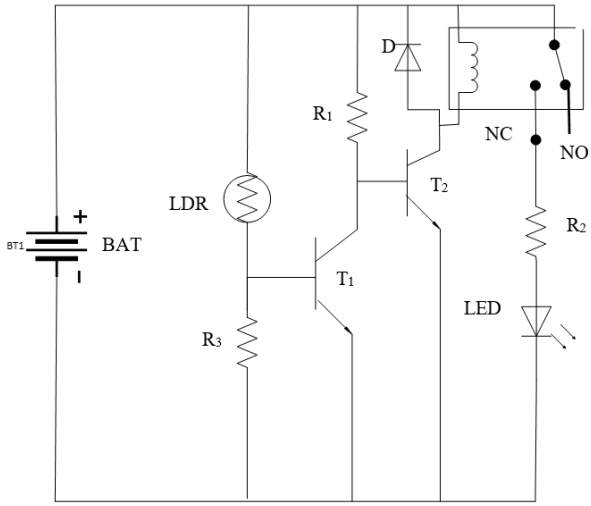

Fig. 7. Control Circuit of Solar Street Light

F. Design and Calculation of Solar Street Light System

The solar street lighting system is tailored for Technological University (Mandalay). This paper presents the design calculations for the PV module, battery sizing, charge controller sizing, lumen and illuminance determination, lamp type selection, light pole height calculation, light pole spacing, and tilt angle. Additionally, it includes a cost comparison between the solar street lighting system and a conventional street lighting system

Road data collection must be completed before building the solar street lighting system for Technological University (Mandalay). The width and length of the road or street that will have solar street lights installed are measured at this stage [2].

Adipati Road, the main entryway, is a two-lane street that is 191 meters (627 feet) long. The width of each lane, including the pedestrian side walk platform, is 7 meters (22 feet).

G. Calculation of Luminaries Spacing

This solar street lighting design uses "GLL WP5" LED light fixtures. These fixtures use a single powerful LED. Compared to high pressure sodium street lights, they can save 50% to 75% electricity. Below is a table 2 detailing the main features of the 35W "GLL WP5" LED street lighting fixture [4].

Lamp output (LED), LL= Efficacy of lamp ×Watt of lamp
Lamp output of the lamp (LED), LL= 120 lm/W × 35 W
= 4200 lm

Luminaries spacing or distance between light poles can be obtained by the following equation.

$$S = \frac{LL \times CU \times LLD \times LDD}{E \times w} \quad (1)$$

Lumen depreciation factor (LLD) = 80% = 0.8
Luminaire dirt depreciation factor (LDD) = 90% = 0.9

$$S = \frac{4200 \times 0.9 \times 0.8 \times 0.9}{10 \times 7}$$
$$S = 38.88 \approx 39m$$

II. SPECIFICATION OF 35W" GLL WP5" LED STREET LIGHT FIXTURE

Specification	Value
Power	35 W
Luminous efficacy	120 lm/W
Power factor	>0.95
Beam angle	120 deg.
Color rendering index	>75
Color temperature	4000K,4500K,5000K
Light output	4200 lumens
Life span	5000 hours

H. Calculation of Number of Poles

The number of light poles which required for the lighting system is calculated by using following equation.

$$\text{No. of light pole} = \frac{\text{Length of road}}{\text{Luminaries spacing}} \quad (2)$$
$$= \frac{191}{39}$$
$$= 4.89 \approx 5\text{poles}$$

I. Calculation of Pole Height

To calculate the height of light pole, beam angle is required. Most of LED light fixtures in the market have a beam angel of 120°.

$$\tan(60) = \frac{19.5}{h}$$
$$h = \frac{19.5}{\tan(60)}$$
$$h = 11.25 \approx 11m$$

J. Calculation of Solar Module Size

System nominal voltage = 12V

Power consumption of LED = 35 W

Working hour = 12hour/day

Daily load consumption = Power consumption of LED × Working hour
= 35 × 12
= 420 Whr/day

For PV system,

Cable loss = 5%

% of max: use of cable = 100% - 5% = 95%

Depth of discharge (DOD) of battery = 80%

Efficiency of conversion = 90%

Total solar energy requirement

$$= \frac{\text{Daily load consumption}}{\%\text{ of cable} \times \text{DOD \% of battery} \times \eta_{con}} \quad (3)$$
$$= \frac{420}{0.95 \times 0.8 \times 0.9}$$
$$= 614\text{Whr / day}$$

$$\text{Module size} = \frac{\text{Total solar energy requirement}}{\text{Average peak sun hour in Mandalay}} \quad (4)$$
$$= \frac{614}{5.5}$$
$$= 111.63 \approx 120W$$

The selected solar module is 120W "CNBM 6M-120". The following table 3 show the specification of 120W "CNBM 6M-120" solar panel.

III. SPECIFICATIONS OF 120W "CNBM 6M-120" SOLAR MODULE

Specification	Value
Rated Maximum Power, (M_p)	120 W
Power Tolerance	∓ 5W
Module Efficiency	18.60 %
Open Circuit Voltage, (V_{oc})	22.7 V
Maximum Power Voltage, (V_{mp})	18.6 A
Short Circuit Current (I_{sc})	6.84 V
Maximum Power Current, (I_{mp})	6.4 5A
Temperature Coefficient of I_{sc}	+ 0.06 %
Temperature Coefficient of V_{oc}	- 0.32 %
Temperature Coefficient of P_{mp}	- 0.45 %
Operating Temperature	- 45 ~ + 80℃
Standard Test Temperature	25℃

In this solar street lighting system design, monocrystalline type "CNBM 6M-120" solar panels are used as they are well-designed to illuminate large area with the highest intensity of light and their fair prices. The following table shows the specifications of 120W "CNBM 6M-120" solar panel and this data are for reference only.

Then, the battery size is calculated by the following equation:

$$\text{Battery size} = \frac{\text{Daily load consumption}}{\text{DOD \% of battery} \times \text{System nominal voltage}} \quad (5)$$

$$= \frac{420}{0.8 \times 12}$$

$$= 43.75\text{Ah} \approx 44\text{Ah}$$

So, selected battery is 46 Ah.

IV. Data Summary For Solar Street Light System

Specification	Single Lamp Pole
Solar Module	120W
Controller	7A
Battery	46Ah
LED	35W
Pole Height	11m
Max: Wire Run	5m

The approximately initial cost 1,420,000 kyats is needed to design the solar street lighting. The approximately initial cost of the conventional street lighting 1,000,000 kyats is needed to design it. The comparing of the cost of conventional street lighting is more than the solar street lighting cost during 20 years. When the cost of solar street light and conventional street light was compared over a twenty-year period, conventional street light were more expensive.

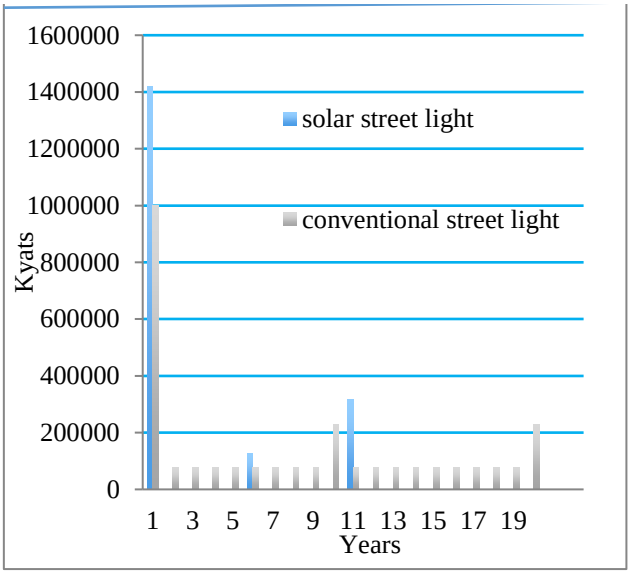

Fig. 8. Comparing Annual Costs of Solar Street Lighting System and Conventional Street Lighting System in Twenty Years

V. Conclusion

The system design is based on Technological University (Mandalay). This statement outlines the process of designing a solar-powered street light system, including calculations for various aspects such as the average brightness (lumen), spacing between light fixtures (luminaries), the number of light poles required, and the height of these poles. The calculations for these parameters have been performed manually. After performing these calculations, the results regarding the average brightness, spacing between fixtures, the number of light poles needed, and the height of these poles are explained. The comparison of the cost of solar street lights and conventional street lights is expressed.

Acknowledgment

The author is deeply gratitude to Daw Moe Moe, Associated Professor and Head of Electrical Power Engineering Department, Technological University (Mandalay), for his kind help and invaluable suggestions. The author wishes to extend grateful thanks to her supervisor, Daw Myat Myat Moe, Lecturer, Electrical Power Engineering Department, Technological University (Mandalay) for her supervision and her kind support all the time of this research work. The author would like to express the deepest gratitude to all of teachers from Department of Electrical Power Engineering, Technological University (Mandalay) and also grateful to her friends who helped her towards the successful completion of this work.

References

[1] Terrell Crof, Wilford I. Summers Frederic P. Hartwell: *American Electrician Handbook.*, fifteenth edition McGraw-Hill Companies, Inc. (2009)

[2] Paul,L., Don,M., and Joseph,C.: *FHWA Lighting Handbook* Office of Safety, Federal Highway Administration, New Jersey Avenue, Washinton DC, August (2012).

[3] Matthew Brooks, LO4-Professor Keezer, DK-2: *High Power White LED Technology* ., 21, Janary, (2009).

[4] John Hesketh, LPA Excil Electronics Technical Director: *The LED Revolution and Emergency Lighting.*, (2008).

[5] Lenardic,D.2008:PhotovoltaicModules., http://www.trilos.de/atomstromfrei, September (2008).

[6] Garg, H.P. and Prakash, J.: *Solar Energy, Fundamentals and Applications*, (2000).

[7] Gilbert M. Masters: Renewable and Efficient Electric Power Systems, (2004)

[8] Harvey: battery Chargers and Charging (1989).

Analysis and Simulation of DPFC under Various Fault Conditions

Htar Htar Hlaing[1], Khine Zar Maw[2], May Thingyan Myint[3]
[1]*Department of Electrical Power Engineering, Technological University (Yamethin)*
[2]*Department of Electrical Power Engineering, Technological University (Yamethin)*
[3]*Department of Electrical Power Engineering, Mandalay Technological University*

E.mail: [1]htarhtarhlaing11111@gmail.com,[2]khinezarmaw@gmail.com, [3]maythingyan.ltu@gmail.com

***Abstract*- DPFC originates from the Unified Power Flow Controller achieves its design by removing the shared direct current link. Unlike the UPFC's single three-phase converter setup, the DPFC employs three individual single-phase series converters, enhancing redundancy and elevates system reliability. Moreover, the DPFC offers a cost-effective compared to the UPFC while retaining identical control capabilities. These capabilities include adjusting line impedance, transmission angle, and bus voltage, ensuring effective power flow management within the grid. In this paper, distribution line between Pyinmana primary substation and Paung Laung Extension substation with distributed loads is presented as case study area to analyze the voltage sag (dip) and swell (rise) conditions. The system has been simulated both with and without a DPFC, focusing on voltage sag (dip) and swell (rise) mitigation under various fault conditions using MATLAB Simulink.**

Keywords–DPFC, FACTS, various fault conditions, sag and swell mitigation, load voltage

I. INTRODUCTION

The power quality disturbances have garnered significant attention from researchers seeking optimal solutions. In today's power systems, power quality is a critical concern for industrial, commercial, and residential applications. The voltage problem is particularly under-voltage (voltage sag) conditions caused by over-currents resulting from short circuits or faults in the system, are of primary concern. Numerous research efforts have focused on mitigating voltage sag (dip) and swell (rise) conditions. Voltage sag is widely acknowledged as a crucial power quality disturbance [1]. This paper introduces the concept of a Distributed Power Flow Controller, which comprises series and parallel converters. By employing two strategies—eliminating the shared direct current link and distributing the series converter across the system—the UPFC is enhanced into a novel combined FACTS device: the DPFC, depicted in Fig.1.

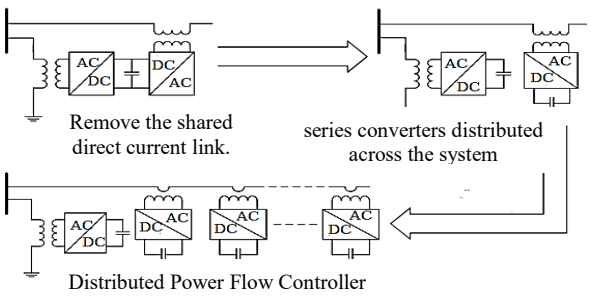

Fig.1. Flow chart from UPFC to DPFC

Just like the UPFC, the DPFC is comprised of parallel and series-connected converters across the system. The parallel converter operates as a STATCOM, while series converters utilize the DSSC concept, employing multiple single-phase converters rather than a single three-phase converter. Each converter within a DPFC functions independently and is equipped with its individual DC capacitor to deliver the necessary DC voltage. Fig.2 illustrates the DPFC configuration.

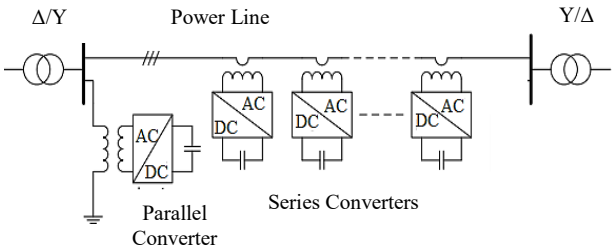

Fig.2. DPFC configuration [2]

II. DPFC OPERATION FOR VOLTAGE SAG (DIP) AND SWELL (RISE) REGULATION

The voltage sag (dip) and swell (rise) regulation is done by controlling reactive power stored in DC capacitor. In both parallel controller and series controller, constant DC voltage is stored in storage capacitor via transformer and IGBT converter. When the parallel controller and series controller sense the load terminal voltage is in sag and swell conditions, the controllers provide parallel and series pulses to the IGBT converters. When the voltage is in sag (dip) condition, parallel and series controller provide pulses to converter so that reactive power is injected to the system and load voltage is maintain nearly reference i.e. regulated value. In the same way, when the voltage is in swell (rise) condition, parallel and series controller provide pulses to converter so that reactive power is absorbed from the system and load voltage is maintain nearly reference i.e. regulated value.

III. MATHEMATICAL MODEL FOR DPFC

The equivalent circuit depicted in Fig.3 of the DPFC is utilized to formulate the mathematical equation for the DPFC dynamic model. V_{SA}, V_{SB}, and V_{SC} denote the three-phase source voltages at the connection point. $V_{se,a}$, $V_{se,b}$, and $V_{se,c}$ represent the AC output voltage of the series converter. The resistance (R) and inductance (L) symbolize the resistance and reactance of the distribution line. The current i_{sa}, i_{sb} and i_{sc} represent line current. A simple model DPFC is used in distribution system for improving the load voltage.

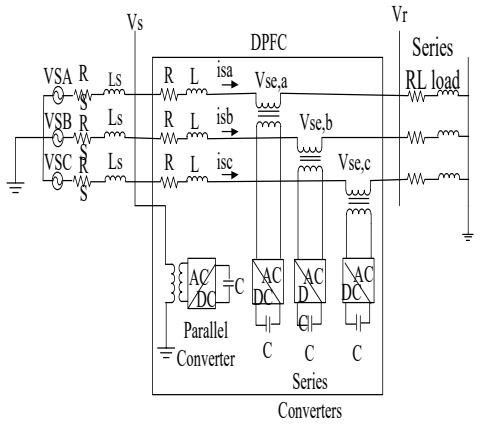

Fig.3. Equivalent circuit of DPFC

When connecting a DPFC in distribution line of two buses system, the synchronization system must be used. The synchronization system can be done with a conventional phase locked loop (PLL). The system voltage is measured to be sent to the PLL for angle estimation. The estimate angle is then used for dq transformation. The reference frame coordinate system is established in a manner where the d-axis aligns directly with the instantaneous system voltage vector, while the q-axis is positioned at a right angle to it. All the controllers will be derived in the d-q system. It is easier to compare the reference with the actual value in the controller.

A. Parallel Device Model

The representation of the parallel device model as a voltage source with series resistance R_{sh} and inductance L_{sh} can be seen in Fig.4 [3].

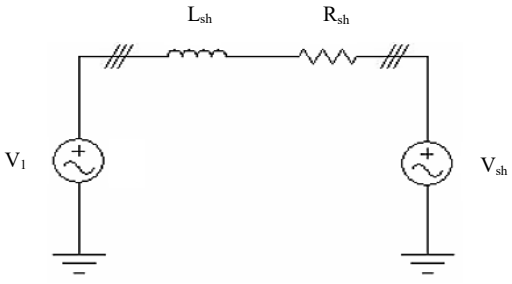

Fig.4. Parallel device model

In the a−b−c axis system, the circuit equation is expressed as:

$$\begin{aligned} V_{1a} + V_{sha} - V_{ra} &= R_{sh} i_{sha} + L_{sh} \frac{d}{dt} i_{sha} \\ V_{1b} + V_{shb} - V_{rb} &= R_{sh} i_{shb} + L_{sh} \frac{d}{dt} i_{shb} \\ V_{1c} + V_{shc} - V_{rc} &= R_{sh} i_{shc} + L_{sh} \frac{d}{dt} i_{shc} \end{aligned} \quad (1)$$

The equation can be organized in matrix format as follows:

$$\frac{d}{dt}\begin{bmatrix} i_{ash} \\ i_{bsh} \\ i_{csh} \end{bmatrix} = \begin{bmatrix} -\frac{R_{sh}}{L_{sh}} & 0 & 0 \\ 0 & -\frac{R_{sh}}{L_{sh}} & 0 \\ 0 & 0 & -\frac{R_{sh}}{L_{sh}} \end{bmatrix} \begin{bmatrix} i_{sha} \\ i_{shb} \\ i_{shc} \end{bmatrix} + \frac{1}{L}\begin{bmatrix} V_{1a} - V_{sha} \\ V_{1b} - V_{shb} \\ V_{1c} - V_{shc} \end{bmatrix} \quad (2)$$

Convert the equation into the d−q-0 axis system:

$$\frac{d}{dt}\begin{bmatrix} i_{shd} \\ i_{shq} \end{bmatrix} = \begin{bmatrix} -\frac{R_{sh}}{L_{sh}} & \omega \\ -\omega & -\frac{R_{sh}}{L_{sh}} \end{bmatrix} \begin{bmatrix} i_{shd} \\ i_{shq} \end{bmatrix} + \frac{1}{L}\begin{bmatrix} V_{1d} - V_{shd} \\ V_{1q} - V_{shq} \end{bmatrix} \quad (3)$$

B. Series Device Model

The device in a balanced three-phase system is represented individually per phase. It is modeled as a voltage source with series resistance R and inductance L, as depicted in Fig.5 [3].

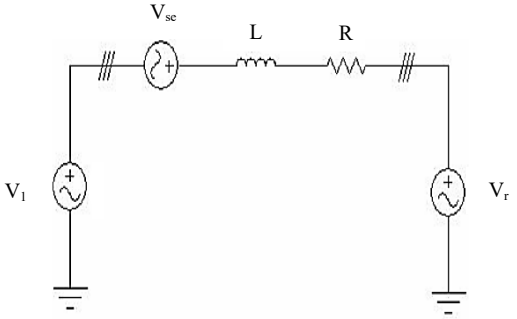

Fig.5. Series device model

The equation set for the resulting three-phase circuit can Be formulated as:

$$\begin{aligned} V_{1a} + V_{sea} - V_{ra} &= R i_a + L \frac{d}{dt} i_a \\ V_{1b} + V_{seb} - V_{rb} &= R i_b + L \frac{d}{dt} i_b \\ V_{1c} + V_{sec} - V_{rc} &= R i_c + L \frac{d}{dt} i_c \end{aligned} \quad (4)$$

Arrange the equations into a matrix format:

$$\frac{d}{dt}\begin{bmatrix} i_a \\ i_b \\ i_c \end{bmatrix} = \begin{bmatrix} -\frac{R}{L} & 0 & 0 \\ 0 & -\frac{R}{L} & 0 \\ 0 & 0 & -\frac{R}{L} \end{bmatrix} \begin{bmatrix} i_a \\ i_b \\ i_c \end{bmatrix} + \frac{1}{L}\begin{bmatrix} V_{1a} + V_{sea} - V_{ra} \\ V_{1b} + V_{seb} - V_{rb} \\ V_{1c} + V_{sec} - V_{rc} \end{bmatrix} \quad (5)$$

Convert the equation into the d−q axis system.

$$\frac{d}{dt}\begin{bmatrix} i_d \\ i_q \end{bmatrix} = \begin{bmatrix} -\frac{R}{L} & \omega \\ -\omega & -\frac{R}{L} \end{bmatrix} \begin{bmatrix} i_d \\ i_q \end{bmatrix} + \frac{1}{L}\begin{bmatrix} V_{1d} + V_{sed} - V_{rd} \\ V_{1q} + V_{seq} - V_{rq} \end{bmatrix} \quad (6)$$

IV. Overview of the Case Study Area

For analysis of various types of fault, the detailed study is carried out at Paung Laung Extension Substation. This substation is located at Paung Laung Extension ward, Pyinmana Township, Myanmar, and constructed for distributing electricity for customers load.

The capacity of Paung Laung Extension Substation is 20 MVA. The incoming line of Paung Laung Extension Substation is 33 kV bus bar of Pyinmana Primary Substation. There is one 20 MVA, 33/11 kV transformer. This transformer converts the incoming 33 kV level to 11 kV level and then distributed to the four feeders are separately operated. The single line diagram of power supply for Paung Laung Extension Substation is shown in Fig.6.

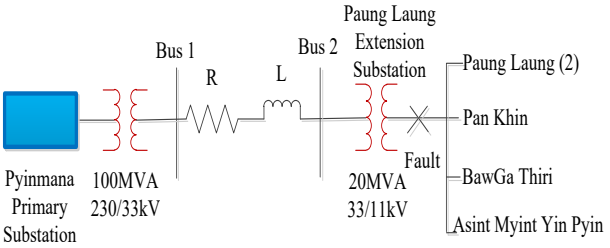

Fig.6. One-line diagram of distribution line of two buses system

At the Paung Laung Extension substation, power quality disturbances such as voltage fluctuations, sag and swell are observed due to system faults.These conditions are in normal operating of the substation. Moreover, the main transformer of the substation cannot provide the sufficient power to the loads. Due to these disturbances, the load current is non-sinusoidal and lags behind the voltage due to inductive impedance characteristics.

TABLE I

LOAD PROFILE IN PAUNG LAUNG EXTENSION SUBSTATION

Parameters	Main Transformer	Total Distribution Load
Active power	16MW	15MW
Reactive power	12MVAR	13MVAR
Power factor	0.8	0.75

V. Modelling of Case Study Area

The simulation model of distribution system without DPFC is illustrated in Fig.7. To analyze voltage sag and swell conditions before using DPFC device, a simulation model is constructed for 33 kV Pyinmana Primary substation to Paung Laung Extension substation with distributed loads. There are three bus bars to measure the values of voltage in the simulation model. To observe sag and swell clearly, system fault conditions are applied near the load side [4].

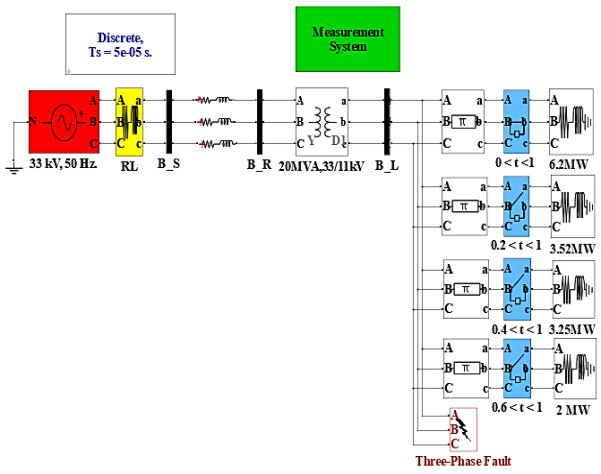

Fig.7. Simulation model of the system without DPFC at various fault conditions

A. Parallel Controller

The parallel controller comprises a three-phase converter connected back-to-back with a single-phase converter. The three-phase converter absorbs active power from the grid at the fundamental frequency and regulates the DC voltage of the capacitor between this converter and the single-phase one. Fig.8 illustrates the block diagram of the parallel controller in the Matlab/Simulink environment.

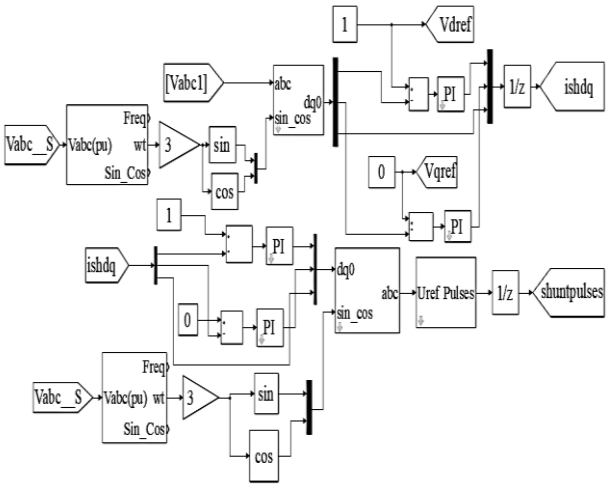

Fig.8. Block diagram of parallel controller [5]

The primary goal of the parallel control is to introduce third harmonic currents into the line, thereby supplying active power to the series converters and regulating the DC voltage across the series capacitors. This third harmonic current is synchronized with the bus voltage operating at the fundamental frequency. To achieve this synchronization, a Phase-Locked Loop (PLL) is utilized to track the frequency of the bus voltage. The output phase signal of the PLL is then tripled to establish a virtual rotating reference frame for the third harmonic component.

Establish a synchronous reference frame transformation for formulating the dynamic model of the parallel controller.

$$\begin{aligned} V_d &= 2/3\,(V_a \sin\omega t + V_b \sin(\omega t - 2\pi/3) + V_c \sin(\omega t + 2\pi/3)) \\ V_q &= 2/3\,(Va\cos\omega t + V_b \cos(\omega t - 2\pi/3) + V_c \cos(\omega t + 2\pi/3)) \\ V_0 &= 1/3\,(V_a + V_b + V_c) \end{aligned} \quad (7)$$

The voltage components in the d-q frame, $V_{d,ref}$ and $V_{q,ref}$ are transformed into the abc frame using Park's transformation.

$$\begin{aligned} V_a &= V_{d,ref} \sin\omega t + V_{q,ref} \cos\omega t + V_0 \\ V_b &= V_{d,ref} \sin(\omega t - 2\pi/3) + V_{q,ref} \cos(\omega t - 2\pi/3) + V_0 \\ V_c &= V_{d,ref} \sin(\omega t + 2\pi/3) + V_{q,ref} \cos(\omega t + 2\pi/3) + V_0 \end{aligned} \quad (8)$$

B. Series Controller

In the series controller depicted in Fig.9, series converter in a DPFC is managed by its dedicated controller. These controllers maintain a uniform control scheme across all series converters. The control strategy employs distinct control loops for managing the two frequency components. Additionally, a separate control loop, focused on the third harmonic, is employed for DC voltage regulation.

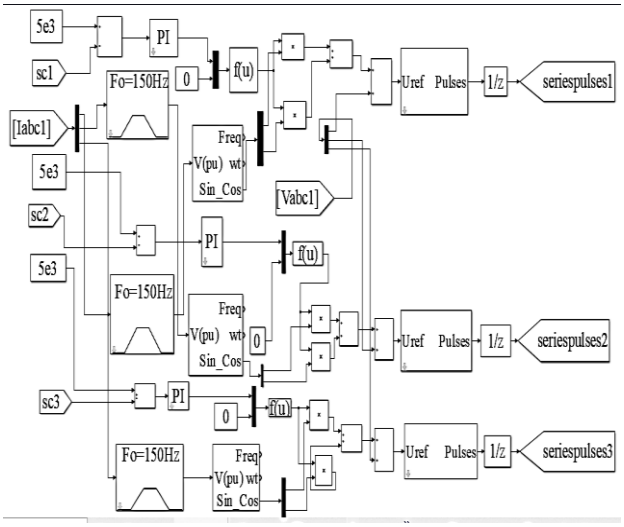

Fig.9. Block diagram of series controller [5]

The representation of voltages in the d-q frame is expressed as:

$$V_d \sin \omega t \quad V_q \cos \omega t \tag{9}$$

The error signal in the DC link capacitor voltage is typically expressed as:

$$V_{se,dc} = V_{se,dc,ref} - V_{dc} \tag{10}$$

The voltage reference in the fundamental component is:

$$V_{se,ref,1} = V_d \sin \omega t + V_q \cos \omega t \tag{11}$$

The voltage reference in the third harmonic component is:

$$V_{se,ref,3} = V_d \sin 3\omega t + V_q \cos 3\omega t \tag{12}$$

The aggregate voltage in a series converter is:

$$V_{se,ref} = V_{se,ref,1} + V_{se,ref,3} \tag{13}$$

VI. DPFC Simulation Model

This model was developed using MATLAB software, as illustrated in Fig.10 [6]. The system is configured with a three-phase programmable voltage source connected to a load. This source is linked to the load via a distribution line spanning 4.7 miles at 33 kV. The DPFC is integrated between the distribution line and RL series loads for dynamic performance analysis. The parallel converter is paralleled with the distribution line through a three-phase transformer, while the series converter is connected to the distribution line in series via three independent single-phase transformers. Various fault conditions are simulated to assess dynamic performance, with time duration of 0.05 seconds (0.3-0.35 seconds). Prior to DPFC implementation, significant voltage sag/swell occurs during different fault conditions, without any compensation, as depicted in Fig.11, 12, 13, and 14. The voltage sag measures about 0.8 per unit, while the voltage swell is 0.6 per unit during various fault conditions. Following the addition of a DPFC, load voltage sag and swell can be effectively mitigated, as demonstrated in Fig.15, 16, 17, and 18.

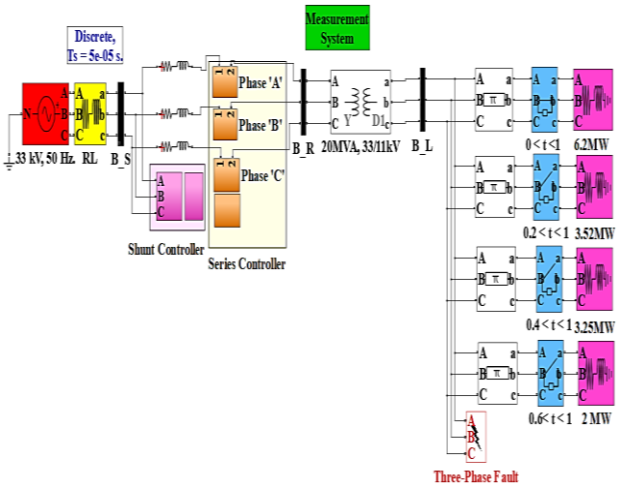

Fig.10. DPFC simulation model

VII. Simulation Outcomes

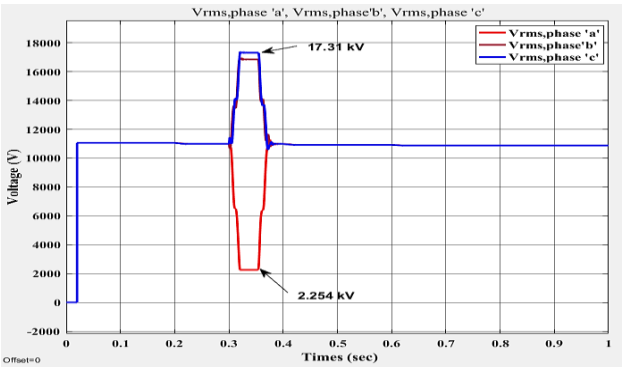

Fig.11. Voltage for three phase load during single line to ground fault without DPFC

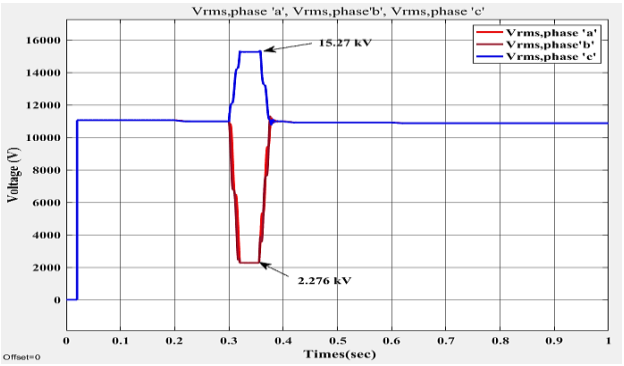

Fig.12. Voltage for three phase load during double line to ground fault without DPFC

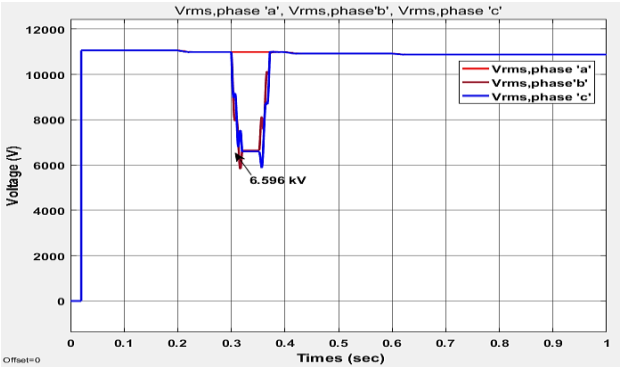

Fig.13. Voltage for three phase load during line to line fault without DPFC

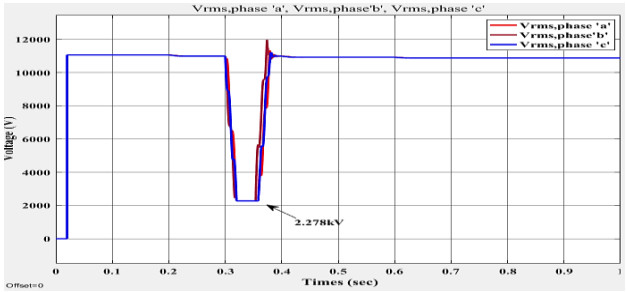

Fig. 14. Voltage for three phase load during three phase fault without DPFC

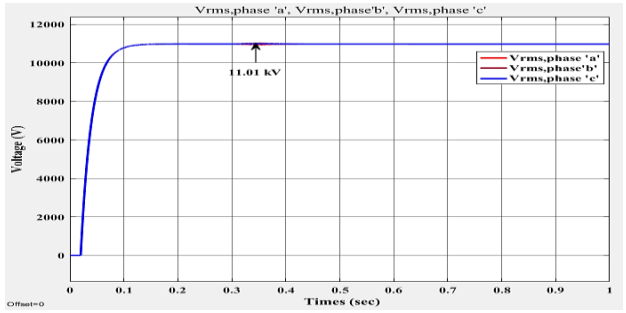

Fig.15. Voltage for three phase load during single line to ground fault with DPFC

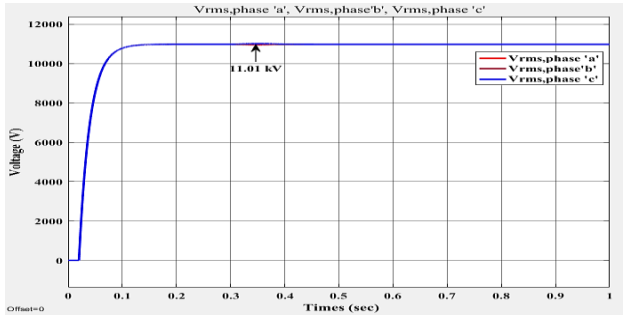

Fig.16. Voltage for three phase load during double line to ground fault with DPFC

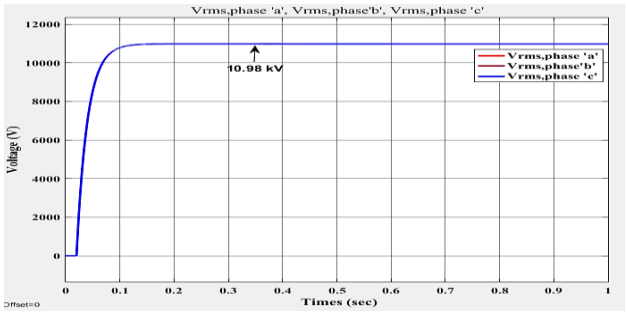

Fig.17. Voltage for three phase load during line to line fault with DPFC

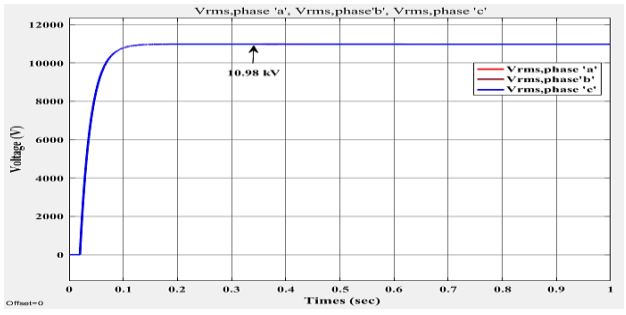

Fig.18. Voltage for three phase load during three phase fault with DPFC

TABLE II

LOAD VOLTAGES ON VARIOUS FAULT CONDITIONS

System Conditions	Case Study	Without DPFC	With DPFC
Single Line to Ground Fault	V_Load	2.254 kV(Sag) 17.31kV(Swell)	11.01 kV
Double Line to Ground Fault	V_Load	2.276kV (Sag) 15.27kV (Swell)	11.01 kV
Line to Line Fault	V_Load	6.596kV (Sag)	10.98 kV
Three Phase Fault	V_Load	2.278kV (Sag)	10.98 kV

VIII. CONCLUSION

In this study, we explore methods to enhance voltage quality within distribution systems. Specifically, we introduce voltage sag and swell compensation through the application of a novel FACTS device known as the Distributed Power Flow Controller. The DPFC shares structural similarities with the UPFC and possesses equivalent control capabilities for balancing line parameters such as line impedance, transmission angle, and bus voltage magnitude. However, this device boasts several advantages over the UPFC, such as heightened control capability, enhanced reliability, and reduced cost. We present a detailed model of the DPFC and design two control loops: series control and parallel control. Through simulation of a distribution system both with and without the DPFC, accounting for various fault conditions, we demonstrate the DPFC's efficacy in mitigating voltage sag (dip) and swell (rise), thereby ensuring acceptable performance across dynamic scenarios.

ACKNOWLEDGMENT

The author extends heartfelt gratitude to Dr. Khine Zar Maw, Professor in the Department of Electrical Power at Technological University (Yamethin), for her invaluable support, guidance, constructive advice, and editing assistance throughout the preparation of this paper.

REFERENCES

[1] Norbert. E: "Effects of voltage sags, swell and other disturbances on electrical equipment and their economic implications," 20th International Conference on Electricity Distribution, Prague, 8-11 June 2009.

[2] Narain and Hinogarni. G: "Understanding FACTS: concepts and technology of flexible ac transmission systems," John Wiley and Sons Inc., (2000).

[3] Jamshidi.A, Masoud Baraka ti.S, and M.M.Ghahderijani et.al.: "Power quality improvement and mitigation case study using distributed power flow controller," IEEE Industrial Electronics,2012.

[4] Heather Gorr: "Simscape power systems, version R2016a (9.0.0.341360), 64-bi (Win64)," February 11, 2016, http://www.mathworks.com.

[5] Papic. I, Zunko.P and D et.al.: "Basic control of unified power flow controller, "power systems, IEEE Transactions on, 1997.

[6] Padiyar K. R: "FACTS controller in power transmission and distribution," Department of Electrical Engineering Indian Institute of Science Bangalore, (2007).

Analysis of Power Factor Correction with Capacitor Bank for Industrial Loads

May Thingyan Myint[1], Dr.Wunna Swe[2], Htar Htar Hlaing[3]

[1]Department of Electrical Power Engineering, Mandalay Technological University
[2]Department of Electrical Power Engineering, Mandalay Technological University
[3]Department of Electrical Power Engineering, Technological University (Yamethin)

Email: [1]maythinggyan.ltu@gmail.com, [2]swethunay@gmail.com, [3]htarhtarhlaing1111@gmail.com

***Abstract*— The overall power factor of modern industries is very poor because of inductive loads absorbing reactive power. There are few solutions, that allow handle the problem of power factor correction. One of those is reactive power compensator based on capacitor banks. Mandalay Soap Factory where all data are collected with variable load conditions has large inductive loads and its power factor is very poor. Before power factor correction, overall power factor of that plant is around 0.74. The main purpose of this paper is to improve power factor and reduce losses. The performance analysis of power factor correction is simulated by using MATLAB software. The finding from calculation and simulation indicated that 120 kVAr and 170 kVAr capacitor banks are the most suitable size for whole loads of that factory. The plant consisting of seventy-two numbers of induction motor is taken as a designed plant from Mandalay soap factory. The ratings of induction motors are from 0.45 hp up to 30 hp. The required reactive power is provided by capacitor banks that are connected parallel to the loads.**

Keywords*— power factor, capacitor banks, induction motor, reactive power, loads, MATLAB/Simulink.

I. Introduction

Problems of power quality in industrial plants are growing due to the increasing number of inductive load and poor power factor. The objectives of an industrial power system are to provide reducing operating costs, improving efficiency and increasing availability. It is necessary to maximize power quality and improve system performance. In general, the two problems of reactive power compensation are load compensation and voltage support. The objectives of load compensation are to increase the value of system power factor, to balance the real power drawn from the AC supply, to compensate the voltage regulation and to eliminate the current harmonic components produced by large and fluctuating nonlinear industrial loads. All power factor of industrial plants may be very poor because of absorbing reactive power in inductive loads. In power distribution system of the plant, shunt capacitors are used for power factor correction. Generally, capacitor installations are economical because of low operating cost and ease of installation to improve industrial power factor.

II. Theory of Power Factor Correction

Electricity is becoming more and more important due to the increasing usage of electricity in our daily life. Nowadays, many loads in industry are inefficient inductive machines, particularly motors and transformer. Most of the distribution systems are faced many problems in poor voltage regulation, poor efficiency, poor power factor, high losses, overloading and less reliability for continuity of supply. One of the solutions to solve this problem is power factor correction. It is defined as the compensation of reactive power for AC power system. Correction of power factor can be applied to improve the transmission network stability and the efficiency for the utility of electrical power transmission or it can be installed to reduce the cost charge for individual electrical customers [1].

A. Power Factor

A power factor of an AC circuit is defined as the cosine of the angle between the current and voltage vectors and the terms leading or lagging indicate that the current leads or lags on the voltage. A voltage applied to a capacitor produces a current which leads the voltage by 90 electrical degrees, a voltage applied to a pure resistance produces a current in phase with it, and a voltage applied to an inductance produces a current lagging it by 90 electrical degrees.

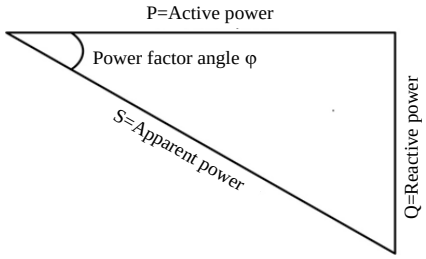

Fig.1. Relationship among active, reactive and apparent power

$$S = \sqrt{P^2 + Q^2} \quad (1)$$

$$P = S\cos\varphi \quad (2)$$

$$Q = S\sin\varphi \quad (3)$$

$$\frac{Q}{P} = \tan\varphi \quad (4)$$

In general, the power factor of the industrial load is lagging and the effects of low lagging power factors are considerable. To supply a fixed amount of kW to a load, it is necessary to provide a greater amount of kVA. The lower power factor which becomes in kVA implication increases losses in generation, transmission and distribution and also requires greater generation and distribution capacity. Maximum efficiency and utilization of generation and distribution capacity would be obtained if the power factor was increased to unity.[1]

B. Power Factor Improvement

Installation of power factor improvement device, to raise the power factor, results in one more of the following effects and advantages [2].

- Reduction in circuit current
- Increasing in voltage level at load
- Reduction in copper losses in the system due to reduction in current.
- Reduction in investment in the system facilities per kW of the load supplied.

There are two disadvantages of low power factor. They are-

- Supplies point of view- Low power factor increases the line current flowing in the supply system and therefore increases the cost of cables, switches, transformers, and generators. Then more initial investment costs.
- Customer point of view- At consumer side, low power factor effects increase the line voltage drop at receiving ends.

C. Power Factor Correction Devices

The power factor correction devices which control the reactive power distribution and flows are:

- Generator
- Synchronous Condenser
- Capacitor bank
- Static VAR compensator (SVC)
- Static synchronous compensator (STATCOM)

I. POWER FACTOR CORRECTION DEVICES AND PERFORMANCE CHARACTERISTICS

Equipment Types	Speed of Response	Ability to support Voltage	Capital Cost per KVAr	Operating Cost
Generator	Fast	Excellent	Difficult to separate	High
Synchronous Condenser	Slow, Stepped	Excellent	Medium	High
Capacitor bank	Fast	Poor	Low	Very low
SVC	Fast	Poor	High	Medium
STATCOM	Fast	Fair	High	Medium

D. Capacitor Bank

The functions of capacitor bank are to reduce maximum kVA demand, improve voltage profile, reduce line/feeder losses, and decrease for energy payments. The best result can be obtained as the shunt capacitors are installed at the load. Depending on situation, 1the capacitor banks are installed at extra–high voltage (above 230 kV), high voltage (66 –145 kV), and feeders at 13.8 and 33 kV. In industrial and distribution systems, capacitor banks are installed at 4.16 kV.

Power factor correction capacitors can be installed at high voltage bus, distribution, or at the load. The following power factor correction approaches are commonly used [2].

- Group Capacitor Bank
- Branch Capacitor Bank
- Local Capacitor Bank

$$C_T = \frac{10^6 \times kVAR}{2\pi \times f \times X_C} = \frac{1000 \times Q_T}{2\pi \times f \times V^2} \quad (5)$$

When the capacitor bank is designed with 3 capacitors in parallel,

$$C_1 = \frac{C_T}{3} \quad (6)$$

III. CALCULATION RESULTS OF POWER FACTOR CORRECTION WITH CAPACITOR BANK

There are nine sections of soap making in the Mandalay soap factory. In the Carbolic section, there are four numbers of 7.5hp induction motors, two numbers of 5.5hp induction motor and one number of 1hp induction motor. One number of 20hp, three numbers of 15hp, three numbers of 5.5hp, one number of 2.2hp, one number of 2hp and one number of 1hp induction motors are operated in the NEEM section. In the Mazzon I, there are two numbers of 30hp, two numbers of 15hp, four numbers of 10hp, three numbers of 5.5hp, two numbers of 1hp and 0.45hp induction motors. Totally seventy-two induction motors are loaded from two numbers of 315kVA, 11kV/400V three-phase transformer.

A. Existing Load Distribution of Transformer No.1 for Mandalay Soap Factory

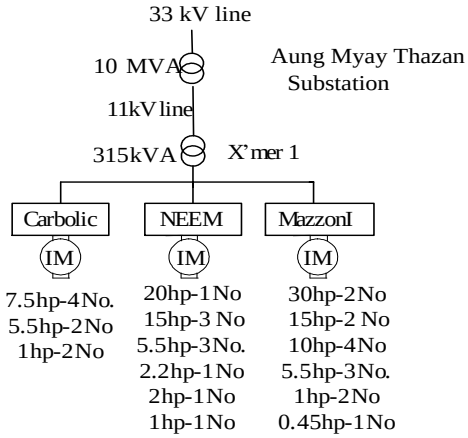

Fig.2. Existing load distribution of transformer No.1 for Mandalay soap factory

II. EXISTING MAXIMUM AND MINIMUM REAL AND REACTIVE POWER LOADINGS FROM TRANSFORMER NO.1 OF MANDALAY SOAP FACTORY

Induction Motor	Total Number	Power Factor		Active Power (kW)		Reactive Power (kVAr)	
		For Max	*For Mini*	*Max*	*Mini*	*Max*	*Mini*
30 hp	2	0.74	0.78	44.76	40.56	40.68	32.54
20 hp	1	0.74	-	14.92	-	13.56	-
15 hp	5	0.74	-	55.95	-	50.85	-
10 hp	4	0.74	0.78	29.84	25.32	27.12	20.31
7.5 hp	4	0.74	0.78	22.38	18.24	20.34	14.63
5.5 hp	8	0.75	0.79	32.82	27.67	28.94	21.47
2.2 hp	1	0.75	0.79	1.64	0.54	1.45	0.42
2 hp	1	0.75	0.79	1.49	0.44	1.31	0.34
1 hp	5	0.76	0.8	3.73	1.76	3.2	2.79
0.45 hp	1	0.76	0.8	0.34	0.21	0.29	0.16
Total				207.87	114.94	187.74	92.66

$S_{T1} = \sqrt{P^2 + Q^2} = \sqrt{207.87^2 + 187.74^2} = 280$ kVA

$\cos \phi = P_{T1}/S_{T1} = 207.87/280 = 0.742$ lagging

$\phi = \cos^{-1} 0.742 = 42.09°$

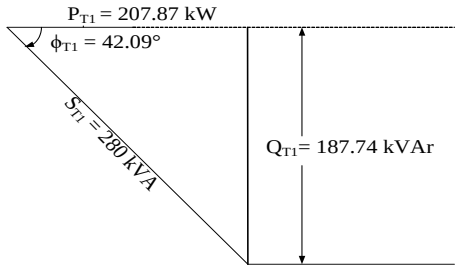

Fig.3. Power triangle of existing maximum load for transformer No.1

Capacitor bank rating for Transformer No.1 required to improve power factor from 0.742 to 0.95 is 120 kVAr.

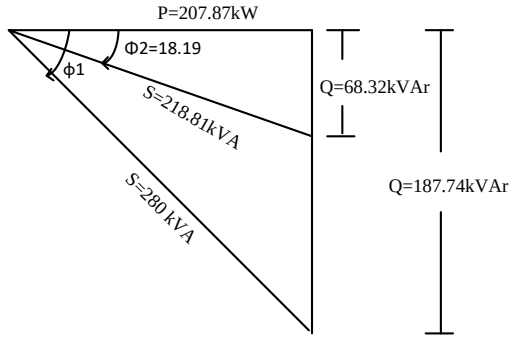

Fig.4. Power triangle for before and after power factor correction (at 95% power factor)

Before power factor correction, maximum overall power factor of that factory for transformer no. 1 is 0.742. 120 kVAr capacitor bank should be chosen for improving the value of power factor from 0.743 to 0.95 to get best result.

- Calculation result for 120 kVAr Capacitor Bank

To improve the overall power factor from transformer no. 1 of the soap factory to 0.95, 120 kVAr capacitor should be chosen and designed.

$$Q_T = 120 \text{ kVAr}, C_T = \frac{10^6 \times \text{kVAR}}{2\pi \times f \times X_C} = \frac{1000 \times Q_T}{2\pi \times f \times V^2} = 2387 \ \mu\text{F}$$

Capacitor bank can be designed to install 3 capacitors which are connected in parallel,

$C_1 = C_T/3 = 795.67$ μF.

$$Q_1 = \frac{(2\pi \times f \times C \times kV^2)}{1000} = 40 \text{ kVAr}$$

Therefore, the total number of 40 kVAr Capacitors should be 3 to get 120 kVAr.

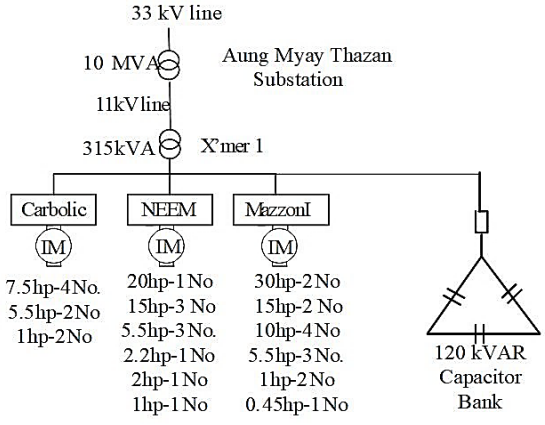

Fig.5. Induction motors and 120 kVAr capacitor bank for transformer No.1

B. Existing Load Distribution of Transformer No.2 for Mandalay Soap Factory

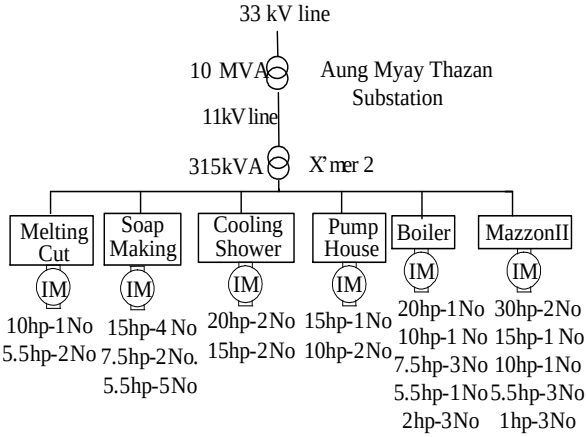

Fig.6. Existing load distribution of transformer No.2 for Mandalay soap factory

III. EXISTING MAXIMUM AND MINIMUM REAL AND REACTIVE POWER LOADINGS FROM TRANSFORMER NO.2 OF MANDALAY SOAP FACTORY

Induction Motor	Total Number	Power Factor		Active Power (kW)		Reactive Power (kVAr)	
		For Max Load	*For Mini Load*	***Max***	***Mini***	***Max***	***Mini***
30 hp	2	0.74	0.78	44.76	41.54	40.76	33.32
20 hp	3	0.74	0.78	44.76	40.78	40.76	32.71
15 hp	8	0.74	-	89.52	-	81.36	-
10 hp	5	0.74	-	37.3	-	33.9	-
7.5 hp	5	0.74	0.78	27.98	23.65	25.43	18.97
5.5 hp	11	0.75	0.79	45.13	40.29	39.8	31.27
2 hp	3	0.75	0.79	4.48	1.23	3.95	0.95
1 hp	3	0.76	0.8	2.24	0.47	1.92	0.35
Total				296.17	147.96	267.88	117.57

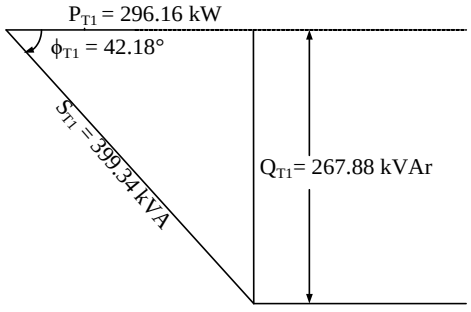

Fig.7. Power triangle of existing maximum load for transformer No.2

Capacitor bank rating for Transformer No.2 required to improve power factor from 0.74 to 0.95 is 170 kVAr.

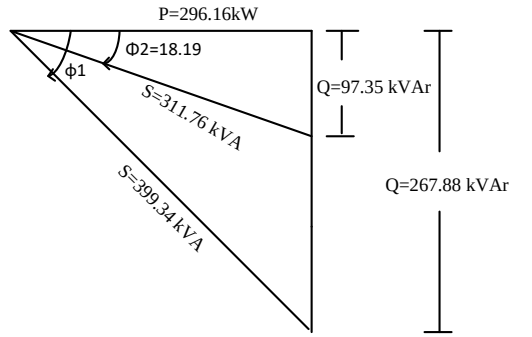

Fig.8. Power triangle for before and after power factor correction (at 95% power factor)

Before power factor correction, maximum overall power factor of that factory for transformer no. 2 is 0.741. 170 kVAr capacitor bank should be chosen for improving the value of power factor from 0.741 to 0.95 to get best result.

- Calculation result for 170 kVAr Capacitor Bank

To improve the overall power factor from transformer no. 2 of the soap factory to 0.95, 170 kVAr capacitor should be chosen and designed.

Q_T = 170 kVAr, C_T = 3382 μF

Capacitor bank can be designed to install 3 capacitors which are connected in parallel, C_1 =1127.3 μF

Q_1 = 57 kVAr

Therefore, the total number of 57 kVAr Capacitors should be 3 to get 170 kVAr.

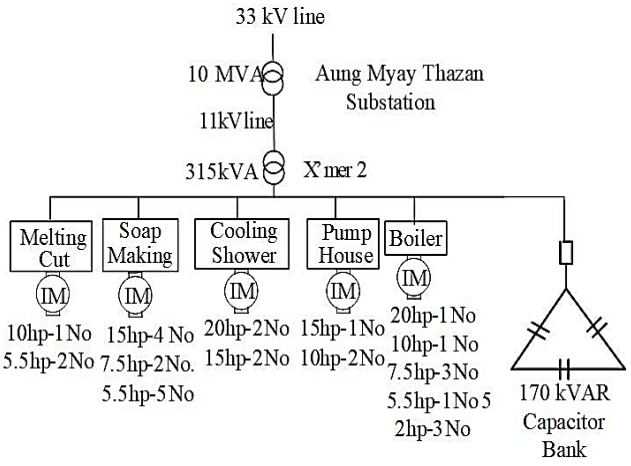

Fig.9. Induction motors and 170 kVAr capacitor bank for transformer No.2

IV. Simulation Results of Power Factor Correction with Capacitor Bank

The load distribution network is the Mandalay Soap Factory in Aung Myay Thazan Township consists of two 315 kVA, 11/0.4 kV step down transformers. The single line diagrams are used as design scheme to construct the complete simulation model in SIMULINK environment. Existing load distribution system consists of three phase supply system, transformer and inductive loads.

The Mandalay Soap Factory which has 11/0.4kV supply source. The 3-phase voltage source block is used to modulate the internal voltage of 11kV source. In the RL series circuit, the value of resistance and inductance are specified from the X/R ratio. The value of X/R ratio is 7 and this value is used for short circuit protection.

A. Simulink Models and Results before Power Factor Correction

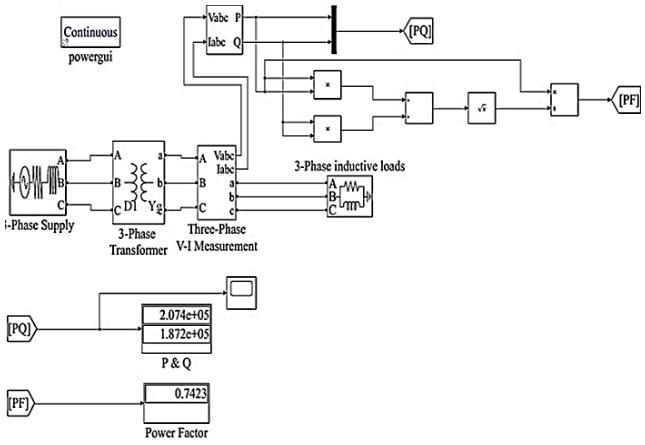

Fig.10(a). Simulink model of existing loads for transformer No. 1

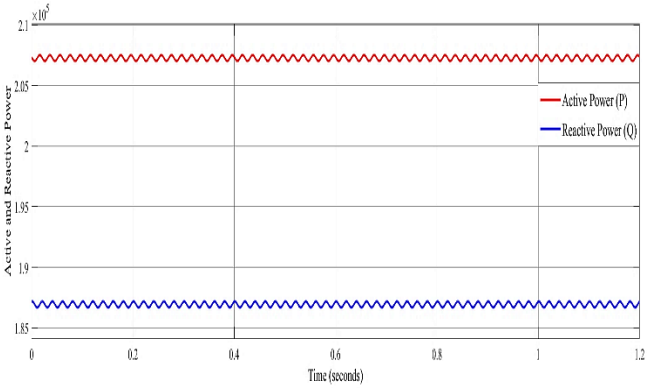

Fig.10(b). Wave form of active and reactive power before power factor correction for transformer No. 1

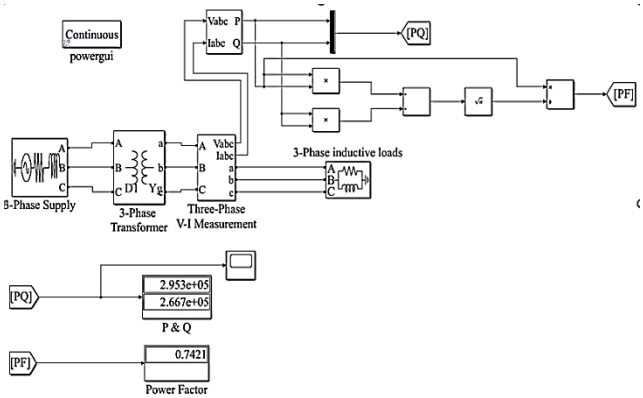

Fig.11(a). Simulink model of existing loads for transformer No. 2

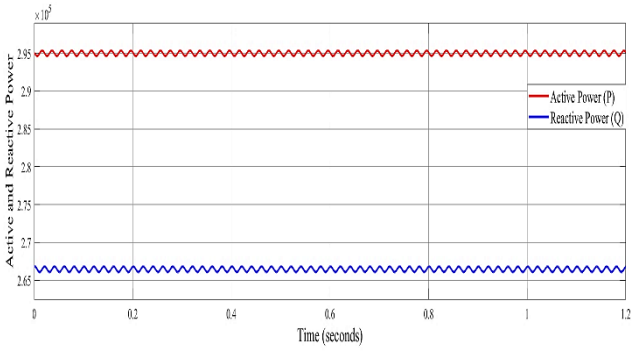

Fig.11(b). Wave form of active and reactive power before power factor correction for transformer No. 2

B. Simulink Models and Results after Power Factor Correction

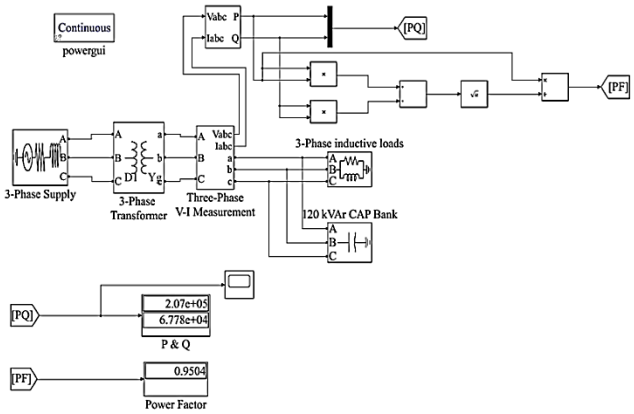

Fig.12(a). Simulink model after power factor correction with 120 kVAr capacitor bank (T1)

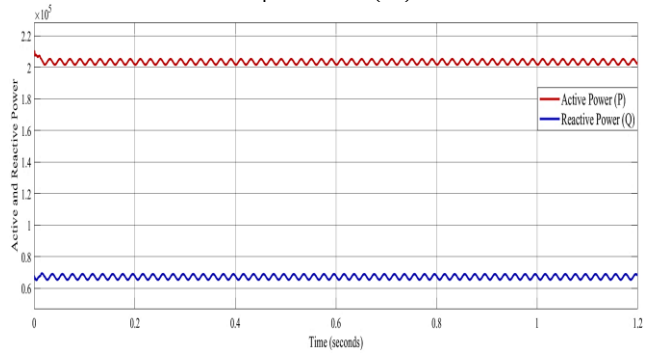

Fig.12(b). Wave form of active and reactive power after power factor correction with 120 kVAr capacitor bank

After installing 120 kVAr rating of capacitor bank, overall power factor of the factory from transformer no. 1 is improved from around 0.74 to 0.95. So 120 kVAr capacitor bank should be installed for transformer no. 1 to get best result, 95% power factor.

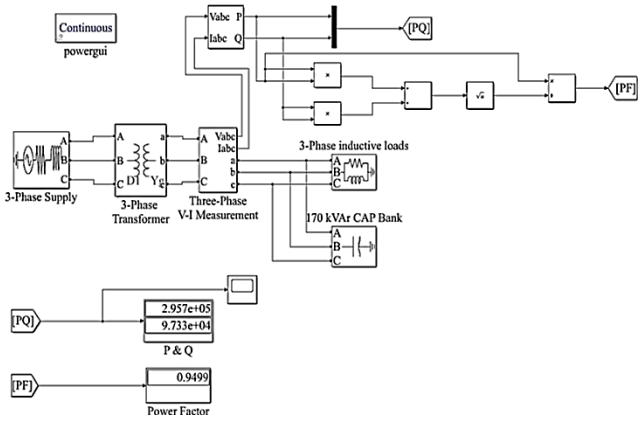

Fig.13(a). Simulink model after power factor correction with 170 kVAr capacitor bank (T2)

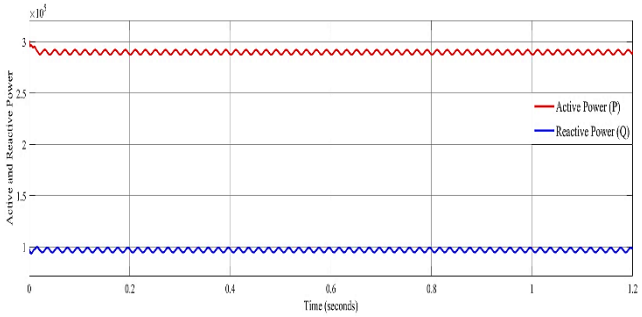

Fig.13(b). Wave form of active and reactive power after power factor correction with 170 kVAr capacitor bank

After installing 170 kVAr rating of capacitor bank, overall power factor of the factory from transformer no. 2 is improved from around 0.74 to 0.95. So 170 kVAr capacitor bank should be installed for transformer no. 2 to get best result, 95% power factor.

IV. Required Capacitor Bank Rating for Desired Power Factor

Loads	Existing Q (kVAr)	Required Q (kVAr)	Existing PF (Before CB)	Desired PF (After CB)	CB Rating (kVAr)
For X`mer 1	187.74	68.32	0.742	0.95	120
For X`mer 2	267.88	97.35	0.741	0.95	170

V. Conclusion

The power factor correction requirements are analyzed. The various compensation solutions for various power factors are compared to choose the suitable size of capacitor banks. The power factor correction using capacitor bank can increase the power factor. Before power factor correction, all power factor is around 0.74 in Mandalay Soap Factory, so this condition is very poor. Therefore, power factor correction is required to improve power factor nearly unity. After installing capacitor bank, the overall power factor of factory is improved from around 0.74 to 0.95. The rating of capacitor banks 120kVAr and 170kVAr for transformer T1 and T2 have the ability to improve the power factor to near unity, reduce reactive power costs, and diminish power quality.

Acknowledgment

The author would like to the heartfelt gratitude to Dr. Wunna Swe, Professor and Head of Department of Electrical Power Engineering, Mandalay Technological University, for his support, guidance constructive advice and editing this paper.

References

[1] Mandar V. Pathak: *"*Review on automatic power factor improvement of induction motor*"*, Assistant Professor, Department of electrical Engineering, DES's College of Engineering & Technology Dhamangaon (Rly), Maharashtra, India, February, (2017)

[2] Utpal: "Automatic power factor correction using capacitor banks", B.E. in Electrical, Assistant Professor, SIET, Jabalpur, M.P., Research interest in field of renewable energy, power distribution, November' (2016)

[3] Heather Gorr: "Simscape power systems", Version 9.0, February 11, 2016, http://www.mathworks.com.

[4] Vijay Kumar Garg: "Power factor improvement of induction motor by using capacitors", Assistant Professor & Electrical Department & UIET, Kurukshetra University, July, (2013)

[5] Pamela Ackerman: "Power factor correction for power systems", Department of Electrical and Computer Engineering, Colorado State University, Fort Collins, April, (2007).

[6] Murthy, M.N.: "Reactive power fundamentals", Director, PSTI, Bangalore, January, (2003).

Speed Control of Induction Motor Used in Escalator Implementing with Fuzzy Logic Controller

Moe Moe[1], Soe Win[2], Soe Soe Ei Aung[3]

[1]*Department of Electrical Power Engineering, Technological University (Mandalay)*

[2]*Department of Electrical Power Engineering, Yangon Technological University*

[3] *Department of Electrical Power Engineering, Yangon Technological University*

Email: [1]ms.dawmoemoe@mail.com, [2]soewin1982@mail.com, [3]soesoeeiaung80@mail.com

***Abstract*—In this paper, the simple method for controlling of induction motor is presented and this method can be used to drive the escalator with constant speed. For escalators, three phase induction motor are commonly used. Because they are more robust, requires less maintenance and a cheaper than other types of motor of equal kilowatt and speed ratings. It is protected against overheating, over speeding and reversing. The major contribution is to control the three-phase squirrel-cage induction motor of continuous power rating 7.5 kW (10 h.p), 1500 rpm, 4 poles and 50 Hz and is compatible for use in 48 inches, step width, 42 steps in order to connect the up floor and the down floor, inclination angle with horizontal floor level 30 degree and vertical rise 17 feet, escalator. The speed of escalator is 40 rpm which is reduced by the gear ratio 1:37. The main function of this paper is to keep the speed at constant speed, instead of fluctuation speed due to the load torque change. The torque changes are considered depending upon the number of person on the escalator. The 130 lb person is approximately 579 N.m. The speed control of indirect field oriented controlled (FOC) induction motor drive with fuzzy logic controller which can be used in escalators are investigated. The proposed system has been developed and simulate by using MATLAB/Simulink.**

***Keywords*—Escalator, Field Oriented Control, Fuzzy, Induction Motor, Motor Drive, Speed.**

I. Introduction

The elevator is crucial in getting people to the intended floor of the building. To operate an escalator, it is necessary to have its own motor and speed controller because it is a mechanical device that demands continuous movement at a constant speed. Electric motors are usually used to move the walk ways of escalators by connecting them to the steps via a belt or chain mechanism. To drive escalator with a constant speed, direct torque control technique is used to drive three-phase squirrel-cage induction motor [1]. It is needed to control for the accelerating and deceleration in order to get the smooth condition because people can find the difficulties to enter and exit an escalator due to the variation of speed when stepping in and moving out due to the sudden change from rest to motion when we enter or exit an escalator, as an effect of Inertia.

AC induction motors are the most commonly used type of motor in escalators due to their unique structure and advantages. To meet the demands of high-performance driving, it is important to have fast dynamic response, accurate speed, and accurate torque.

The most commonly used controller for the speed control of induction motor is field oriented control. The fuzzy set theory is intelligent control. The main advantage of fuzzy logic controller when compared to the conventional controller is that no mathematical model is required for the controller design [2].

The primary objective of this paper is to develop a control method that will maximize the performance of an Induction Motor by using a fuzzy logic controller with FOC drive. This paper presents the speed control of induction motor used in escalator using fuzzy controlled FOC and is analyzed using MATLAB/Simulink.

II. Specification of Induction Motor

In this paper, the reversible type AC three-phase squirrel cage induction motor is used. The specification of induction motor is described in Table. 1.

I. Specification of Induction Motor

Parameter	Symbol	Value
System Frequency	f	50 Hz
Rated voltage	V	400 V
Maximum Voltage	V_{max}	565 V
Rated Power	P	10 HP
Friction	B	0.1 N.m.s
No. of Pole	P	4
Slip	S	1
Rated Torque	T_r	49.13 N.m
Maximum Torque	T_{max}	1311 N.m

For a person (130 lb) = 59.02 kg =579 N.m

Assume the speed of the escalator is 40 r.p.m.

The gear ratio is

$$\frac{\text{Escalator Torque } (T_2)}{\text{Motor Torque } (T_1)} = \frac{\text{Motor Speed } (N_1)}{\text{Elevator Speed } (N_2)}$$

$$= \frac{1500}{40}$$

$$= 37.5$$

The relationship of escalator and motor torque depending upon persons is summarized in Table. 2. For maximum 84 persons, the escalator may have 42 steps.

II. ESCALATOR AND MOTOR TORQUE RELATIONSHIP DEPENDING UPON PERSONS

No. of Person	Person+Escalator (N.m)	Motor Torque (N.m)
84 (T_{max})	49162	1311
11	6750	180
78	45000	1200
50	30000	800
1	750	20

III. MODELING OF FIELD-ORIENTED CONTROLLED INDUCTION MOTOR

The simulink model of induction motor with FOC is shown in Figure.1. In this simulation model block, the induction motor is fed by a PWM voltage source inverter. The speed control of induction machine is simulated for speed curve by MATLAB/Simulink at different load torque.

The closed loop control scheme consists of the mathematical modeling of induction motor, 6-pulse inverter and speed and current controller for generating to satisfy the required logic, sequence and timing for triggering the gate signals for IGBT. Here a speed error is obtained by comparing actual speed with the reference speed. An actuating signal is obtained as the output of fuzzy controller which is fed by an error signal. In order to decide the values to be used for the gains, an experimental simulation has been performed with field-oriented control.

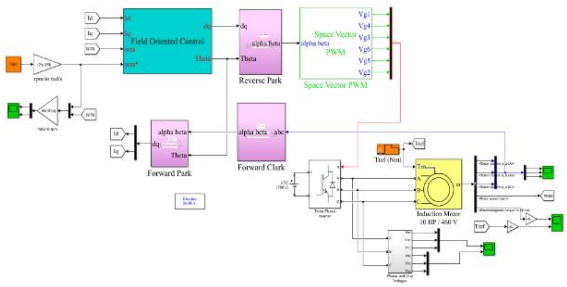

Fig. 1. Simulink Model of Induction Motor with Field Oriented Control

IV. MODELING AND SIMULATION RESULTS OF FUZZY LOGIC CONTROLLER

The indirect field-oriented control of fuzzy controller algorithm has been simulated in MATLAB as shown in Figure.2. The membership functions for the speed error and change in error as input are shown in Figure.3 and Figure.4. The membership function for output is shown in Figure.5 and for rule editor is shown in Figure.6.

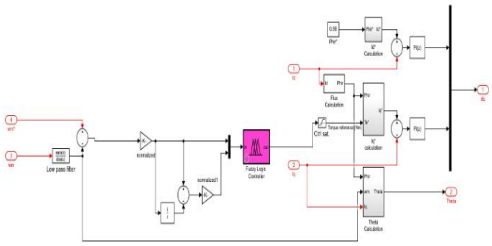

Fig. 2. Fuzzy Logic Controlled FOC

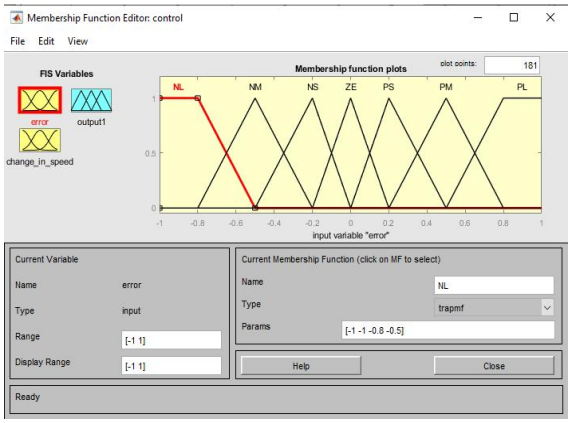

Fig. 3. Membership Function for Speed Error

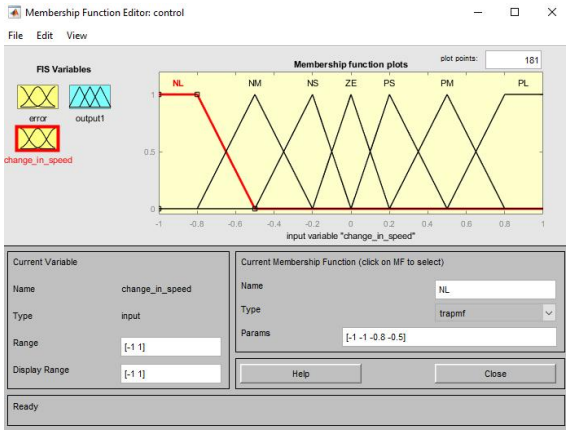

Fig. 4. Membership Function for Speed Change

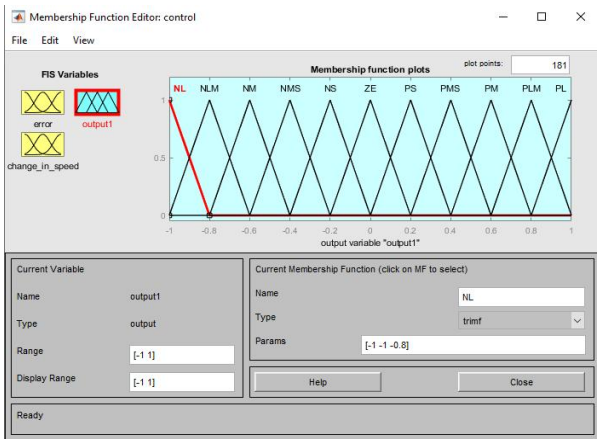

Fig. 5. Membership Function for Output

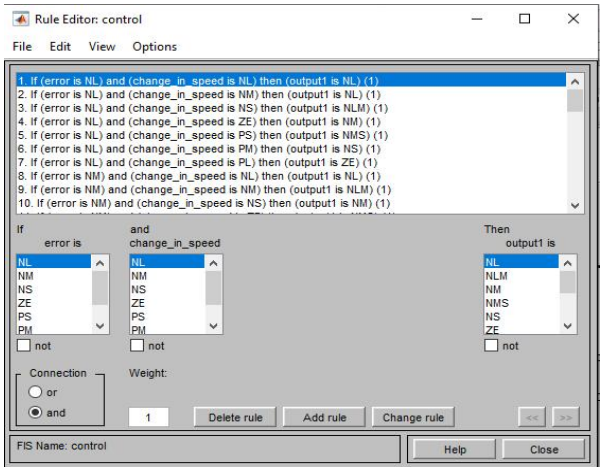

Fig. 6. Membership Function for Rule Editor

V. Simulation Results

The simulation results of the fuzzy-based speed controller are performed using MATLAB/SIMULINK. Torque changes are set as 180, 1200, 800 and 20 N.m at constant speed 1500 r.p.m. To observe the torque control performance, the motor speed and torque are set in simulation as shown in Figure. 7. The resultant load torque of three-phase induction motor is shown in Figure.8.

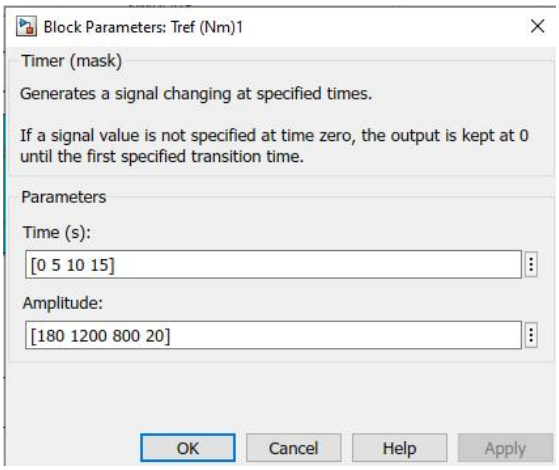

Fig. 7. Torque Change Parameters

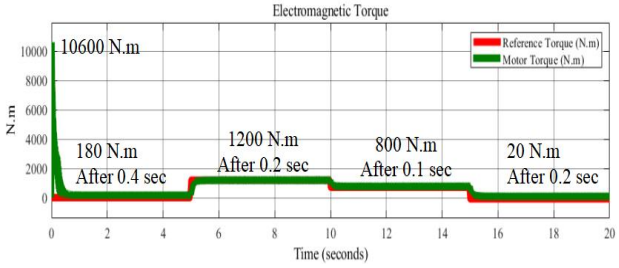

Fig. 8. Measurement for Torque Changes

Figure.9 is shown the resultant stator current of induction motor. The starting current is 562 A but the stable current is reached after 0.4 second. The curves of the R.M.S values for the stator current and phase voltage are shown in Figure.10 and Figure.11.

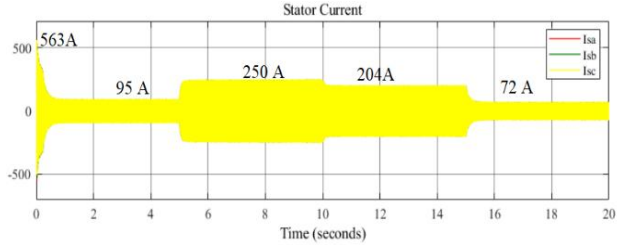

Fig. 9. Stator Current with Fuzzy Logic Controller

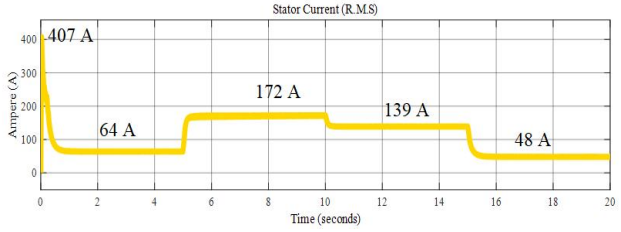

Fig. 10. R.M.S Value of Stator Current

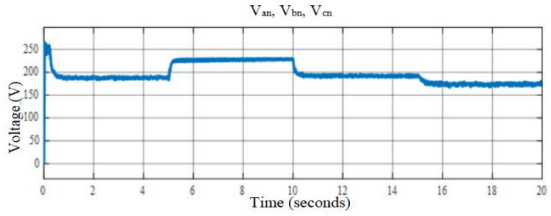

Fig. 11. R.M.S Value of Stator Output Voltage

The rotor speed of the machine at difficult load torque is shown in Figure.12 and Figure.13. The motor shaft receives a sudden load, resulting in a small dip or rise in the rotor speed that quickly recovers.

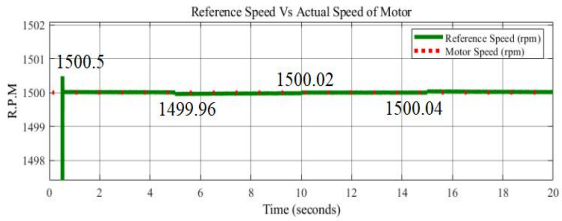

Fig.12. Speed of Motor with Torque Changes using Fuzzy Logic controller

When the load torque changes from no-load to 100 Nm, the speed decreases to the 1499.98 rpm and return to the desired speed in 0.01 seconds. The speed increases to the 1500.02 rpm when the load torque changes from 100 Nm to 10 Nm but the desired speed is reached after 0.01 second. And then the speed slightly increases to.1500.025 rpm, return to desired in 0.01 second.

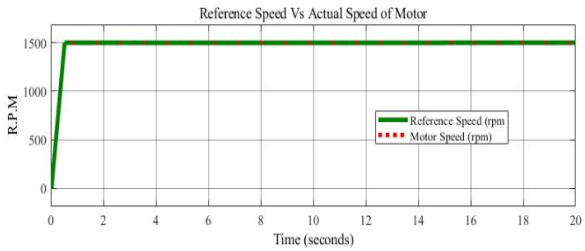

Fig. 13. Result of Speed with Torque Changes

Table.2. shows performance analyses of different speed controllers for induction motor 1500 rpm reference speed and different load torque. According the results, Fuzzy has fast transient response and less overshoot than other controllers.

III. Comparative Analysis for Speed Under Torque Varying Condition

Load Torque (N-m)	Setting Time (seconds)	Speed Over/Under Shoot (rpm)	Speed Rise Time (second)	Steady State Speed (N-m)
180	0	1500.5	0.4	1500
1200	5	1499.96	0.2	1500
800	10	1500.02	0.1	1500
20	15	1500.04	0.2	1500

VI. CONCLUSIONS

In conclusion, the analysis of a fuzzy speed controller for closed loop operation of the induction motor drive system has revealed that it provides improved speed response and higher levels of robustness and effectiveness. In order to control this machine, rating is 7.5 kW (10 hp), 400 V, 1500 rpm, 50 Hz and 4 poles and is compatible for use in 48 inches' step width, 42 steps in order to connect the up floor and the down floor, inclination angle with the horizontal floor level 30 degree and vertical rise 17 ft, escalader. For escalator, three phase induction motor are commonly used. Because they are more robust, requires less maintenance and a cheaper than other types of motor of equal kilowatt and speed ratings. Simulation carried out and the resultant outputs are compared with the results obtained from PI and Fuzzy logic controller. From the simulation results, the output speed (1500 rpm) can be exactly obtained with minimum time during torque changes on escalator depending upon the number of persons, for example, 11 persons (800 N.m), 78 persons (1800 N.m), 50 persons (800 N.m) and 1 person (20 N.m). The performance of Fuzzy controlled-FOC is given smooth condition during torque change conditions. Therefore, the escalator will be moving steadily with 40 rpm which is reduced by gear ration whenever the torque using FOC controlled induction motor with Fuzzy controller.

ACKNOWLEDGMENT

The author is thankful to the Organization of ESEJ and deeply thankful to all persons who give support and encouragement.

REFERENCES

[1] Soe Sandar Aung and Thet Naing Htun, "Speed Control System of Induction Motor by using Direct Torque Control Method used in Escalator" Published in International Journal of Trend in Scientific Research and Development (ijtsrd), ISSN: 2456-6470, Volume-3, Issue-5, August 2019, pp.2250-2253, https://doi.org/10.31142/ijtsrd27903.

[2] Fattah, Ahmed, "Design and Analysis of Speed Control Using Hybrid PID-Fuzzy Controller for Induction Motors" (2015). Master's Theses.595. https://scholarworks.wmich.edu/masters_theses/595

[2] Roshan Varghese Rajan , Ganesh. H , Sumith Mathai , Faizal.S and Aby Thomas Baby. 2016. *Escalator Speed Control.* International Journal of Advanced Research in Management, Architecture, Technology and Engineering. Volume 2, Issue 2.

[3] K Rajaraman and S. K. Nagaraja . 1984. *An Elevator Speed-Control System Using Squirrel-Cage Induction Motors*. IEEE Transactions on Industrial Electronics. Volume IE-31. No.2.

[4] Fathalla Eldali. 2012. *A Comparative Study Between Vector Control and Direct Torque Control of Induction Motor Using Matlab Simulink. Department of Electrical and Computer Engineering*. Degree of Master of Science Colorado State University Fort Collins, Colorado.

[5] Ned Mohan. 2020. *Electric Drives: An Integrative Approach*. Department of Electrical Engineering, University of Minnesota, USA.

Performance Analysis of the Incremental Conductance (INC) Based MPPT Control Algorithm for Solar Power System

Nann Pa Pa Linn[1], Moe Moe[2], Myat Myat Moe[3]

[1]*Technological University (Mandalay)*

[2]*Technological University (Mandalay)*

[3]*Technological University (Mandalay)*

Email: [1]nanpapalinn.npp1500@gmail.com, [2]ms.dawmoemoe@mail.com, [3]myatmyatmoe88@mail.com

***Abstract*— These days, more and more people are coming around to the idea of producing power utilizing renewable energy sources (RES). There are basically three types of renewable energy sources (RES) for the generating process: wind, photovoltaic (PV) cells, and fuel cells. Solar power systems, despite being highly effective, face challenges such as low efficiency and dependence on daylight. To enhance their performance, maximum power point tracking (MPPT) is crucial. This study analyzes the performance of a 20-kW solar power system equipped with MPPT, specifically utilizing the Incremental Conductance (INC) algorithm. Using MATLAB/Simulink, the simulation model integrates the INC MPPT algorithm, DC-to-DC boost converters, and solar panels. As a result, the INC MPPT algorithm works effectively in variable weather situations. Comparing scenarios with and without an MPPT controller under different irradiance levels, the findings demonstrate that the developed INC MPPT controller significantly improves the efficiency of the solar PV system.**

Keywords*— *Photovoltaic (PV) cells, Maximum Power Point Tracking or MPPT, DC-to-DC Boost Converter, Incremental Conductance or INC, MATLAB/Simulink.

I. Introduction

Renewable energy sources can be included into the supply of energy to help with the issues related to the production of power from fossil fuels. The light emitted by the sun is one renewable energy source that can be utilized for this. Through the use of photovoltaic technology, this light may be transformed into clean electricity. Beginning in the 1970s of the 20th centuries, photovoltaic (PV) systems have been used to generate electricity, and their use is currently expanding quickly throughout the world [1]. However, there is an issue with employing PV systems for generating because of their low system efficiency [2]. Throughout the day, the sun's position varies. Consequently, the PV system's output varies. In this case, producing the maximum power requires a tracking system known as a Maximum Power Tracking or MPPT.

MPPT controllers have advanced quickly in terms of simplicity, efficiency, precision, speed of tracking, and dependability. The best MPPT algorithm often responds quickly to changes in output power and oscillates less around the maximum power point or MPP. There exist numerous implemented MPPT control mechanisms available at the moment. These controllers track either a PV system with numerous maximum power points or the PPP under uniform irradiation for a distinct MPP [3]. Any PV system's MPP should be distinct, meaning that tracking it doesn't need a complicated algorithm. Most of the time, unexpected occurrences can happen. One of the best ways to consistently influence the amount of power that can be extracted from any PV system is by partial shading or PS. Under Partial Shading, the MPPT algorithms' efficiency is low [4][5]. This paper examined and discussed INC MPPT algorithm, which was suggested by the researchers as a way to improve solar system efficiency. Additionally, a system model built on the INC MPPT algorithm is created. MATLAB software is used to construct the whole model, which is used to assess the proposed system's capabilities.

The structure of the paper is as follows. The DC-to-DC Boost converter and the 20 MW PV system's design and calculations are shown in Section 2. The INC MPPT controllers and their MATLAB/Simulink implementation are shown in Section 3. and also explains the outcomes of the simulation. Section 4 contains the conclusions.

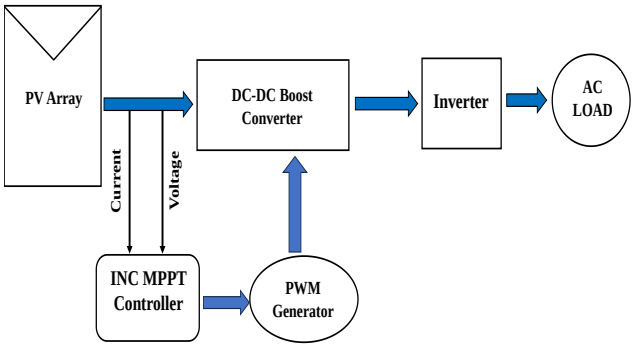

Fig. 1. The Schematic Representation of the INC MPPT Solar-Powered Apparatus

II. Design Calculation of 20kW Solar Power System and DC-to-DC Boost Converter

A. Single-Diode PV Cells

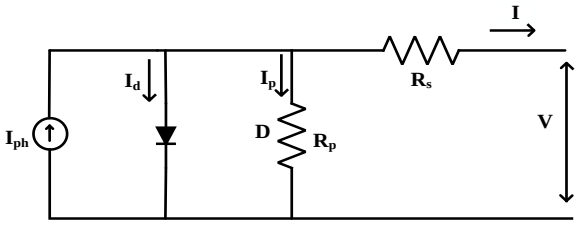

Fig. 2. Equivalent PV Cell Circuit for a Single Diode

A comparable electric circuit model is created to simulate the PV array and ascertain its output characteristic under various operation conditions. The just one diode photovoltaic model is the one used in this work, despite the fact that there are several models in the literature. The comparable circuit for a solar cell has a current source coupled in parallel to a diode while accounting for series and shunt resistances. The electrical design of this device is shown in "Fig. 2". One diode, crossed by a current (I_d), and

a current source, which produces the photocurrent (I_{ph}), make up the analogous model. At the shunt resistance R_p, the leakage current is I_p.

By Kirchhoff's Current Law (KCL),

$$I = I_{ph} - I_d - I_p \quad (1)$$

An expression for the association between the current (I_d) and voltage (V_d) of the diode is as follows:

$$I_d = I_o\left(e^{\frac{qV_d}{KT}} - 1\right) \quad (2)$$

The current of leakage brought on by the resistivity of shunts R_p is known as the I_p. The following can be used to express the connection between the electrical voltage(V) throughout the cell and the I_p current:

$$I_p = \frac{V + R_s I}{R_p} \quad (3)$$

Replacing (2) and (3) by their expressions, equation (1) becomes:

$$I = I_{ph} - I_o\left\{\exp\left[\frac{q(V + I \times R_s)}{n \times K \times N_s \times T}\right] - 1\right\} - \frac{V + IR_s}{R_p} \quad (4)$$

With,

N_s = Quantity of PV cells connected in series
k_i = 0.0032
T = Temperature(°K)
G = Irradiance (W/m2)
T_n = Nominal Operating Temperature (°K)
n = diode ideality factor
I_0 = diode saturation current
K = The Boltzmann constant ($1.3806 \times 10{-}23J/K$)
q = charge of electron ($1.602 \times 10{-}19C$)
I_{ph} = photo-generated current
I = PV output current

"Table I" provides the PV module's electrical parameters under Standard Test Conditions or STC.

I. 555W PV MODULE'S PARAMETER INFORMATION

PV Parameter	The Values
Peak Power, P_{mp}/W	555
Maximum Power Level Voltage, V_{mp}/V	42.93
Maximum Power Level Current, I_{mp}/A	12.93
Voltage of Open Circuit, V_{oc}/V	50.45
Current of Short Circuit, I_{sc}/A	13.73
Module Effectiveness, %	21.7
Tolerance for Power Output, W	0~ +5

Finding the total quantity of PV modules for a 20-kW solar PV system is the first stage in system design. The number of modules that should be placed in series as well as parallel must then be considered. According to the information described in "Table I". The calculated sizing of 20-kW solar PV system is showed in "Tabel II".

As illustrated in "fig. 3", It is evident to us that the amounts of current as well as voltage alter as the irradiance does. As irradiance decreases, the worth of the current also decreases.

"Fig. 4." makes it abundantly evident that changes in temperature also affect the amounts of current as well as voltage. The temperature and voltage have an inverse relationship.

II. CASE STUDY AREA OF PROPOSED SYSTEM

PV System Parameters	Specifications at STC
System Power Rating	20kW, 440 V
System Voltage	1500 V DC
Module Type	SUN EVO5 SE5-72H
Series Connected Modules/String	9
Parallel String/Array	4
Voltage of Open Circuit, V_{oc}	454.05 V
Current of Short Circuit, I_{sc}	54.92 A
Voltage at the Point of Maximum Power, V_{mp}	386.37 V
Current at the Point of Maximum Power, I_{mp}	51.72 A

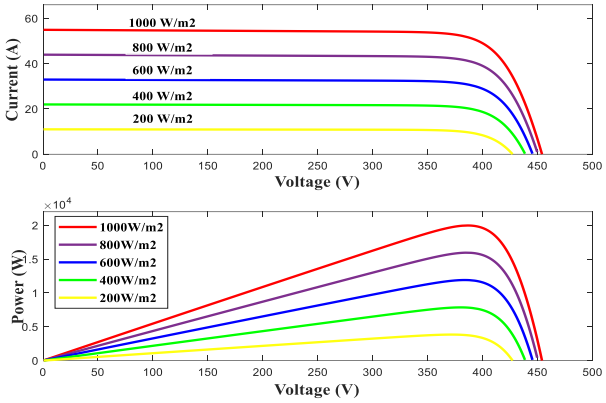

Fig. 3. PV array's V-I and P-V Features with Varying Irradiances

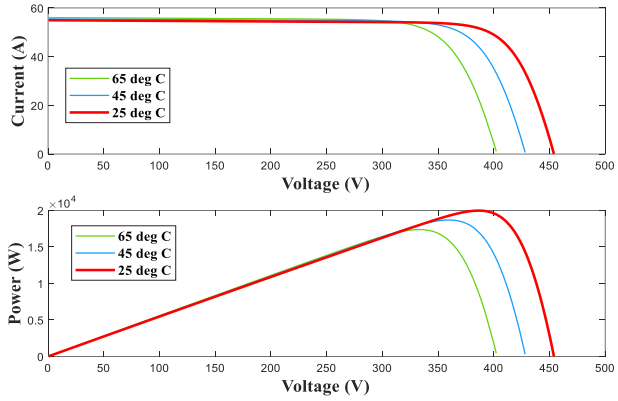

Fig. 4. PV array's V-I and P-V Features at Varying Temperatures

B. Design Calculation of DC-to-DC Boost Converter

PV systems frequently use the Boost converter to boost the low solar panel input voltage to the required voltage. An apparatus for electronic link to get past the disadvantages of the solar power module and demand being directly connected, a DC-to-DC converter is required [6].

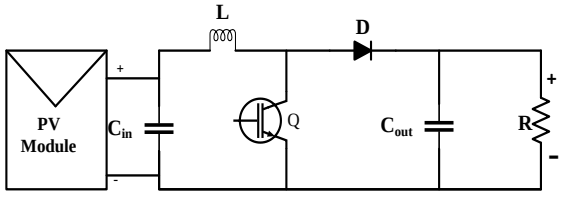

Fig. 5. The Electrical DC-to-DC Boost Converter Circuit

Regardless of temperature and illumination levels, the converter's duty ratio serves as an interaction of the MPPT

between the demand and the source. The following mathematical equations can be employed to figure out the dc-to-dc boost converter's parameters:

$$D = 1 - \frac{V_{in}}{V_{out}} \quad (5)$$

$$R = \frac{V_{out}}{I_{out}} \quad (6)$$

$$L = \frac{D\left(1 - D^2\right)R}{2F_s} \quad (7)$$

$$C = \frac{D}{R\left(\frac{\Delta V_o}{V_o}\right)F_s} \quad (8)$$

With,

D	= Duty Cycle
V_{in}	= PV output or Converter input voltage
V_{out}	= Converter Output Voltage
R	= Resistive Load
F_s	= Switching Frequency
L	= Inductor
C	= Capacitor
$\frac{\Delta V_o}{V}$	= Voltage Ripple Factor

"Table III" shows the calculated values of the dc-to-dc boost converter.

III. PARAMETERS OF DC-TO-DC BOOST CONVERTER

Dc-to-Dc Boost Converter Parameters	Value
Input Capacitor	65.7462 μF
Inductor	0.38 mH
Resistive Load	30.42 Ω
Output Capacitor	65.7462 μF

III. INCREMENTAL CONDUCTANCE (INC) MPPT ALGORITHM AND SIMULATION RESULTS

Maximum power point tracking or MPPT Controller, is a key tactic in solar power systems for maximizing energy collected from solar panels [7]. The primary principle behind MPPT is to run the solar-powered panels at their maximum output power point which is where they can generate the most power given the present environmental circumstances such as sunlight intensity as well as warmth. This paper discusses and simulates the incremental conductance or INC based MPPT algorithm.

A. Incremental Conductance (INC) Algorithm

An MPPT method used in solar power generation is called "Incremental Conductance (INC)". An enhanced version of the perturbation & observation method is the Incremental Conductance. INC based algorithm has several advantages over other traditional techniques, including greater efficiency, high tracking speed, and ease of implementation [8]. This method operates by continually observing and contrasting the progressive panel conductance (ΔI/ΔV) with the instantaneous panel conductance (I/V).

The principle behind incremental conductance is to align the operational point of a solar panel with the point at which the power is maximized. When either (dP/dV) = 0 or (dI/dV) = - I/V, the MPP is reached.

P = VI

From the PV curve at MPP, dP/dV = 0

I + V (dI/dV) = 0

If dI/dV = - I/V, the MPP serves as the operational point.

If dI/dV > - I/V, to the left of MPP is the functioning point.

If dI/dV<-I/V, the functioning point is located to MPP's right.

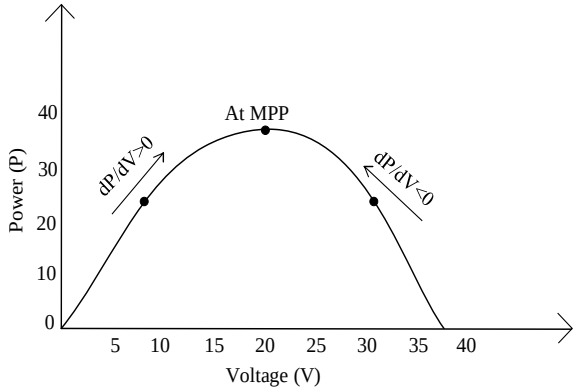

Fig. 6. PV Curve for INC MPPT

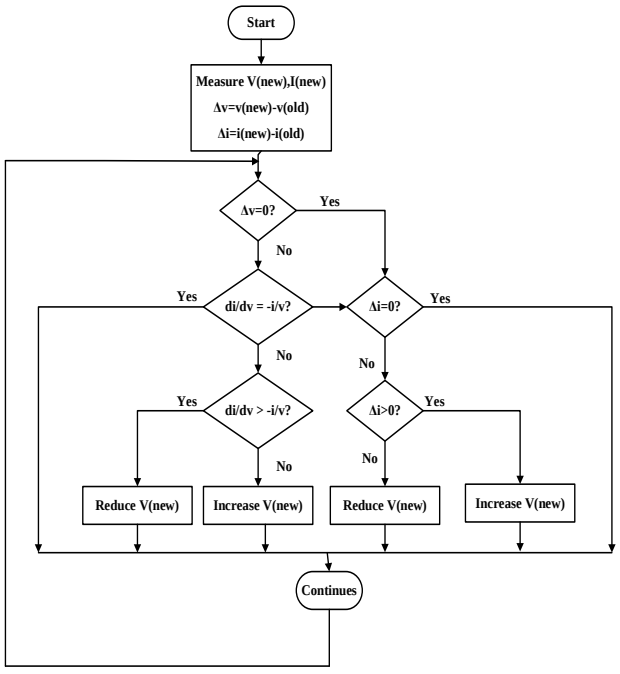

Fig. 7. Schematic of the INC MPPT Flow

The algorithm is represented in "Fig. 7". Similar algorithms are available for voltage-based incremental conductance MPPT and current-driven management, which involves measuring, differentiating, and adjusting current. There isn't disturbance up until an alteration in the environment circumstances is detected, meaning that if dv = 0 and di = 0, MPP is reached and dP/dV = 0, the maximum power point value is equivalent to the voltage required for functioning. The MPP voltage rises as the PV power increases and there is an increase in insolation, as indicated by dV = 0 and dI>0. The way to monitor the MPP, the MPPT needs to raise the operating voltage. Conversely, if dI<0, then MPP voltage and solar energy are impacted by a

reduced insolation, requiring a decrease in PV array operating voltage from the MPPT.

If ΔI/ΔV = - I/V, continues at same direction.

If ΔI/ΔV > - I/V, need to increase operating voltage to arrive at MPP.

If ΔI/ΔV< -I/V, need to decrease the voltage needed to operate at MPP.

To regulate the MPP, PV operating voltage is adjusted by adjusting the DC-to-DC converter's duty cycle. When implementing MPPT with modifying step magnitude, the problem of set tiny or large steps can be handled [9][10]. The customized adaptable size of steps INC method proposes that the PV array's capabilities decide the size of steps instinctively.

B. Modelling and Analysis of Simulation Outcomes

MATLAB software is used to model the entire system. Fig. 8. (a) and (b) shows the model of the suggested system in Simulink.

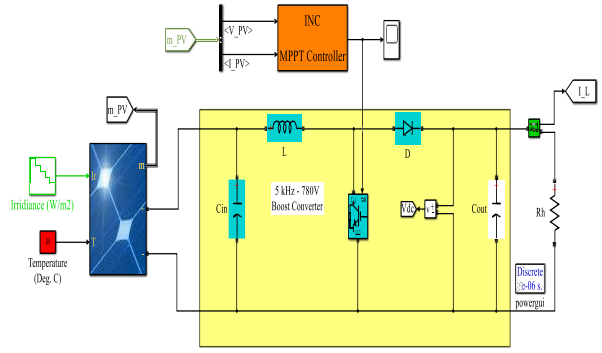

Fig. 8 (a). The Model of Solar Power System with INC in Simulink

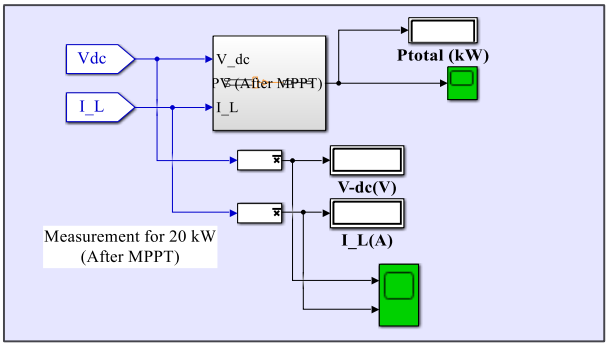

Fig. 8(b). Measuring Block of Solar Power System

It is evident from "fig. 8(a)" that the boost converter is connected to the solar module's output in order to convert DC to DC. Here, the MPPT method is based on conduction and is applied incrementally. The generated voltage and current are measured through the sensors for voltage and current in order to use the INC approach. The MPPT generates the pulse essential to turn on and off the boost converter switch.

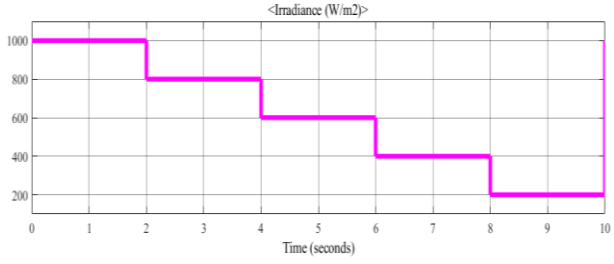

Fig. 9. Irradiance Changes (1000-200-200) W/m^2

The system's performance is examined by varying external factors like irradiation in order to confirm the efficacy of the INC control technical algorithms. Every two seconds, the light intensity changes from 1000W/m^2 to 800W/m^2, 600W/m^2, 400W/m^2, and 200W/m^2. The generated power, voltage generated, and current generated of the indicated PV unit can be observed by changing irradiance from "Fig. 10" to "Fig. 11".

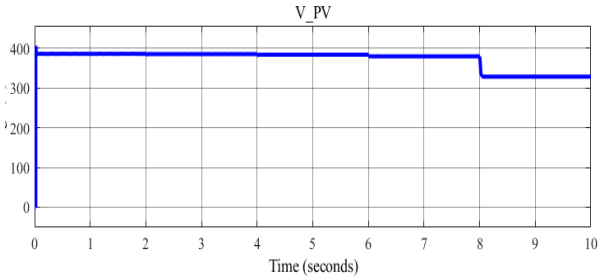

Fig. 10. Voltage Output of Proposed PV Panels

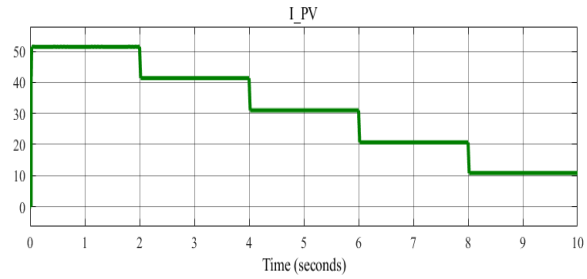

Fig. 11. Current Output of Proposed PV Panels

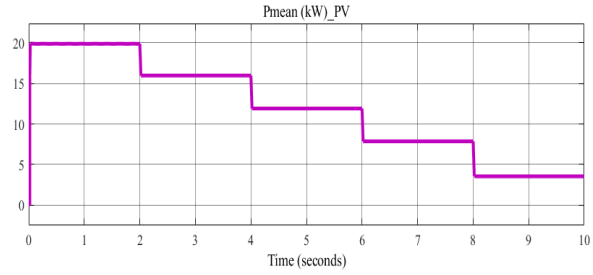

Fig. 12. Power Output of Proposed PV Panels

In Fig. (10), the PV array's voltage output is not steady but is not greatly impacted by the irradiance change conditions. Still, "Fig. (11) makes it clear that the current fluctuates together with the irradiance. Consequently, as shown in "Fig. (12), fluctuations in voltage and current also have an impact on the PV's power production.

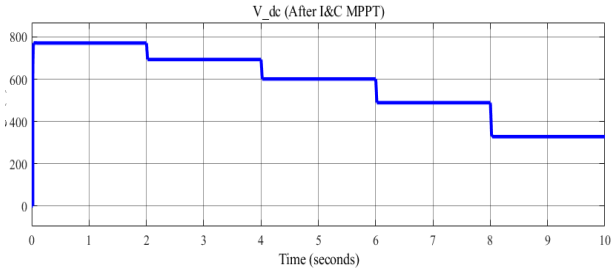

Fig. 12. Voltage Output of Proposed PV Panels with INC MPPT

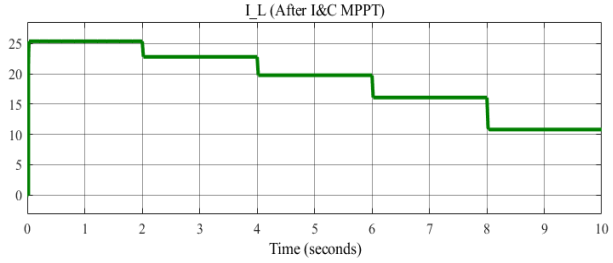

Fig. 13. Current Output of PV Panels with INC MPPT

PV panels implementing INC that have different irradiance are shown in "Fig. 4.12" through "Fig. 4.14," displaying the generated power, voltage, and current. PV array output in “Fig. (10)” and “Fig. (11)” are not constantly changes according to the irradiance. But after using INC MPPT the output of the PV array is constantly changes in irradiance in “Fig. (12)” and “Fig. (13)”.

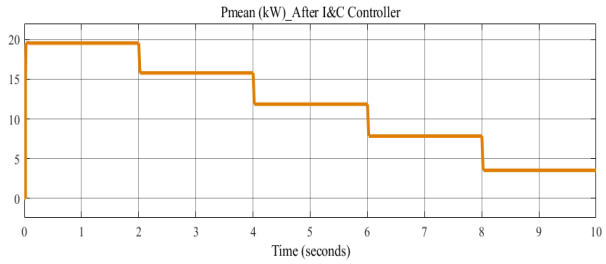

Fig. 14. Power Output of PV Panels with INC MPPT

“Fig. (14)” shows that the INC approach can track the maximum power point. The INC MPPT approaches simulation results can swiftly, precisely, and with less oscillation monitor the maximum power point.

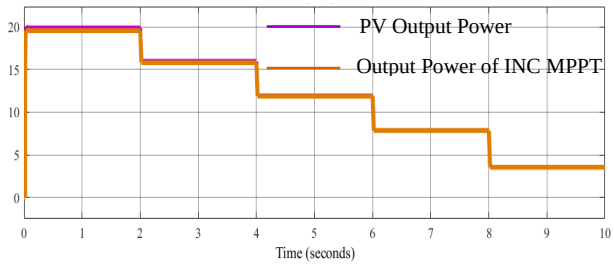

Fig. 15. Comparison of Output Power with Irradiance Change

"Fig. 4.15" demonstrates the selected system's generation of electricity under conditions of variable irradiance regardless of INC MPPT. In contrast, the PV array's power output in "Fig. (12)" and "Fig. (14), with and without INC, is shown. In relation to the PV array output time, the PV output value with INC is almost same in “Fig. (15)”.

IV. Conclusion

In the PV generation industry, maximum power point tracking (MPPT) systems are increasingly important due to the rapid growth of PV systems. The focus here is on MPPT, with the commonly used Perturb and Observe (P&O) algorithm having several drawbacks. This work discusses an alternative MPPT technique based on Incremental Conduction, which effectively measures the maximum power point (MPP) of PV panels under various climatic conditions, ensuring optimal power output and maximizing energy harvest, as illustrated in “Fig. (15)”. The proposed tasks are implemented and analyzed using MATLAB software. Future research could explore other MPPT methods, such as soft computing and hybrid techniques, for solar generation.

Acknowledgment

Gratitude is extended to everyone who has contributed valuable time and effort to assist in finishing this study. Without such support, comprehending and evaluating this research would not have been feasible.

References

[1] Xiao, W. and Dunford, W.G.: A modified adaptive hill climbing MPPT method for photovoltaic power systems, Power Electronics Specialists Conference, (2004).

[2] K.H. Hussein, I. Muta, T. Hoshino and M. Osakada, “Maximum photovoltaic power tracking:an algorithm for rapidly changing atmospheric conditions,” IEEEploc.-Gener. Transmission and Distribution, Vol. 142, No. 1 , Jan. 1955.

[3] C.Thulasiyammal and S Sutha, “An Efficient Method of MPPT Tracking System of a Solar Powered Uninterruptible Power Supply Application,” 1st International Conference on Electrical Energy Systems, 2011.

[4] TrishanEsram and Patrick L.Chapman, “Comparison of Photovoltaic Array Maximum Power Point Tracking Techniques,”IEEE Transactions on Energy Conversion, Vol. 22, No. 2, June 2007.

[5] M. A. G. Brito, L. Galotto, Jr., L. P. Sampaio, G. A. Melo, and C. A. Canesin, “Evaluation of the Main MPPT Techniques for Photovoltaic Applications”, Journals, IEEE transactions on industrial electronics, vol. 60, no. 3, march 2013.

[6] Venkata Reddy Kota, Muralidhar Nayak Bhukya, “A novel linear tangents-based P & O scheme for MPPT of a PV system”, Renewable and Sustainable Energy Reviews, ELSEVIER 2017.

[7] Hala, R. K. T.: A Review Study of Photovoltaic Array Maximum Power Tracing Algorithms, Electrical Engineering Department, Saudi Arabia, (2016).

Developing High Accuracy Trash Classification Model

Aung Khaing Soe[1], Pa Pa Winn San[2], Hnin Yu Wai[3]

[1]*Department of Electronic Engineering, Technological University (Mandalay)*

[2]*Department of Electronic Engineering, Technological University (Mandalay)*

[3]*Department of Electronic Engineering, Technological University (Mandalay)*

Email: [1]davidheel855@gmail.com, [2]papawinsan.1@gmail.com, [3]powerlay@gmail.com

***Abstract*— This paper focuses on accuracy increasing in trash classification model development of any trash management systems, especially for the school, hotel, hospital, shopping mall, and industry. As trash classification and correct rubbish destruction are important, it is critical to classify the trash types with high accuracy first. The rapid increase in urban populations and consumption patterns around the world causes an unpredicted growth in trash generation [6]. Trash classification is currently a big challenge without a good solution [8]. This Trash Classification Model (Office) has effectively classified the most common human used materials (office-used materials) like glass, metal, paper, plastic, and cardboard. The model predicted answer is displayed with the label and feature together. The model's learning method is supervised, and the classifier Softmax is used for its classification. Python programming language, machine learning toolkit, Scikit-learn library, TensorFlow framework, and Jupyer IDE are used in model training. This model used 400 trash images for its training process and 165 images for its testing process. This paper presents today's trash management situation, artificial intelligence (AI), model development, and detailed accuracy calculations with confusion matrix, recall, precision, and F1 score evaluation methods. This paper discusses manual hyperparameter tuning with the CNN technique and ConVNet architecture design.**

Keywords—trash classification model (office), classification, accuracy, AI, CNN, ConVNet, hyperparameter tuning

I. Introduction

According to the World Bank estimates (1992), between 0.7 and 1.8 kg per capita of waste is produced every day in developed countries' urban areas, and approximately 0.4 to 0.9 kg is produced in the cities of developing countries. The World Bank estimates (1992) that "the manner in which power is exercised in the management of a country's economic and social resources for development" [8].

Trash management policy and its implementation strategy are urgent problems in developed countries, as well as in the economic framework of a country. The trash management system is important because it is directly linked to the protection of public health, safety, and the environment. Proper trash management should not only protect public health and the environment but also promote natural resource recovery, recycling, reducing pollution, saving time, manpower, and reducing risk.

The present issue of waste management, which relies on manual labour, is not efficient, and poses health and environmental risks. The main goal of the research is to develop a real-time application that can recognize and separate different types of trash based on the images. The research achieved varying levels of accuracy, with different datasets and deep learning models [6].

One of the recent works on recycling is the automatic trash bin by the TechCrunch Disrupt Hackathon team to determine whether the garbage is suitable for recycling with the Raspberry Pi and a camera module. The work of this research focused on garbage classification and whether the garbage is suitable for recycling or not [7].

Nowadays, artificial intelligence (AI) is the key to fulfilling this solution. Since it is also an up-to-date technology, artificial intelligence (AI) technology is improving day by day [1]. New classification algorithms are being developed these days. Among popular algorithms, Deep Learning's CNN is trending for classification and automation [4].

Presently, there is no automatic trash classification system at the domestic level. Therefore, the need today is to develop a low cost, eco-friendly, and feasible trash classification model for offices (locations like the office's situation). Therefore, the Trash Classification Model (Office) is to fully fill the above factors using the deep learning method's CNN technique. Sample trash images are shown in Fig. 1 for Trash Classification Model (Office).

Fig. 1. Sample trash images of model (office)

There are four sections in the paper. Section 1 is an introduction to today's trash classification situation around the world and today's technologies. Section 2 presents related work, which includes architecture design, model training, its training and testing flow charts, the model evaluation methods, and its calculation. In Section 3, model testing results and discussion about the hyperparameter tuning to develop a good trash model are presented. Finally, the conclusion is outlined in Section 4.

II. System Design Of The Model (Office)

This proposed system uses convolutional neural networks to classify the trash images correctly. There are two main parts to the high accuracy Trash Classification Model (Office) that are developing. The first one is training the Trash Classification Model (Office) using the convolutional neural network, and the second is testing the Trash Classification Model (Office) with an unknown image dataset. For the training and testing of the model, the following flowcharts are shown in Fig. 2. and Fig. 3.

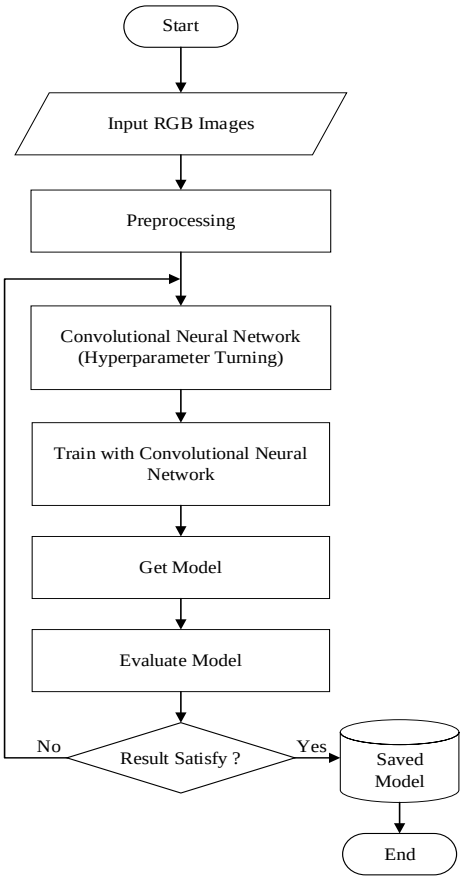

Fig. 2. Flowchart diagram for model training

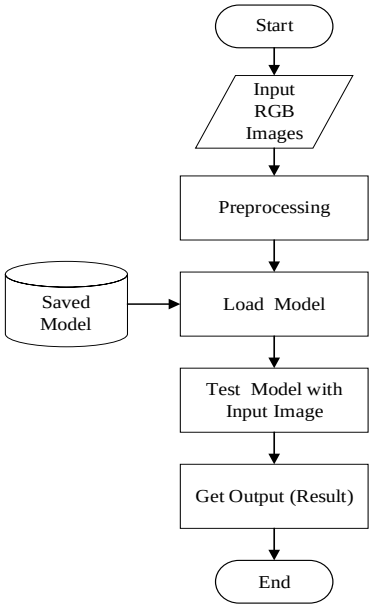

Fig. 3. Flowchart diagram for model testing

For the model's robustness, it uses multiple views of images, which include white background images, grey background images, and background free images. Research used its own datasets. The images belonging to the three datasets were collected by photographing with my own Android phone; some were collected from the internet and some from the Kaggle site. The model uses total 400 images for its training process, which is 80 images in each class. The total number of 165 images, which is 33 images for each class, is used for the testing process.

A. *Preprocessing*

The proposed system receives the RGB images. In the data preprocessing, there needs to be uniformity in all the input image sizes. Therefore, this proposed system resizes all images to 200 x 200, as shown in Fig. 4.

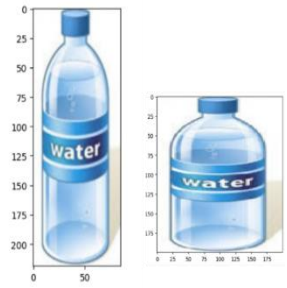

Fig. 4. Original image and after preprocessing image

After the preprocessing step, there is a need to develop a model with a convolutional neural network by tuning the hyperparameters.

B. *Classification Model Developing with CNN*

This step has to choose a technique to develop a model. This proposed system uses convolutional neural networks to develop a Trash Classification Model (Office). It uses the ConVNet architecture design to implement the model. The following Fig. 5 is its architectural design.

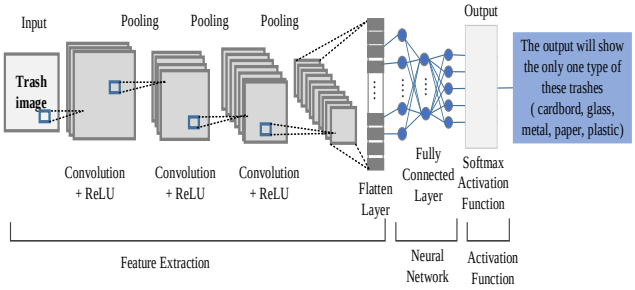

Fig. 5. Architecture design of the convolutional neural network

In model development uses a learning rate of 0.05, an optimizer Adam, a loss function Categorical, the Python programming language, and the integrated development environment Jupyter Notebook. In this system development, the two main sections, namely training and testing, are all included together. Therefore, again and again, data clearing, correct data grouping in each class, and retraining the model according to the experience conducted are being done during the time limitation. After only acceptable accuracy is achieved in model training, it is saved as this system's model. When the model is tested with an external image, pattern features are extracted with convolution, ReLU and pooling layers, and the extracted features are checked with the developed model's equation.

The tested image's properties are checked to see how similar they are to the properties of the model's defined classes, and then the most similar class is defined as a model's predicted answer (the output), which is displayed with the label and feature together as shown in Fig. 6.

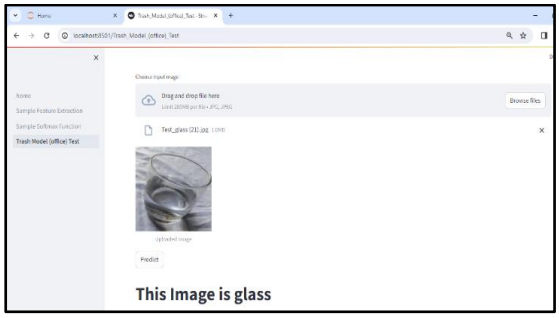

Fig. 6. Testing the trash classification model (office)

In the model development, numbers of hyperparameters are used, and finally the proposed model reaches its target goal with following hyperparameters, as shown in Fig. 7.

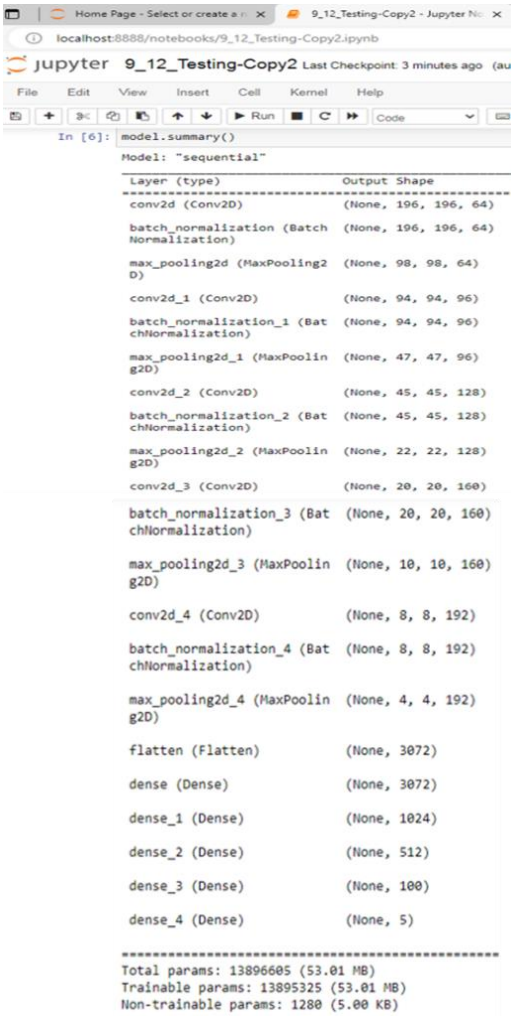

Fig. 7. Model hyperparameter summary

C. Evaluation

There are many methods to evaluate the accuracy of the trained model. The proposed system used the confusion matrix, precision, recall, and F1 score to check the model's accuracy and robustness [3].

The following Table I shows the summary prediction result of a model with predicted values and the actual values for the confusion matrix.

Table I

CONFUSION MATRIX

Predicted / Actual	0	1
0	True Negatives	False Positive
1	False Negatives	True Positive

The Trash Classification Model (Office) is tested for 33 images for each trash image. It can classify trash images like the following, Fig. 8 as a confusion matrix results.

```
from sklearn.metrics import confusion_matrix
confusion_matrix = confusion_matrix(y_test,y_predict)
print(confusion_matrix)
```

```
[[29  0  2  1  1]
 [ 0 30  1  1  1]
 [ 1  0 31  0  1]
 [ 0  3  4 26  0]
 [ 0  0  1  0 32]]
```

Fig. 8. Confusion matrix of the office model 3

The proposed system can classify 30 images correctly for the cardboard, 24 images for the glass, 27 images for the metal, 20 images for the paper, and 23 images for the plastic.

To calculate the model's accuracy, the proposed system calculates the following:

$$\text{Accuracy} = \frac{\text{No.of correctly predicted}}{\text{Total no. of predictions}} \quad (1)$$

$$= \frac{29+30+31+26+32}{29+2+1+1+30+1+1+1+1+31+1+3+4+26+1+32}$$

$$= 0.89696$$

The next method is precision and recall. Here are the precision and recall results.

$$\text{Precision} = \frac{\text{TruePositives}}{\text{TruePositives} + \text{FalsePositives}} \quad (2)$$

$$= \frac{29+30+31+26+32}{(29+30+31+26+32)+(1+3+8+2+3)}$$

$$= 0.89696$$

$$\text{Recall} = \frac{\text{True Positives}}{\text{True Positives} + \text{False Negatives}} \quad (3)$$

$$= \frac{29+30+31+26+32}{(29+30+31+26+32)+(4+3+2+7+1)}$$

$$= 0.89696$$

The next evaluation method for this classification model is the F1 score. It combines the above two methods into a single one, which can be used as a fair judge of the model and is equal to the harmonic mean of precision and recall.

Here is the F1 score result.

$$F1Score = 2 \times \frac{Precision \times Recall}{Precision + Recall} \quad (4)$$

$$= 2 \times \frac{0.89696 \times 0.89696}{0.89696 + 0.89696}$$

$$= 0.90$$

After training the model, its accuracy is 0.96 and its loss is 0.1217 for the training dataset, the validation is 0.89 accuracy for the testing dataset, and the testing loss is 0.5846, as shown in the following Fig. 9.

```
20/20 ━━━━━━━━━━━━━━━━━━━━ 26s 910ms/step - accuracy: 0.2954 - loss: 2.4021 - val_accuracy: 0.5455 - val_loss: 1.1438
Epoch 2/8
20/20 ━━━━━━━━━━━━━━━━━━━━ 22s 882ms/step - accuracy: 0.6280 - loss: 0.9912 - val_accuracy: 0.6424 - val_loss: 1.0712
Epoch 3/8
20/20 ━━━━━━━━━━━━━━━━━━━━ 24s 992ms/step - accuracy: 0.7342 - loss: 0.7186 - val_accuracy: 0.7576 - val_loss: 0.6063
Epoch 4/8
20/20 ━━━━━━━━━━━━━━━━━━━━ 22s 890ms/step - accuracy: 0.8252 - loss: 0.4734 - val_accuracy: 0.7576 - val_loss: 0.6689
Epoch 5/8
20/20 ━━━━━━━━━━━━━━━━━━━━ 21s 823ms/step - accuracy: 0.8096 - loss: 0.5100 - val_accuracy: 0.8000 - val_loss: 0.7862
Epoch 6/8
20/20 ━━━━━━━━━━━━━━━━━━━━ 20s 782ms/step - accuracy: 0.8956 - loss: 0.2855 - val_accuracy: 0.8364 - val_loss: 0.6310
Epoch 7/8
20/20 ━━━━━━━━━━━━━━━━━━━━ 21s 792ms/step - accuracy: 0.9514 - loss: 0.1878 - val_accuracy: 0.8848 - val_loss: 0.5161
Epoch 8/8
20/20 ━━━━━━━━━━━━━━━━━━━━ 20s 745ms/step - accuracy: 0.9671 - loss: 0.1217 - val_accuracy: 0.8970 - val_loss: 0.5846
```

Fig. 9. Accuracies and losses of the office model 3

The following Fig. 10 is an accuracy graph, which shows variation between the training dataset and the testing dataset. This graph shows model can predict well on the unknown images because there is less variation between training dataset testing and testing dataset testing.

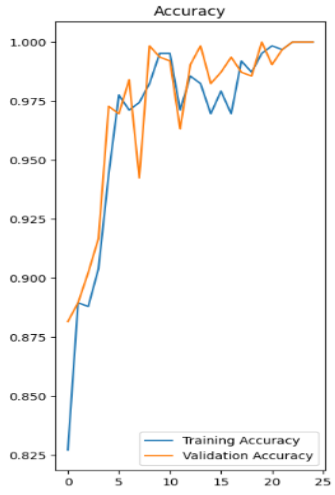

Fig. 10. Accuracy graph of the office model 3

The following Fig. 11 is the total evaluation results record of the proposed model (Office).

```
print('Accuracy of Trash Model',accuracy_score(y_test,y_predict)*100,'%')
print('Precision  of Trash Model',precision_score(y_test,y_predict,average='macro')*100,'%')
print('Recall of Trash Model',recall_score(y_test,y_predict,average='macro')*100,'%')
print('F1 Score of Trash Model',f1_score(y_test,y_predict,average='macro')*100,'%')
```

```
Accuracy of Trash Model 89.6969696969697 %
Precision  of Trash Model 90.26973026973029 %
Recall of Trash Model 89.6969696969697 %
F1 Score of Trash Model 89.68944855637237 %
```

Fig. 11. Evaluation results of the office model 3

The balance among the evaluation methods is correct because the results of accuracy, precision, recall, and F1 score are high and similar to each other. This result shows the model training situation is correct, as there is neither training under fitting nor training over fitting. So, this model will work well in the real world.

Moreover, the model has been checked for external real images for its robustness test. According to the experimental result, its accuracy score is shown in Table II. It shows the accuracy of each trash with the evaluation method's result and its experimental testing result.

Table II

ACCURACIES AND EVALUATION RESULTS OF THE OFFICE MODEL 3

Class	Pre-cision	Recall	F1 Score	Accuracy (Testing Dataset)	Accuracy (Experi-mental Result)
Card-board	96 %	87 %	91 %	87 %	81 %
Glass	90 %	90 %	90 %	90 %	82 %
Metal	79 %	93 %	85 %	93 %	79 %
Paper	92 %	78 %	84 %	78 %	77 %
Plastic	91 %	96 %	93 %	96 %	82 %

III. RESULTS AND DISCUSSION

The work focuses on accuracy increasing in trash classification as accuracy is the first priority for this work. So, this research took a long time on hyperparameter tuning and data cleaning to be able to organize its dataset with the correct images. In time duration, research work had remarkable success with three models like in Table III.

Table III

ACCURACIES WITH THREE OFFICE MODELS

Model	Train Data	Test Data	No. of Class	Accuracy (Testing Dataset)	Accuracy (Experimental Results)
Office Model 1	800	150	5	83 %	68 %
Office Model 2	400	150	5	88 %	76 %
Office Model 3	400	165	5	89 %	80.2 %

The second and third models use five convolutional layers, but the first convolutional layer uses only three. The image usage for the first model is eight hundred, while the second and third models use carefully cleaned images with a number of four hundred. The model's accuracy and robustness are quite different among these three models. The first model has notably less accuracy than the others. The third model's performance (the proposed model's performance) is significantly better than the second one in terms of accuracy and also in the model's robustness. The last two models have the same structures, but two main reasons for different performances among them are different dense layer usage (160 units and 192 units) and batch

normalization, absent and present. The combination of dropout rate and batch normalization really decreases overfitting and enhances the performance of the model.

Data indicators for achieving a good model are situations of losses, accuracy, and evaluation methods' results. The choice of evaluation methods depends on the specific task, dataset characteristics, and desired balance among the evaluation methods [5]. Continuous experimentation and fine-tuning are often necessary for the art to achieve results. This research used the manual tuning method because it allows for a deep understanding of the model's behavior and the influence of different hyperparameters [3].

The key hyperparameters to tune according to priority are learning rate, batch size, number of epochs, kernel size, number of layers, pooling size, number of filters (dense), number of neurons, and dropout rate. Batch size should be proportional to the number of classes used in the training process, although it doesn't know how many batch sizes should be used exactly. Defining too many epochs in one section may cause damage to the training machine because the processor is heating more and more, as training times are longer. The trainer should test the training machine's ability and make the training process patient. The training process should have appropriate epoch numbers, and it should be continued when the processor is cold enough. Checking the results of losses and accuracy is always done while the machine is running.

The convolutional kernel size is used to differentiate the input images. Different kernel sizes capture different features in the input images. A smaller kernel size provides more detail in taking out the feature extraction. It can be said that a smaller kernel size is correct for most types of images, generally. Increasing filters (denseness) allows the model to learn a more complex nature, but it may increase computational costs. Common values used in dense choice include 16, 32, 64, and 128, while they should be increased slowly and proportionally [2]. The number of layers impacts the depth of convolutional work. More layers can capture more complex features, which may increase computation demand and cause a load for the training machine. Generally, it can be said that more layers can produce better feature extraction than fewer layers. Most CNN-utilizing models achieve their goal above three layers. Pooling reduces spatial dimensions and helps invariance in small translations. Most CNN models use a 2 x 2 pooling size. More neurons can capture intricate relationships, which may lead to overfitting. The common neuron dropout rate range is commonly 0.2 to 0.5 [2].

Every good model has boundaries or limitations in its predictions, which is a normal condition, while hyperparameter tuning is very nice. Knowing well, the model prediction boundary is also a need for a good model. Moreover, it is a sign of a good model.

IV. Conclusion

The work analyzed the accuracy increasing factors of the CNN technique by using office image datasets. This work focused the study on five classes of each dataset only. Generally, the performance of a model is almost directly related to the learned parameters or the trained dataset. Quality images are more important than quantity images for a good model to develop. The main aim of this research paper is to increase the efficiency of the trash processing solution, reduce the workload of people, save time, money, and reduce risk. The proposed model predicted 96% with a training dataset and 89% with a testing dataset. According to the experimental results, the model's average prediction result is 80.2% for each class of total testing images for five hundred. These prediction results and experimental results of the proposed model are satisfied to be a support for any office image datasets usage trash management systems.

Acknowledgment

The author would like to deeply thank all of the teachers from the Department of Electronic Engineering, Technological University (Mandalay) and also grateful to the colleagues who helped me accomplish for this work really.

References

[1] Tom Taulli "Artificial Intelligence Basics: A Non-Technical Introduction", Ed. Shiva Ramachandran, 2019.

[2] Himanshu Singh "Practical Machine Learning and Image Processing for Facial Recognition, Object Detection, and Pattern Recognition Using Python", 2018.

[3] Benjamin Johnston and Ishita Mathur "Applied Supervised Learning with Python", Ed. Taabish Khan, April 2019.

[4] S.Lucci, S.Musa, D.Kopec "Artifical Intelligence in the 21st Century", 3rd ed.

[5] Eugene Charniak "Introduction to Deep Learning", Cambridge, Massachusetts London, England, 2018.

[6] Ishika Mittal, Anjali Tiwari, Bhoomika Rana, and Pratibha Singh "Trash Classification: Classifying Garbage using Deep Learning", July, 2020.

[7] J. Donovan, "Auto-trash sorts garbage automatically at the techcrunch disrupt hackathon".

[8] Julianne M Mungure, "Governance and community participation in Municipal Solid Waste management, case of Arusha and Dares Salaam Tanzania", Master thesis, Aalborg University, 2008.

Analysis of Lumped Elements Bandpass Filter and Microstrip Coupled Line Bandpass Filter

Bo Bo Wai[1], Hnin Yu Wai[2], Aye Min Soe[3]

[1]*Department of Electronic Engineering, Technological University (Mandalay)*

[2]*Department of Electronic Engineering, Technological University (Mandalay)*

[3]*Department of Electronic Engineering, Technological University (Mandalay)*

Email: [1]bobowai64@gmail.com, [2] powerlay@gmail.com, [3]ayeminsoeec@gmail.com

***Abstract*— This paper presents the analysis of lumped elements bandpass and microstrip coupled lines bandpass filter by using the Chebyshev frequency response method with a 3dB passband ripple. The frequencies are passed inside a certain range and rejected the frequencies exterior the range in the bandpass filter. The lumped elements filter is a resonator circuit and capacitors, inductors and resistors are used to design and simulate the filter. The lamped elements filter is designed in 8th order and is simulated for filter performances. The microstrip coupled line filter is designed in 8th order with FR4 substrate materials and the specified centered frequency is 5.48 GHz with a bandwidth of 680MHz. If the performances of microstrip coupled line filters do not match the specifications, optimization will be done, such as varying the filter parameters. These two types of filters are simulated and compared for their performances such as insertion loss (S_{21}), return loss (S_{11}), and sharpness of the stop band attenuation. The electronic design automation (EDA) software tool such as ADS (Advanced Designed System) is used for these simulations.**

Keywords—Lumped Elements, coupled line bandpass filter, FR4 materials, Chebyshev Response Method, Insertion Loss, Return Loss

I. INTRODUCTION

Filters play vital roles in radio-frequency and microwave communication systems. Some wideband applications, such as wireless applications, require microstrip coupled line and strip line filters because they need minute filters due to space and cost limitations. In broadband communication systems, size reduction becomes a main consideration for practical devices [1]. The function of the bandpass filter is that pass frequencies within a certain range and reject frequencies outside this range. There are two types of methods in designing the RF filter, that are image parameter methods and insertion loss methods. The image parameter method is simple and has drawbacks because this method must be repeated many times to get the desired results. The insertion loss method practices network synthesis techniques to get a designed filter with a desired frequency response [2]. Therefore, the filters used in high frequency are designed by using the insertion loss method.

There are four types of frequency response methods. Among them, Chebyshev-type filters are common for their high-frequency selectivity.

The lumped elements filter is a kind of passive filter. This filter type consists of the appropriate inductance (Ls), capacitance (Cs), and resistance (Rs) to meet the requirements of applications [3]. It can operate in a range of 1 Hz to 2 GHz. The lumped elements filter is easy to design, and this filter type is larger compared to the microstrip coupled line filter. In distributed element filters, microstrip and strip line filter types are widely used in many RF applications because they are compact. The parallel transmission lines are designed using the microstrip line technology, which is routed on the PCB surface. Designing the microstrip coupled line bandpass filter includes four main processes as shown in Fig. 1.

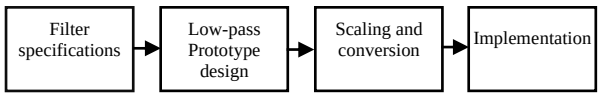

Fig. 1. Block diagram of filter design process [3]

II. THEORY OF MICROSTRIP COUPLED LINE BANDPASS FILTER

Coupled transmission lines refer to, that is, when two unprotected transmission lines are in closeness, power can be coupled from one line to the other because of the interaction of the electromagnetic fields and are supposed to operate in the TEM mode. Coupled transmission lines are symmetric, which means the two conducting strips have an equal width and position as shown in Fig. 2 [2].

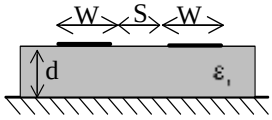

Fig. 2. Microstrip coupled line geometrics [2]

A general layout of a parallel coupled microstrip bandpass is shown in Fig. 3.

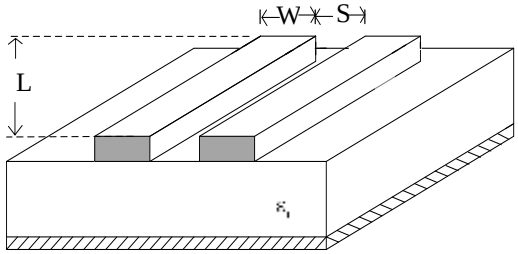

Fig. 3. General structure of microstrip coupled line topology [3]

In the filter structure, open-circuited coupled microstrip lines are contained. These coupled lines are quarter wavelength, (λ/4) lengthy, and are ready for shunt resonant circuits. The coupling gaps link to the admittance inverters at the low-pass prototype circuit. By using the

admittance inverter, even mode and odd mode characteristics impedance of parallel coupled line resonators can be designed. These even-mode and odd-mode impedances are used to compute the physical dimensions of the filter [4]. The microstrip coupled line bandpass filter is a filter composed of a cascade of N+1 coupled line sections as in Fig. 4.

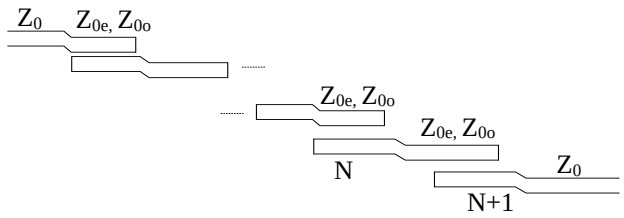

Fig. 4. Layout of an (N+1) section coupled line bandpass filter [2]

The parallel coupled sections are denoted from left to right by number, with the load at the right. Therefore, each coupled line sections have an equivalent circuit as in Fig. 5.

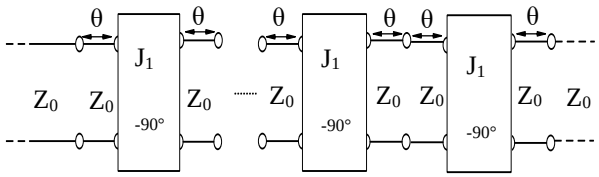

Fig. 5. Equivalent circuit for each coupled line section [2]

The admittance inverter is very important in filter design process. They are used in the transformation of a filter circuit to an equivalent form. The equivalent form of coupled line sections can be easily implemented using various microwave structures. The equivalent circuit of admittance inverter is shown in Fig. 6.

In designing a bandpass filter, first of all, a low-pass prototype circuit is changed to include admittance inverters. These low-pass structures are then converted to bandpass circuits by applying conventional low-pass to bandpass transformation.

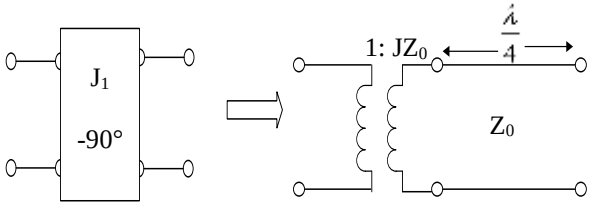

Fig. 6. Equivalent circuit of admittance inverters [2]

III. Design Methodology

Microwave filters can be designed as two types, that are lumped elements filters and distributed elements filters in general. The performance of the distributed elements filter is effective at higher microwave frequencies. So, most of the microstrip bandpass filters are based on the distributed elements such as waveguides, microstrip lines, and coplanar waveguides [5]. In designing the microstrip line filters, there are two types of design methods; image parameter method and insertion loss method. From these two methods, the insertion loss method is used because this method uses network synthesis techniques to get the designed filter easily.

The process of designing the microstrip coupled line bandpass filter is shown in Fig. 1. In the first stage, filter specifications must be specified, and then the bandpass filter prototype must use resistors, capacitors, and inductors at the second stage of the process. At the third state, the designed low pass filter prototypes are converted to the bandpass filter as lumped elements bandpass filters, and the required calculations have to be computed. At the last stage, the designed lumped elements bandpass filters are replaced by the distributed transmission line such as microstrip transmission lines.

A. Filter Specifications

Table I describes the filter specifications. That specifications are taken from the UNII Band of 5GHz wireless frequency ranges. UNII Band means Unlicensed National Information Infrastructure.

I. Designed Specifications Of Filter

Required Specifications	**Specifications Values**
Lower cut off frequency (f_{c2})	5.15 GHz
Upper cut off frequency (f_{c1})	5.83 GHz
Center frequency (f_0)	5.48 GHz
Bandwidth (BW)	680 MHz
Filter Type	Chebyshev Bandpass Filter
Pass band attenuation	3 dB
Stop band attenuation	25 dB

After specifying the operated frequency ranges of the filter, the filter orders have been calculated by using the bilinear transformation method [6].

$$\varepsilon = \sqrt{10^{0.1\alpha_p} - 1} \quad (1)$$

$$\lambda = \sqrt{10^{0.1\alpha_s} - 1} \quad (2)$$

Where, α_p and α_s are passband and stopband attenuations respectively.

$$K = \frac{f_{c1}}{f_{c2}} \quad (3)$$

$$A = \frac{\lambda}{\varepsilon} \quad (4)$$

By using (1) to (4), the filter order can be calculated as,

$$N = \frac{\cosh^{-1} A}{\cosh^{-1} \frac{1}{K}} \quad (5)$$

After calculating, the value of N, designed filter order is 7.18. So, bandpass filter can be designed N > 7.18. So, 8th order bandpass filter is appropriate for this specified frequency range.

B. Designing Lowpass Filter prototype

After specifying the filter order, the low pass filter prototype have been designed by using the inductors, capacitors and resistors for 8th order filter as shown in Fig. 7.

Where g_0 is generator resistance or conductance, g_k is either inductance for series inductors or capacitance for shunt capacitors (k = 1 to N), g_{N+1} means either load resistance if g_N is a shunt capacitor or load conductance if

g_N is a series inductor. The values of 'g' parameters have been described in Table II. This 'g' parameters are used in calculation of lumped elements values such as capacitance and inductance, and then used in calculation of even and odd mode impedance. [7]

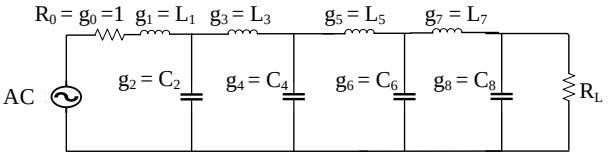

Fig. 7. Circuit diagram of 8th Order lumped elements lowpass filter

II. LOW PASS PROTOTYPE ELEMENTS VALUES

N	8
g_1	3.5277
g_2	0.7745
g_3	4.6575
g_4	0.8089
g_5	4.6990
g_6	0.8018
g_7	4.4990
g_8	0.6073
g_9	5.8095

C. Scaling and Conversion

The low pass filter prototypes were normalized designs having a source impedance of $R_s = 1\ \Omega$ and cutoff frequency of $\omega_c = 1$ rad/s. Impedance scaling is when all impedances of the prototype design are multiplied by R_0 to get a source resistance of R_0.

Lowpass filter designs are transformed to the bandpass filters for 8th Order is illustrated in Fig. 8. At the transformation of the bandpass, the inductor L_k is transformed to the series LC circuit and capacitor C_k is transformed to the shunt LC circuit.

The edges of the passband are defined by ω_1 and ω_2. The fraction bandwidth of the pass band is

$$\Delta = \frac{\omega_2 - \omega_1}{\omega_0} = 0.124 = 12.4\% \tag{6}$$

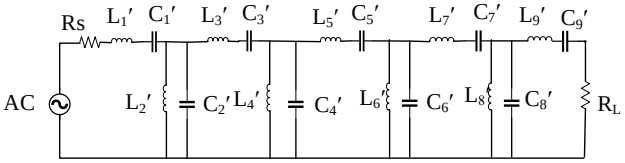

Fig. 8. Circuit diagram of 8th Order lumped elements bandpass filter

The values of lumped elements components, capacitance and inductance, have been calculated.

For a series inductor L_k,

$$L_k' = \frac{L_k R_0}{\omega_0 \Delta} \tag{7}$$

$$C_k' = \frac{\Delta}{\omega_0 L_k R_0} \tag{8}$$

For a shunt capacitor C_k,

$$L_k' = \frac{\Delta R_0}{\omega_0 C_k} \tag{9}$$

$$C_k' = \frac{C_k}{\Delta \omega_0 R_0} \tag{10}$$

The value of source and load impedance, R_0 is 50 Ω and the values of capacitance and inductance for 8th Order filter is shown in Table III.

III. THE VALUES OF LUMPED ELEMENTS FILTER'S COMPONENTS

k	**L'_k (nH)**	**C'_k (pF)**
1	41.18	0.02044
2	0.2327	3.625
3	54.5	0.01548
4	0.2228	3.787
5	54.99	0.01534
6	0.2248	3.753
7	52.65	0.01602
8	0.2968	2.843

D. Filter Implementation of Microstrip Coupled Line Bandpass Filter

The lumped element filters can operate at low frequencies. Its capacitors and inductors are available for a limited range of values and it is difficult to implement at microwave frequencies. So, lumped element filters are replaced by distributed elements such as microstrip coupled line filters to operate at higher microwave frequencies. The j-inverter method is used to transform the bandpass filter to a distributed elements filter by using the values of 'g' parameters, in designing the coupled line bandpass filter [8]. The values of 'g' parameters have been shown in Table II.

Making use of admittance inverters convert a lumped elements filter circuit into an equivalent form that would be more suitable for microwave structures. Equation (11), (12) and (13) are used to compute the admittance inverter constants.

For the first coupling,

$$Z_0 J_1 = \sqrt{\frac{\pi \Delta}{2\, g_1}} \tag{11}$$

For the intermediate coupling,

$$Z_0 J_n = \frac{\pi \Delta}{2\sqrt{g_{n-1}\, g_n}} \quad (n = 1, 2, \ldots, N) \tag{12}$$

For the final coupling,

$$Z_0 J_{N+1} = \sqrt{\frac{\pi \Delta}{2\, g_N\, g_{N+1}}} \tag{13}$$

Where, $g_1, g_2, \ldots, g_N, g_{N+1}$ are 'g' parameters, this means that the coefficient of the Chebyshev filter design, $J_1, \ldots, J_n$, J_{N+1} is the characteristics admittance of the J inverters, Z_0 is defined the characteristics impedance of source and lode side of the filters. From the results of admittance inverters, the even and odd mode impedance values can be calculated by using (14) and (15). [8]

For the even mode impedance,

$$Z_{0e} = Z_0\ [1 + Z_0 J_1 + (Z_0 J_n)^2] \tag{14}$$

For the odd mode impedance,

$$Z_{0o} = Z_0 [1 - Z_0 J_1 + (Z_0 J_n)^2] \quad (15)$$

The results of admittance inverters ($Z_0 J_n$), even and odd mode impedances are shown in Table IV.

IV. EVEN AND ODD MODE IMPEDANCES OF THE MICROSTRIP COUPLE LINIE BANDPASS FILTER

Line Description	Admittance Inverter	Even mode impedance (Z_{0e}) (Ω)	Odd mode impedance (Z_{0o}) (Ω)
1st Coupling	0.234	64.44	41.038
2nd Coupling	0.117	56.534	44.834
3rd Coupling	0.102	55.62	45.42
4th Coupling	0.1	55.5	45.5
5th Coupling	0.099	55.44	45.54
6th Coupling	0.1	55.5	45.5
7th Coupling	0.102	55.62	45.42
8th Coupling	0.117	56.534	44.834
9th Coupling	0.234	64.44	41.038

Table IV shows the even mode and odd mode impedance for each coupling of the 8th order microstrip coupled lines filter. There are nine couplings in the 8th order microstrip coupled lines filter. .

The even and odd mode impedance values from Table VI are used in calculation of width (W), length (L) and space between each strip (S) of each coupling of the coupled line filter. Line calculation tool in ADS software is used to calculate the filter's dimension such as width, length and space and substrate material's parameters are also needed in this calculation. The required substrate parameters are shown in Table V.

V. THE PARAMETERS OF SUBSTRATE MATERIAL

Name of Substrate Materials	FR4
Dielectric constant (Er)	4.4
Thickness of the Substrate (H)	1.6 mm
Thickness of the copper line (T)	0.02 mm
Loss tangent	0.002
Roughness	0 mil

IV. SIMULATION RESULT

Lumped elements band pass filter and microstrip coupled line bandpass filter simulation are simulated with ADS (Advanced Design System) simulation tool. The simulation results of 8th order of lumped elements bandpass filters are shown in Fig. 9.

In the Fig. 9, the pointer 'm_1' indicates the insertion loss (S_{21}) , -0.066 dB and the pointer 'm_2' indicates the return loss, -18.216 dB of the lumped elements bandpass filter. The IL of the lumped elements filter is nearly closed to 0 dB at the f_0, that is good and acceptable results. And, the RL is greater than the -10 dB at the f_0, it also be the acceptable result. But, the type of lumped element filter is larger in size to use in portable wireless device and there is no sharper to the stopband attenuation compared to the coupled lines filter. So, the designing is continued to the microstrip coupled line filter implementation.

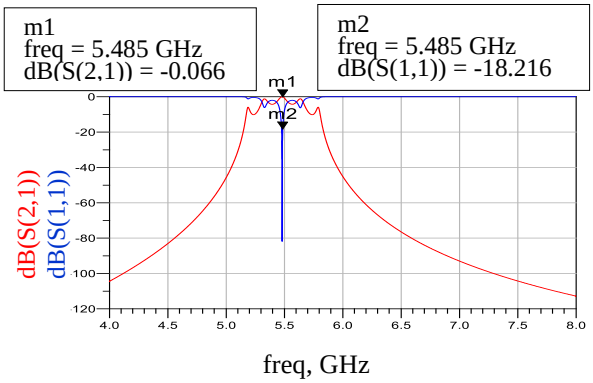

Fig. 9. Frequency response curve of 8th Order lumped elements filter

From the Line Calculation tool of the ADS, the values filter parameters of the 8th order coupled line filters are shown in Table VI and their simulation results are shown in Fig 10.

VI. THE 8TH ORDER MICROSTRIP COUPLED LINE BANDPASS FILTER PARAMETERS

n	Width (W) (mm)	Space (S) (mm)	Length (L) (mm)
1	2.69098	0.7823	7.62146
2	2.96775	1.8903	7.55100
3	2.99042	2.1818	7.49907
4	2.99294	2.2278	7.49068
5	2.99355	2.2384	7.48882
6	2.99294	2.2278	7.49068
7	2.99042	2.1818	7.49907
8	2.96775	1.8903	7.55100
9	2.69098	0.7823	7.62146

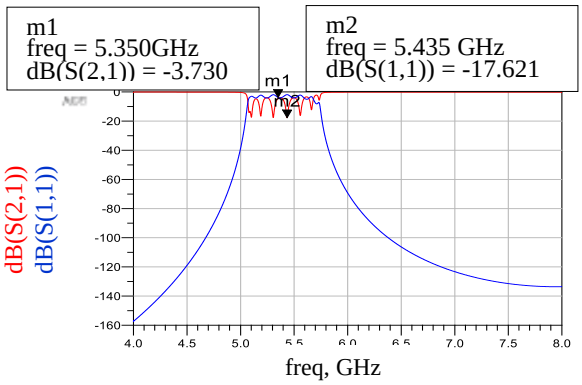

Fig. 10. Frequency response curve of 8th Order microstrip coupled line filter

In the Fig. 10, 'm_1' indicates the insertion loss (S_{21}) of 8th order microstrip coupled line bandpass filter, -3.730 dB, 'm_2' indicates the return loss (S_{11}), -17.621 dB. The IL of the microstrip coupled line filter is higher than the lumped elements filter due to the material effects, but this result can acceptable. Bandwidth is 476 MHz, it needs to extend to get the desired values.

According to Fig. 10, the center frequency of 8th Order microstrip coupled line filters is 5.35 GHz. It is less than desired center frequency 5.48 GHz. It needs to shift the passband to the right. The bandwidths are narrower than the desired bandwidth 680MHz. So, for fitting the coupled lines filter with the desired specifications, the filter's parameters have to been varied. According to theory, the wide of the bandwidth depends on the space between the two strips of the coupling. If the space between strips is increased, the bandwidth becomes decrease, while space is decreased, then

the bandwidth becomes increase. The more increase the length of coupled lines, the more shift the passband to the left and the more decrease the length of coupled lines, the more shift the passband to the right. Therefore, the varied values of filter's parameters are shown in Table VII.

VII. VARIED VALUES OF WIDTH, LENGTH AND SPACE OF 8TH ORDER MICROSTRIP COUPLED LINES FILTER

N	Width (W) (mm)	Space (S) (mm)	Length (L) (mm)
1	2.69098	0.6823	7.49146
2	2.96775	1.5903	7.42100
3	2.99042	1.8818	7.36907
4	2.99294	1.9378	7.36068
5	2.99355	1.9384	7.35882
6	2.99294	1.9278	7.36068
7	2.99042	1.8818	7.36907
8	2.96775	1.5903	7.42100
9	2.69098	0.6823	7.49146

The response curve of the 8th Order microstrip coupled line bandpass filter after varying the filter's parameters is shown in Fig. 11.

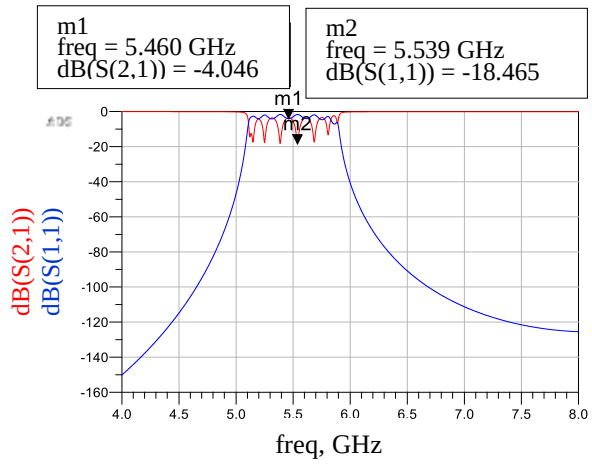

Fig. 11. Varied frequency response curve of 8th Order microstrip couple lines filter

The comparison of before and after optimization results are described in Table VIII.

VIII. COMPARISON OF BEFORE AND AFTER OPTIMIZATION OF 8TH ORDER COUPLED LINES FILTER

Desired Specifications	Expected Results	Before Optimization	After Optimization
f_0	5.48 GHz	5.35 GHz	5.46 GHz
BW	680 MHz	476 MHz	677 MHz
S_{21}	< -3dB	-3.73 dB	-4.046 dB
S_{22}	>-10dB	-17.621 dB	-18.465 dB

After varied the filter parameters, the center frequency is 5.46 GHz, it is closed to the desired f_0. The bandwidth is wider to meet the desired bandwidth, 680 MHz. The insertion loss (S_{21}) is greater than the before optimization state, but it can be accepted. The maximum peak of the return loss (S_{11}) is -18.465 dB that is greater than the before state.

V. CONCLUSION

In this paper, lumped elements bandpass filter and microstrip coupled lines filer are analyzed. The lumped elements filters met the desired values, but its size is larger compare to the microstrip coupled line filter. According to the nature of bandpass filter, the more the order, the higher the values of insertion losses. The insertion loss of lumped elements filter (S_{21}) is -0.066 dB and the return loss (S_{11}) is -18.216 dB. Although, S_{21} of the coupled line filter is larger than the lumped elements filter, lumped elements filters cannot be used in the wireless system because of its size. The insertion loss of the microstrip coupled line filter is –4.046 dB can be acceptable and the stopband attenuation is sharper than the lumped elements bandpass filter. So, the microstrip coupled line bandpass filter is more convenient than the lumped elements bandpass filters in the RF devices.

ACKNOWLEDGMENT

The author would like to thank to Dr. Pa Pa Winn San, Professor and Head of the Department of Electronic Engineering, Technological University (Mandalay) for her support and guidance. In particular, the author would like to thank Dr. Hnin Yu Wai, Associate Professor, Department of Electronic Engineering, Technological University (Mandalay), for her help and guidance, support and encouragement. The author would like to thank to Dr. Aye Min Soe, Associate Professor, Department of Electronic Engineering, Technological University (Mandalay) for her support and guidance. The author also would like to thank to his parents and all of his teachers from Department of Electronic Engineering, Technological University (Mandalay).

REFERENCES

[1] V. Thangasamy and S. Duraikannan. "Λ-type 5.75GHz Chebyshev Bandpass Filter for WLAN Applicationis", *International Journal of Advanced Research in Electrical, Electronics and Instrumentation Engineering*, vol. 3, Issue 1, January 2014.

[2] D. M. Pozar, "Microwave Engineering", John Wiely & Sons, Inc. 2011

[3] C. Bowick, J. Blyler and C. Ajluni, "RF Circuit Design", Elsevier, 2008.

[4] R. Levy, S. B. Cohn, "A History of Microwave Filter Research, Design, and Development", *Microwave Theory and Techniques, IEEE Transactions*, vol. 32, no. 9, pp. 1055,1067, Sep 1984.

[5] E. O. Hammerstard, "Equations for microstrip circuit design," in Proceedings of the European Microwave Conference, Hamburg, Germany,

[6] V. Thangasamy and S. Duraikannan. "Design and Simulative Analysis of Chebyshev Band Pass Filter For LMDS Band", Journal of Science Technology Engineering and Management-Advanced Research & Innovation, ISSN: 2581-4982, Vol. 1, Issue 2, May 2018.

[7] S. Seghier, N. Benahmed, F. T. Bendimerad and B. Benyoucef, "Parallel Coupled Microstrip Bandpass Filter for G.S.M Band Applications.

[8] J. T. Kou, Senior M. Jiang and H. Jen Chan, "Design of parallel coupled Microstrip Fiters with Sppression of Spurious Resonances Using Substrate Suspensio", IEEE Transactions on microwave theory and techniques. Vol. 52, No 1, January 2004.

Simulation and Optimization of Pyramidal Horn Antenna for UAV Video Link

Hnin Wai Wai Aung[1], Aye Min Soe[2], Htet Htet Aung[3]

[1]*Department of Electronic Engineering, Technological University (Mandalay)*

[2]*Department of Electronic Engineering, Technological University (Mandalay)*

[3]*Department of Electronic Engineering, Technological University (Mandalay)*

Email: [1]hninwaiwaiaung2017@gmail.com, [2]ayeminsoeec@gmail.com, [3]htethtetaunginle@gmail.com

***Abstract*— This paper enlightened on the significance of the pyramidal horn antenna for video link, especially applied to the Unmanned Aerial Vehicle (UAV) at the 5.8 GHz frequency range. This UAV's video link communication requires high bandwidth and needs to support long ranges. The existing ground station antennas have the problems of less coverage area, narrow beamwidth, and low antenna gain. It is also needed to increase the capacity of these functions. Pyramidal horn antennas solve this problem because it provides long-range video transmission and high gain resolution. This paper uses CST Studio Suite software to apply to the horn antenna with a pyramidal shape at a frequency range of 5.8 GHz. The optimization process is carried out to enhance the data achieved from the simulation results. After the optimization process, antenna parameters such as main lobe beamwidth, far-field radiation pattern, side lobe levels, and voltage standing wave ratio (VSWR) values are improved. The desired horn antenna design provides a well reliable gain of 15dB operating at 5.8 GHz.**

Keywords* – *pyramidal horn antenna, UAV, beamwidth, CST Studio Suite, 5.8 GHz

I. Introduction

A horn antenna is an aperture antenna family member, widely used in microwave communication. A horn antenna is utilized in two primary ways. It transmits electromagnetic waves from a waveguide into open space, ensuring effective signal radiation. Additionally, it receives electromagnetic waves from open space, directing them into a waveguide for further processing [6].

The various varieties of horn antennas are each designed for specific applications and offer different radiation patterns and performance characteristics. The main types include pyramidal horns, sectoral horns, conical horns, corrugated horns, and exponential horns. This antenna's wide bandwidth, excellent directivity, heightened antenna gain, straightforward design, and relatively better radiation properties are further reasons to utilize it [1]. These characteristics make the horn antenna suitable for applications such as radar systems, antenna testing, satellite communications, remote sensing, and various forms of wireless communication.

This research explores important antenna design techniques for UAV video link communications. The proposed antenna is used as a receive antenna in video communication systems using a frequency range of 5.8 GHz. This research presents the detailed design procedure calculations and simulations for a pyramidal horn antenna intended for the frequency range of 5.8GHz. The dimensions of the antenna are calculated using MathCAD software according to the horn antenna design calculation methodologies. The MathCAD results are then used to create and simulate in CST simulation software, and the antenna parameter results are archived. After the antenna design simulation, optimization tools of CST were employed to improve the antenna's performance [4].

The design process outlined crucial parameters such as waveguide dimensions, aperture size, flare angle, and feeding element at the designated frequency. Increasing far-field radiation, antenna gain, antenna directivity and bandwidth, lowering side-lobe levels, and low voltage standing wave ratio (VSWR) of an antenna are some of the primary golds for this research. This research's main goals are designing a video link ground station antenna based on a horn antenna, performing the design calculation of the horn antenna, and the antenna simulation.

II. Specifications Of Design

To design a pyramidal-shaped horn antenna, the design procedure is computed with the aid of MathCAD software [3]. The specifications play a crucial role when designing a pyramidal horn antenna. The primary consideration when designing a horn is the frequency range. The flowchart of the pyramidal horn antenna design is illustrated in Fig. 1.

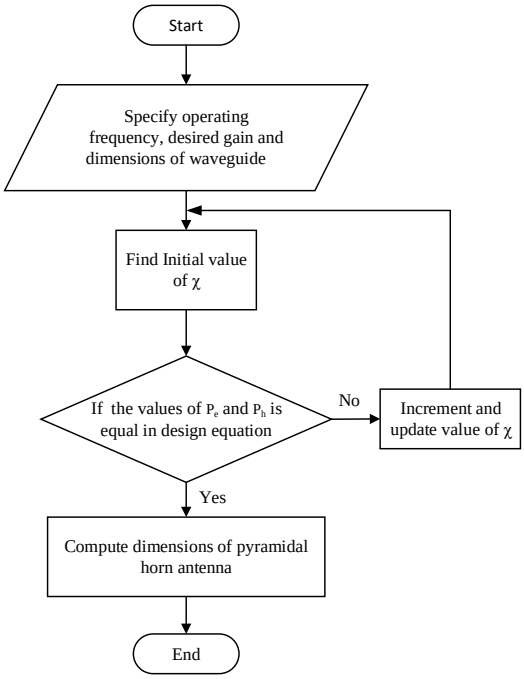

Fig. 1. Flowchart of pyramidal horn antenna design

The horn design in pyramidal shape encompasses the configuration of the waveguide, aperture, flared angle, and radiating elements.

A. Waveguide Design

A hollow conductive tube utilized for efficiently transferring electromagnetic power from one point to another is called a "waveguide" [8]. In waveguide types, the rectangular waveguide is an essential component in high-frequency transmission systems, providing efficient and reliable means of guiding electromagnetic waves with minimal loss. The waveguide of horn antenna is determined in Fig. 2.

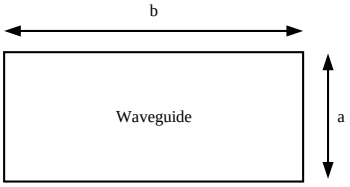

Fig. 2. Waveguide of horn antenna

The WR187 waveguide is used to excite the horn across the desired frequency range. The symbols (a) and (b) are represented by the larger and smaller parameters of the waveguide, respectively.

B. Aperture Design

The aperture of a pyramidal horn antenna refers to the rectangular opening at the end of the horn where electromagnetic waves are radiated or received [5]. The geometry of a pyramidal horn is described in Fig. 3. The dimensions of this aperture are critical in determining the performance characteristics of the antenna, such as its gain, beamwidth, and directivity. The E-plane and H-plane view of horn antenna is shown in Fig. 4 and 5.

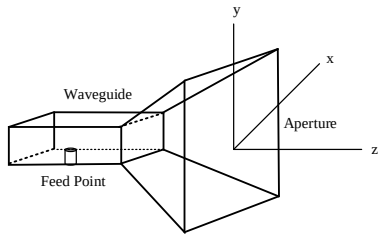

Fig. 3. Geometry of a pyramidal horn

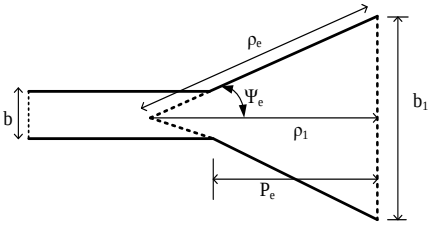

Fig. 4. E-plane view of horn antenna

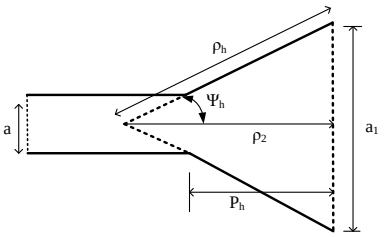

Fig. 5. H-plane of horn antenna

As shown in Fig. 4 and 5, (b_1) and (a_1) represent the measurements of the mouth of the horn. The symbols (Ψ_e) and (Ψ_h) are stand for half of the flare angles. Then, (ρ_e) and (ρ_h) are the distances along the side of the horn from the waveguide to the aperture, and the signs (ρ_1) and (ρ_2) are the horizontal distance from the waveguide to the point where the flare angle stats to open out towards the aperture. Furthermore, (P_e) and (P_h) indicate the distances from the start of the horn's flare to the midpoint of the mouth of the horn along the indicated axis.

Initially, the desired gain (G_0) and the parameters of rectangular waveguides (a) and (b) are known for designing a pyramidal horn [2]. And then, the dimensions of (a_1, b_1, P_e, P_h) are calculated to acquire an ideal gain.

The values of (ρ_2) and (ρ_h) are the same and the values of (ρ_1) and (ρ_e) are also equal for a long-horn. To ensure that a pyramidal horn is perceptibly dependable, (P_e) and (P_h) values are equal.

$$\left(\sqrt{2\chi}-\frac{b}{\lambda}\right)^2\left(2\chi-1\right)=\left[\frac{G_0}{2\pi}\sqrt{\frac{3}{2\pi}}\frac{1}{\sqrt{\chi}}-\frac{a}{\lambda}\right]^2\left[\frac{{G_0}^2}{6\pi^3}\frac{1}{\chi}-1\right] \quad (1)$$

At the initial stage of the design process, determine the χ value that completes the equation for the desired gain (G_0). The constant value of χ is obtained by solving (1).

By using (2) and (3), the values of ρ_e and ρ_h are computed after obtaining the accurate value of χ.

$$\rho_e = \chi \cdot \lambda \quad (2)$$

$$\rho_h = \frac{{G_0}^2}{8\pi^3}\left(\frac{1}{\chi}\right)\lambda \quad (3)$$

Where, ρ_e = horn antenna's slant length in the E-plane

ρ_h = horn antenna's slant length in the H-plane

The correlative values of a_1 and b_1 are evaluated by applying (4) and (5) individually.

$$a_1 = \frac{G_0}{2\pi}\sqrt{\frac{3}{2\pi\chi}}\cdot\lambda \quad (4)$$

$$b_1 = \sqrt{2\cdot\chi}\cdot\lambda \quad (5)$$

Where, a_1 = width of the aperture in the H-plane

b_1 = width of the aperture in the E-plane

The values of ρ_1 and ρ_2 are calculated by means of (6) and (7).

$$\rho_1 = \frac{b_1^2}{2\lambda} \quad (6)$$

$$\rho_2 = \frac{a_1^2}{3\lambda} \quad (7)$$

Where, ρ_1 = the aperture's slant length in the E-plane

ρ_2 = the aperture's slant length in the H-plane

After computing ρ_e and ρ_h, P_e and P_h values are estimated by using (8) and (9).

$$P_e = (b_1 - b)\left[\left(\frac{\rho_e}{b_1}\right)^2 - \frac{1}{4}\right]^{1/2} \quad (8)$$

$$P_h = (a_1 - a)\left[\left(\frac{\rho_h}{a_1}\right)^2 - \frac{1}{4}\right]^{1/2} \quad (9)$$

Where,

P_e = distance from the start of the horn's flare to the midpoint of the mouth in the E-plane

P_h = distance from the start of the horn's flare to the midpoint of the mouth in H-plane

C. Flared Angle

The flare angle of a horn antenna, which is the angle between the horn's axis and the slant of its side walls. This angle is crucial in determining the directivity and the gain of the horn antenna. For a pyramidal-shaped horn, two flared angels exist: one in the E-plane (parallel to the electric field) and one in the H-plane (parallel to the magnetic field). [7]. The flare angle requires an optimum value and is closely related to the antenna's length. Fig. 6 indicates the flare angle of horn antenna.

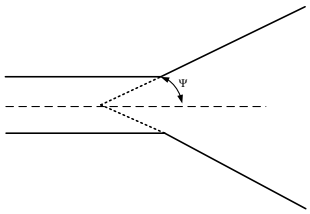

Fig. 6. Flare angle of horn antenna

The flare angle for the E and H plane views are calculated by using (10) and (11).

$$\psi_e = \tan^{-1}\left(\frac{\frac{b_1}{2}}{\rho_1}\right) \quad (10)$$

$$\psi_h = \tan^{-1}\left(\frac{\frac{a_1}{2}}{\rho_2}\right) \quad (11)$$

Where, Ψ_e = E-plane flared Angle

Ψ_h = H-plane flared Angle

D. Radiation Element Design

The radiation element of a horn antenna is the part of the antenna structure responsible for emitting or receiving electromagnetic waves [1]. In a horn antenna, this element typically consists of a flared opening that allows for the efficient transmission or reception of electromagnetic radiation. The E-plane view with radiation element is determined in Fig. 7.

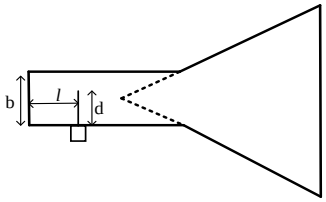

Fig. 7. E-plane view with radiation element

The waveguide wavelength is calculated by using (12).

$$\lambda_g = \frac{c}{f} \times \frac{1}{\sqrt{1 - \left(\frac{c}{2a.f}\right)^2}} \quad (12)$$

Where, λ_g = Waveguide wavelength

The feed antenna is positioned from the waveguide edge corresponding to one-quarter of a wavelength within the waveguide, which is calculated as (13).

$$l = \frac{\lambda_g}{4} \quad (13)$$

Where, l = feed antenna's distance from the waveguide

The feed antenna's height is equivalent to one by fourth of the wavelength, calculated using (14).

$$d = \frac{\lambda}{4} \quad (14)$$

Where, d = height of the feed antenna

The total length of the waveguide part is calculated by using (15).

$$L = \lambda_g \quad (15)$$

According to the calculation by using (1) to (15), the dimensions of the proposed horn antenna are obtained. The dimensions of calculation results are described in Table I.

I. DIMENSIONS OF CALCULATION RESULTS

Section	Description	Dimension (cm)
Waveguide	Width, a	4.755
	Height, b	2.22
	Length, L	6.157
Horn Aperture	E-plane, b_1	9.799
	E-plane, ρ_1	9.288
	E-plane, P_e	6.103
	H-plane, a_1	13.41
	H-plane, ρ_2	11.597
	H-plane, P_h	6.103
Flared Angle	E-plane	27.811 deg.
	H-plane	30.036 deg.
Radiation Element	Distance, l	1.538
	Length, d	1.292

III. Simulation And Optimization Results In CST Studio Suite

The numerical values for the desired horn antenna are obtained by using CST studio suite simulation software. The obtained results are voltage standing wave ratio (VSWR), return loss at the desired frequency, gain, directivity, bandwidth, and radiation pattern. And then varying the radiation element and aperture dimensions by ±10% to maximize antenna efficiency and overall performance. The 3D view of a horn antenna in CST is represented in Fig. 8.

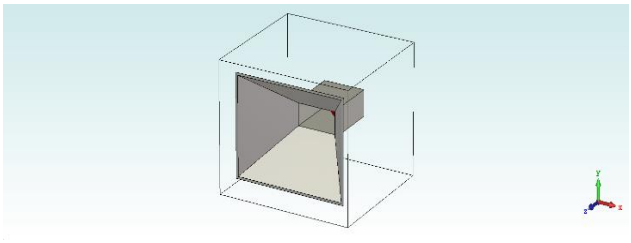

Fig. 8. 3D view of a horn antenna in CST

From the simulation results, the value of VSWR is 1.7976 at 5.8 GHz as displayed in Fig. 9. A VSWR value close to 1 is highly effective and desirable in horn antenna design, indicating excellent impedance matching between the antenna and the transmission line.

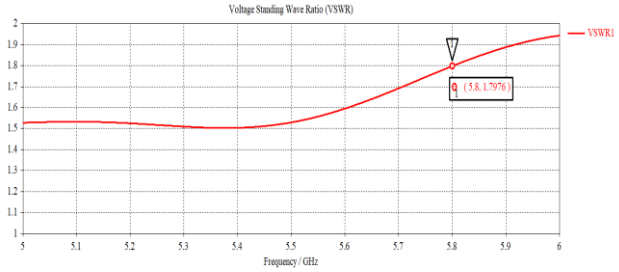

Fig. 9. VSWR result in CST

After optimizing, the result of the VSWR value is 1.277 as shown in Fig. 10. Comparing the results of a VSWR value before optimization (1.7976) and after optimization (1.277) in a horn antenna design improves performance and efficiency.

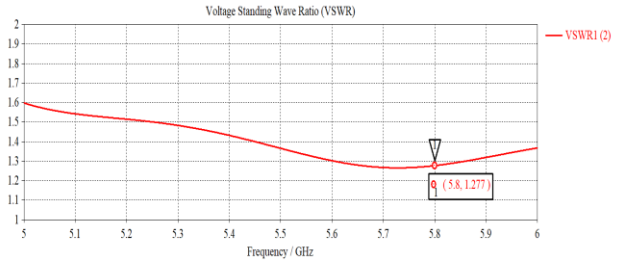

Fig. 10. VSWR result after optimization

The S_{11} represents the return loss graph. Fig. 11 represents the S_{11} curve in CST and -10.9 dB of return loss is attained at the 5.8 GHz operating frequency.

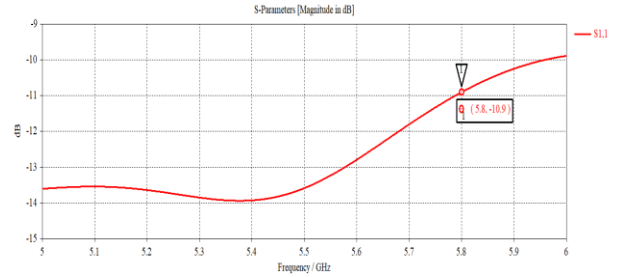

Fig. 11. S_{11} curve in CST

After the optimizing process, the return loss is reduced from -10.9 to -18.297. This return loss value indicates a good impedance match. Fig. 12 shows the S_{11} curve after optimization at 5.8 GHz.

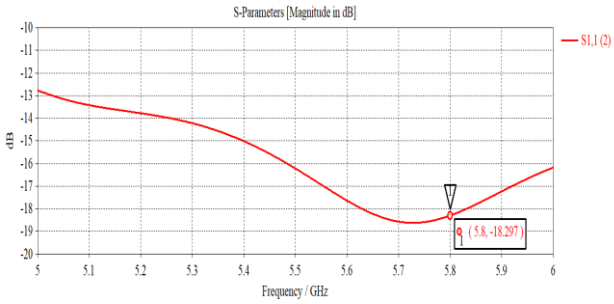

Fig. 12. S_{11} curve after optimization

Fig. 13 represents the 2D far field pattern in CST at 5.8 GHz. The magnitude of the main lobe result is 15.2 dB, the direction of the main lobe is 0.0 degrees, the value of angular width at 3dB is 28.6 degrees, the gain is 15.17 dB, and the side lobe level is -23.0 dB.

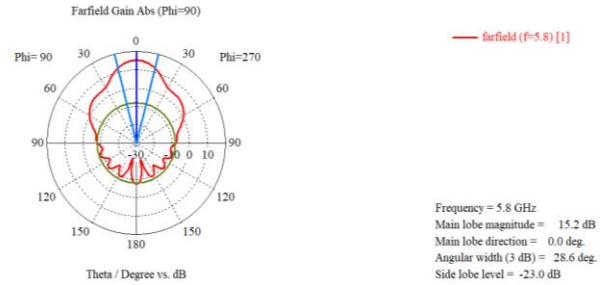

Fig. 13. 2D far field pattern in CST at 5.8 GHz

After the optimization process, the result of the 2D far-field pattern after optimization is shown in Fig. 14. The results of the main lobe magnitude are changed to 15 dB, the direction of the main lobe is 0.0 degrees, the angular width at 3dB is 30.4 degrees and the value of side lobe level is -23.1 dB at 5.8GHz frequency.

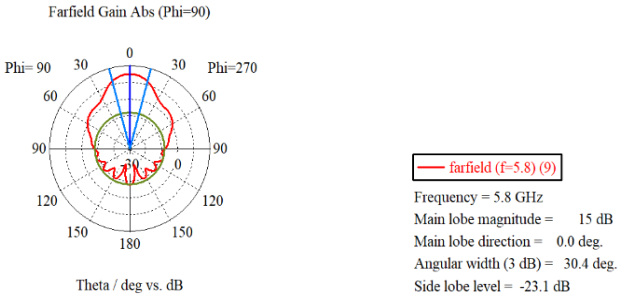

Fig. 14. 2D far field pattern after optimization

The 3D view of the radiation pattern for the horn antenna is expressed in Fig. 15. This figure describes the antenna's radiating energy in 3D space, with the colors indicating the intensity of the radiation in different directions.

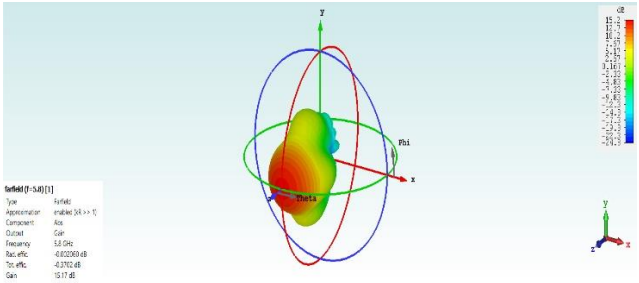

Fig. 15. 3D radiation pattern of the horn antenna

Fig. 16 describes the results of the three-dimensional radiation pattern of the horn antenna after the optimization process.

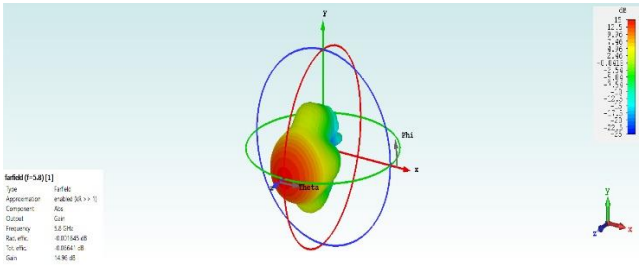

Fig. 16. 3D radiation pattern of the horn antenna after optimization

By systematically varying the radiation elements and aperture dimensions by 10%, and employing an optimization algorithm, identified the optimal design parameters that enhance the performance of the desired horn antenna. This methodical approach ensures a balanced improvement, resulting in a highly efficient antenna design. The comparison results of before and after optimization are presented in Table II.

II. RESULTS COMPARISON OF BEFORE AND AFTER OPTIMIZATION

Description	**Values**	
	Before Optimization	***After Optimization***
Frequency	5.8 GHz	5.8 GHz
Polarization	Linear Polarization	Linear Polarization
Impedance	50 Ohm	50 Ohm
Radiation Efficiency	99.953 %	99.962 %
Angular Width (3dB)	28.6 deg.	30.4 deg.
Main Lobe Magnitude	15.2 dB	15 dB
Side Lobe Level	-23 dB	-23.1 dB
VSWR	1.7976	1.277
Return Loss (S_{11})	-10.9	-18.297

IV. CONCLUSION

The research paper discusses "Simulation and Optimization of Pyramidal Horn Antenna for UAV Video Link" at 5.8GHz. In this research, an optimization process is undertaken to enhance the capability of antenna. The horn antenna is achieved with a typical gain value of 15 dB. Optimizing the main antenna dimensions improves the antenna's gain, beamwidth, side lobe level, VSWR, and S-parameter values. According to the simulation results, it has a high radiation efficiency of 99.962% ensuring minimal energy loss. The VSWR value of 1.277 and S-parameter of -18.297 indicate good impedance matching and minimal signal reflection. The angular width (3 dB) of 30.4 degrees indicates a suitable coverage area and the low side lobe level (-23.1 dB) signifies reduced interference from unwanted directions. The presented design methodology, simulation results, and optimized antenna characteristics demonstrate the feasibility and effectiveness of the desired horn antenna for 5.8 GHz video link applications.

ACKNOWLEDGMENT

First of all, the author conveys special thanks to Dr. Pa Pa Winn San, Head of the Department, for her support and motivation. The author expresses immense gratitude to her supervisor, Dr. Aye Min Soe, for her exceptional supervision, patient guidance, invaluable advice, and suggestions throughout the journal. The author extends sincere gratitude to her Co-Supervisor, Daw Htet Htet Aung, for her valuable advice and guidance on this journal. Lastly, the author offers heartfelt appreciation to all of the teachers from the Department of Electronic Engineering, Technological University (Mandalay), and also grateful to the colleagues who have contributed to the accomplishment of this work.

REFERENCES

[1] Simon R. Saunders Alejandro Aragon Zavala, "*Antennas and Propagation for Wireless Communication Systems*."

[2] Robert S. Elliot, "*Antenna theory and design*."

[3] Brent Maxfield, "*Engineering with Mathcad: Using Mathcad to Create and Organize your Engineering Calculations*," 2006.

[4] Abdelali El Bouanani, "*CST Studio Suite: Modeling and Simulation of High-Frequency Structures*," 2019.

[5] Mrs. Nitin Gupta, Mrs. Ritika Gohil, "*Design and Analysis of Pyramidal Horn Antenna*," (IJCRT), Vol-8, Issue 3, March 2020.

[6] P. Gowtham Kumar, S. Sai Rama Raju, and P. Chandrasekhar, "*Waveguide Pyramidal Horn Antenna with Enhanced Directivity*," Volume 3, Issue 3, 2015.

[7] Karim Gurney, "*Design of Pyramidal Horn Antennas*," Pure Sciences Marmara, Journal 2002.

[8] Aniket Bhumika, "*Design and implementation of Pyramidal Horn Antenna*," May 2015.

Design and Simulation of FTTH System for Talote City using Optisystem

Nyan Phyo Aung[1], Mo Mo Myint Wai[2]

[1]*Department of Electronic Engineering, Technological University (Mandalay)*

[2]*Department of Electronic Engineering, Technological University (Mandalay)*

Email: [1]nyanphyoaung@gmail.com, [2]2moemyint@gmail.com

***Abstract*—This paper focuses on the design and analysis of optical fiber communication systems, which is essential to meet the increasing demands for high-speed data transmission in various applications such as live broadcasting, internet video, and video conferencing in Talote City, Myanmar. By utilizing Optisystem for simulating network topology, we ensure thorough design, testing, and performance evaluation of optical networks. This explanation emphasizes the importance of high-speed data transmission, the choice of Optisystem for simulation, and the significance of the Power Link Budget and BER in evaluating system performance. It also highlights the positive simulation results, suggesting a reliable and adaptable system. The simulation results indicated that the power levels at both ends of the spectrum are within the acceptable range for the receiver. This finding reinforces the feasibility of the implementation across varying power levels and distances. It provides confidence in the reliability and adaptability of the optical communication system designed for Talote City.**

Keywords— optical fiber, Optisystem, Power Link Budget, BER, Talote City

I. INTRODUCTION

Fiber-to-the-Home (FTTH) is a GPON technology that uses fiber optic cables to deliver high-speed internet, telephone, and television services directly to homes and businesses. Talote City, like many other cities, has seen a growing demand for high-speed internet services, and FTTH infrastructure is becoming increasingly important to meet this demand. To build an FTTH network infrastructure in Talote City, several key steps need to be taken. First, a feasibility study should be conducted to determine the optimal locations for fiber optic cables and other equipment. This study should take into account factors such as population density, existing infrastructure, and potential obstacles to installation. Once the feasibility study is complete, the actual installation process can begin. This typically involves laying fiber optic cables overhead, connecting them to distribution points, and then connecting those points to individual homes and businesses. The process can be time-consuming, but the benefits of high-speed internet access are well worth the investment.

FTTH (Fiber to the Home) network using OptiSystem is a high-speed fiber optic network that provides internet, phone, and TV services to homes and businesses. OptiSystem is a software tool used to design and simulate optical communication systems. The FTTH network consists of an Optical Line Terminal (OLT) at the central office or headend, optical fiber cables that connect the OLT to ONTs located at the customer premises, and customer equipment such as modems and routers. The network uses Passive Optical Networks (PON) to deliver services to customers.

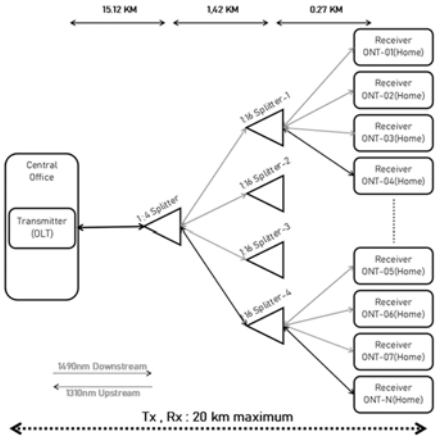

Fig. 1. The Block Diagram of FTTH System

The OLT is responsible for providing the high-speed data stream and for converting the electrical signals into optical signals for transmission over the fiber optic cable. The ONTs are located at the customer premises and are responsible for receiving the optical signal and converting it back into an electrical signal for use by the customer's equipment. OptiSystem is used to design and simulate the FTTH network to ensure optimal performance and reliability. It allows engineers to model the entire network, including the optical fiber cable, the OLT, the ONTs, and customer equipment, and to test different configurations and parameters to optimize performance. In this paper, the BER and link loss budget of two homes are described.

In conclusion, while building an FTTH network infrastructure in Talote City may present challenges, the potential benefits far outweigh the costs. By undertaking careful planning, investment, and collaboration, the city can establish a modern and reliable telecommunications infrastructure that supports the needs of its residents and contributes to overall socio-economic development.

II. BACKGROUND THEORY

A. Fiber to the Home

Fiber to the Home (FTTH), also known as Fiber to the Premises (FTTP), represents a significant advancement in internet connectivity by installing optical fiber from a central point directly to individual buildings, ensuring high-speed internet access. This technology vastly improves connection speeds for users compared to traditional technologies such as cable modems or DSL.

FTTH offers connection speeds of up to 100 megabits per second (Mbps), which are 20 to 100 times faster than typical cable modem or DSL connections. This substantial increase in speed enables smoother and more reliable internet experiences, supporting demanding applications like live broadcasting, internet video, and video conferencing.

Implementing FTTH on a large scale can be costly due to the need for new cable installations over the last mile from existing optical fiber infrastructure to individual users. While some communities already benefit from fiber to the curb (FTTC) services, which use optical fiber to the curbs near homes or businesses and copper for the final connection, FTTH involves direct optical fiber connections to residences, apartment buildings, and businesses. This approach eliminates the limitations of copper and maximizes the performance benefits of optical fiber.

In an FTTH network, optical fiber cables run from a central office through a fiber distribution hub, then through a network access point, and finally into homes via a terminal junction box. The key components of the network include:

- **Optical Line Terminal (OLT):** Located at the provider's central office, the OLT manages the overall operation of the network.
- **Optical Network Units (ONUs):** Placed closer to end-user premises, these units receive and convert optical signals for delivery to individual users.
- **Optical Distribution Network (ODN):** Situated between the OLT and ONUs, this network includes splitters to distribute signals.
- **Fiber Distribution Terminals (FDTs):** These serve as intermediate points where incoming fibers from the central office are split to serve different neighborhoods or areas.
- **Fiber Access Terminals (FATs):** Located closer to end-users, FATs distribute optical signals from FDTs to individual residences or businesses and typically include equipment for signal conversion and distribution.

Two primary types of systems enable data transmission in FTTH:

- **Active Optical Networks (AONs):** Utilize electrically powered switching equipment to direct signals to specific users.
- **Passive Optical Networks (PONs):** Use optical splitters instead of electrical switches to distribute signals. PONs still require powered equipment at the source and receiving ends but are generally more cost-effective and offer high performance.

The PON topology consists of:

- An **Optical Line Terminal (OLT)** at the central office.
- **Optical Network Units (ONUs)** near end-user premises.
- An **Optical Distribution Network (ODN)** that includes splitters to distribute signals along the PON.

FTTH's direct optical fiber connections to end-users represent the future of high-speed internet access, promising significant improvements in connection speeds and reliability. Despite the higher initial installation costs, the long-term benefits in performance and scalability make FTTH a compelling choice for modern telecommunications infrastructure, especially in data-demanding environments like Talote City, Myanmar. Utilizing tools like Optisystem for simulation and analysis ensures that these networks are designed and evaluated for optimal performance, reliability, and adaptability. [1]

B. Gigabit Passive Optical Network (GPON)

Gigabit Passive Optical Network (GPON) is an advanced technology in fiber optic communication systems, designed to deliver high-speed internet and other telecommunication services to end-users. GPON is characterized by its use of a point-to-multipoint (P2MP) architecture, employing a passive optical distribution network (ODN) to interconnect the central office with multiple end-user locations. OLT was located at the service provider's central office. It manages the overall operation of the GPON system, including signal transmission and reception. ONU **r**eceives optical signals from the OLT, converts them to electrical signals for user devices, and vice versa. ODN **i**ncludes passive splitters to distribute optical signals from one fiber into multiple fibers. Split ratios of ODN can vary, commonly 2, 4, 16, 32, or 64, allowing one fiber from the OLT to serve multiple ONUs/ONTs. The nominal bit rate of signals from the OLT to ONUs (downstream) is 2488.32 Mbit/s, as specified by ITU-T G.984.2 Recommendation. The nominal bit rate of signals from ONUs to the OLT (upstream) is 1244.16 Mbit/s.

GPON systems operate by transmitting data in a P2MP configuration using passive splitters to divide a single optical signal from the OLT into multiple signals for various ONUs. This method is efficient for serving multiple users with a single fiber infrastructure, reducing the cost and complexity of the network.

GPON represents a robust and efficient solution for modern telecommunication needs, offering high-speed connectivity and the ability to support multiple users with a single fiber infrastructure. Its point-to-multipoint architecture and use of passive components make it a cost-effective and scalable option for delivering broadband services, particularly in densely populated areas or regions with high demand for bandwidth-intensive applications.[2]

C. Optsystem

OptiSystem is a comprehensive simulation software tool designed by Optiwave for designing, testing, and optimizing optical communication systems. It supports the end-to-end development of optical networks, including Fiber to the Home (FTTH) systems, enabling users to simulate various aspects of optical communication networks and components. OptiSystem offers advanced tools for performance analysis, including bit error ratio (BER), eye diagrams, Q-factor, and power link budget calculations.

These tools help assess the feasibility and reliability of optical communication systems. The software supports industry standards and recommendations, such as ITU-T and IEEE, ensuring that the simulated systems meet real-world specifications. Users can simulate the entire FTTH network topology, including the Optical Line Terminal (OLT) at the central office, passive optical distribution network (ODN) with splitters, and Optical Network Units (ONUs) at end-user premises. OptiSystem is a powerful tool for designing and optimizing optical communication systems, including FTTH networks. Its comprehensive simulation capabilities, extensive component libraries, and advanced analysis tools make it an invaluable resource for engineers and researchers working to develop high-performance and reliable optical networks. By using OptiSystem, users can ensure that their FTTH systems are designed to meet the growing demands for high-speed, high-quality data transmission in a cost-effective manner.[3]

D. Power Link Budget

The power link budget, a remarkable and necessary calculation for communication networks, is designed beyond the threshold of the required power. Hence, the power link budget calculation is applied on the basis of ITU-TG.984 standardizations and implemented via industry instruction. The coverage distance is a maximum of 20 km while the receiving power is a maximum of −28 dBm. Consequently, equations (1) is used to calculate the power budget link of total damping.The total attenuation for the FTTH device is calculated as follows [4]:

Link Loss = [fiber length(km) x fiber attenuation per km] + [splice loss x (N) of splices] + [connector loss x (N) of connectors] +[splitter loss] (1)

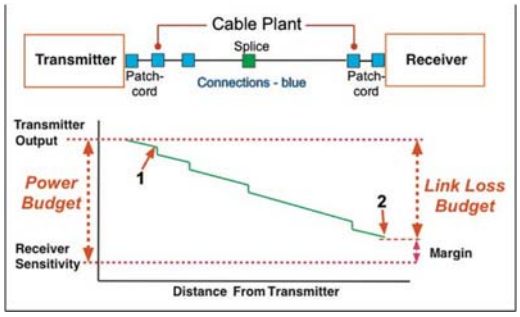

Fig. 2. The Link Loss Budget [5]

The standard attenuation values are as followed:

Fiber length Loss 1 km = -0.25dBm

Splice loss 1 joint = -0.05dB

Connector 1 head = -0.02dB

Splitter loss 1:4 Splitter = 10log(1/4) = -6.02dB

Splitter loss 1:16 Splitter = 10log(1/4) = -12.04dB

III. Proposed System and Simulation Setup

The FTTH system is design in area of Talote City of Myanmar. There are two geographical locations in this design to develop FTTH the system in the city. The google earth photo of two area of FDT in the city. The Fig 3 show the two area of the FDT in city to implement FTTH. In this work, there simulation of the two homes for two different location and dirrrnce FDT for BER and link loss.

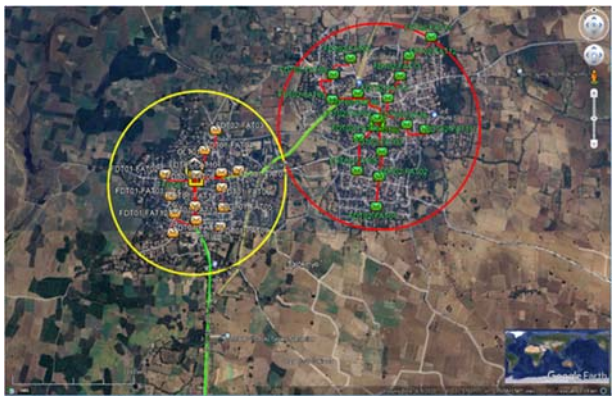

Fig. 3. The Google Earth Photo of Talote City with Two FDT

The fiber core plan of this city has two depends on the two FDTs which are called FDT-01 and FDT02 as shown in Fig. 4 and 5. The transmission path of the signal from the central office to the homes, which involves passing through Fiber Distribution Terminals (FDTs) and Fiber Access Terminals (FATs) depending on the city's core plan. The signal transmission path from the central office to homes involves passing through multiple FATs, which are strategically placed based on the city's core plan to ensure efficient coverage and distribution of high-speed internet services.

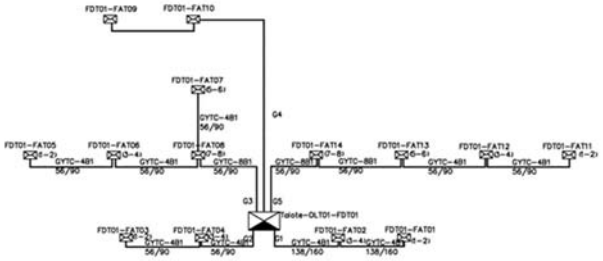

Fig. 4. The Core Plan For FDT-01

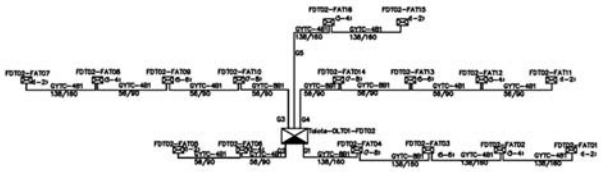

Fig. 5. The Core Plan With FDT-02

Fig 6 likely illustrates this transmission path, showing the interconnected network of FDTs and FATs along with the flow of signals from the central office to the individual homes. This is called simulation model of each user in city.

Fig. 6. The Simulation Model of User Home in City

IV. Simulation Results

The simulation of FFTH system of houses in city are developed by Optisystem. In this work, the two homes are different location in the city area. The home 1 is located in FDT-01 area in city. The fiber layout plan of home 1 which is near at FAT10 can be setup as following:

At transmitter component - 1490 nm / +5dBm

OLT to FDT-01 = 15118 m

FDT-01 to FAT-10 = 268 m

FAT-10 to ONT-01(User Home) = 250 m

Connector Attenuation = -0.02 dB x 7 connectors = -0.14 dB

Splicing Attenuation = -0.05 dB x 6 joints = -0.3 dB

1:4 Splitter Formula : 10log(1/4) = -6.02dB

1 : 16 Splitter Formula : 10log(1/16) =-12.04dB

After calculation of fiber layout out of home 1 in city, the simulation model of this home can be done by optisystem as shown in Fig. 7. In this model of optisystem, there are detail of fiber core layout and FDT-01 and FATs from OLT to ONT. And BER results can be calculate in this model. The simulation result of home 1 is as shown in Fig. 8. The BER analysis revealed that the network of home 1 had a low BER of $3.3e^{-035}$, which indicates a high signal quality. The BER values for home in the network are shown in Fig. 9. The low BER values indicate that the network's design and simulation parameters were optimal for achieving a high signal quality. Therefore, the ONT located farthest from the OLT had a slightly higher BER than the others.

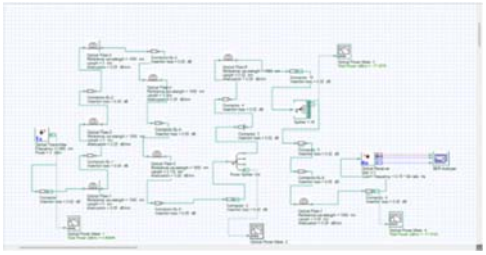

Fig.7. The Simulation Model of Home 1 In City

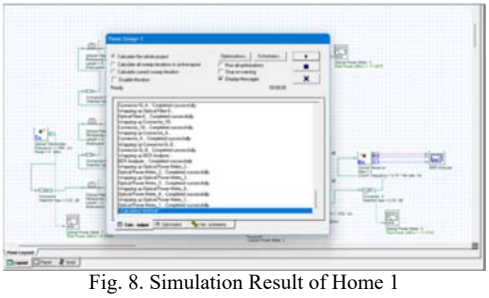

Fig. 8. Simulation Result of Home 1

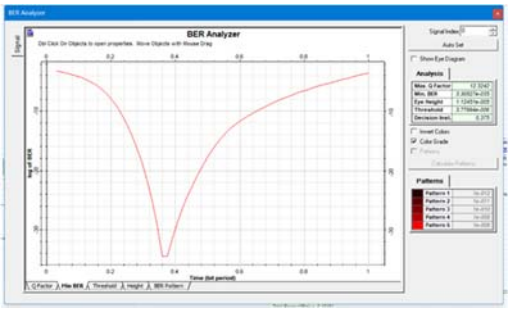

Fig. 9. BER analysis of Home 1

This suggests that there may be signal degradation due to distance and attenuation. The link losses budget of home can be calculated by eq:1 and the result are as shown in Table I.

I. LINK LOSS BUDGET OF HOME 1

No.	Item Name	Power	Attenuation	Total Power(dBm)
1	Output Power	4.9385	1.00	4.9385
2	Connector	-0.0200	1.00	-0.0200
3	Optical Fiber	-3.0000	0.25	-0.7500
4	Splice	-0.0500	1.00	-0.0500
5	Optical Fiber	-3.0000	0.25	-0.7500
6	Splice	-0.0500	1.00	-0.0500
7	Optical Fiber	-3.0000	0.25	-0.7500
8	Splice	-0.0500	1.00	-0.0500
9	Optical Fiber	-3.0000	0.25	-0.7500
10	Splice	-0.0500	1.00	-0.0500
11	Optical Fiber	-3.1180	0.25	-0.7795
12	Splice	-0.0500	1.00	-0.0500
13	Connector	-0.0200	1.00	-0.0200
14	1:4 Splitter	-6.0206	1.00	-6.0206
15	Connector	-0.0200	1.00	-0.0200
16	Connector	-0.0200	1.00	-0.0200
17	Optical Fiber	-0.0200	0.25	-0.0050
18	Connector	-0.0200	1.00	-0.0200
19	1:16 Splitter	-12.0412	1.00	-12.0412
20	Connector	-0.0200	1.00	-0.0200
21	Splice	-0.0500	1.00	-0.0500
22	Optical Fiber	-0.2500	0.25	-0.0625
23	Connector	-0.0200	1.00	-0.0200
				-17.41031 dBm

The home 2 is located in FDT-02 area in city. The fiber layout plan of home 2 which is near at FAT13 and it must be pass through the FDT-01 to FDT-02 can be setup as following:

At Transmitter component - 1490 nm
OLT to FDT-01 = 15118 m
FDT-01 to FDT-02 = 1518 m
FDT-02 to FAT-13 = 293 m
FAT-13 to ONT-02(User Home) = 272 m
Connector Attenuation = -0.02 dB x 7 connectors = -0.14 dB
Splicing Attenuation = -0.05 dB x 7 joints = -0.35 dB
1:4 Splitter Attenuation = 10log(1/4) = -6.02dB
1 : 16 Splitter Attenuation = 10log(1/16) =-12.04dB

After calculation of fiber layout out of home 2 in city, the simulation model of this home can be done by optisystem as shown in Fig. 10. In this model of optisystem, there are detail of fiber core layout and FDT-02 and FATs from OLT to ONT. And BER results can be calculate in this model. The Fig. 11 shows the simulation results of optisystem model of home 2 in the city

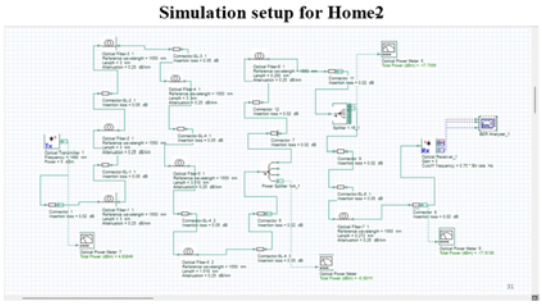

Fig. 10. The Simulation Model of Home 2 In the City

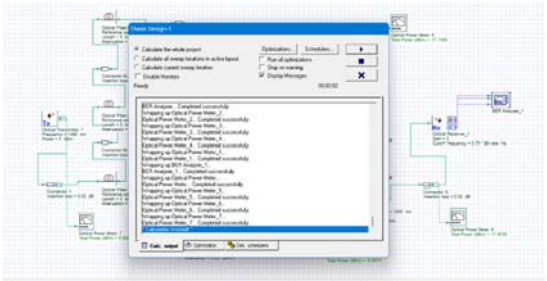

Fig. 11. The Results of Simulation Model Of Home 2 In The City

The BER results of the home 2 in the city as shown in Fig. 12.

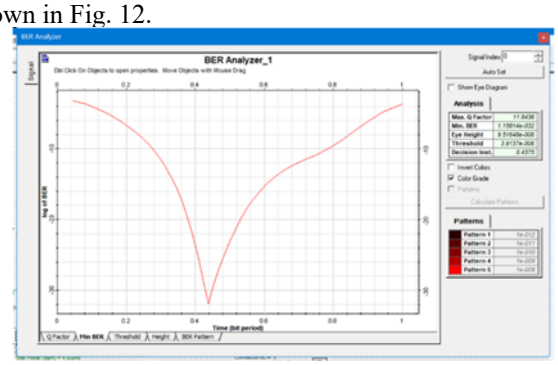

Fig. 12. BER Result of Home 2

The link losses budget of home 2 can be calculated by eq:1 and the result are as shown in Table II.

II. LINK LOSS BUDGET OF HOME 2

No.	Item Name	Power	Attenuation	Total Power
1	Output Power	4.9385	1.00	4.9385
2	Connector-1	-0.0200	1.00	-0.0200
3	Optical Fiber	-3.0000	0.25	-0.7500
4	Splice	-0.0500	1.00	-0.0500
5	Optical Fiber	-3.0000	0.25	-0.7500
6	Splice	-0.0500	1.00	-0.0500
7	Optical Fiber	-3.0000	0.25	-0.7500
8	Splice	-0.0500	1.00	-0.0500
9	Optical Fiber	-3.0000	0.25	-0.7500
10	Splice	-0.0500	1.00	-0.0500
11	Optical Fiber	-3.1180	0.25	-0.7795
12	Splice	-0.0500	1.00	-0.0500
13	Optical Fiber	-1.518	0.25	-0.3795
14	Splice	-0.0500	1.00	-0.0500
15	Connector	-0.0200	1.00	-0.0200
16	1:4 Splitter	-6.0206	1.00	-6.0206
17	Connector	-0.0200	1.00	-0.0200
18	Connector	-0.0200	1.00	-0.0200
19	Optical Fiber	-0.2930	0.25	-0.0733
20	Connector	-0.0200	1.00	-0.0200
21	1:16 Splitter	-12.0412	1.00	-12.0412
22	Connector	-0.0200	1.00	-0.0200
23	Splice	-0.0500	1.00	-0.0500
24	Optical Fiber	-0.2720	0.25	-0.0680
25	Connector	-0.0200	1.00	-0.0200
				-17.9136

The link loss budget between home 1 and home 2 in the city. The comparisons of link loss budge of these home are as shown in Table III.

III. COMPARISONS OF LINK LOSS BUDGET BETWEEN TWO HOMES

	Home 1	Home 2
Total fiber length	15636 m	17201 m
Total joints	13	14
1:4 Splitter	1	1
1:16 Splitter	1	1
Total Link Budget	-17.47231dBm	-17.9136dBm
Difference		-0.4413dBm

Generally, the longer the fiber optic cable, the greater the link loss. Expanding the distance of the fiber length from 5 km to 20 km between the central office and ONT is a significant extension that reflects real-world scenarios where longer distances need to be covered. Your observation that this increase causes the bit error rate to rise from 4.3e^-57 to 5.02e^-16 is important, as it highlights the impact of distance on the performance of the optical communication system. Despite the increase in bit error rate, it's notable that the values still meet the minimum acceptable level, indicating the robustness of in this design. Furthermore, considering the effect of received power, with values ranging from -16 dBm to -20 dBm, is crucial for ensuring proper signal reception at the ONT.

V. CONCLUSION

The study described seems to have provided valuable insights into optimizing FTTH (Fiber to the Home) networks for improved signal quality. By using Optisystem for simulation and BER analysis, the researchers were able to assess the performance of the network under different conditions. The observation that the ONT (Optical Network Terminal) located farthest from the OLT (Optical Line Terminal) experienced slightly higher BER due to distance and attenuation highlights the real-world challenges faced in FTTH deployments. This underscores the importance of optimizing network design to mitigate these issues. Adjusting optical power levels and implementing dispersion compensation are effective strategies for improving signal quality, as demonstrated by the study's results. By optimizing the network design based on these parameters, the researchers were able to achieve a significantly lower BER, indicating a substantial improvement in signal quality. Overall, this paper underscores the importance of rigorous simulation and analysis in designing and optimizing FTTH networks. It also emphasizes the significance of BER analysis in evaluating network performance and identifying areas for improvement. By addressing factors such as distance, attenuation, and dispersion, network engineers can enhance signal quality and ensure reliable performance in FTTH deployments.

ACKNOWLEDGMENT

I would like to extend my sincere gratitude to my rector and prorector for their unwavering support and guidance throughout the development of this journal. Their insights and encouragement have been invaluable. I am also deeply thankful to my wife for her constant support and understanding, which has been a source of strength during this project. Furthermore, I would like to acknowledge my pupil, Aung Win Zaw, whose dedication and assistance have been crucial in the development of this work.

REFERENCES

[1] Ben Lutkevich," Fiber to the Home (FTTH)," Available: https://www.techtarget.com/searchnetworking/definition/fiber-to-the-home [April, 2013].

[2] Frank Effenberger, "An Introduction to PON Technologies," presented at IEEE Communications Magazine, 2007.

[3] Glen Kramer. " Ethernet PON (ePON): Design and Analysis of an Optical Access Network.," presented at Photonic Network Communications, April 2001.

[4] Arafat Abdallah Shabaneh, and Masa Loai Melhem. "Execution Simulation Design of Fiber-to-the-home (FTTH) Device Ingress Networks Using GPON with FBG Based on OptiSystem," in Proc. International Journal of Electronics and Telecommunications VOL. 68, PP. 783-791, Dec 2022.

[5] The Fiber Optic Association. "Power Budgets and Loss Budgets," Available: https://www.thefoa.org/tech/lossbudg.htm [2004].

Performance of SDR Based FSK Transceiver with USRP and LabVIEW

Swe Zin Win Tun[1], Nyan Phyo Aung[2], Htet Htet Aung[3]

[1] *Department of Electronic Engineering, Technological University (Mandalay)*

[2] *Department of Electronic Engineering, Technological University (Mandalay)*

[3] *Department of Electronic Engineering, Technological University (Mandalay)*

Email: [1]ecszwt@gmail.com, [2]nyanphyoaung@gmail.com, [3] htethtetaunginle@gmail.com

***Abstract*— This paper discusses the performance of Software Defined Radio (SDR) transceiver in LabVIEW and USRP. This system is implemented to design a Frequency Shift Keying (FSK) transmitter and receiver using the Universal Software Radio Peripheral (USRP) board and LabVIEW. This paper describes the use of the USRP Board for transmitting and receiving FSK signals and the experimental implementation of LabVIEW and USRP for wireless channel transmission. The system tests three different testing schemes by sample per symbol and IQ sampling rate to get the best performance in communication with USRP in the FSK communication system.**

***Keywords*— FSK, LabVIEW, SDR, Transceiver, USRP**

I. INTRODUCTION

SDR is a software-defined wireless communication technology that offers efficient and inexpensive solutions for building multimode, multicarrier, multiband, and multifunctional wireless devices. It has the capability to be reprogrammed and reconfigured for use with various waveforms and protocols. SDR is useful for radio interoperability and spectrum reuse, covering a substantial frequency range and executing software for various modulation techniques. Benefits include ease of design, manufacturing, multimode operation, advanced signal processing techniques, fewer discrete components, flexibility, reduced obsolescence, and ubiquitous connectivity. To develop this system, there are software and hardware components that combine to create a complete system [1].

Frequency Shift Keying (FSK) is a digital modulation technique where the carrier frequency is shifted between discrete values to represent different symbols in a binary data stream. The transmitter modulates the carrier frequency based on the symbols, while the receiver demodulates the signal [2].

Binary FSK (or "BFSK") uses two frequencies:

Mark: corresponds to logical 1 and Space: corresponds to logical 0

Laboratory Virtual Instrument Engineering Workbench (LabVIEW), a popular graphical programming language, is used for simulation, control, and DAQ applications. It supports various instrumentation I/O interfaces, networking protocols, and underapplication communication protocols. It offers powerful features for network operations, mathematics, signal processing, and signal theory.

USRP, a hardware component used in capturing real-time signals, allows general-purpose computers to function as high-bandwidth software radios, serving as a digital baseband and IF section in a radio communication system. The USRP performs waveform-specific processing on the host CPU using LabVIEW, while high-speed general-purpose operations are performed on the FPGA. The Universal Software Radio Peripheral (USRP) 2920 board is used to design the Frequency Shift Keying (FSK) transmitter and receiver. This paper describes the transmission and receiving of the FSK signal in the form of binary data using USRP. There are three FSK modulation scheme varieties with IQ values and sample per symbol values to get the best signal received in this work. The proposed implementation of system setup is as shown in Fig. 1 [3].

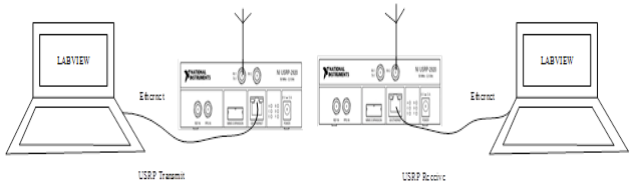

Fig. 1. The block diagram of the implementing of system of FSK transceiver using USRP

Software-Defined Radio (SDR) is a technique that uses software to make radio functions hardware-independent and is used in advanced wireless communication systems like the Joint Tactical Radio System (JTRS). GNU Radio emerged as an open-source tool that supports SDR, and Universal Software Radio Peripheral (USRP) was developed as a low-cost, high-speed SDR platform. GNU Radio and USRP are employed for developing software-based wireless transmission systems, implementing retransmission schemes, buffering, and the Leaky Bucket Algorithm to solve transmission error and environmental interference problems. Traditional radios have low flexibility to adapt to new services, standards, and technology, and the process of redesigning, manufacturing, and replacing hardware requires longer time and higher cost. USRP is an interesting option due to its relatively cheap cost and wide frequency range of 0–5 GHz.FPGA is a high-bandwidth mathematical calculator used for signal processing processes, and USB 2.0 is used for transmitting and receiving data between USRP and host computers. Several communication systems projects have been developed using both USRP and GNU Radio, with USRP being an integral part of the system. A simple file transmission system using GNU Radio and USRP is described, addressing issues like buffering and retransmission. A repeater is placed between the sender and receiver to increase transmission distance. The text introduces the concept of software-defined radio and the

capacity of GNU Radio, showing that USRP with GNU Radio is a powerful tool for developing and testing wireless systems [4].

In this paper, a bit stream of data is modulated using the FSK technique and transmitted in the 915 MHz center frequency ISM band, utilizing LabVIEW programming through a USRP. This process involves modulating the bit stream with FSK and programming it on LabVIEW for transmission via USRP.

II. Implementation Procedure

This work has a software and hardware portion of the system. The transmitter and receiver software block models are developed by LabVIEW. As shown in Fig. 1, the software portion of the LabVIEW block model of the transmitter and receiver of the system is combined by the USRP section block and the FSK modulation and demodulation techniques block. The flow chart of the transmitter and receiver of LabVIEW program software is shown in Fig. 2 and Fig. 3.

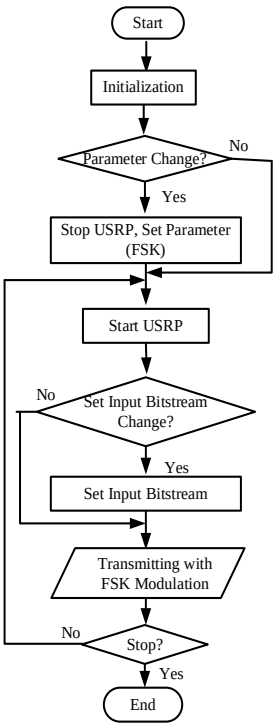

(2)

Fig. 2. The flow chart of transmitter of LabVIEW program software

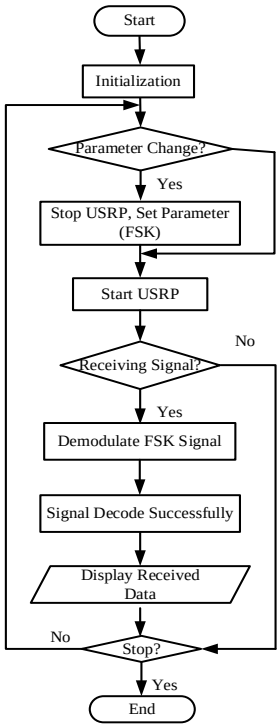

(3)

Fig. 3. The flow chart of transmitter of LabVIEW program software

LabVIEW is used to develop the software for this work, as mentioned earlier. The operation of the transmitter section and receiver section is shown in the flow chart in Fig. 2 and Fig. 3. After the software portion is completed, the hardware portion has a computer with LabVIEW and USRP connected via Gigabit Ethernet cables. Two USRPs of transmitter and receiver are wireless communication. The antenna is connected at TX 1 of the FSK transmitter USRP. FSK receiver USRP's antenna is coupled at RX2. Fig. 4 shows the hardware setup for two computers and the USRP.

These are connected to USRP via a gigabit Ethernet cable, as shown in Fig. 4. The bit stream transmitter with FSK modulation technique is developed by LabView block programming, as shown in Fig. 5. The FSK demodulation with USRP receiver section is also programmed with LabVIEW, as shown in Fig. 6.

Fig. 4. The hardware setup for two computer and USRP

Table I shows the experimental parameters of FSK modulation and demodulation using USRP.

I. Table the Parameters of FSK Modulation and Demodulation Using USRP

No.	FSK Modulation and Demodulation Parameters	
1.	Eye Length	12
2	PN Sequence Order	9
3	TX Filter	Gaussian
4	Filter Length	4
5	FSK M(-ary)	2
6	Carrier Frequency	915MHz (ISM Band)

III. Experimental Results of FSK Transceiver

After the software and hardware of this system are combined, the data bit starts transmitting with the FSK modulation technique using the test 1 parameter as described in Table II. These values are using an IQ sampling rate of 100k with samples per symbol 2.

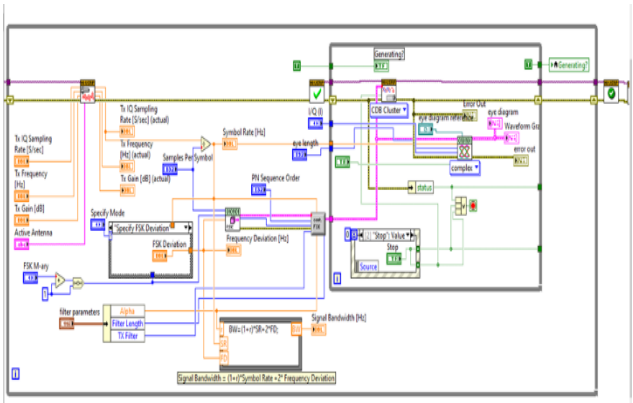

Fig. 5. FSK modulation of LabVIEW block programming Tx

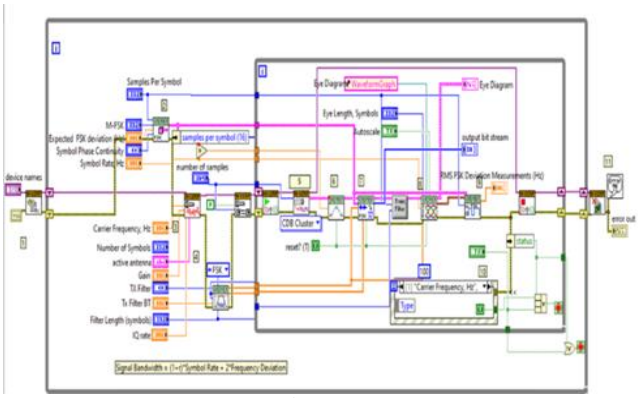

Fig. 6. FSK demodulation of LabVIEW block programming Rx

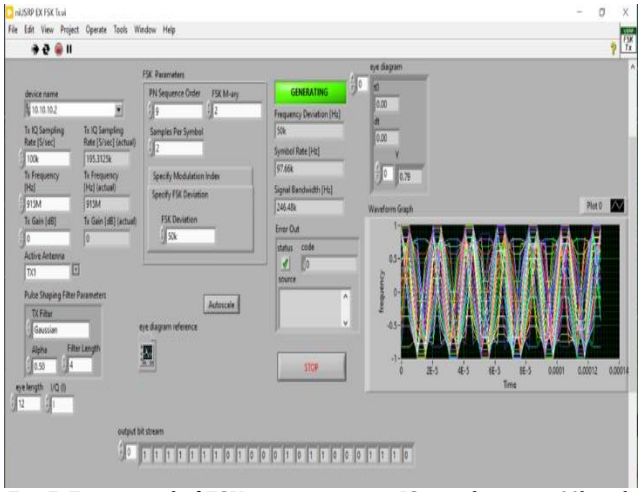

Fig. 7. Front pannel of FSK transmitter using IQ sampling rate 100k with samples per symbol 2

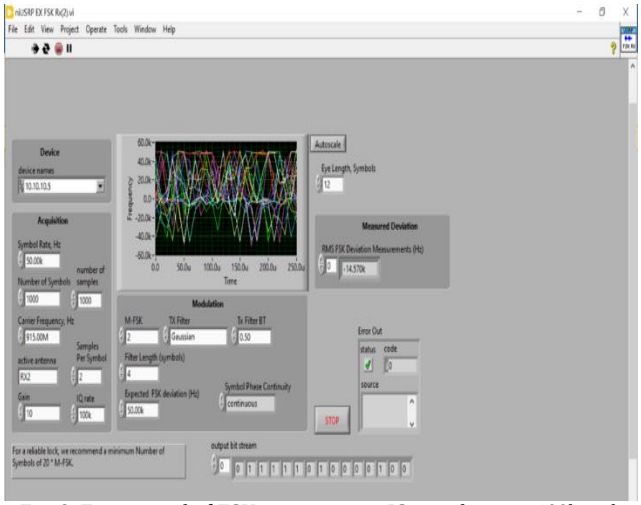

Fig. 8. Front pannel of FSK receiver using IQ sampling rate 100k with samples per symbol 2

The modulated waveform in LabVIEW is as shown in Fig. 7. The receiver side of the computer on LabVIEW has received a signal, and the demodulated results are shown in Fig. 8 with the same value as the transmitter.

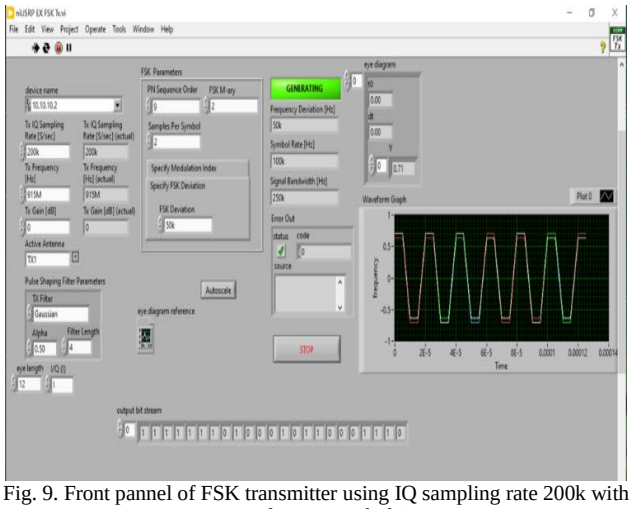

Fig. 9. Front pannel of FSK transmitter using IQ sampling rate 200k with samples per symbol 2

The IQ sampling rate is 200k with samples per symbol 2. The modulated waveform in LabVIEW is as shown in Fig. 9. The receiver side of the computer on LabVIEW has received a signal, and the demodulated results are shown in Fig. 10 with the same value as the transmitter.

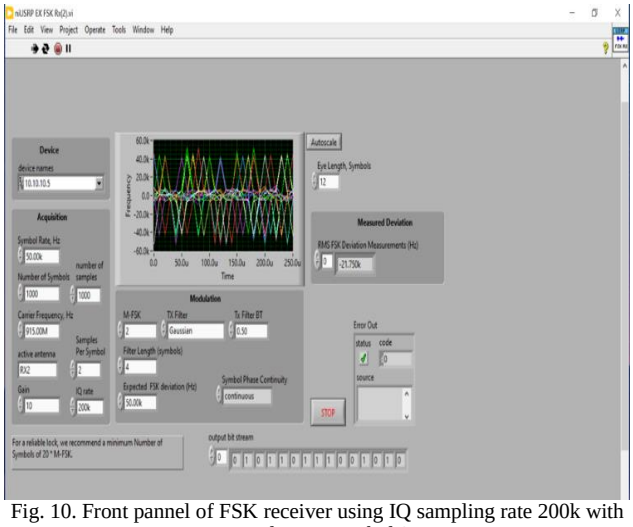

Fig. 10. Front pannel of FSK receiver using IQ sampling rate 200k with samples per symbol 2

After that, the same samples per symbol value and the IQ value of 300k of the transmition of FSK modulation and demodulation of data are as shown in Fig. 11 and Fig. 12. The test scheme is changing samples per symbol to 4, which is testing the system. In this test 2 scheme, the three values of the IQ sampling rate are tested with 100k, 200k, and 300k. The results of these tests are shown in Fig. 13, Fig. 14, Fig. 15, Fig. 16, Fig. 17, and Fig. 18.

Fig. 11. Front pannel of FSK transmitter using IQ sampling rate 300k with samples per symbol 2

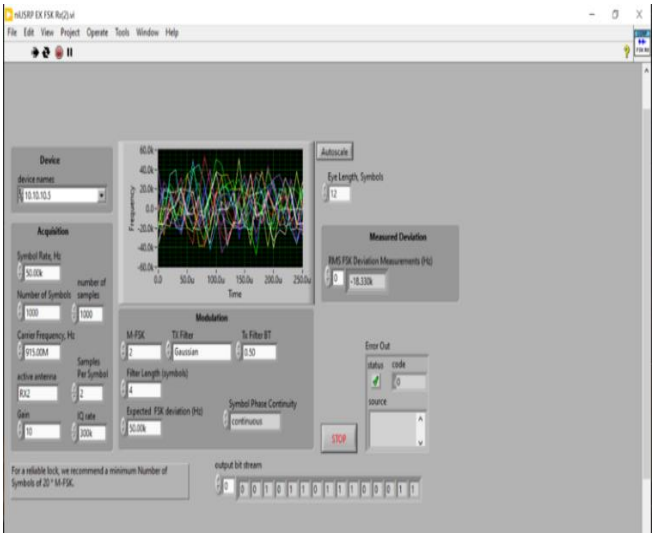

Fig. 12. Front pannel of FSK receiver using IQ sampling rate 300k with samples per symbol 2

Fig. 13. Front pannel of FSK transmitter using IQ sampling rate 100k with samples per symbol 4

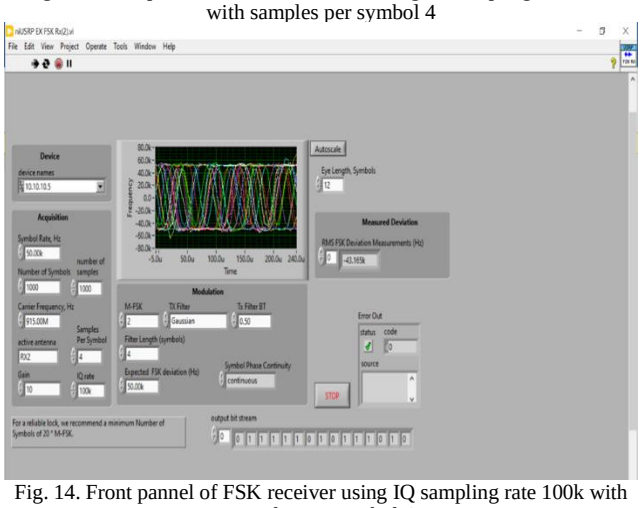

Fig. 14. Front pannel of FSK receiver using IQ sampling rate 100k with samples per symbol 4

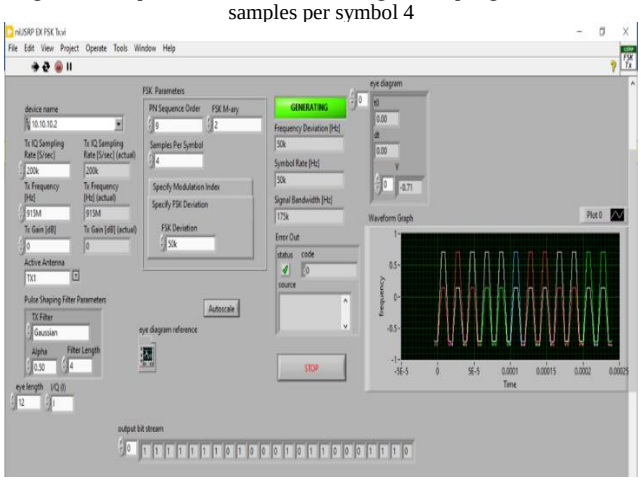

Fig. 15. Front pannel of FSK transmitter using IQ sampling rate 200k with samples per symbol 4

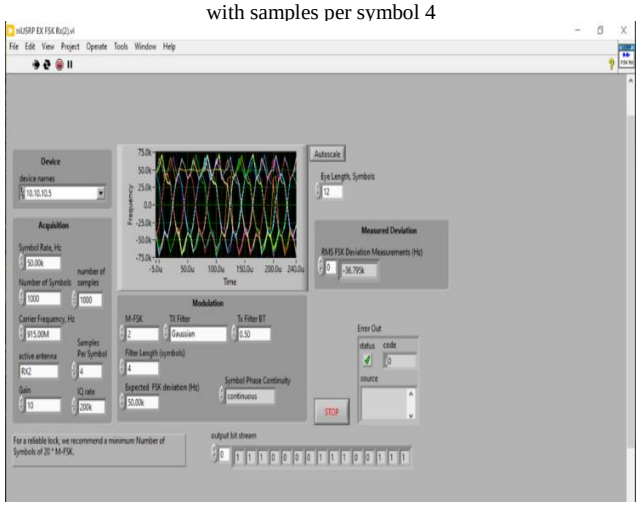

Fig. 16. Front pannel of FSK receiver using IQ sampling rate 200k with samples per symbol 4

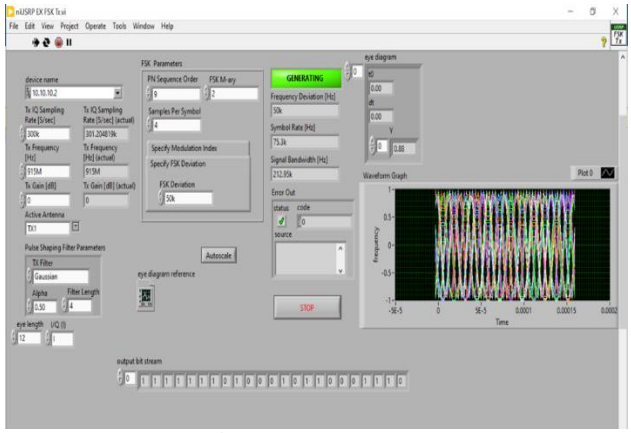

Fig. 17. Front pannel of FSK transmitter using IQ sampling rate 300k with samples per symbol 4

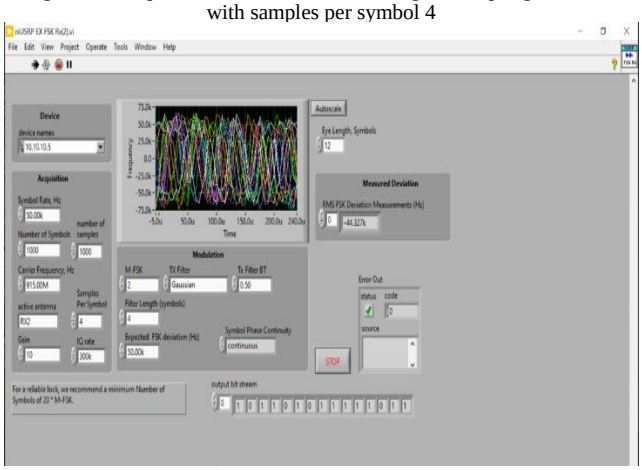

Fig. 18. Front pannel of FSK receiver using IQ sampling rate 300k with samples per symbol 4

The results of Fig. 13, Fig. 14, Fig. 15, Fig. 16, Fig. 17, and Fig. 18 show samples per symbol 4 and an IQ sampling rate of 200k, achieving a clear waveform result.

Fig. 19. Front pannel of FSK transmitter using IQ sampling rate 100k with samples per symbol 6

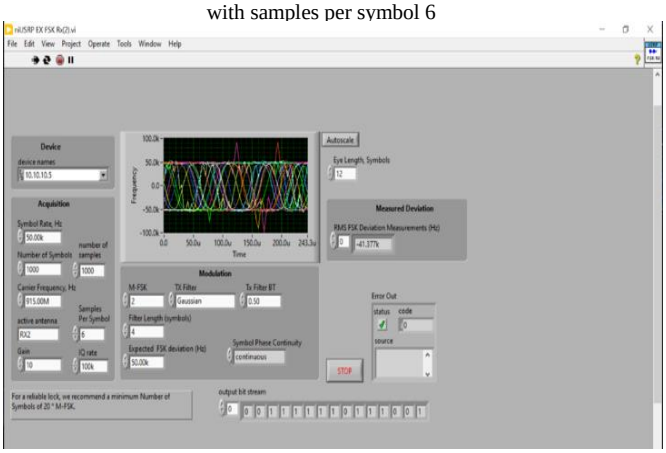

Fig. 20. Front pannel of FSK receiver using IQ sampling rate 100k with samples per symbol 6

The test 3 scheme is changing the samples per symbol value to 6. The other three values of IQ are the same as the test scheme. The transmitter and receiver LabVIEW waveforms are as shown in Fig. 19, Fig. 20, Fig. 21, Fig. 22, Fig. 23, and Fig. 24.

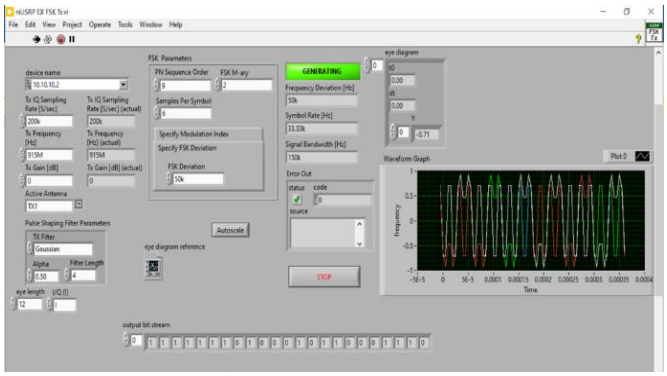

Fig. 21. Front pannel of FSK transmitter using IQ sampling rate 200k with samples per symbol 6

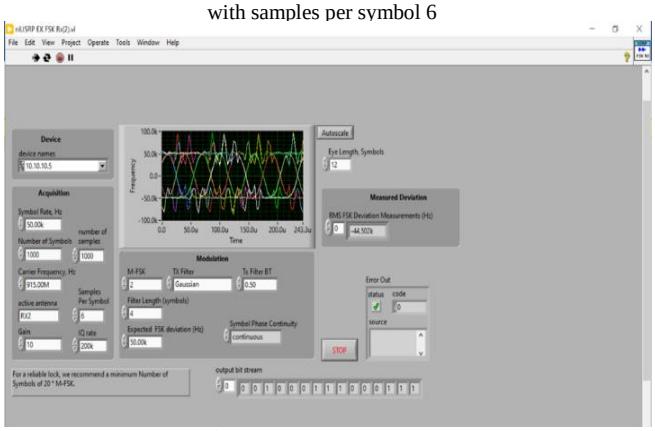

Fig. 22. Front pannel of FSK receiver using IQ sampling rate 200k with samples per symbol 6

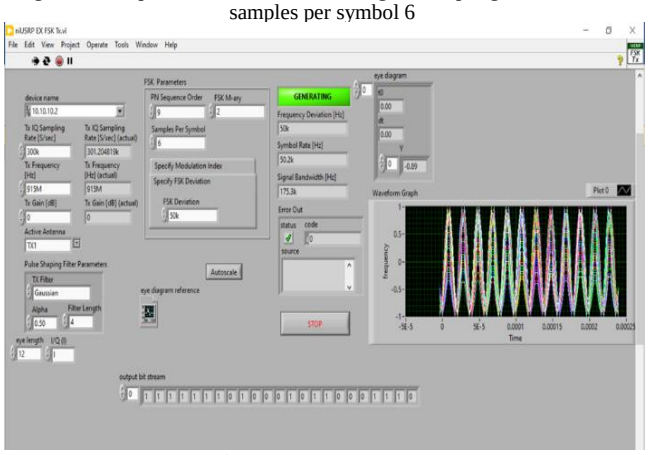

Fig. 23. Front pannel of FSK transmitter using IQ sampling rate 300k with samples per symbol 6

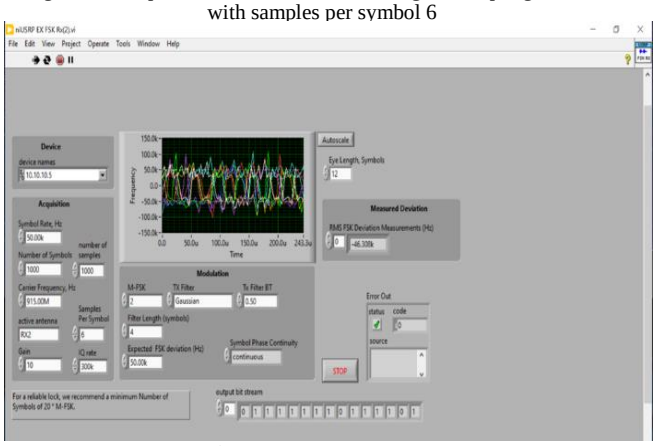

Fig. 24. Front pannel of FSK receiver using IQ sampling rate 300k with samples per symbol 6.

The transmitter and receiver of waveforms result in Fig. 19, Fig. 20, Fig. 21, Fig. 22, Fig. 23, and Fig. 24 show samples per symbol is 6 and the output waveform is distortion.

The summary of the three testing Schemes is as shown in Table II.

II. TABLE FSK SYSTEM PARAMETERS RESULTS

Testing Scheme	Tests Results				
	samples per symbol (S/s)	***IQ sampling rate (kHz)***	***symbol rate (kHz)***	***Signal Bandwidth (kHz)***	***Expected Freq: Deviation (kHz)***
1.	2	100	50	175	50
	2	200	100	250	50
	2	300	150	375	50
2	4	100	25	13.37	50
	4	200	50	175	50
	4	300	75	212.5	50
3	6	100	16.67	125	50
	6	200	3.33	150	50
	6	300	50	175	50

IV. CONCLUSION

Data (a bit stream) is modulated with FSK and transmitted in the center frequency ISM band (915 M) using LabVIEW programming via USRP. The data (a bit stream) is modulated using the FSK modulation technique and programmed on LabVIEW to transmit via USRP. Data is modulated with FSK and received by the LabVIEW program on a PC with NI USRP in three conditions: samples per symbol (2, 4, 6) and IQ sampling rate (100k, 200k, 300k). In test scheme (1, 2, 3), given that the IQ sampling rate is increased, the bandwidth is also increased. Samples per symbol value is 2, the output waveform is complex with noise, samples per symbol value is 4, the output waveform is clear, and samples per symbol value is 6, the output waveform is distortion. The above three condition parameters to consider are the IQ sampling rate (200k) and samples per symbol (4) for optimal performance.

ACKNOWLEDGMENT

The author also wishes to acknowledge special thanks to all the teachers to all the instructors from the Department of Electronic Engineering at Technological University (Mandalay) and extends heartfelt appreciation to the colleagues whose assistance was instrumental in completing this work.

REFERENCES

[1] J. R. Machado-Fernández, "Software defined radio." *Software defined radio: Basic principles and applications*, vol. 24, pp. 79-96, Jan 2015.

[2] Bob Watson, "FSK signals and demodulation," Internet: https://www.rfcafe.com/references/articles/wj-tech-notes/fsk-signals-demodulation-v7-5.pdf. May 5, 2021 [Accessed Feb 20, 2024].

[3] Dr. Thad B. Welch. "LabVIEW, the USRP, and their Implications on Software Defined Radio," presented at 2011 ASEE Annual Conference & Exposition, 2011.

[4] Z. Tong, M. S. Arifian to and C. F. Liau. "Wireless Transmission using Universal Software Radio Peripheral," Space Science and Communication, Port Dickson, Negri Sem bilan, Malaysia,2009.

Performance Analysis of MIMO Using Delay Profile Models in Wi-Fi 7 Technology

Than Than Swe[1], Htet Htet Aung[2], Yin Hnin Thet Htun[3]

[1]*Department of Electronic Engineering, Technological University (Mandalay)*

[2]*Department of Electronic Engineering, Technological University (Mandalay)*

[3]*Department of Electronic Engineering, Technological University (Mandalay)*

Email: [1]nanswethanswe@gmail.com, [2]htethtetaunginle@gmail.com, [3]yinhninthettun@gmail.com

***Abstract*—This research focuses on the performance analysis of MIMO using delay profile models in IEEE 802.11be or Wi-Fi 7 technology. MATLAB software is used to simulate and implement it. Multiple packets are transmitted using a noisy TGax indoor channel model. This next-generation standard aims to enhance the performance of wireless networks. The exceptionally high-capacity multi-user, or EHT MU packet is modeled using 4x4 MIMO, channel bandwidth of 320 MHz, scheme for modulation and coding (MCS) and delay profile models. The enhancement of numerous wireless communication systems is being significantly explored through multiple inputs, multiple outputs (MIMO) technology. This research demonstrates that utilizing an improved model and maintaining a significant SNR results in excellent performance, characterized by a low packet error rate (PER), for the IEEE 802.11be Wi-Fi network or WLAN standard. The performance of PER between different delay profile models is measured and evaluated using MATLAB software.**

Keywords – Delay Profile Models, IEEE 802.11be, MIMO, MATLAB, PER

I. INTRODUCTION

The IEEE 802.11 working team is advancing the next generation of Wi-Fi technology with the development of IEEE 802.11be, also referred as Wi-Fi 7 or extremely high data rates (EHT) [1]. This new standard operates within the 1 GHz and 7.125 GHz frequency ranges. The seventh generation of Wi-Fi enhances the existing concepts and techniques of the HE PHY layer, introducing enhancements such as multiple resource unit assignments to a single user, expanded bandwidths up to 320 MHz, support for up to 16 spatial streams (antennas), and 4096-QAM modulation [2]. At the MAC layer, it brings significant innovations, like multilink operation (MLO), which facilitates multiple links between a station (STA) and an access point (AP). This feature helps Aps conserve STA resources, resulting in more predictable traffic with reduced latency and increased reliability. Over the past two decades, IEEE 802.11 or Wi-Fi networks have mainly operated within the 2.4 gigahertz and 5 gigahertz bands, even as Wi-Fi usage has surged [3].

Wireless local area network or WLAN technology is the standard for establishing high-speed wireless connections, particularly for indoor devices, due to its straightforward deployment and cost effectiveness [4]. The evolution of wireless communication technologies has witnessed remarkable advancements in recent years, enabling faster and more efficient data transmission. One such significant hmilestone is the emergence of the wireless network standard, commonly referred to as the seventh version of Wi-Fi, which promises to revolutionize Wi-Fi connectivity with unprecedented performance and capabilities.

In order to understand, analyze, and optimize the behavior of IEEE 802.11be, it is essential to develop accurate and reliable models. MATLAB, a widely used high-up programming language and simulation environment, provides powerful tools and libraries that facilitate the modeling and simulation of wireless communication systems. This introduction aims to provide an overview of the process involved in modeling IEEE 802.11be using MATLAB, highlighting key aspects and techniques that can be employed to gain insights into the behavior of this advanced wireless standard. Table I describes the physical parameters of IEEE 802.11be [5].

I. IEEE 802.11BE PHYSICAL PARAMETERS

Parameters	Values
Frequency bands	2.4, 5, and 6 GHz
Channel bandwidth	320 MHz
Delay profile models	6 types (A, B, C, D, E, and F)
Modulation and coding scheme (MCS)	0 to 13, and 15
Modulation	4096-QAM
Spatial streams and MIMO	2 to 16, and MU-MIMO (2x2, 4x4, 8x8, 16x16)
Maximum throughput	46 Gbps

II. BACKGROUND THEORY

The error rate of the packet for six delay profile models is simulated. The channel bandwidth of 320 MHz is used for an extremely high capacity multi-user or EHT MU packet. The 4x4 multiple input, multiple output (4x4 MIMO) is used to transmit and receive 500 packets. The SNR ranges 8:1:13, 8:2:18, 16:2:26, and 18:2:28 and MCS 0 to 3 are used to test packet error rates between different models.

A. Delay Profile Models

In Wi-Fi 7, delay profile models are essential for characterizing the wireless channel. These models help simulate the various propagation environments that Wi-Fi devices must encounter, which is crucial for evaluating performance and ensuring robustness. The delay profile model is specified as Model A, Model B, Model C, Model D, Model E, or Model F. Each model has its own parameter. These parameters are used to develop realistic channel models for simulating Wi-Fi 7 performance in various scenarios [6]. By accurately characterizing the delay profile, manufacturers and researchers can ensure that Wi-Fi 7 devices perform optimally under different propagation

conditions. Table II presents the parameters of the models A, B, C, D, E, and F [7].

II. MODELS PARAMETERS

Parameters	Models					
	A	B	C	D	E	F
Breakpoint Distance (m)	5	5	5	10	20	30
RMS delay spread (ns)	0	15	30	50	100	105
Maximum delay (ns)	0	80	200	390	730	1050
Rician K-factor (dB)	0	0	0	3	6	6
Number of taps	1	9	14	18	18	18
Number of clusters	1	2	2	3	4	6

B. Modulation and Coding Scheme (MCS)

Modulation and Coding Scheme (MCS) plays a pivotal role in determining the data rate and reliability of wireless transmission. Modulation is the process of varying a carrier signal to transmit data. Coding Schemes are essential for error detection and correction. Wi-Fi 7 employs advanced modulation techniques to enhance throughput. Key among these techniques is 4096-QAM (Quadrature Amplitude Modulation). The higher the modulation order, the more data can be transmitted, but this also requires a stronger and more stable signal. MCS 0 to 3 are used to test packet error rates between different models. Table III describes the modulation type and code rate for each MCS [8].

III. MODULATION TYPE AND CODING RATE FOR EACH MCS

MCS	Modulation	Coding Rate
0	Binary phase-shift keying (BPSK)	1/2
1	Quadrature phase-shift keying (QPSK)	1/2
2		3/4
3	16-point quadrature amplitude modulation (16-QAM)	1/2
4		3/4
5	64-QAM	2/3
6		3/4
7		5/6
8	256-QAM	3/4
9		5/6
10	1024-QAM	3/4
11		5/6
12	4096-QAM	3/4
13		5/6
15	Binary phase-shift keying-Dual carrier modulation (BPSK-DCM)	½

C. Multiple-Input, Multiple-Output (MIMO)

The MIMO technology uses multiple transmitting and receiving antennas to improve communication performance. A 4x4 MIMO configuration includes two transmitting and two receiving antennas, which can enhance signal quality through spatial diversity and increase data rate via spatial multiplexing [9]. The MIMO systems take advantage of the independent paths between antennas to mitigate the effects of fading and interference, resulting in enhanced SNR and lower PER.

III. PERFORMANCE ANALYSIS

There are six delay profile models in Wi-Fi 7. These are models A, B, C, D, E, and F. Fig. 1. describes the screenshot packet error rate plot for model A with 4x4 MIMO in this simulation result.

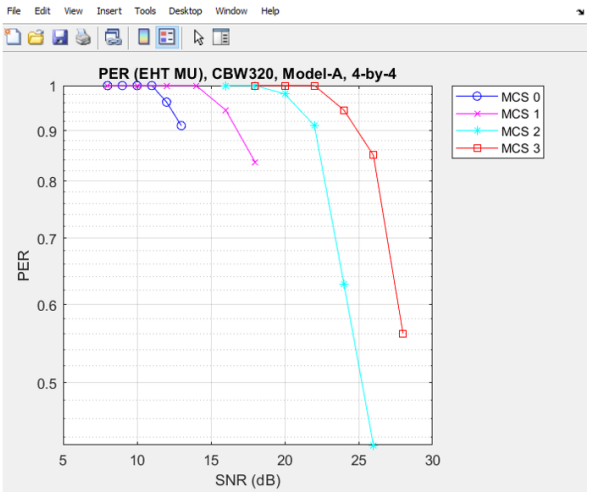

Fig. 1. PER plot for Model A with 4x4 MIMO

The packet error rates are 1, 0.96226, and 0.91071 at MCS 0, and at the SNRs of 8, 9, 10, 11, 12, and 13 after completing 51, 53, and 56 packets. For MCS 1, the packet error rates are 1, 0.94444, and 0.83607 at the SNRs of 8, 10, 12, 14, 16, and 18 after completing 51, 54, and 61. After completing 51, 52, 56, 81, and 118, the packet error rates are 1, 0.98077, 0.91071, 0.62963, and 0.4322 at the SNRs of 16, 18, 20, 22, 24, and 26 for MCS 2. After completing 51, 54, 60, and 91 packets, the packet error rates are 1, 0.94444, 0.085, and 0,56044 at MCS 3 and at the SNRs of 18, 20, 22, 24, 26, and 28 for Model A.

Fig. 2. represents the simulation result of PER (packet error rate) for model B with channel bandwidth (CBW) 320 MHz, MCS (modulation and coding scheme) 0 to 3, and 4x4 MIMO.

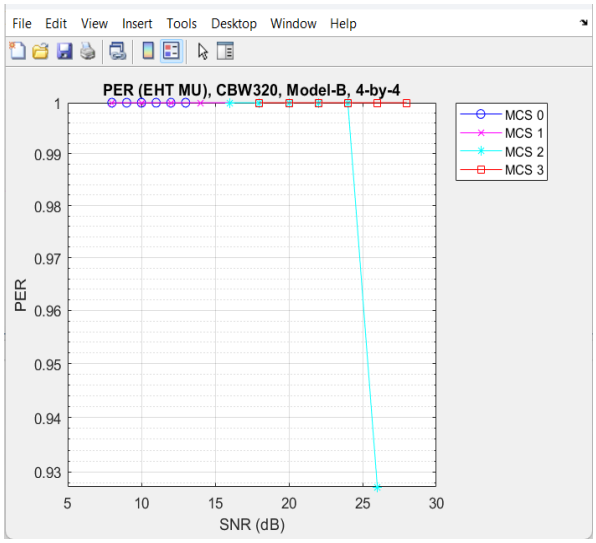

Fig. 2. PER plot for Model B with 4x4 MIMO

The packet error rate is 1 at MCS 0, and at the SNRs of 8, 9, 10, 11, 12, and 13 after completing 51 packets. For MCS 1, the packet error rate is 1 at the SNRs of 8, 10, 12, 14, 16, and 18 after completing 51 packets. After completing 51 and 55, the packet error rates are 1 and 0.92727 at the SNRs of 16, 18, 20, 22, 24, and 26 for MCS 2. After completing 51 packets, the packet error rate is 1 at MCS 3 and at the SNRs of 18, 20, 22, 24, 26, and 28 for Model B.

Fig. 3. illustrates the outcome of PER (packet error rate) for model C with 4x4 MIMO, channel bandwidth 320 MHz, and MCS 0 to 3. The PER of an EHT MU packet is one for MCS 0 to 3 and a SNR of 8 to 28.

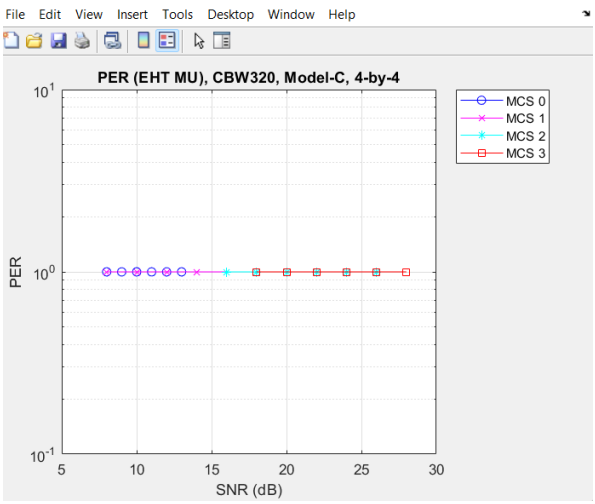

Fig. 3. PER plot for Model C with 4x4 MIMO

The packet error rate is 1 at MCS 0, and at the SNRs of 8, 9, 10, 11, 12, and 13 after completing 51 packets. For MCS 1, the packet error rate is 1 at the SNRs of 8, 10, 12, 14, 16, and 18 after completing 51 packets. After completing 51, the packet error rate is 1 at the SNRs of 16, 18, 20, 22, 24, and 26 for MCS 2. After completing 51 packets, the packet error rate is 1 at the SNRs of 18, 20, 22, 24, 26, and 28 for Model C.

Fig. 4. demonstrates the PER (packet error rate) plot for delay profile model D with 4x4 MIMO, channel bandwidth (CBW) 320 MHz, and MCS (modulation and coding scheme) 0 to 3.

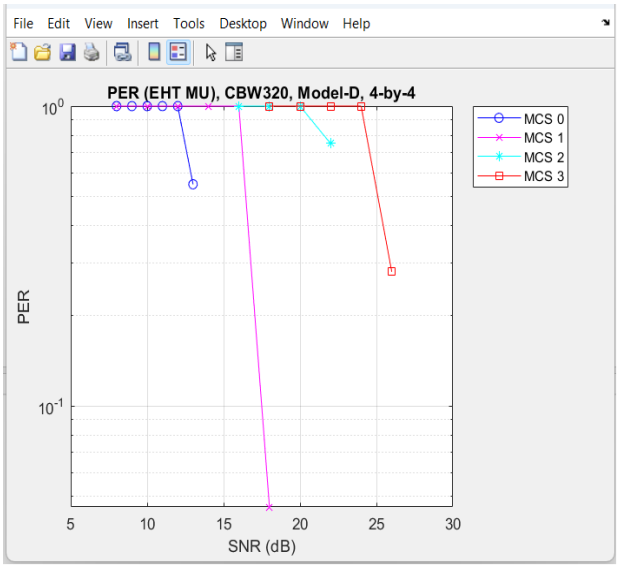

Fig. 4. PER plot for Model D with 4x4 MIMO

The packet error rates are 1 and 0.54839 at MCS 0, and at the SNRs of 8, 9, 10, 11, 12, and 13 after completing 51 and 93 packets. For MCS 1, the packet error rates are 1 and 0.046 at the SNRs of 8, 10, 12, 14, 16, and 18 after completing 51 and 500 packets. After completing 51, 68, and 500 packets, the packet error rates are 1, 0.75, and 0 at the SNRs of 16, 18, 20, 22, 24, and 26 for MCS 2. After completing 51, 182, and 500 packets, the packet error rates are 1, 0.28022, and 0 at MCS 3 and at the SNRs of 18, 20, 22, 24, 26, and 28 for Model D.

Fig. 5. represents the PER (packet error rate) plot for model E with 4x4 MIMO, channel bandwidth (CBW) of 320 MHz, a SNR of 8 to 28, and the scheme for modulation and coding (MCS) of 0 to 3.

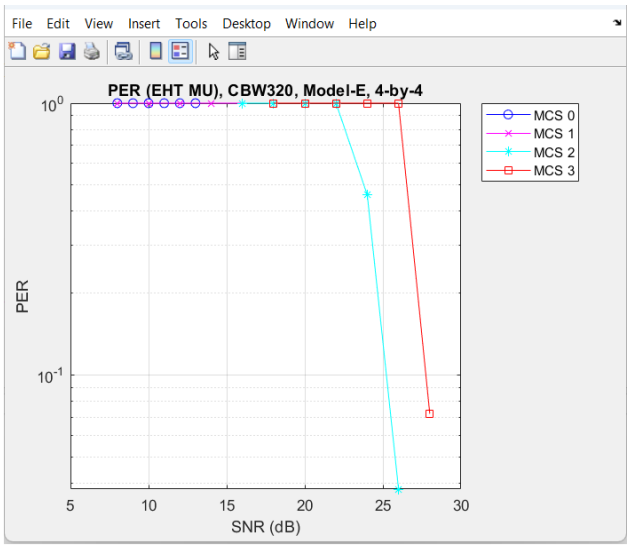

Fig. 5. PER plot for Model E with 4x4 MIMO

The packet error rate is 1 at MCS 0, and at the SNRs of 8, 9, 10, 11, 12, and 13 after completing 51 packets. For MCS 1, the packet error rate is 1 at the SNRs of 8, 10, 12, 14, 16, and 18 after completing 51 packets. After completing 51, 111, and 500 packets, the packet error rates are 1, 0.45946, and 0.038 at the SNRs of 16, 18, 20, 22, 24, and 26 for MCS 2. After completing 51 and 500 packets, the packet error rates are 1 and 0.072 at MCS 3 and at the SNRs of 18, 20, 22, 24, 26, and 28 for Model E.

Fig. 6. illustrates the PER plot for model F utilizing a 4x4 multiple-input multiple-output (MIMO) configuration, a channel bandwidth (CBW) of 320 MHz, an SNR of 8 to 28, and an MCS from 0 to 3. As the SNR value increases, the PER value decreases, leading to an enhancement in system performance.

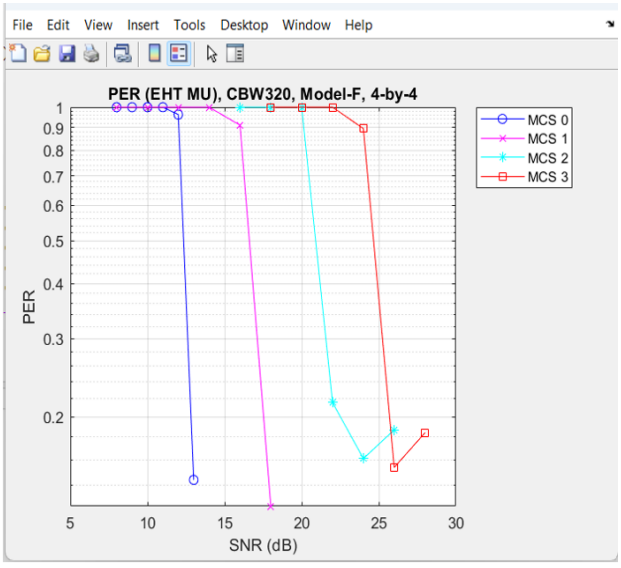

Fig. 6. PER plot for Model F with 4x4 MIMO

The packet error rates are 1, 0.96226, and 0.14407 at MCS 0, and at the SNRs of 8, 9, 10, 11, 12, and 13 after completing 51, 53, and 354 packets. For MCS 1, the packet error rates are 1, 0.91071, and 0.12562 at the SNRs of 8, 10, 12, 14, 16, and 18 after completing 51, 56, and 406 packets. After completing 51, 237, 317, and 273 packets, the packet

error rates are 1, 0.21519, 0.16088, and 0.18681 at the SNRs of 16, 18, 20, 22, 24, and 26 for MCS 2. After completing 51, 57, 332, and 277 packets, the packet error rates are 1, 0.89474, 0.15361, and 0.18412 at MCS 3 and at the SNRs of 18, 20, 22, 24, 26, and 28 for Model F.

IV. PERFORMANCE COMPARISON OF SIX MODELS FOR MCS 0

PER	Models						SNR
	A	B	C	D	E	F	
	1	1	1	1	1	1	8
	1	1	1	1	1	1	9
	1	1	1	1	1	1	10
	1	1	1	1	1	1	11
	0.96	1	1	1	1	0.96	12
	0.91	1	1	0.55	1	0.14	13

Table IV presents the performance analysis comparison of the six models (models A, B, C, D, E, and F) for MCS 0 at the SNR range of 8:1:13. The PER of all models is 1 at the SNRs of 8, 9, 10, and 11 for MCS 0. At the SNR of 12, the PER of models B, C, D, and E is 1, and the PER of models A and F is 0.96. At the SNR of 13, the PER of models B, C, and E is 1, and the PERs of models A and D are 0.91 and 0.55, but the PER of model F is 0.14 for MCS 0. When the PER is one, the performance is not good. The PER is closer to zero, and the performance is better. If the PER is zero, the performance is the best. So, the performance of model F is better than that of the other models for MCS 0.

V. PERFORMANCE COMPARISON OF SIX MODELS FOR MCS 1

PER	Models						SNR
	A	B	C	D	E	F	
	1	1	1	1	1	1	8
	1	1	1	1	1	1	10
	1	1	1	1	1	1	12
	1	1	1	1	1	1	14
	0.94	1	1	1	1	0.91	16
	0.84	1	1	0.05	1	0.13	18

Table V presents the performance analysis comparison of the six models (models A, B, C, D, E, and F) for MCS 1 at the SNR range of 8:2:18. The PER of all models is 1 at the SNRs of 8, 10, 12, and 14 for MCS 1. At the SNR of 16, the PER of models B, C, D, and E is 1, and the PERs of models A and F are 0.94 and 0.91. At the SNR of 18, the PER of models B, C, and E is 1, and the PERs of models A and F are 0.84 and 0.13, but the PER of model D is 0.05 for MCS 1.Therefore, the performance of model D is better than that of the other models for MCS 1.

VI. PERFORMANCE COMPARISON OF SIX MODELS FOR MCS 2

PER	Models						SNR
	A	B	C	D	E	F	
	1	1	1	1	1	1	16
	1	1	1	1	1	1	18
	0.98	1	1	1	1	1	20
	0.91	1	1	0.75	1	0.22	22
	0.63	1	1	0	0.46	0.16	24
	0.43	0.93	1	0	0.04	0.19	26

Table VI describes the performance analysis comparison of the six models (models A, B, C, D, E, and F) for MCS 2 at the SNR range of 16:2:26. The PER of all models is closer to 1 at the SNRs of 16, 18, and 20 for MCS 2. At the SNR of 22, the PER of models A, B, C, and E is closer to 1, and the PERs of models D and F are 0.75 and 0.22. At the SNR of 24, the PER of models B and C is 1, and the PERs of models A, E, and F are closer to zero, but the PER of model D is 0 for MCS 2. At the SNR of 26, the PERs of models B and C are closer to 1, and the PERs of models A, E, and F are closer to zero, but the PER of model D is 0 for MCS 2. Therefore, the performance of model D is better than that of the other models for MCS 2.

VII. PERFORMANCE COMPARISON OF SIX MODELS FOR MCS 3

PER	Models						SNR
	A	B	C	D	E	F	
	1	1	1	1	1	1	18
	1	1	1	1	1	1	20
	1	1	1	1	1	1	22
	0.94	1	1	1	1	0.89	24
	0.85	1	1	0.28	1	0.15	26
	0.56	1	1	0	0.07	0.18	28

Table VII describes the performance analysis comparison of the six models (models A, B, C, D, E, and F) for MCS 3 at the SNR range of 18:2:28. The PER of all models is 1 at the SNRs of 18, 20, and 22 for MCS 3. The PER of all models is closer to 1 at the SNR of 24 for MCS 3. At the SNR of 26, the PER of models B, C, and E is 1, and the PER of model A is closer to 1, but the PERs of models D and F are closer to 0. At the SNR of 28, the PERs of models A, B, and C are closer to 1, and the PERs of models E, and F are closer to zero, but the PER of model D is 0 for MCS 3. Therefore, the performance of model D is better than that of the other models for MCS 3.

IV. CONCLUSION

In this study, the performance of PER is analyzed with MIMO using delay profile models A, B, C, D, E, and F in Wi-Fi 7. The error rate of the packet is an essential metric that evaluates the reliability and quality of data transmission in communication systems. The number of packets tested at each SNR point is determined by the maximum allowable packet errors and the maximum packet parameters. The PER is used to measure the performance of wired and wireless systems. Packets are transmitted using 4x4 multiple-input multiple-output (MIMO). The communication quality improved as the SNR increased and the PER decreased. A high packet error rate can significantly impact the performance of a Wi-Fi network.

The higher PER leads to retransmissions and delays in data transmission, affecting the overall throughput and user experience. A Wi-Fi network performs poorly when the PER is one. So, the performance is not good when the PER is one. The optimal performance is achieved when the PER is zero, with the network performing better as the PER approaches zero. If the PER is zero, the performance is the best. At MCS 0, the performance of model F is better than that of the other models. At MCS 1 to 3, the performance of model D is better than that of the other models. So, the performance of delay profile model D is the best, according to the overall simulation result.

ACKNOWLEDGMENT

The author wishes to extend heartfelt thanks to Dr. Pa Pa Winn San, Professor and Head of the Department of Electronic Engineering at Technological University (Mandalay), for her kindness and encouragement. Special appreciation goes to Daw Htet Htet Aung, Associate Professor in the same department, for her exceptional supervision, kindness, friendliness, encouragement, patient guidance, invaluable advice, and continuous support throughout the research. Deep gratitude is also expressed to Dr. Yin Hnin Thet Htun, Associate Professor in the Department of Electronic Engineering, for her patience and guidance. Lastly, the author sincerely thanks all of the

teachers from the Department of Electronic Engineering at Technological University (Mandalay) and expresses deep gratitude to her parents for their support in completing this research.

REFERENCES

[1] G. Bianchi, *''Performance analysis of the IEEE 802.11 distributed coordination function,''* IEEE J. Sel. Areas Commun., Mar. 2000.

[2] S. Vermani, A. Chen, B. Tian, and Y. Kim, *"Further Ideas on EHT Preamble Design,"* document IEEE 802.11, Nov. 2019.

[3] Oscar Bejarano and Edward W. Knightly, *"IEEE 802.11ac : From Channelization to Multi-User MIMO,"* October 2013.

[4] Yong Soo Cho, Jaekwon Kim Won Young Yang, Chung-Gu-Kang, *"MIMO-OFDM Wireless Communication with MATLAB,"* John Willey & Sons (Asia) Pte Ltd., Singapore, 2010.

[5] Y. Seok, G. Bajko, J. Yee, J. Liu, and T. Pare, *"EHT Multi-Link Operation, document IEEE 802.11,"* May 2019.

[6] 802.11ax-2021 – *"IEEE Standard for Information Technology--Telecommunications and Information Exchange between Systems Local and Metropolitan Area Networks--Specific Requirements Part 11: Enhancements for High-Efficiency WLAN."* IEEE, May 2021.

[7] D. Lopez-Perez et al. *"IEEE 802.11be Extremely High Throughput: The next generation of Wi-Fi technology beyond 802.11ax,"* in IEEE Communications Magazine, v. 5, n. 9, Sept. 2019.

[8] E. Au, *''IEEE 802.11be: Extremely high throughput [standards],''* IEEE Veh. Technol. Mag., Sep. 2019.

[9] Z. Li, H. Fang, H. Wang, and M. Daneshmand, *''A data-centric cognitive gateway with distributed MIMO for future smart homes,''* IEEE Wireless Commun., Jun. 2019.

State of Charge Prediction for Lithium-ion Battery in Electric Vehicles using Feed Forward Neural Network

Thandar Aung[1], Yin Hnin Thet Htun[2], Hnin Yu Wai[3]

[1]*Department of Electronic Engineering, Technological University (Mandalay)*

[2]*Department of Electronic Engineering, Technological University (Mandalay)*

[3]*Department of Electronic Engineering, Technological University (Mandalay)*

Email: [1]thandar.aung.831991@gmail.com, [2]yinhninthettun@gmail.com, [3]powerlay@gmail.com

***Abstract*—This paper researches into the prediction of state of charge for lithium-ion batteries in electric vehicles utilizing a Feed Forward Neural Network. State of charge (SoC) serves as a crucial parameter, particularly in electric vehicles, necessitating determination by the battery management system. As SoC remains unmeasured, it is inferred from other measured quantities such as discharge current and battery terminal voltage. The primary objective is to show the mathematical relationship between the input and output parameters of the battery through simulation using MATLAB. Additionally, the paper proposes a design for a Feed Forward Neural Network (FFNN) based SoC observer for lithium-ion batteries, aimed at ensuring safe and reliable battery operations by preventing overcharging or over-discharging. Finally, the dataset demonstrates favorable outcomes, with both training and test errors yielding satisfactory results. The development of the Levenberg Marquardt algorithm in this situation marks significant progress in SoC estimation.**

Keywords – Battery Management System, Electric Vehicle, Feed Forward Neural Network, Lithium-Ion Battery, MATLAB, State of Charge

I. INTRODUCTION

BMS are employed across various applications including microgrids, portable electronics, telecommunications, and EVs. The BMS is an electronic system that manages and controls different battery parameters such as state of charge, state of health, depth of discharge, and more. Batteries are the primary power source for electric vehicles [1]. Various types of batteries include Ni-MH, Li-ion, and lead-acid batteries. Li-ion batteries are commonly used in energy storage systems due to their high energy density, high specific cell voltage, and low cost [6].

SoC represents the percentage of the battery's rated capacity that remains, providing a snapshot of the battery's current capacity. Precise SoC estimation is crucial for the BMS to manage energy efficiently and ensure the safe charging and discharging of EV batteries [4]. Various methods for calculating SoC include the Ampere-hour integral method, internal resistance method, Artificial Neural Network, Kalman Filtering method, and discharge experimental method and so on.

This paper presents an artificial neural network algorithm designed to enhance the accuracy of SoC estimation in batteries by improving the FFNN's design and performance [5]. This method has been applied to estimate the SoC of a battery pack during a drive cycle, and a comparison has been made between the training data and test data of SoC using FFNN.

II. FEED FORWARD NEURAL NETWORK ESTIMATOR THEORY

Neural networks are categorized into various types, each serving different purposes. The most common types include Feedforward Neural Networks (FFNN), Convolutional Neural Networks (CNNs), and Recurrent Neural Networks (RNNs) [3]. Artificial Neural Networks (ANNs) are universal approximators capable of modeling any nonlinear function with precision. ANNs are structured as either single-layer or multi-layer networks and are composed of numerous parallel nonlinear artificial neurons. Among the most widely used networks with reliable performance predictions is the feedforward neural network [8]. This basic type of neural network processes input in a single direction without loops, consisting of an input layer, one or more hidden layers, and an output layer. The feedforward neural network is easy to implement and capable of handling a variety of functions, offering precise estimation and straightforward implementation without requiring complex equivalent circuit battery models for SoC estimation [2].

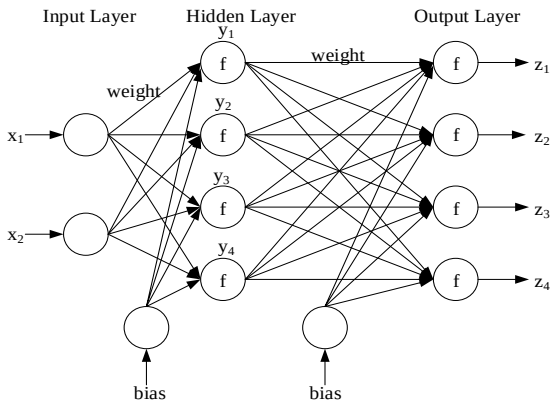

Fig. 1. A multi-layer feed forward neural network [5]

A multi-layer feedforward neural network in Fig.1 is a type of artificial neural network where the connections between the nodes do not form a cycle. It consists of an input layer, hidden layers, and an output layer. Input Layer consists of nodes that represent the input features. Each node in this layer corresponds to one input feature from the dataset. Hidden Layers are between the input and output layers. Each hidden layer consists of nodes that process the inputs from the previous layer and pass the output to the next layer. The number of hidden layers and the number of

neurons in each hidden layer can vary depending on the complexity of the problem. Output Layer consists of nodes that produce the final output of the network. The number of neurons in the output layer depends on the type of problem [6]. Weights and Biases are connecting between the nodes of different layers have weights associated with them. Each neuron also has an associated bias. The weights and biases are adjusted during the training process to minimize the error in the output. Each neuron (except those in the input layer) applies an activation function to its input to introduce non-linearity into the model [5].

At each neuron in the hidden layer and output layer, the processing operation is performed through the activation function. Additionally, in the proposed neural network, the activation functions in both layers are piecewise functions, as described in (1) [7].

$$a = f(z_k) = \begin{cases} 0, & \text{if } z_k < x_{min} \\ wx + b, & \text{if } x_{min} \le z_k \le x_{max} \\ 1, & \text{if } z_k > x_{max} \end{cases} \quad (1)$$

where,

x_{min}, x_{max} = input layer values

w = weight of neural network

b = bias in hidden layer and output layer

z_k = output layer value

a = output values

Piecewise linear is calculated using a range of numbers required for the particular equation, anything less than the range is 0, and anything greater is 1. Between 0 and 1, the signals going from one layer to the next are linearly-interpolated [5]. A node in a hidden layer receives inputs from all the nodes in the previous layer, processes these inputs, and then passes the output to the nodes in the subsequent layer in Fig.2. Each node in a hidden layer receives inputs from all nodes in the previous layer [9]. Each input is multiplied by a corresponding weight. The weighted inputs are summed together along with a bias term [8]. The summed value is passed through an activation function to introduce non-linearity. The result of the activation function is the output of the hidden layer node, which is passed to the nodes in the next layer in Fig.2.

The following equations define the mathematical relationship for the hidden layer or output of the FFNN [3] and [8]:

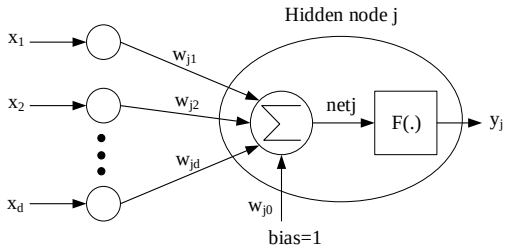

Fig. 2. Hidden Layer Node

$$netj = x_1 w_{j1} + x_2 w_{j2} + ... + x_d w_{jd} + w_{j0} \quad (2)$$

$$netj = \sum_{i=1}^{d} x_d w_{jd} + w_{j0} \quad (3)$$

$$netj = \sum_{i=0}^{d} x_d w_{jd} = w_j^T x \quad (4)$$

$$\text{where, } w_j = \begin{bmatrix} w_{j1} \\ w_{j2} \\ : \\ . \\ w_{jd} \\ w_{j0} \end{bmatrix}, x = \begin{bmatrix} x_1 \\ x_2 \\ : \\ . \\ x_d \\ 1 \end{bmatrix} \quad (5)$$

$$\therefore y_j = f(netj) \quad (6)$$

Where, x_d = the output at the previous layer

w_{id} = the weight of the previous layer to the present layer

w_{j0} = the bias

netj = hidden node j

III. Training and Testing Data

The training algorithm is built on a five-step approach, which is clearly shown in the flowchart in Fig.3.

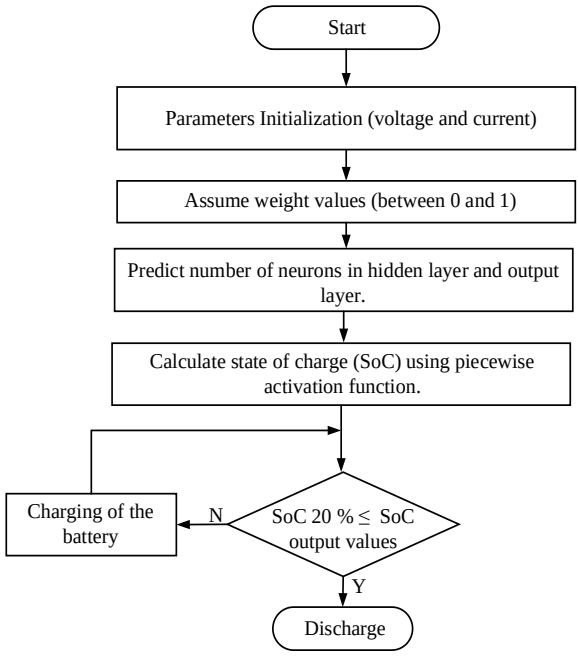

Fig. 3. Flowchart of SoC estimation using FFNN

A. Training Data for Voltage and Current

Firstly, the input current and voltage data are set and considered how much neurons are used in the hidden layer to get accurate output results. And then, calculated the output results with FFNN estimator theory. In the hidden and output layers, the processing operation at each neuron is carried out using the Piecewise Linear (PL) activation function. Both current weight and voltage weight of the hidden layer set the same values because current data and voltage data are trained in neural network tool box (nntool) in MATLAB software to calculate MSE values using Levenberg Marquardt algorithm and predict accurancy and their performance.

In Fig.4, desires the initial current value is 180AH, the percentage of battery state is 100%. Weight value is set to random values between 0 and 1 and bias value is set to constant value 1. Calculating for one output value result and the other output is similar to calculate in this algorithm.

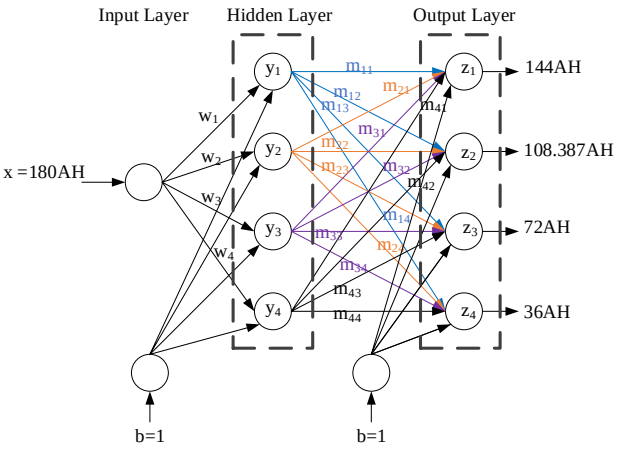

Fig. 4. A Diagram of Multi-Layer FFNN for current

Input values, x_{max} = 180AH, x_{min} = 36AH

Desired Weight values, w = 0.2, 0.4, 0.6, 0.8 (SoC % is differed 20% in CC method)

Hidden layer, y = (wx + b) (7)

y = (0.2×180) +1 = 37

Output layer, z = f(my + b) (8)

z = [(0.99×37) + (0.35×73) + (0.35×109) + (0.3×145) + 1]

z = 144 AH

Using piecewise activation function,

$x_{min} < z < x_{min}$ = 37 < 144 < 180 (9)

Therefore, the algorithm is continued running before less than x_{min}. Table I is current dataset based on FFNN theory use in (7),(8) and (9) to get 144.83, 108.387, 71.56 and 36.019 current output values.

I. CURRENT TRAINING DATASET

Input Data, x (AH)	Weight, w	Bias, b	Hidden Layer, y (AH)	Weight, m	Bias, b	Output Result, z (AH)
180	0.2	1	36	0.99	1	144.83
180	0.2	1	36	0.35	1	144.83
180	0.2	1	36	0.35	1	144.83
180	0.2	1	36	0.3	1	144.83
180	0.4	1	73	0.001	1	108.387
180	0.4	1	73	0.7	1	108.387
180	0.4	1	73	0.25	1	108.387
180	0.4	1	73	0.2	1	108.387
180	0.6	1	109	0.001	1	71.56
180	0.6	1	109	0.001	1	71.56
180	0.6	1	109	0.5	1	71.56
180	0.6	1	109	0.11	1	71.56
180	0.8	1	145	0.001	1	36.019
180	0.8	1	145	0.001	1	36.019
180	0.8	1	145	0.001	1	36.019
180	0.8	1	145	0.24	1	36.019

In Fig.5, desires the initial voltage value is 356V, the percentage of battery state is 100%. Weight value is set to random values between 0 and 1 and bias value is set to constant value 1. Calculating for one output value result and the other output is similar to calculate in this algorithm.

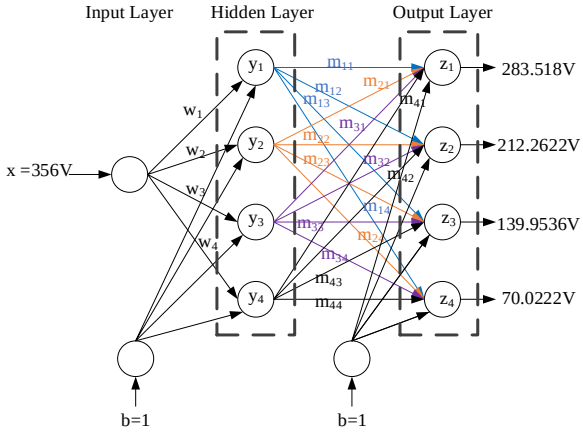

Fig. 5. A Diagram of Multi-Layer FFNN for voltage

Input values, x_{max} = 356V, x_{min} = 71V

Desired Weight values, w = 0.2, 0.4, 0.6, 0.8 (SoC % is differed 20% in CC method)

Hidden layer, y = (wx + b) (10)

y = (0.2×356) +1 = 72.2

Output layer, z = f(my + b) (11)

z = [(0.99×72.2) + (0.35×143.4) + (0.35×214.6) + (0.3×285.8) + 1]

z = 283.518V

Using piecewise activation function,

$x_{min} < z < x_{min}$ = 71 < 283.518 < 356 (12)

Therefore, the algorithm is continued running before less than x_{min}. Table II is voltage dataset based on FFNN theory in use (10), (11) and (12) to get 283.518, 212.2622, 139.9536 and 70.0222 voltage output values.

II. VOLTAGE TRAINING DATASET

Input Data, x (V)	Weight, w	Bias, b	Hidden Layer, y (V)	Weight, m	Bias, b	Output Result, z (V)
356	0.2	1	72.2	0.99	1	283.518
356	0.2	1	72.2	0.35	1	283.518
356	0.2	1	72.2	0.35	1	283.518
356	0.2	1	72.2	0.3	1	283.518
356	0.4	1	143.4	0.001	1	212.2622
356	0.4	1	143.4	0.7	1	212.2622
356	0.4	1	143.4	0.25	1	212.2622
356	0.4	1	143.4	0.2	1	212.2622
356	0.6	1	214.6	0.001	1	139.9536
356	0.6	1	214.6	0.001	1	139.9536
356	0.6	1	214.6	0.5	1	139.9536
356	0.6	1	214.6	0.11	1	139.9536
356	0.8	1	285.8	0.001	1	70.0222
356	0.8	1	285.8	0.001	1	70.0222
356	0.8	1	285.8	0.001	1	70.0222
356	0.8	1	285.8	0.24	1	70.0222

B. *Testing Data for Voltage and Current*

Firstly, taken voltage and current data values from Table I and Table II, written script in nntool box of the MATLAB software. The second is set input vector and target error, chosen number of neurons for hidden layer and output layer, and selected Levenberg-Marquardt algorithm in the nntool box to calculate mean square error for training and testing performance. To prevent under-fitting, the neural network was trained to achieve a reasonable MSE suitable for simulating the battery's dynamics. Depending on the actual application, it is advisable to maintain the battery SoC within a safe operating range, typically 20% to 90% for lithium-ion batteries [10]. The training data determines the biases and net weights using the Levenberg-Marquardt algorithm. Processing occurs at each neuron in both the hidden and output layers via the Piecewise Linear activation function. The primary function of FFNN fitting tools in MATLAB is to fit a nonlinear function between the input and output data [7]. While the architecture is customized, a typical design consists of three layers: input, hidden, and output layers. This architecture is depicted in Fig.6.

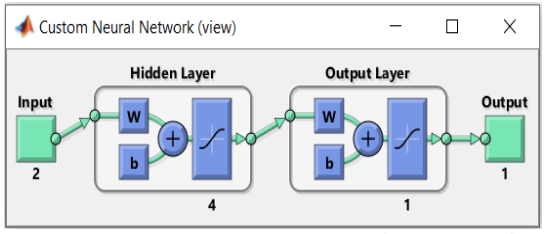

Fig. 6. Training and testing data set in nntool of MATLAB software

IV. Result and Discussion

In Fig.7 shows the training and testing data result for current and voltage using nntool box of MATLAB software. In figure, the blue line is training data, the red line is testing data and the green line is validation. The blue line and the red line results are synchronized in Fig.7(a) and (b). Therefore, the training and testing results are best performance.

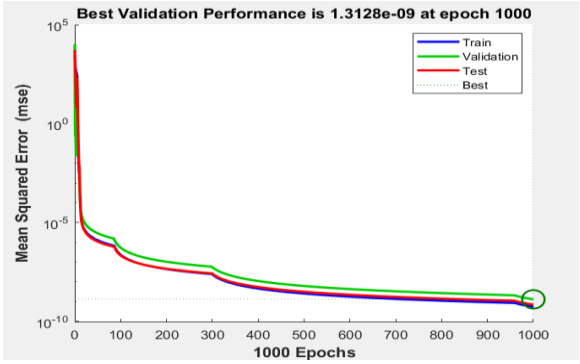

(a)

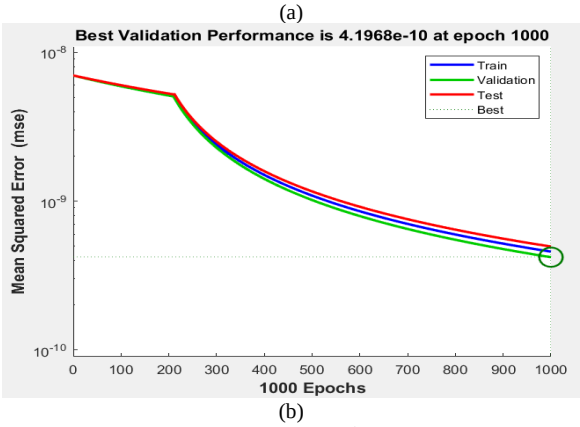

(b)

Fig. 7. (a) Training and testing data result for current using nntool box, (b) Training and testing data result for voltage using nntool box

Fig.8(a) and (b) represent the comparison of data and fit line of the voltage and current training datasets. For the best performance and accuracy, combination of validation and test results are the same as training result. The good performance of MSE is greater than 0.8 and the best is 1. In Fig.8(a) and (b), the training result and all result are the same. The mean square error value is 1. Therefore, the training and testing results are best performance and the accuracy is 100%.

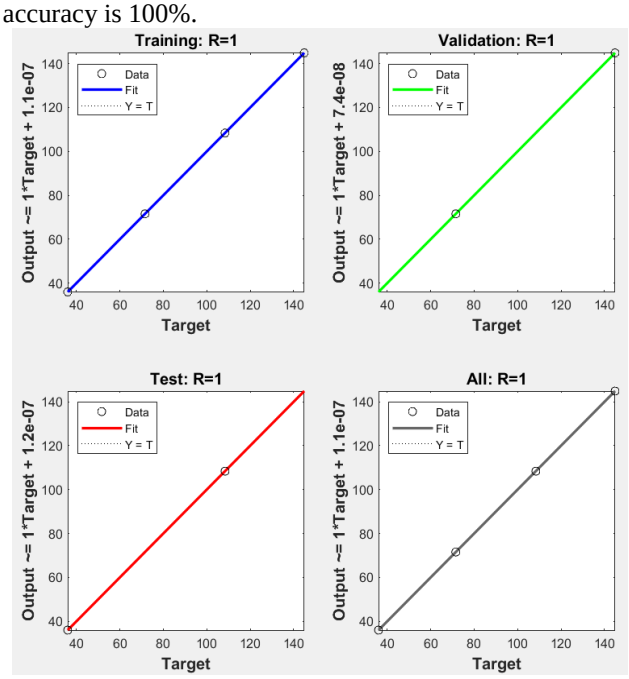

(a)

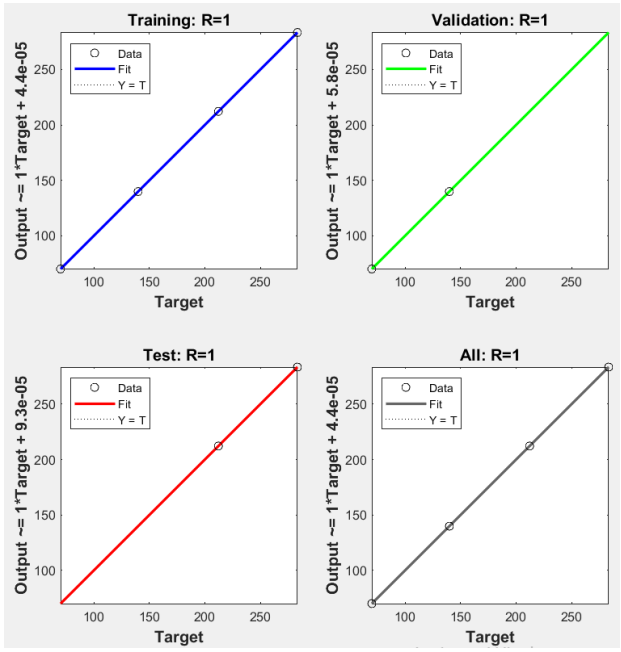

(b)

Fig. 8. (a) Comparison of MSE values and accurancy for current, (b) Comparison of MSE values and accurancy for voltage using nntool box

Fig.9(a) illustrates the State of Charge Estimation Curve, showing how voltage (V) and current (AH) vary over time during a 5-hour usage period. The voltage and current both exhibit a step-wise decline, dropping significantly at the end of each hour. The state of charge decreases by 20% after each hour of usage. By the end of the 5-hour period, both voltage and current have decreased significantly from their initial values. In Fig.9(b) shows the relationship between voltage (V) and time (hours) for two different current

capacities: 36AH (green curve) and 18AH (blue curve). The duration of the steady voltage phase is proportional to the capacity of the battery. The 36AH battery maintains its voltage for 5 hours, while the 18AH battery maintains its voltage for 10 hours.

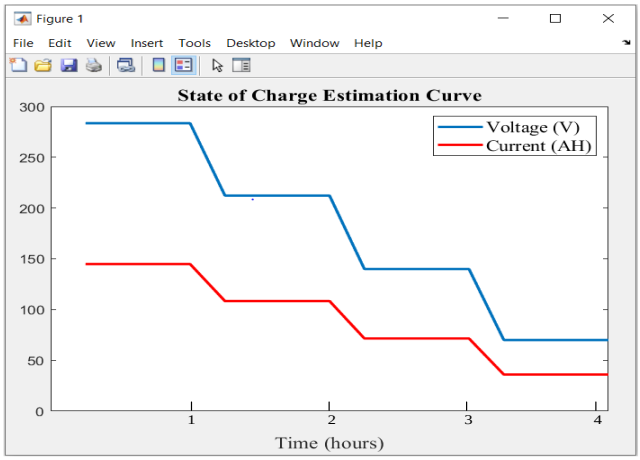

(a)

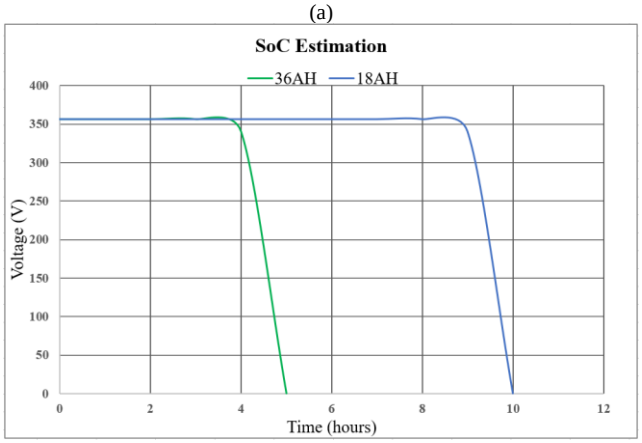

(b)

Fig. 9. (a) SoC result curve using nntool box, (b) State of charge (SoC) estimation for 36AH and 18AH batteries

V. Conclusion

In this paper, a state of charge estimation method for lithium-ion batteries is developed using a Feed Forward Neural Network. As part of a data-driven learning machine approach, the FFNN offers precise estimation and simple implementation without the need for complex Equivalent Circuit battery models, unlike other SoC estimation methods. Using MATLAB's Neural Network Toolbox (nntool) to design the FFNN and defining the architecture:input layer, hidden layers and output layer. Selecting Levenberg-Marquardt algorithm and training the network using the voltage and current training datasets, adjusting weights and biases to minimize the error between the predicted and actual SoC. Evaluating the performance on the test set to ensure the model's accuracy. The good performance of MSE is greater than 0.8 and the best is 1. In Fig.8(a) and (b), the training result and all result are the same. The mean square error value is 1. Therefore, the training and testing results are best performance and the accuracy is 100%.

FFNNs model the nonlinear relationship between voltage, current, SoC and provide high accuracy in SoC estimation. Once trained, the FFNN quickly process inputs to provide real-time SoC estimates. It allows for the accurate, real-time monitoring of battery SoC, improving the efficiency and safety of battery-powered systems. Proper data preprocessing, network design, and training are crucial steps to ensure the model's performance and reliability.

Acknowledgment

I am deeply grateful to my supervisor Dr. Yin Hnin Thet Htun for her solid support, insightful feedback, and continuous encouragement throughout this paper. I extend my heartfelt thanks to Dr. Pa Pa Winn San for her support and encouragement. I am also grateful for Dr. Hnin Yu Wai's commitment to excellence and their willingness to share their knowledge and insights. Moreover, I desire to express my classmates for their collaboration and support. Lastly, I would love to express my family for everything you've done and continue to do for me.

References

[1] CHENG C, RUI X, SHEN W. 2018 "A lithium-ion battery-in-the-loop approach to test for state of charge and capacity estimation".

[2] Vidal C, Malysz P, Kollmeyer P, et al. 2020 "Machine Learning Applied to Electrified Vehicle Battery State of Charge and State of Health Estimation".

[3] Cheddadi Youssef, Diouri Omar, Gaga Ahmed, Errahimi Fatima, Es-Sbai Najia. 2017 "Design and Simulation of an Accurate Neural Network State-of-Charge Estimator for Lithium Ion Battery Pack".

[4] Yang F, Li W, Li C, et al. 2019 "State-of-charge estimation of lithium-ion batteries based on gated recurrent neural network".

[5] Golam Kabir.2023 "Deep neural network for predicting the state-of-charge of lithium-ion battery in electric vehicles".

[6] MENG J, LUO G, GAO F.2015 "Lithium Polymer Battery State-of-Charge Estimation Based on Adaptive Unscented Kalman Filter and Support Vector Machine".

[7] CHENG C, RUI X, SHEN W. 2018 "A lithium-ion battery-in-the-loop approach to test and validate multi-scale dual H infinity filters for state of charge and capacity estimation".

[8] YUE L, CHATTOPADHYAY P, XIONG S, et al. 2016 "Dynamic data-driven and6 model-based recursive analysis for estimation of battery state-ofcharge".

[9] Fangfang Yang, Weihua Li, Chuan Li, Qiang Miao. 2019 "State-of-charge estimation of lithium-ion batteries based on gated recurrent neural network".

[10] Hannan M A, Lipu M S H, Hussain A, et al. 2018 "Neural Network Approach for Estimating State of Charge of Lithium-ion Battery Using Backtracking Search Algorithm".

Design and Simulation of Water Supply Networks using PLC with PID and SCADA System

Tyie Lynn Aung[1], Nyan Phyo Aung[2], Yin Hnin Thet Htun[3]

[1]*Department of Electronic Engineering, Technological University (Mandalay)*

[2]*Department of Electronic Engineering, Technological University (Mandalay)*

[3]*Department of Electronic Engineering, Technological University (Mandalay)*

Email: [1]tyinlinaung@mail.com, [2]nyanphyoaung@gmail.com, [3]yinhninthethtun@mail.com

***Abstract*— The paper details a comprehensive approach to designing and simulating water supply networks incorporating S7-1500 PLC, WinCC SCADA systems, Siemens PID compact, water level sensor and TIA portal software. Through SCADA technology, the system facilitates real-time monitoring and control of water distribution, while the PID control algorithm manages modulating valves and tank levels to improve performance. The methodology involves system identification, PID controller design, SCADA integration, historical data, simulation, and testing, utilizing software to analyze system behavior for optimal performance and stability. The paper emphasizes the collaboration of PID control and SCADA systems to achieve efficient and reliable water supply networks. Overall, the paper contributes to advancing smart water management systems by providing insights into integrating SCADA and PID control for improved operation and management of water distribution networks.**

Keywords*— *PID, PLC, SCADA, SENSOR, TIA PORTAL

I. Introduction

Water supply networks are pivotal for efficiently delivering clean water to communities and industries. Effective management of these networks is essential to fulfill water demand, minimize losses, and maintain quality standards.

SCADA systems have become indispensable in industries, offering simplified control and monitoring features. This research concentrates on incorporating a control unit into a filling system using SCADA technology to enhance manufacturing processes. By employing microcontrollers and control circuits, the system efficiently handles data exchange with the master station. SCADA applications, driven by advanced technologies and skilled personnel, play a crucial role in modern industrial settings, aiding in technical reengineering endeavors. Initially relying on relay logic, SCADA has progressed to integrate digital electronics, with programmable logic controllers (PLCs) now serving as a pivotal element in industrial control systems, highlighting their continued significance and broad acceptance. [1]

Designing and tuning PID controllers is theoretically simple but faces practical hurdles, especially when striving for multiple goals like swift transient response and strong stability. Consequently, engineers have developed "intelligent" tools to aid in achieving optimal PID control under diverse conditions. This article offers a current examination of PID functionalities and tuning approaches found in patents, software packages, and commercial hardware. Integrating system identification and "intelligent" methods into software-based PID systems streamlines design and tuning, laying the groundwork for future "plug-and-play" PID controllers. These advancements promise heightened productivity, superior quality, and reduced maintenance demands [2].

Technological advancements have enabled the integration of Siemens PLC and WinCC SCADA systems with PID control algorithms, offering a promising avenue to enhance the efficiency and reliability of water supply networks. SCADA systems furnish real-time monitoring, control, and data acquisition capabilities, empowering operators to remotely oversee and manage various components. Meanwhile, PID control regulates system parameters such as tank levels to maintain desired settings and adapt to changing demands or disruptions. [3]

The paper focuses on designing and simulating water supply networks integrated with SCADA systems and PID control to enhance efficiency, reliability, and resilience. It aims to establish a systematic approach for designing and simulating such networks while evaluating systems under different conditions.

II. Implementation Of the System

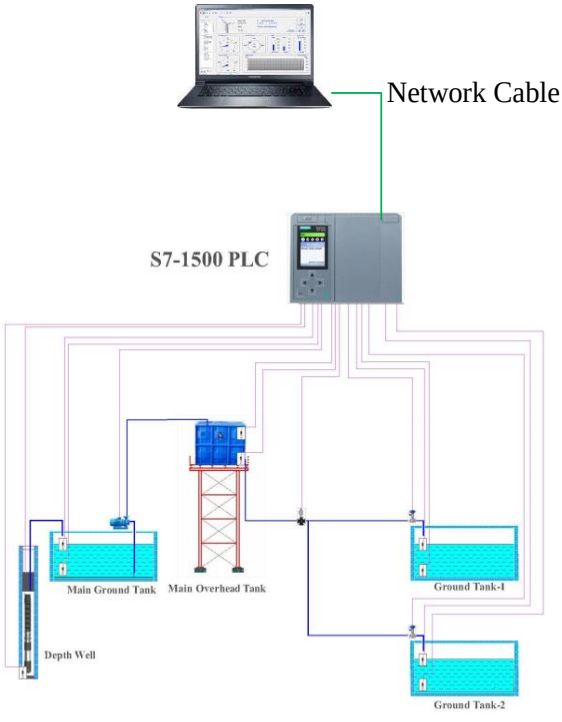

Fig. 1. Schematic diagram of the system

The system configuration, illustrated in Fig. 1, initiates with water extraction from a deep well via a submersible pump, directing it towards the primary ground tank. A booster pump then facilitates the transfer of water to the main overhead tank. Water filling for both tanks relies on upper and lower-level sensors. If water levels drop below a specified threshold, the sensors trigger the filling process, which halts if levels exceed the upper threshold. Modulating valves regulate the distribution between ground tank-1 and ground tank-2 using PID Control, ensuring efficient water distribution.

The system ensures optimal utilization of water resources and maintains stable tank levels. Modulating valves, integrated with PID control, offer significant advantages in water distribution systems. Adjusting valve positions based on real-time feedback enables the system to promptly respond to changes in demand, ensuring precise regulation of water flow. Communication between the PLC and SCADA systems over a local network facilitates the exchange of control information and historical data. The SCADA computer efficiently oversees both monitoring and controlling the entire water supply network.

The installation of a programmable logic controller (PLC) using TIA portal software is highlighted as essential for the water supply network's smooth operation. The specifications of the chosen S7-1500 PLC model, as detailed in Table I highlight its reputation for robust performance and versatility, positioning it as a key element in industrial automation systems. [4]

I. SOME SPECIFICATIONS OF S-7 PLC

No.	S7-1500 PLC	
1.	Product type designation	CPU 1511-1 PN
2.	Firmware version	V2.5
3.	Display	3.45 cm
4.	Power loss	5.7 W
5.	Rated value (DC)	24 V
6.	Central processing unit with working memory	150 KB for program and 1 MB for data
7.	Number of IO modules	1 024; max. number of modules / submodules
8.	RJ 45 (Ethernet)	Yes; 2
9.	IP protocol	Yes; IPv4
10.	PID Compact	Yes; Universal PID controller with integrated optimization
11.	Programming language	LAD, FBD, STL, SCL, GRAPH

Additionally, a laptop computer is employed as the SCADA computer, running TIA V15 software. The operating system is customized for SCADA software requirements, and the SCADA software is configured to establish connections with field devices for real-time data acquisition and control. [5]

The PID control method utilizes Siemens PID compact, and the PID control formula is:

$$y = K_p\left[(b\times(w-x)) + \frac{(w-x)}{T_i\times s} + \frac{(T_d\times s)(c\times(w-x))}{((a\times T_d)(s+1))}\right] \quad (1)$$

Where:

y = Output value of the PID algorithm

K_p = Proportional gain

b = Proportional action weighting

w = Setpoint

x = Process value

T_i = Integral action time

s = Laplace operator

T_d = Derivative action time

a = Derivative delay coefficient

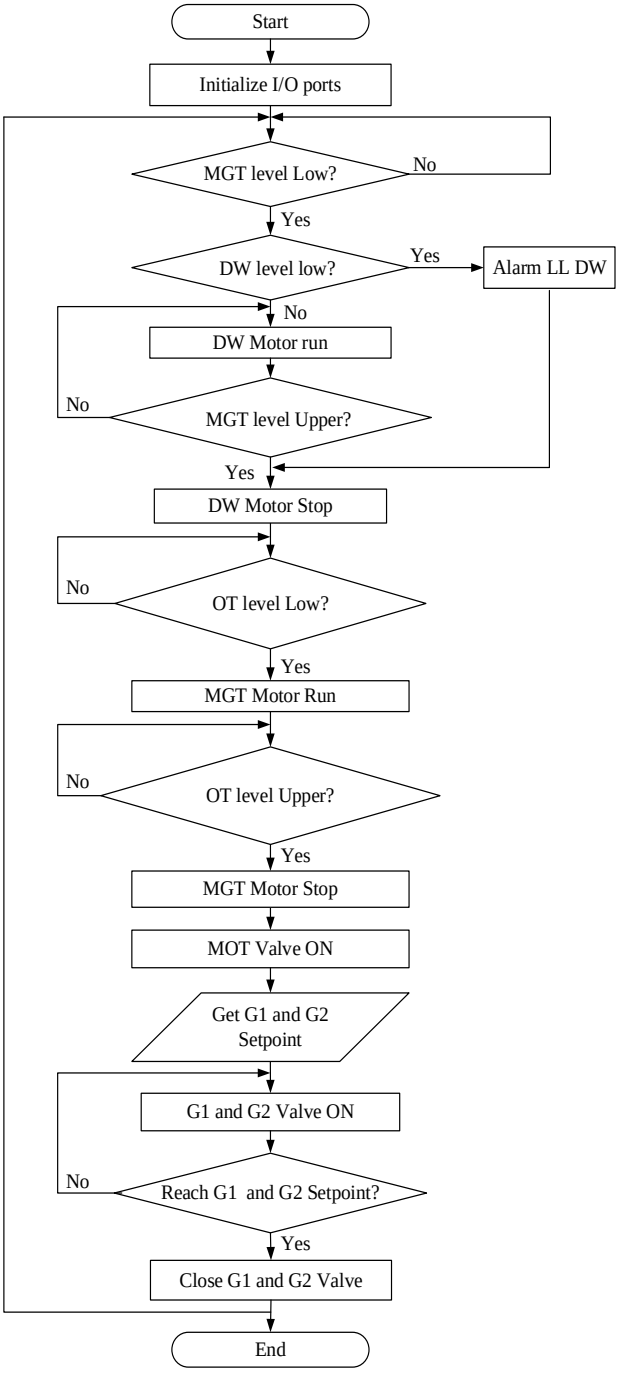

Fig. 2. Flowchart of the system

The system's flowchart, depicted in Fig. 2, serves as a visual representation of the program's structure and logic. It helps in understanding the sequence of operations, decision points, and interactions within the system. This flowchart aids in troubleshooting, as it allows users to identify potential issues and locate specific areas of the program that may require adjustment or improvement. [6]

III. Simulation Results of the System

Fig. 3 illustrates the water distribution screen of the SCADA system. This screen offers a visual depiction of the water distribution process, enabling operators to oversee and regulate the flow of water to various tanks and components within the system. It provides real-time updates on water levels, valve positions, and other pertinent parameters, facilitating efficient management and optimization of water distribution. Using the information on this screen, operators possess the ability to make smart choices to keep the system running smoothly and make the most of available resources.

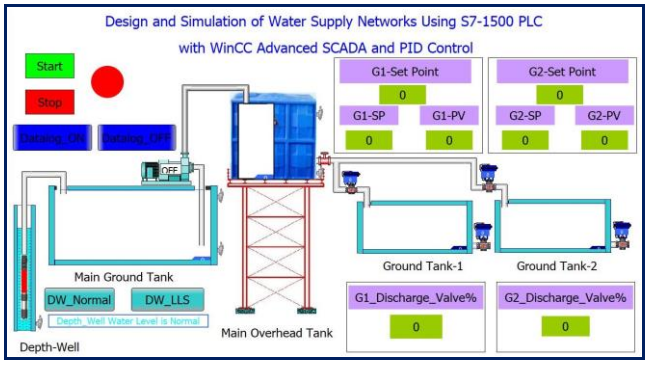

Fig. 3. Water supply networks with WinCC advanced SCADA screen

The operational sequence depicted in Fig. 4 elucidates the interactions among various components within the system. Upon the water level in the main ground tank falling below a predetermined threshold, low-level sensors within the tank are activated, prompting the submersible pump in the deep well to replenish the main ground tank. Once the sensors detect the desired water level, they automatically deactivate the submersible pump in the deep well.

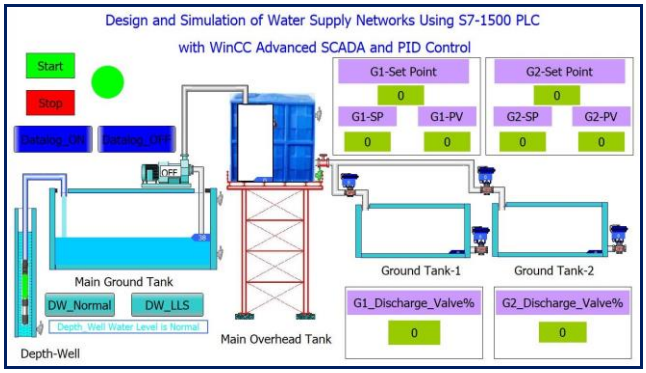

Fig. 4. Main ground tank water filling process

The synchronized operation illustrated in Fig. 5 guarantees effective oversight of water levels throughout the system. As the water level in the depth well diminishes to a critical point, triggering the activation of low-level sensors, the submersible pump's operation in the depth well is promptly halted. Additionally, a low-level alarm for the depth well water level is displayed on the screen, alerting operators to the situation.

Following this process, the low-level sensors detect the low water level in the main overhead tank, causing the booster pump to activate and transfer water from the main ground tank to replenish the main overhead tank. However, if the low-level sensors detect a lower water level in the main ground tank, the booster pump remains inactive. Conversely, if the water level in the main ground tank is normal, the filling process in the main overhead tank continues without interruption, as depicted in Fig. 6.

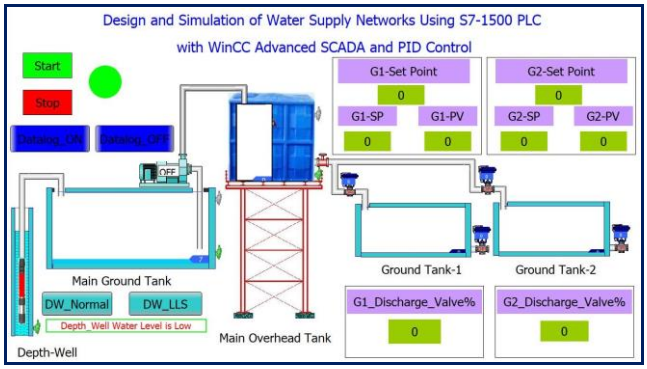

Fig. 5. Depth well water level low alarm activated

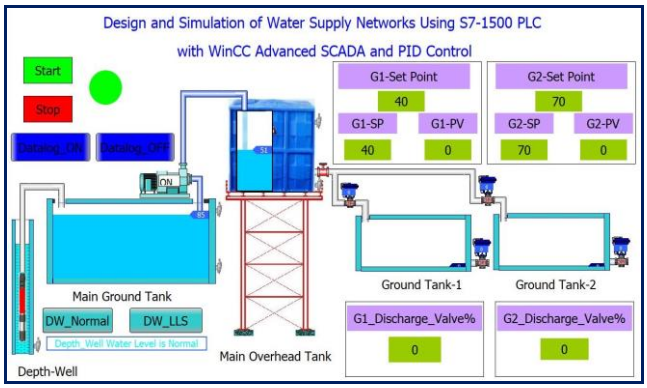

Fig. 6. Main overhead tank water filling process

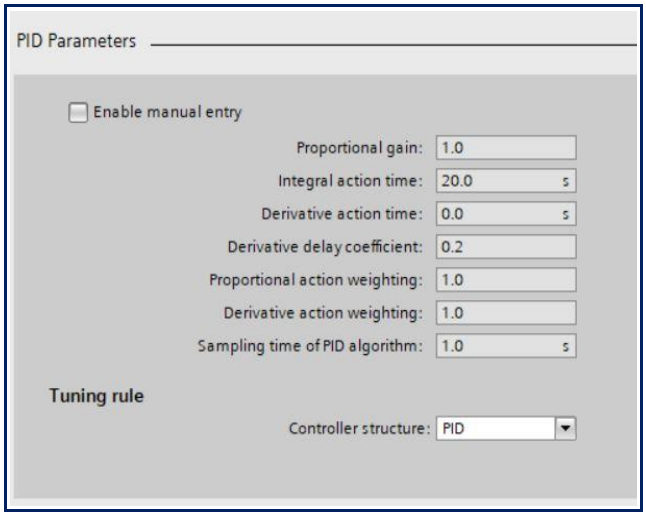

Fig. 7. PID algorithm default parameters with ground tank-1 and ground tank-2 PID compact

When the water level in the main overhead tank reaches the upper threshold, the discharge valve of the main overhead tank automatically opens. Simultaneously, the modulating valves controlling ground tank-1 and ground tank-2 are also open to initiate the filling process. Ground tank-1 and ground tank-2 are regulated by the PID control method. In the TIA portal software, the default parameters of the PID algorithm are configurable and programmable, as depicted in Fig. 7. This allows for precise adjustment and optimization of the PID controller to suit the specific requirements of the system. Utilizing Fig. 7 as a guide, users

can streamline the setup process and ensure that the PID controller operates efficiently and effectively to maintain desired system performance.

Fig. 8 and Fig. 9 display the automatic tuning method process for ground tank-1 and ground tank-2, presenting tuning graphs that offer insights into optimizing the control parameters for these tanks. By examining the tuning graphs provided in Fig. 8 and Fig. 9, engineers and operators analyze the effectiveness of the tuning process and make informed adjustments to achieve desired control outcomes. These visual representations enable the identification of any deviations from target setpoints, facilitating the fine-tuning of control parameters to enhance the stability and efficiency of the tanks. With the information presented in Fig. 8 and Fig. 9, users can iteratively refine the tuning settings to ensure precise control and reliable operation of ground tank-1 and ground tank-2 within the system.

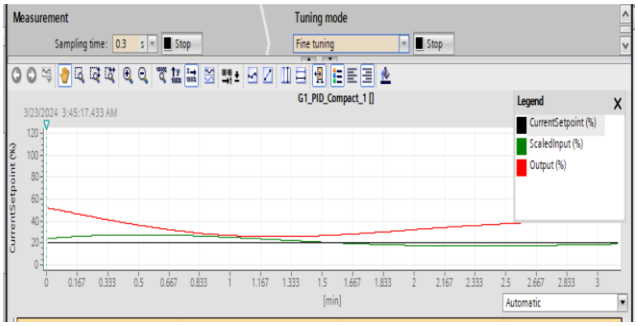

Fig. 8. Tuning graphs for ground tank-1

By employing the PID control method, ground tank-1 and ground tank-2 successfully reach the specified setpoints, setpoint-20 and setpoint-40, respectively. Once the setpoints are achieved, the modulating valves controlling the flow close, thereby maintaining the water levels within the tanks. Despite variations in user water consumption, ground tank-1 and ground tank-2 are able to sustain their target levels. This consistent water level stability is a result of the accurate operation of the modulating valves, ensuring the tanks continuously meet the desired conditions.

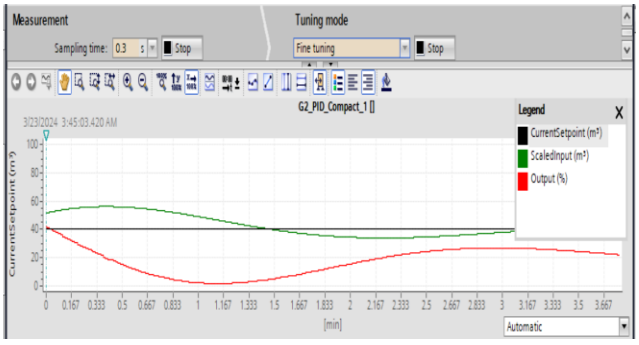

Fig. 9. Tuning graphs for ground tank-2

The tuned results of ground tank-1 and ground tank-2 are presented in Fig. 10 and Fig.11, accompanied by graphical representations that depict the outcomes of the tuning process.

These graphs offer a comprehensive view of the performance of ground tank-1 and ground tank-2 following the tuning adjustments. By analyzing the data presented in Fig. 10 and Fig. 11, engineers and operators assess the effectiveness of the tuning process and evaluate whether the control parameters have been optimized to achieve the desired system performance. The graphs help understand how ground tank-1 and ground tank-2 behave in various situations, making it easier to adjust control settings for accurate and dependable operation in the system.

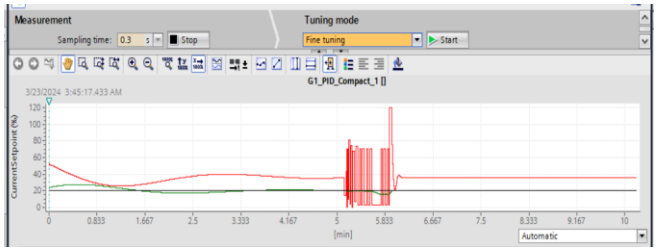

Fig. 10. PID tuned results of ground tank-1

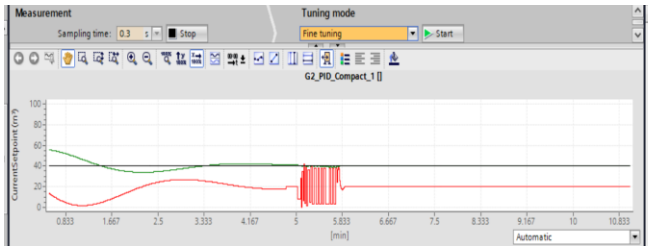

Fig. 11. PID tuned results of ground tank-2

Fig. 12 and Fig. 13 display the tuned parameters of ground tank-1 and ground tank-2, respectively, showcasing values for proportional gain, integral action time, and derivative action time. Throughout this filling process, PID control operates as the operator sets the desired setpoint to maintain an appropriate water level.

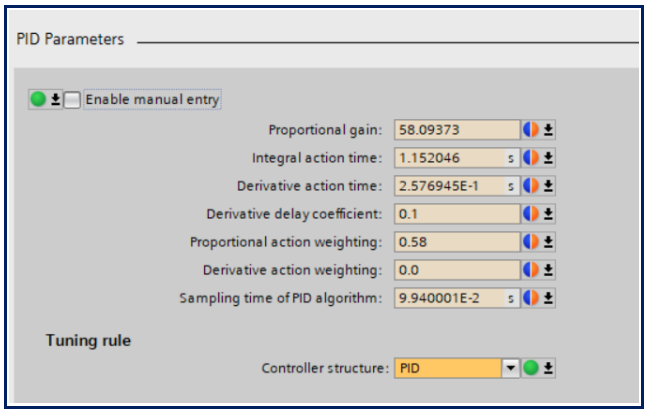

Fig. 12. PID tuned parameters of ground tank-1

Once the water levels in ground tank-1 and ground tank-2 reach their respective setpoint levels, the modulating valves controlling the flow close, as shown in Fig. 14, ensuring that the water levels in their respective tanks are maintained. Ground tank-1 and ground tank-2 can keep their desired levels in ground tank-1 and ground tank-2, no matter how much water users consume.

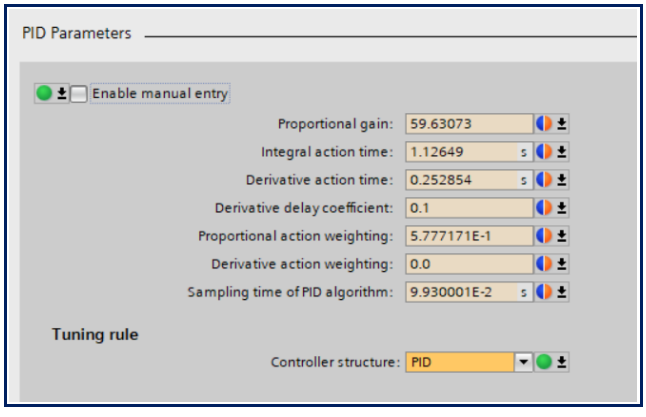

Fig. 13. PID tuned parameters of ground tank-2

This ensures consistent water levels in these tanks, meeting the desired conditions achieved through the operation of the modulating valves. The results of PID control tuning for ground tank-1 and ground tank-2 in the system are shown in Fig. 15 and Fig. 16, respectively.

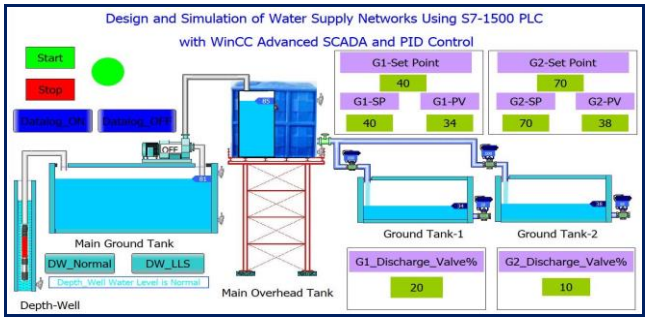

Fig. 14. Ground tank-1 and ground tank-2 water filling process with PID control

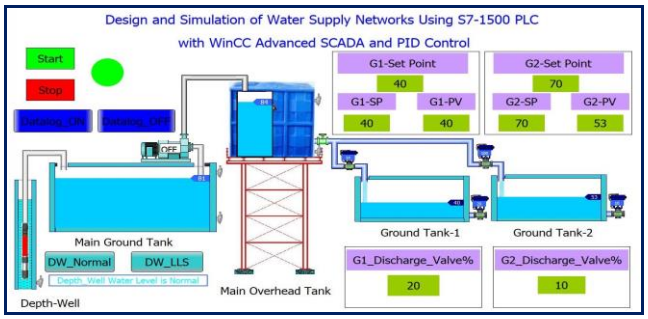

Fig. 15. Ground tank-1 at setpoint and ground tank-2 filling to setpoint

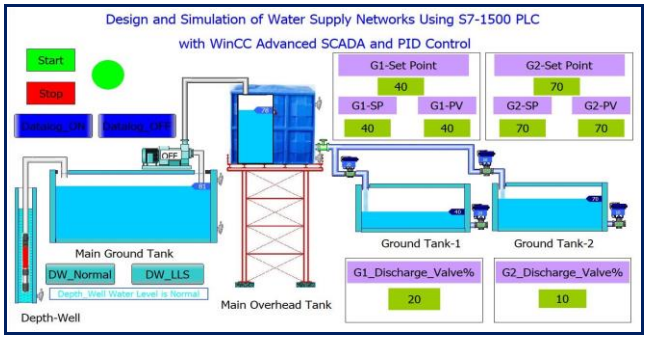

Fig. 16. Ground tank-1 and ground tank-2 reached setpoint

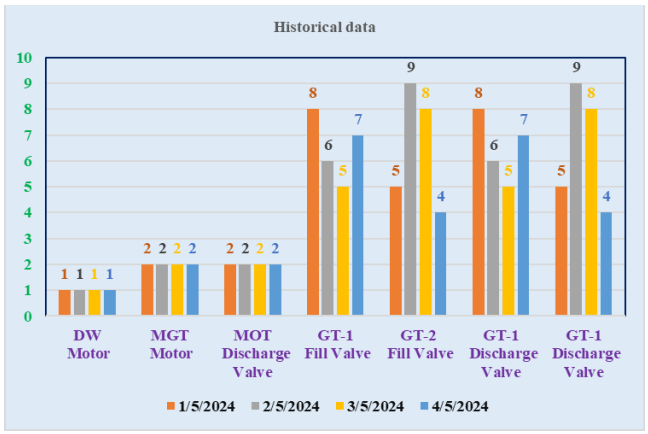

Fig. 17. Historical data of the SCADA system

Figure 17 displays historical data from a four-day trial of the SCADA system, focusing on evaluating key components and collecting operational data. Initially, the depth well motor, main ground tank motor, and main overhead tank discharge valve maintained stable values of 1, 2, and 2, respectively, while ground tank-1 and ground tank-2 fill valves were set at 8 and 5. Over subsequent days, minor variations were observed in the fill and discharge valves, whereas the depth well motor, main ground tank motor, and main overhead tank discharge valve consistently retained their values. The second day, slight changes occurred with the ground tank-1 fill valve increasing to 9 and the ground tank-2 fill valve decreasing to 6, accompanied by corresponding shifts in discharge valve readings. The third day saw the ground tank-1 fill valve rise to 7 and the ground tank-2 fill valve drop to 5, maintaining variability in discharge valve values. Finally, on the fourth day, the ground tank-1 fill valve increased to 7 and the ground tank-2 fill valve decreased to 4, continuing the trend of fluctuations in component operations throughout the testing period.

IV. Conclusion

The simulation results confirm the effectiveness of the water supply network's management and control. Integration of the SCADA system and PID control ensures precise regulation of water supply, optimizing resource distribution. Simulations illustrate the coordinated operation of pumps, valves, and sensors to maintain ideal water levels. The SCADA system's historical data offer insights into daily operations, aiding in monitoring pump activities and system performance. Overall, the results demonstrate the system's reliability in managing water supply networks efficiently. The integration of the SCADA system and PID control shows promise for improving system performance, with ongoing research necessary for further advancement.

Acknowledgment

Firstly, the author wishes to express gratitude to the Union Minister of the Ministry of Science and Technology for inaugurating the Master of Engineering course at Technological University (Mandalay). The author is particularly thankful to the Rector of Technological University Mandalay. Finally, the author is deeply grateful to all the teachers in the Department of Electronic Engineering at Technological University Mandalay.

References

[1] L. Talwar and H. K. Khajuria. “SCADA system.” *Design and selection of SCADA system using PLC for power control*, vol. 4, pp. 101-106, October 2015.

[2] K. H. Ang. “PID control.” *PID Control System Analysis, Design, and Technology*, vol. 13, pp. 599-576, October 2005.

[3] Siemens, "Closed-Loop Control with 'PID Compact V2.2,” Internet: https://support.industry.siemens.com/cs/ww/en/view/79047707.Mar. 2017. [Accessed: Feb.19,2024].

[4] J. Paulusova. “PID Controller.” *Design of PID controller for PLC*, vol. 15, pp.35-41 May 2012.

[5] Yin Yin Soe and Pann Ei San, "PID closed-loop control analysis for automation with Siemens PLC using TIA V13." Internet: http://www.ijciras.com/PublishedPaper/IJCIRAS1361.pdf. August 11, 2019. [Accessed: Jan. 20,2024]

[6] N. Nadgauda and S. A. Muthukumaraswamy, "Design and development of industrial automated system using PLC-SCADA," *in Proc. IEEE-GCC*,2019, pp. 425-431.

Analysis of Ten Myanmar Indigenous Medicines from Mon State for the Treatment of Anaemia and Ailments

Hla Thidar Aung[1], Cherry Than[2], Yin Yin Aye[3]

[1] *Professor, Department of Engineering Chemistry, Technological University* (*Mandalay)*

[2] *Associate Professor, Department of Engineering Chemistry, Technological University* (*Mandalay)*

[3] *Associate Professor, Department of Engineering Chemistry, Technological University* (*Mandalay)*

Email: [1]aunghlathidar@mail.com, [2]royal.cherry01@mail.com, [3]yinyinmdy75@mail.com

***Abstract*— The main aim of this research is to evaluate some minerals contents in Myanmar indigenous medicines containing Kyauk-thway .In this research work, ten brand Myanmar indigenous medicines containing Kyauk-thway were analyzed according to ash, nitrogen contents, citric acid percent and trace minerals such as iron .These medicines were good remedies for the treatment of anemia and other ailments. Most of Myanmar medicines recipes applied kyauk-thway for the betterment of their potencies. The essential nutritive element of iron was determined by atomic absorption spectroscopy (AAS). In the selected ten Myanmar medicines from Mon State, the ash percent was performed by incineration method and nitrogen contents were evaluated by micro Kjeldahl method. And alternatively, the iron contents of each sample were measured by atomic absorption spectroscopy(AAS) and visible spectrophotometry. Citric acid contents of these samples were calculated by volumetric method.**

Keywords—Thwaysay, atomic absorption spectroscopy, furnace, Kjeldahl method, visible spectroscopy

I. INTRODUCTION

The development of new versatile medicines in the laboratory either extracted from medicinal plants or synthesized-stretches herbs back to the late and early of 19th century, when pharmacists first isolated and identified the constituents. From that time onwards of isolating and identifying, scientists made tremendous progress in understanding how isolated chemicals affect the body, as well as how the body works in health and diseases of developing world. [1]. Even today its use in various sectors such as medicinal compounds in medicine, agro chemicals in agricultural, facial and skin compound in cosmetic etc. is well known. There are millions of natural organic compounds which have been well documented. But still there are many unknown compounds that stick await discovery. The use of modern techniques and instruments enables to analyze and elucidate the structural natural of these compounds [2]. Simultaneous advancement in the fields of chemistry, biochemistry, biosynthesis and pharmacology has developed pharmacognosy, which is concerned with the study of crude drugs of plant and animal origins. Various active compounds have been isolated from plants which are used in modern medicine. With the advancement of synthetic organic chemistry, most of the active constituents of plants used in medicine have been synthesized [3]. Local indigenous physicians use Thwaysay in the treatment of various kinds of diseases cause by blood. It is almost suitable for female in the treatment of dizziness, gynecological disorders and fever. .It can be used by sniffing or taken orally. In general, thwaysay contains the following raw materials ;Kyauk-thway, Nathaphyu, Nathani, Ponmathein, Gangaw, Payok,Hpala, Kantchokeni ,Paikchin, and Thitkyabo,.Each powdered raw material mentioned above is mixed to get one course of Thwaysay The quantity of each dosage is instructed one teaspoon, two tamarind seeds, half betel nut and one medicine spoon equivalents [4].

The uses of Thwaysay of different brands are similar to each other .Its therapeutic uses are as follows;

- Dizziness can be relieved by sniffing these drugs or it can be taken orally with sugar.
- It can be taken with water for depression, unsleeping, debility, loss of appetite, afraid and anemia.
- It can also be taken with juice of sugar cane for treatment of palpitation, dizziness, tiredness and giddiness.
- It can be taken with warm, firstly boiled, water for gastroenteritis.
- It can be used with juice of lemon for dyspepsia ulence, nausea and vomiting.
- When one has painful micturition, it can be given with infusion of pennywort leaves.
- It can be given with coconut milk for treatment of asthma.
- When one has fever, it can be taken by infusing betel leaves; this makes the patient sweat profusely to reduce the body temperature.
- Generally, when menstrual cycle disappears or irregular between the ages of 13 to 40 years, it can be used with decoction of ginger and betel leaves.
- It can be also taken with an equal amount of hypertension.
- It can be given with infusion of betel leaves for children with diarrhea [5].

In brief, Thwaysay can be used in varies ways for the treatment of various kinds of diseases.

A. Iron

Iron is the most trace element deficiency anemia, characterized by a low concentration of hemoglobin in the blood or by a low volume of packed red blood cells, is the usually symptom. The recommended dietary allowance for ages 23 to 50 years is 80%higher than for men in the same

age group because of the iron lost from menstrual bleeding. Children between the ages of 0.5 and 4.0 years, because of the rapid rate of growth at this time and because the infants iron stores are not sufficient to the last beyond the age of 6 months .Children in early adolescences are also at risk factor because of the their rapid growth .In addition, menstruations is a risk factor of deficiency. Pregnancy is another risk factor because of the mother`s expanding blood volume, the demands of the fetus and placenta and blood losses during childbirth. Anemia in infants, for example can be treated with 6mg of iron /kg body weight per day. The iron can be supplied as oral ferrous sulphate. Iron deficiency anemia in adults can be treated with 50mg of iron three times a day .The iron can be supplied as ferrous sulfate. Early rises in serum ferritin may not occur at these doses ,but can occur at higher doses .With the use of standard dose, serum ferritin may rise into the nor mal range only after the anemia has been corrected.

II. Experimental

A. Sample Collection

Ten brands of Myanmar indigenous medicines were collected from no.1 market of Mawlamyine in Mon state.

Fig. 1. Ten brands of Myanmar Indigenous Medicines from Mon State

B. Determination of Single dose, Daily dose in Myanmar Indigenous Medicines

All of the samples were weighed with digital balance to get the accurate weigh of single dose and daily dose asdescripted instruction on each of the sample bottle.

C. Determination of Ash Contents in Myanmar Indigenous Medicines

A porcelain crucible was heated at 60 °C for 30 minutes. Then it was cooled in a desiccator for 30 minutes until it gets at room temperature and the weight was noted. Sample (3 g) was placed in a pre-weighed porcelain crucible and it was heated carefully on a hot plate until the organic matter dried and burned off without flaming. The partially decomposed sample was then incinerated in a muffle furnace at 400 °C until the resultant ash become uniform in color. When the sample was completely ashed, the crucible was allowed to cool in a desiccator and weighed. The process of heating, cooling, and weighing was repeated until a constant weight was obtained. And then ash content was calculated. All the samples were done according to the above mention method.

D. Determination of Nitrogen Contents in Myanmar Indigenous Medicine

The homogenized sample 0.5 g was introduced into a dried Kjeldahl flask [6]. The catalyst mixture (0.2 g anhydrous copper II sulphate and 4.0 g potassium sulphate) and concentrated sulphuric acid (10 mL) were then added. The contents were digested by heating the flask in a inclined position in a fume hood. The mixture was heated gently for about thirty minutes and heating was continued for about 3 hours until the solution become clear. The flask was shaken gently from time to time during the digestion process.

Then the flask was allowed to cool and transferred into 100 mL volumetric flask and made up to the mark with distilled water. After boiling the distilled water in round bottom flask, 20 mL of made up solution was added in the middle flask. The 40% sodium hydroxide solution (12 mL) was poured in this flask. The ammonia evolved was allowed to absorb in 10mL of 0.5 % boric acid solution contained 1 drop of mixed indicator solution. The ammonia distillate was titrated with 0.05 M sulphuric acid until the colour change from green to gray. Then the nitrogen content in the sample was calculated.

E. Determination of iron contents by atomic absorption spectroscopy

Ash 3 g of Myanmar medicine was placed in a 150 mL beaker and 8 mL of concentrated nitric acid was added slowly [7]. Then the resulting mixture was evaporated to dryness and the residue, after cooling was dissolved in 6 mL of 10 % nitric acid (v/v) solution. The above solution was transferred to a 100 mL volumetric flask and the volume made up to the mark with distilled water. Then, the amounts of the iron contents were determined by atomic absorption spectroscopy.

F. Determination of Iron Contents in Myanmar Indigenous Medicines by Visible Spectrophotometry

Ash 0.1 g of Myanmar indigenous medicine was placed in a 250 mL beaker and 25 mL of 6 M hydrochloric acid was added. The beaker was covered with watch glass and then heated at a slow boil for 20 minutes on a hot plate. The beaker was removed from hot plate and, the bottom side of watch glass over the beaker was tilted and washes down with a small amount of deionized water. The hot mixture was filtered through the filter paper into a 100 mL volumetric flask. The beaker was rinsed with 10mL of hot deionized water and poured this through the filter paper while after most of the first mixture has been collected in the volumetric flask. When no more liquid remained in the bottom of the filter paper, it was removed and the inside of the funnel with a few mL of deionized water at room temperature. The filtrate was

cooled at room temperature and diluted to the mark with deionized water to mark 100 mL solution and mixed well.

The resulting solution 5mL was pipette into a 100 mL volumetric flask and the volume made up to the mark with deionized water and mixed well. Then the solution 1 mL was added into a 100 mL volumetric flask, 6 drops of sodium citrate solution, 2 mL of hydroquinone solution, 3 mL of 1, 10-phenanthroline solutions were added and diluted to the mark with deionized water and all were mixed well. The orange colour Fe(II)-phenanthroline complex was obtained. After 15 minutes, the absorbance of prepared solution was measured at the λ_{max} of 513 nm.

G. Determination of Citric Acid Contents in Myanmar Indigenous Medicine

The citric acid solution 10 mL was pipetted into a 150 mL conical flask and 2 drops of thymol blue indicator was added. It was then titrated with 0.05 M sodium hydroxide solution until the colour change from yellow to blue. The sample solution 10 mL was pipetted into a 150 mL conical flask and 2 drops of thymol blue indicator were added [8]. It was then titrated with 0.05 M sodium hydroxide solution until the colour changed from yellow to blue. Then the citric acid content was calculated.

III. Results and Discussion

A. Determination of Ash Contents

The ash content in the traditional drug is the residue of inorganic minerals remaining after the incineration. The simplest method for preliminary ashing is the use of flame [8]. The temperature of the detected sample must be kept as low as possible. It should not produce the flame but carbon and some organic matter must be burned off in a reasonable time. The final ashing of the sample must be accomplished by using furnace with appropriate temperature.

The ash percent in a foodstuff is actually the residual inorganic materials remaining after the organic matter has been burnt [7]. The ash percent is a measure of the quality of food. The smaller the ash percent, the better will be the food quality. However, in the case of Myanmar medicines, the main ingredients are the inorganic materials so that the ash percent should be reasonable amount. Generally, the ash percent is directly proportional to its elemental contents.it has been found that sample no.4 has the highest amount of ash 31.44% and lowest ash percent was 5.77 in sample no.6.the smaller the value of ash percent in sample no.6 is better for the food quality but it is not related to the properties of Myanmar medicine.

B. Determination of Nitrogen Contents

Organic substance of Proteins is the high molecular weight formed by a number of amino acids united by a peptide linkage. The groups of non-amino acid may also be present. Proteins are amphoteric, *i.e.*, they may possess both acidic and basic properties, depending upon the reaction of the solution in nature. They usually almost form colloidal solution in water. They are the basic components of protoplasm in the cells of flora and fauna. It is necessary for the formation of the various enzymes and hormones found in the body [6]. Proteins are nitrogenous substances.

Regarding to the values of nitrogen percent in selected samples, it was indicated that the sample no.7 has the highest amount of 2.25% and sample no.4 has the smallest amount of nitrogen, 1.32%.Nitrogen content is also plays important role in foodstuff and secondary metabolites. The higher amount of nitrogen is essential in the formation of cells and cytoplasm.

C. Determination of Single Dose and Daily Dose of Myanmar Medicines

In Myanmar medicine, the amount of single dose is illustrated as the amount of ywei seed, tamarind seed, betel-nut, tea-spoon full and the number of tablets and capsules. The daily dose is the amount of single dose multiplied by maximum intake of one day.

In this work, the single dose and daily dose of the selected samples were determined by the instruction pamphlets. The weight of the single dose, daily dose and maximum intake of the samples were shown in “Table II”. Daily dosage amount of Myanmar Traditional medicines affected the health of consumer directly. For adult, sample no.1 showed the highest daily dose for three times a day and it was weighed 9.381g while sample no.5 weighed 0.872g. In the case of child, sample no.1 also showed the highest daily dose of 4.596g and sample no.5 expressed the smallest weight of 0.436g.The weight of sample greatly affected the quality of medicines and it was the base concept to calculate the minerals percent of each of the sample by AAS.

I. The Ash Percent and Nitrogen Content Percent in ten Brands of Myanmar Indigenous Medicines

Sample no.	Ash%	Nitrogen%
1.	6.238	1.98
2.	6.965	1.76
3.	5.987	1.45
4.	31.44	1.32
5.	23.56	2.01
6.	5.77	1.98
7.	17.98	2.25
8.	6.32	1.91
9.	6.49	1.85
10.	23.54	1.43

D. Determination of Elemental Contents by Atomic Absorption Spectroscopy

The mineral elements are crucial to many vital system operations [5]. Some of essential mineral elements, especially sodium and potassium are the major factors in osmotic control of water metabolism. Atomic absorption is a modern technique for the determination of minerals in

the samples. It is commonly used for the analysis of food. The food is the first digested in acid to release the minerals into a soluble form for determination). Atomic absorption method has been widely applied used to the estimation of about 60 minerals elements and it is a major useful method in studies of involving trace metals in the environmental and biological samples [6]. Determining the values of iron content in each of the sample, sample no.1 has the highest amount of iron (4.01mg) and sample no.2 has the lowest amount of iron content (0.30mg).The maximum intake of iron for individual varies from 16 to 18 mg/day. So these ten selected samples were safe for the consumer.

II. WEIGHT OF SINGLE DOSE, DAILY DOSE AND MAXIMUM INTAKE OF DRUG

Sample no	Adult			Child		
	Single dose (g)	*Intake (time)*	*Daily dose (g)*	*Single dose (g)*	*Intake (time)*	*Daily dose (g)*
1	3.127	3	9.381	1.532	3	4.596
2	0.297	3	0.891	0.297	2	0.594
3	0.288	3	0.864	0.288	2	0.576
4	0.423	3	1.269	0.215	3	0.645
5	0.436	2	0.872	0.218	2	0.436
6	0.985	2	1.970	0.498	2	0.996
7	0.545	3	1.635	0.545	2	1.090
8	1.927	2	3.854	0.964	2	1.928
9	2.023	2	4.046	1.012	2	2.024
10	2.433	2	4.866	1.213	2	2.426

E. Determination of Iron Contents in Myanmar Indigenous Medicines by Visible Spectrophotometry

Absorption spectroscopy based on ultraviolet and visible radiation is one of the most useful tools for quantitative analysis. The important characteristics of spectrophotometric methods are (i) wide applicability (ii) high sensitivity (iii) moderate to high selectivity (iv) good accuracy (v) ease and convenience [7].

The class of organic compound known as 1, 10-phenanthroline formed stable complexes with iron (ii) and certain other ions. The parent compound has a pair of nitrogen atoms located in such position that each can form a covalent bond with the ion (II) ion.

Comparative study of iron concentrations between AAS results and spectrophotometric results were carried out statistically using Student T test. There is no significance difference between iron concentration calculated from AAS and spectrophotometric method. It also observed that sample no.1 has greatest amount of iron (4.19mg) and sample no.2 has smallest iron content (0.32mg).

F. Determination of Citric Acid Contents in Myanmar Medicines

Citric acid ($C_6H_5\ O_7.H_2O$) is one of the most widely found natural acids, and it plays a vital role in the Kerbs metabolic cycle as well as in the photosynthesis process. It is a white crystalline soluble inorganic tribasic acid. It has a sour taste and occurs as free acid in lemons and other sour fruits [6]. The citric acid is dealt with the final stages of the oxidation of carbohydrates and fats and involved in the synthesis of amino acid.

It was showed that all the samples were in the range of between 0.19% in sample no.10 and 0.98 % in sample no.3.These results were acceptable for the safety of consumer.

III. IRON CONTENTS AND CITRIC ACID CONTENT IN DAILY DOSE OF MYANMAR INDIGENOUS MEDICINES

Sample no.	Iron Contents (mg)		
	AAS	*UV_VIS*	*Citric acid (%)*
1	4.01	4.19	0.21
2	0.30	0.32	0.27
3	0.67	0.45	0.98
4	3.79	3.21	0.56
5	1.65	1.53	0.79
6	0.67	0.66	0.54
7	1.24	1.27	0.75
8	3.47	3.45	0.53
9	1.29	1.22	0.68
10	5.45	5.61	0.19

IV. CONCLUSION

The main aim of this research work is to analyses the minerals contents, ash contents, protein contents and citric acid in some Myanmar Medicine containing Kyauk thway and to determine their recommended dose by comparing the values of allowable percentage in foodstuff.

The ash percent (%) in the selected samples were determined by incineration method and then incinerated at 400 °C in crucible. They were found to be in the range of 5.77 to 23.56% (sample no.6 and sample no.5).

The nitrogen contents % of the samples were detected by Kjeldahl method. The respective values were noted as 1.32 % (sample no.4) to 2.25 % (sample no.7).

Highest iron values contents were found to be sample no.10, because the weight of single dose, numbers of dosage per day and constituents of parasays were different. It was indicated that there is no prominent differences between atomic absorption spectroscopy and visible spectroscopy. It can be applied to the anaemia related diseases without any side effects. The median dietary intake of iron is approximately 16 to 18mg/day for man ad 12mg/day for woman. For children, 10mg/day is the recommended amount of iron a day. Children under age of 14 should not take more than 40mg a day. Because of its rich citric acid contents, it can be cured high blood pressure to a certain extent. This research revealed the high citric acid content in sample no.3 (0.98%).There are no specific recommended amounts of natural citric acid from fruits. Consuming citric acid in high amount can lead to stomach upset and erosion of tooth enamel.

By observing the data resulted from comparing their constituents, Myanmar indigenous medicines were benefit for consumers. .

ACKNOWLEDGMENT

I am grateful to the committee of ESEJ and editorial board for permitting this paper to publish. I would like to express my sincere gratitude to pro-rectors for their kind provision and submission of this paper. I am also thanks to all, who helped me during all courses of this research.

REFERENCE

[1] Mnimh, A. G. 1996. "The Encyclopedia of Medicinal Plants".

[2] "Medicinal Plants of Myanmar", Ministry of Health, Department of Traditional Medicine. 2000. vol 1.

[3] World Health Organization 2005. "WHO Traditional Medicine Strategy 2002-2005". Report of WHO Study Group, No. 905: 54-59.

[4] Chatterjee, C.C., (1981), "Human Physiology", Medical Allied Agency, Calcutta, pp.160-161.

[5] Day, R.A. and Underwood, A.L.,(1991), "Quantitative Analysis", *Prentice Hall International Inc*., New York, pp.431-432.

[6] Harper, J.L., Marcel, E.C. and Emmanuel, C. B., (2015), "Iron Deficiency Anemia: Practice essentials, Pathophysiology and Etiology. Medscape" .

[7] Joslyn, M.A., (1970), "Methods in Food Analysis, Physical, Chemical and instrumental Methods of Analysis", Academic Press Inc., New York, pp.109-110.

[8] Kalthoff, M. and Elving, P.J., (1961), "Treatise on Analytical Chemistry", Interscience *Pub*., *Inc*., New York, vol.13, pp.780-781.

Identification of Binding Energy and Atomic State of Ξ^- Hyperon in Ξ^- - ^{14}N System

Htet Htet Wai Moe[1], Khin Than Tint [2], Wai Wai Aung [3], Aye Mar Khin[4], Maw Maw Kyu [5]

[1]*Lecturer, Engineering Physics Department, Technological University Mandalay*

[2]*Professor, Dr, Department of Physics, University of Mandalay*

[3] *Lecturer, Department of Academic, Government Technical Institute (Myingyan)*

[4]*Associate Professor, Engineering Physics Department, Technological University Mandalay*

[5]*Assistant Lecturer, Engineering Physics Department, Technological University Mandalay*

Email: [1]htethtetwaimoe9@gmail.com, [2]khinthantint045@gmail.com, [3]myatnoewai616@mail.com, [4]yccayemarkhin@gmail.com, [5]mawmawkyu87@gmail.com

***Abstract*—In this research work, the binding energies of the Ξ^- hypernuclei; Ξ^- -^{14}N system and atomic state at which Ξ^- hyperon is absorbed by the nucleus have been calculated. Firstly, nonrelativistic Schrödinger equation have been solved by using Gaussian basis wave function and Gaussian potential. At the potential strength -24 MeV, the binding energy of Ξ^- hyperon in Ξ^--^{14}N system was obtained to be 1.93 MeV which is nearly consistent with experimental result (1.93 ± 0.64 MeV) at p-atomic state. Therefore, Ξ^- hyperon was absorbed at the p-state by the nucleus in the emulsion. This atomic state of Ξ^- hyperon in Ξ^--^{14}N system which is the same as the IBUKI event and the KISO event.**

Keywords— Ξ^- hypernuclei, Gaussian potential, binding energy, atomic state, Gaussian basis wave function

I. Introduction

The nucleus is made of one or more protons and a number of neutrons. A hypernucleus is a bound system of the protons, neutrons and at least one hyperon and having a non-zero value of strangeness [1]. Hyperons are baryons heavier than nucleons. There are four types of hyperons; lambda hyperon (Λ^0), sigma hyperon (Σ^+, Σ^0, Σ^-), xi hyperon (Ξ^-, Ξ^0) and omega hyperon (Ω^-). Being baryons, hyperons are composed of three quarks including at least one strange quark [4]. The cascading particle is Ξ hyperon. Ξ^- and Ξ^0, are composed of dss and uss quarks. They are strangeness -2 particles.

A twin single-Λ hypernuclei event [6], named "KINKA event" which is found in the KEK E373 experiment. The event was uniquely interpreted as the decay mode of $\Xi^- + {}^{14}\mathrm{N} \rightarrow {}^{9}_{\Lambda}Be + {}^{5}_{\Lambda}He + \mathrm{n}$. The B_{Ξ^-} value of the KINKA event was also revised to be 8.00 ± 0.77 MeV if the daughter nucleus, ${}^{9}_{\Lambda}Be$, was in the ground state. If the ${}^{9}_{\Lambda}Be$ was in an excited state, the B_{Ξ^-} was 4.96 ± 0.77 MeV. In 2014, the KEK E373 experiment presented a twin single-Λ hypernuclei event [7], named "KISO event".

The event was uniquely interpreted as the decay mode of $\Xi^- + {}^{14}\mathrm{N} \rightarrow {}^{10}_{\Lambda}Be + {}^{5}_{\Lambda}He$. The B_{Ξ^-} value of the KISO event was also revised to be 3.87 ± 0.21 MeV or 1.03 ± 0.18 MeV for production of the ${}^{10}_{\Lambda}Be$ nucleus as either the ground state or the first excited state, respectively [12]. The IBUKI event [8,13], a twin single-Λ hypernuclei event detected in the E07 emulsion. The reaction process was clearly identified as $\Xi^- + {}^{14}\mathrm{N} \rightarrow {}^{10}_{\Lambda}Be + {}^{5}_{\Lambda}He$. The binding energy of the Ξ^- + ^{14}N system was determined to be 1.27 ± 0.21 MeV by applying kinematic fitting. The energy level of Ξ^- is likely a nuclear 1p state.

A single Λ hypernucleus event via the Ξ^- hyperon capture at rest in nuclear emulsion in J-PARC E07 experiment [9]. In this experiment, Ξ^- hyperons were produced via the quasi free p (K^-, K^+) Ξ^- reaction with momentum of K^- meson beam, 1.8 GeV/c in a diamond target [10,11]. The single-Λ was generated with the stopped Ξ^- hyperon was captured by an atom in nuclear emulsion [14]. Decay fragments were produced from the stop point of the Ξ^- hyperon. One of the single-Λ hypernucleus events was found at plate #6 of module #26 in J-PARC E07 experiment have been analyzed in Fig. 1. [2, 3].

The reaction process was clearly identified as $\Xi^- + {}^{14}_{7}N \rightarrow {}^{12}_{\Lambda}B + p + \Lambda + n$. The single-$\Lambda$ hypernucleus was identified as ${}^{12}_{\Lambda}B$ and its decay products were helium 4, helium 3, deuteron and three neutrons. Finally, the value of the binding energy of Ξ^- hyperon was 1.93 ± 0.64 MeV that observed from difference between Q value and total energy. In this paper, the binding energy and atomic state of Ξ^- hyperon in the nucleus of Ξ^--^{14}N system was investigated by solving nonrelativistic Schrödinger equation.

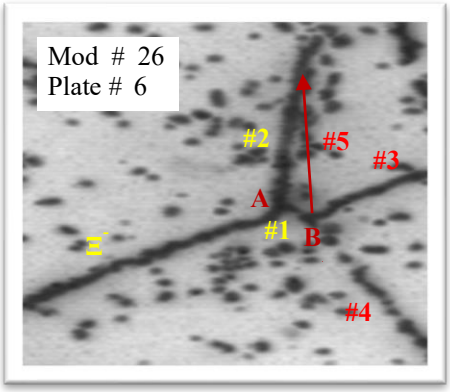

Fig. 1. Photograph of a single Λ hypernucleus event occurred in plate #6 of module #26 in J-PARC E07 experiment.

II. Mathematical Formulation

A. Derivation of Kinetic Energy, Centrifugal Potential Energy and Norm Matrix elements

In order to calculate the energy eigen value, i.e. binding energy of Ξ^--Nucleus was theoretically solved Schrödinger equation.

$$(H_0 + V)\Psi = E\Psi \tag{1}$$

Here, H is the Hamiltonian operator, E is energy eigenvalue, Ψ is eigen-vector, H_0 is the kinetic energy operator and V is the potential energy operator.

The spherical coordinate for the wave function was chosen,

$$\Psi(\vec{r}) = R(r)\,\Theta(\theta)\,\Phi(\varphi)$$

where, R(r) is a radial part and spherical $\Theta(\theta)\,\Phi(\varphi)$ is the angular part. And then, the following radial equation was derived by applying the separable method.

$$\left\{-\frac{\hbar^2}{2\mu}\frac{d^2}{dr^2}+\frac{\hbar^2}{2\mu}\frac{\ell(\ell+1)}{r^2}+V(r)\right\}u(r)=E\,u(r) \tag{2}$$

In this calculation, we use Gaussian basis wave function as follows,

$$u(r) = r^{\ell+1}\sum_{j=1}^{N_b} c_j\, e^{-\left(\frac{r}{b_j}\right)^2} \tag{3}$$

By substituting the equation (3) in equation (2), we get this equation,

$$\left\{-\frac{\hbar^2}{2\mu}\frac{d^2}{dr^2}+\frac{\hbar^2}{2\mu}\frac{\ell(\ell+1)}{r^2}+V(r)\right\}\sum_j c_j r^{\ell+1}e^{-\left(\frac{r}{b_j}\right)^2}=E\sum_j c_j r^{\ell+1}e^{-\left(\frac{r}{b_j}\right)^2} \tag{4}$$

By multiplying the equation (4) with $r^{\ell+1}e^{-\left(\frac{r}{b_i}\right)^2}$ and integration through the equation,

$$\int r^{\ell+1}e^{\left(\frac{r}{b_i}\right)^2}\left\{-\frac{\hbar^2}{2\mu}\frac{d^2}{dr^2}+\frac{\hbar^2}{2\mu}\frac{\ell(\ell+1)}{r^2}+V(r)\right\}\sum_j c_j r^{\ell+1}e^{-\left(\frac{r}{b_j}\right)^2}dr$$

$$=E\int r^{\ell+1}e^{-\left(\frac{r}{b_i}\right)^2}\sum_j c_j r^{\ell+1}e^{-\left(\frac{r}{b_j}\right)^2}dr \tag{5}$$

Equation (5) can be described as the follows:

$$\sum_j [T_{ij}^{\ell} + F_{ij}^{\ell} + V_{ij}^{\ell}]\,c_j = E\sum_j N_{ij}^{\ell} c_j$$

where,

The kinetic energy matrix as follows,

$$T_{ij}^{\ell} = \int r^{\ell+1}e^{-\left(\frac{r}{b_i}\right)^2}\left\{-\frac{\hbar^2}{2\mu}\frac{d^2}{dr^2}\right\}r^{\ell+1}e^{-\left(\frac{r}{b_j}\right)^2}dr \tag{6}$$

The centrifugal potential energy matrix element,

$$F_{ij}^{\ell} = \frac{\hbar^2}{2\mu}\int r^{\ell+1}e^{-\left(\frac{r}{b_i}\right)^2}\frac{\ell(\ell+1)}{r^2}r^{\ell+1}e^{-\left(\frac{r}{b_j}\right)^2}dr \tag{7}$$

The potential energy matrix element,

$$V_{ij}^{\ell} = \int r^{\ell+1}e^{-\left(\frac{r}{b_i}\right)^2}V(r)r^{\ell+1}e^{-\left(\frac{r}{b_j}\right)^2}dr \tag{8}$$

The norm matrix element,

$$N_{ij}^{\ell} = \int r^{2(\ell+1)}e^{-\left(\frac{r}{b_i}\right)^2}e^{-\left(\frac{r}{b_j}\right)^2}dr \tag{9}$$

In this calculation, we obtained equation (10), (11) and (12) by using standard integral.

$$N_{ij}^{\ell} = \frac{(2\ell+1)!!}{2^{\ell+2}}\frac{\sqrt{\pi}}{\left(\frac{1}{b_i^2}+\frac{1}{b_j^2}\right)^{\ell+\frac{3}{2}}} \tag{10}$$

$$T_{ij}^{\ell} = -\frac{\hbar^2}{2\mu}N_{ij}^{\ell}\left[\frac{2(2\ell+3)}{b_j^4\left(\frac{1}{b_i^2}+\frac{1}{b_j^2}\right)}-\frac{(4\ell+6)}{b_j^2}+\frac{2\ell(\ell+1)\left(\frac{1}{b_i^2}+\frac{1}{b_j^2}\right)}{(2\ell+1)}\right] \tag{11}$$

$$F_{ij}^{\ell} = \frac{\hbar^2}{2\mu}N_{ij}^{\ell}\frac{2\ell(\ell+1)\left(\frac{1}{b_i^2}+\frac{1}{b_j^2}\right)}{(2\ell+1)} \tag{12}$$

By adding equation (11) and (12), we get

$$T_{ij}^{\ell} + F_{ij}^{\ell} = \frac{\hbar^2}{2\mu}N_{ij}^{\ell}\frac{(4\ell+6)}{b_i^2+b_j^2}.$$

The potential energy matrix element with Gaussian basis wave function becomes as follows:

$$V_{ij}^{\ell} = \int r^{\ell+1}e^{-\left(\frac{r}{b_i}\right)^2}[V_{\Xi^- - \text{Nucleus}}]r^{\ell+1}e^{-\left(\frac{r}{b_j}\right)^2}dr \tag{13}$$

B. Interaction for Ξ^--Nucleus System

In the present work, binding energy of Ξ^- hyperon was calculated that a Ξ^- hyperon moves in a nuclear potential which is an average effect of the nucleons in the core nucleus. By using the phenomenological Gaussian potential, the Ξ^--Nucleus potential was derived. The Gaussian potential can be expressed as follows [5],

$$V(r) = Ve^{-\left(\frac{r}{\beta}\right)^2} \tag{14}$$

Thus, the potential energy matrix element with Gaussian basis wave function become as follows:

$$V_{ij} = V\frac{(2\ell+1)!!}{2^{(\ell+2)}}\frac{\sqrt{\pi}}{\left(\frac{1}{b_i^2}+\frac{1}{b_j^2}+\frac{1}{\beta^2}\right)^{\ell+3/2}} \tag{15}$$

To obtain the value of binding energy of our consideration system, the Schrödinger equation will be solved by using power inverse iteration method which was written in FORTRAN code.

III. Results and Discussions

A. Results of Ξ⁻-Nucleus Interaction

The structure analysis of light Ξ⁻ hypernuclei namely Ξ⁻ -^{14}N have been theoretically investigated. Firstly, nonrelativistic Schrödinger equation have been solved by using Gaussian basis wave function and Gaussian potential. The Gaussian potential is displayed in Fig.2 with the potential strength -24.0 MeV. The interaction range is about 3 fm in this figure.

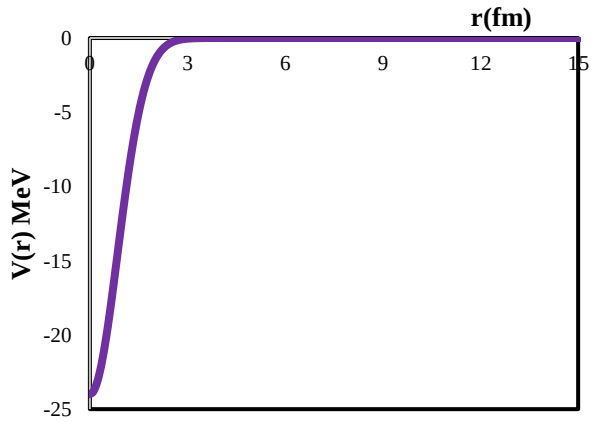

Fig. 2. Gaussian potential with potential strength -24 MeV

B. Results of Theoretical Estimation of Level State of Ξ⁻ Hyperon in Ξ⁻ -^{14}N System

The binding energies and atomic state of light Ξ⁻ hyperon in Ξ⁻ -^{14}N system have theoretically investigated by using Gaussian potential in two-body calculation. Tables I give the binding energy for each possible state of Ξ⁻ hyperon in Ξ⁻ -^{14}N system. At the potential strength -24 MeV, the binding energy was obtained to be 1.93 MeV at p-atomic state. This value is nearly consistent with experimental result and was compared with the result of twin single-Λ hypernuclei events in the E373 and the E07 experiments. Table II give the binding energy values of Ξ⁻ hyperon in Ξ⁻ -^{14}N system. Fig.3 show schematic diagram of the binding energy of Ξ⁻ hyperon and the corresponding states.

TABLE I

THE BINDING ENERGY FOR EACH POSSIBLE STATE OF LIGHT Ξ⁻ HYPERNUCLEUS BY USING GAUSSIAN POTENTIAL

State	Calculated results of Binding Energies of Ξ⁻ -^{14}N (MeV)	Binding Energies of Ξ⁻ -^{14}N from the experimental results (MeV)
s (l=0)	4.97	**1.93 ± 0.64**
p (l=1)	**1.93**	
d (l=2)	1.74	
f (l=3)	1.59	

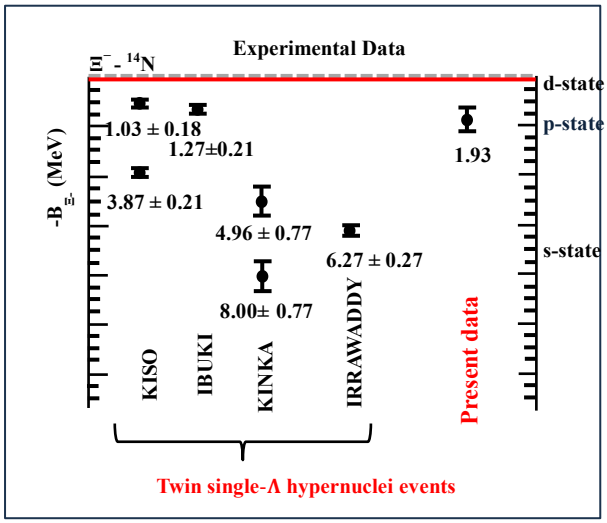

Fig. 3. Schematic diagram of the binding energy of Ξ⁻ hyperon in Ξ⁻ -^{14}N system and the corresponding states.

C. Discussions

In this research work, the binding energies of the Ξ⁻ hypernuclei; Ξ⁻ -^{14}N system and atomic state at which Ξ⁻ hyperon is absorbed by the nucleus have been calculated. Firstly, nonrelativistic Schrödinger equation have been solved by using Gaussian basis wave function and Gaussian potential. Fig. 2 show the Gaussian potential with potential strength, -24 MeV. The interaction range is about 3 fm. The binding energies of Ξ⁻ hyperon in Ξ⁻ -^{14}N system ($^{15}_{\Xi}$C) was also calculated by using Gaussian potential. Table I give the binding energy for each possible state of Ξ⁻ hyperon in Ξ⁻ -^{14}N system by using Gaussian potential. At the potential strength -24 MeV, the binding energy was obtained 1.93 MeV which is consistent within the error of experimental result 1.93 ± 0.64 MeV at p-atomic state. The binding energy values of Ξ⁻ hyperon in Ξ⁻-^{14}N system for twin single-Λ hypernuclei events and our results were shown in Fig. 3 and Table II. It is found that the level state of Ξ⁻ hyperon in Ξ⁻-^{14}N system of the present

data was the same "p" atomic state as the IBUKI event and the KISO event.

TABLE II
THE VALUE OF BINDING ENERGY OF Ξ^- HYPERON IN Ξ^--^{14}N SYSTEM

Event		Reaction	B_{Ξ^-} (MeV)
E373	KISO	$\Xi^- + {}^{14}\mathrm{N} \rightarrow {}^{10}_{\Lambda}Be + {}^{5}_{\Lambda}He$	3.87 ± 0.21 (or) 1.03 ± 0.18
E373	KINKA	$\Xi^- + {}^{14}\mathrm{N} \rightarrow {}^{9}_{\Lambda}Be + {}^{5}_{\Lambda}He + \mathrm{n}$	8.00 ± 0.77 (or) 4.96 ± 0.77
E07	IBUKI	$\Xi^- + {}^{14}\mathrm{N} \rightarrow {}^{10}_{\Lambda}Be + {}^{5}_{\Lambda}He$	1.27±0.21
E07	IRRAWADDY	$\Xi^- + {}^{14}\mathrm{N} \rightarrow {}^{5}_{\Lambda}He + {}^{5}_{\Lambda}He + {}^{4}He + \mathrm{n}$	6.27 ± 0.27
Present data			1.93

IV. CONCLUSION

One of the single-Λ hypernucleus events which was found in plate #6 of module #26 in J-PARC E07 experiment have been analyzed. The reaction process was clearly identified as $\Xi^- + {}^{14}_{7}N \rightarrow {}^{12}_{\Lambda}B + p + \Lambda + n$. The value of the binding energy of Ξ^- hyperon was 1.93 ± 0.64 MeV that observed from difference between Q value and total energy. The binding energy of Ξ^- hyperon in Ξ^--^{14}N system by using Gaussian potential becomes 1.93 MeV which is nearly consistent with our experimental result at p-atomic state. Ξ^- hyperon is absorbed at the p-state by the nucleus in the nuclear emulsion. This level state of Ξ^- hyperon in Ξ^--^{14}N system which is the same as the IBUKI event and the KISO event.

ACKNOWLEDGMENT

I wish to express our warmest thanks to Dr. Su Yin Win, Pro-Rectors, Dr. Hnit Thit Shein, Pro-Rectors and members of ESEJ at the Technological University Mandalay for their kind permission to submit this research paper. I would like to express my gratitude to Professor Dr. Khaing Khaing Thinn, Head of Department of Engineering Physics, Technological University Mandalay for her kind permission.

REFERENCES

[1] S. S. Aye. *et al*., "Determination Type of Hypernucleus from a Single Lambda Hypernucleus Event in Nuclear Emulsion of KEK-E373 Experiment". J. Myanmar Acad. Arts Sci. Vol. XVIII No.2B, 2020.

[2] Htet Htet Wai Moe *et al*., "Analysis of a single-Λ hypernucleus event in J-PARC E07 experiment." University of Mandalay Research Journal, vol. 13, no. 2, pp. 83-89, Dec 2022.

[3] Htet Htet Wai Moe *et al*., "Identification of Level State of Ξ^- hyperon in Ξ^--^{14}N system." University of Mandalay Research Journal, vol. 14, no. 2, pp. 177-186, Dec 2023.

[4] Phyo Wai Wai Lwin *et al*., "Structure analysis of light Ξ^- hypernuclei." University of Mandalay Open Access Repository, 2016.

[5] S. Nandi, "The quantum Gaussian well". arxiv: 1011.3637v1[quant-ph]. Nov 16, 2010.

[6] M. Yoshimoto *et al*., "First observation of a nuclear s-state of a Ξ hypernucleus, ${}^{15}_{\Xi}C$", Prog. Theor. Exp. Phys. **2021** (2021) 073D02.

[7] K. Nakazawa *et al*., "First evidence of a deeply bound state of Ξ^--^{14}N System", Prog. Theor. Exp. Phys. **2015** (2015) 033D02.

[8] S. H. Hayakawa *et al*., "Observation of Coulomb-Assisted Nuclear Bound State of Ξ^--^{14}N System", Phys. Rev. Lett. **126** (2021) 062501.

[9] M. Yamaguchi *et al*., "ΞN and ΞΞ OBEP and Ξ^-- Nucleus Bound States", Prog. Theor. Phys. **105** (2001) 627.

[10] K. T. Tint. *et al*., "Observation of a Be Double- Lambda Hypernucleus in the J-PARC E07 Experiment". Prog. Theor. Exp. Phys. 021D02, 2019.

[11] K. T. Tint. *et al*., (2021). "Observation of Coulomb Assisted Nuclear Bound State of Ξ^--^{14}N System". arXiv: 2010. 14317v3 [nucl-ex].

[12] A. N. L. Nyaw. "Double hypernuclei with nuclear-emulsion detector". D.Sc. Thesis, Gifu University, 2021.

[13] S. H. Hayakawa. "Study of Ξ^- nucleus interaction by measurement of twin hypernuclei with hybrid emulsion method". D.Sc. Thesis, Osaka University, 2019.

[14] H. Takahashi, "Study of Double-Hypernuclei with Hybrid Emulsion Method". D.Sc. Thesis, Department of Physics, Kyoto University, 2003.

Composition of Elements in Sue-La-Na-Phar and Their Utilization

Htike Htike Aung[1], Khaing Mar Htay[2], War War[3]

[1]*Lecturer, Engineering Physics Department, Technological University Mandalay*

[2] *Lecturer, Engineering Physics Department, Technological University Mandalay*

[3] *Lecturer, Engineering Physics Department, Technological University Mandalay*

Email. [1]htikehtikeaung55555@gmail.com, [2]khingmarhtay2018@gmail.com, [3]wwar0441@gmail.com

***Abstract*— The Energy Dispersive X-ray Fluorescence (EDXRF) detection technique examines in *Sue-La-Na-Pha* (*Fumaria Parviflora)* and it is used for traditional medicine. Fundamental Parameter method (FP balance), the composition of elements can be useful to evaluate by the Shimadzu EDX- 700 spectrometer and assessment software. From measurement calcium, silicon, potassium and phosphorus describe as major elements, and chlorine, sulphur and iron show as minor elements. Zinc, manganese, strontium, rubidium, copper and bromine are trace elements. These elements are advantages for human and animal in their daily life. *Sue-La-Na-Pha* is applicable for human health and the usage of each element are presented.**

Keywords— Composition, elements, Sue-La-Na-Pha, calcium, medicine.

I. Introduction

Funaria parviflora, or Sue-La-Na-Pha, is a type of flowering plant. Indian fumitory, fine-leaved fumitory, and fine-leaf fumitory are some of its common names. Although it is common and extensively distributed in many other parts of the world, it is native to Europe, Asia, and Africa and belongs to the Papaveraceae family. It can be weedy at times. The tiny flowers have purple tips and are dull white in colour. Round nutlets with a central crest make up the fruit [1,2].

The entire plant can be used as medication to treat buffalo toxaemia and a number of illnesses such as diabetes [3,4]. It has been an ingredient in about fifty traditional remedies in Myanmar [5].

Sue-La-Na-Pha, Fig. 1 and Fig. 2, were collected from *Law-Ka-Nan-Da*, Mandalay Region and prepared by drying under average thermal condition. The baked samples were crumble and flooring so as to get thin powder by using agate mortar and pestle. Then, the powder sample was analyzed by EDXRF spectrometer to get composition of elements.

Fig 1. *Sue-La-Na-Pha* plant, flowers and fruits

Fig 2. *Sue-La-Na-Pha* plant growing at *Law-Ka-Nan-Da*, Mandalay Region

II. Theoretical Background

Electromagnetic radiation with wavelengths typically ranging from 0.05 to 100 A˙ is known as an X-ray or Roentgen ray. It overlaps with gamma radiation and UV radiation, the former is at the short wavelength end and the later is at the long wavelength end. Wilhelm Conrad Roentgen made the discovery of X-rays in 1895 at the University of Warzbur in Bavaria.

The various interactions occured by the time a beam of X-ray photons keep in touch with matter. These interactions result in an attenuation of the incident X-ray beam's intensity. The photoelectric effect and X-ray scattering are the two fundamental XRF analysis techniques. The three sub-interactions such as X-ray outpouring, the photoelectron emission, and the Auger electron exudation are made up by the photoelectric effect. It is possible for there to be both coherent and incoherent scattering. The composition of sample and these interactions have been distincte by the incident X-ray beam's spectral distribution [6]

When the binding energy of the atom's electron is lower than the incident photon energy E, a photoelectron is decreased in the photoelectric interaction. The atom to become unstable is caused by the removal of a bonded electron, and it must rearrange itself to return to its normal condition. X-ray photons reduce when outer to inner shell are moved by an electron. Either the atom can decrease these X-ray photons or they can be absorbed to expel an auger electron, which is an electron in the outer shell. Each chemical element emits significant the lines of X-ray when radiation stimulâtes chemical element with a higher energy and go through quickly above the element's absorption edge. Each element has a properties spectrum, and there is a distinctly correlation between the atomic number and the characteristic X-ray line of energy in each of the transition series K, L, and M. One can distinguish the element and quantity of an element consists of a sample by evaluating

the energy and intensity of these characteristic lines. X-ray fluorescence spectrometry used in quantitative and qualitative assessment. The analysis is equally useful at high and low concentration levels, and sensitive considerable for the majority of elements attain the low parts per million ranges.

The "fundamental" methods for handling matrix effects in XRF analysis have been established recently. Most scenarios that are reasonably simple can be handled with the fundamental parameters method. Hai Fe has created a quantitative method for EDXRF and used on a desktop PC. It may get almost in every sample coming out of a matrix and produce reliable findings level in situations when there aren't many standards available [7].

The three primary components of the X-ray fluorescence spectrometer are the excitation source, the specimen presentation device, and the X-ray spectrometer. The aim of the excitation source is used the X-ray fluorescence technique to excite the specimen's distinctive X-ray. The device for presenting the specimen allows for the introduction and extraction of the specimen from the excitation position while maintaining the specimen in a precisely defined position during analysis. The different wavelengths or energy of X-rays that the object emits must be separated and counted by the X-ray spectrometer. The set of parts that are utilised to distribute, identify, quantify, and show the spectrum of X-ray photons released by the object is referred to as an X-ray spectrometer [8].

Differential X-rays are excited by radioactive sources and X-ray tubes. In addition to primary energy dispersive systems, secondary target energy dispersive spectrometers also commonly use X-ray tubes. A filament that has a variable current control is heated in an X-ray tube in order to release free electrons. The electrons at the anode (Rh or W) accelerate and then release X-rays. An atom in the sample may absorb X-rays if their energy is high enough, releasing a unique X-ray in the process. The X-ray travels in the direction of the detector after leaving the material. When biassing an X-ray tube, the tube voltage needs to be set higher than the maximum absorption edge energy. Tube voltage ranges from 4 to 50 kV with 1 V increments, while tube current ranges from 0.01 to 0.99 A with 0.01 A increments. In order to minimise background in the energy region, estimate characteristic lines of the X-ray tube that overlap with an element of interest, and transmit X-rays with enough energy for the excitation, filters are occasionally placed between the X-ray tube and the sample [9,10].

III. Sample Preparation

Sue-La-Na-Pha was let to air dry at ambient temperature. An agate mortar and pestle was used to smash and grind the dried sample into a fine powder. It was sufficiently ground to assure measurement reproducibility and to satisfy the requirements for homogeneous dense materials. After that, these powders were put into a steel die and compressed into a pallet using a 3-ton hydraulic press. The pallet has a 2.5 centimetre diameter.

Since uniform fine powder is necessary for the best results in the EDXRF analysis, sample preparation is crucial. Because biological samples are typically heterogeneous, they must be homogenised, powdered, and dried. In X-ray emission spectrometry, sample preparation is crucial to obtaining accurate results.

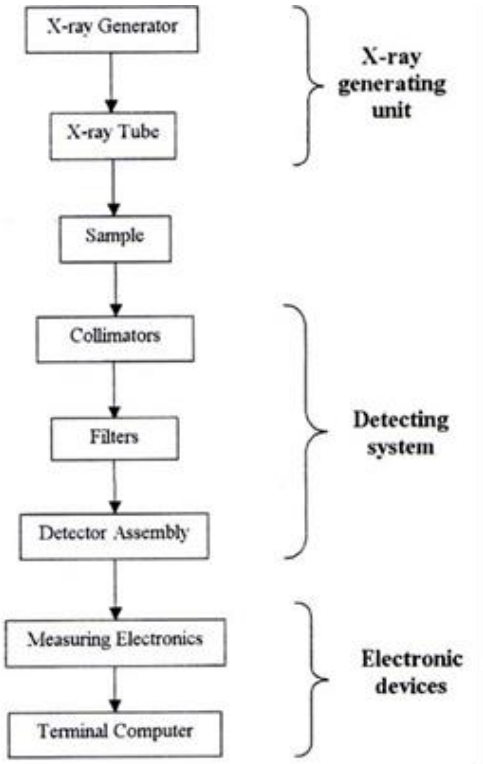

Fig 3. Flow diagram of a sequential EDXRF Analysis

Specimen preparation is crucial procedure before the experiment itself. The flow diagram for a sequential EDXRF analysis is displayed in Fig. 3. The Shimadzu EDX-700 Spectrometer at the University of Yangon's Universities' Research Centre (URC) is shown in Figure 4.

Care must be taken when preparing samples to avoid contaminating grinding equipment. To reduce the impact of particle size, the grinding process needs to be attended to. The following criteria should guide specimen preparation methods: low cost, quick preparation time, simplicity, accuracy, and reproducibility.

The connection between element composition and spectral line intensity depends critically on specimen preparation. This association may be impacted by surface roughness, particle size, shape, homogeneity, distribution, and mineralization variables.

Sue-La-Na-Pha was examined using the Shimadzu EDX-700 energy dispersive X-ray fluorescence (EDXRF) equipment in this study. The elements included in the sample were analysed using the fundamental parameter (FP balance) method. One significant analysis technique is the FP approach. The Shimadzu EDX-700 comes pre-installed with high performance FP software as a result.

Fig 4. Shimadzu EDX-700 Spectrometer are used to analyze the elements at the University of Yangon's Universities' Research Centre (URC)

IV. Results and Discussion

Results from the EDXRF analysis are both quantitative and qualitative. Despite having low resolution, the energy dispersive possesses high counting rates. In vacuum, the measurement time was 100s. During measuring time, some pallets ended in failure because of moisture and loose powder. Therefore, the pallets had to be stored in the desiccators before measuring. From this measurement calcium, silicon, potassium and phosphorus were found as major elements, and chlorine, sulphur and iron as minor elements, and zinc, manganese, strontium, rubidium, copper and bromine as trace elements. The composition of elements in Sue-La-Na-Pha are described in Table 1 and Fig. 5.

TABLE 1. COMPOSITION OF ELEMENTS (%) IN *Sue-La-Na-Pha* USING EDX- 700 SPECTROMETER

Element	Composition (%)
Calcium (Ca)	26.522 ± 5.15
Silicon (Si)	25.923 ± 5.09
Potassium (K)	19.726 ± 4.44
Phosphorous (P)	13.392 ± 3.66
Chlorine (Cl)	7.429 ± 2.73
Sulphur (S)	3.398 ± 1.84
Iron (Fe)	2.168 ± 1.47
Zinc (Zn)	0.437 ± 0.66
Manganese (Mn)	0.279 ± 0.53
Strontium (Sr)	0.246 ± 0.49
Rubidium (Rb)	0.209 ± 0.46
Copper (Cu)	0.161 ± 0.40
Bromine (Br)	0.111 ± 0.33

The elements Mn, Sr, Rb, Cu, and Br are not very noticeable in Fig. 5 because of their extremely minor composition.

Calcium is the most common mineral in the human body which is almost entirely observed in teeth and bones. Paradoxically, physiological processes similar as muscle contraction, keeping a normal heartbeat, sending and receiving nerve signals, releasing hormones and other chemical, clotting blood and protein regulation where calcium is the most of the greatest importance. Calcium may have benefits in protecting against cancer, diabetes and high blood pressure. On the other hand, if calcium deficient in a person's diet, their body will actually draw calcium from their bones, most significant to issues like osteoporosis. The average adult needs 1000mg of calcium per day. The amount of calcium increases to 1200 mg per day for women over the age of 50 and men over the age of 71. Calcium should be taken in the morning (about 1 hour after breakfast) or in the afternoon with plenty of water.

The body needs silicon, and significant trace mineral, for stronger bones (osteoporosis), heart disease, stoke (cardiovascular disease), Alzheimer's disease, more radiant skin, and more flexible and robust joints. A dietary supplement is often used; silicon is recognized to strengthen skin, hair, nails, and connective tissues in addition to bones. This is why it is referred to as the "beauty mineral."

Potassium is a crucial electrolyte. It helps regulate the heartbeat and is essential for electrical signalling in nerves. It reduces the effect of sodium (present in table salt) on blood pressure. It helps move nutrients into cells, and waste products out of cells. People with high blood pressure should aim to eat foods that provide 3500-5000mg of potassium daily. Taking potassium citrate can help prevent kidney stones from reoccurring.

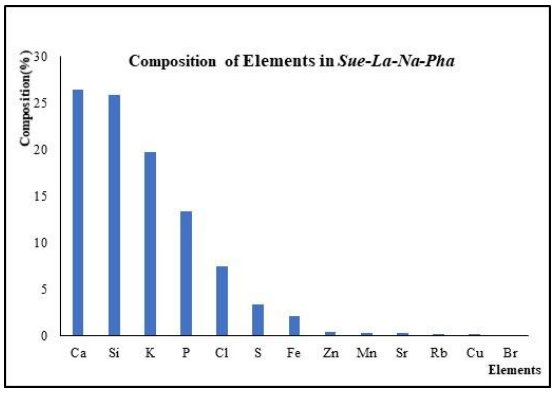

Fig 5. Elemental concentration in *Sue-La-Na-Pha*

Most phosphorus is found in bone, but it is also present in the molecule ATP, which gives cells the energy they need to power chemical operations.

The body often contains chloride, a negative ion, which is the form of chlorine. Keeping the fluid balance normal requires this electrolyte.

Two amino acids that are crucial for giving proteins their structure contain sulphur.

For practically all living things, iron is an essential component of their metabolism. Haemoglobin, the oxygen carrier in red blood cells, also contains it. Less than half of women's diets contain enough iron.

For all living organisms, zinc is a trace element that is necessary. "Zinc fingers" are structural elements found in several proteins that aid in gene regulation. In poorer nations, dwarfism has been linked to zinc deficiency.

Manganese is necessary for several enzymes, especially those that shield the mitochondria, the area inside cells where useful energy is produced, from harmful oxidants.

As an electron donor in a variety of biological processes, copper is essential. Iron cannot function well in the body if there is not enough copper.

The lack of strontium resulted in a worsening of tooth and bone calcification as well as an increased risk of carious teeth. One of the most prevalent and possibly dangerous radioactive byproducts of nuclear fission is ^{90}Sr, and plants are better at absorbing strontium than animals are. Because strontium is eliminated preferentially, particularly in the urine, it offers some protection against ^{90}Sr.

Adjoining cesium (Cs) or rubidium (Rb) to a low-potassium diet aid rats improve commonly in a short period of time, keep away from the damage typical of potassium insufficient meager.

Mice and chicks increase rapidly by the time exposed to bromine. It does not turn aside goiter, and if iodine is reintroduced into the diet, it is quickly restored. Bromine absorbed more than a third of the iodine in the thyroid gland.

Quantitative data caused by the EDX-700 software for this study is built only on the mass of inorganic components available in 100% of the sample of absorption. Organic compounds and dark matrix elements are not examined. This indicates that the data display the relative elemental composition found in the analysis sample.

V. Conclusion

Thirteen (13) elements in Sue-La-Na-Pha was analyzed by the Energy Dispersive X-ray Fluoresence (EDXRF) detection technique. Calcium, silicon, potassium and phosphorus are the most abundant elements, chlorine, sulfur and iron as less common elements and zinc, manganese, strontium, rubidium, copper and bromine are trace elements. Thus, Sue-La-Na-Phar is used in medicinal treatment material for human. Calcium in Sue-La-Na-Phar has many benefits for healthcare. Silicon in Sue-La-Na-Phar is mainly useful for Alzheimer's disease and osteoporosis. The pros of potassium in Sue-La-Na-Phar are prevent kidney stones, sodium effect on blood pressure and nutrients into cells.

Acknowledgments

I would like to thank the ESEJ team members, the Technological University (Mandalay).

References

[1] "Glossary of Indian Medicinal Plants," A. N. Chopra, S. L. Nayar, and I. C. Chorpra, Council of Scientific and Industrial Research, New Delhi, 1956.

[2] African Journal of Food Science, vol. 4, no. 5, pp. 200–222, May 2010. K. O. Soetan, C. O. Olaiya, and O. E. Oyewole, "The Importance of Mineral Elements for Humans, Domestic Animals, and Plants: A Review."

[3] Buffalo Bulletin, vol. 33, no. 4, pp. 350-354, 2014; A. Shakoor, A. Hussain, T. Abbas, S. A. Muhammad, and M. Kashif, "The Comparative Efficacy of Three Indigenous Plants (Fumaria Parviflora, Artemesia Maritima, and Swertia Chirata) Alone or in Combination for the Treatment of Toxaemia in Buffaloes."

[4] "Hypoglycemic Activity of Fumaria Parviflora in Streptozotocin-Induced Diabetic Rats," by F. Fathiazad, S. Hamedeyazdan, M. Karim Khosropanah, and A. Khaki, Advanced Pharmaceutical Bulletin, vol. 3, no. 1, pp. 207–210, 2013.

[5] ဦးစည်သူ (သုခချမ်းသာ)။ "စူလာနဖာဂယက်နှင့် နောက်ဆက်တွဲ ဆေးနည်းများ" (ဒုတိယအကြိမ်)၊ အလင်းသစ် စာပေ၊ ရန်ကုန်မြို့၊ ၂၀၀၉ ခုနှစ်၊ မေလ။

[6] "An Introduction to X-ray Spectroscopy: An Introduction," by B. K. Agarwal Springer- Verlag, Berlin, 1979.

[7] "Gamma and X-ray Spectroscopy with Semiconductor Detectors," K. Deberlin and R. G. Helmer,North-Holland, , New York, 1998.

[8] Shimadzu Co., Tokyo, EDX-700 Manual, 2002.

[9] Hand Book of X-Ray Spectroscopy, R. E. V. Grieken and A. Markowicz, London: Dekker, 1993.

[10] S. Norton, "Quantitative Assessment of Mast Cells Breakdown via Compound," 48/80. Ed. *J. Pharmacol*, vol. 2, 1964.

Characteristics of (π^+, K^+) and (K^-, π^-) Reactions for Λ Hypernuclear Production

Khaing Mar Htay[1], War War[2], Htike Htike Aung [3]

[1] *Lecturer, Engineering Physics Department, Technological University Mandalay*

[2]*Lecturer, Engineering Physics Department, Technological University Mandalay*

[3]*Lecturer, Engineering Physics Department, Technological University Mandalay*

Email: [1]khingmarhtay2018@gmail.com, [2] warwaar0441@gmail.com, [3]htikehtikeaung55555@gmail.com

***Abstract*—The primary purpose of the research is to determine the backward momentum transfer of Λ hyperon as based on the incident momentum for $n(\pi^+, K^+)\Lambda$ reaction at various scattering angles. As a result of the reaction, the hyperon replaces the nucleon in this system. Initially, the threshold energy is calculated to ensure the momentum transfer of the hyperon. Later on, the momentum transfer of Λ hyperon is calculated at different scattering angles to the $n(\pi^+, K^+)\Lambda$ reaction. In addition, it was calculated the momentum transfer of Λ hyperon for $n(K^-, \pi^-)\Lambda$ with various discrete angles. The results show that the calculated hypernuclear recoil momentum transfer matches the experimental results at angles of $0^\circ, 5^\circ and\ 10^\circ$ respectively.**

Keywords—threshold energy, Λ hyperon recoil momentum, algebra method, endothermic reaction, exothermic reaction.

I. Introduction

Hyperons are baryons heavier than nucleons and consisting of one or more strange quarks. They have a lifetime of the order of 10^{-10}s and they decay weakly while their formation time is 10^{-23}s which is typical for strong interaction. All hyperons are fermions. That is they have half-integer spin and obey Fermi-Dirac statistics. There are four types of hyperon; lambda(Λ), sigma (Σ) , Xi (Ξ) and omega (Ω) . The lambda baryon $\Lambda^0$was first discovered in October 1950, by V.D. Hopper and S. Biswas of the University of Melbourne, as a natural Λ particle with a proton as a decay product, thus correctly distinguishing it as a baryon [1]. The Λ hyperon is an isospin singlet of strangeness -1. The mean lifetime of the lambda is found to be $2.517 \pm 0.024 \times 10^{-10}$s. The quark structure of lambda is u(up), down(d), and s(strange) quarks. The $\sum$ hyperon occurs as an isospin triplet of baryons Σ^+, Σ^0, Σ^- the masses of which increase as the charge becomes more negative:1189.42 MeV, 1192.52 MeV, and 1197.37 MeV respectively[2]. They all have strangeness -1, spin $^1/_2$ and baryon number 1. The quark structure of Σ^+, Σ^0, $\Sigma^-$are uus, uds, and dds quarks. Lambda also known simply as lambda particle or lambda baryon is a type of subatomic particle classified as a baryon. Baryons are a family of elementary particles composed of three quarks held together by the strong nuclear force. The lambda hyperon consists of three quarks, two "up" quarks (u) and one "down" quark (d). Its quark composition is denoted as uud. The mass of a lambda is approximately 1.115683 amu (atomic mass units) [3].

II. Momentum Matching

To create a hypernucleus, the hyperon produced by reaction with the nucleon of the target must be inside the nucleus. This probability called the sticking probability is dominated by the momentum tuning of the reaction, particularly the magnitude of the momentum transfer to the hyperon. If the momentum transfer q_Y is much greater than the nuclear Fermi momentum, the hyperon will likely remain in the nucleus and escape normally. Conversely, when q_Y is very small, the probability of sticking is high. This means that the hyperon is more likely to remain in the position of the original nucleon.

A. Calculation of Threshold Energy for Reaction

In this reaction process, an incoming particle interacts with a stationary target particle, and the resulting product particle is positioned as shown in Fig.1.

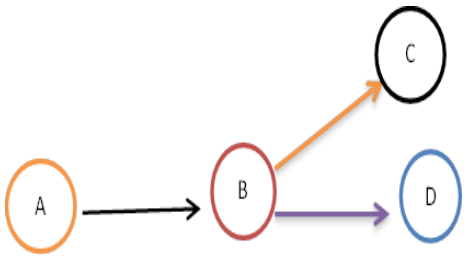

Fig.1. Decay process for $A + B \rightarrow C + D$ reaction

Before the crash in a laboratory setting, the total momentum for four vectors.

$$\vec{P}_{total} = \left(\frac{E_{total}}{c}, \vec{P}_{total}\right) \quad (1)$$

$$\vec{P}_{total} = \left(\frac{E_{K^-}}{c} + m_n c, \vec{P}_{K^-}\right) \quad (2)$$

After the collision, in the frame of the center of mass, all particles are at rest, a total of four-momentum vectors

$$P'_{total} = \left(\frac{E'_{total}}{c}, \vec{P}_{total}\right) \quad (3)$$

$$P'_{total} = \left((m_{\pi^-} + m_\Lambda)c, 0\right) \quad (4)$$

For any frame the square of the four-momentum is invariant,

$$P_{total}^2 = P'^2_{total} \tag{5}$$

$$P_{total}^2 = \left[\left(\frac{E_{K^-}}{c} + m_p c\right)^2 - \left|\vec{P}_{K^-}\right|^2\right] \tag{6}$$

$$P_{total}^2 = \left[\frac{E_{K^-}^2}{c^2} + m_n^2 c^2 + 2\frac{E_{K^-}}{c} m_n c - \left|\vec{P}_{K^-}\right|^2\right] \tag{7}$$

$$\left[\frac{E_{K^-}^2}{c^2} + m_n^2 c^2 + 2\frac{E_{K^-}}{c} m_p c - \frac{E_{K^-}^2}{c^2} + m_{K^-}^2 c^2 = (m_{\pi^-} + m_\Lambda)^2 c^2\right] \tag{8}$$

$$E_{K^-} = \left[\frac{(m_{K^-} + m_\Lambda)^2 - m_n^2 - m_{K^-}^2}{2m_n}\right] c^2 \tag{9}$$

The above equation is threshold equation.

B. Calculation of Λ Recoil Momentum for $n(K^-, \pi^-)\Lambda$ Reaction

In the (K^-, π^-) reaction, the elementary process is $K^- + n \rightarrow \pi^- + \Lambda$ and when Λ is released it is attached to the nucleus ${}^{A}_{\Lambda}X$.

By the law of conservation of energy, the (K^-, π^-)reaction is written as follows,

$$E_n + E_{K^-} \rightarrow E_\Lambda + E_{\pi^-} \tag{10}$$

$$E = \sqrt{P^2c^2 + m^2c^4} \tag{10a}$$

Equation (10) becomes

$$\sqrt{P_{K^-}^2 c^2 + m_{K^-}^2 c^4} + m_n c^2 = \sqrt{P_\Lambda^2 c^2 + m_\Lambda^2 c^4} + \sqrt{P_{\pi^-}^2 c^2 + m_{\pi^-}^2 c^4} \tag{11}$$

By the law of momentum conservation,

$$\vec{p}_{K^-} + \vec{p}_n = \vec{p}_{\pi^-} + \vec{p}_\Lambda \tag{12}$$

Since the target is rest, equation (12) can be expressed as

$$\vec{p}_{K^-} = \vec{p}_{\pi^-} + \vec{p}_\Lambda$$

$$\vec{p}_\Lambda = \vec{p}_{K^-} - \vec{p}_{\pi^-}$$

$$p_\Lambda^2 = p_{K^-}^2 + p_{\pi^-}^2 - 2p_{K^-}p_{\pi^-}cos\theta$$

$$p_\Lambda = \sqrt{p_{K^-}^2 + p_{\pi^-}^2 - 2p_{K^-}p_{\pi^-}cos\theta} \tag{13}$$

Let $2p_{K^-}cos\theta = D$,

$$p_\Lambda^2 = p_{K^-}^2 + p_{\pi^-}^2 - Dp_{\pi^-}$$

Equation (12) is becomes,

$$\sqrt{p_{K^-}^2 + m_{K^-}^2} + m_n = \sqrt{p_{\pi^-}^2 + m_{\pi^-}^2} + \sqrt{p_{K^-}^2 + p_{\pi^-}^2 - Dp_{\pi^-} + m_\Lambda^2}$$

Let $A = \sqrt{p_{K^-}^2 + m_{K^-}^2} + m_n$

$$A = \sqrt{p_{\pi^-}^2 + m_{\pi^-}^2} + \sqrt{p_{K^-}^2 + p_{\pi^-}^2 - Dp_{\pi^-} + m_\Lambda^2} \tag{14}$$

Let $B = \sqrt{p_{K^-}^2 + m_\Lambda^2}$

$$A = \sqrt{p_{\pi^-}^2 + m_{\pi^-}^2} + \sqrt{B + p_{\pi^-}^2 - Dp_{\pi^-}}$$

$$A - \sqrt{p_{\pi^-}^2 + m_{\pi^-}^2} = \sqrt{B + p_{\pi^-}^2 - Dp_{\pi^-}}$$

Squaring both side,

$$A^2 + P_{\pi^-}^2 + m_{\pi^-}^2 - 2A\sqrt{m_{\pi^-}^2 + P_{\pi^-}^2} = B - DP_{\pi^-} + P_{\pi^-}^2$$

$$A^2 + m_{\pi^-}^2 - 2A\sqrt{m_{\pi^-}^2 + P_{\pi^-}^2} = B - DP_{\pi^-} \tag{15}$$

Let $G = A^2 + m_{\pi^-}^2$

$$G - 2A\sqrt{m_{\pi^-}^2 + P_{\pi^-}^2} = B - DP_{\pi^-}$$

$$G - B + DP_{\pi^-} = 2A\sqrt{m_{\pi^-}^2 + P_{\pi^-}^2} \tag{16}$$

Let H = G-B

$$H + DP_{\pi^-} = 2A\sqrt{m_{\pi^-}^2 + P_{\pi^-}^2}$$

Squaring both side,

$$H^2 + D^2P_{\pi^-}^2 + 2HDP_{\pi^-} = 4A^2(P_{\pi^-}^2 + m_{\pi^-}^2)$$

$$H^2 + D^2P_{\pi^-}^2 + 2HDP_{\pi^-} = (4A^2P_{\pi^-}^2 + 4A^2m_{\pi^-}^2)$$

$$H^2 + D^2P_{\pi^-}^2 + 2HDP_{\pi^-} - (4A^2P_{\pi^-}^2 + 4A^2m_{\pi^-}^2) = 0$$

$$(D^2 - 4A^2)P_{\pi^-}^2 + 2HDP_{\pi^-} + H^2 - 4A^2m_{\pi^-}^2 = 0$$

Let $X = (D^2 - 4A^2)$, $Y = 2HD$ and $Z = H^2 - 4A^2m_{\pi^-}^2$ (17)

$$\therefore XP_{\pi^-}^2 + YP_{\pi^-} + Z = 0$$

$$P_{\pi^-} = \frac{-Y \pm \sqrt{Y^2 - 4XZ}}{2X} \tag{18}$$

Substituting equation (18) into equation (12) gives the numerical values of the recoil momenta of Λ hyperon, by using the FORTRAN program.

III. Results and Discussion

A. Momentum transfer of $n(\pi^+, K^+)\Lambda$ reaction

In 1980, Thiesse and Dover et.al., proposed the (π^+, K^+) reaction as an efficient method for the spectroscopic studies of heavy hypernuclei. This (π^+, K^+) reaction provides extensive spectroscopic information on Λ hypernuclei bound states, as has been done in experiments at BNL and KEK. The original process involved is $\pi^+ + n \rightarrow K^+ + \Lambda$, which produces two odd particles, K^+ and Λ simultaneously, hence referred to as correlated production. The (π^+, K^+) reaction is notable for its large momentum transfer, reaching 350MeV/c, comparable to the Fermi momentum.

The momentum transfer for endothermic reaction (π^+, K^+) was determined through equation (18) using Fortran Code. Fig .2 illustrates the momentum transfer for this reaction across various projectile momenta. Remarkably, the maximum momentum transfer occurs at the threshold of the reaction and marks the onset of hyperon production. In this reaction, the reversal speed of the hyperon exceeds the Fermi momentum ($P_F \approx 280$ MeV/c). In addition, an increase in projectile momentum is associated with a decrease in hyperon recoil momentum. The experimental results shown in Fig. 2 are in close agreement with the theoretically calculated momentum transfer $n(\pi^+, K^+)\Lambda$ reaction. Therefore, it can be concluded that the theoretical findings validate the experimental results.

B. Momentum Transfer of $n(K^-,\pi^-)\Lambda$ Reaction

The $n(K^-,\pi^-)\Lambda$ reaction is an exothermic reaction (positive Q value). (K^-,π^-) can be reactive without the need to provide the threshold energy. Therefore, the product momentum transfer of Λ was found at zero incident momentum. After that, the momentum transfer is zero at incident momentum of 530MeV/c and recoiless Λ hyperon production is observed for this reaction. The product momentum of Λ is found to increase with the increasing momentum of the incident K^- as shown in fig.7,the formation of Λ hypernucleus can be studied by selecting incident velocities and scattering angles where the incident velocity is greater than 530Mev/c for scattering angles the $n(K^-,\pi^-)\Lambda$ reaction favors substitution state according to its small momentum transfer. By choosing the incident momentum and scattering angles, the formation of Λ hypernucleus can be observed.

For this reaction, the hyperon product momentum is found to be lower the Fermi momentum ($P_F \approx 280$ MeV/c). Fig.7 shows that the momentum transfer of $n(K^-,\pi^-)\Lambda$ reaction was found experimental result. Therefore, it was found that theoretically results also agreed with the experimental results.

C. Momentum Transfer of Λ hyperon

The elementary process is $n(\pi^+,K^+)\Lambda$ reaction which produces a hyperon on the nucleon target. To produce a hypernucleus, the hyperon resulting from a reaction on a nucleon of the target has to stay inside the nucleus. If the momentum transfer is too large compared to the nuclear Fermi momentum, the hyperon will have little chance to stick to the nucleus and will usually leave. The probability of sticking should be high and the hyperon will retained the state of the original nucleon. The $n(\pi^+,K^+)\Lambda$ reaction is an endothermic reaction, and threshold momentum for reaction $n(\pi^+,K^+)\Lambda$ reaction is about 1040 MeV/c. The variation of momentum transfer to Λ hyperon with the projectile momentum for scattering angle $\theta = 5°, 10°$ are displayed in Fig.4 and Fig.5. Fig.6 was shown the momentum transfer of Λ hyperon for various scattering angles. According to this graph, the greater the momentum of the projectile, the higher the momentum transfer is to Λ hyperon for scattering angle $0°, 5° and 10°$. However, the momentum transfer to Λ hyperon is maximum at the threshold momentum and comes down to the constant value as the projectile momentum increases for scattering angles $\theta = 0°$.The transferred momenta to Λ hyperon for all scattering angles are larger than the Fermi momentum.

The variation of momentum transfer to Λ hyperon with the projectile momentum for scattering angle $\theta = 5°, 10°$ are displayed in Fig.9 and Fig.10. Fig.11 was shown the momentum transfer of Λ hyperon for various scattering angles. According to this graph, the greater the momentum of the projectile, the lower the momentum transfer is to Λ hyperon for scattering angle $0°, 5° and 10°$. The transferred momenta to Λ hyperon for all scattering angles is smaller than the Fermi momentum.

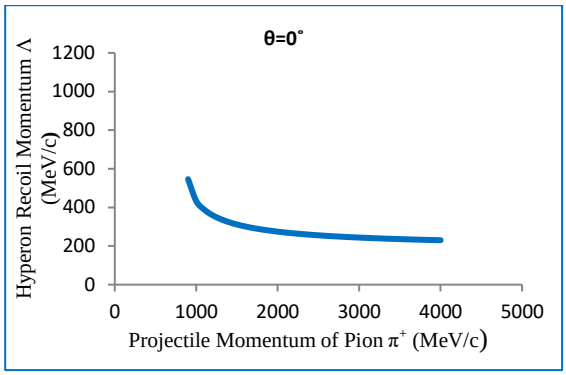

Fig.2. Hyperon momentum transfer (Λ) vs momentum of (π^+) at θ =0°.

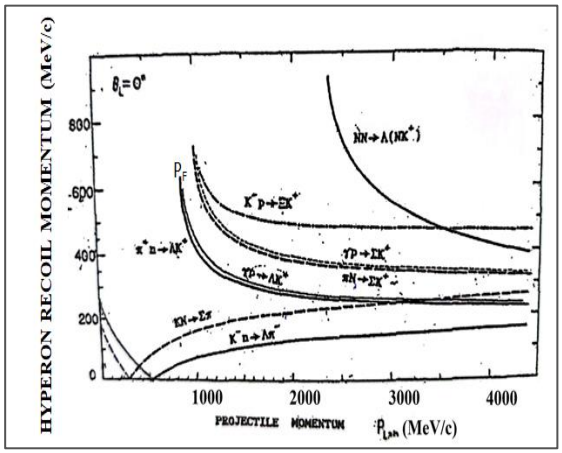

Fig.3.The momentum q_Y transferred to the hyperon Y as a function of the projectile momentum $P_{proj=}\ P_\alpha$ in the reaction $\alpha N \rightarrow Yb$ at $\theta_{bl=0°}$[4].

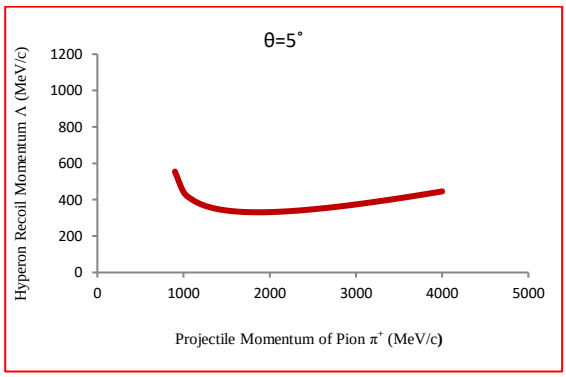

Fig.4. Hyperon momentum transfer (Λ) vs momentum of (π^+) at θ =5°

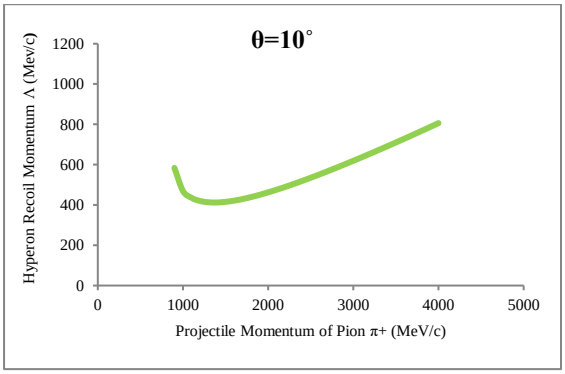

Fig.5. Hyperon momentum transfer (Λ) vs momentum of (π^+) at $\theta = 0°$

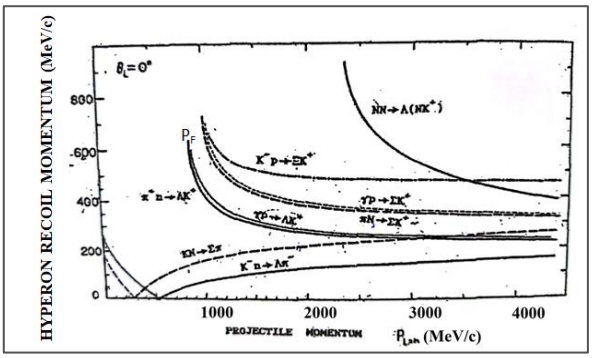

Fig.8. The momentum q_Y transferred to the hyperon Y as a function of the projectile momentum $P_{proj=}\ P_\alpha$ in the reaction $\alpha N \rightarrow Yb$ at $\theta_{bl=0°}$[4].

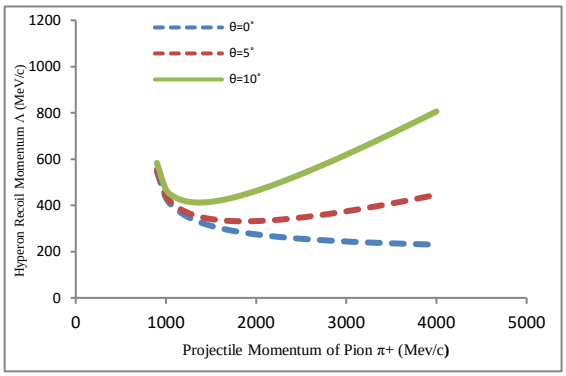

Fig.6. Hyperon momentum transfer (Λ) versus the projectile momentum for $n(\pi^+, K^+)\Lambda$ with scattering angles.

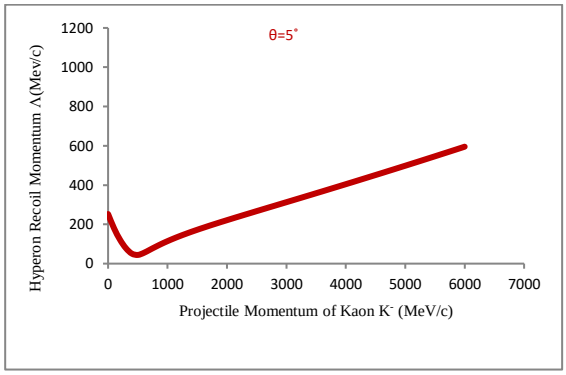

Fig.9. Hyperon momentum transfer (Λ) vs momentum of (K^-) at $\theta = 5°$.

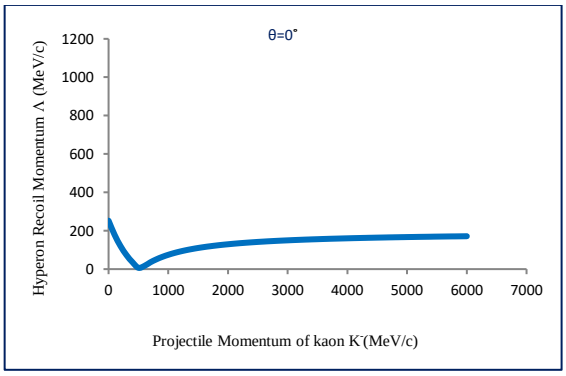

Fig.7. Hyperon momentum transfer (Λ) vs momentum of (K^-) $at\ \ \theta = 0°$.

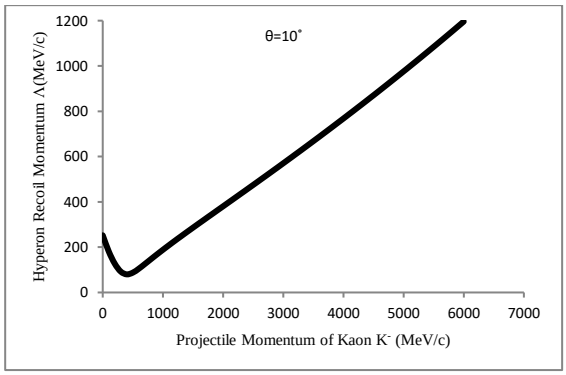

Fig.10. Hyperon momentum transfer (Λ) vs momentum of (K^-) at $\theta = 10°$.

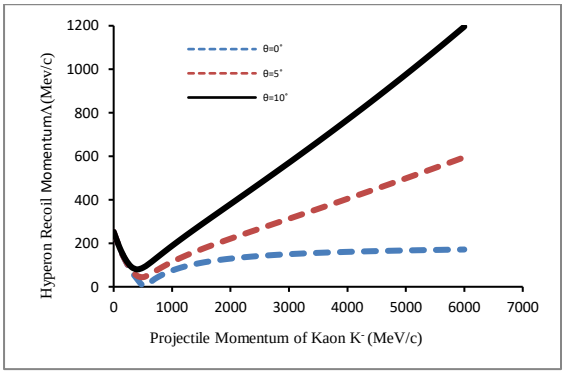

Fig.11. The (Λ) momentum transfer versus the projectile momentum for $n(\mathrm{K}^-,\pi^-)\Lambda$ with scattering angles.

IV. Conclusion

In this research, the variation of momentum transfer to the Λ hyperon from $n(\pi^+,\mathrm{K}^+)\,\Lambda$ reaction has been investigated. The momentum transfer to Λ hyperon is maximum the threshold momentum and comes down to the constant value as the projectile momentum increases for various scattering angles. This study demonstrates that shows that the momentum transfer of hypernuclei is greater than Fermi level at angles $0^\circ, 5^\circ$ and 10°. In this$n(\pi^+,\mathrm{K}^+)\,\Lambda$ reaction, Λ hyperon was found decay. In this calculation, the momentum transfer to the Λ hyperon from $n(\mathrm{K}^-,\pi^-)\Lambda$ reaction has been investigated. This research work, show that the momentum transfer of hypernuclei is lower than Fermi level at angles $0^\circ, 5^\circ$ and 10°.Then, the Λ hypernuclear was found bound state. Therefore, the calculated results agree with experimental results.

Acknowledgment

The author would like to thank Dr Khaing Khaing Thinn, Professor and Head of Physics Department, Technological University Mandalay for her encouragement. I am grateful to Professor Dr Sandar Min, Department of Physics, Yadanabon University .

References

[1] V.D. Hopper and S.Biswas,"Evidence concerning the existence of the new unstable elementary neutral particle", Rev.80 (1950) 1099. [online] https://journals. aps.org/pr/abstract/10.1103/phys

[2] Yin Yin Nu"Characteristics of Some elementary process for Hypenuclear Production"10Vol. [online] www.bmwuni.edu.mm

[3] L.S.Hughes, Elementary Particles (1930).

[4] H. Bando *et al* "Production Structure and Decay of Hypernuclei" 5V1, (1990).

Study of Soil Samples from Peanut Farms in Uyintaw Village at Amarapura Township

Maw Maw San[1], Aye Mar Khin[2], Sandar Oo[3]

[1]*Leacture, Engineering Physics Department, Technological University (Sagaing)*

[2]*Associated Professor, Engineering Physics Department, Technological University (Mandalay)*

[3]*Tutor, Engineering Physics Department, Technology University (Sagaing)*

Email: [1]mawmawsan222.@gmail.com, [2]yccdawayemarkhin@mail.com, [3]sandarsgg997@mail.com

***Abstract*— There is a lot of cultivated land in Uyintaw village, Amarapura Township. The problem for modern agriculture is the physical and chemical condition of the soil layer rather than the natural fertility. Therefore, it is necessary to systemically evaluate the soils from different peanut plantations. In this study, three soil samples were collected from three peanut farms in Uyintaw village, Amarapura township in early November 2021. After that, the second sampling was done at the end of January 2022. pH of the soil: moisture appearance bulk density; porosity, organic carbon percentage physicochemical parameters such compost percentage were determined. According to the data, the pH of the soil from this farm was found to be slightly acidic in 2021. However, they become slightly alkaline in 2022. Soil moisture were found to be higher than in 2021 than those of year 2022. The organic carbon concentration of the soil is the same in the two periods. Also, Bulk density and porosity were found to agree with the value of plant growth is limited.**

Keywords—organic carbon, bulk density, porosity percent, macronutrients

I. INTRODUCTION

Uyintaw village is situated in Amarapura Township, Mandalay region. It is bounded by Ayeyarwady river in the west, Chanmyathazi township in the north, and the ancient capital site of Ava (Inwa) in the south [7]. Uyintaw village is 3.5 miles far away from Mandalay and along the river bank in Amarapura township, vegetable trees and fruit trees are grown on a market scale. During the rainy season, peanut fields are flooded, and after the monsoon, they are irrigated. Compared to the unirrigated dry lands of the nearby desert, they are considered arid irrigated lands because of their high productivity. In modern agriculture, the lack of natural fertilizers is no longer a problem, and the necessary plant nutrients can be added as manure, although there are practical difficulties in how to apply them in some tropical soils. There are various constraints that prevent high crop yields: e.g. soil salinity and alkalinity; weather or short growing season due to flooding to limited drainage; hard pans appear: during the monsoon season. The water of the Ayeyarwaddy river is submerged, so the peanuts are wet. The grass flooded. And then as the river receded, the locals various crops, especially peanuts, a variety of crops such as fruit trees.

II. MATERIALS AND METHODS

A. Study of Some Physicochemical Properties of Soils Sample from Peanut areas in Uyintaw village

The three samples from different peanut farms were started in year of November 2021 and in January 2022. Sampling location of soil from peanut areas are as shown in table I and Fig. 1(a),(b), and(c).

I. SAMPLE LOCATION OF SOIL FROM PEANUT FARMS

No.	Sample	Location	
		Longitude	Latitude
(i)	S1	96.1619 E	21.9414 N
(ii)	S2	96.0502 E	21.9416 N
(iii)	S3	96.1599 E	21.9396 N

Fig. 1. (a) Sampling location (S1).

Fig. 1. Sampling location (S2).

Fig 1.(c) Sampling location (S3).

Three soil samples were collected from peanut farms using a cross pattern, which is an iron mining method. The depth was 20-25 cm [1]. In addition to determining the moisture content of the soil, each soil sample brought to the laboratory was spread on an aluminum tray and stones, removed the root fragments and unnecessary material left behind. Mix the collected soil samples with clean paper towels and the composite samples were reduce waste by coming together to the retain approximately 500 g of composite samples individually. Each sample was stored in polyethylene bag with appropriate description. A base for developing fresh surfaces samples were mixed during incubation to reveal fresh surfaces [4]. After the air-drying, the soil samples gently crush with the 2 mm sieve in a mortar and pestle sieve. Then, the above -mentioned biochemistry parameters were applied to agriculture, it was determined by traditional method in the Laboratory of the Department of Livestock and Ministry of Land Use.

III. Results And Discussion

A. *pH, Moisture, Organic Carbon percent, and Humus percent of Soil from Different Farms*

Table II and Fig. 2 depict pH values of the soil samples from peanut farms for 2021 and 2022. Peanuts from different farms over the years, the pH value of (5.35-5.52) was illustrated. pH in 2021 a few substances were found. However, in 2022 pH values of those were getting nearly neutral, (5.89-6.51). However, both values of pH in two times were acceptable for many plants, particularly oil crops.

II. pH Values of Soil from Peanut Farms

No.	Sample	pH	
		2021	2022
(i)	S1	5.35	6.13
(ii)	S2	5.32	6.51
(iii)	S3	5.52	5.89

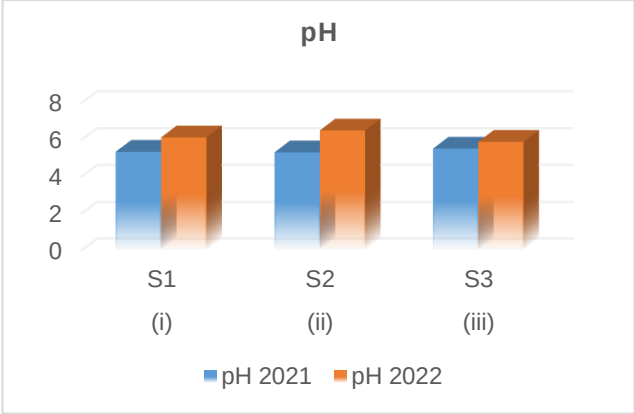

Fig. 2. pH values of Soil from Peanut Farms.

Table III and Fig. 3 (a), (b), and (c) denote moisture percentage of soil samples; organic carbon and humus percentage in two times. Other range of above values in two times are as follows: moisture percent (6.31-8.42) % and (2.81-3.27)%, organic carbon percent (1.79-1.89)% and (1.78-1.80)%, humus percentage were found, in the same distance; (2.29-2.49)%. Organic carbon and humus were found in the soil samples. These values are below for the plant growth so natural fertilization may be carried out occasionally. The both values of moisture in two times were significantly different. Very few in 2022. This may be due to nearly harvesting period of peanut plants.

III. Moisture Percent, Organic Carbon and Humus Percent of Soil from Peanut Farms

No.	Sample	Moisture %		Organic Carbon%		Humus%	
		2021	2022	2021	2022	2021	2022
(i)	S1	7.97	2.81	1.79	1.78	2.29	2.29
(ii)	S2	6.31	2.94	1.89	1.87	2.49	2.42
(iii)	S3	8.42	3.27	1.84	1.80	2.37	2.49

<4.00% low, 4.00-10.00% Medium, >10.00% High organic carbon
4.20-6.00% High humus content
2.00-4.20% Medium Humus content [2]

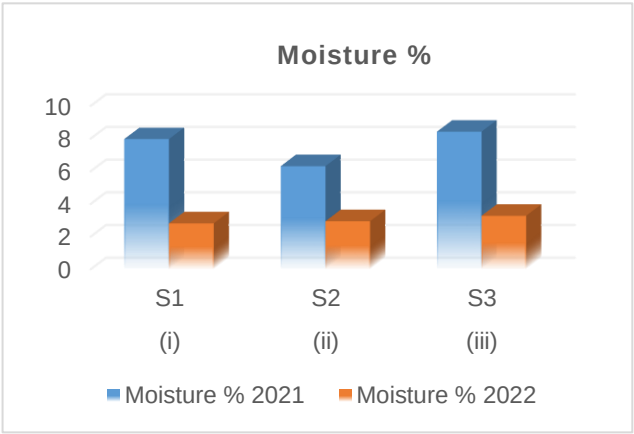

Fig. 3. (a) Moisture percent of Soil from Peanut Farms.

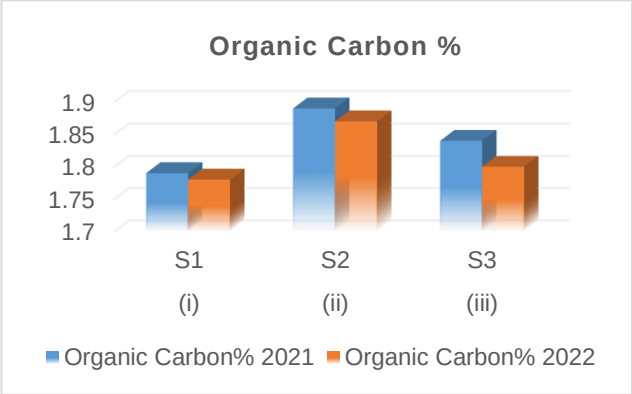

Fig. 3. (b) Organic Carbon percent of Soil from Peanut Farms.

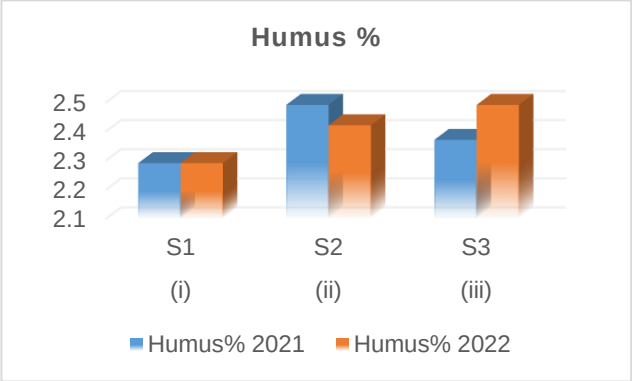

Fig. 3. (c) Humus percent of Soil from Peanut Farms.

B. Bulk Density Percent and Porosity Percent of Soil from Different Peanut forms

Table IV and Fig. 4 show the Bulk density percentage of three soil samples at two times. The range: (1.23-1.45) g/cm^3 and (0.98-1.45) g/cm^3 in 2021 and 2022. Lower values were found in 2022. They were found to limit the value of the plant grows.

IV. BULK DENSITY OF SOIL FROM PEANUT FARMS

No.	Sample	Bulk Density g/cm^3	
		2021	2022
(i)	S1	1.23	1.45
(ii)	S2	1.23	0.98
(iii)	S3	1.45	1.35

Permissible limit 1.60 g/cm^3 [3]

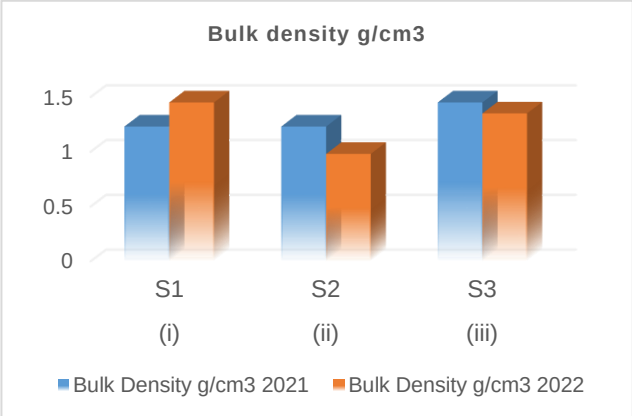

Fig. 4. Bulk density of Soil from Peanut Farms.

Table V and Fig. 5 show porosity percentage of soil samples in the range of (47.22-48.72) % and (45.95-47.30) % in 2021 and 2022. Higher values in 2021 were found. Bulk density and porosity percent are negatively correlated to each other. They are for plant growth, good porosity is found [4].

V. POROSITY OF SOIL FROM PEANUT FARMS

No.	**Sample**	**porosity %**	
		2021	**2022**
(i)	S1	47.22	46.95
(ii)	S2	48.72	45.95
(iii)	S3	47.92	47.30

30.00-40.00%; low
40.00-45.00%: moderate
45.00-50.00% high [2]

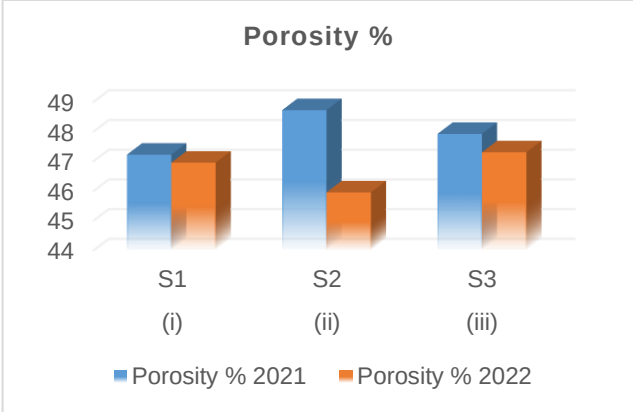

Fig. 5. Porosity percent of Soil from Peanut Farms.

C. Nitrogen Percent, Phosphorus and Potassium contents of Soil From Peanut Farms

Table VI and Fig. 6 denote the nitrogen percentage of soil samples at both periods. The value was found (0.17-0.23)% in two periods. The percentage of nitrogen is low in two periods. Moderate fertilization and timely schedule must be applied.

VI. NITROGEN PERCENT OF SOIL FROM PEANUT FARMS

No.	**Sample**	**Nitrogen (%)**	
		2021	**2022**
(i)	S1	0.17	0.23
(ii)	S2	0.23	0.23
(iii)	S3	0.23	0.10

< 0.150% low
0.15-0.250% medium
>0.250% high [5]

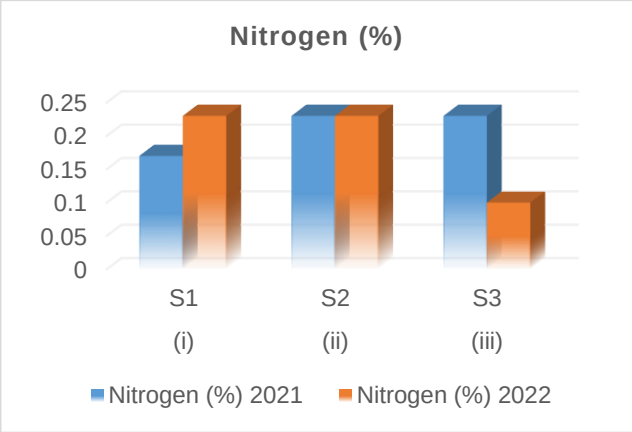

Fig. 6. Nitrogen percent of Soil from Peanut Farms.

Table VII and Fig. 7 show that the phosphorus content of the soil samples was detected at both times. It was from (20.38-21.96) ppm and (20.19-20.82) ppm respectively. High levels of phosphorus were found in soil samples during both periods. This may be due to the number of perennials in these areas.

VII. PHOSPHOROUS OF SOIL FROM PEANUT AREAS

No.	Sample	Phosphorus(ppm)	
		2021	2022
(i)	S1	20.38	20.19
(ii)	S2	20.91	20.76
(iii)	S3	21.96	20.82

>12 ppm high phosphorous
8-11 ppm medium phosphorous
4-7 ppm low phosphorous [5]

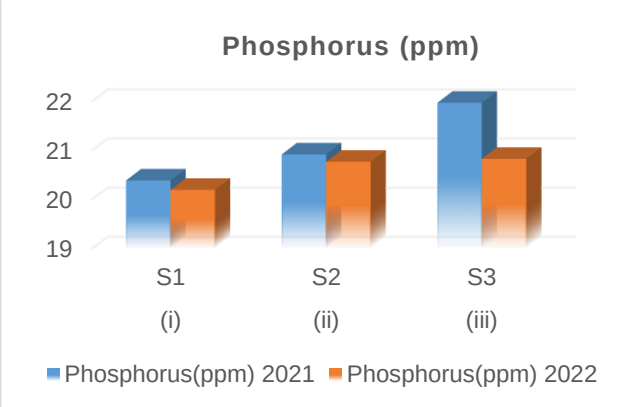

Fig. 7. Phosphorus of Soil from Peanut Farms.

Table VIII and Fig. 8 show that the potassium content of the soil samples was detected in years 2021 and 2022. (2.16-2.55) and (2.19-2.55) ppm range were found in 2021 and 2022 Both periods were found to have very low levels of potassium in the soil samples. Low potassium values were found in both periods. Potassium concentrations in the soil should be included in fertilizer program.

VIII. POTASSIUM OF SOIL FROM PEANUT FARMS

No.	Sample	Potassium (ppm)	
		2021	2022
(i)	S1	2.55	2.10
(ii)	S2	2.18	2.19
(iii)	S3	2.16	2.55

>30 ppm medium potassium contents [6]

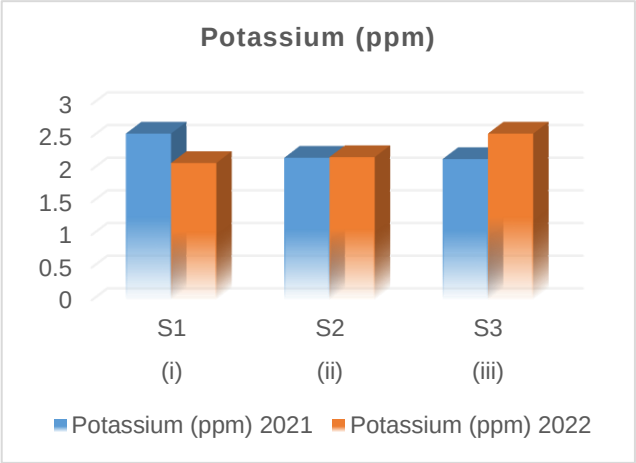

Fig. 8. Potassium contents of Soil from Peanut Farms.

IV. CONCLUSION

In this study, a two years study of soil samples from peanut areas found that slightly acidic soil samples in 2021 became slightly alkaline in 2022. Bulk density was found to be within the permissible limit of the plant grows. It was found to be within the limits. A good percentage was found, organic carbon and humus percentage values are below for the plant growth so natural fertilization may be carried out occasionally. All in all, macronutrients like nitrogen percent, contents of phosphorous and potassium were found inappropriate contents as physical nature of the soil such as bulk density, porosity and texture conditions were found optimum for oil crops. So, rain-fed conventional farming should be transformed to irrigated farming should be transformed to irrigated farming system. Also, it will bring the sustainable development for farming for oil crops.

ACKNOWLEDGMENT

The authors would like to thank Technological University (Mandalay), for valuable guidance and feedback throughout this paper. This work was supported by Dr Myat Sandar Hla, Professor Yangon University and she shared her experiment in this paper. Finally, the author thanks their families for their unwavering support and encouragement.

REFERENCES

[1] Jones. (1998). " Soil Testing and Plant Analysis": *Procedure and Use*. Taipei: Tech. Bell.109. Food and Fertilizer Technology Center, Taiwain,14

[2] Beernear. (1994). "Sample and Practical Methods to Evaluate Analysis Data of Soil Profiles". Dschang: Soil Science Department Belgian Coorperation,111

[3] McKenzie, etal., (2004). “Australian Soils and Landscape”. *An Illustrated Compendium.* Collinwood. CSIRO Publishing

[4] Levy, et al., (1997). ” Aggregate Stability of Some Southern US Soils”. *Soil Science Society of America Journal*, 61, 1176-1182

[5] Havlin, et al., (1999). “Soil Fertility and Fertilizer”: *An Introduction to Nutrient Management*. New Jersey: 6th ed., Upper Saddle River, Prentice Hall

[6] Jackson. (1958). “ Soil Chemical Analysis”. New Jersey: Prentice Hall Inc., 214-221

[7] http://en.mwikipeda.org/wiki/ Township

Influence of Sintering Temperature on Characteristics of Hematite (α - Fe_2O_3) Nanoparticles by Co-precipitation Method

Myint Myint Than[1], Kyi May San[2], Yee Mon Tun[3]

[1]*Lecturer, Natural Science Department, University of Information Technology*

[2]*Professor, Natural Science Department, University of Information Technology*

[3]*Lecturer, Academic Department (Physics), Government Technical Institute (Insein)*

Email: [1]myintmyintthany2k40@gmail.com, [2]kyimaysan@uit.edu.mm, [3]yeemontun186@gmail.com

***Abstract* — The iron oxide (α-Fe_2O_3) nanoparticles were created by co-precipitation method following with sintering process at several temperatures at (900 °C, 1000 °C, 1100 °C) for 2 hours. Ferric nitrate nano-hydrate ($Fe(NO_3)_3.9H_2O$) was chosen as a precursor and sodium bicarbonate ($NaHCO_3$) as a form of precipitator. Making use of Fe_2O_3 nanoparticles were characterized by X-ray diffraction (XRD), fourier transform infrared spectroscopy (FTIR), scanning electron microscopy (SEM), and electron-dispersive spectroscopy (EDS). The effect of sintering temperatures on properties of synthesized particles was investigated. XRD patterns were confirmed the iron oxide nanoparticles exhibited hematite (α-Fe_2O_3) phase with a hexagonal structure. The crystalline size was the nano range. In the FTIR spectrum, the two strong band below 700 cm^{-1} was appeared Fe-O metal oxide vibrations mode at 542-557 cm^{-1} and 472-476 cm^{-1}. The morphological investigations from SEM illustrated spherical-like shaped particles and the grain size of the particles 0.52 μm – 0.649 μm. According to the EDS micrograph, the element composition consists of oxygen and iron.**

Keywords*— *Iron oxide nanoparticles, Hematite, co-precipitation, precursor, precipitator.

I. INTRODUCTION

Novel nanostructures in materials, especially metal oxides have recently received more attention due to the rapidly evolving fields of nanoenergetics and nano electronics. Transition metal oxide nanostructures have attractive benefits in energy storage applications, specifically as a supercapacitors electrodes. Because energy storage devices are in popular demand, a significant amount of research has been performed on metal oxides such as RuO_2, IrO_2, NiO, SnO_2, V_2O_5, CeO_2, PbO_2, CO_3O_4, etc; for energy storage devices. These metal oxides were used as supercapacitor electrodes, demonstrate pseudo capacitive actions, featuring extremely high specific capacitance values. Instead, the restrictions of the majority of these metal oxides are connected to their toxicity, price and availability. Among all of the transition metal oxides, ferric oxide, Fe_2O_3 is promising electrode because of its cost, ready availability, environmental friendliness and corrosion resistance. However, the toxicity, cost, and availability of the majority of these metal oxides are their main drawbacks [1].

The presence of unknown Fe_2O_3 has four polymorphs consisting of alpha phase (α-Fe_2O_3), beta phase (β-Fe_2O_3), gamma phase (γ-Fe_2O_3), and epsilon phase (ε-Fe_2O_3). Each polymorph has a unique crystal structure and set of physical characteristics. The two most common prevalent polymorphs, the cubic spinel structure "gamma" and the hexagonal corundum structure "alpha", are found in hematite and maghemite materials. In recent years, the other polymorphs, orthorhombic structure "epsilon" and the cubic bixbyite structure "beta" have been manufactured and thoroughly analyzed. Forms of Fe_2O_3 (Gamma and epsilon) are ferromagnetic while beta type Fe_2O_3 is a paramagnetic substance, alpha Fe_2O_3 is a set antiferromagnetic. In particular, Hematite (α-Fe_2O_3) is compared with the additional polymorphs of iron oxide, it is discovered to be especially encouraging for use in a variety of applications, including supercapacitor, rechargeable electrodes , batteries [2], gas sensor [3], magnetic resonance imaging, photo catalytic applications [4], solar cells, field-effect transistor [5], phenyl hydrazine sensor, electrode for lithium ion batteries [6], photo-anode for photo assisted electrolysis of water, etc.

(α-Fe_2O_3) is significant among these polymorphs because of its easy manufacture, cheaply priced, abundance, kindness toward the environment, strongly cracking resistance, chemical inertness, biocompatibility, and superior substance adhesion [7]. Different methods have been developed to create (α-Fe_2O_3) nanoparticles with distinct physical and chemical properties, including the micro emulsion method, sol-gel method, co-precipitation method, spray pyrolysis, hydrothermal synthesis, solvothermal synthesis [8], and others.

In this paper, we produced (α-Fe_2O_3) using the co-precipitation method, which is a simple, straightforward, low-effort, well- crystallized product, high homogeneity short preparation time and cost effective way to create nanostructures. The ferric nitrate ($Fe(NO_3)_3.9H_2O$) and sodium bicarbonate ($NaHCO_3$) were used as a precursor and a precipitator to co-precipitate (α-Fe_2O_3) nanoparticles. To produce nanoparticles with various particle sizes, (α-Fe_2O_3) was sintered at three distinct temperatures. In this study, nanoparticles was examined their crystalline size, structure, morphology, chemical composition and functional groups properties of nanoparticles were investigated.

II. MATERIALS AND METHOD

A. Materials

The iron precursor was ferric nitrate nano - hydrate ($Fe(NO_3)_3.9H_2O$), while the precipitating agents were sodium

bicarbonate ($NaHCO_3$), distilled water, and ethanol (C_6H_6O). All solutions were prepared with deionized water. All the chemicals and solvents were purchased from Academy chemical shop from Yangon in Myanmar. All reagents were lab grade and were utilized any additional purification.

B. Experimental Detail of Iron Oxide Nanoparticles (hematite, α - Fe_2O_3)

Iron oxide (Hematite, α-Fe_2O_3) were employed by co-precipitation method. In a typical experiment, ferric nitrate precursor solution was prepared by dissolving 50g of ferric nitrate nano-hydrate ($Fe(NO_3)_3.9H_2O$) in 500ml of deionized water with magnetic stirring for 90 mins at room temperature. After that, 30g of sodium bicarbonate ($NaHCO_3$) in a 200 ml of deionized water and stir it for 90 mins at room temperature by magnetic stirrer. To ensure all the base granules was dissolved and the aqueous solution was completely clear until continued stir. After placing the ferric nitrate solution on a magnetic stirrer and turning on the magnetic engine, drop by drop of room temperature sodium bicarbonate solution was stirred. During stirring, the solution color changed from orange color to reddish brown color. Each time a base is added, brown precipitate starts to form and monitors the pH level of the solution (using litmus paper) until the pH reaches 8, at which point the reaction is finished. At room temperature, the resultant solution was continuously agitated for two hours at 500 rpm. After that, the beaker's contents were left unattended for 36 hours to permit the precipitate settle. After that, the resulting solution was separated into precipitate and water. During collection and centrifugation at 2000 rpm for 10 minutes, the precipitate solutions were repeatedly cleaned with distilled water until the pH level was nearly equal to 7. Finally, the precipitate was washed with ethanol to remove impurity, and then separated by centrifuge. When the precipitate was dried in an oven at 90 °C for 4 hours, reddish brown powder was obtained.

The transformation of ferric nitrate into ferric hydroxide and then into ferric oxide is illustrated in the following equations.

$$2Fe\ (NO_3)_3.\ 9H_2O + 6NaHCO_3 = 2Fe\ (OH)_3 + 6NaNO_3 + 6CO_2 + 18H_2O$$

$$2\ Fe\ (OH)_3 = Fe_2O_3 + 3H_2O \qquad (1)$$

The finally equation is;

$$2Fe\ (NO_3)_3.9H_2O + 6NaHCO_3 = Fe_2O_3 + 3H_2O + 6NaNO_3 + 6CO_2 + 2H_2O$$

Using a refractory ceramic crucible, the reddish-brown powder was sintered in a furnace at various temperatures of 900 °C, 1000 °C, 1100 °C for 2 hours. And then, hematite (α-Fe_2O_3) nanoparticles were obtained.

C. Characterization of Iron Oxide (α-Fe_2O_3) Nanoparticles

Different kinds of techniques were utilized to analyze the structural, chemical, and morphological features of the iron oxide nanoparticles that were generated. Using Cu-K radiation (α = 1.54060°A) as the source, the X-ray diffraction patterns of the materials had been examined using D/te X Ultra 250 detectors. The intensity data compiled over the range 20°- 80° using a step width 0.02°. The synthetic nanoparticles were subjected to elemental and chemical composition evaluations using energy dispersive spectroscopy (EDS) coupled with scanning electron microscopy (SEM) and Fourier transform infrared spectroscopy (FTIR) on an IR-Tracer 100 Shmadzu, Japan. At room temperature, FTIR measurements were performed in the 400 cm^{-1} - 4000 cm^{-1} range. The sample's morphological characteristics were examined using a scanning electron microscope (SEM: ZEISS).

Fig 1. Sample preparation of Fe_2O_3 step by step (a) ferric nitrate (b) DI water (c) precursor solution (d) sodium bicarbonate (e) sodium bicarbonate solution (f) added precipitator solution drop by drop (g) reaction complete (h) settle 36 hours (i) centrifuged by solution (j) filtered by sample (k) dried brown powder (l) sintered in furnace (m) α-Fe_2O_3 nanoparticles

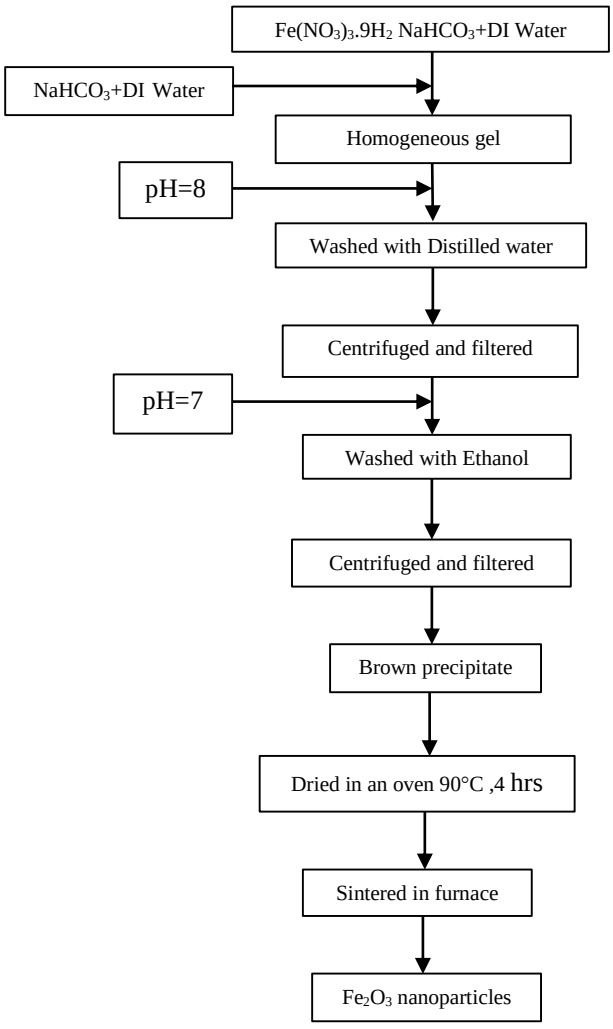

Fig 2. Block diagram of sample preparation of (α - Fe_2O_3) nanoparticles

III. Results and Discussions

A. XRD Analysis of (α-Fe_2O_3) Nanoparticles

The XRD is achieved for the classification and understanding the crystalline progress behavior of (α-Fe_2O_3) nanoparticles. The crystallite size of the particle was calculated from Debye-Scherer's equation which is given by

$$D = K\lambda/\beta \cos\theta \quad (2)$$

where; D is crystallite size, λ is the X-ray wavelength (1.54060 °A), β is the diffraction peak at Full Wave Half Maximum(FWHM) in radians, β is shape factor, about 0.9 for iron oxides and θ is the Bragg's angle (degree).

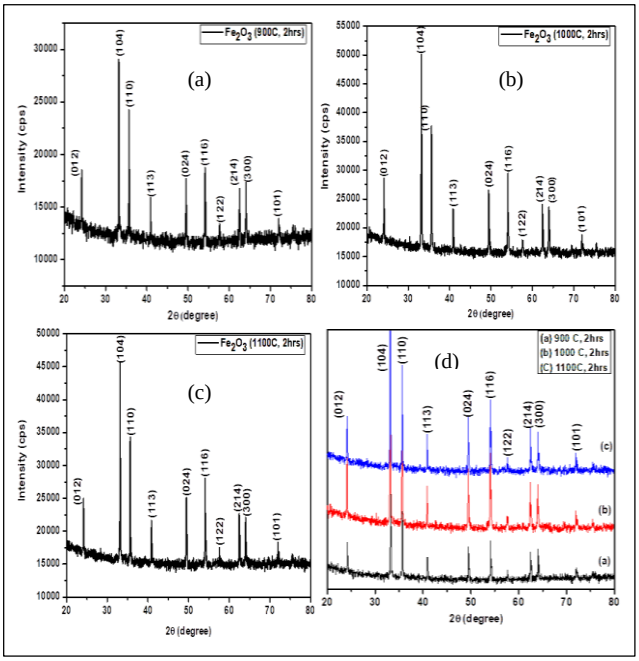

Fig. 3 XRD patterns of α-Fe_2O_3 nanoparticles (a) 900 °C, (b) 1000 °C, (c) 1100 °C for 2 hours, (d) XRD patterns of α-Fe_2O_3 nanoparticles at (900°C,1000°C,1100°C) for 2 hours

Using X-ray diffraction equipment, a sample is predicted to be (α-Fe_2O_3), the retrieved XRD pattern and Fig. 3(a-d) show the peaks in the spectrum range of 20 to 80 degrees (in terms 2θ), which it is confirmed, are consistent with the standard card number (Card No: 04-008-7627), and no other impurity peaks can be seen. XRD patterns which are confirmed to iron oxide nanoparticles (α-Fe_2O_3) with the hexagonal structure. The largest peak intensity of this image matching to sheet (104) displayed in an $2\theta^{\circ}$ = 35.75 angle and other peaks linked to sheets (012), (104), (110), (113), (024), (116), (122), (214), (300) and (101) is continuous with what identified in articles.

From XRD results, calculated that the variation of crystallite size for (α-Fe_2O_3) nanoparticles are 89.1 nm, 94.2 nm and 113.2 nm at 900 °C, 1000 °C and 1100 °C respectively. At sintering temperatures 900 °C and 1000 °C, the average crystallite size of (α-Fe_2O_3) was about 89.1 nm and 94.2 nm exist in the nano-range below 100 nm [9]. Crystallite size increased from ~ 89 to 113 nm when temperature raised from 900 to 1100 °C. In this result, the crystallize size increased when the temperature increased because the rate of the deposition reaction increases at higher temperature and the crystallites grow faster resulting in a larger size [10]. Fig. 3(d) shows the comparison of three different temperatures of (α-Fe_2O_3) nanoparticles.

B. Effect of Sintering Temperature on FTIR

FTIR spectra of (α-Fe_2O_3) were identified the chemical compositions and the functional groups of the sample. The spectrum of (α-Fe_2O_3) were observed with three different sintering temperatures (900 °C, 1000 °C, 1100 °C) for 2 hours as shown in Fig. 4(a-c).

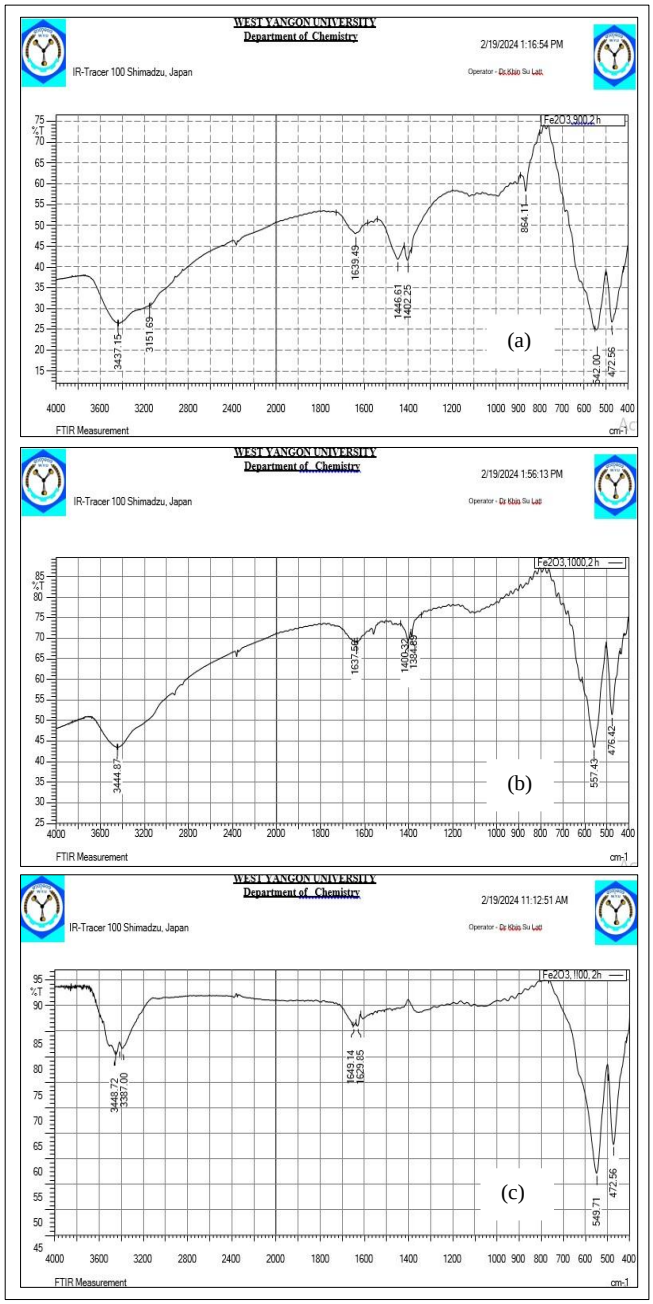

Fig 4. FTIR spectra (a) 900 °C (b) 1000 °C (c) 1100 °C of (α-Fe_2O_3) particles for 2 hours

Fig. 4(a) shows the absorption bands of (α-Fe_2O_3) particles at 3437, 1639, 1446, 864, 542 and 472 cm^{-1} at 900 °C. The strong board band at 3437 cm^{-1} is assigned to the O-H stretching vibration in OH - hydroxyl groups, and 1639 cm^{-1} were attributed due to bending vibration of H-O-H water molecules. The two strong band below 700 cm^{-1} was appeared metal oxygen stretching vibration modes. In addition, the peak at 1446 cm^{-1} is assigned to the deformation of CH_3. The small peak at 864 cm^{-1} was showed due to the existence of nitrate group. The two sharp peaks at 542 cm^{-1} and 472 cm^{-1} were identified to the Fe-O stretching vibration mode respectively of (α-Fe_2O_3) [11].

Fig. 4(b) shows the absorption bands of (α-Fe_2O_3) nanoparticles at 3444, 1637, 1400, 557 and 476 cm^{-1} at 1000 °C. The peaks positions at 1637 cm^{-1} and 3444 cm^{-1} are due to the bending vibration of absorbed water and surface hydroxyl and O-H stretching mode respectively. The high frequency band at 557 cm^{-1}can be attributed to Fe - O deformation in the octahedral and tetrahedral site while the low frequency band at 476 cm^{-1} is attributed to Fe-O deformation in the octahedral site of hematite [12].

Fig. 4(c) shows the absorption bands of (α-Fe_2O_3) nanoparticles at 3448, 1649, 549, 472 cm^{-1} at 1100 °C. The band at 3448 cm^{-1} is positioned to adsorbed water which also gives rise to the stretching mode of hydroxyl at 3387 cm^{-1} and the bending mode of hydroxyl at 1649 cm^{-1} [13]. The intensity of the high frequency band is stronger than the low frequency. Metal-Oxygen vibrational bands was occurred slightly shift at 549 cm^{-1} and 472 cm^{-1}. According to the recorded FTIR data confirmed that the synthesized nanoparticles are iron oxide without any identifiable impurities.

C. Morphological Properties

The surface morphology of the (α-Fe_2O_3) particles has been observed through scanning electron microscope (SEM). Fig. 5(a-c) show the SEM and EDS images of the (α-Fe_2O_3) particles at different sintering temperatures. Fig. 5(a) shows the SEM image of the (α-Fe_2O_3) particles that were heated to 900 °C for 2 hours, the sample size and morphology are irregular, formation of more clusters and irregular shaped grain of random agglomerated particles have occurred. The grains were connected with each other to form clusters with some clusters of overgrowth. Fig. 5(b) shows the SEM image of the (α-Fe_2O_3) particles that were heated to 1000 °C for 2 hours, the particles were seen as equally sized distribution , smooth, tiny, spherical particles on the surface. SEM micrograph of the samples sintered at 1100 °C for 2 hours is shown in Fig. 4(c). As seen, particles have developed on the surface as single clusters with few agglomerates.

When the particles collided at a lower temperature, numerous smaller – sized particles were appeared. On the other hand, because of the growing and union of microscopic grains following the sintering steps, particles sintered at increased temperature were made up of less, larged - sized particulates. Particle diameter distribution of (α-Fe_2O_3) at different temperature as shown in Fig. 5(d-f). The mean particles dimension of (α-Fe_2O_3) at temperatures 900 °C, 1000 °C and 1100 °C are 0.524 μm, 0.558 μm and 0.649 μm respectively. It is noted that the (α-Fe_2O_3) particles imposed at 900 °C seems to be less particles size 0.524 μm. As the temperature grows to 1000 °C and the particle size decreases to 0.558μm, strong intensity peaks were appeared. Particle size grows with increasing temperature, this may be caused by an increase in the interplanar distance (d) put on by the excess oxidization with process, in which oxygen atoms acquire reference-congruent oxygen vacancies [14]

D. Energy-Dispersive Spectroscopy (EDS)

Energy-Dispersive Spectroscopy (EDS) was developed to analyze the element composition of a sample attached with SEM. EDS spectra of (α-Fe_2O_3) sintering temperatures at (900 °C,1000 °C, 1100 °C) for 2 hours are shown in Fig.6(a-c) which confirms the evidence of iron (Fe), oxygen (O) and other element with mass percent express. Fig 6(a),

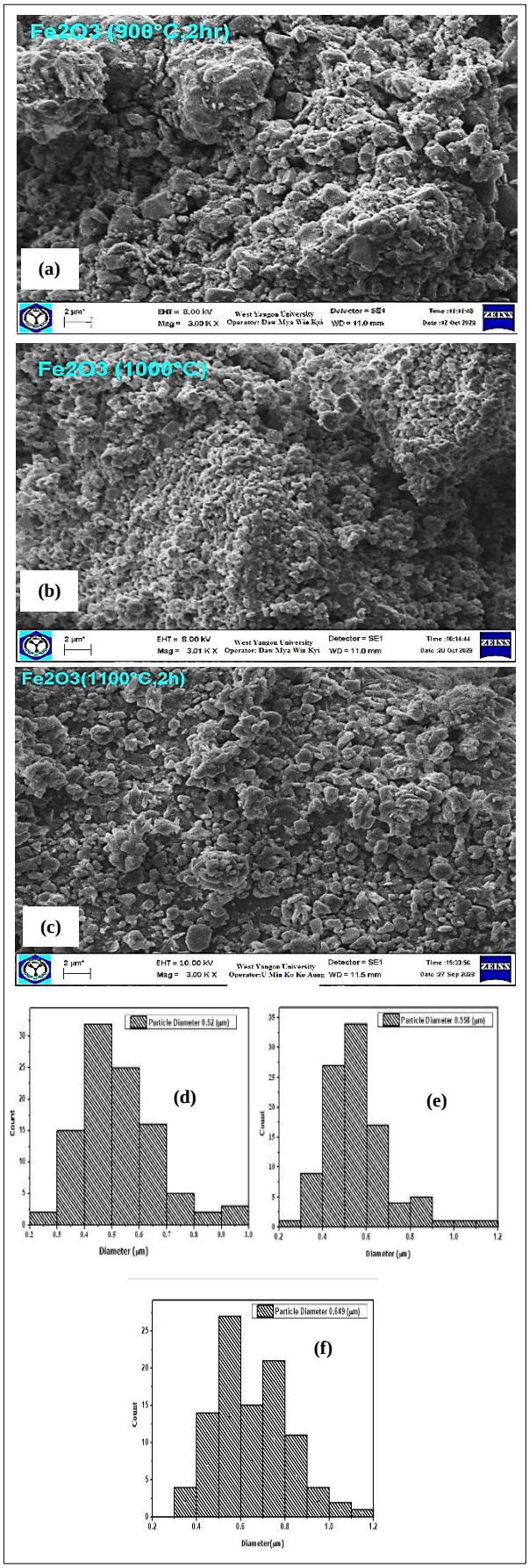

Fig. 5(a-c) SEM images and fig.5 (d-f) particle diameter distribution of (α-Fe_2O_3) at different temperature

shows EDS analysis of (α-Fe_2O_3) sintering temperatures at 900 °C for 2 hours. EDS was revealed Fe (57.66%), Na (19.15%) and O (23.18%) consist. The appearance of sodium in the EDS spectrum is because of the $NaHCO_3$ as

precursors used in the synthesis. Fig. 6(b) and 6(c) show EDS analysis of (α-Fe_2O_3) sintering temperatures at 1000 °C and 1100 °C for 2 hours. EDS was showed Fe (77.73%) and O (22.27%) consist. The presence of Fe and O, no other elements were identified in the tracked spectrum, which indicates that the synthesized iron oxides are purity [15]. All EDS spectral analysis revealed that "Fe" and "O" is the main elements in the attained product, which was determined by the occurrence of strong intense peak 0.705 keV corresponding to "Fe". The obtained EDS analysis confirmed the formation of Fe_2O_3 nanoparticles.

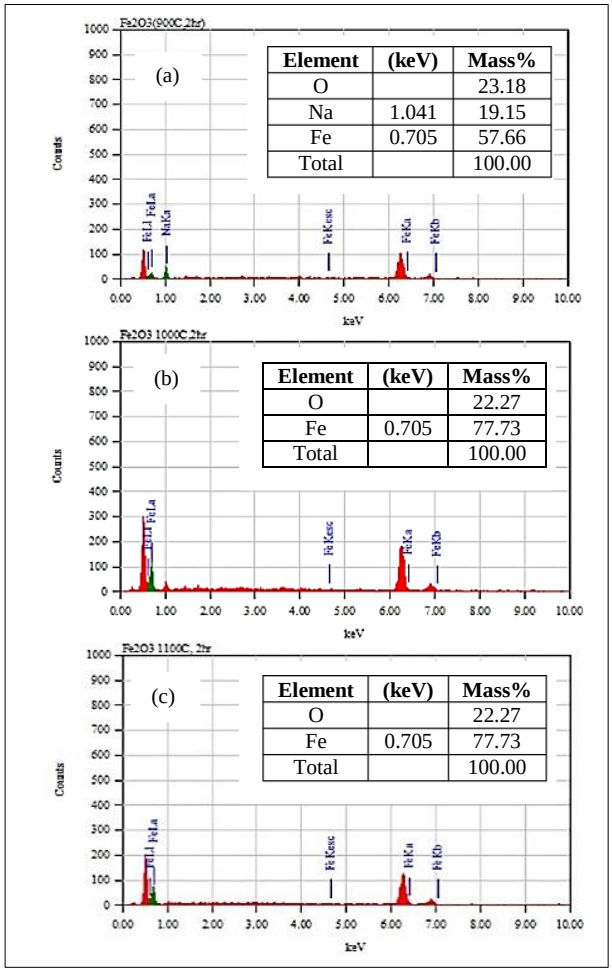

Fig 6. EDS spectral of α-Fe_2O_3 nanoparticles (a) 900°C (b) 1000°C (c) 1100°C for 2 hours

IV. Conclusion

In conclusion, it is necessary to summarize the α-Fe_2O_3 nanoparticles was produced by the co-precipitation method with good crystalline quality. As we sintered at a higher temperature, XRD analysis shows narrow, sharp peaks and large crystalline. (α-Fe_2O_3) nanoparticles at 1000 °C show that they are highly crystalline, with the average crystalline size being 94.2 nm, which is definitely in the nanometer range. FTIR result of (α-Fe_2O_3) nanoparticles established the occurrence of Fe-O stretching vibration mode of the sintered temperatures at 1000 °C. SEM images clearly show that as temperature increased, the particle morphology transformed to a more sphere-like shape and the quantity of nanoparticle agglomeration decreased. When (α-Fe_2O_3) is synthesized at 1000 °C, EDS only detect peaks of iron and oxygen, indicating that there are no impurities present. Continuously, this synthesized nanoparticles can be studied electrochemical properties and fabricated ways of electrode materials for energy storage devices. In this study, preparation of α-Fe_2O_3 sintered at 1000 °C was choice excellent to different applications used as the anode material for a Li ion electrode asymmetric hybrid supercapacitor, electrode for electrochemical capacitor, polyelectrolyte membrane for DMFC applications. In future, we believed α-Fe_2O_3 nanostructures can only be used as supercapcitor electrodes, but could also be implemented in other various different energy storage applications.

Acknowledgment

The author was deeply indebted to Dr. Kyi May San, Professor and Head of Department of Natural Science Department (Physics), University of Information Technology, for her kind permission to carry out this research.

References

[1] G.Binitha *et al.*, "Electrospun α-Fe_2O_3 nanostructures for supercapacitor applications," *J. Mater. Chem. A*, vol. 1, no. 38, pp. 11698–11704, 2013, doi: 10.1039/c3ta12352a.

[2] C. T. Cherian *et al.*, "Electrospun α-Fe_2O_3 nanorods as a stable, high capacity anode material for Li-ion batteries," *J. Mater. Chem.*, vol. 22, no. 24, pp. 12198–12204, 2012, doi: 10.1039/c2jm31053h.

[3] S. W. Hwang, A. Umar, G. N. Dar, S. H. Kim, and R. I. Badran, "Synthesis and characterization of iron oxide nanoparticles for phenyl hydrazine sensor applications," *Sens. Lett.*, vol. 12, no. 1, pp. 97–101, 2014, doi: 10.1166/sl.2014.3224.

[4] J. Sundaramurthy, P. S. Kumar, M. Kalaivani, V. Thavasi, S. G. Mhaisalkar, and S. Ramakrishna, "Superior photocatalytic behaviour of novel 1D nanobraid and nanoporous α-Fe_2O_3 structures," *RSC Adv.*, vol. 2, no. 21, pp. 8201–8208, 2012, doi: 10.1039/c2ra20608k.

[5] A. Lassoued, B. Dkhil, A. Gadri, and S. Ammar, "Control of the shape and size of iron oxide (α-Fe_2O_3) nanoparticles synthesized through the chemical precipitation method," *Results Phys.*, vol. 7, pp. 3007–3015, 2017, doi: 10.1016/j.rinp.2017.07.066.

[6] Y. Wang, J. Roller, and R. Maric, "Novel flame synthesis of nanostructured α-Fe_2O_3 electrode as high-performance anode for lithium ion batteries," *J. Power Sources*, vol. 378, no. December 2017, pp. 511–515, 2018, doi: 10.1016/j.jpowsour.2017.12.047.

[7] G. BOZKURT, "Synthesis and Characterization of α-Fe_2O_3 Nanoparticles by Microemulsion Method," *Erzincan Üniversitesi Fen Bilim. Enstitüsü Derg.*, vol. 13, no. 2, pp. 890–897, 2020, doi: 10.18185/erzifbed.742160.

[8] M. Farahmandjou and F. Soflaee, "Synthesis and characterization of -Fe_2O_3 nanoparticles by simple co-precipitation method," *Phys. Chem. Res.*, vol. 3, no. 3, pp. 191–196, 2015, doi: 10.22036/pcr.2015.9193.

[9] R. RT, A.-A. SD, K. HH, and M. HS, "Preparation and Characterization of Hematite Iron Oxide (α -Fe_2O_3) by Sol-Gel Method,"*Chem.Sci.J.*,vol.09,no. 04, pp. 2–8, 2018, doi: 10.4172/2150-3494.1000197.

[10] A. Banerjee, S. Patra, M. Chakrabarti, D. Sanyal, M. Pal, and S. K. Pradhan, " Microstructure, Mössbauer, and Optical Characterizations of Nanocrystalline α - Fe_2O_3 Synthesized by Chemical Route ," *ISRN Ceram.*, vol. 2011, pp. 1–8, 2011, doi: 10.5402/2011/406094.

[11] S. Basavaraja, D. S. Balaji, M. D. Bedre, D. Raghunandan, P. M. Prithviraj Swamy, and A. Venkataraman, "Solvothermal synthesis and characterization of acicular α-Fe_2O_3 nanoparticles," *Bull. Mater. Sci.*, vol. 34, no. 7, pp. 1313–1317, 2011, doi: 10.1007/s12034-011-0321-z.

[12] A. Mirzaei *et al.*, "Synthesis and characterization of mesoporous α-Fe_2O_3 nanoparticles and investigation of electrical properties of fabricated thick films," *Process. Appl. Ceram.*, vol. 10, no. 4, pp. 209–218, 2016, doi: 10.2298/PAC1604209M.

[13] A. S. Al-Kady, M. Gaber, M. M. Hussein, and E. Z. M. Ebeid, "Structural and fluorescence quenching characterization of hematite nanoparticles," *Spectrochim. Acta - Part A Mol. Biomol. Spectrosc.*, vol. 83, no. 1, pp. 398–405, 2011, doi: 10.1016/j.saa.2011.08.052.

[14] A. Ibrahim and B. A. Abubakar, "Some wet routes for synthesis of hematite nanostructures," *African J. Pure Appl. Chem.*, vol. 7, no. 3, pp. 114–121, 2013, doi: 10.5897/ajpac12.002.

[15] M. Waseem, S. Munsif, U. Rashid, and Imad-ud-Din, "Physical properties of α - Fe_2O_3 nanoparticles fabricated by modified hydrolysis Technique,"*Appl. Nanosci.*, vol.4, no.5, pp.643–648, 2014, doi: 0.1007/s132040 -013-0240-y.

Analysis of a Xi Minus (Ξ^-) Hyperon Stopped Event in Nuclear Emulsion of J-PARC E07 Experiment

Wai Wai Aung[1], Khin Than Tint[2], Htet Htet Wai Moe[3]

[1]*Lecturer, Department of Academic, Government Technical Institute (Myingyan)*

[2]*Professor, Department of Physics, University of Mandalay (Mandalay)*

[3]*Lecturer, Department of Engineering Physics, Technological University (Mandalay)*

Email: [1]myatnoewai616@mail.com, [2]khinthantint045@mail.com, [3]htethtetwaimoe9@mail.com

***Abstract*—One of the main goals of hypernuclear research is to study the interaction between the Λ hyperon and the nucleus. In this research, one of the Ξ^- stopped events, (a single-Λ hypernucleus event) that was found in nuclear emulsion pl #10, module # 084 in J-PARC E07 experiment has been analyzed.**

Keywords— single-Λ hypernucleus, nuclear emulsion, Ξ^- hyperon, Ξ^- stopped events, J-PARC E07 experiment

I. Introduction

The Ξ^- hyperons were produced through the reaction $K^- + p \rightarrow K^+ + \Xi^-$ in a diamond target with a K^- momentum of 1.81 GeV/c in J-PARC E07 experiment. An atom in nuclear emulsion captured a stopped Ξ^- hyperon. Firstly, it was captured on an atomic orbit in a highly excited level. A captured Ξ^- hyperon was transferred into lower orbits with emitting Auger electrons or X rays. Finally, it was absorbed by the nucleus, and then they formed, with some probability, double-Λ hypernucleus, twin single-Λ hypernuclei and single-Λ hypernucleus [1, 7].

In E07 experiment, total 118 emulsion stacks were used. An emulsion stack consists of 13 emulsion sheets with an area of 34.5 x 35.0 cm^2. Two SSDs (Silicon Strip Detectors) were used to reconstruct vertex positions and tracks of particles with high precision [8].

II. Xi Minus (Ξ^-) Hyperon Stopped Event

A. Event Description

In E07 experiment, 10^4 (Ξ^-) stopped events in nuclear emulsion were observed. Among them, one of the Ξ^- stopped events with two vertex topology was analyzed. It was observed in nuclear emulsion pl #10 of mod #084 in J-PARC (Japan Proton Accelerator Research Complex) E07 experiment. According to the characteristics of sequential weak decay topology of this event, it was denoted as single-Λ hypernucleus event. The photograph was taken by 100x magnification objective lens microscope. In this event, the Ξ^- hyperons were produced through the 'p' (K^-, K^+) Ξ^- reaction in a diamond target and came to rest at vertex A from which two charged particles (track #1 and #2) were emitted. The particles of track #1, #2 and #3 of this event was stopped in nuclear emulsion sheet #10 while the particle of track #4 moved downward direction of the nuclear emulsion sheet #10. It was stopped in the upstream layer of nuclear emulsion sheet #11 as the ρ-stop, i.e., no charged particles were emitted at the stopped point. The photograph and schematic drawing of the single- Λ hypernucleus (Ξ^-Hyperon Stopped) event is shown in Fig.1.

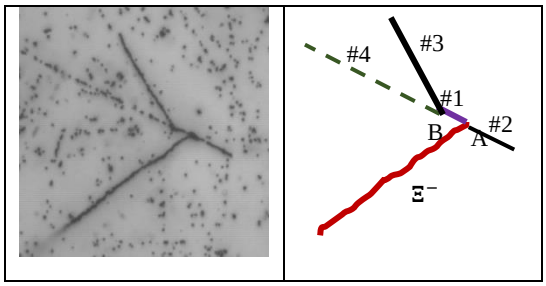

Fig. 1. Photograph and schematic drawing of the single- Λ hypernucleus (Ξ^-Hyperon Stopped) event

B. Range and Angle Measurement

The range measurement is very important to obtain the kinetic energy of particles. The tracks are divided into short segments because tracks are not straight due to the multiple Coulomb scattering. Therefore, the range of a charged particle can be measured by making the points at several straight segments as shown in Fig. 2, by using the computer display with the mouse equipment in microscopic system which was described as in Fig. 3 [5]. The emulsion layers shrunk and distorted during the development process. Therefore, we need to consider about the shrinkage factor and other distortions due to the process of photographic development. The shrinkage factor could be estimated from the thickness of the plate at the exposure time and that at the measurement time [6]. The range, R, of a charged particle from x, y and z coordinates in nuclear emulsion can be obtained by using the equation (1).

$$R = \sqrt{\Delta x^2 + \Delta y^2 + (\Delta z^2 \times S^2)} \quad (1)$$

Where, R is the original range of the track, Δx, Δy and Δz are the lengths in the x, y and z directions, respectively. S is the shrinkage factor for emulsion gel. After the range measurement, the emission angles have to be measured by marking the x, y and z coordinates at the first straight segment of the particle track on the vertex point, as shown in Fig. 2. From these coordinate points, the emission angles were obtained by using the following equations:

$$\theta = cos^{-1}\left(\frac{\Delta z}{\sqrt{\Delta x^2+\Delta y^2+(S\Delta z)^2}}\right) \quad (2)$$

(2)

$$\phi = tan^{-1}\left(\frac{\Delta y}{\Delta x}\right) \quad (3)$$

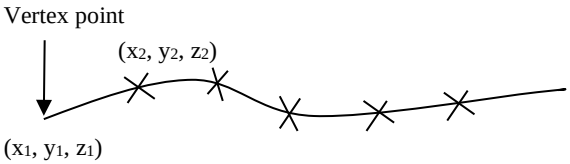

Fig. 2. The schematic drawing of a particle track marked x, y and z coordinates.

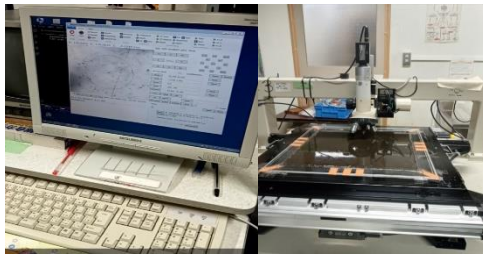

Fig. 3. The photograph of microscopic system.

The angles are expressed by an azimuthal angle ϕ and a zenith angle θ. Where θ is the angle from the z-axis to the x-y plane and ϕ is the angle from the x-axis to the y-axis. The measured ranges and emission angles of the particle tracks in a single- Λ hypernucleus event were summarized in Table I.

TABLE I

RANGES AND EMISSION ANGLES OF EACH TRACK IN SINGLE- Λ HYPERNUCLEUS EVENT

Vertex	Track	Length (μm)	θ (degree)	ϕ (degree)	Comment
A	#1	5.6 ± 0.4	95.9 ± 2.4	338.5 ± 1.3	Single-Λ Hypernucleus
	#2	7.9 ± 0.3	80.8 ± 1.7	157.1 ± 1.3	Stopped in pl#10
B	#3	20.3 ± 0.1	108.1 ± 1.8	303.9 ± 1.0	Stopped in pl#10
	#4	5737.0 ± 1.3	99.9 ± 0.2	337.1 ± 0.5	Stopped in pl#11

III. EVENT RECONSTRUCTION OF Ξ^- STOPPED (SINGLE- Λ HYPERNUCLEUS) EVENT

Event reconstruction was performed to identify the hypernucleus. It was made based on the conservation laws of energy and momentum. At vertex B, possible mesonic decay and non-mesonic decay were considered to identify the decay modes. Since track #4 was a thin track, we considered that track to be a single charged particle, such as a π^-meson, ^{1}H, ^{2}H or ^{3}H particles.

The Q-values for all possible decay modes were calculated from their masses by using the equation (4). The kinetic energies of track #3 and track #4 were obtained from their measured ranges by using the Range-Energy program written by Prof: Nakazawa, Gifu University. The visible kinetic energy, E_{vis}, was by the sum of the kinetic energies of charged particles. without neutron emission. For each reaction, neutral particle emission was also considered. For the modes with neutron emissions, the kinetic energies of the neutron were obtained from the momentum balance by using equations (5), (6), and (7). The total kinetic energy, E_{tot}, was the sum of the kinetic energies of all emitted charged and uncharged particles.

$$Q(MeV) = [M(\#1) - \{M(\#3) + M(\#4)\}]c^2 \quad (4)$$

$$P_x = |\vec{P}|\, sin\theta\, cos\phi \quad (5)$$

$$P_y = |\vec{P}|\, sin\theta\, sin\phi \quad (6)$$

$$P_z = |\vec{P}|\, cos\theta \quad (7)$$

To identify the type of hypernuclei, the invariant masses of single- Λ hypernuclei were calculated the sum of kinetic energy and the rest mass of its decay daughters. It was assumed that the single- Λ hypernucleus rests at vertex B. Therefore, the kinetic energy of a single- Λ hypernucleus is equal to zero.

Then, the invariant masses of single- Λ hypernuclei were compared with the known masses from the particle data group. Moreover, the initial masses need to be calculated to estimate the binding energies of the single- Λ hypernuclei. The binding energies of single-Λ hypernuclei for acceptable decay modes were obtained from equation (10).

$$M_{invariant}\, c^2 = \{M_{\#3} + M_{\#4}\}c^2 + \{KE_{\#3} + KE_{\#4}\} \quad (8)$$

$$M_{initial} = M_{core} + M_\Lambda \quad (9)$$

$$BE = \{M_{initial} - M_{invariant}\}c^2 \quad (10)$$

IV. RESULTS AND DISCUSSIONS

A. *Results of Identification of Type of Single- Λ Hypernucleus from Vertex B of Event*

A single-Λ hypernucleus event was analyzed. Firstly, all possible decay modes of single- Λ hypernucleus were checked at vertex B. The Q-values and total kinetic energies were kinematically calculated for all possible mesonic and non-mesonic decay modes. The comparison of Q-value and E_{tot} for possible mesonic decay modes without neutron emission and with neutron emission were listed in Tables II and III.

The comparison of Q-value and E_{tot} for possible non-mesonic decay modes with neutron emission and without neutron emission were described in Tables IV, V, and VI, respectively. In our analysis, Q-values less than E_{tot} and large differences between Q-value and E_{tot} were rejected. Among them, three acceptable decay modes with a small difference between Q-value and E_{tot} were observed.

TABLE II

THE COMPARISON OF Q-VALUE AND E_{TOT} FOR ALL POSSIBLE MESONIC DECAY MODES OF SINGLE- Λ HYPERNUCLEUS (TRACK #1) WITHOUT NEUTRON EMISSION

No	Track # 1	Track # 3	Track # 4	Q-value (MeV)	E_{vis} (MeV)	E_{tot} (MeV)	Q-E_{tot} (MeV)	Remark
1	${}^{3}_{\Lambda}H$	${}^{3}He$	π^-	43.20	20.81 ± 0.1	20.81 ± 0.1	22.39 ± 0.1	Rejected
2	${}^{4}_{\Lambda}H$	${}^{4}He$	π^-	55.61	21.20 ± 0.1	21.20 ± 0.1	34.41 ± 0.1	Rejected
3	${}^{6}_{\Lambda}He$	${}^{6}Li$	π^-	38.26	25.39 ± 0.1	25.39 ± 0.1	12.87 ± 0.1	Rejected
4	${}^{9}_{\Lambda}Li$	${}^{9}Be$	π^-	46.23	30.33 ± 0.2	30.33 ± 0.2	15.89 ± 0.2	Rejected
5	**${}^{10}_{\Lambda}Be$**	**${}^{10}B$**	**π^-**	**35.31**	**34.95 ± 0.4**	**34.95 ± 0.4**	**0.36 ± 0.4**	**Acceptable**
6	**${}^{12}_{\Lambda}B$**	**${}^{12}C$**	**π^-**	**42.43**	**40.12 ± 0.6**	**40.12 ± 0.6**	**2.31 ± 0.6**	**Acceptable**
7	${}^{14}_{\Lambda}C$	${}^{14}N$	π^-	33.22	45.46 ± 1.1	45.46 ± 1.1	- 12.24 ± 1.1	Rejected

TABLE III

THE COMPARISON OF Q-VALUE AND E_{TOT} FOR ALL POSSIBLE MESONIC DECAY MODES OF SINGLE- Λ HYPERNUCLEUS (TRACK #1) WITH ONE NEUTRON EMISSION

No	Track # 1	Track # 3	Track # 4	neutron	Q-value (MeV)	E_{vis} (MeV)	E_{tot} (MeV)	Q-E_{tot} (MeV)	Remark
1	${}^{4}_{\Lambda}H$	${}^{3}He$	π^-	1n	35.03	20.81 ± 0.11	44.87 ± 0.11	- 9.84 ± 0.11	Rejected
2	${}^{8}_{\Lambda}He$	${}^{7}Li$	π^-	1n	41.10	25.73 ± 0.13	106.46 ± 0.13	- 65.36 ± 0.13	Rejected
3	${}^{13}_{\Lambda}B$	${}^{12}C$	π^-	1n	39.06	40.13 ± 0.69	311.17 ± 0.69	- 272.11 ± 0.69	Rejected

TABLE IV

THE COMPARISON OF Q-VALUE AND E_{TOT} FOR ALL POSSIBLE NON-MESONIC DECAY MODES OF SINGLE- Λ HYPERNUCLEUS (TRACK #1) WITHOUT NEUTRON EMISSION

No	Track # 1	Track # 3	Track # 4	Q-value (MeV)	E_{vis} (MeV)	E_{tot} (MeV)	Q-E_{tot} (MeV)	Remark
1	${}^{4}_{\Lambda}He$	p	t	174.49	60.83 ± 0.08	60.83 ± 0.08	113.66 ± 0.08	Rejected
2	${}^{4}_{\Lambda}He$	t	p	174.49	38.99 ± 0.14	38.99 ± 0.14	135.50 ± 0.14	Rejected
3	${}^{4}_{\Lambda}He$	d	d	170.45	51.71 ± 0.10	51.71 ± 0.10	118.74 ± 0.10	Rejected
4	${}^{5}_{\Lambda}He$	d	t	155.40	61.15 ± 0.08	61.15 ± 0.08	94.25 ± 0.08	Rejected
5	${}^{5}_{\Lambda}He$	t	d	155.40	51.91 ± 0.10	51.91 ± 0.10	103.49 ± 0.10	Rejected

TABLE V

THE COMPARISON OF Q-VALUE AND E_{TOT} FOR ALL POSSIBLE NON-MESONIC DECAY MODES OF SINGLE- Λ HYPERNUCLEUS (TRACK #1) WITH ONE NEUTRON EMISSION

No	Track # 1	Track # 3	Track # 4	neutron	Q-value (MeV)	E_{vis} (MeV)	E_{tot} (MeV)	Q-E_{tot} (MeV)	Remark
1	**${}^{4}_{\Lambda}He$**	**p**	**d**	**1n**	**168.23**	**51.4 ± 0.10**	**166.00 ± 0.10**	**2.23 ± 0.10**	**Acceptable**
2	${}^{4}_{\Lambda}He$	d	p	1n	168.23	38.79 ± 0.14	96.40 ± 0.14	71.83 ± 0.14	Rejected
3	${}^{5}_{\Lambda}He$	p	t	1n	153.18	60.84 ± 0.08	248.53 ± 0.08	- 95.35 ± 0.08	Rejected
4	${}^{5}_{\Lambda}He$	t	p	1n	153.18	38.99 ± 0.14	103.74 ± 0.14	49.44 ± 0.14	Rejected
5	${}^{5}_{\Lambda}He$	d	d	1n	149.15	51.71 ± 0.10	177.77 ± 0.10	- 28.62 ± 0.10	Rejected
6	${}^{6}_{\Lambda}He$	d	t	1n	155.25	61.15 ± 0.08	262.58 ± 0.08	- 107.33 ± 0.08	Rejected
7	${}^{6}_{\Lambda}He$	t	d	1n	155.25	51.91 ± 0.10	187.69 ± 0.10	- 32.44 ± 0.10	Rejected

TABLE VI

THE COMPARISON OF Q-VALUE AND E_{TOT} FOR ALL POSSIBLE NON-MESONIC DECAY MODES OF SINGLE- Λ HYPERNUCLEUS (TRACK #1) WITH TWO NEUTRONS EMISSION

No	Track # 1	Track # 3	Track # 4	neutron	Q-value (MeV)	E_{vis} (MeV)	E_{tot} (MeV)	Q-E_{tot} (MeV)	Remark
1	${}^{4}_{\Lambda}He$	p	p	2n	166.01	38.48	> 63.67	102.34	Rejected
2	${}^{5}_{\Lambda}He$	p	d	2n	146.93	51.40	> 111.24	35.69	Rejected
3	${}^{5}_{\Lambda}He$	d	p	2n	146.93	38.79	> 68.25	78.68	Rejected
4	${}^{6}_{\Lambda}He$	p	t	2n	153.02	60.83	> 161.36	- 8.34	Rejected
5	${}^{6}_{\Lambda}He$	d	d	2n	148.99	51.71	> 117.81	31.18	Rejected
6	${}^{6}_{\Lambda}He$	t	p	2n	153.02	38.99	> 72.19	80.83	Rejected
7	${}^{8}_{\Lambda}He$	t	t	2n	157.09	61.35	> 176.36	- 19.27	Rejected

B. Results of Invariant Masses and Binding Energies of Single- Λ Hypernucleus

The obtained invariant masses for three acceptable decay modes were compared with the known mass from particle data group. Then, the binding energies of single-Λ hypernuclei obtained in the analyzed event were also compared with the other experimental binding energies. The results of invariant masses and binding energies for three acceptable decay modes were described in Table VII.

TABLE VII

THE COMPARISON OF THE INVARIANT MASS AND BINDING ENERGY FOR ACCEPTABLE DECAY MODES AT POINT B

Decay modes	Invariant mass (MeV/c^2) [Our Analyzed Event]	Known mass (MeV/c^2) [6]	Binding Energy (BE) (MeV) [Our Analyzed Event]	Other Experimental BE (MeV) [2, 3, 4]
${}^{10}_{\Lambda}Be \rightarrow {}^{10}B + \pi^-$	9498.961 ± 0.498	9499.326 ± 0.226	9.48 ± 0.58	9.11 ± 0.22
${}^{12}_{\Lambda}B \rightarrow {}^{12}C + \pi^-$	11354.563 ± 0.791	11356.880 ± 0.078	13.67 ± 0.80	11.37 ± 0.06
${}^{4}_{\Lambda}He \rightarrow p + d + 1n$	4828.934 ± 0.401	3921.642 ± 0.58	14.129 ± 0.407	2.39 ± 0.3

C. Results of Estimation of Binding Energy of Ξ^- Hyperonfrom Vertex A of Event

The possible production modes of single-Λ hypernucleus at vertex A were also considered. Kinematical analysis of the production reaction was made by assuming the Ξ^- hyperon was captured by a light emulsion nuclide (^{12}C, ^{14}N or ^{16}O). All production modes from the light nuclides (^{12}C, ^{14}N and ^{16}O) were checked as in Table VIII.

The Q-value and total kinetic energy for each production mode were calculated in the same manner as in decay modes. All possible production modes, their Q values, E_{tot}, the difference between Q value and E_{tot} and comments were shown in Table VIII. The modes were rejected in which Ξ^- hyperon is unbound, i.e., B_{Ξ^-} is negative. Among them, a small difference between Q-value and E_{tot} was observed.

TABLE VIII

POSSIBLE PRODUCTION MODES OF SINGLE- Λ HYPERNUCLEUS AT VERTEX A

No	Xi	Target	Track #1	Track #2	lambda	n	Q-value (MeV)	E_{vis}(MeV)	E_{tot} (MeV)	Q-E_{tot} (MeV)	Remark
1	Ξ^-	${}^{12}C$	${}^{8}_{\Lambda}Li$	${}^{4}He$	Λ	-	10.79	5.20 ± 0.2	8.04 ± 0.2	2.75 ± 0.2	Rejected
2	Ξ^-	${}^{14}N$	${}^{8}_{\Lambda}Li$	${}^{6}Li$	Λ	-	1.99	6.99 ± 0.2	7.07 ± 0.2	- 5.08 ± 0.2	Rejected
3	**Ξ^-**	**${}^{14}N$**	**${}^{10}_{\Lambda}Be$**	**${}^{4}He$**	**Λ**	**-**	**19.52**	**6.47 ± 0.4**	**16.55 ± 0.4**	**2.97 ± 0.4**	**Acceptable**
4	Ξ^-	${}^{14}N$	${}^{12}_{\Lambda}B$	d	Λ	-	13.75	6.22 ± 0.7	45.08 ± 0.7	- 31.33 ± 0.7	Rejected
5	Ξ^-	${}^{14}N$	${}^{7}_{\Lambda}Li$	${}^{7}Li$	Λ	-	0.77	7.05 ± 0.4	7.66 ± 0.4	- 6.89 ± 0.4	Rejected
6	Ξ^-	${}^{14}N$	${}^{13}_{\Lambda}B$	p	Λ	-	14.90	5.99 ± 0.8	55.85 ± 0.8	- 40.95 ± 0.8	Rejected
7	Ξ^-	${}^{14}N$	${}^{9}_{\Lambda}Be$	${}^{4}He$	Λ	1n	15.46	0.51 ± 0.8	11.11 ± 0.8	4.35 ± 0.8	Rejected
8	Ξ^-	${}^{16}O$	${}^{10}_{\Lambda}Be$	${}^{6}Li$	Λ	-	0.26	8.26 ± 0.4	10.03 ± 0.4	- 9.77 ± 0.4	Rejected
9	Ξ^-	${}^{16}O$	${}^{12}_{\Lambda}B$	${}^{4}He$	Λ	-	16.87	7.74 ± 0.2	29.32 ± 0.2	- 12.45 ± 0.2	Rejected
10	Ξ^-	${}^{16}O$	${}^{14}_{\Lambda}C$	d	Λ	-	12.50	7.51 ± 1.2	66.38 ± 1.2	- 53.88 ± 1.2	Rejected

D. Discussions

According to Table VII, the value of the invariant mass of ${}^{10}_{\Lambda}Be$ hypernucleus in our analyzed event was 9498.961 ± 0.498 MeV/$c^{2.}$ The known mass of ${}^{10}_{\Lambda}Be$ hypernucleus was 9499.326 ± 0.226 MeV/c^2 [6]. Therefore, the invariant mass of a single - Λ hypernucleus in the analyzed event was very consistent with the known mass in ${}^{10}_{\Lambda}Be \rightarrow {}^{10}B + \pi^-$ decay mode. And then, the binding energy of ${}^{10}_{\Lambda}Be$ hypernucleus, 9.48 ± 0.58 MeV was also consistent with the other experimental binding energy, 9.11 ± 0.22 MeV. Therefore, the type of single- Λ hypernucleus of this analyzed event was ${}^{10}_{\Lambda}Be$ hypernucleus.

By comparing the results at decay modes and production modes, the most possible production and decay modes were shown in below:

$$\Xi^- + {}^{14}_{7}N \rightarrow {}^{10}_{\Lambda}Be + {}^{4}_{2}He + \Lambda$$

$${}^{10}_{\Lambda}Be \rightarrow {}^{10}_{5}B + \pi^-$$

The Ξ^- hyperon was captured by ${}^{14}_{7}N$ nucleus and ${}^{10}_{\Lambda}Be$ hypernucleus (track #1), ${}^{4}_{2}He$ (track #2) and invisible Λ hyperon were emitted at the production point A. Then, ${}^{10}_{\Lambda}Be$ hypernucleus (track #1) mesonically decays into ${}^{10}_{5}B$ nucleus (track #3) and π^- meson (track #4) at the decay point B. Finally, the binding energy of Ξ^- hyperon in the Ξ^--^{14}N system was 2.97 ± 0.4 MeV.

V. Conclusion

A single- Λ hypernucleus event has been analyzed. It has two vertex points, one production point, and one decay point of Λ hypernucleus. The type of single- Λ hypernucleus was identified from the decay point B. The binding energy between the Λ hyperon in ${}^{10}_{\Lambda}Be$ nucleus was 9.48 ± 0.58 MeV. It shows the bond state of Λ hyperon and beryllium 10 core nucleus. On the other hand, the binding energy of Ξ^- hyperon in Ξ^--^{14}N system was obtained from the production point A. The existence of hypernuclei with strangeness quantum numbers S = -1 and S = -2 was confirmed by this analysis.

Acknowledgment

I would like to thank Pro-Rectors and members of ESEJ, the Technological University (Mandalay) for their kind permission to carry out this research work.

References

[1] S. S. Aye *et al*., "Determination Type of Hypernucleus from a Single Lambda Hypernucleus Event in Nuclear Emulsion of KEK-E373 Experiment". J. Myanmar Acad. Arts Sci. Vol. XVIII No.2B, 2020.

[2] T. Cantwell *et al*., "On the Binding Energy Values and Excited States of Some A ≥ 10 Hypernuclei", 1974.

[3] M. Juric *et al*., "A New Determination of the Binding Energy Values of the Light Hypernuclei A ≤ 15*"*, Nuclear Physics. B 52, 1973.

[4] T. Gogami *et al*., "High Resolution Spectroscopic Study of ${}^{10}_{\Lambda}Be$", Phys. Rev. C **93** (2016) 034314.

[5] K. T. Tint. *et al*., "Observation of a Be Double- Lambda Hypernucleus in the J-PARC E07 Experiment". Prog. Theor. Exp. Phys. 021D02, 2019.

[6] M. Yamaguchi *et al*., "ΞN and ΞΞ OBEP and Ξ^-- Nucleus Bound States", Prog. Theor. Phys. **105** (2001) 627.

[7] S. H. Hayakawa. "Study of Ξ^- nucleus interaction by measurement of twin hypernuclei with hybrid-emulsion method". D.Sc. Thesis, Osaka University, 2019.

[8] H. Takahashi. "Study of Double- Λ Hypernuclei with Hybrid-Emulsion Method", D. Sc. Thesis, Kyoto University, 2003.

Co-Precipitation Method for Characterization of Nickel Oxide Particles with Various Agent Weights

War War[1], Khaing Mar Htay[2], Htike Htike Aung[3], Aye Aye Maw[4], Aye Mar Khin[5], Maw Maw Kyu[6], Chan Thar[7]

[1,2,3]*Lecturer,Engineering Physics Department ,Technological University(Mandalay)*

[4,5]*Associate Professor,Engineering Physics Department,Technological University(Mandalay)*

[6] *Assistant Lecturer,Engineering Physics Department,Technological University(Mandalay)*

[7]*Tutor,Engineering Physics Department,Technological University(Mandalay)*

Email: [1]wwar0441@gmail.com, [2]khingmarhtay2018@gmail.com, [3]htikehtikeaung55555@gmail.com,[4]dawayeayemaw16@gmail.com, [5]yccdawayemarkhin@gmail.com,[6]mawmawkyu87@gmail.com,[7]chanthar313@gmail.com

***Abstract*—Nickel oxide particles have a wide range of applications in a variety of advanced materials. This study was prepared to obtain pure nickel oxide particles,sodium hydroxide with different masses of weights. X-ray diffraction (XRD), Fourier transform infrared spectroscopy (FTIR), and scanning electron microscopy (SEM) were used to characterize the crystal structures and phase purity of the prepared samples. The XRD and FTIR results revealed that the prepared sample was nanocrystalline pure nickel oxide (NiO). SEM image showed that the prepared NiO sample was irregular shaped micro-plates.**

Keywords—nickel oxide (NiO), co-precipitation, XRD, FTIR, SEM.

I. INTRODUCTION

Many inorganic nanoparticles have been the subject of intense research over the past few decades due to their practical uses in a variety of sectors, including biomedicine, photocatalysis, magnetic devices, and sensors. These include zinc oxide (ZnO), titanium oxide (TiO), and nickel oxide (NiO). A lot of interest has been shown in nickel oxide (NiO) nanoparticles due to their exceptional stability, exceptional magnetic, electronic, optical, and catalytic properties, and their wide range of applications, which include gas sensors, electrochromic devices, batteries, fuel cells, dye-sensitized solar cells, solar energy absorbers, and magnetic recording devices. Furthermore, NiO nanoparticles have a broad band gap of 3.6–4.0 eV and are incredibly cheap, notcontaining poisonous substances, and highly durable conductive appliance, in contrast to other metal oxide nanoparticles [1].

Biomedical detection, medication distribution, imaging, and antibiotics are just a few of the medicinal uses for these nanoparticles.In addition to the uses already described, NiO nanoparticles have the potential to effectively remove both organic and inorganic contaminants, which makes them a valuable tool for environmental protection [2].

As a result, several techniques, including as thermal decomposition, micro-emulsion, co-precipitation, chemical vapour deposition, sol-gel, hydrothermal, and microwave-assisted synthesis, have been used in the production of nickel oxide micro/nanostructures. The co-precipitation method is becoming more and more popular among these many techniques since it has the possibility for direct process synthesis together with the benefits of simplicity and high yield [3].

We report on the synthesis of NiO from pure precursors, sodium hydroxide and nickel chloride, via co-precipitation technique. The generated sample was subjected to X-ray diffraction (XRD), Fourier transform infrared spectroscopy (FTIR), and scanning electron microscopy (SEM) to assess its phase clarity, crystal composition.

II. MATERIALS AND METHODS

A. Materials

All of the chemicals used in this work were of analytical grade. They were used without further cleaning. Nickel chloride (NiCL) as used as a precursor and sodium hydroxide (NaOH) was used as a precipitating agent for the solutions. Deionized water has been used for the preparation of all solutions.

B. Preparation of Nickel Oxide

Using distilled water and continuous stirring, a NiCL solution was made using this procedure.

First, the calculated amounts of NaOH and NiCLwere weighed. After that, 30 ml of deionized water, 3 ml of ethylene glycol $(CH2OH)_2$, and 4.5 g of NiCL were combined and agitated for 5 minutes at room temperature. The Ni solution's pH was found to be five. Then, at room temperature, 1.5 g of NaOH and 20 ml of distilled water were combined and stirred for five minutes.

Subsequently, the NaOH solution was gradually added to the Ni solution, and after 30 minutes of stirring the mixed solution at 100 °C, the green-colored precipitate was seen. The mixture's solution had a pH of eight. Centrifugation was used to wash the green precipitate after it had been cleaned with deionized water to remove any remaining ions. Following that, ethanol was used twice to wash the green-colored precipitate.The pH was changed to 7.

The computed amount of NaOH for the second sample (S2) has been adjusted to 2.5 g, while the weighted mass of NiCL remains unchanged. The first sample was subjected to the same experimental protocol. Subsequently, sample three (S3) has the same weighted mass of NiCL and a different determined amount of NaOH (3.5 g).

The green-filtered sample was dried in an oven at 100 °C for six hours during the course of the investigation. After that, the dried sample was calcined for two hours at 400 °C to produce NiO samples (S1, S2, and S3).

TABLE I. NIO THREE SAMPLES WITH THE SAME CALCINED TEMPERATURE

Sample	*Starting Materials*	*Calcined hours*	*Calcination temperature*
S1	NiCL+NaOH	2 hours	400 °C
S2	NiCL+NaOH	2 hours	400 °C
S3	NiCL+NaOH	2 hours	400 °C

C. Characterization

To study the crystal structures and phase purities of synthesized powdered samples (namely S1, S2 and S3) at 400 °C, X-ray powder diffraction (Shimadzu XRD-6100-S) with Cu Kα1 radiation (λ = 0.154 nm), working current (20 mA) and voltage (40 kV) was used. Fourier transform infrared spectrum (FTIR, Shimadzu IR Affinity-1S) was used to investigate the functional group of synthesized samples. The wavenumber range was set up from 400 cm^{-1} to 4000 cm^{-1} with a spectral resolution of 4 cm^{-1}. The morphology of the synthesized samples was observed by scanning electron microscopi(SEM, JEOL JCM-6000).

III. RESULTS AND DISCUSSIONS

A. XRD Analysis

The XRD patterns of synthesized powdered samples (S1, S2, and S3) are shown in Figure 1(a-c). The main diffraction peaks were observed at about 2θ value 37°, 43° and 62°, corresponding to the reflection from the (111), (200), and (220) crystal planes which are in good agreement with the nickel oxide particles of cubic structure. The NiO lattice constant computed from the XRD data is 4.1740 °A, which is also in well accepted with the reported data (JCPDS-ICDD card no.47-1049, a = 4.1771°A). The broad diffraction peaks indicate that the synthesized samples (S1, S2 and S3) are NiO nanoparticles. The crystallite size determined using the Scherrer equation (1) is list in Table III(a - c). As seen, when the amount of NaOH was increased from 1.5 g to 2.5 g and 3.5 g, the intensity of the diffraction peaks and crystallite sizes in S2 and S3 increased.

$$D = \kappa \lambda / \beta \cos \theta \qquad (1)$$

where, D = crystallite size
κ = Scherrer constant (0.899)
β = full width half maximum
λ = wavelength of x ray (1.54056 °Å)
θ = Bragg diffraction angle

TABLE II(A). CRYSTALLITE SIZES OF SYNTHESIZED NIO S1

Sample	*(hkl)*	*2θ (deg)*	*fwhm*	*Crystallize size (nm)*
S1	(111)	37.1515	1.07700	9.243
S1	(200)	43.1993	1.13500	9.596
S1	(220)	62.7214	1.48014	11.713

TABLE II (B). CRYSTALLITE SIZES OF SYNTHESIZED NIO S2

Sample	*(hkl)*	*2θ (deg)*	*fwhm*	*Crystallize size (nm)*
S2	(111)	37.1541	1.06430	9.343
S2	(200)	43.2139	1.12840	9.647
S2	(220)	62.7355	1.20230	14.466

TABLE II(C).CRYSTALLITE SIZES OF SYNTHESIZED NIO S3

Sample	*(hkl)*	*2θ (deg)*	*fwhm*	*Crystallize size (nm)*
S3	(111)	37.1567	1.0516	9.445
S3	(200)	43.2285	1.1218	9.698
S3	(220)	62.7469	0.9245	18.786

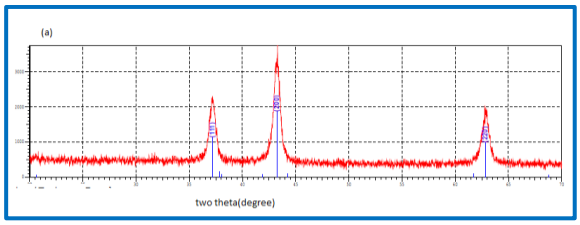

Fig. 1(a). XRD spectrum of prepared NiO (S1).

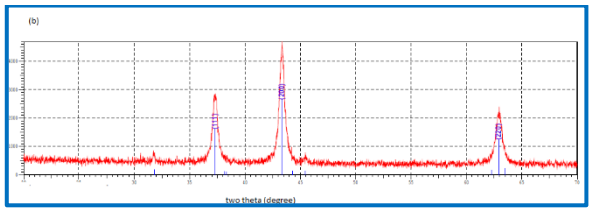

Fig. 1(b). XRD spectrum of prepared NiO (S2).

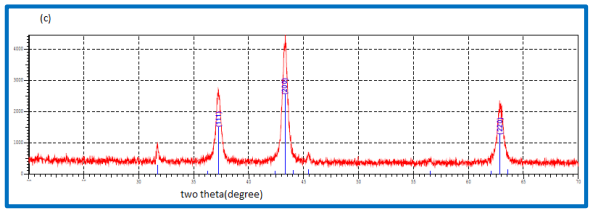

Fig. 1(c). XRD spectrum of prepared NiO (S3).

B. FTIR Analysis

Figure 2(a-c) shows the FTIR spectra of S1, S2, and S3. For S1, the weak bands at 1636 and 3385 cm^{-1} with the intensity of 77 and 64. The strong band at 1108 cm^{-1} with an intensity of 47. For S2, the weak bands at 1630 and 3396.94 cm^{-1} with the intensity of 82 and 69. The strong band at 1111.33 cm^{-1} with an intensity of 73. For S3, the weak bands at 1641 and 3394.50 cm^{-1} with the intensity of 83 and 71. The strong band at 1389 cm^{-1} with an intensity of 67.

The bands at 877 and 1124 cm^{-1} represented in-plane bending vibration mode. The bands at 877 cm^{-1} are

associated with the Ni-O vibration bond. The above information confirms the formation of pure NiO.

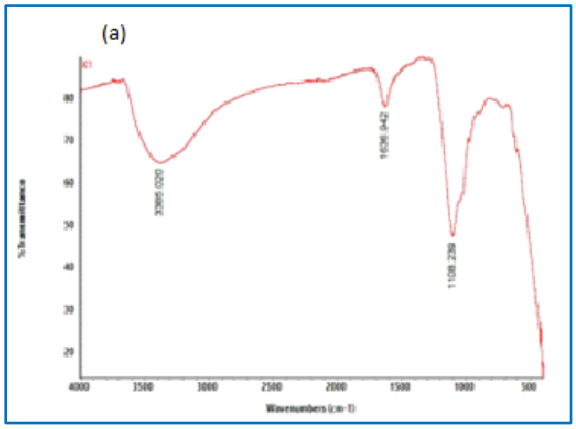

Fig. 2(a). FTIR spectrum of (NiO) particles at 400°C for (S1).

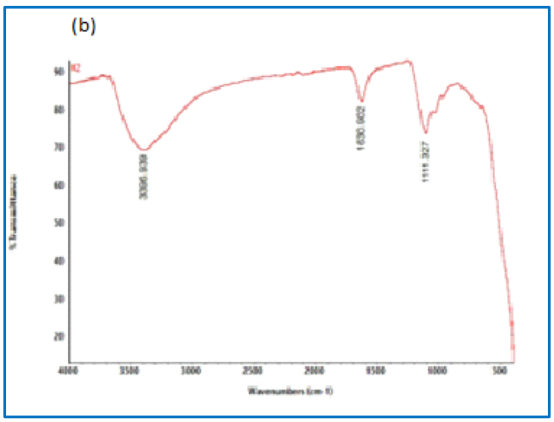

Fig. 2(b). FTIR spectrum of (NiO) particles at 400°C for (S2).

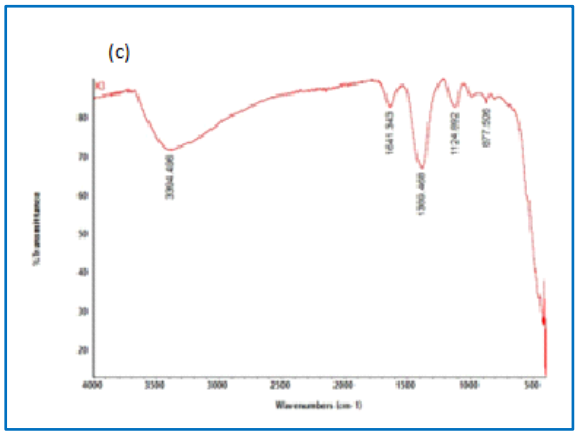

Fig. 2(c). FTIR spectrum of (NiO)particles at 400°C for (S3).

C. SEM Analysis

Figure 3(a-c) shows the morphology of the samples which has been investigated by the use of a scanning electron microscope (SEM). In the SEM images of samples in Figure 3(a-c), agglomerated nanoparticles are observed. Further analysis is required to study the detailed morphology of the samples by either field emission scanning electron microscope (FESEM) or tunneling electron microscope (TEM).

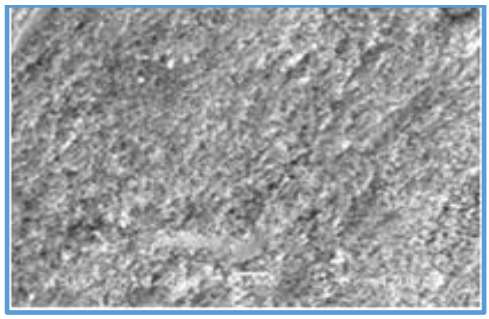

Fig. 3(a). SEM image of prepared NiO (S1).

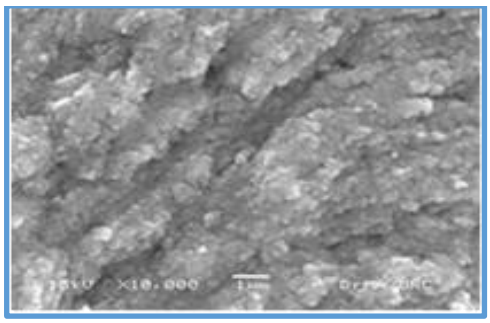

Fig. 3 (b). SEM image of prepared NiO (S2).

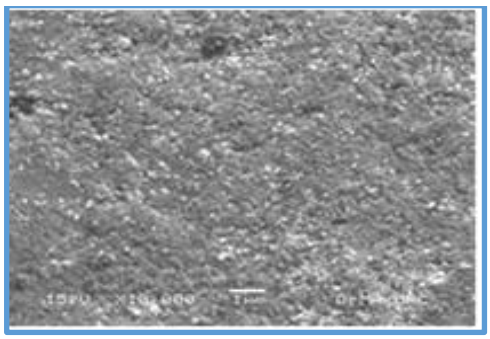

Fig. 3(c). SEM image of prepared NiO (S3).

IV. Conclusion

In conclusion, NiO nanoparticles were successfully prepared by simple co-precipitation method using sodium hydroxide and nickel chloride. The powder X ray diffraction patterns show face centred cubic phase of the synthesized NiO nanoparticles. The SEM images show that the NiO have aggregated nanoparticles. Increasing the amount of NaOH from 1.5 g to 2.5 g and 3.5 g, the intensity of the diffraction peaks and crystallite sizes of S2 and S3 increased. For the future work, the effect of temperature on the phase purity and morphology of the synthesized NiO samples will be study.

Acknowledgments

The author would like to thank Dr. Nwe Ni Hlaing, Professor, University Research Center, Magway University, and Dr. Khaing Khaing Thinn, Professor & Head of Department, Technological University (Mandalay), for their helpful comments and guidance during the production of this work.

REFERENCES

[1] Mearg Gidey Berhe & Yemane Tadesse Gebreslassie(2023,July) ”Biomedical Applications of Biosynthesized Nickel Oxide Nanoparticles”. “International Journal of Nanomedicine” [On-line]. 27:18:4229-4251.doi:10.2147/IJN.S410668.Available: https://pubmed.ncbi.nlm.nih.gov/37534055.

[2] Xiangjun Han, Ke Xu, Olena Taratula and Khashayar Farsad (2019,Jan) "Applications of Nanoparticles in Biomedical Imaging”.”International Journal of Nanomedicine” [On-line] Nanoscale,11(3),pp:799-819.Available: https://pubmed.ncbi.nlm.nih.gov/30603750/

[3] Matti M Van Schooneveld and David P Cormode(2010,July-Aug) “A fluorescent, paramagnetic and PEGylated gold/silica nanoparticle for MRI, CT and fluorescence imaging””International Journal of Nanomedicine”[On-line]2010Jul-Aug;5(4):231-6.doi:10.1002/ cmmi.376 Available: https://pubmed.ncbi.nlm.nih.gov/20812290/

Evaluating the Effectiveness of Teaching Oral Skills by Using Communicative Language Teaching in the Classroom

Daw Phyu Phyu Thet[1], Daw Khaing Mi Mi Htun[2]

[1]*Lecturer, Department of English, Technological University (Mandalay)*
[2]*Lecturer, Department of English, Technological University (Mandalay)*
Email: [1]kyawthet1291985@gmail.com, [2]khaingmi1988@gmail.com

***Abstract*—In the language classroom of second-year engineering students at Technological University (Mandalay), Communicative Language Teaching methods are used to enhance students' English language skills. In this place, whether the effectiveness of using CLT methods can be evaluated is the paradox of determining and evaluating a language teacher. Therefore, the author tries to come up with this situation by using the qualitative approach through the use of mark distribution for students' performance in their group presentations. The qualitative research method allows for detailed exploration and interpretation of students' language use. It brings a subtle understanding of the teaching strategies used in the classroom. However, it is important to acknowledge some limitations inherent in the study, such as the small sample size and the specific context of the language classroom. These limitations may affect the generalizability of the findings and should be considered when interpreting the results. As a result, this research study reveals the improvements of students who are taught oral skills by using CLT as a way to show the effectiveness of CLT in the classroom and to increase confidence in public speaking.**

Keywords—Evaluating, Effectiveness, Oral skills, Communicative Language Teaching, Second-year engineering students

I. Introduction

In this global age, many people use English as a medium of communication, making it easier to interact with people from different countries. Students should master English for some reason, such as getting a job, continuing further studies, or life-long learning. There are different approaches used in teaching English as a foreign language in and outside the classroom, but not all of them help to reach the desired communicative goal. Therefore, it is necessary to select and apply the most effective materials according to the existing level of students. Based on teaching experience, the author believes that students find speaking more difficult than reading and writing. Additionally, students' only language exposure occurs in the classroom, and students do not rely on teachers to employ effective strategies for language production. As a result of this problem, in 2016, the English curriculum in Ecuador was improved, considering the Communicative Language Teaching method as one of the central principles. [5]. This approach involves learning a language through interaction and communication rather than by memorizing different aspects of the language system. Therefore, the author investigates a way in which students' oral skills improve using the Communicative Language Teaching (CLT) method in the second-year engineering classroom. Consequently, this will benefit both teachers and students by providing valuable insights into implementing the CLT approach effectively in the second-year engineering classroom. This study aims to evaluate the effectiveness of CLT in improving the verbal skills of second-year engineering students and to tackle the problem of how to gain insight into its implementation and effects both inside and outside the classroom. By investigating the long-term effects of using CLT on students' oral communication skills, this research aims to enhance pedagogical practices in specialized academic settings and to understand how these skills are utilized in their vocational and professional environments. This connection underscores the broad implications of CLT for lifelong learning and career readiness, making it a central focus for educational innovations and supportive language teaching. Through verifiable analytics and teaching insights, this research contributes to the ongoing discussion of effective language teaching practices in specialized academic fields. Finally, it aims to improve the academic and professional communication skills of engineering students.

II. Literature Review

A. Why Important the CLT Method is

All individuals require communication to convey their ideas, emotions, and thoughts, which is why incorporating communicative activities into the lesson is essential. When an active learning environment inspires students to finish their tasks, they typically speak more fluently. However, teachers have consistently encountered difficulties related to oral tests, including issues like insufficient assessments, the absence of assessments, and the lack of adequate time and resources to develop comprehensive and fair evaluations. Additionally, teachers often invest significant time in creating effective speaking activities, determining the assessment criteria, and selecting the appropriate scoring methods for evaluating English language proficiency. Oral communication skills, in particular, are fundamental for engineering students as they guide their career needs. The pedagogical method used to teach these skills has a significant impact on students' abilities to communicate effectively in real-world situations. One approach that has gained attention in recent years is Communicative Language Teaching (CLT).

According to Richards and Rodgers (2001), CLT is about meaningful language use, circulating contextual content, and learner-centered activities [1]. This approach fits well with the communication needs of engineering students, who must convey technical information effectively. According to Savignon, S.J. (2002), CLT enables learners to use language appropriately in different situations, which is a very relevant skill in engineering situations [3]. Effective communication is essential in

engineering education for cooperation, problem-solving, and project management. So, CLT is the best method to improve students' oral skills.

B. Oral Assessment Criteria

Many teachers require students to give oral presentations that count toward their grades. Teachers must clarify their goals for these performances as well as the student learning objectives they relate to. By including the assignment in course goals and learning objectives, teachers make students clear about their expectations and develop a rule for evaluating presentations. Judging presentations can pose a challenge, especially if teachers must consider multiple criteria and different performance levels. Sadie Louise Winterscheid (2016) notes that "rubrics make presentations more efficient and are important tools in educational sectors, especially when evaluating individual and group presentations." [9]. They guide both teachers and students, outlining specific criteria that presentations need to meet for success. By clearly setting expectations, the core principles help students understand what it takes to achieve high-performance levels and provide a plan for their preparation. This transparency is advantageous because it clarifies the ranking process and makes it clear and fair. "In addition to enhancing the learning experience, rubrics contribute to a fairer and more equitable educational environment." [7]. It ensures that teachers assess all students based on the same standards, regardless of their background or abilities. This is especially important in diverse classrooms, where students may have different levels of prior knowledge and skills. By leveling the playing field, rubrics promote inclusiveness and fairness. They also provide a common language for assessment, which can be particularly useful in collaborative settings where teachers may be involved in the assessment process. Moreover, teachers can adapt rubrics to suit different disciplines and presentation formats. They can tailor rubrics to address the specific requirements of each context, whether it's a scientific presentation, a literary analysis, or a business proposal. Additionally, the use of rubrics aligns with the best practices in educational assessment, which advocate for clear, transparent, and consistent evaluation methods [8]. The rubric usually consists of two components: criteria and grades. The criteria are the aspects or dimensions, such as content, organization, delivery, and visual aids, that teachers want to evaluate. Teachers use grades such as excellence, good, fair, and inadequate to describe how well students meet each criterion. In addition, the rubrics support teachers by providing a clear framework for grading. This saves time and can reduce the uncertainty often associated with subjective assessments. Teachers have to provide constructive feedback. Teachers can use rubrics to highlight specific areas where students excel and where they need to improve. This targeted feedback is invaluable to students, as it guides their learning process and helps them refine their skills. Additionally, teachers can use rubrics as teaching tools. When students share their presentations before they begin, it can help to focus on the key points that are critical to success. This proactive approach encourages students to self-assess and adjust their work against standards, leading to high-quality presentations. Depending on the importance and difficulty of the task, rubrics can allocate points or weights to each criterion and grade. Rubrics can give many advantages in evaluating presentations, such as clarifying goals and expectations, providing specific and constructive feedback, reducing subjectivity and bias, saving time and effort for the evaluator, and facilitating comparison and analysis. However, there are some disadvantages. For example, it can limit creativity and flexibility by imposing a scheduled structure, forgetting about the characteristics or nuances of the presentation, creating a false sense of objectivity, and encouraging discussion between the presenter and evaluator. Creating a rubric for presentation skills requires some planning and preparation. First, it is required to identify criteria that are relevant and appropriate to the presentation's purpose and audience. Then, it is important to define grades that reflect the quality of each criterion and to assign points or weights to each criterion and grade [2].

C. Consideration for Making Effective Oral Presentation Criteria

Rubrics play an important role in group presentations to ensure a fair assessment of all members. They evaluate not only collective output but also the contributions of individual team members, promoting accountability and collaboration. Team presentations often involve different roles and responsibilities, and this is important because a well-designed rubric captures the unique aspects of each member's participation. In addition, rubrics can help reduce biases in ratings. Based on these undeniable reasons, teachers must follow the steps below to create an effective rubric for measuring presentation skills, ensuring standardized criteria for assessing all students and increasing the objectivity and consistency of the assessment process. Here are some steps and strategies that can help teachers use the rubric effectively: Before the presentation, the organizers explain the purpose, explanation, and evaluation process to the presenters. After studying and recording the presentation, it is important to carefully consider the criteria and steps involved in creating rubrics. This step is the foundation for the rubric development process and is essential. Subsequently, it is important to identify evidence or examples to support scoring and provide commentary on the presentation using rubrics. Teachers base their evaluations on this assessment and assign scores or grades based on it. Finally, providing the presenter with specific positive feedback that highlights their strengths and areas for improvement is important to further improve students' oral skills.

The author assesses each member's presentation skills based on six specific criteria: content, delivery, organization, engagement, visual aids, and time management. Under assessment by these standards, each participant receives a score that represents their unique contribution to the presentation. But for more specific performance of teamwork, the author evaluates the entire group by two additional factors: collaboration and Q&A handling. This comprehensive assessment method recognizes that each student's abilities are different, and that each grade is also different.

For individual presentations, rubrics provide detailed recommendations for various aspects, such as content, delivery, and visual aids. This feedback is for students to identify their strengths and areas that need improvement. It is essential to promote their growth and development.

In conclusion, the author cannot overstate the importance of rubrics in evaluating individual and group presentations. They are clear and concise for assessment. It provides an objective and consistent framework that benefits students and teachers. Rubrics outline specific standards and performance levels, guiding students in their preparation and helping them understand what to expect. They provide fair and unbiased ratings, improve accountability and collaboration in team settings, and save teachers' time while providing meaningful feedback. Ultimately, the rules are

fair and enhance the educational experience by fostering an inclusive and effective learning environment. The clearest part of creating and using a rubric as an assessment tool for students' oral skills is that it measures how effectively the CLT method, used for teaching oral skills in the classroom, links with and assesses students' application of knowledge and understanding during group presentations.

III. Research Methodology

Assessment approaches within the education sector are a broad field. A variety of tasks, such as topic discussions and role-plays, serve as common tools for assessing students' oral skills. Teachers typically rely on criteria such as range, accuracy, ability, interaction, and coherence to measure performance. In addition, oral assessments typically adopt an analytical scoring method. Teachers recognize assessing speaking skills as one of the most complex aspects of evaluating language ability. In this study, the author used group presentations to evaluate how effectively the CLT method enhances students' oral skills in the classroom. Since CLT, in its meaning, is communicative language teaching, the author observed communication in group work. Therefore, the research method here is making comparisons to find out whether CLT is successful or not by setting concise rubrics for group presentations.

3.1 Rubric for the Group Presentation

The author utilizes the following rubric criteria to evaluate students' oral skills through group presentations, referencing the works of Prof. Magdy M. Aly (2020) and Anderson, Joseph S., and Mohrweis, Lawrence C. (2008). [4] [6]. Teachers must assess students' speaking skills through direct and conversational interactions**.** The group presentation rubric is an essential tool for comprehensively evaluating the performance of group presentations. Measuring efficient communication and the speaker's ability involves eight different criteria. They are content, organization, delivery/presentation, engagement, visual aids, time management, collaboration, and overall presentation. Speaking scoring methods evaluate a learner's language performance in oral tasks and indicate the proficiency level of their spoken language skills. Teachers can use either numerical form or verbal categories such as 'excellence', 'good', or 'fair', etc. Teachers evaluate each criterion on a scale of 1 to 5, with the highest score indicating excellent performance by the students and the lowest indicating significant deficiencies.

1) *Content*: This criterion assesses the depth and relevance of the information presented. An excellent score (5) reveals thorough coverage with strong supporting details, while an inadequate score (1) shows little or irrelevant information.
2) *Organization*: It evaluates how logically the presentation is structured. The best score (5) is a different introduction; it reflects a clear and logical flow with a body and conclusion. A score of 1 shows cohesion, making the presentation difficult to follow.
3) *Delivery/Presentation*: This standard is based on the clarity, emphasis on trust, and engagement of all group members. A score of 5 means that all team members speak clearly and confidently, engaging the audience effectively. A score of 1 indicates poor speaking skills and a lack of audience participation.
4) *Engagement*: This assesses the ability to engage an audience. A high score (5) reflects continuous engagement with interactive elements or engaging content, while a low score (1) indicates a failure to maintain audience interest.
5) *Visual Aids*: This principle reviews the effectiveness of visual aids in enhancing their presentation. A score of 5 was given for relevant aids designed to enhance understanding, and a score of 1 for irrelevant or distracting aids.
6) *Time Management*: This criterion analyzes whether the presentation fits within the allowed time. For effective time management, a score of 5 means the presentation is well-timed, while a score of 1 indicates significant timing issues.
7) *Collaboration*: It measures the contribution and teamwork among the group members. A score of 5 indicates equal and effective collaboration, whereas a score of 1 reflects poor or no collaboration.
8) *Q&A Handling*: It examines the team's ability to handle audience questions. A score of 5 indicates thorough and confident responses, while a score of 1 indicates a failure to handle the questions effectively.

This outline supplies a detailed framework for evaluating group presentations, ensuring that all essential aspects are considered. It helps identify strengths and areas that need improvement and guides students toward more effective group presentation skills.

IV. Class Contribution to Evaluation using CLT Methods

The author employs the above eight criteria of the group presentation rubrics to evaluate the presentations of 17 groups comprising about 100 second-year engineering students at Technological University (Mandalay). There are between 5 and 7 members in one group. The author explained to the students these criteria before starting their presentations. Some students are enthusiastic, and some are not active in the presentations. This formative assessment not only provides transparency in grading but also supports detailed feedback and continuous improvement of presentation skills. This systematic approach will help identify top-performing teams and identify those in need of support and guidance. The author gives a total of 40 marks for each group. The author rates each criterion on a scale of 1 to 5, with 5 indicating excellent, 4 referring to good performance, 3 indicating fair, 2 representing needed improvements, and 1 indicating inadequate.

The author shows that 1 represents "inadequate" (between 1 and 8 marks), 2 indicates "needs improvements" (between 9 and 16 marks), 3 refers to "fair" (between 17 and 24 marks), 4 represents "good" (between 25 and 32 marks), and 5 refers to "excellent" (between 33 and 40 marks) based on 40 marks.

I. Criteria Explanation

Criteria No.	**Criteria Name**
1.	Content
2.	Organization
3.	Delivery/Presentation
4.	Engagement

Criteria No.	Criteria Name
5.	Visual Aids
6.	Time Management
7.	Collaboration
8.	Q & A Handling

In the above table, the author reveals that 1 represents "content," 2 indicates "organization," 3 refers to "delivery/presentation," 4 represents "engagement," 5 expresses "visual aids," 6 illustrates "time management," 7 exemplifies "collaboration," and 8 represents "Q&A handling.".

II. MARK DISTRIBUTION FOR GROUP PRESENTATION

Group No.	Criteria									
	1	**2**	**3**	**4**	**5**	**6**	**7**	**8**	**Total**	**Grades**
1.	4	3	2	3	3	2	3	3	23	**3**
2.	4	4	3	3	3	3	4	3	27	**4**
3.	4	3	2	3	3	2	3	2	22	**3**
4.	5	5	4	4	3	5	5	5	36	**5**
5.	4	3	2	2	3	3	3	2	22	**3**
6.	4	4	2	3	2	2	3	2	20	**3**
7.	5	5	4	4	3	5	5	5	36	**5**
8.	4	4	3	4	3	4	4	4	30	**4**
9.	4	4	3	4	3	4	4	4	30	**4**
10.	5	5	4	4	3	5	5	5	36	**5**
11.	4	3	3	4	3	3	4	3	27	**4**
12.	4	3	2	3	3	2	3	3	23	**3**
13.	4	4	3	4	3	4	4	4	30	**4**
14.	4	3	2	4	3	4	3	3	26	**4**
15.	4	4	3	4	3	4	4	4	30	**4**
16.	4	3	3	4	3	4	4	3	28	**4**
17.	4	4	3	4	2	4	4	4	29	**4**

The author shows the scores of the 17 groups of about 100 students. These scores represented an evaluation of the effectiveness of teaching oral skills using the CLT method.

4.1 Detailed Explanation for Mark Distribution

According to Table 2, group 1 received a score of 4 for their content, 3 for organization, 2 for presentation/delivery, 3 for engagement, 3 for visual aids, 2 for time management, 3 for collaboration, and 3 for Q&A handling. This group got 23 marks in total. Their performance showed middling or fair competence in most criteria but struggled with delivery and visual aids.

In Group 2, they got 4 for their content, 4 for organization, 3 for presentation/delivery, 3 for engagement, 3 for visual aids, 3 for time management, 4 for collaboration, and 3 for Q&A handling. This team had 27 marks and good overall performance, particularly in collaboration and Q&A handling, but delivery needs improvement.

Group 3 earned a score of 4 for their content, 3 for organization, 2 for presentation/delivery, 3 for engagement, 3 for visual aids, 2 for time management, 3 for collaboration, and 2 for Q&A handling. This group got 22 marks in total. They lacked presentation and visual aids, indicating a need for better preparation.

In group 4, they scored 5 for their content, 5 for organization, 4 for presentation/delivery, 4 for engagement, 3 for visual aids, 4 for time management, 5 for collaboration, and 5 for Q&A handling. This team had 36 marks and excelled in all criteria, showing strong engagement, collaboration, and handling of Q&A.

The next group's scores were 4, 3, 2, 2, 3, 3, 3, 2, representing the scheduled criteria such as content, organization, etc. Their total scores were 22, and their performance was similar to that of group 3, with a significant lack of delivery and visual aids.

Group 6 scored 4, 4, 2, 3, 2, 2, 3, and 2, demonstrating the above eight criteria. Their total scores were 20, and this group had the lowest score, highlighting significant weaknesses in most criteria.

In group 7, they got a score of 5 for their content, 5 for organization, 4 for presentation/delivery, 4 for engagement, 3 for visual aids, 5 for time management, 4 for collaboration, and 4 for Q&A handling. This group got 36 marks in total and matched Group 4 superbly, showing thorough coverage and teamwork.

Group 8 accepted a score of 4, 4, 3, 4, 3, 4, 4, 4, for their given criteria. This group won 30 marks. They performed very well, with little improvement in cooperation.

The next group's scores were 4, 4, 3, 4, 3, 4, 4, 4, representing the scheduled criteria such as content, organization, etc. Their total scores were 30. This group showed similar strengths to Group 8, with excellent visual aids and organization.

Group 10 scored 5, 5, 4, 4, 3, 5, 5, and 4, demonstrating the above eight criteria. Their total scores were 36. Their performance was consistent and good in all criteria, indicating strong preparation and teamwork.

In Group 11, they scored 4 for their content, 3 for organization, 3 for presentation/delivery, 4 for engagement, 3 for visual aids, 3 for time management, 4 for collaboration, and 3 for Q&A handling. This team had 27 marks and scored well on organization and delivery, but needed improvement in content and engagement.

In group 12, they got a score of 4 for their content, 3 for organization, 2 for presentation/delivery, 3 for engagement, 3 for visual aids, 2 for time management, 3 for collaboration, and 3 for Q&A handling. This team had 27 marks. Their performance indicated a need for better organization and more engaging delivery.

Group 13 accepted a score of 4, 4, 3, 4, 3, 4, 4, 4 for their given criteria. This group won 30 marks in total. This group excelled in visual aids and engagement, with minor areas for improvement in collaboration.

Group 14 received a score of 4 for their content, 3 for organization, 2 for presentation/delivery, 4 for engagement, 3 for visual aids, 4 for time management, 3 for collaboration, and 3 for Q&A handling. Their total scores were 26. They

performed well on delivery and engagement but scored low on organization and collaboration.

Group 15 accepted a score of 4, 4, 3, 4, 3, 4, 4, 4 for their given criteria. This group obtained 30 marks in total. Their presentation was comprehensive and showed strength in all parameters, especially in delivery and visual aids.

Group 16 scored 4, 3, 3, 4, 3, 4, 4, and 3, demonstrating the above eight criteria. This group gained 28 marks in total. They showed good performance but needed to improve in cooperation and engagement.

The last group's scores were 4, 4, 3, 4, 2, 4, 4, 4, representing the scheduled criteria such as content, organization, etc. Their total scores were 29. Their presentation was strong in most areas but needed better visual aids and question-and-answer handling.

V. Discussion

The author evaluated the effective use of CLT methods in the second-year engineering classroom. According to the evaluation, the findings reveal significant insight into the teaching approach's effectiveness and areas for improvement. The analysis of group presentations based on specific criteria revealed a wide range of skills and abilities among groups. This survey had the groups that similarly achieved the highest scores (36), such as groups 4, 7, and 10. They performed well in all standards, indicating thorough preparation and strong teamwork. Groups 8, 9, 13, and 15 had high scores (30) that showed flexibility and effectiveness in their presentations.
Groups 2, 11, 16, 14, and 17 scored between 27 and 29, indicating generally good performance with minor areas requiring improvement.

Groups 1, 3, 5, and 12 scored between 22 and 23, highlighting several areas needing improvement.

Group 6 received the lowest scores at 20 marks, reflecting significant inadequacies in several criteria.

Similarly, the findings identified different groups. Most groups generally remembered the topic well, indicating that they adequately covered it. Group 6 obviously lacked content.

A high-scoring groups like 4, 7, and 10 had clear and logical presentations, while groups 6 and 12 showed no cohesion. Top-performing teams demonstrated confident and clear speech. Low-performing groups such as 3 and 5 lacked clarity and engagement in presentations. Using visual aids effectively was a common strength in the highest-scoring groups. Conversely, groups with low scores tend to have less relevant or poorly designed aids. Excellent teams demonstrate effective collaboration. Groups with low scores showed less cooperation, which affected their overall performance. The teams that achieved good scores struggled to maintain interest while low-scoring teams kept the audience engaged. While most teams managed their time well, some low-scoring teams deviated significantly from the allowed time. Top-scoring teams answered questions thoroughly and confidently while low-scoring teams had difficulty with that.

Then, the author presents that this survey had multiple levels from 1 to 5, indicating different levels of performance across the groups. Several groups achieved grades ranging from 3 to 5, indicating that most groups performed moderately well. All three groups, such as 4, 7, and 10, received the highest 5 grades, showing exceptional performance in their presentations. The grade of 5 suggested that these groups consistently excelled in various criteria such as content, organization, presentation, engagement, visual aids, time management, collaboration, and Q&A handling. These three groups showed superior quality in their presentations, distinguishing them from other groups with their high level of effectiveness and proficiency. Getting high grades in presentations often reflected effective communication skills, suggesting that these groups were able to articulate their ideas and successfully engage their audience. Groups 2, 5, 8, 9, 11, 13, 14, 15, 16, and 17 obtained a grade of 4 on various criteria, suggesting a consistent level of activity across the groups. Obtaining grade 4 meant that these groups had prepared their presentations well and had a thorough understanding and organization. These groups demonstrated effective communication skills and were able to successfully convey their ideas and engage the audience. Although these groups performed well, there might still be minor areas for improvement that could raise their performance to a good level (Grade 5). Then groups 1, 3, 6, and 12 had the same grade of 3, indicating a moderate level of performance in their presentations. All four groups performed poorly compared to other groups. This suggested that they performed below average on several criteria compared to other groups. Group 6 had the lowest level of these four groups. Overall, most groups performed moderately well on levels 3 to 5. The main differences were in the distribution of grades across criteria. Some groups showed stronger performance in certain areas compared to others. As overall consideration for the results, it demonstrated that CLT techniques improved presentation skills, as corroborated by the high-scoring groups' excellent planning, productive teamwork, and skillful use of visual aids. The study's recommendations for improved teaching methods, including better preparation and the use of interactive technologies, directly support better oral communication skills. All things considered, the study provides insightful analysis and practical recommendations for enhancing oral presentations in the context of engineering education, making sure that its contributions are in line with the declared goal**.**

So, the author illustrates that this detailed assessment highlights strengths and areas for improvement for each group and provides a clear framework for future presentations. It emphasizes the importance of preparing and effectively using visual aids and interactive technologies to improve teamwork and overall performance. By examining these performance trends, the discussion aims to provide a comprehensive understanding of the impact of the CLT approach on student presentations and support recommendations for enhancing the teaching and learning experience in the engineering classroom.

VI. Conclusion

The survey aims to evaluate the effectiveness of using Communicative Language Teaching (CLT) approaches to improve the oral skills of second-year engineering students by contributing adequate and precise rubrics at the University of Technology (Mandalay). By using qualitative research methods and analyzing grades based on rubric criteria that focused on the performance of students in their group presentations, this study supported a comprehensive evaluation of the impact of CLT on students' oral skills. The survey results show clear differences between high-performing and low-performing groups and highlight the potential for improvement.

Then, the findings varied but generally indicated significant improvement in students' oral communication skills, as evidenced by positive performance scores. The highest-grading groups demonstrated thorough preparation, strong teamwork, and effective use of visual aids, highlighting the strengths of CLT in fostering a collaborative and interactive learning environment. These excellent groups, such as 4, 7, and 10, spoke clearly and confidently, in effective engagement with the audience. The Q&A sessions were expertly handled.

On the other hand, groups with lower scores needed to improve areas such as content organization, clarity of delivery, and engagement strategies. The lowest scoring group (6) showed a significant lack of several criteria, highlighting the need for more targeted support and practice.

The author provides detailed rubrics for group presentations to promote transparency, consistency, and fairness in grading through a structured framework. This approach allows teachers to identify specific areas for improvement and encourages students to self-assess and actively improve their oral skills

In general, the study confirms that CLT methods are effective in improving engineering students' oral skills, contributing to their confidence, ability to communicate well, and ability to demonstrate technical information effectively. The author would like to mention here that this evidence remains inconclusive due to annual student transfers, making it uncertain whether these methods are suitable for the skills of these students. However, this research certainly highlights the importance of incorporating interactive and communicative activities in language teaching, especially in specialized academic settings, to better prepare students for professional and career environments. By highlighting these performance trends, the study supports a clear framework for future improvements in teaching and learning experiences in engineering education, emphasizing the impact of the CLT approach on student presentation. The insights gained from this study can inform pedagogical practices, support the ongoing development of effective language teaching strategies, and enhance the academic experience and career readiness of engineering students. To address the limitations identified in this study and further validate the effectiveness of CLT methods, future research could explore long-term studies that would track the progress of engineering students over several academic years. By continuously evaluating the sustained impact of CLT interventions on oral communication skills, teachers can gain deeper insight into the long-term effectiveness of this pedagogy in the classroom. In addition, this study points out the need to conduct comparative studies across diverse student populations and educational contexts, which can explain contextual factors that influence the usability of CLT methods. Additionally, qualitative investigations into students' performance under CLT teaching methods can reveal valuable insights into the underlying mechanisms driving its effectiveness, aiding further teaching and learning processes.

ACKNOWLEDGMENTS

As the very first, I would like to thank Daw Zin Mar Hnin, Associate Professor and Head of the Department of English at Technological University (Mandalay), for her insightful comments and encouragement. I give my deepest gratitude to my advisor, Daw Khing Mi Mi Htun, Lecturer, Department of English, Technological University (Mandalay), for her continuous support and invaluable guidance throughout this research. I would like to express my heartfelt appreciation to all the second-year engineering students who participated in this research because their enthusiasm and cooperation were essential for the successful completion of this research. I am also deeply grateful to my family for their unwavering support and understanding during this research journey.

REFERENCES

[1] Richards, J.C & Rodgers, T.S. (2001). Approaches and Methods in Language Teaching. Cambridge University Press.

[2] Richards, J.C & Rodgers, T.S. (2001). Approaches and Methods in Language Teaching (2nd ed.). Cambridge University Press

[3] Savignon, S. J. (2002). Interpreting Communicative Language Teaching: Contexts and Concerns in Teacher Education. Yale University Press.

[4] Prof. Magdy M. Aly (2020). Rubrics for EFL Oral Presentations

[5] Toro, V., Camacho-Minuche, G., Pinza-Tapia, E., & Paredes, F. (2018). The Use of the Communicative Language Teaching Approach to Improve Students' Oral Skills. English Language Teaching, 12(1), 110-118.

[6] Anderson, Joseph S. and Mohrweis, Lawrence C (2008). Using Rubrics to Assess Accounting Student's Writing, oral presentations, and Ethics Skills

[7] https://cte.alliant.edu/resources-for-teaching/assessment/rubrics-for-oral-presentations/

[8] https://www.linkedin.com/advice/3/how-can-you-use-rubric-evaluate-presentations-vabke

[9] Sadie Louise Winterscheid (2016) Rubrics: Effectiveness of Feedback

Vedic Astrology System (Vedicware)

Daw Moh Moh Khaing [1], Mg La Win Tun[2], Dr. Khin Myo Chit[3]

Department of Information Technology Engineering, Technological University (Mandalay)

Student, Information Technology Engineering, Technological University (Mandalay)

Department of Information Technology Engineering, Technological University (Mandalay)

dawmoh2khaing@gmail.com, lawintun1000@gmail.com, miss.khinmyochit@gmail.com

***Abstract*—The paper presents a computational system designed to visualize and analyze Doshas and planetary influences in Vedic Astrology, focusing on the fluctuations in a native's insights into human life through celestial influences, yet modern visualization tools for its analysis are lacking. Key features include graphical depictions of Karmic fluctuations influenced by planetary positions when a native birth, are in each Dosha(729 divisional sectors of 120 years duration). Results show the system's effectiveness in illustrating the dynamic nature of a native's Karma, acting as a powerful tool for astrological analysis. This research integrates traditional astrological knowledge with modern computational methods, advancing the field of astrological studies.**

Keywords— Vedic Astrology, Dosha Analysis, Karmic Visualization, Planetary Influences, Accuracy conclusion, incidences studies, Data Visualization, Predictive Analytics.

I. INTRODUCTION

In traditional practices, astrologers provided interpretations through text, spoken words, or audio forms, complemented by Vedic charts and some astrological illustrations. These traditional tools were comprehensible primarily to professional astrologers. Today, there is a demand for more effective and comprehensive services, such as lifetime predictions and daily, monthly, and yearly fortune assessments. This raises the question: why haven't astrologers integrated technology between interpretation and analysis? The answer lies in the nature of Vedic astrology, which combines data, algorithms, mathematics, astronomy, relational logic, and belief systems. These elements fall within the realm of information and computation, positioning Vedic services within the technological sector. The lack of integrated techniques for the Vedic Astrology from the Information Technology sector has been a significant gap. This paper addresses this gap by exploring and proposing potential techniques to bridge this area effectively. Integration of Numerology and Dosha System in Vedic Astrology, it includes a time division system based on the influence of planets over time, known as the Dosha system. By integrating numerology with the Dosha system and benefic scores, we can outline a native's karmic path more accurately. Time Periods and Planetary Life Spans in Vedic astrology, the total time periods considered amount to 120 years, each influenced by the life spans of various planets.

II. RELATED WORK

In Myanmar, Vedic services industry, most of astrologers used Eastern Indian Chart Style. Myanmar called "Htan Phu Zatar" pronouncing in Burmese ascent. Types are "Rasi" , "Bhava" and Navam" Charts. Different charts are used by different analysis techniques. All of charts represents 360° and 12 sectors of celestial bodies, called "Rasi", each occupied 30°. 12 Zodiac signs are represented by 12 of cells. Not only Eastern but also Western charts consist of 12 cells for dividing 12 sectors.

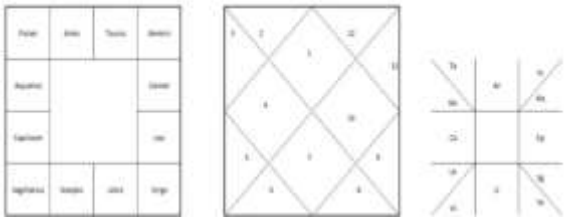

Fig. 1. Different styles of Vedic Astrological Charts

A. Rasi chart investigation

This paper explained how to Input formatting, the Planets, Rasi, Bhava, Navam and Nakshatras are listed in the excel files. Reading the file with Pandas module (Python). For Rasi chart investigation, define the weight values for types of relationships between Planet and signs. A planet fall in a sign may be 4 conditions. The strengths of planets could be defined in Vedic astrological belief system.[1] If a planet sit in

1. Owned Sign, it gives positive results.
2. Exalted Sign, it is benefic to a native
3. Debilitated Sign, it is malefic to a native
4. Reverse of Owned Sign, it gives negative results.

Planets and Signs relationships (owned)

Planets and Signs relationships (exaltation)

Planets and Signs relationships (debilitation)

Planets and Signs relationships (reversed owned)

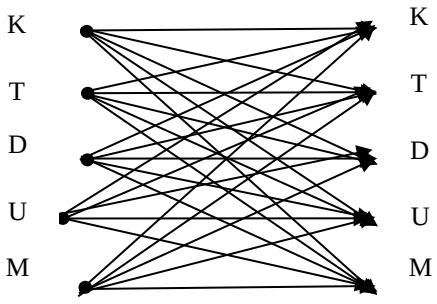

Fig. 2. Type of relationships

B. Navam chart investigation

It is also the same as Rasi chart Investigation but the house diving system and Rasi Sign arranging system is differ. "Navam" meant the 9 , 9th or Nine. In Vedic astrology , 9 is the most powerful. This belief concept was deployed in the chart dividing system , it formed the Navamsa chart.The whole chart represents the 360 degrees , 12 of cells represents the 12 sectors of 360 degrees, a sector had 30 degrees. In Navam system, 30 degrees is divided by 9 .[1]

C. Bhava chart investigation

Current step, planetary positions might be changed by the house boundaries shifting by the position of Lagna in the degree of sign. The dependency of planetary position lied on the chart dividing system. In this case, equal house system. It is meant that if the Lagna (ascendant) is over or lower the mid degree , the boundaries were adjusted in an accordance with the left 15 and right 15 degrees spacing of Lagna. (exactly 15 degrees).

The houses (Bhava) haves quantities 12 same as Rasi. However, the counting start cell is differ from Rasi. In Rasi chart, the starting cell that represents Aries sign. In Bhava chart, the starting cell that the Lagna is existedl, this cell would be the first house in Bhava chart.[2]

If the planet is included in a list of friendship of the house lord, it had good strengths. If the planet is included in a list of foe of the house lord, it would not be favored condition.

D. Nakshatra investigation

In Nakshatra investigation , the investigation process is the defining the relationship Nakshatra Lord (planets) and the planets sitting in this Nakshatra. The relationships type is Planets to Planets. However , they would be the secondary relationships that were the dependency on the primary relationships (Planets and Nakshatra). [2]

The results of 4th investigations

Rasi chart investigation gives R = [a,b,c,d,e,f,g,h,i,]

Navam chart investigation gives N = [a,b,c,d,e,f,g,h,i]

Bhava chart investigation gives B = [a,b,c,d,e,f,g,h,i]

Nakshatra chart investigation gives K = [a,b,c,d,e,f,g,h,i]

The vedic astrology, known as Jyotisha, is an ancient system of knowledge that uses the positions and movements of celestial bodies to predict and understand human affairs and natural phenomena. The Vedic Planetary Theory (VP Theory) is a core component of this system, detailing the roles and effects of planets in shaping individual destinies. This research paper delves into the intricacies of VP Theory, illustrating its principles, methodologies, and applications.

The Vedic Planetary Theory provides a comprehensive framework for understanding the karmic influences of celestial bodies. By integrating traditional astrological principles with modern analytical methods, this research paper aims to offer more precise and accessible astrological insights.[2]

III. METHODOLOGY

This paper serves as a bridge between the ancient wisdom of Vedic astrology and contemporary computational analysis, providing a deeper understanding of planetary influences on human life.

The different results of different investigations are needed to determine a single result. In this case, the following sample data is applied, planetary positions are in excel file.

I. VISUALIZATION EACH RESULT TABLE

	A	B	C	D	E
1	Planet	rasi	bhava	navam	nakshatra
2	1	6	6	4	13
3	2	2	2	12	3
4	3	9	9	1	19
5	4	6	7	6	14
6	5	1	2	8	2
7	6	7	7	12	15
8	7	6	6	5	14
9	8	10	11	6	23
10	9	4	5	12	9
11	L	7	7	9	18
12					

Birth date : 7/10/1952

Birth Time : 09:30:00

Birth Place : St. Petersburg

Moon Degree : 39.71

For Rasi chart investigation the relationships are the 180 degrees signs of owned signs. The system had to give the +6 scores when a planet transits in own sign or exaltation sign, else condition, would give the -6 scores when a planet transits in debilitated sign or reversed of its owned sign. The Rasi chart investigation give 9 numerical values of 9 planets.

	K	T	D	U	M
K	6	6	-6	6	6
T	6	6	-6	6	6
D	-6	-6	6	-6	-6
U	6	6	-6	6	6
M	6	6	-6	6	6

Fig. 3. Relationships and weights

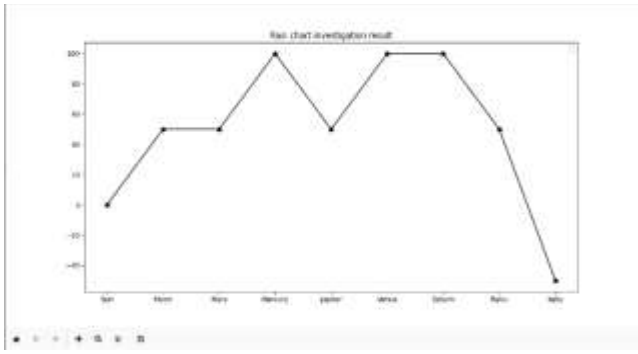

Fig. 4. The result of Rasi chart investigation method

For Navam chart investigation

A Navam sector = (30 degree)/9 = 3 degree 20 minutes

For the whole charts,

12*9 = 108 sectors

108 sectors * (3 degree 20 minutes) = 360 degrees

12 Rasi signs are arranging in 108 sectors,

first sector is former Aries (30 degrees), Now , 9 Divisions had been (Aries to Sagittarius) signs are in it. Therefore, Aries is changed from degree range (0 <x< 30) to degree range (0 < x<3.33333). The second sector is former Taurus

(30 degrees), Now , 9 Divisions gave, (Capricorn to Virgo) signs are in it. The degree changes would be the same as first sector.

All sectors would had been 12 . Rasi occupied degrees area had been separated into many areas more than one. lthough a planet was sitting a Rasi in Rasi chart would not be possible the same in Navam chart.The Navam chart investigation gives 9 numerical values of 9 planets. [3]

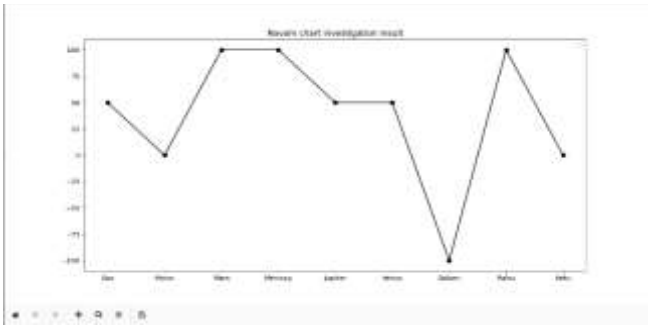

Fig. 5. The result of Navam chart investigation method

For Bhava chart investigation, Five Parties in Bhava Houses

1. Kendra Party (1st , 2nd , 4th , 10th houses)

2. Trikona Party (1st ,5th ,9th houses)

3. Dusthana Party (6th , 8th , 12th houses)

4. Upachaya Party (3rd ,11th houses)

5. Maraka Party (2nd house) , it also called Dhana house.

In reality, 2nd house and this house lord had gaven dual natures, this house had related with the wealth accumulation of native and in the other hand , the lord of it , had the most spirit to terminate the native , it was defined the killer of house, called Maraka house in Vedic astrology. In this condition, the complex natures were eliminated in system application.Sun to Ketu , 9 of planets might be a lord of house from the four parties such as Kendra,Trikona,etc.[2]

Associative properties could interpret the possible relationships.

[“Sun”,”Moon”,”Mars”,”Mercury”,”Jupiter”,”Venus”,Saturn”,”Rahu”,”Ketu”] * [“Kendra”,”Trikona”,”Dusthana”, ”Upachaya”,”Maraka”]

9*5 = 45 relationships (planets and parties)

After that, the planet was the member of a party, the lord of a house. It could sit in it own house or other house . At that time, the party the planet had been membership and the party the planet sitting house, would form the possible relationships between two parties.

[“Lord of Kendra”, ”Lord of Trikona”, ”Lord of Dusthana”, “Lord of Upachaya”,”Lord od Maraka”] * [“Kendra House”, “Trikona House” , “Dusthana House” , “Upachaya House”,”Maraka House”]

5*5 = 25 relationships (parties and parties)

Defining weight values for each relationship

If a planet was a lord in otherwise a membership of “Kendra”,”Trikona” or “Upachaya” party. It would got +6 scores and else conditions, being a member of “Dusthana” party, it would got -6 scores.If the lord of Kendra , Trikona or Upachaya house had associated with Dusthana , it score would be multiplied by -1. And any relationships between them except of Dusthana, their scores would not be needed to do nothing. In special case the Dusthana Lord stayed in Dusthana House, the planet score would change to positive integer. In Vedic astrology , although the Dusthana is a house of malefic but the Dusthana Lord sit in Dusthana , gives the benefic result.[3]

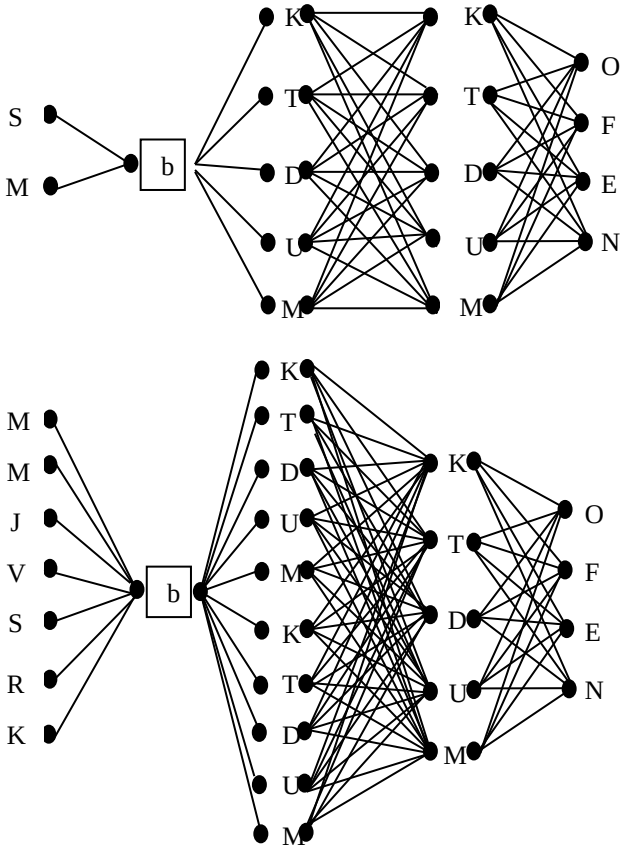

Fig. 6. Relationships of 5 parties Lords and Houses.

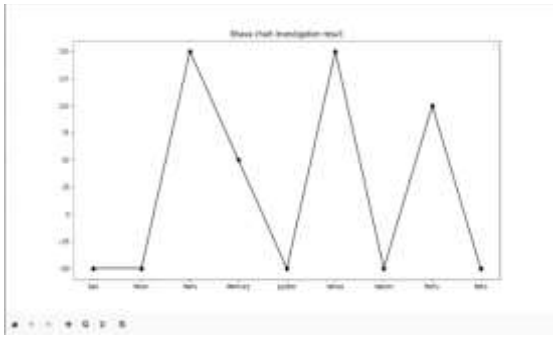

Fig. 7. The result of Bhava chart investigation method

For Friend or Foe identifying, this different conditions, +6 for friendly and -6 for enemy condition.

[“Sun”,…,”Ketu”] * [“Sun”,…,”Ketu”]

9*9 = 81 relationships (planets and planets)

The result of identifying, the possible relationships might be 81. (if a planet sit in it house, this condition under the own Rasi relationship) planets and parties → parties and parties → planets and planets → [a,b,c,d,e,f,g,h] , alphabets represent the numerical values , they might be positive or negative, 9 of them are the result weight values of 9 planets from the Bhava investigation. [3]

Above JSON format data (JavaScript Objects) represents the Python dictionary data structure {“key”:[“list of keys”]}. In this case, nested dictionaries were applied for three nature “friend”,”foe” and “neutral”.

The keys, “1”, ,”9” represents “Sun”,…,”Ketu” planets. For the friend or foe identifying process , the system searches and matching the relationships to identify the two planets are being friend or foe. “neutural” is to checking the two planets are being neutral.[2]

For Nakshatra investigation

9*27 = 243 relationships (Primary Relationships)

72*9 = 243 relationships (Secondary Relationships)

Above relationships would met the planet and planet , that one would sit in Nakshatra and another would rule it Nakshatra. The sitting planet and the ruling planet may be friend or foe. If friend , the system would give +6 to this sitting planet and If foe , the system would give -6 to this sitting planet. In this process , the ruler would not be gotten any score. The result of this process, gives the 9 numerical values of 9 planets.[2]

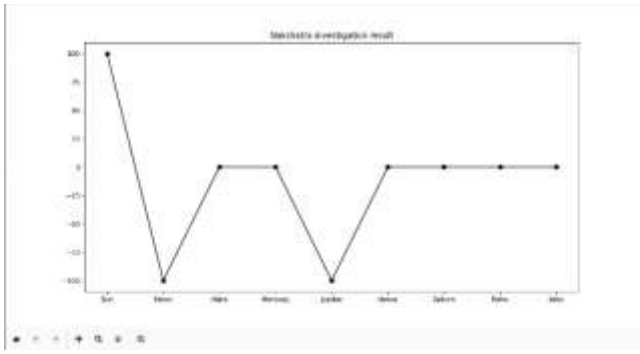

Fig. 8. The result of Nakshatra investigation method

VP Theory identifies nine primary celestial bodies, also known as Navagrahas, each with unique characteristics and influences:

In Vedic astrology, the relationships between planets significantly impact their influence.

VP Theory incorporates the Dasha system, which divides a person's life into periods ruled by different planets. The most common system is the Vimshottari Dasha, which spans 120 years, distributed among the nine planets:

These periods influence the timing of events and the overall direction of a person's life.[1]

The application of VP Theory can be enhanced using modern computational tools and visualization techniques. For instance, creating visual representations of planetary influences over time can help individuals and astrologers better understand and interpret astrological data.

IV. Implementation

In this system includes four patterns , “main.py” is the system entry point program file.“Model” is a module that collection of program files (only data manipulations and logical algorithms works).“View” is a module that collection of program files (only UI processes work).“Controller” is a module that collection of program files (only coordination works between Model and View) . Our system utilizes Python and libraries like Matplotlib to process astrological data and generate visual representations.

These architecture of the organizational pattern is shown in Fig. 9.

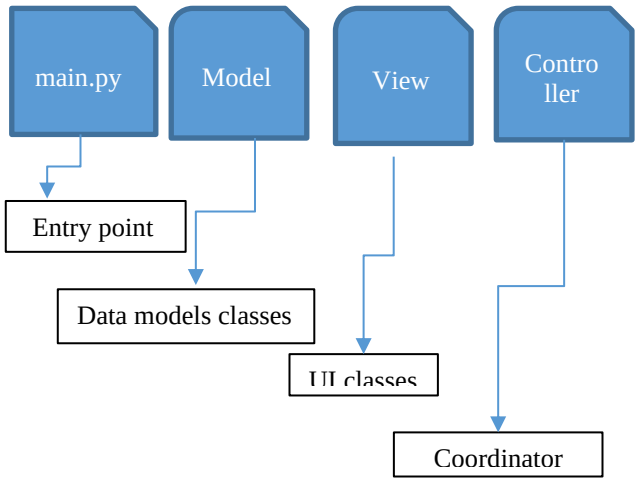

Fig. 9. System organizational pattern

The System Flow Chart is shown in Fig.10. The first process is to input data from the user , calculation with internal storage data and then display result. In the system flow chart, the difference between “Predefined Data” and “Internal Storage” block are that the location of data and the extracting data(planetary score data) which are predefined.

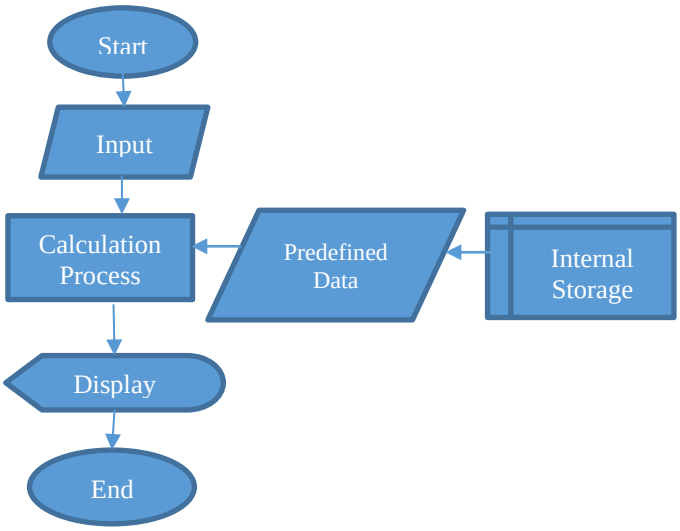

Fig. 10. System flow chart

To visualize the "Kama" fluctuation of a native, "Vimshottaris Dosha" System (Time division techniques and planets influencing belief system) is useful, providing Karmic path of a native. The combination of the results of birth chart analysis and time division system could make the Karmaic journey of a native.

Native : One of the 21st century’s most influential leaders, the former foreign intelligence Officer at KGB, The former prime minister of USSR, The President of Russian Federation.Acurate : Reference source (Astrosage astro databank, the most reliable and applicable sources in Vedic Astrological field).

Full name : Vladimir Vladimirovich Putin.

Birth date : 7/10/1952

Birth Place : Saint Petersbarg (Post Leningrad)

Birth Time : 09:30:00 AM

Offset : UTC + 3

Moon degree: 39.71

Finding first Dosha Planet and date

The user data , Moon degree that aparting from Aries (Meana) Sign 0° 0' 0". Start from Mena Rasi, the width of a single Nakshatra (stellar) had 13° 20" (13.333333° in degree form).Integer 2 would be post nak numbers. Therefore, the moon degree would be in third nak.

Finding first Dosha planet (Maha)

Third Nakshatra name is "Krittika" , its lord is Sun. Sun has the 6 years life span.

Finding start date

All Nakshatra, including Krittika wide 13.333333° . The lord life span is 6 years. Putin Dosha would be started from 1946 to end in 2066. (120 years).

In this case, the values of X,Y and Z would be the results from the applying of methods that had been described in Chapter 3.The out put data of calculation for all date. The system generates the result in a dictionary data structure.

{“Date 1”:“Karmic point”,…,“Date 729 ”:“Karmic point” }

The system would manipulate the keys and values of dictionary to visualize the Karmic journey of Putin as follows.

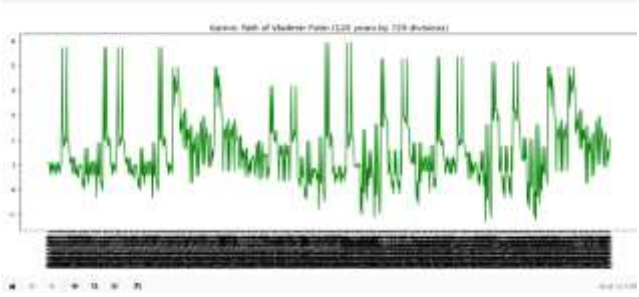

Fig. 11. The Karmic fluctuation the whole Dosha life time.

For the Karmic fluctuations are grouping 27 and 27 divisions of mean values show in Fig.12.

Total Karmic fluctuated points are divided by 27 = 729/27= 27 (divisions)

Summation of 27 Karmic fluctuated points = k1+…+k27

Mean = (k1+…+kn)/n , n = 27

The result = [1st D mean values, … , 27th D mean values]

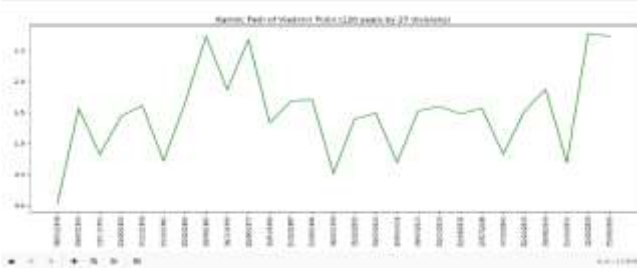

Fig. 12. The Karmic fluctuations are grouping 27 and 27 divisions of mean values

For the Karmic fluctuations are grouping 9 and 81 divisions of mean values show in Fig.13.

Total Karmic fluctuated points are divided by 9 = 729/9= 81 (divisions)

Summation of 9 Karmic fluctuated points = k1+…+k9

Mean = (k1+…+kn)/n , n = 9

The result = [1st D mean values, … , 81th D mean values]

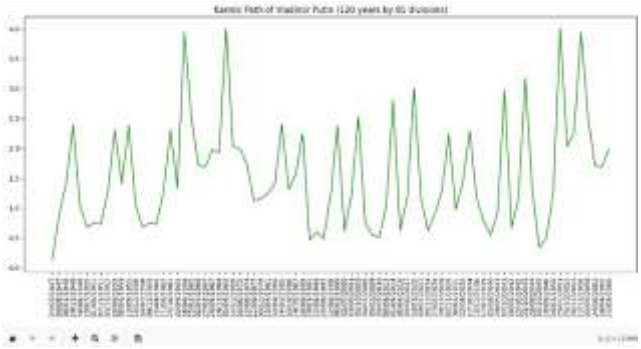

Fig. 13. The Karmic fluctuations are grouping 9 and 81 divisions of mean values

V. Conclusion

This research paper delves into the intricate methods of Vedic astrology, specifically focusing on birth chart analysis and the Vimshottari Dasha system, to visualize and interpret the karmic fluctuations of Vladimir Vladimirovich Putin, one of the 21st century’s most influential leaders. Utilizing accurate data from the Astrosage astro databank, we systematically analyzed Putin’s birth chart and applied time division techniques to generate a comprehensive karmic journey.

In conclusion, this paper demonstrates the efficacy of combining Vedic astrology birth chart analysis with the Vimshottari Dasha system to create a detailed and insightful karmic profile. The visualization of karmic fluctuations provides a unique perspective on how astrological influences shape the life path of a significant global figure like Vladimir Putin. This approach not only enhances our understanding of individual karmic journeys but also validates the profound impact of celestial dynamics on human destiny.

Acknowledgment

The author would like to thank and appreciate Dr. Su Yin Win and Dr. Hnit Thit Shein Pro Rector of Technological University (Mandalay), for her kind permission to develop this paper.

The author is also deeply thankful to Dr. Khin Myo Chit, Professor and Head, Department of Information Technology Engineering, Technological University (Mandalay), for her numerous suggestions concerned with this paper, for her supporting, and for her encouragement.

The author is also especially indebted to Daw Thiri Kyaw, Associate Professor, all teachers Department of information Technology Engineering and Mg La Win Tun, VIT-8, Technological University (Mandalay) for their imagination, enthusiasm, expertise and technical knowledge in diversified areas.

References

[1] B. V. Raman, "Graha and Bhava Balas," Raman Publications, 1992.

[2] David Frawley, "Astrology of the Seers," Motilal Banarsidass, 2000.

[3] Sanjay Rath, "Crux of Vedic Astrology," Sagar Publications, 2003.

Design Analysis of Solar Cooker by Using Flat Plate Collector

Hla Thu Zar Oo[1], Cho Cho Khaing[2], Aye Mya Thandar[3]

[1]*Mechanical Engineering Department, Technological University (Mandalay), Myanmar*

[2]*Mechanical Engineering Department, Technological University (Mandalay), Myanmar*

[3]*Mechanical Engineering Department, Technological University (Mandalay), Myanmar*

[1]hlathuzaroo2020@gmail.com, [2]khaingcho999@gmail.com, [3]ayemyathandar2023@gmail.com

***Abstract*— This writing paper describes theoretical and numerical thermal analysis of the sun-powered cooker by utilizing flat plate collector. This cooker can be utilized for different low and medium-temperature applications. In this research work, at first, angle of incidence, sun-oriented declination, zenith angle of the sun, and effective solar constant are based on Mandalay, Myanmar, and heat flux, water outlet temperature, and efficiency of the collector are calculated from 9:00 am to 4:00 pm for 31st December 2023. In addition, to get the ideal collector water outlet temperature has utilized experimental equations and ANSYS computer programs by changing the breadth of the indicated coil. A palatable qualitative sun-powered cooker is obtained between the theoretical and numerical results. The box type sun-powered cooker design is cheap, easy to construct and useful in rural areas where there is no electricity.**

Keywords*— sun-powered cooker, water outlet temperature, efficiency, ANSYS software

I. INTRODUCTION

Energy is defined that a thermodynamic amount which is expressed as the working ability of a physical system framework. Energy is essential in our environment. So, investigating energy-related issues is quite important. Thus energy specifically influences our life and its utilization. Fossil fuel-based energy assets still prevail with the biggest share in worldwide energy utilization [4].

In cooking, sun-powered cooking is renewable energy sources, which is basic, secure, and helpful without expending power and decrease contaminating the environment. It is suitable for many people around the world with rare fuel and budgetary assets for cooking by using fuel. Moreover,sun-powered cookers can be utilized for bubbling drinking water and give secured drinking water to many people around the world to avoid water-borne sicknesses. Using sun-powered cookers offers numerous benefits like no repeating costs, make the food more nutritious. It has the potential to reduce hunger, and not easy to break[4,10]. Moreover, sun-powered cookers has numerous benefits for health, time, user income and the environment.

II. METHODOLOGY

A. Theoretical Analysis

The design location is considered in Mandalay and the design month is December 2023. Specification data are as follows;

North Latitude – 21.98°N

East Longitude – 96.1°E

Solar constant, I_o –1373W/m^2

Elevation above sea level –74.646 m

Climate type – tropical

Local Standard time of meridian – 97°E

The diagrammatic view for the proposed flat plate sun-powered cooker design is described in "Fig. 1''.

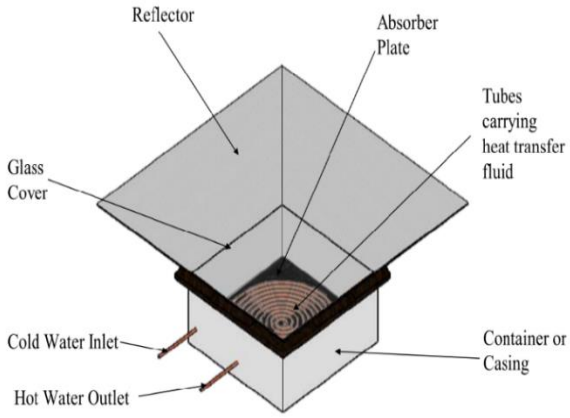

Fig. 1. Diagrammatic view of Level Plate Sun-Powered Cooker.

B. Total Solar Insolation Flux

Under clear sky conditions, the equation of beam irradiance at the surface can be expressed as:

$$I_b = I_{o,eff} \left[a_o + a_1 \exp\left(\frac{-k}{\cos\theta_z}\right) \right] \quad (1)$$

Effective solar constant varies with the time of year according to the formula,

$$I_{o,eff} = I_o \left[1 + 0.033 \cos\left(\frac{360\, n}{365.25}\right) \right] \quad (2)$$

The clear sky diffuse irradiance can be estimated from a relation;

$$I_d = [0.2710\, I_{o,eff} - 0.2939\, I_b] \cos\theta_z \quad (3)$$

The hemispherical irradiance I_h is given by,

$$I_h = I_b \cos\theta_z + I_d \quad (4)$$

The effective irradiance for the flat plate collector was calculated by using Equation;

$$I = I_b \cos\theta + I_d (1+\cos\beta)/2 + I_h \rho_{ground} (1-\cos\beta)/2 \quad (5)$$

"Fig. 2'' shows the results of effective irradiance for December 31 by assuming the collector angle is 45˚ from the horizontal.

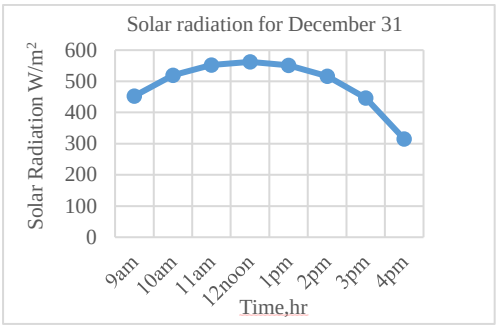

Fig. 2. Effective Irradiance Varies with Time.

The design procedure for flat plate sun-powered cooker collector is presented below.

I. Proposed Design Of Flat Plate Solar Cooker

No.	Design Parameter	Symbol	Value	Unit
1.	Box Length	l	609.6	mm
2.	Box Width	b	609.6	mm
3.	Box Height	t	304.8	mm
4.	Back Insulation thickness	t_b	50.8	mm
5.	Absorber Plate Thickness	t_p	1	mm
6.	Coil Diameter	D	7.9375	mm
7.	Tube Length	L_{tube}	15000	mm
8.	Type of Insulation		Foam insulation	
9.	Material of Tube		Copper	
10.	Glazing Cover		Glass	

C. Calculation of Overall Heat Loss Coefficient

In this paper, convection losses and radiation losses are considered to calculate the collector's overall heat loss coefficients. Conduction loss has occurred at the insulation. The loss of energy passed the collector is the resultant of convection and radiation within parallel plates as shown in "Fig. 3''.

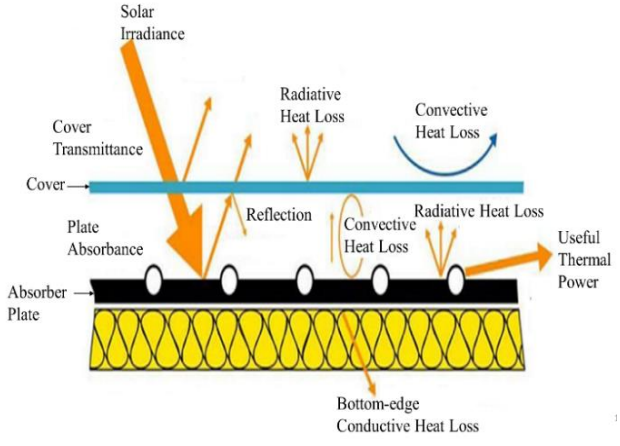

Fig. 3. Diagrammatic view of Various Heat Exchange Components in a Flat-plate Collector

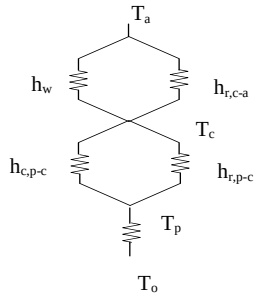

Fig.4. Thermal Network for One Glass Shield Flat-Plate Collector

The thermal network for one glass shield flat-plate collector is described in "Fig. 4''.

The calculation of Rayleigh number is,

$$R_a = \frac{g\beta' \Delta T L^3}{v\alpha} \quad (6)$$

The calculation of Nusselt number is,

$$N_u = 1+1.44\left[1-\frac{1708[\sin(1.8\beta)]^{1.6}}{R_a \cos\beta}\right]\left[1-\frac{1708}{R_a \cos\beta}\right]+\left[\left(\frac{R_a \cos\beta}{5830}\right)^{\frac{1}{3}} -1\right] \quad (7)$$

The calculation of convection heat exchange coefficient within plate and shield is

$$h_{c,p-c} = \frac{N_u\, k}{L} \quad (8)$$

The calculation of radiation heat exchange coefficient within plate and shield is

$$h_{r,p-c} = \frac{\sigma(T_p+T_c)(T_p^2+T_c^2)}{\frac{1}{\varepsilon_p}+\frac{1}{\varepsilon_c}-1} \quad (9)$$

The calculation of radiation heat exchange coefficient from shield to atmosphere is

$$h_{r,c-a} = \varepsilon_c\, \sigma\, (T_c^2+T_a^2)\,(T_c+T_a) \quad (10)$$

The calculation of wind convection and radiation from the absorber plate to the atmosphere is

$$h_w = 5.7+3.8V \quad (11)$$

The collector peak heat loss coefficient is given by,

$$U_t = \left[\frac{1}{h_w+h_{r,c-a}} + \frac{1}{h_{c,p-c}+h_{r,p-c}}\right]^{-1} \quad (10)$$

The collector bottom heat loss coefficient is given by,

$$U_b = \frac{k}{l} \quad (13)$$

The collector corner heat loss coefficient is calculated by using equation;

$$U_e = \frac{(UA_{edge})}{A_c} \quad (14)$$

The entire heat loss coefficient of the collector can be calculated by using equation;

$$U_l = U_t + U_b + U_e \quad (15)$$

D. Calculation of Useful Energy

The occurrence on the opening plane of the sun-powered collector having a collector surface region, at that point the quantity of sun-powered radiation accepted by the collector is calculated by using the equation;

$$Q_i = I\,(\tau\alpha)A_c \quad (16)$$

The heat loss of collector can be solved by the relationship:

$$Q_{loss} = U_l\,A_c(T_c - T_a) \quad (17)$$

The collector is absorbed the rate of useful energy that can be calculated by the equation,

$$Q_u = Q_i - Q_{loss} \quad (18)$$

E. *Calculation of Water Outlet Temperature*

The water outlet temperature for flat plate collector is:

$$T_o = \frac{Q_u}{mc_p} + T_i \quad (19)$$

F. *Flat-plate Collector's Efficiency*

The flat plate collector's efficiency can be solved by the expression:

$$\eta_c = \frac{Q_u}{A_c I} \quad (20)$$

"Fig. 5''. and "Fig. 6''. show the results of water outlet temperature and efficiency for December 31 by assuming the collector angle is 45˚ from the horizontal.

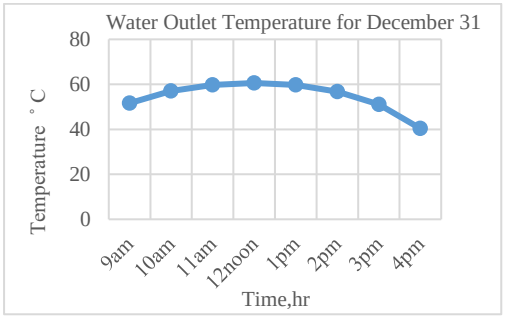

Fig. 5. Water Outlet Temperature Varies with Time.

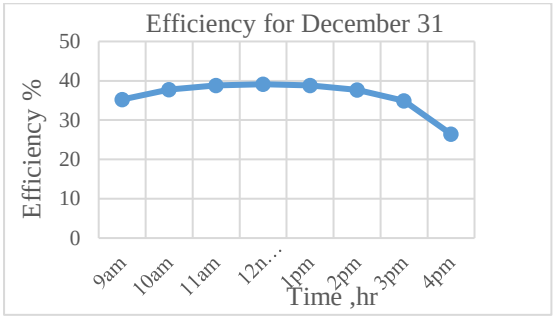

Fig. 6. Efficiency Varies with Time.

G. Numerical Analysis

Computational Fluid Dynamics (CFD) is a split inside liquid flow where numerical strategies and calculations are utilized to unravel liquid stream issues that are distant as well as complex to fathom logically. The results of a CFD analysis ought to be systematically analyzed and this item should be verified before acceptance. It is too imperative to comprehend that this answer is an estimate for decision around the world.

H. CAD Modeling and Meshing with ANSYS 2022

The modeled assembly of water pipe of a level plate sun-powered cooker consists of two header tubes and fourteen flow tubes. The modeled assembly consists of an inlet and outlet. The modeling has been done in ANSYS Workbench 2022. The meshing of the water pipe domain was done at spear shapes and the meshing of the water pipe domain for fillet spear shape is shown in "Fig. 7'', "Fig. 8'' and "Fig. 9''.

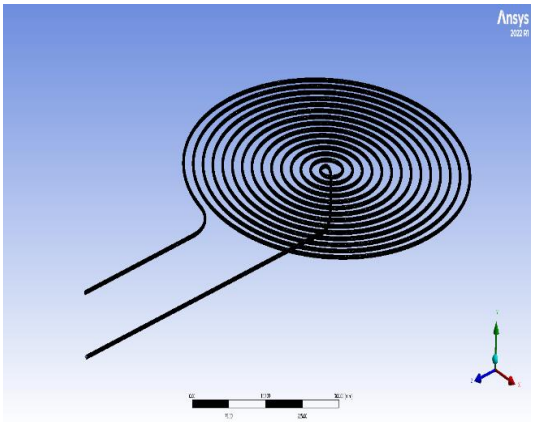

Fig. 7. Meshing of water pipe for Flat Plate Collector (5mm diameter coil).

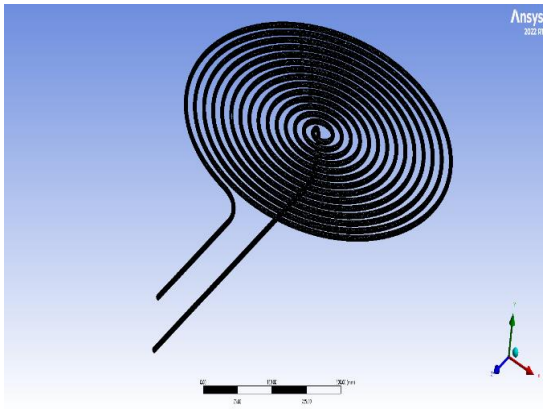

Fig. 8. Meshing of water pipe for Flat Plate Collector (7.9375mm diameter coil).

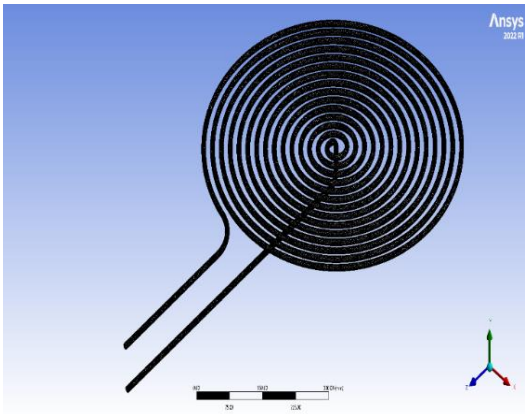

Fig. 9. Meshing of water pipe for Flat Plate Collector (10mm diameter coil).

I. MESH DATA FOR WATER PIPE (5MM, 7.9375MM AND 10MM DIAMETER COIL)

No.	Domain	Nodes	Elements
1.	Default Domain	522908	2275851
2.	Default Domain	601662	2766720
3.	Default Domain	597488	2329334

The mesh is changed over into the necessary format and is entered the data into ANSYS CFX- program. In ANSYS CFX-Pre the properties of the domains and liquid are characterized across with their interface properties. The concise of the domain1 properties is described in "Table III''. The terminus condition of flat plate coil is described in "Table IV''.

II. DOMAIN SETUP FOR CFD

Domain	Boundaries
Boundary 1(inlet)	
Location	Inlet
Static Temperature	28˚C
Turbulence	Intensity and Viscosity Ratio
Boundary 2 (Outlet)	
Location	Outlet
Backflow Reference Frame	Absolute (Total Pressure)
Gauge Pressure	1 atm
Boundary 3 (wall)	
Location	Wall
Heat transfer	Heat Flux
Heat Flux in	585 W/m^2
Momentum	No Slip Wall
Wall	Standard

III. BOUNDARY SETUP FOR CFD

Component	Feature	Details
Space Claim		Geometry Creation
		Named Selection
CFD (Fluid Flow Fluent)	User Mode	Quick Setup mode
	Location	From Geometry Input
	Domain Type	Fluid Domain
	Fluid List	Water-Liquid
	Reference Pressure	1 atm
	Heat Transfer Model	Thermal Energy
	Buoyancy Model	Not Buoyant
	Turbulence Model	k-Epsilon

III. RESULTS AND DISCUSSION

A. *Simulation Results*

The water outlet temperature is obtained using insert form and enter streamline instructions of the menu bar in ANSYS CFX-Post.

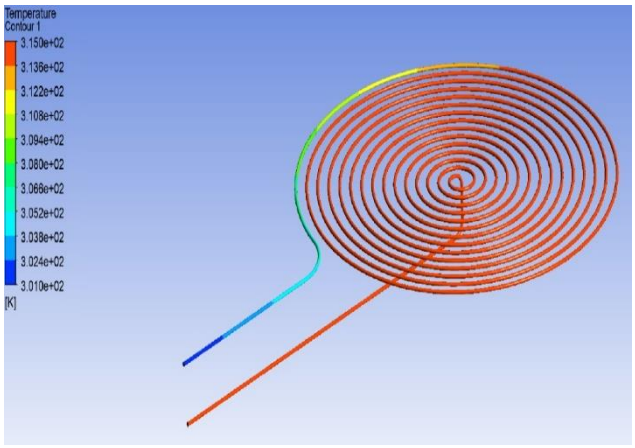

Fig. 10. Simulation Results of Water Outlet Temperature (5mm diameter coil).

"Fig. 10" shows the water outlet temperature of 5mm diameter flat plate coil. In this figure, the water inlet temperature is 301K and the water outlet temperature is 315K.

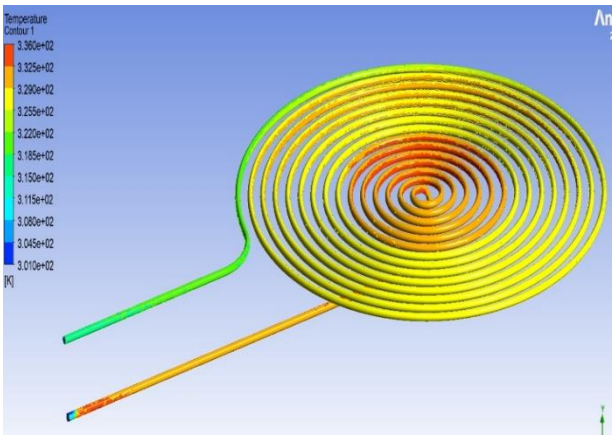

Fig. 11. Simulation Results of Water Outlet Temperature (7.9375mm diameter coil).

"Fig. 11" shows the water outlet temperature of 7.9375mm diameter flat plate coil. In this figure, the water inlet temperature is 301K and the water outlet temperature is 332K.

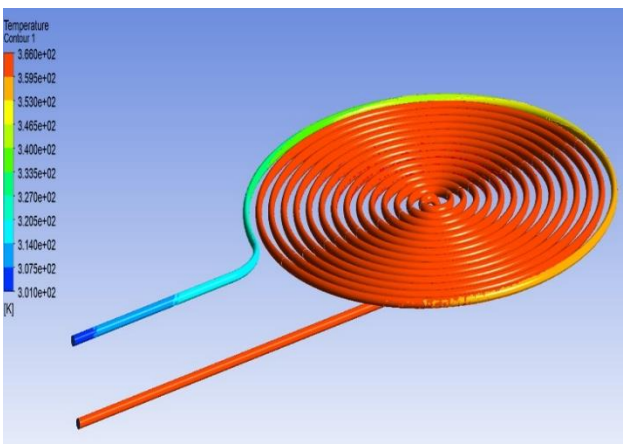

Fig. 12. Simulation Results of Water Outlet Temperature (10mm diameter coil).

"Fig. 12" shows the water outlet temperature of 10mm diameter flat plate coil. In this figure, the water inlet temperature is 301K and the water outlet temperature is 366K.

B. Discussion

The water outlet temperature from theoretical is compared with numerical result as shown in "Table IV''.

IV. COMPARISON OF THEORETICAL AND NUMERICAL WATER OUTLET TEMPERATURE RESULT FOR DESIGNED SOLAR COOKER

Coil Sizes	Water Outlet Temperature	Theoretical Result	Simulation Result	% Deviation
7.935 mm	$T_{w\text{-}out}$	334 K	332 K	1%

According to the theoretical result of designed solar cooker, the maximum water outlet temperature is obtained 334 K at ambient temperature 303 K. Numerical water outlet temperature is 332 K.

As shown in "Fig. 5'' the water outlet temperature for flat plate solar cooker varies with time that the water outlet temperature raise before noon and comes to the highest level at twelve hour. After that it starts to diminish amid the eventide.

As shown in "Fig. 6" the efficiency for flat plate solar cooker curve also follows the same pattern.

IV. CONCLUSION

In this paper, the flat plate solar cooker was studied both theoretically and numerically with free convection. Solar radiation, collector overall heat loss coefficient, collector incident radiation, collector heat loss, useful energy, water outlet temperature and collector efficiency were calculated. As a result, solar radiation, water outlet temperature and efficiency for flat plate solar cooker varied according to daily required heat. The water outlet temperature of flat plate collector by using ANSYS Software is analyzed by changing three different coil sizes. If the area of the collector is small, the amount of collecting heat will be less. To get the maximum temperature, the area of the collector is increased as high as possible. The theoretical and simulation results of water outlet temperature for designed solar cooker are compared. The percentage deviation is 1%.

There are many types of sun-powered cooker, namely box type sun-powered cooker, parabolic sun-powered cooker and panel sun-powered cooker. Among them, the box type sun-powered cooker design has been utilized in this paper. This design is simple, easy to construct, easy to use for cooking at any of the tropical zone. Therefore, if it is built according to this design, hopefully it will help the rural areas without electricity. There should be effective technology transfer from researchers to the rural areas, where solar cooker is favorable in the country.

ACKNOWLEDGMENT

The writer want to describe her deep appreciation to Dr. Su Yin Win, Rector of Technological University (Mandalay)(acting) for her valuable suggestions and guidance. Moreover, the writer is deeply indebted to Dr. Aye Mya Thander, Professor and Head of Department of Mechanical Engineering, Technological University (Mandalay), for her support and encouragement along with paper. And also special thanks to Daw Cho Cho Khaing, Associate Professor, Department of Mechanical Engineering, Technological University (Mandalay), for her editorial help, kindly advice, valuable suggestions and guidance throughout this paper.

REFERENCES

[1] Chinnumol Francis, Victor Jose, "A Review On Performance Improvements In Box Type Solar Cookers",2015.

[2] D.Yogi Goswami, "Principles of Solar Engineering",Third Edition.

[3] Emmanuel Yeboah Osei, Araba Amo-Aidoo, "Experimental Water Heating Studies of Flat Box And Inclined Box Solar Cooker Designs In Ghana,"2018.

[4] Erdem Cuce, Pinar Mert Cuce, "A comprehensive review on solar cookers,"Applied Energy, vol.102,pp.1399-1421, 2013

[5] John Twidell and Tony Weir, "Renewable Energy Resources", Second Edition.

[6] John A. Duffie (Deceased),William A. Beckman, "Solar Engineering of Thermal Process",Fourth Edition.

[7] Mulu Bayray Kahsay, John Paintin, Anwar Mustefa, Asfafaw Haileselassi,Meseret Tesfay, Biniam Gebray, "Theoretical and Experimental Comparison of Box Solar Cookers with and without Internal Reflector",2013.

[8] O.A. Ogunwole," Flat Plate Collector Solar Cooker,"2006.

[9] Paras Soni and Dr. B.K. Chourasia, "A Water White Glazed Box Type Solar Cooker: Perfomance Testing And Analysis",2015.

[10]Subodh Kumar, "Estimation of design parameters for thermal performance evaluation of box-type solar cooker,"Renewable Energy, vol.30, pp. 1117-1126, 2005.

[11]T Sitepu, S Gunawan, D M Nasution, H Ambarita, R E T Siregar, A D Ronowikarto, "Experimental Study on Performance of a Box Solar Cooker with Flat Plate Collector to Boil Water,".

Design and Fabrication of Solar-Wind Powered Hybrid Vehicle

Min Khant Zaw[1], Dr. Aye Mya Thandar[2], Dr. Aye Aye Khaing[3]

[1]*Technological University, Mandalay, Myanmar*

[2]*Technological University, Mandalay, Myanmar*

[3]*West Yangon Technological University, Myanmar*

Email: [1]m04382678@gmail.com, [2]ayemyathandar2023@gmail.com, [3]ayeyaekhaing2@gmail.com

***Abstract*—Wind and sun-oriented vitality, being promptly open and Eco-conscious, give a more try and true control source when coordinates. Half-breed vehicle joining these economic vitality sources will reduce dependence on oil, picking up notoriety for their natural benefits. Thinks about demonstrate that significant government and car segment financing in half-breed vehicle is basic for the pending for a long time. These vehicles are seen as the imminent mode of transportation, requiring as it will negligible assets for promoting and deals endeavors. This article looks for to investigate the necessities for the plan, working, and control of wind-solar half-breed vitality frameworks, underscoring the monetary focal points and basic nature of half-breed vehicles in the car sector. The designed for solar-wind hybrid vehicle is 0.75 kW motor power and 2900 revolution/min rotation speed.**

Keywords—Wind vitality, Sun based vitality, Cross breed vehicle, Car, Crossover vitality system.

I. INTRODUCTION

A. Solar Energy

Solar energy from the sun is a promising renewable source, with vast potential. Earth's surface has 1016 watts of solar power, offering a sustainable energy solution. Advancements in technology make solar power a viable alternative to fossil fuels, reducing our carbon footprint and promoting environmental sustainability.[3] The global power demand required to sustain civilization is 1013 watts. Consequently, the sun provides us with a surplus of power that exceeds our needs by a factor of 1000.[2] The practical application of solar energy, which harnesses the power of the sun to generate electricity and heat, has the potential to bring about numerous benefits to society and the environment.

B. Wind Energy

Wind energy is an incredibly promising power source, boasting an estimated availability of 16 million megawatts, which is on par with the current global energy consumption levels. The first power source we will discuss is the photovoltaic solar cell, a technology that efficiently converts sunlight into direct current (DC) power without releasing any harmful emissions. The second power source we will delve into is wind energy, which harnesses the kinetic energy of moving air to generate electricity. This clean and renewable energy source has the potential to revolutionize the way we power our world, offering a sustainable alternative to traditional fossil fuels.. [6]

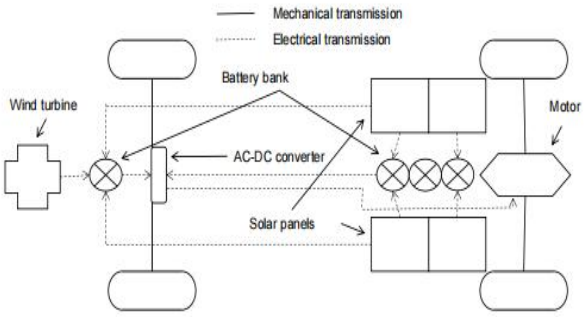

Fig. 1. Working diagram of solar-wind hybrid vehicle

II. METHODOLOGY

A. Hybrid Solar Energy

On-Grid solar PV system used for house and factory utilities. Standalone PV system with photovoltaic panels, not connected to grid. Charges during day, stores power in battery, used as needed. Placed on top of car or appliances.[1] In the system, one or more PV panels and electrical switches are installed. Then inverter is arranged to modify DC power as per our requirement.

B. Hybrid Wind Energy

Hybrid solar PV system combines solar PV with other power sources for utilities. PV-wind hybrid system combines solar PV and wind power generation. They operate at different times of the day.[5] Solar energy available during the day, wind energy depends on wind speed. Combined system provides steady power for vehicles and utilities with minimal fluctuations. Installation more complex than traditional designs.[1] For optimal utilization of wind energy, a minimum average speed of 20 kilometers per hour (20 km/h) must be maintained.

C. Hybrid System

A solar-wind hybrid system combines PV solar panels and wind turbines to generate renewable energy. Solar panels convert sunlight into electricity during the day, while wind turbines capture wind power, which is stronger at night or in cloudy conditions. This setup includes inverters for DC to AC power conversion and a battery storage system. Using both energy sources ensures a reliable power supply, reducing dependence on one source and minimizing fluctuations. These systems are ideal for

remote areas, off-grid applications, and enhancing grid stability with a sustainable energy solution.

III. Design Of Solar System

Solar energy in vehicles uses photovoltaic cells to convert sunlight into electricity, promoting energy efficiency and sustainability..[1] Solar panels on vehicles are commonly associated with electric vehicles (EVs) and hybrids.

I. Design Specification of Solar System

No.	Name	Symbol	Values	Units
1.	Propulsion power	$P_{propulsion}$	745.7	W
2.	Auxiliary power	$P_{auxiliary}$	0	W
3.	Daily driving time	t_{daily}	2	hrs
4.	Length of the available solar area	L	0.9144	m
5.	Width of the available solar area	W	0.762	m
6.	Motor voltage		48	V
7.	Solar constant	G_{total}	1361	W/m^2
8.	Solar zenith angle	θ	60	°
9.	Solar zenith angle at noon	θ_z	90	°
10.	Area of single solar panel	A_{solar}	0.1575	m^2
11.	Efficiency of the solar panels	η_{solar}	15	
12.	Days of autonomy	D	1	day
13.	Voltage of solar panels	V	48	V
14.	Ampere of solar panels	I	1.04	A
15.	Sun hour of a day		6	hrs
16.	Voltage of battery bank	$V_{battery}$	48	V

A. Calculation of Solar System

The power demand (P_demand) of the vehicle can be estimated using the equation (1).

$$P_{demand} = P_{propulsion} + P_{auxiliary} \quad (1)$$

The energy demand (E_demand) over a specific period of time can be calculated by integrating the power demand over that period.

To estimate the daily energy demand is using equation (2).

$$E_{demand} = P_{demand} \cdot t_{daily} \quad (2)$$

Calculate the average sunlight at the vehicle's location to estimate solar panel energy generation. Panel space on a vehicle varies based on design, size, and layout.

$$A_{available} = L.W \quad (3)$$

Solar irradiance (G) is the power per unit area received from the Sun's rays. It varies depending on factors such as time of day, season, geographic location, and weather conditions.

Solar irradiance (G) is calculated by using equation (4).

$$G = G_{total} \cdot \frac{Sin\theta}{Sin\theta_z} \quad (4)$$

Several factors influence the efficiency of solar panels, including type of solar cell technology, cell temperature (higher temperatures reduce efficiency), incident angle of sunlight and spectral distribution of sunlight.

Calculate the power output (P_out) of a single solar panel using the equation (5).

$$P_{out} = A_{solar} \times G \times \eta_{solar} \quad (5)$$

Adjust for days of autonomy is calculated by using equation (6).

$$E_{required} = E_{total} \times D \quad (6)$$

The selection of the battery type depends on factors such as energy density, weight, cycle life, and cost.

Calculate required battery capacity is using equation (7).

$$C_{required} = \frac{E_{required}}{V_{battery}} \quad (7)$$

Adjust for battery efficiency is using equation (8).

$$C_{battery} = \frac{C_{required}}{\eta_{battery}} \quad (8)$$

The power output of the solar panels are calculated by using equation (9).

$$P = V.I \quad (9)$$

II. Results Data for Solar System

No.	Name	Symbol	Values	Units
1.	Power demand	P_{demand}	745.7	W
2.	Energy demand	E_{demant}	1491.4	Whr
3.	Area available for solar panels	$A_{available}$	0.6968	m^2
4.	Power output	P_{out}	27.85	W
5.	Energy required	$E_{required}$	1491.4	Whr
6.	Required battery capacity	$C_{required}$	31.07	Ah
7.	Required battery capacity with battery efficiency	$C_{battery}$	36.55	Ah
8.	Power output of the solar panels	P	49.92	W
9.	Power output of a day	P_{day}	299.52	Whr
10.	Ampere output of a day	I	6.24	Ah
11.	Solar irradiance	G	1178.661	W/m^2

IV. Design Of Wind System

To create a wind energy system, evaluate the site, select components tailored to the location. Conduct feasibility analysis to measure wind speed, direction. Consider site features like topography, obstructions, distance from grid. Choose turbines based on evaluations, specs, dimensions, elevation for optimal power generation..[4]

III. Design Specification of Wind System

No.	Name	Symbol	Values	Units
1.	Pressure of the air	P	1013	hPa
2.	Gas constant	R	287	Nm
3.	Temperature	T	307	K
4.	Radius of the rotor	r	0.12	m
5.	Velocity of the wind	V_{wind}	11.1	m/s
6.	Lift coefficient	C_l	0.6	
7.	Drag coefficient	C_d	0.2	
8.	Power coefficient	C_p	0.4	
9.	Generator efficiency	η_{solar}	85	%
10.	Driving time for no wind	$t_{no\ wind}$	2	hr
11.	Battery efficiency	$\eta_{battery}$	85	%
12.	Battery voltage	V	12	V
13.	Power demand	P_{demand}	50	W
13.	Generator voltage	V	12	V

A. Calculation of Wind System

Calculate the available wind power using the equation (10).

$$P_{wind} = \frac{1}{2}\rho A V_{wind}^3 \quad (10)$$

The air density is calculated by using equation (11).

$$\rho = \frac{P}{RT} \quad (11)$$

Calculate the swept area of the wind turbine is using equation (12).

$$A = \pi r^2 \quad (12)$$

The efficiency of the wind turbine is using equation (13).

$$\eta = \frac{P_{actual}}{P_{theo}} \quad (13)$$

Wind turbine blade's lift and drag forces from airflow affect aerodynamic performance, efficiency, and power output..

The lift force of the wind blade is calculated by using equation (14).

$$F_L = \frac{1}{2}\rho A V_{air}^2 C_L \quad (14)$$

The drag force of the wind blade is calculated by using equation (15).

$$F_D = \frac{1}{2}\rho A V_{air}^2 C_D \quad (15)$$

Generator power output = mechanical power from wind turbine rotor x generator efficiency.

The generator's efficiency is calculated by using equation (16).

$$P_{gen} = P_{mech} \cdot \eta_{gen} \quad (16)$$

The mechanical power from the wind turbine is calculated by using equation (17).

$$P_{mech} = \frac{1}{2}\rho A V_{wind}^3 C_p \quad (17)$$

The total energy required to operate the vehicle without wind is calculated by using equation (18).

$$E_{required} = P_{demand} \cdot t_{no\ wind} \quad (18)$$

Adjust the required energy to account for losses in the battery system.

Required energy for losses in the battery is calculated by using equation (19).

$$E_{battery} = \frac{E_{required}}{\eta_{battery}} \quad (19)$$

To obtain the required battery capacity is calculated by using equation (20).

$$C_{required} = \frac{E_{battery}}{V_{battery}} \quad (20)$$

The power equation is same as equation number (9).

IV. Results Data for Wind System

No.	Name	Symbol	Values	Units
1.	Air density	ρ	1.1497	kg/m^3
2.	Swept area of wind turbine	A	0.0113	m^2
3.	Power from the wind	P_{wind}	9	W
4.	Wind turbine efficiency	η	34	%
5.	Lift force	F_L	0.4858	N
6.	Drag force	F_D	0.1619	N
7.	Mechanical power	P_{mech}	3.6	W
8.	Generator power	P_{gen}	3.06	W
9.	Energy required	$E_{required}$	100	Whr
10.	Energy of the battery	$E_{battery}$	117.64	Whr
11.	Required battery capacity	$C_{battery}$	9.8	Ah
12.	Ampere of wind turbine	I	0.255	A

V. Manufacture of Hybrid Vehicle

Solar and wind powered hybrid vehicle is built by the taking after procedures

- Fabric selection
- Motor selection
- Battery selection
- Development of frame
- Installation of solar panels
- Installation of wind turbine
- Assembly
- Testing

A. Fabric Selection

Solar-wind hybrid car uses AISI 4340 OQT 400, AISI 4140, and AISI 4340 steel for strength, lightweight, and ease of use.

B. Motor Selection

In this car, motor control is 0.75 kW for driving the vehicle. The motor is driven by four batteries (12 V). Rotational speed of motor is 2900 rpm (revolution per minute). Most extreme speed of motor is 40 km/hr.

Fig. 2. Installation of motor

C. Battery Selection

There are four batteries utilized in this vehicle extend. The course of action of the batteries is arrangement to get the required voltages. The capacity of battery is 100 Ah.

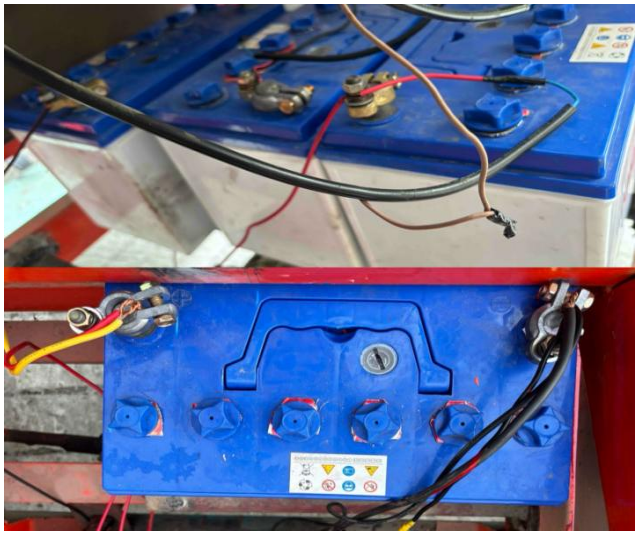

Fig. 3. Installation of four batteries

D. Development of Frame

After selecting the reasonable fabric, alloy steel empty (AISI 4140) and alloy steel level (AISI 4340) was cutting to degree required estimation. Concurring to plan, the cutting materials is bored to motor and steering. At that point, cutting materials is joined by welding prepare. Frame built using nearby fabric in Mechanical Workshop.

E. Installation of Solar Panels

Four 25W solar panels are introduced in a square shape on the rear frame of the vehicle.

Fig. 4. Installation of solar panels

F. Installation of Wind Turbine

The wind turbine is mounted on an press plate at the front of the vehicle in conjunction with a 12V dynamo motor.

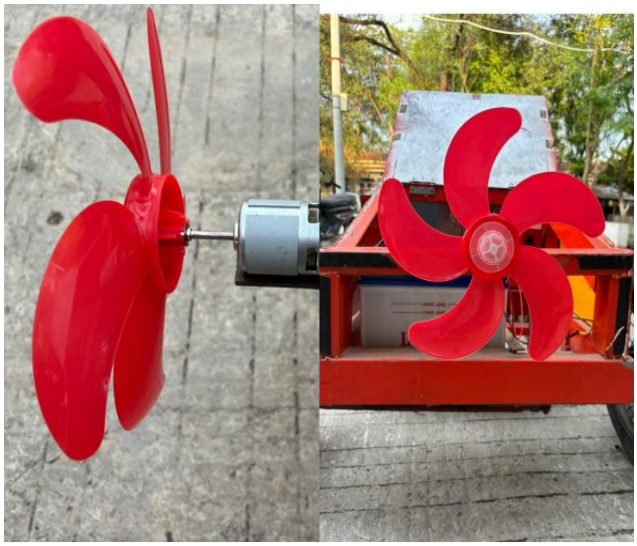

Fig. 5. Installation of wind turbine

G. Assembly

The assembly line for the solar-wind hybrid car is designed with a focus on successive component expansion to ensure thorough testing and seamless integration, which are key factors in boosting productivity. The final product of this innovative process is a sustainable mode of transport that utilizes both solar and wind power. For a more in-depth look at the assembly process, refer to Figure 5 for detailed information and insights.

Fig. 6. Assembly of hybrid vehicle

H. Testing

The graph below shows the power output depending on the speed of the wind turbine.

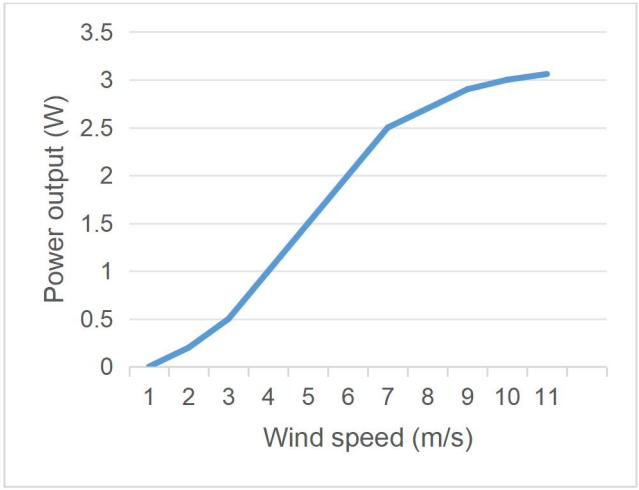

Fig. 7. Wind turbine performance

VI. Conclusion and Recommendation

The design of solar-wind powered hybrid vehicles represents a significant step towards maintainable transportation and renewable vitality integration. By tackling the control of the sun and wind, these vehicles offer the potential to decrease greenhouse gas emissions, diminish dependence on fossil fuels, and moderate natural affect. In summary, the combination of solar and wind using renewable vitality has an vital put to decrease and supplant fossil fuels in the power utilized in lament. It is the appropriate for driving inside the Technological University (Mandalay) campus. It is reasonable for driving as a teaching aid to students who will be going to in the next academic year.

Solar-wind hybrid vehicles offer benefits like sustainable energy use, lower costs, and reduced environmental impact. However, there are challenges like high initial investment, energy storage issues, reliance on weather, and complex design. Other concerns include weight, component durability, and the need for consumer acceptance and infrastructure.

Reduce the weight of the vehicle to make strides the execution. The greater the wind turbine, the superior the productivity. Need to more solar power, have to utilized more solar panel watts and utilized superior batteries.

In this system, all the power from the solar panels will be used for the motor, and the power from the wind system will be used as auxiliary power for the vehicle's horn and bulbs.

Acknowledgment

The author would like to thank to Dr. Aye Mya Thandar, Professor and Head of the Department of Mechanical Engineering, Technological University (Mandalay) for her support and guidance. In specific, the author would like to thank Dr. Aye Aye Khaing, Professor, Department of Mechanical Engineering, West Yangon Technological University, for her offer assistant and direction, bolster and support. The author also would like to thank to his parents and all of his instructors from Department of Mechanical Engineering, Technological University (Mandalay).

References

[1] A. Ameri et al. "Design and optimization of a solar wind hybrid power system for an electric vehicle" (International Journal of Hydrogen Energy, 2016).

[2] S. Ogunnaike et al. "Design and development of a solar and wind energy powered electric vehicle" (Energy Proceed, 2016).

[3] R. Reddy et al. "Modeling and analysis of a solar wind hybrid energy system for electric vehicle charging stations" (Applied Energy, 2018).

[4] S. Rajasekaran et al. "Solar-Wind Hybrid Electric Vehicle (SWEV): Overview, Design, and Simulation" (2017 SAE Technical Paper Series).

[5] Y. Wang et al. "Design and Implementation of a Solar-Wind Hybrid Energy System for Electric Vehicle Charging Station" (2018 IEEE Power & Energy Society General Meeting).

[6] C.C. Chan and K.T. Chau. "Hybrid Electric Vehicles: Principles and Applications with Practical Perspectives" (Wiley, 2011).

[7] Banal, V., et al. "Design and Performance Evaluation of a Solar-Wind Hybrid Vehicle" . Energy, 190, 116365.(2020)

[8] Jain, M., et al. "Design and Fabrication of a Solar-Wind Hybrid Vehicle Prototype". International Journal of Engineering Trends and Technology, 36(7), 357-361.(2016).

[9] Li, S., et al. "Design and Optimization of Solar-Wind Hybrid Power System for Electric Vehicle" . Applied Energy, 215, 243-257.(2018)

Performance Analysis of Wave Power and Buoyancy Force

Swe Swe Maw[1], Thida Win[2]

[1] *Department of Mechanical Engineering Technological University (Mandalay)*

[2] *Department of Mechanical Engineering Mandalay Technological University*

Email: [1]sweswemaw22@gmail.com, [2] maythidawinkyi@gmail.com

***Abstract*— This research aims to produce power by means of waves. The wave energy converter (WEC) generates power on harnessing the energy produced by the waves of the ocean. Mechanical labor that harvests wave energy is transformed into electrical energy via a generator. The wave up power in this study is computed using local data (the Ayeyarwady River near Sagaing city in Myanmar). The amount of power generated depends on the waves' intensity. Wave power converters have traditionally exclusively used the buoy's vertical motion to generate electricity. It is a way to directly produce mechanical power from waves. In this case, the rack and pinion mechanism is utilized. The system consists of a DC generator, sprocket, and rack & pinion. The buoy is attached using a rack and pinion system, which is linked to the generator and chain sprockets. When the wave height ranges from 0.1778 meters to 0.3048 meters at normal saturation, the buoy design and wave up power can produce 64.6788 watts.**

Keywords- buoyancy, rack and pinion, sprocket, chain, wave energy

I. INTRODUCTION

Numerous ways of producing renewable energy have been discovered. Among the best renewable energy sources is water wave energy. The majority of wave energy equipment is made to capture energy from waves in the deep sea. Vibrations of elastic media, like air, crystalline solids, or stretched strings, are the most basic forms of wave motion. Large waves are typically created when the wind transfers its energy to the water and causes waves to form on the ocean's surface. When the mean depth of these is compared to the group velocity, the most prevalent type of wave is discovered [1].

Water wave power is the utilization of the wind energy produced from water waves for beneficial applications like electricity production or water pumping. An apparatus that produces wave power is called a wave energy converter, or WEC. Although wave speed, wavelength, and water density can have an impact on wave power, larger waves are typically more potent. The scale of operation must be established, just like with any renewable energy source. Current trends support the generation of moderate power at 100 kW–1 MW using modular devices that individually capture energy from waves that measure between 5 and 25 meters in length. Sea waves in deep water can experience extremely significant energy flows. The water wave's strength is directly proportional to the motion's period and the square of its amplitude [2–3].

In addition to this, waves with a huge height of 2 m and a long wavelength of 10 m are of great interest for power generation. Energy flows typically average between 50 and 70 kW/m breadth of the approaching wave. A basic prototype was created and put to the test locally in order to better comprehend wave energy devices. The wave power and wave-up force can be calculated using information obtained from the surrounding environment.

The buoy is stretched using a form of connection by the fixed-type wave power mechanism, which is designed to remain in place. The waves' periodic motion is directly used to extract power. The renewable energy source is wave energy, and numerous technologies and ideas have been developed. By evaluating the wave motions, a new model was constructed and tested for the new energy in the research. The buoy was designed to produce more buoyant force [2].

In this study, the wave-up force is calculated from the data of the Ayeyarwady River near Sagaing City in Myanmar. The wave energy is mostly dependent on the wave-up force, and the wave-up force is related to the wind speed. In an ordinary situation, the river beside it can get the required wave-up force for as light changes. The side of the river can give wave-up force (about 56.3975 N), and that force was calculated from the average wave height of 0.1778 m and depth of not over 0.3048 m.

When the wave-up force is calculated, the buoy (the floating part of the mechanism) is considered the material for the buoy, which has less density than the water, so enough buoyant force can be obtained. The buoy is designed to accept almost all upcoming waves that lead to the front of the mechanism. The mechanical design of the device and the operation process were presented in detail, and several devices are currently being used to extract mechanical energy from the waves. Mechanical and electrical outputs of the system are recorded for different wave heights varying from 0.0508 to 0.3048 m for a time interval of 3s. The mechanical design of the device along with the working process are presented in detail, and the test results show an increase in power generation.

II. MECHANICAL WAVE ENERGY CONVERTER

The entire configuration of the Mechanical Wave Energy Converter (MWEC) is depicted in Fig. 1. It is made up of a buoy that floats and a system of racks and pinions that is used to change vertical, reciprocating action into oscillatory, rotating motion. In order to protect the floating buoy from ocean waves, two vertical shafts are assembled with the gear rack and surrounded by guide supports. The floating buoy is connected to the gear rack through the shaft. Ball bearings support driving sprockets that are mounted on these shafts, and the free-wheel sprocket is then coupled to secured pinion gears. The rpm multiplier that is connected to the shaft of the electric generator is fixed by the whole unit, which is transversely mounted on a shaft supported by ball bearings. The entire MWEC assembly is fixed to a platform deck that is anchored to the sea floor or a floating vessel. The toothed gear rack attached to the buoy turns the pinion gear (5) clockwise and the second pinion gear (6) counterclockwise as the approaching wave pushes the buoy upward [4].This is because the free wheel sprocket keeps the

pinion gear's rotation from being interfered with (5). Conversely, as the waves push the floating buoy down, the toothed gear rack fixed to the buoy turns the pinion gear (5) counterclockwise, and the free wheel sprocket (17) causes the pinion gear (6) to turn clockwise. An RPM multiplier is fitted to increase the output shaft's rotational speed. Power transfer occurs through pinion gear (5) in upward motion and pinion gear (6) in downward motion [3- 5].

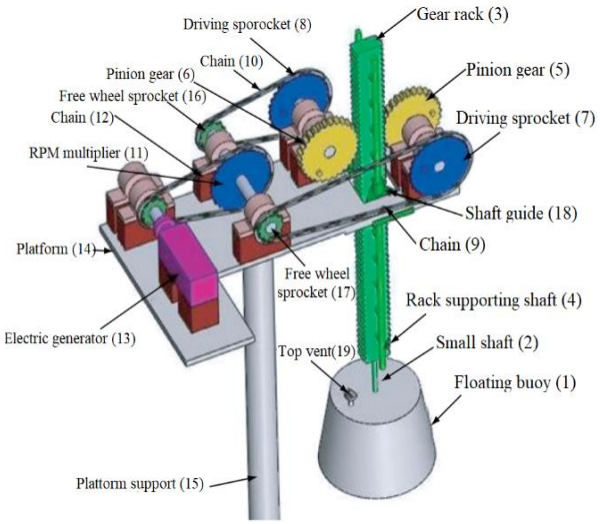

Fig. 1. Overall assembly of mechanical wave energy converter

A. Components of Wave Energy Convector

The working of the system has been shown in Fig. 2's flow diagram for fixed type wave energy convertors.

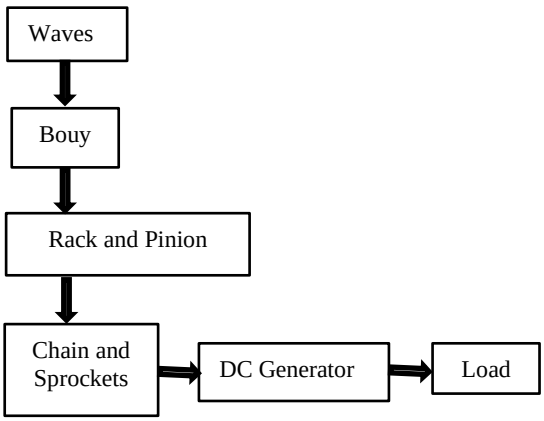

Fig. 2. Working flow diagram of wave energy convertors

Table I shows the various component materials that were implemented in the fabrication.

I. MATERIAL USED OF WAVE ENERGY CONVERTER

No.	Components	Materials
1.	Frame	Galvanized Iron
2.	Pinion	Cast Iron
3.	Rack	Cast Iron
4.	Rod	Cast Iron
5.	Buoy	Polyurethane Elastomer
6.	Chain and Sprockets	Mile steel

B. Power of Water Wave

The wave power formula is given by,

$$P_w = \frac{\rho g^2 t h^2 l}{32\pi} \quad (1)$$

Where,
P_w = power of water wave presents in depth, Watts
ρ = water density, kg/m^3
g = acceleration due to gravity, 9.81 m/s^2
t = wave period, second
h = wave height, m
l = length of wave front, m

C. Total Buoyant Force From the Buoy

The buoyant force is present whether the object floats or sinks. Let's consider a floating object, but the analysis is basically the same for a submerged object [6-7] .

$$F_b = F_{bottom} - F_{top} \quad (2)$$

Where,
F_b = Buoyant force of an object, N
F_{bottom}= The force exerted on the bottom, N
F_{Top} = The force exerted on the upper surface, N

$$F_b = \rho g\, Ah \quad (3)$$

Where,
F_b = the buoyant force, N
A = total area of buoy, m^2
h = average height of the buoy, m

D. Rack and Pinion Drive

The torque on the pinion is just the tangential force (force on the rack) divided by the pinion radius [6].

$$T_p = F_r \times r_p \quad (4)$$

Where,
T_p = torque on pinion, N.m
r_p = pinion radius , m
F_r = Tangential force, N

Power is the ratio between the work done and the time taken and can be expressed as

$$P_p = \frac{2\pi \times n_{rpm} \times T_p}{60} \quad (5)$$

Where,
P_p = power ,Watts
n = speed , rev/s
T_p = Torque on pinion, Nm

E. Chain Drive Design

Chain drive is a method of moving mechanical power across a sprocket gear by using the teeth of the gear meshing with the grooves in the chain links. Center distance (C), chain length (L), the number of teeth in the large sprocket, and the number of teeth in the small sprocket in pitches are conveniently related to each other [6].

$$C = \frac{1}{4}\left[L - \frac{N_1 + N_2}{2} + \sqrt{\left(L - \frac{N_1 + N_2}{2} \right)^2 - \frac{8(N_1 - N_2)^2}{4\pi^2}} \right] \quad (6)$$

Where,
C = Center distance (m)
L = Chain length (m)

N_1 = Number of teeth on driver sprocket
N_2 = Number of teeth on driven sprocket

F. Sprocket Ratio

The tooth ratio between the front and rear sprockets is known as the sprocket ratio. The ratio establishes the transmission of driver sprocket RPM to driven sprocket [6].

$$\text{Sprocket ratio} = \frac{N_1}{N_2} = \frac{n_2}{n_1} = \frac{T_1}{T_2} \quad (7)$$

Where,
N_1= Number of teeth on driver sprocket
N_2= Number of teeth on driven sprocket
n_1= Speed of the driver sprocket (rpm)
n_2= Speed of the driven sprocket (rpm)
T_1=Torque of the driver sprocket (Nm)
T_2=Torque of the driven sprocket (Nm)

G. Shaft Design

The torsion equation can be used to calculate the shaft's diameter when it is shaft subjected to a twisting moment, also known as torque. The formula is [6]:

$$\frac{T}{J} = \frac{\tau}{r} \quad (8)$$

Where,
T = Twisting moment (or torque) acting upon the shaft, N.m
J = Polar moment of inertia of the shaft about the axis of rotation, m^4
τ = Torsional shear stress, N/m^2
$r = \frac{d}{2}$; where d is the diameter of the shaft, m

III. Design Of Wave Energy Converter

The following specifications must be known in Table II.

II. Design Parameters for Wave Energy Converter

No.	Descriptions	Value
1.	Length of buoy	0.7112 m
2.	Breadth of buoy	0.508 m
3.	Height of buoy	0.2286 m
4.	Length of rack	0.2974 m
5.	No. of teeth in pinion	20
7.	No. of teeth on smaller and larger sprockets 1	38-38
8.	Sprocket 1 ratio	1:1
9.	No. of teeth on smaller and larger sprockets 2	48-16
10.	Sprocket 2 ratio	3:1

A. Working Procedure

The apparatus is capable of producing power and converting it into electricity through the use of waves. The buoy, three shafts, sprockets, bar-linkages, generator, lightbulb, and bearings make up the equipment. The buoy helps the machine float on water and is fastened to the bar linkages. The rack is fastened to the bar-linkage, and the pinion is situated on the first shaft. Additionally, the first shaft features a sprocket. The second shaft has three sprockets on it. The last sprocket assists the second sprocket in producing higher speed and rotating smoothly. The first sprocket is connected to the other sprocket on the first shaft, and the second sprocket is connected to the other sprocket on the third shaft via a chain. The third shaft has a flywheel and a sprocket. The lightbulb is connected to the generator, which is connected to the third shaft. The buoy will float when waves form on the water's surface, and the bar links will follow it. The rack will likewise go vertically along the bar links.

That makes to rotate the pinion and to the first shaft. When the first shaft rotates, the second shaft will rotate too and also to the third shaft. The third shaft will generate power and sent it to the generator to convert into electric which will lighten the bulb. The complete schematic diagram of the prototype convector is displayed in Fig. 3(a) and Fig. 3 (b) is testing of wave energy convector in the Ayeyarwady River.

Prototype of WEC

(b) Testing of WEC

Fig. 3. Overview and testing of the wave energy convertor

B. Result and discussion

Table III shows the calculated results of wave energy convector.

III. Result Data Of Wave Energy Converter

No	Descriptions	Value	Units
1.	Displacement of wave	1.0025	m
2.	Wave Heigh	0.1778	m
3.	Pitch circle diameter	0.0384	m
4.	Force of rack	1038.86	N
5.	Torque on pinion	20.98	N.m
6.	Diameter of sprockets 1	153.79	mm
7.	Larger diameter of sprocket 2	194.18	mm
8.	Smaller diameter of sprocket 2	66.1	mm
9.	Center distance 2	318.77	mm
10.	Speed of sprockets 2	26,78	rpm
11.	Wave power	225.667	Watt
12.	Water wave force	56.3975	N
13.	Total buoyant force	929.5145	N
14.	Force on pinion	1176.6	N
15.	Torque on pinion	23.7673	N.m
16.	Mechanical output power	64.6788	Watts

Design consideration is based on the local area and it was the averages of waves. The maximum and minimum saturation are considered. Wave comes up about 28 crests per minute which the depth of about 0.3048 m. At the depth of 0.3048 m the upcoming wave height is varies from 0.0508 m to 0.3048 m. If length of wave front 1.2198m, the power of wave can be calculated. The wave up force can be calculated by using the power of wave from the depth and

variable wave height. The wave up force must be given to the buoy and then the rise and fall periodic motion of the buoy can give the power to start the mechanism.

The length of rack is based on the height of the water wave. The diameter of the pinion is based on the length of the rack that is connecting with pinion. The material used for rack and pinion is cast iron. In gear design, selected pressure angle is 20° full depth. In design calculation, spur gear set is satisfied at module is 0.002 m, outside diameter is 0.0404 m. The circular pitch of 0.0063 m has addendum 0.002m and dedendum is 0.0025m. The whole depth of 0.0045m has clearance 0.0005m and working depth is 0.004m. It has pitch circle diameter of 0.0384m and tooth thickness is 0.0032 m. The pinion has a base circle diameter of 0.0361 m, fillet radius is 0.0006 m and root diameter was 0.03m. The face width of the pinion is used 0.026 m for strength and dynamic check. Rack gear has a module of 0.002m and its length has 0.2794m. The numbers of teeth are designed to 41 teeth for strength and dynamic check. Square type aluminum alloy pipe for weight on the buoy is used for bar linkage. This square pipe has 1276.27 N weights and its area is 0.0254 m width. It has 0.0254 m thickness and 2.997 m long.

The first shaft has 0.2931 N-m in bending moment, 23.7673 N-m in torque, 17.2002 mm in diameter, the speed of 39 rpm and 64.6788 W in power. The second shaft has 0.8892 N-m in bending moment, 23.7673 N-m in torque, 17.2048 mm in diameter, the speed of 37. The third shaft has 6.2356 N m in bending moment, 64.6788 N-m in torque, 23.2134 mm in diameter, the speed of 112 rpm.

In chain drive design, cast iron coated with aluminum is used and chain no. 40 is designed, which is used on motorbike and bicycle. The chain pitch is 12.7 mm and roller diameter is 8 mm. Roller width is also 8mm and link plate thickness is 1.5 mm. The average tensile strength is 16.46 kN. In design calculation first stage, it is satisfied at diameter of the driver sprocket is 153.79 mm and diameter of the driven sprocket is also 153.79 mm. The number of teeth on driver and driven sprocket are same and 38 teeth for designing the sprockets ratio 1. The center distance between two sprockets is 317.5 mm and the required chain length is 88 pitches for designing the chain. In second stage, it is satisfied at diameter of the driver sprocket is 194.18 mm, diameter of the driven sprocket is 66.1 mm, the number of teeth on driver sprocket is 48 teeth and the number of teeth on driver sprocket is 16 teeth, for designing the sprockets according to sprockets ratio is 3. The center distance between two sprockets is 318.77 mm and the required chain length is 83 pitches for designing the chain.

The Mechanical output power can be also calculated in the following MATLAB program.

```
>> k=[10,19,28];
h=[0.0508,0.1778,0.3038];
l=1.2192;
t=60;
g=9.81;
rho=1000;
pi=3.14;
Pw=(rho*g*t.*h.^2*l)/(32*pi)
lambra=2*pi./k
v=sqrt(g.*h)
c=(((g.*lambra)/(2*pi)).^2)
fv=0.0076.*lambra;
V=v+c+fv;
F=v./lambra
fx=c./lambra
Fa=F+fx+0.0076;
D=V/(Fa.*lambra)
T=1./(F+0.0076)
Fw=(Pw.*T)/(D)
Fb=3424.44
FB=4297.557-Fb+Fw
b=10.68;
c=8.4372;
Fc=FB.*b/c
rp=0.0202;
Tp=Fc.*rp
n=26;
Pp=(2*pi*n.*Tp)./60
plot(h,Pw),grid
xlabel('wave height,m'),ylabel('wave power,W'),
title('wave height and wave power')
plot(Pw,Fw),grid
xlabel('wave power,W'), ylabel('water wave force,N'),
title('wave power and water wave force')
plot(Fw,FB),grid
xlabel('water wave force,N'), ylabel('Total bouyant
force,N')
title('water wave force and total bouyant force')
plot(FB,Fc),grid
xlabel('total bouyant force,N'), ylabel('force on pinion,N')
title('total bouyant force and force on pinion')
plot(Fc,Tp),grid
xlabel('force on pinion,N'), ylabel('torque on pinion,N-m')
title('force on pinion and torque on pinion')
plot(Tp,Pp,'*'),plot(Tp,Pp),grid
xlabel('torque on pinion,N-m'), ylabel('mechanical output
power,W')
title('torque on pinion and mechanical output power')
D = 1.0000
T = 0.8836    0.2498    0.1298
Fw = 16.2858   56.3975   85.5531
Fb = 3.4244e+03
FB = 889.4028  929.5145  958.6701
Fc = 1.0e+03 *     1.1258    1.1766    1.2135
Tp = 22.7417   23.7673   24.5128
Pp = 61.8877   64.6788   66.7076
```

The graphs in Fig. 4 through Fig.10 below, which were created using MATLAB program, show the mechanical power resulting from wave height.

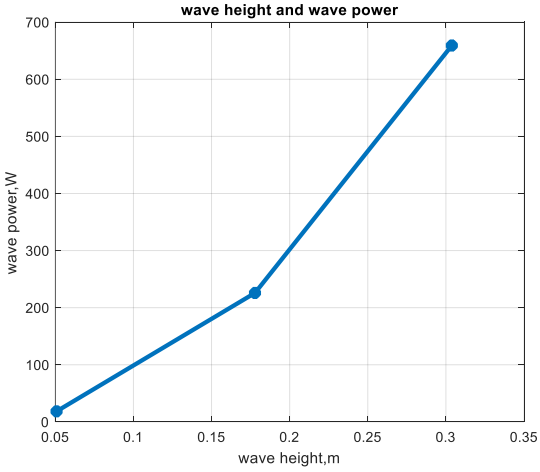

Fig. 4. Wave height and wave power graph

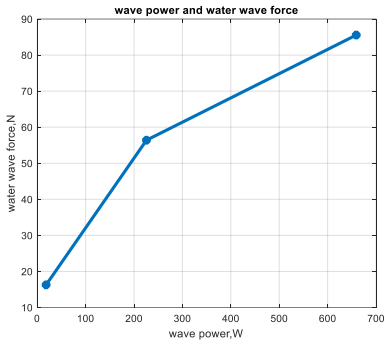

Fig. 5. Wave power and water wave force graph

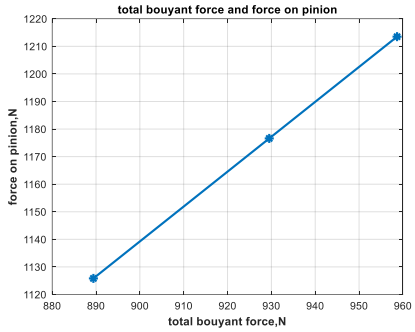

Fig. 6. Water wave force and total buoyant force graph

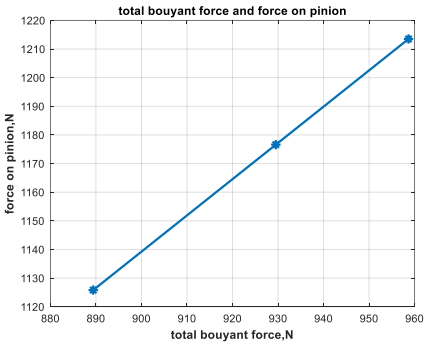

Fig. 7. Total buoyant force and force on pinion graph

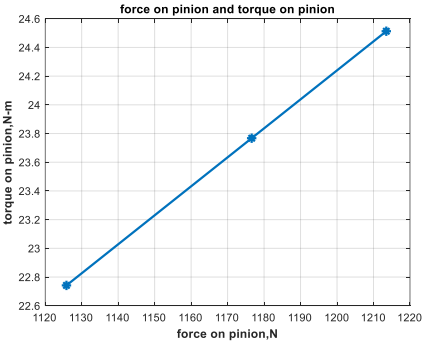

Fig. 8. Force on pinion and torque on pinion graph

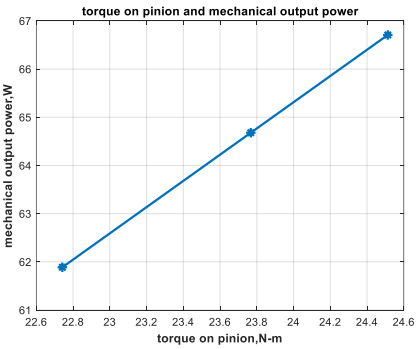

Fig. 9. Torque on pinion and mechanical power graph

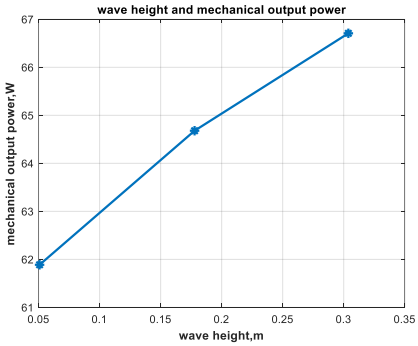

Fig. 10. Wave height and mechanical power graph

It can be seen from the graphs that the output power increases with wave height.

IV. Conclusion

The two most important elements of the fixed-type wave energy convertor are the buoyant force and the wave up force. The mechanism is genuinely powered by a small percentage of the total power produced. When the variable changes as known data, the computed wave up force from the wave at one minute in time is obtained. Wave averages are taken into account when designing, taking into account the surrounding environment. Saturation at its highest, medium, and minimum are taken into account. When the wave height ranges from 0.1778 meters to 0.3048 meters at normal saturation, the buoy design and wave up force can produce 64.6788 watts. The buoy design is not the only foundation for the wave energy convertor design. The buoy can provide sufficient power, and the more buoyant force can also provide power. The rack and pinion is also regarded as significant in this design since it provides the force necessary for the entire mechanism to execute the secondary forces that begin providing sufficient force. Because the rack and pinion come in contact with water most of the time, it is susceptible to rust. The weight needs to be light, have a good density, and be able to withstand unexpected high torques. Thus, when selecting a material, the rack length and the pinion must be taken into account. Therefore, the fixed-type wave energy convertor is operating fully and should provide more electricity if the generator is able to use it.

Acknowledgment

The author wishes to express the deepest gratitude to her parents for their moral support and encouragement and all teachers who taught her everything since childhood till now and to everyone who assisted in completing this paper. The author thanks her family and friends for supporting.

References

[1] Bret Bosma, On the Design, Modeling, and Testing of Ocean Wave Energy Converters, July 16, 2013

[2] Srinivasan Chandrasekaran, Power Generation Using Mechanical Wave Energy Converter, Volume 3 · Number 1 · 2012

[3] A.ANISH, Modification of Wave Energy Convector Using Buoy, Volume 4, Issue 05, JETIR (ISSN-2349-5162) May 2017

[4] Eugen Rusu, Evaluation of the Wave Energy Conversion Efficiency in Various Coastal Environments, June 2014,Dr. K.R. (Fluid mechanics and hydraulic machines) buoyant force.

[6] Robert R Creamer, “Machine Design” by Temple University Technical Institute.

[7] Dr.Rajendar Karwa “A text book of MACHINE DESIGN”, Published by Laxmi Publication (P), LTD; New Delhi

Performance Test of Domestic Solar Dryer with Double-glass Flat Plate Collector

Yin Myo Thu[1], Swe Swe Maw[2], Thinzar Win[3]

[1]*Mechanical Engineering department, Technological University, Mandalay, Myanmar*

[2] *Mechanical Engineering department, Technological University, Mandalay, Myanmar*

[3]*Mechanical Engineering department, Technological University, Mandalay, Myanmar*

Email: [1]yinmyothu322@mail.com, [2]sweswemaw22@mail.com, [3]tinzarwin.tu@mail.com

***Abstract*—This mentioned paper introduces the study of performance test of mixed-mode sunlight drying machine on potato, chili, eggplant. The dryer was installed at 21.98° latitude and 96.1° longitude in Mandalay region, Myanmar. A mixed mode solar dryer consists of the air heater (collector of the sunlight) and the drying room with two trays. The temperature of air in the mixed mode solar drying machine was varying 27°C-50°C at the noon of a clear day in January 1st, no load test and the maximum temperature is about when the environmental temperature was 36° C. The drying capacity for potato, eggplants and chili is 1 kg and 500 g of each capacity is in the upper tray and in the lower tray. Mixed-mode solar dryer is used to dry fruits and vegetables for rural areas.**

Keywords—Flat-plate Collector, Mixed-mode Solar Dryer, methodology, Collector efficiency, Performance Test

I. INTRODUCTION

Drying is the useful and ancient technology to preserve food. The waste of excessive production can be reduced and also products can be made to be light-weight, small and easy for handling [1]. Drying is a wetness removal method because of simultaneously thermal and mass transfer [2]. Excessive wetness participation amount in some farming products after reaping can be easy and smooth the development of disease-causing germs resulting in decomposition of the products. Decreasing wetness participation amount of food is between 10% and 20% prevents, disease-causing germs, fermentation agent, mold and enzymes from damaging it [3].

For effective drying, sufficient heat to extract wetness without making the food and enough dry air circulation to carry it away the released wetness should be applied. Loaded test of the sunlight drying machine is carried out utilizing one kilogram of fresh potato sheets, eggplant and chili. The thickness of the sheets between 3mm and 4 mm. The sheets put on the level of each tray and in traditional sun drying. These sheets avoid to overlap each other and ensure uniform drying. The instruments for data collection are needed that are digital thermometer, anemometer, thermo-hygrometer, infrared thermometer and digital balance.

Only sunlight energy is utilized as the heat original resources for drying. The temperature of air in the environment, dryer temperature and the air temperature of the collector are documented every hour. The wetness of the participation amount of the product samples is also recorded for one hour interval.

Damp based wetness informs the mass of water as a percentage of total mass of a specimen and dry basis indicates the mass of water included in a given mass of dry solids [4]. As a result, wetness participation amount is decided in terms of both wet basis and dry basis. The performance test of drying efficiency and drying rate is also calculated.

II. MAIN COMPONENTS OF FLAT PLATE SOLAR DRYER

A. *Flat Plate Collector's Components*

A levelled sheet collector is a fundamental and uncomplicated heat absorber to absorb heat from the sun radiation. Parts of levelled sheet collector with their functions are as follow:

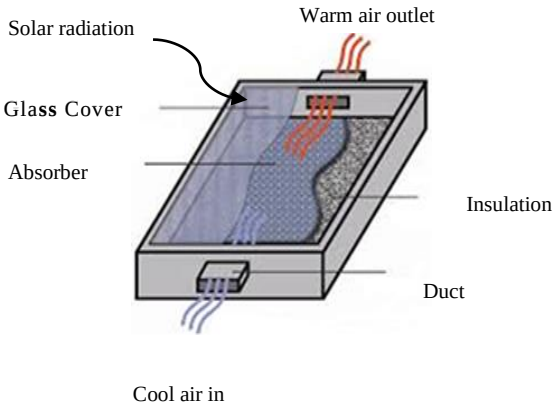

Fig.1. Solar Flat plate Collector by using air

The solar radiation strikes the sunlight scattering the cover glass of sunlight air collector. Absorber plate with black painting absorb solar energy, and the air from environment enters into the collector's inlet channel. The heat is transferred from the absorber plate to the air and the heated air escape from the air outlet to the drying room. It accomplishes the changing process from sunlight energy. Insulators prevent heat lost from the lowest layer and lateral surfaces of the collector.

B. *Working principles of Combined Model Sunlight Dryer*

Combined model sunlight drying is one of the modern sunlight's drying methods, in which both direct and indirect sunlight drying are carried out at the same time. This way is also known as passive drying machine.

The combined model sunlight drying machine has no movable portions, which is why it is called the passive drying machine. This type of dryer obtains the heating energy from the sunlight that comes in through the collector shinning. The air permitted in through air inlet is became hotter inner the sunlight collector channeled through the drying room. In drying room, it is completed in drying and eliminating the wetness content from the farming product.

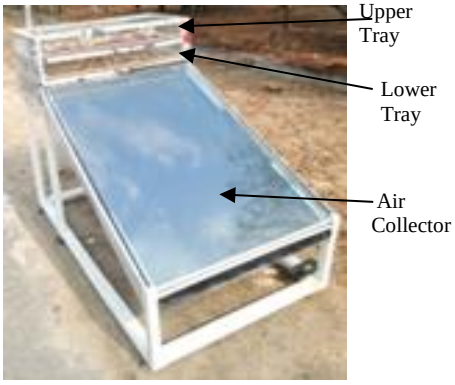

Fig. 2. Mixed Mode Solar Dryer

III. METHODOLOGY

A. Determination of Solar Radiation

The solar radiation can be calculated by using the following specifications. Weather is fine and then, do not blow. The collector is faced to the sun's track. The seasonal variation is negligible.[5] Plan location is Mandalay. Climate type is tropical.

Latitude, = 21.98º North
Longitude, L_{loc} = 96.1º East
The elevation above sea level, H = 74.676 m
The solar constant, I_0 = 1373 W/m^2
Local standard time of meridian, L_{st} = 97.5º E
Number of days, n = 365(for December 31st,2023)

1) Solar Zenith Angle (θz)

Sunlight Zenith Angle is an angle between the vertical and the line to the sun [5]. The sunlight zenith angle θ_z is of the form,

$$\theta_z = \cos^{-1}[\sin\lambda \sin\delta + \cos\lambda \cos\delta \cos\omega] \quad (1)$$

2) Clear Sky Radiation

By using, zenith angle and effective solar constants I_{0eff}, the beam irradiance I_b at the earth's surface is indicated [5] by,

$$I_b = I_{0,eff}\left[a_0 + a_1 \exp\left(-\frac{k}{\cos\theta_z}\right)\right] \quad (2)$$

The coefficients are,

$$a_o = r_0\, a_0^*,$$
$$a_1 = r_1\, a_1^*,$$
$$k = r_k\, k^*.$$

The constants a_0^*, a_1^* and k^* for the 23 km visibility standard atmosphere are:

$$a_0^* = 0.4237 - 0.00821\,(6 - H)^2,$$
$$a_1^* = 0.5055 + 0.00595\,(6.5 - H)^2,$$
$$k^* = 0.2711 + 0.01858\,(2.5 - H)^2,$$

where, H - elevation above sea level (km).

The clear sky diffuse irradiance, Id (on the horizontal) can be calculated from an equation,

$$I_d = [0.2710\, I_{0,eff} - 0.2939\, I_b]\cos\theta_z \quad (3)$$

3) Effective Solar Constant

The effective solar constant varies with the time of year according to the formula; [5]

$$I_{0,eff} = I_0\left[1 + 0.033\cos\left(\frac{360\ n}{365.25}\right)\right] \quad (4)$$

4) Hemispherical Irradiance

The beam and diffuse radiations after reflection from the ground is determined according to the formula; [5]

$$I_h = I_b \cos\theta_z + I_d \quad (5)$$

5) Seasonally adjusted solar panel tilt angles for Mandalay, Myanmar

At the winter, solar panel's angle adjusts to a 37° towards the south for the best energy production. [8]
The best tilt angle of collector, β = 37°

6) Total Solar Insolation Flux

The total solar insolation flux falling on an inclined surface any instant [5]is

$$I = I_b\cos\theta + I_d\frac{(1+\cos\beta)}{2} + I_h\rho_{ground}\frac{(1-\cos\beta)}{2} \quad (6)$$

B. Design procedure

The design calculation contained environmental conditions of the test location, the temperature of dryer, quantity of wetness to be removal, heat energy requirement and determination of airflow requirement.

1)Drying Temperature

The drying temperatures of fruits and vegetables are recommended from 37.7℃ to 54.4℃. [6]

2) Amount of Moisture to be removed

The formula for the all quantity of wetness to be removal (Mw) is calculated by [6]:

$$M_W = \frac{W_W \times (M_i - M_f)}{1 - M_f} \quad (7)$$

3) Heat Energy Required to Remove Water

It is considered drying process as a two-stage. Where, the first one is raised the temperature of the wet material to needed level at which the wetness will be removed. [6] This is calculated by the following equation:

$$Q_1 = C_P \times W_W (T_d - T_a) \quad (8)$$

The heat energy needed to evaporate is represented by:

$$Q_2 = L \times M_W \quad (9)$$

The latent heat of vaporization for liquid and vapour,

$$L = h_g - h_f \quad (10)$$

The total heat requirement, [6]

$$Q = Q_1 + Q_2 \quad (11)$$

4) Sizing the Collector

To obtain the best deign, the efficiency of level plate collector is between 35% and 50%. The area of the collector can be expressed as follow [6]:

$$A_c = \frac{Q}{I_T \eta_c t_d} \quad (12)$$

5) Air Flow Requirement

The depth of air channel can be calculated by:

Depth of air channel, [6]

$$D_c = 0.05 \times L_c \quad (13)$$

6) Performance Evaluation of the Dryer,

Calculation of Moisture Content, [6]

$$MC = \frac{w\text{-}d}{w} \times 100\% \ (w.b) \quad (14)$$

7) Calculation of Overall Heat Energy Received from the Sun (Q g)

The overall heat energy received from the sun,

$$Q_g = I_T (\tau\alpha) A_c \quad (15)$$

The total energy transmitted and absorbed is given by:[5]

$$I_T A_C (\alpha\tau) = Q_U + Q_L \quad (16)$$

Calculation of Collector Bottom Heat Loss Coefficient (U_b) [5]

The thermal energy loss across the base of the collector is represented by

$$U_b = \frac{k}{L_b} \quad (17)$$

For convection thermal transfer coefficient between absorber levels and first glass,[5]

$$h_{c(p\text{-}c1)} = \frac{N_U \times k}{L_C} \quad (18)$$

For convection thermal transfer coefficient between first glass and second glass,[5]

$$h_{c(c1\text{-}c2)} = \frac{N_U \times k}{L_C} \quad (19)$$

Calculation of Radiation Heat Transfer Coefficient

The heat radiation transfer from the second glass to the air in the environment is represented by,[5]

$$h_{r,c2\text{-}a} = \frac{\sigma \varepsilon_{C2} (T_S + T_{C2})(T_S^2 + T_{C2}^2)(T_S + T_{C2})}{(T_{C2} - T_S)} \quad (20)$$

The sky temperature [5] is

$$T_s = 0.0552 \ (T_a)^{1.5} \quad (21)$$

The heat transfer coefficient for radiation between the first glass and absorber level is following. [5]

$$h_{r,\,p\text{-}c1} = \frac{\sigma (T_P + T_{C1})(T_P^2 + T_{C2}^2)}{\frac{1}{\varepsilon_P} + \frac{1}{\varepsilon_{C1}} - 1} \quad (22)$$

The heat transfer coefficient for between first glass and second glass is following. [5]

$$h_{r,\,c1\text{-}c2} = \frac{s (T_{C1} + T_{C2})(T_{C1}^2 + T_{C2}^2)}{\frac{1}{\varepsilon_{C1}} + \frac{1}{\varepsilon_{C2}} - 1} \quad (23)$$

The resistance R_1 to surrounding can be expressed as,[5]

$$R_1 = \frac{1}{h_W + h_{r,C1\text{-}C2}} \quad (24)$$

The resistance to heat flow between the upper glass and lower glass,[5]

$$R_2 = \frac{1}{h_{c,c1\text{-}c2} + h_{r,c1\text{-}c2}} \quad (25)$$

The resistance R_3 between absorber plate and lower glass cover,[5]

$$R_3 = \frac{1}{h_{c,p\text{-}c1} + h_{r,p\text{-}c1}} \quad (26)$$

The Collector Upper Part Heat Loss Coefficient (U_t) can be calculated by:[5]

$$U_t = \frac{1}{R_1 + R_2 + R_3} \quad (27)$$

The wind convection and radiation from the absorber plate transfer heat to the ambient air. [5]

$$h_w = 5.7 + 3.8V \quad (28)$$

Collector border Heat Loss Coefficient (U_e),

The border heat loss coefficient, based on the collector area A_c, can be calculated [5] by

$$U_e = \frac{(UA)_{edge}}{A_c} \quad (29)$$

Collector Total Heat Loss Coefficient (U_L) [5]

$$U_L = U_t + U_b + U_e \quad (30)$$

The heat removal factor for collector is given as: [5]

$$F_r = \frac{\dot{m_a} c_{pa} (T_c - T_a)}{A_C \left[(\alpha\tau) I_T - U_L (T_c - T_a)\right]} \quad (31)$$

The utilizing energy gained of the collector is, [7]

$$Q_U = A_C \left[(\alpha\tau) I_T - U_L (T_c - T_a)\right] \quad (32)$$

8) Flat Pate Collector Efficiency (η_c)

The level plate collector's efficiency can be calculated [5] by:

$$\eta_c = Q_u / A_c * I_T \quad (33)$$

IV. Result Data Of Flat Plate Mixed Mode Solar Dryer

I. Result Data of Flat Plate Solar Dryer.

No	Design Parameter	Symbol	Value	Unit
1	Collector length	l	1.2192	m
2	Collector width	b	0.9044	m
3	Collector thickness	t	0.00056	m
4	Collector air channel depth	D_c	0.06	m
5	Collector area	A_c	1.1148	m^2
6	Collector top heat loss coefficient	U_t	2.7970	W/m^2
7	Collector base heat loss coefficient	U_b	0.8	W/m^2
8	Collector total heat loss coefficient	U_L	3.617	W/m^2
9	Collector border heat loss coefficient	Ue	0.02	W/m^2
10	Useful energy gain	Q_u	474.5	W
11	Collector efficiency	η_c	57	%

The results data of level plate sunlight dryer are expressed in Table I.

1) The result Data of solar insolation for Annually

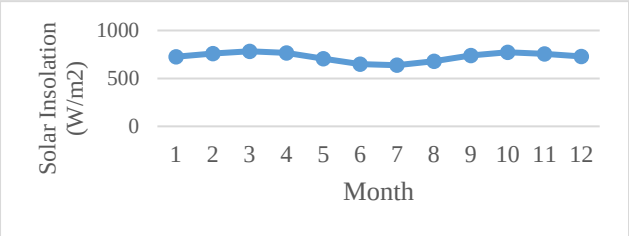

Fig.3. Solar Insolation for Annually

The result of solar insolation for Annually is also shown in Fig. 3. This result is for the collector tilt angle 37° from the horizontal. The maximum solar insolation occurred in March and April, and the minimum solar insolation occurred in June and July.

IV. Performance Test Of Solar Dryer

Fig.4.Drying Test of Chili

Fig.5.Drying Test of Eggplant Slices

Drying tests for chili, eggplant and potato is shown Fig.4, Fig.5 and Fig.6.They are measured moisture loss, collector air outlet temperature, ambient air temperature, upper tray and lower tray temperature one- time every one-hour interval. In Fig.4, maximum collector air outlet temperature is 50 °C and minimum is 37 °C. In Fig.5, the maximum collector air outlet temperature is 45 °C and minimum collector air outlet temperature is 34 °C.

Fig.6.Drying Test of Potato Slices

In Fig.6, the ambient air temperature at inlet is 20 °C at 9:00 am. It increases 34 °C at 12 noon and decreases to 28.4 °C. Moreover, the collector air outlet temperature is 31°C at 9:00 AM and increases 40.8°C at 11 am. And then, collector's air outlet temperature fluctuates each time and finally it reaches 30 °C at 3 pm.

1) Moisture Content in loaded test for potato in 7nd January

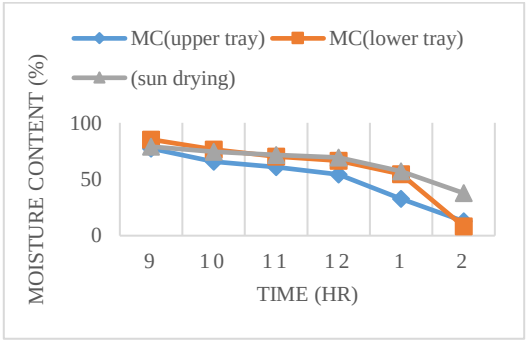

Fig.7. Various Wetness Content with Time for Potato

In Fig. 7, the moisture content of potato in the upper tray reach from 77% to 33%. The weight of potato slices in upper tray loss approximately 0.06 kg every one-hour. The moisture content of the potato slices in the lower tray decreases from 85% to 8%. The weight of potato slices in lower tray loss nearly 0.07 kg every one-hour. The traditional moisture content is slightly decreased from 78% to 34 %. In the sun drying, total weight of potato slices decreases 0.065 kg on one hour.

2) Moisture Content from Experiment for Eggplant in 26th, January

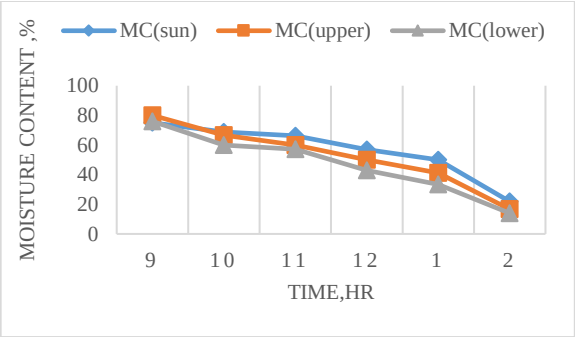

Fig.8. Various Wetness Content with Time for Eggplant

In Fig.8, the moisture content of eggplants in the upper tray is 80% to 17%. The moisture content of the eggplant in the lower tray is 76 % to 14%. The traditional moisture content is 75 % to 22%. The weight of eggplants in upper tray loss approximately 0.04 kg every one-hour. The weight of eggplants in lower tray loss nearly 0.05 kg every one-hour. In the sun drying, total weight of eggplants decreases 0.03 kg on one hour.

3) Moisture Content in loaded test for Chili in 29th January

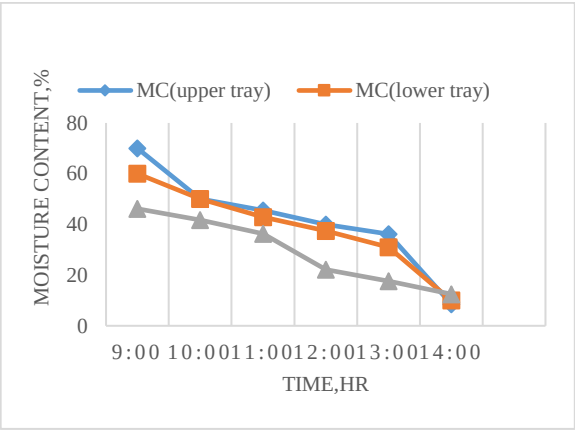

Fig.9.Various Wetness Content with Time for Chili

In Fig.8, the weight of eggplants in upper tray loss approximately 0.05 kg every one-hour. The weight of eggplants in lower tray loss nearly 0.065 kg every one-hour. In the sun drying, total weight of eggplants decreases 0.075 kg on one hour. The moisture content of eggplants in the upper tray is from 70% to 9%. The moisture content of the potato in the lower tray is from 60% to 10%. The traditional moisture content is from 46 % to 13%. The least moisture content of chili is in the upper tray.

VI.CONCULSIONS

In this study, the maximum air outlet temperature of the collector is collected at 50˚C.Average upper tray temperature of the collector and average collector lower tray temperature are at 48˚C and 47 ˚C. Dryer average tray temperature measured at 45 ˚C. In the same time the average ambient temperature is 34 ˚C during sunlight hour. The average efficiency of collector obtained without loading test is 57%. This value is in the range recommended by various literature for flat plate collector well. It also depends on air flow rate, temperature difference and radiation intensity.

The least moisture content of potato is in the lower tray in 7nd January and that of eggplant is in the lower tray in 26th, January. The least moisture content of chili is in the upper tray in 29th January. Solar dyer can be utilized for drying various types of fruits, vegetables, meat and fish, medicinal leaves and roots and Thanatkha solid etc. Moreover, by using mixed mode solar dryer, it can prevent from getting bad of food grains which cause huge loss to farmers.

ACKNOWLEDGMENTS

The writer wishes to describe her deep gratitude to Dr. Su Yin Win, Rector of Technological University Mandalay (TUM) for her kind authorization to submit this journal. The writer would like to thank to Dr. Aye Mya Thandar, Professor and Head of Mechanical Department, Technological University Mandalay, for her valuable supervision to complete this journal. And also special thanks to Dr. Swe Swe Maw, Professor, Daw Thinzar Win, Associate Professor, and to all her teachers from Mechanical Engineering Department at Technological University Mandalay, for their valuable supervision, guidance and encouragement throughout this research. Eventually, the writer would like to describe her deepest gratitude to her mother.

REFERENCES

[1] Green, M. G. and Schwarz, D., "*Solar Drying Technology for Food Preservation"*, Gate Information Service/GTZ, Eschborn, Germany, (2001).
[2] Ertekin. C. and Yaldiz. O., *"Drying of Eggplant and Selection of a Suitable Thin Layer Drying Model"*, (2004).
[3] D. Scanlin, "*Design, Construction and use of an Indirect, Through –pass, Solar Food Dryer"*, Homebrew, (1997).
[4] Mercer, D. G, "*An Introduction to the Dehydration and Drying of Fruits and Vegetables"*, Canada, (2014).
[5] William A. Beckman, "*Solar Engineering of Thermal Processes",* Fourth Edition.
[6] Zin Mar Oo, "*Design and Construction of Solar Dryer for Potato"*, (2018).
[7] Akoy, E. O. M., Ismail, M. A. and Ahmed, E. A. and L. W., "*Design and Construction of A Solar Dryer for Mango Slices",* Sudan, (2014).
[8] NASA's Prediction of Worldwide Energy Resources (power)API, https://profilesolar.com/countries/MM

Investigation of Radiator Performance in Electric Vehicle Thermal Management System Using MATLAB/ Simulink-Simscape Simulation

Zin Lay Nwe[1], Phone Myint Thein[2], Dr. Aye Mya Thandar[3]

[1]*Technological University, Mandalay, Myanmar*

[2]*Automotive Technology Research Institute, Pyin Oo Lwin, Myanmar*

[3]*Technological University, Mandalay, Myanmar*

Email: [1]zinlay.n@gmail.com, [2]phonemyintthein@gmail.com, [3]ayemyathandar2023@gmail.com,

***Abstract*—This study investigates the performance of the radiator within an Electric Vehicle Thermal Management System (EVTMS) using MATLAB/Simulink-Simscape simulations. Despite significant advancements in electric vehicle technology, several issues and areas for improvement persist in EVTMS. Modelling and simulations play a crucial role in assessing new designs, identifying issues in current designs, and analysing a system's performance under challenging conditions that may not be easily replicated in reality. Our research focuses on creating dynamic and scalable models to gain a deep understanding of intricate systems and facilitate swift changes in the architecture and control design of EVTMS. Through a detailed simulation comparison using the Nissan Leaf EV as a case study, we demonstrate the effectiveness of the specified radiator. The results indicate that, even at higher speeds, the radiator can maintain components within their ideal operating temperatures, ensuring optimal performance and reliability of the EVTMS. This investigation highlights the importance of simulation tools in optimizing thermal management systems for electric vehicles.**

Keywords— thermal management system, electric vehicle, MATLAB, Simulink, Simscape, radiator

I. INTRODUCTION

Since around 1884 which is roughly 140 years from 2024 cars have been utilizing internal combustion engines ICE for power. The escalating consciousness among the public about the scarcity of earth's natural resources and the impacts of climate change has spurred advancements in efficiency and the creation of innovative propulsion systems [1]. Battery electric vehicles (BEVs) have the potential to drastically lower greenhouse gas emissions worldwide and reduce reliance on fossil fuel imports. For the past six years, there has been a sharp increase in consumer demand for BEVs [2]. International Energy Agency (IEA) reported that in 2023 the global registration of new battery electric and plug-in hybrid cars reached nearly 14 million increasing the total count of such vehicles on the roads to 40 million [3].

Despite significant advancements in electric vehicle technology, there are still several issues and areas for improvement in Thermal Management System for Electric Vehicle (EVTMS), such as thermal uniformity, energy efficiency, cold weather performance, thermal runaway prevention, component integration, environmental impact, cost and affordability [4][5]. Searching and identifying of these challenges are critical for improving the overall efficiency, safety, and performance of EVs. The complex thermal dynamics involved in the high voltage battery system, combined with varying driving and environmental conditions, make it a difficult task to achieve efficient and effective thermal management. Electric Vehicle's high voltage (HV) batteries are prone to rapid deterioration if they operate outside the specified temperature range. This could lead to increased expenses and reduced dependability. General Motors has estimated that without a thermal management system, an electric vehicle could lose up to 85% of its range in an environment at 0°C [6]. Moreover, the incidence of fires involving EV HV batteries has been increasing, and these fires are notably more challenging to extinguish. Traditional trial-and-error approaches to design and optimization of EVTMS are time-consuming, expensive, and often lead to suboptimal results.

II. MODELLING AND SIMULATION IN MATLAB®

Modelling is a technique utilized in engineering and science to generate a digital replica of a physical system. Simulations play a crucial role in assessing new designs, identifying issues in current designs, and analysing of a system's performance in potentially challenging conditions that may not be easily replicated in reality. If any components of the system operate based on mathematical relationships, they can be modelled and simulated across various scenarios to observe their performance. System simulation is the process of examining the behaviour of systems by using mathematical models that replicate the physical characteristics of real-world systems [7]. Through the use of modelling and simulation, the design quality of a system can be enhanced during the initial phases, ultimately diminishing the occurrence of errors in later stages of design. Consequently, this results in a drastic reduction in both the time and financial resources allocated to the development process.

MATLAB®, Simulink® and Simscape™ are well-known tools for designing various systems. These platforms serve as tools for scientists and engineers who employ model-based design. This method supports design and simulation at the system level across various domains, automatic code creation, and continuous testing and verification of dynamic systems. The concept of multidomain physical modelling was introduced in MATLAB® R2008a, and a modelling tool known as Simscape® was launched. This tool facilitates the physical modelling of mechanical, electrical, electronic, and control systems in a modular way. System simulation technology has been successfully implemented in all scientific and engineering disciplines [7].

III. THERMAL MANAGEMENT MODEL FOR ELECTRIC VEHICLE

A Thermal Management System for Electric Vehicle (EVTMS) consists of various heat source, heat sink and fluid delivery components. EVTMS model needs to include physical models associated with fluid mechanics and thermodynamics to simulate radiator, coolant pumps, fans, HVAC components and heat sources. In this study, component models are integrated into a cooling system architecture designed for a Nissan Leaf EV (1st Generation model) using MATLAB® (R2023b version) to investigate the performance and the power consumption of the cooling system. All component models were developed and validated by MATLAB® Simulink®.

Fig. 1. Nissan Leaf EV (1st Generation model)

This EV TMS includes a network of coolant circulation a refrigeration cycle and a heating circuit for passenger compartment. The thermal load components are the powertrain (traction motor), power electronics (inverter, DC-DC converter, on-board charger) and cabin. In this setup, the motor and inverter are cooled through a water-based cooling system that is circulated via an electric pump. The heat is eliminated in the primary radiator without any form of recycling. Heating for the cabin is achieved through a distinct loop system utilizing a 5 kW PTC heater (Positive Temperature Coefficient) with its own pump. The final loop manages the air conditioning, following the traditional design found in vehicles with internal combustion engines (Fig. 2).

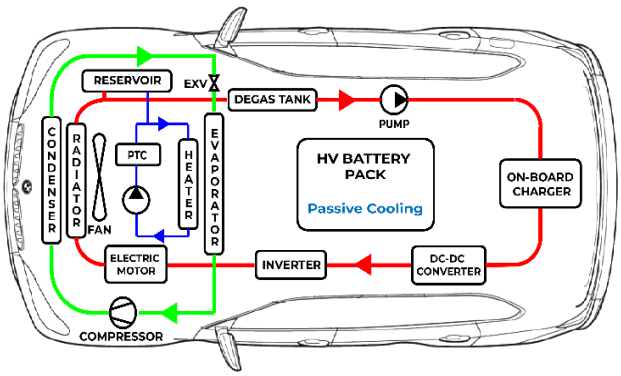

Fig. 2. Nissan Leaf's EV thermal management system

As the first mass-produced battery-electric car, the Nissan Leaf included one design compromise that it did not include the active thermal management for the 24-kWh battery pack under the floor. That is why HV battery pack model is not added in this EVTMS model.

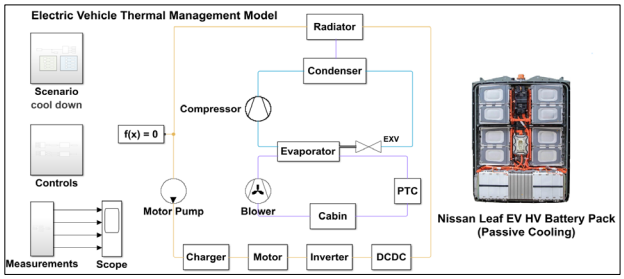

Fig. 3. Simulink model of EV thermal management system

IV. MODELLING OF THE RADIATOR

In this study, Heat Exchanger (thermal liquid – moist air) Simscape™ block is used to represent the radiator, utilizing the radiator's physical dimensions, the thermodynamic characteristics of the two fluids, and the heat transfer properties of the materials used in the radiator.

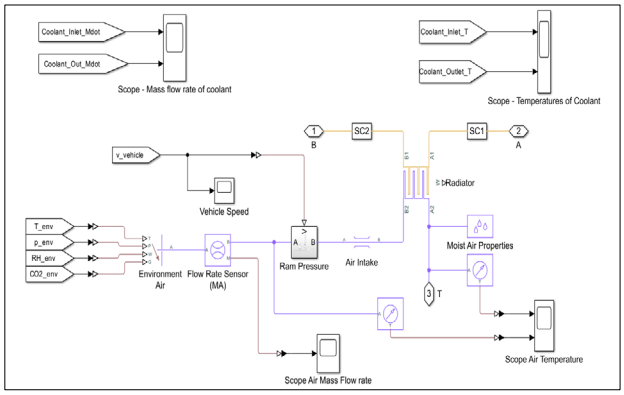

Fig. 4. Simulink model of radiator

As the interest of this simulation is inlet and outlet temperatures of radiator's fluids (coolant and air), temperature sensor and mass flow rate sensor blocks are added to the radiator model and connected at relevant signal lines. And to view the simulation results, corresponding scope blocks are added.

A. Measurements and Properties Given for the Radiator Model Block

Measurements taken on Nissan Leaf radiator, such as length, width, height of the radiator, number of radiator fluid tubes, height of each individual fluid tube, distance between adjacent fins, wall thickness of the radiator fluid tubes, thermal conductivity of tube material are shown in Table I.

I. RADIATOR DIMENSION

No.	Items		Dimensions
1.	Length of radiator	L_{rad}	0.63 m
2.	Height of radiator	H_{rad}	0.34 m
3.	Width of radiator0.15	W_{rad}	0.016 m
4.	Height of coolant tube	H_{tube}	0.002 m
5.	Width of coolant tube	W_{tube}	0.016 m
6.	Length of coolant tube	L_{tube}	0.63 m
7.	Number of tubes	N_{tube}	35
8.	Fin spacing		0.002 m
9.	Fin thickness	T_{fin}	0.00025 m
10.	Fin height	H_{fin}	0.00794 m
11.	Fin width	W_{fin}	0.016 m
12.	Number of fins per tube	N_{fin}	315
13.	Thermal conductivity of Al	k_{Al}	238.5644 W/m K

In Heat Exchanger Block configuration, "Flow arrangement" parameter is assigned to "Cross flow" and "Thermal mixing" parameter have to change to "Both fluids unmixed" because EV radiator understudied (Nissan Leaf 2010 Model) is single row compact type heat exchanger. Some of the radiator dimensions have to add at "Parameters" MATLAB Code data file. Complete radiator block parameters are shown in Fig. 5.

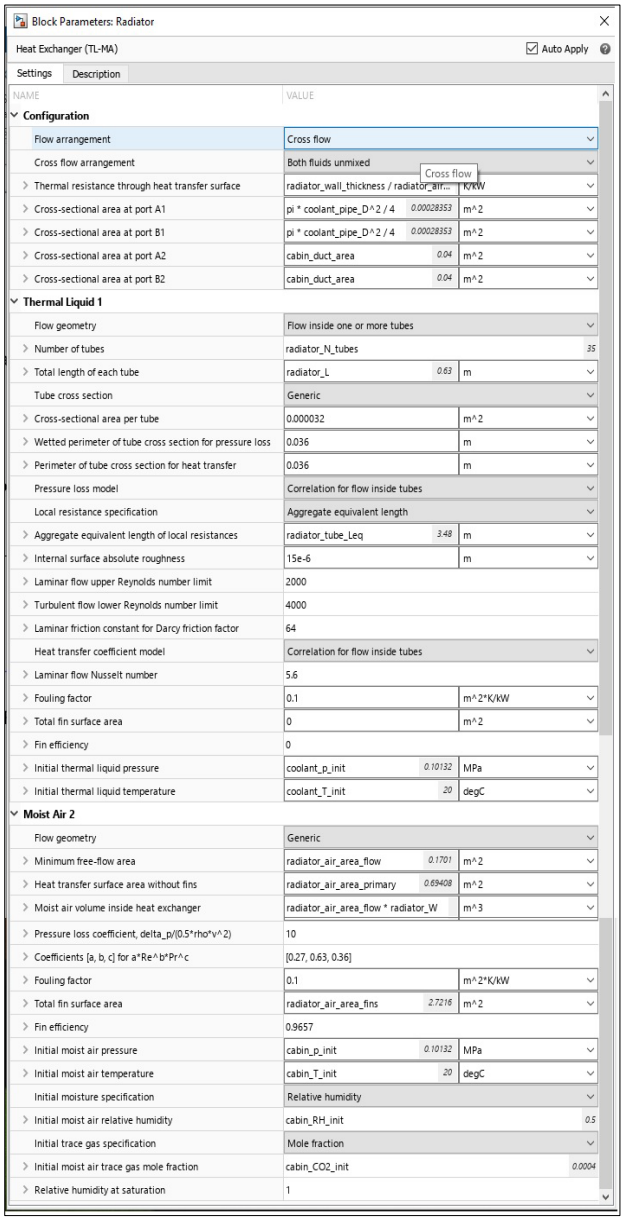

Fig. 5. Radiator model's block parameters

B. Equations Used in Radiator Calculation

The heat transfer rate is computed over the averaged properties of moist air and coolant by using effectiveness-number of transfer units (NTU) heat transfer method.

The heat transfer is calculated as [8]:

$$Q = \varepsilon\, C_{min}\,(T_{in,CL} - T_{in,MA}) \tag{1}$$

C_{min} = the lower heat capacity rate between the two fluids.

The rate of heat capacity is determined by multiplying the specific heat of the fluid, denoted as C_p, with the mass flow rate of the fluid. The value of C_{min} is positive in every case.

$T_{in,CL}$ = the coolant's inlet temperature, K
$T_{in,MA}$ = the moist air's inlet temperature, K
ε = the effectiveness of heat exchanger.
The NTU is calculated as [8]:

$$\text{NTU} = \frac{1}{C_{min}\,R}, \tag{2}$$

R = the total thermal resistance from convection, conduction, and any fouling on the surface of tubes and fins [8]:

$$\text{R} = \frac{1}{U_{CL}A_{Th,CL}} + \frac{F_{CL}}{A_{Th,CL}} + R_W + \frac{F_{MA}}{A_{Th,MA}} + \frac{1}{U_{MA}A_{Th,MA}} \tag{3}$$

U = the convective heat transfer coefficient of the air or coolant
F = the fouling factor on the respective fluid side
R_W = the thermal resistance of tube wall through heat transfer surface
A_{Th} = the heat transfer surface area of the air or coolant side of the exchanger (m^2) [8]:

$$A_{Th} = A_W + \eta_F A_F \tag{4}$$

A_W = the surface area of tube wall (m^2)
A_F = the total surface area of fin (m^2)
η_F = the fin efficiency

The effectiveness of heat exchanger is dependent on the flow setup and the degree of mixing in each fluid. This is particularly true when the flow is arranged in a "Cross flow" pattern and both fluids are set to remain "unmixed" [8]:

$$\varepsilon = 1 - e^{\{(\frac{NTU^{0.22}}{C_r}\times(e^{(-C_r\times NTU^{0.78})}-1)\}} \tag{5}$$

C_r represent the ratio between the heat capacity rates of the air and coolant [8]:

$$\text{C}_\text{r} = \frac{C_{min}}{C_{max}} \tag{6}$$

C. Vehicle Simulation Results

The drive cycle scenario simulates driving conditions in 30.253°C weather with air conditioning on. The vehicle speed is based on the New European Driving Cycle (NEDC) (urban part) followed by 16 min of 130 km/h high speed to push the heat load as seen in Fig. 6. In this TMS model there is only one coolant loop for power electronic components and traction motor. Even at highway driving with higher speeds and fewer stops, those component's temperatures (max 38.7°C) didn't higher than their optimum working temperatures (as for motor < 60°C) as can be seen in Fig. 7.

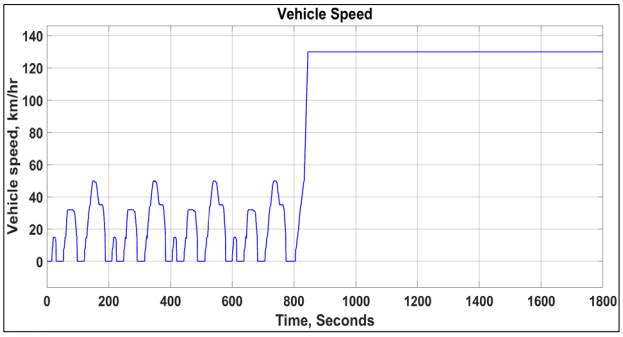

Fig. 6. Scope view which shows the simulation results of drive cycle

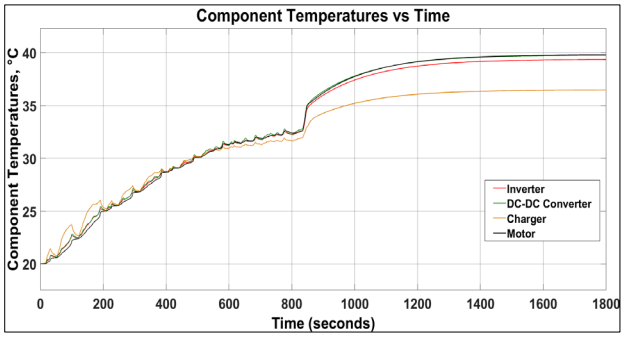

Fig. 7. Scope view which shows the simulation results of component temperatures

In Fig. 8 and Fig. 9, the dynamic changes of inlet and outlet temperatures of radiator coolant and air due to the driving cycle had been shown. From these temperature signals scope, radiator performance can be analysed. This analysis calculates how well an existing heat exchanger performs. It considers pre-set flow rates and inlet temperatures of the fluids, and predicts the amount of heat transferred and the resulting temperatures at the exchanger's outlet. This type of calculation is often used for pre-made heat exchangers with standard sizes offered by manufacturers [9].

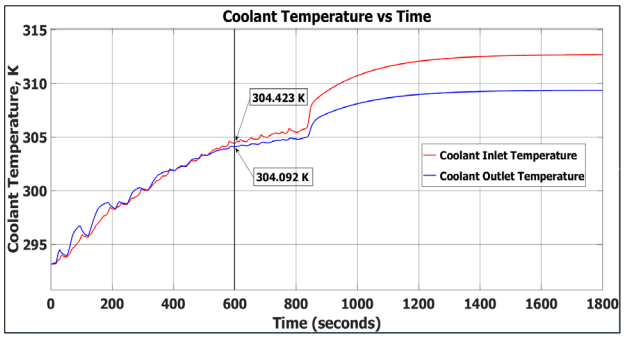

Fig. 8. Scope view which shows the simulation results of radiator inlet and outlet temperatures of coolant

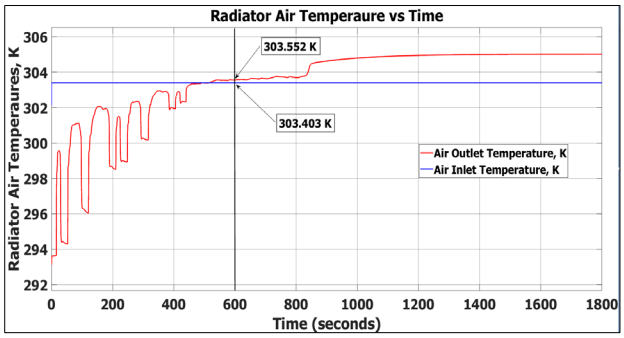

Fig. 9. Scope view which shows the simulation results of radiator inlet and outlet temperatures of air

D. Measurements of Radiator Performance

To compare and analysis the result of simulation results, data measurements were carried out several time by driving Nissan Leaf EV (2010). Real-world data measurements were performed using following instruments to obtain the temperatures of coolant and air passing through radiator.

The Pico thermocouple data logger (TC-08) is a temperature and voltage data logger designed to measure and records up to 8 thermocouples at once with up to high accuracy 10 measurements per second. The TC-08 is capable of sustaining a resolution superior to 0.025°C for commonly used Type K thermocouples, across a wide range from -250°C to 1370°C [10]. In this study, Pico TC-08 data logger (shown in Fig. 10) is used to measure the inlet and outlet temperatures of radiator, inlet and outlet temperatures of air, ambient temperature during test driving.

Fig. 10. Pico data logger with PicoLog® software

The G-Scan 2 is the multifunction scan tool which cover both Petrol and Diesel vehicles. G-Scan functions include system search mode [searches all available electronic control units (ECU)], diagnostic trouble codes (DTC) analysis, data analysis, flight recording, flight record review, actuation tests and special functions. In this study, G-Scan 2 (shown in Fig. 11) is used to measure and record the vehicle speed, coolant outlet temperature, ambient temperature, coolant fan request duty and coolant pump speed duty by using real-time data analysis and flight recording functions.

Fig. 11. G-Scan 2 scanner

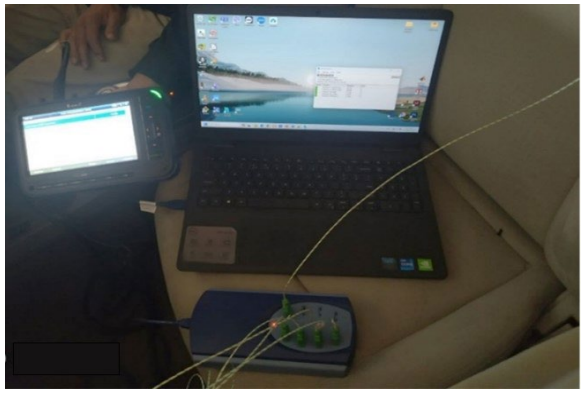

Fig. 12. Data measurement setup

In Fig. 13, inlet and outlet temperatures of radiator coolant and air against date time data were captured and displayed by PicoLog® software in Graph format. While a radiator's job is to cool the coolant, it might not function as expected at first. This can happen when the car is just starting, and the surrounding air is actually warmer than the coolant. In such cases, the radiator won't immediately bring down the coolant temperature. This is evident in the simulation results of Fig. 8, and real-world measurements confirm this behaviour, as shown in Fig. 13.

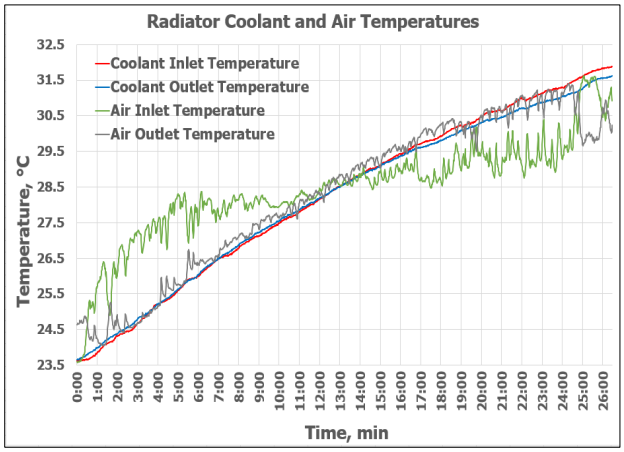

Fig. 13. Inlet and outlet temperatures of radiator coolant and air against date time shown in PicoLog® software

V. Result and Discussion

The goal of this study is to use the analytical heat transfer process to determine outlet coolant and air temperatures and to compare this data with experimental results. The heat transfer performance of the electric vehicle radiator is analysed by theoretical calculation, simulation and test drive values in a real-life situation. And those results are checked and validated by comparing with text drive data as shown in Table II.

As observed in Table II, the values obtained from the test drive for the outlet temperature of both air and coolant deviate from the theoretically calculated predictions for a variety of potential reasons. This could be due to several assumptions made during the analytical computations, such as - the temperature of the coolant and air is consistent throughout, there are no phase changes in the fluids, the specific heats of the coolant and air remain constant across the radiator, even flow distribution on both sides of the radiator, and there is no fouling within the radiator, among others.

II. Result Comparison

Results	Coolant, K			Air, K		
	Inlet	Outlet	ΔT	Inlet	Outlet	ΔT
Calculation	304.42	304.20	0.22	303.4	303.74	0.34
Test drive	304.42	304.14	0.28	303.4	303.82	0.41
Simulation	304.42	304.09	0.33	303.4	303.55	0.15

Therefore, the values derived from analytical methods may vary from those obtained through simulations and experiments. In real-world scenarios, the properties of air and coolant can vary across different points in the radiator core, affecting the rate of heat transfer. Nonetheless, analytical values offer a safer approach to radiator design as the actual conditions during vehicle operation are unpredictable. Regarding the test drive data, the precision of Type K thermocouples used in the Pico TC-08 data logger is the sum of ±0.2% of the reading and ±0.5°C. Hence, there might be minor differences in the results of measurements and calculations.

The current BEV TMS model is designed in a straightforward and modular manner, allowing it to operate faster than in real-time. The Simulink model only needs 26.535s of simulation time when run on an HP Z440 workstation (Intel Xeon E5 3.5 GHz, RAM 32 GB). It is apt as a reference model for drive cycle simulation to estimate the thermal efficiency of the vehicle and other vehicle-level data. The use of modelling and simulation techniques can assist in addressing highly complex problems that have traditionally been challenging for individuals with limited expertise to tackle.

VI. Conclusion

Electric vehicle mainly prioritizes the energy efficiency due to current limitations in battery technology, which affects driving range. So, most EVs used light weight, compact-type radiators, which compromise in the decrease thermal effectiveness of the radiator. The results of this study indicate that the outlet temperatures of both coolant and air deviate slightly between the theoretical calculations, simulations, and test drive data. These deviations can be attributed to assumptions made during analytical computations and precision of measurement instrument. This analysis concludes that the specified radiator, with its given dimensions and number of fins, can function effectively under optimal operating temperatures, even at higher speeds.

The current study focuses solely on a basic EVTMS due to the unavailability of inventory and manufacturer data. In the future, more advanced systems should be considered for simulation, including additional battery cooling circuits that regulate battery temperature using various components such as chillers, coolers, heat pumps, or a combination of those. This could lead to the development of a more detailed and sophisticated control strategy, based on factors like the power consumption of the cooling components and the rate of heat generation by the battery, to devise energy-efficient cooling system operations.

Acknowledgment

The authors would like to thank the Automotive Technology Research Institute, Pyin Oo Lwin for providing workshop facilities, technical support and guidance for this paper.

References

[1] J. C. Menken, K. Strasser, T. Anzenberger, and C. Rebinger, "Evaluation of the energy consumption of a thermal management system of a plug-in hybrid electric vehicle using the example of the Audi Q7 e-tron." *Journal of SAE International*. 11(3):203-211, 2018, doi:10.4271/06-11-03-0017.

[2] S. G. Garrow, C. T. Aksland, S. Sharma. and A. G. Alleyne, "Integrated modeling for battery electric vehicle transcritical thermal management system." *Presented at the 2018 Annual American Control Conference (ACC)*, Wisconsin Center, Milwaukee, USA, 2018.

[3] E. Connelly et al., "Global EV Outlook 2024." IEA, Paris https://www.iea.org/reports/global-ev-outlook-2024.

[4] D. Dan, Y. Zhao, M. Wei and X. Wang, "Review of thermal management technology for electric vehicles", *Journal of Energies*, Vols 16(12), pp. 4693, June 2023.

[5] W. Ferraris, M. Rostagno and F. Bettoja, "Thermal management architectures virtual evaluation for HEV/PHEV", SAE Technical Paper 2018-37-0025, 2018.

[6] Z. Wang, C. Lu, and P. Liu, "Reviews of studying on thermal management system in EV/HEV battery pack." *Advanced Materials Research*, Vols. 291-294, pp. 1674-1678, 2011.

[7] D. Xue, "*Modeling and simulation with Simulink®*", Tsinghua University Press and De Gruyter, 2022, pp. 1-8.

[8] D. P. Sekulic, R. K. Shah, "*Fundamentals of heat exchanger design*", Wiley, 2023, pp. 123-135.

[9] B. L. Theodore, L. S. Adrienne, "*Fundamentals of heat and mass transfer*", Hoboken, NJ: Wiley, 2017, pp. 670-678.

[10] Picotech.com, "TC-08 data sheet", Internet: September 13, 2021. [May 19, 2024].

Design and Fabrication of Gorlov Helical Turbine

Zin Mar Nwe[1], Dr.Pa Pa Minn[2], Dr.Swe Swe Maw[3]

[1] *Department of Mechanical Engineering, Technological University (Mandalay)*

[2] *Department of Mechanical Engineering, Technological University (Mandalay)*

[3] *Department of Mechanical Engineering, Technological University (Mandalay)*

Email: [1]87zinmarnwe@gmail.com, [2]dr.papaminn@gmail.com, [3]sweswemaw22@gmail.com

***Abstract*— The purpose of Gorlov helical turbine (GHT) is to provide the electricity for rural areas where is no power grid. The GHT can be used in areas of sea, rivers and water channel. This paper is mainly divided by three main portions which are design calculation, fabrication and performance test of 50 Watts GHT. In the first portion, 50 Watts GHT was designed based on water velocity 1.5 m/s. The calculated results are expressed by changing the aspect ratio. The diameter and height of turbine is 0.2504 m and 0.3756 m and the helical blade angle is 55.08°. The chord length of hydrofoil is 0.07 m and steel shaft diameter is 0.0093 m. The torque of turbine is 1.855 N-m and turbine power is 55.55 Watts. The water power is 158.79 Watts and electrical power is 50 Watts. Three blades which profile is NACA 0018, used in this turbine. In the second portion, the model of 50 Watts GHT with suitable fiber plastic (plus) is constructed by using 3D printing. And then, frame and generator are fabricated in workshop. Finally, the performance testing results are described in this paper.**

Keywords*—Gorlov helical turbine, Water velocity, Aspect ratio, Fabrication, Electrical power

I. Introduction

The annual consumption of electrical energy has been increasing in Myanmar. All the sources of the country are produced the electrical power. Traditional used natural energy resources are spending in long term. Consequently, it impacts on environment negatively. Raw material called fossil fuels such as coal, oil, natural gas causes climate changes and natural disaster because it makes greenhouse gas emissions and ecosystem destruction. To be environmentally friendly, renewable energy sources, especially hydrokinetic energy sources is of almost important and used full. Hydrokinetic energy oldest and the most renewable energy resource. In addition, in current situation, it becomes more and more popular energy sources [1].

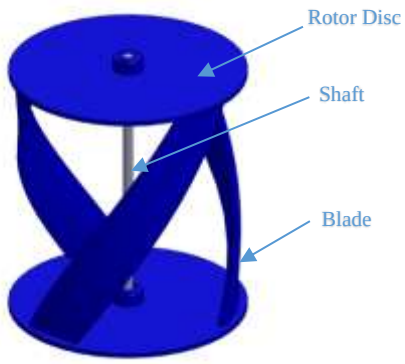

Fig. 1. Gorlov helical turbine

This paper is about the Gorlov helical turbine is easy to be used without building reservoir and dam. The kinetic energy is come from flow of water impacted on turbine blades. Due to kinetic energy, shaft rotates and transmit mechanical energy. After mechanical energy to electrical energy converted from the generator. So, the Gorlov helical turbine blades is converted energy [5].

II. Main Components of Gorlov Helical Turbine

The main components of Gorlov helical turbine includes;

- Rotor Discs
- Turbine Blades Profile
- Transmission Shaft
- Generator

A. Rotor Discs

There are various rotor designs in hydrokinetic turbines. Rotor discs are most stressed in the circumference area. The Gorlov helical turbine blade root connect occurs, and the focus of the turbine discs is required to be large in the circumference depending on the blades.

B. Turbine Blades Profile

There are various blades profile designs in hydrokinetic turbines. Among them, airfoil blade design is used in this research and the most use of the hydrokinetic turbine designs are airfoil blade designs. The turbine blades are commonly fixed to the focus at a congruent angle of attack for the lift force to act upon and make the turbine blade rotate. The twist and taper on blade occur variation in the blade setting angle along the length of the blade when the water flows on it. This blade profile is called the blade's hydrodynamic profile. Two type of airfoil blade design are symmetric and unsymmetric. The symmetric design NACA0018 is used in this paper because its starting torque is strong in rotation [58Ira H].

C. Transmission Shaft

The hydrokinetic turbine consists of a transmission shaft that converts power generated by the turbine blades rotation. The rotor is directly connected to the generator with the shaft.

D. Generator

Generator is a device that transforms mechanical power to electrical power. The generator AC (alternating current) or DC (direct current) can be used and difficult types of generators are used in hydrokinetic turbines depending on their size and design. Three basic types of generators include dynamo (DC) generator, synchronous (AC) generators and asynchronous (AC) generators. Dynamo

(DC) generator is selected for this paper.

III. Design of Gorlov Helical Turbine

The design calculation is divided into three parts. Firstly, the design specifications of Gorlov helical turbine are described in Table I. Rotor design of the turbine is calculated by changing aspect ratio (shown in table II), then, detail design of blade parameter (as shown in table III) and shaft design for the Gorlov turbine are calculated.

I. Design Specifications of Gorlov Turbine

Description	Symbol	Data	Unit
Generator Power	P_e	50	W
Water Current Velocity	V_w	1.5	ms^{-1}
Water Density	ρ	1000	kg/m^3
Generator Efficiency	η_g	0.9	-
Blade Number	B	3	-
Tip Speed Ratio	λ	2.5	-
Coefficient of Turbine	C_p	0.35	-
Solidity Ratio	σ	0.3	-

A. Calculation of theoretical results for Gorlov helical turbine

The Gorlov helical turbine area can be calculated by using an average water flow velocity of 1.5 m/s.

$$P_e = \frac{1}{2}\rho A V_w^3 C_P \eta_g \quad (1)$$

The ratio of the turbine height to diameter is called aspect ratio (AR). In hydrokinetic turbines, aspect ratio is usually between "0.5 to 1.5". So, this paper changed the values of aspect ratio to predict the performance of Gorlov hydrokinetic turbine.

$$AR = \frac{H}{D} \quad (2)$$

In Gorlov helical turbine, the tip speed ratio (λ) is between 2 to 2.5 to reduce the cavitations [12Ada]. The turbine angular velocity is based on the tip speed ratio, the angular velocity of the turbine is given

$$\omega = \frac{\lambda V_w}{R} \quad (3)$$

Turbine rotational speed is calculated from the following equation.

$$N = \frac{60\omega}{2\pi} \quad (4)$$

The chord length, c is calculated from the below equation.

$$c = \frac{\sigma \pi D}{B} \quad (5)$$

The turbine torque, T is calculated from the below equation.

$$T = \frac{1}{2}\left(\frac{C_p \rho A V_w^3}{\omega}\right) \quad (6)$$

The turbine power, P_t is calculated from the below equation.

$$P_t = T\omega \quad (7)$$

The water power, P_w is calculated from the below equation.

$$P_w = \frac{1}{2}\rho A V_w^3 \quad (8)$$

Helical angle (α) for a Gorlov helical turbine refers to the pitch angle that the blade makes with a horizontal plane. The helical angle is calculated from the below equation.

$$\alpha = \tan^{-1}\left\lfloor \frac{BH}{\pi D} \right\rfloor \quad (9)$$

II. Result Data on Changing Aspect Ratio of Gorlov Turbine

No.	Parameter	Aspect Ratio		
		0.5	*1*	*1.5*
1.	Swept area, A (m^2)	0.0941	0.0941	0.0941
2.	Average water speed, v_w (m/s)	1.5	1.5	1.5
3.	Turbine diameter, D (m)	0.4338	0.3067	0.2504
4.	Turbine height, H (m)	0.2169	0.3067	0.3756
5.	Rotational speed of turbine, N (rpm)	165.09	233.50	286
6.	Number of blades	3	3	3
7.	Chord length, c (m)	0.1362	0.0963	0.07
8.	Maximum torque, T (N-m)	3.214	2.272	1.855

Table II show the theoretical result data of Gorlov helical turbine by changing the aspect ratio. According to theoretical results data, if the aspect ratio is increased, rotational speed of turbine is gradually increased and turbine torque is gradually decrease. The geometrical point of view, as aspect ratio increase, the number of revolution of the turbine increase, which improves the turbine performance. So, the number of aspect ratio 1.5 is chosen.

III. Theoretical Result Data of Power (Water, Turbine, Electrical) by Changing Water Velocity

Sr No	D (m)	H (m)	V_w (m/s)	P_w (W)	P_t (W)	P_e (W)
1	0.2504	0.3756	0.5	5.88	2.05	1.85
2			1	47.05	16.46	14.82
3			1.5	158.79	55.57	50.02
4			2	376.4	131.7	118.5
5			2.5	735.15	257.3	231.5

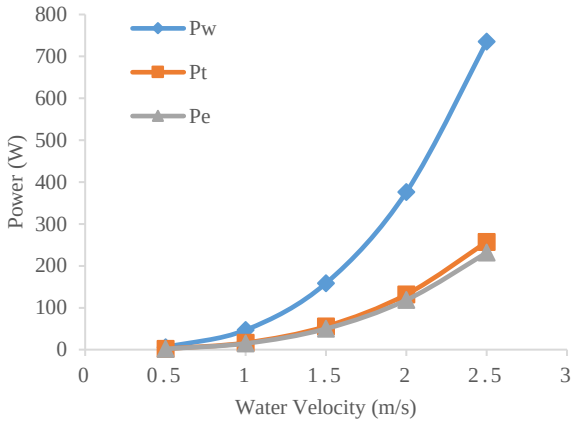

Fig. 2. Theoretical results of water power and turbine power at different velocity

Table III shows the theoretical results data of power (water, turbine, electrical) by changing the water velocities. If the water velocity is increased, turbine power, water power and electrical power are also increased. Fig. 2 shows water power is the greatest and generator power is smaller than turbine power. In Fig. 2 and Table III, water power is obtained by converting kinetic energy directly from water velocity. And then, the water power to turbine power conversion decreases turbine power because of turbine efficiency. And, the turbine power to electrical power conversion reduces the output of electrical power because of generator efficiency.

B. Calculation of Turbine Shaft Design

The transmission shaft converts power generated by using by the turbine blades rotation. And then, it is to transmit the turbine torque generated at the turbine blades to the generator. The torsional moment or twisting moment acting on the shaft can be determined from the equation,

$$T = \frac{P_w \times 60}{2\pi N} \tag{10}$$

The shaft design is calculated by using the equivalent twisting moment equation or ASME code equation.

For solid shaft,

$$T_{eq} = \sqrt{(k_b M_b)^2 + (k_t M_t)^2} \tag{11}$$

The diameter of shaft is calculated by using the below equation.

$$d_0^{\,3} = \frac{16}{\pi \sigma_s} \sqrt{(K_b M_b)^2 + (K_t M_t)^2} \tag{12}$$

(or)

$$d^3 = \frac{32 n_s}{\pi \sigma_s} \sqrt{M^2 + T^2} \tag{13}$$

IV. Construction Procedures Of Gorlov Helical Turbine

Gorlov helical turbine is constructed by the following procedures;

- Material Selection
- Manufacture of Turbine model by 3D printing
- Construction of frame
- Generator Selection
- Assembly
- Site Selection
- Performance Testing

A. Material Selection

In this paper, alloy steel solid shaft and turbine blade plastic (plus) are used because they are light weight, low cost and easy to manufacture.

B. Manufacture of Turbine Model by 3D Printing

In the first stage, Gorlov helical turbine is start model of rotor disc diameter is 0.2504 m, then, the profile of the blade was NACA 0018 and the chord length was 0.07 m production turbine half printing. The helix angle is 55.08° and index of revolution is 0.25. Finally, complete printing of turbine height is 0.3756 m and it is coated with durability emulsion paint and dyed into white color.

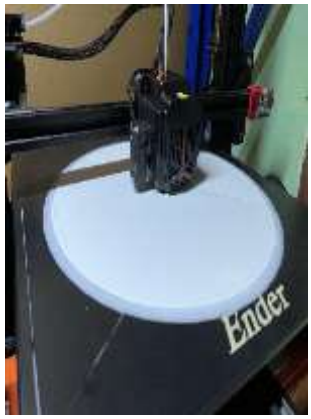

Fig. 3. Model of rotor disc

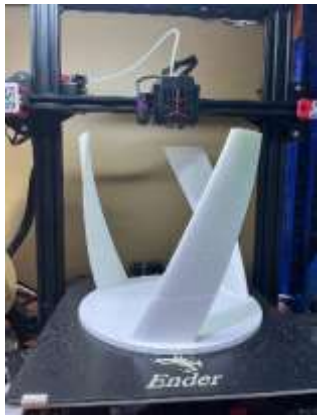

Fig. 4. Blade profile

Fig. 5. 3D-Printing complete for Gorlov helical turbine

C. Construction of Frame

After 3D printing turbine model and alloy steel shaft were assembled. Frame is constructed by using square mild steel from local material in the Mandalay mechanics workshop.

Fig. 6. Turbine and frame constructed

D. Generator Selection

In this paper, turbine rotational speed is 286 rpm (revolution per minute) for driving generator. A Sanyo dynamo or dynamo hub that is a small electrical generator is used.

E. Assembly

An assembly line is a fabrication process of Gorlov helical turbine in which all sub parts are added as shaft, and dynamo, A dynamometer is connected to the turbine by using bearing. These bearing was employed at the other end of the shaft too. Finally, the Gorlov helical turbine is assembled as shown in Fig.7.

Fig. 7. Assembly of Gorlov helical turbine

F. Site Selection

The performance site is the channel at Shintawkone Village, in Patheingyi township. for Gorlov helical turbine. The channel is 5 m long, 2.5 m wide, and the height of the gate is 0.9 m, which meets the requirements for the Gorlov helical turbine testing, as shown in Fig. 8. The water velocity of the channel is controlled by operating the gate of dam, and its flow is between 0.5–2 m/s. The flow rate is obtained by increasing the level of water stored at the congruent height. The different flow rates of the water velocity are measured accurately three times per test, and then, the average velocity was calculated.

Fig. 8. Measuring of water velocity

G. Performance Testing

This section includes performance testing of Gorlov helical turbine. The rpm (revolution per minute) was measured by using contact tachometer. The contact tachometer is physically attached to the shaft, and providing an RPM reading. Fig.9. shows the contact tachometer. In the performance test, tachometer can be measured the speed for free loading (357 rpm) and 50 Watts loading (280 rpm) in water velocity 1.5 m/s.

Fig. 9. Contact tachometer

Fig. 10. Performance testing of Gorlov helical turbine

IV. DATA FROM PERFORMANCE TESTING

Velocity Water (m/s)	**0.5**	**0.7**	**1**	**1.2**	**1.5**	**2**
Turbine Speed (For Free Load)	100	206	230	276	357	490
Turbine Speed (For Loading)	80	120	180	212	280	379
	Loading 5 W	Loading 5 W	Loading 10 W	Loading 25 W	Loading 50 W	Loading 117W

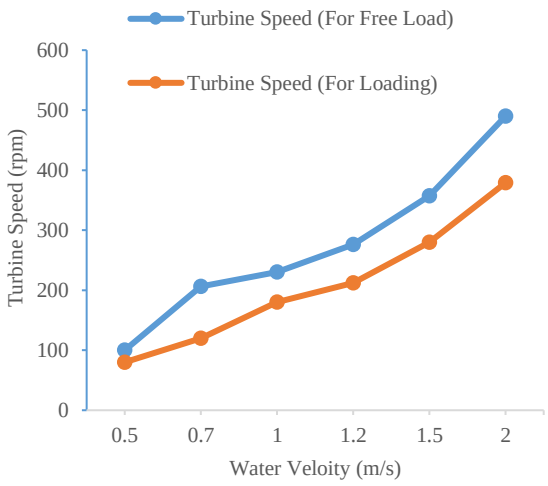

Fig. 11. Turbine speed at various velocity

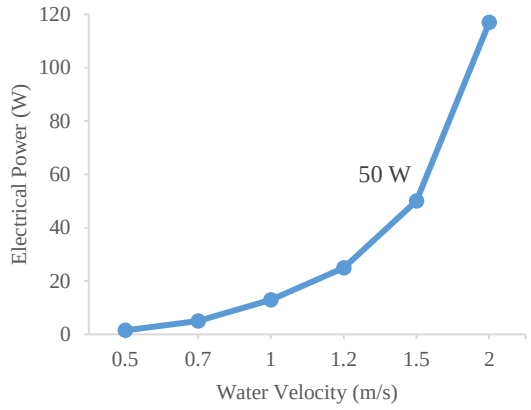

Fig. 12. Electrical power at various velocity

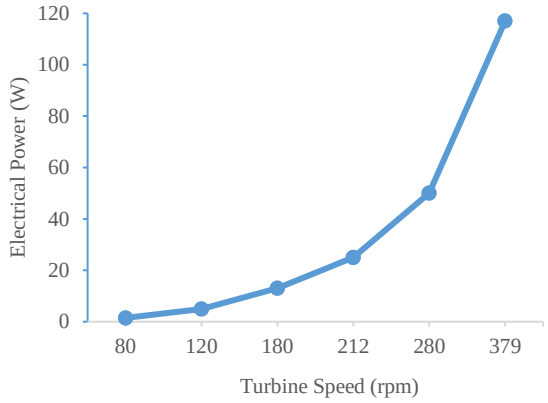

Fig. 13. Electrical power at various turbine speed

V. Discussion and Conclusion

The water velocity, density, tip speed ratio, solidity ratio, blade number, generator and turbine efficiency are the design specification data of 50 Watts GHT. The swept area is calculated by using equation (1), the diameter and height of GHT is calculated from the aspect ratio equation. The rotational speed of turbine and maximum torque can be adjusted to get the required power output. For this research the impact of water power on the turbine blade, water velocity and rotational speed are more essential than the maximum torque. So that, the aspect ratio 1.5 is selected because the rotational speed is maximum. If the speed of turbine is increase, the turbine experiment will improve.

According to the theoretical results, if the water velocity is increased, the turbine power is gradually increased as shown in Fig. 2.

The model of the GHT is created by using SolidWorks software. And then, turbine model is manufacture by using 3D printing. The frame and generator are fabricated in the Mandalay mechanics workshop. The site location for GHT testing is the channel of Shintawkone Village, in Patheingyi township. The different flow rates of water velocity are measured accurately three time per test to obtain the average velocity. In the experimental test, free loading and various loading are tested by changing water velocity. The rotational speed is measured with tachometer and turbine speed 357 rpm is found that in free loading at water velocity 1.5 m/s. For 50 Watts loading test, turbine speed is 280 rpm at water velocity 1.5 m/s. So, the rotational speed for loading is less than free loading.

Acknowledgment

The author would like to thank Dr. Aye Mya Thandar, Professor and Head of the Department of Mechanical Engineering, Technological University (Mandalay), for her immeasurable help throughout the research. And also, special thanks to Dr.Pa Pa Minn, Professor, Department of Mechanical Engineering, Technological University (Mandalay), for her invaluable supervision, support, and guidance throughout this study. The author also would like to thank her parents for their support and all her teachers from Department of Mechanical Engineering, Technological University (Mandalay).

References

[1] Jayarm Vijayana[a] and Bavanish Balac Retnam[b], "A Brief Study on the Implementation of Helical Cross Flow Hydrokinetic Turbines for Small Scale Power Generation in the Indian SHP Sector", ISSN: 2252-4940/2022.

[2] AiMing Zhang, "Field Tests on Model Efficiency of Twin Vertical Axis Helical Hydrokinetic Turbines", PR China,2022.

[3] Clement N,"Design of an Experimental Plug- Plow Helical Hydrokinetic Turbine for Power Generation in Kenya", ISSN 2519-5115 research article, 2019

[4] Jayaram.V, "Viability Study of Implementing Cross Flow Helical Turbine for Micropower Generation in India", international journal of renewable energy research, No. 1, March, 2018.

[5] Ei Ei Nwe, "Design and Performance of Vertical Axis Helical Cross Flow Turbine Blade for Micropower Generation", ISSN: 2454-4116, Volume-4, Issue-6, June 2018.

[6] Dr.Nader Sawalhi, Senior Design Project Report Helical Wind Turbine, Prince Mohammad Bin Fahd University,2017.

[7] Dr. Bharat Jhamnani, Performance Evaluation of Helical Turbine,Delhi Technological University, July-2017.

[8] Adam L.Niblick, "Experimental and Analytical Study of Helical Cross Flow Turbines for a Tidal Micro Power Generation System", University of Washington, 2012.

Real Time Door Lock Security System with Face Recognition using Haar Cascade Classifier and Eigenface(PCA)

Ahunt Min Maung[1], Su Myat Hlaing[2], Ei Wai Phyo[3], Myint Htun Naing[4]

[1]*Technological University, Mandalay, Myanmar*

[2]*Technological University, Mandalay, Myanmar*

[3]*Technological University, Mandalay, Myanmar*

[4]*Technological University, Mandalay, Myanmar*

Email: ahuntmin1995@gmail.com[#1], sumyathlaing963tum@gmail.com[#2], eiwaiphyo981@gmail.com[#3], dr.myinthtunnaing@gmail.com[#4]

***Abstract*—Security Door Lock System is a major problem faced by the houses, offices and other privacy areas. Therefore, information privacy is essential in today's automation system, and it is necessary to use the face recognition system to increase the security of the system. Face recognition system is a biometric recognition technology that confirms identity using about human facial features, and this system is used for door access control system. The main aim of this paper is to control the door lock security system based on face recognition and keypad door lock system for the real time monitoring using raspberry Pi3. In this research work, Haar-Cascade Classifier is presented for face detection and Eigenface algorithm is used for face recognition based on Principal Component Analysis (PCA). In this research, Face detection and recognition of door lock system is used in graphical user interface (GUI) and this algorithm is used to manage the interaction with the system. In this study, it is done by collecting different face shapes from 8 people with the aim of getting 300 images for each person. The experimental accuracy result of face recognition is 98.3% for door lock system. The proposed face detection and recognition system is a better method than the conventional method.**

***Keywords*—Face Detection and Recognition, Door Lock, Haar, Eigenface (PCA), GUI, Open CV**

I. Introduction

Nowadays, the security door lock system is faced in every aspect and security systems are now essential [1]. Face recognition system is a domain of computer vision-based system with search and recognition capabilities. This system is the matching procedure of identification face of recognized person between test images and train images. facial recognition technology is also used for a variety of applications namely, banks, airports, railway stations, public security departments, hotels, automotive systems, many commercial and enforcement applications, laboratories and important areas. Therefore, Face recognition system is a system that should be used in today's security-related areas [2]. This research is a method using face recognition system with door lock system for security purposes by connecting with Raspberry pi3 and Python (OpenCV). The system implementation is for observing whether any unknown person is entering through the door [3]. With the help of a webcam camera, the system is connected to electronic components through face recognition is a technology that solves the door lock system. In this research work, Haar-Cascade Classifier is used for face detection algorithm and Eigenface is used for face recognition algorithm based on Principal Component Analysis (PCA). When the database images and test images match, the door will be unlocked. If the system has an error, an alarm will be triggered. Then enter the secure password using the keyboard and the door will be opened.

II. Methodology

This system has two portions: (1) Face Detection and Recognition Door Lock System in GUI and (2) Keypad Door Lock System. In this system, Eigenface (PCA) is used for face recognition and Haar-Cascade Classifier is used to face detection algorithm. If the face recognition system is also recognizer, the door lock will unlock. If the facial recognition was an error state, move to toggle switch C from the key switch to open the door. Toggle switch slide B is set to inactive mode.

A. Face Detection for door lock system

A Haar-Cascade Classifier is used as a pre-trained process using Open CV in python for real-time system. It has 7 steps for the face detection Haar-Cascade Classifier algorithm, namely, import open CV Package, read the image, convert the image to grayscale, load the classifier, perform the face detection, drawing a bounding box, display the image are shown in Fig. 1 and 2.

```python
import cv2

# Load the pre-trained face detection model
face_cascade = cv2.CascadeClassifier(cv2.data.haarcascades + 'haarcascade_frontalface

# Read the input image
image = cv2.imread('path/to/your/image.jpg')

# Convert the image to grayscale
gray_image = cv2.cvtColor(image, cv2.COLOR_BGR2GRAY)

# Perform face detection
faces = face_cascade.detectMultiScale(gray_image, scaleFactor=1.3, minNeighbors=5)

# Draw rectangles around the detected faces
for (x, y, w, h) in faces:
    cv2.rectangle(image, (x, y), (x+w, y+h), (255, 0, 0), 2)

# Display the result
cv2.imshow('Detected Faces', image)
cv2.waitKey(0)
cv2.destroyAllWindows()
```

Fig. 1. Haar cascade classifier in OpenCV for face detection

Fig. 2. The proposed system of Face Detection

B. *Face Recognition for door lock system*

In this research work, PCA face recognition algorithm using eigenfaces approach utilizes two steps, namely, initialization (acquire a set of training images and evaluate the eigenfaces from the training set) and recognizing new face images. This approach enables accurate face recognition by representing and comparing facial features through eigenfaces, making it robust for recognizing individuals from different angles or expressions. PCA focuses on the study and development of an automated face recognition system considering three main factors, namely, illumination, distance, and subject's head orientation, with the potential application for door security system.

C. *Keypad door lock system*

In the door lock system, only registration persons can unlock and enter the room by clicking the secure code on the keypad. If codes are not shared or managed properly. There is a risk that unauthorized individuals can easily access sensitive areas.

Fig.3. Keypad Door Lock System

This Fig. 3 is the Keypad Door Lock System. In this research, if the human face is recognized, the door lock system will unlock by turning the magnetic lock. However, even if it's a specific face. In certain error situations; if the face is not recognized, the system will start alarm. If a switch works Slide C for keypad door lock system. So, the user will enter the defined password using keypad. If the password is correct, the system will unlock the door. Thus, if the password is wrong, the system will alarm work.

III. System Implementation

In this paper, the proposed system consists of eight subsystems: hardware components linked together, namely, motion sensor, webcam, Raspberry Pi-3, personal computer/laptop/ tablet, Arduino UNO, buzzer, keypad, and DC 12V Solenoid Lock. The block diagram of the door security control is based on the face recognition as shown in Fig. 4.

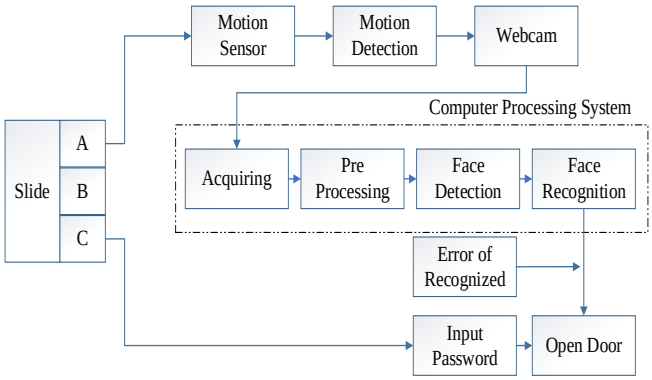

Fig. 4. Block diagram of Door Security Control with Face Recognition

A. *Flowchart system*

In this system, a combination of hardware and software is used. The Face Recognitions algorithm was used to secure for door lock system.

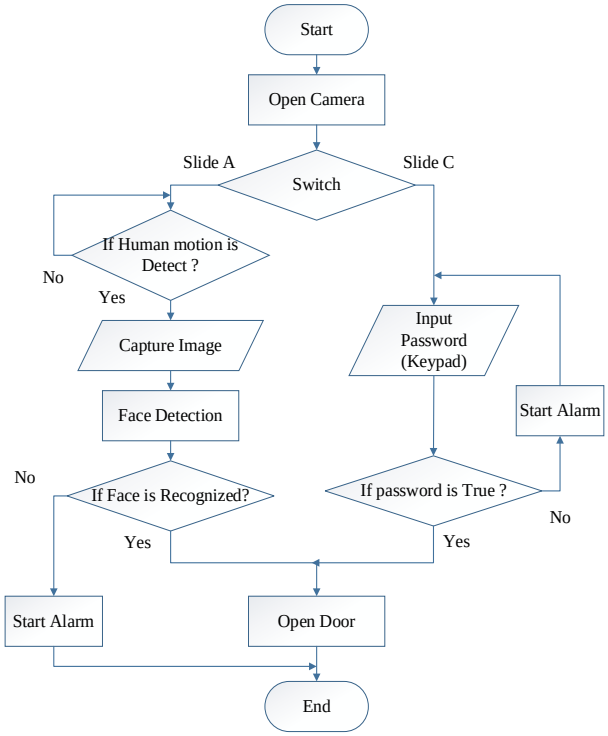

Fig. 5. Overall operation of door security control system

In this Fig. 5, Motion Detection, Face Detection and Recognition, and Keypad door lock system are operated in this research. Additionally, a switch is put between the face recognition system (Slide A) and keypad (Slide C) to make more easy working for door lock security System.

B. *Installation of Component for Door Lock System*

The hardware implements for door lock security system is shown in Fig. 6. In this research, a door lock system using a camera with OpenCV implementation has been successfully developed on Raspberry Pi3, which is stored the images using face recognition, collaborated to form an effective motion detection mechanism using motion sensor for real time door lock application. On the other hand, the keypad is applied for this proposed door access system. If the face is not recognized, it needs to be typed using the keypad by alerting the buzzer. Arduino UNO type, which is connected to Raspberry Pi3, relay, motion sensor, buzzer, and keypad, is used for door lock motor and servo motor for auto door opening and closing system.

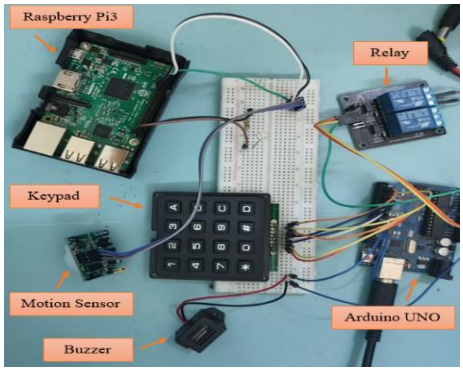

Fig. 6. Overall hardware components of the system

C. *Circuit Diagram of Door Lock System*

The following Fig. 7 is a circuit diagram of door lock system. In this figure, Arduino UNO is connected with Raspberry Pi 3 via the USB cable connected to webcam through motion sensor in port number pin 9 (red wire) and 11 (black wire). The keypad is connected to the pin number 2 to 9 in Arduino UNO. The buzzer is connected to the yellow wire in A5 and the ground black wire in Arduino UNO. Solenoid lock consisting of 12V DC adapter for power supply is connected to the relay via the pink wire (input pin 10), the black wire (ground), and the red wire (5V) in Arduino UNO.

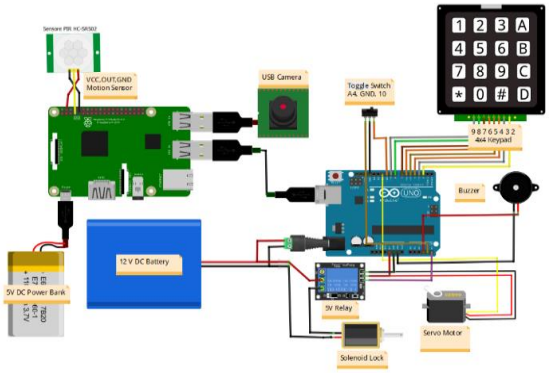

Fig. 7. Circuit Diagram of Door Security System

IV. Results and Discussion

A. *Graphical User Interface (GUI)*

The following Fig. 8 shows the result of face detection Harr classifier algorithm using database for detecting and creating images.

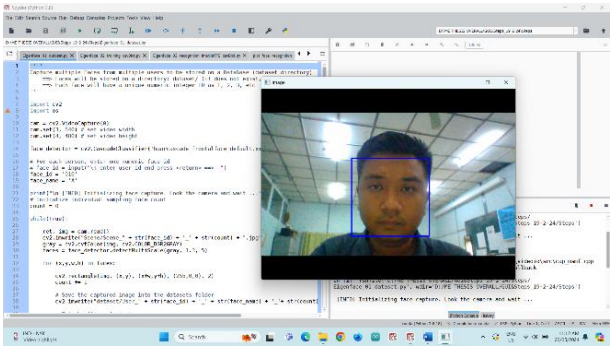

Fig. 8. Human Face detection algorithm based on Harr cascade classifier

In Fig.9, the face recognition system based on PCA eigienface algorithm can be calculated in database using Open CV Python in real time door seurity system.

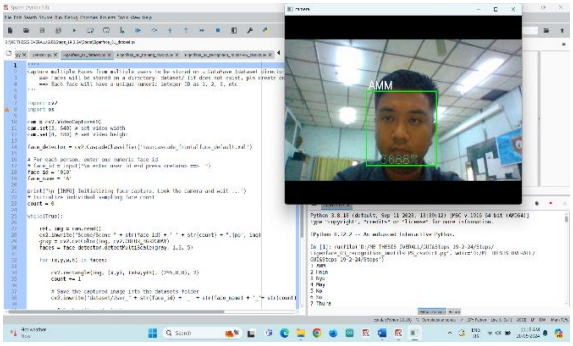

Fig. 9. Human Face recognition algorithm based on PCA

Fig. 10 shows the result of GUI door lock system view of face recognition based on PCA, namely, three main buttons, Register, Door lock, Quit.

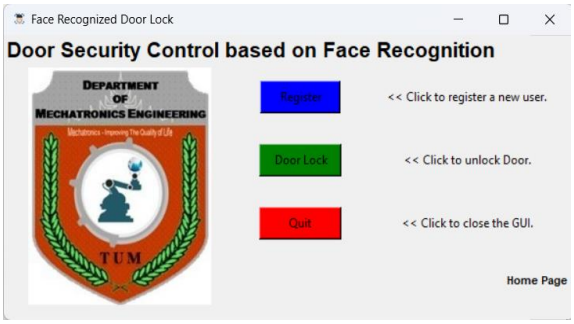

Fig. 10. Door Lock System View, Home Page

After taking 300 pictures of human faces, these 300 pictures were trained with the help of GUI. The following Fig. 11 shows the system is already checked in model for door lock system when the face is recognized.

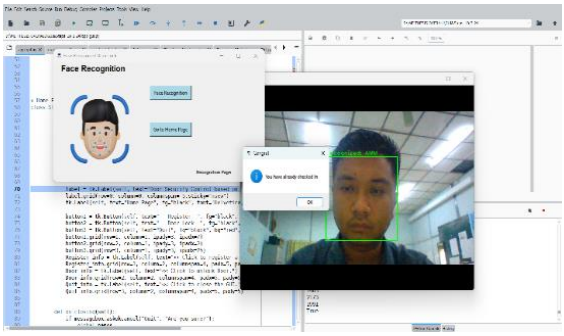

Fig. 11. Recognized Condition of the detection of authorized person

The door lock system will open when the user is recognized in GUI Database using PCA. The result of matched people and algorithm as shown in Fig. 12.

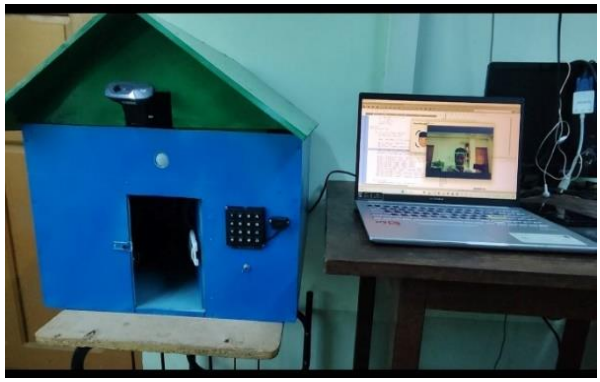

Fig. 12. Operation condition of the door lock system

If the result of test images and train images is not matched, the database with PCA algorithm, the door lock system will not operate as shown in Fig. 13.

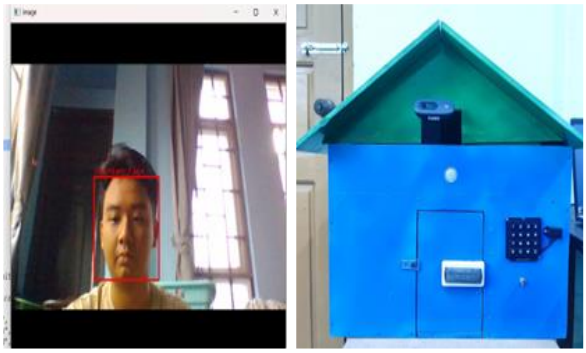

Fig. 13. Un-Recognized condition of the detection of un- authorized person

B. *Facial Recognition*

The proposed system was designed and implemented using Haar feature-based cascade classifiers for face detection and eigenfaces approach PCA algorithm for face recognition. Fig. 14 and Fig. 15 show the results of facial images for 5 persons in database.

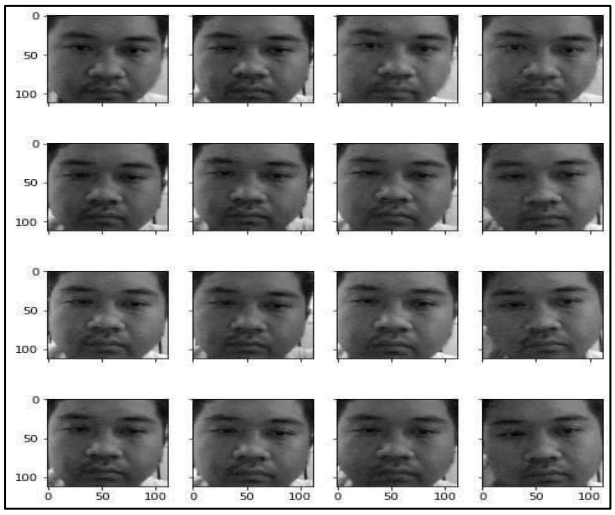

Fig. 14. Eigenfaces of AMM in database

Fig. 15. Eigenfaces of 4 authorized persons in database

By using PCA algorithm, extracted the feature from 300 training images in database. Each single face of volunteers was identified and tested under the PCA face recognition algorithm to determine query and best match in database. The experimental results are shown in Fig. 16.

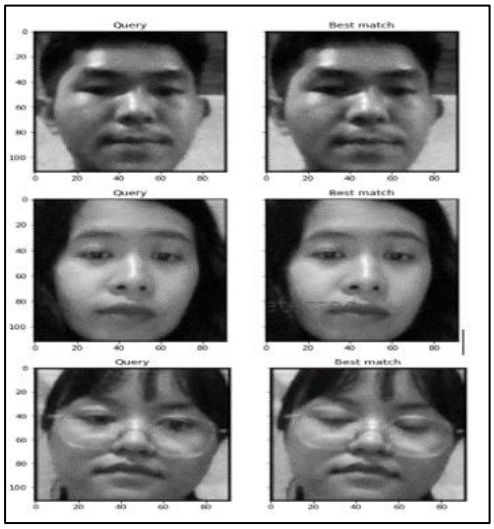

Fig. 16. Facial Identification of 3 Persons

Table I. **Prediction accuracy results for 8 persons**

Predicting people's names on the test set
done in 0.079s

	precision	recall	f1-score	support
AMM	1.00	1.00	1.00	202
B	1.00	1.00	1.00	111
Hnin	1.00	1.00	1.00	92
Ei	1.00	0.99	0.99	97
Ko	1.00	1.00	1.00	92
May	1.00	1.00	1.00	99
Su	0.99	1.00	0.99	93
Thura	1.00	1.00	1.00	110
accuracy			1.00	896
macro avg	1.00	1.00	1.00	896
weighted avg	1.00	1.00	1.00	896

Table 1 shows the result of prediction accuracy for 8 volunteers based on precision, recall, and f1-score, support vectors/features of the proposed system. In table 1, the result of 7 persons gets the accuracy of 1 in precision and FI scores, except the one person Su. However, Su obtains the comparable accuracy result 0.99. In recall, Ei and Su achieves nearly to 0.99 compared with others. We can clearly see that AMM get the best result of 202 in support features.

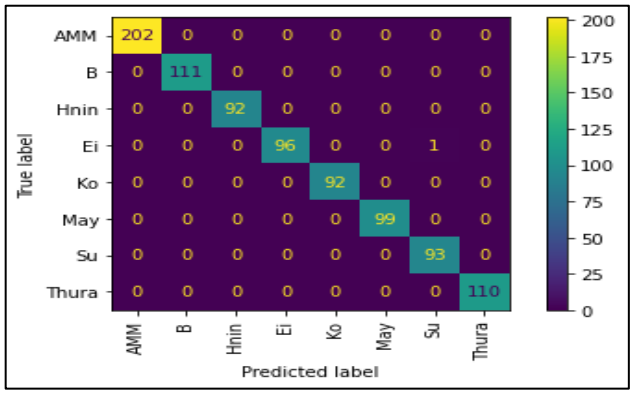

Fig.17. Confusion matrix of the Face Recognition System

Fig. 17 shows the result of confusion matrix for true label and predicted label PCA for 8 persons. We can clearly see that the best accuracy result is 202 of AMM with yellow color achieved zero error true negative (TN) and false

positive (FP). However, the name of Hnin and Ko obtain the lowest accuracy result (92). Moreover, Su (93) has the error one time compared with Ei although Ei achieves the good accuracy result (96). It is the normal case when we train and test image datasets of many persons in real time and it is not affected on the system. For other persons, the zero result of TN and FP are comparable. Therefore, we can clearly say that the proposed system is achieved the best performance.

V. Conclusion

In this research work, the door lock security system is successfully performed on hardware and software implementation. In this proposed system, the face recognition method based on Principal Component Analysis (PCA) approach is developed and Haar-Cascade Classifier is presented for face detection algorithm. For real time monitoring, this paper proposes a smart approach using raspberry Pi3 of the door security system. Moreover, if the face recognition system is not recognized, the proposed system is developed using the keypad by alerting the buzzer, Arduino UNO type, which is connected to Raspberry Pi3, relay, motion sensor, buzzer, and keypad for auto door lock motor and servo motor opening and closing system. In this research, based on the PCA algorithm, the accuracy result rate of 8 people obtained from the calculation of confusion matrix was 98.3%. The proposed face recognition technique is better than the traditional method. This may be a suggested future direction to improve the accuracy efficiency of many people.

Acknowledgment

Firstly, the author is very grateful to his parents who helped and encouraged his goal without difficulty. The author wishes to express special thanks Daw Ei Wai Phyo, Associate Professor and Head, Department of Mechatronic Engineering, Technological University (Mandalay) for their kind help, generous guidance, suggestions and supporting to carry out this result. And also, special thanks and sincere gratitude to his supervisor, Daw Su Myat Hlaing, Lecturer, and his Co-supervisor, Dr. Myint Tun Naing, Tutor, and for valuable suggestion, generous guidance, instructions and supervision throughout the research work. The author special thanks to all his teachers from Department of Mechatronic Engineering, Technological University (Mandalay). Finally, I would like to thank the author's wife and friends for their support and kindness.

References

[1] Nourman S. Irjanto. "Home Security System with Face Recognition based on Convolutional Network." (IJACSA) International Journal of Advanced Computer Science and Applications, vol. 11, pp.408-412, no.11, 2020.

[2] Shrutika V. Deshmukh1, Prof Dr. U. A. Kshirsagar. " Implementation of Human Face Detection System for Door Security using Raspberry Pi." International Journal of Innovative Research in Electrical, Electronics, Instrumentation and Control Engineering, vol. 5, pp. 186-191, Issue 4, April 2017.

[3] Nwukar Frances Nkem. " Face Recognition Door Lock System using Raspberry Pi." Globel Scientific. [Online]. vol. 10, issue. 8, ISSN.2320-9186. Available: www.globalscientificjournal.com [Aug, 2022].

[4] R.Manjunatha. " Home Security System and Door Access Control Based on Face Recognition." International Research Journal of Engineering and Technology (IRJET), vol. 4, pp. 437-442, Issue 3, Mar 2017.

[5] Peng Peng, "A Face Recognition Software Framework Based on Principle Component Analysis", Jul 22, 2021.

[6] Ali Javed, "Face Recognition Based on Principal Component Analysis", Jul 22, 2021.

ကံ့ကော်မြိုင်စာတမ်းလာ “နွေဦးကျက်သရေ”စာတမ်းမှ ဆရာဇော်ဂျီ၏ စာပေလက်ရာ

အေးအေးသန်း
မြန်မာစာဌာန
မန္တလေးကွန်ပျူတာတက္ကသိုလ်
ayethanaye252@gmail.com

စာတမ်းအကျဉ်း- ဤစာတမ်းသည် မြန်မာစာပေနယ်ပယ် စကားပြေကဏ္ဍတွင် ပါဝင်သော ကံ့ကော်မြိုင်စာတမ်းလာ ဆရာဇော်ဂျီ၏ စာပေလက်ရာကို လေ့လာတင်ပြထားသော စာတမ်းဖြစ်ပါသည်။ ရည်ရွယ်ချက်မှာ ဆရာဇော်ဂျီ၏ စာပေလက်ရာကို ဖော်ထုတ်တင်ပြလိုခြင်း ဖြစ်သည်။ အလေ့လာခံအဖြစ် ကံ့ကော်မြိုင်စာတမ်းလာ ဆရာဇော်ဂျီ၏ စာပေလက်ရာဖြစ်သည့် နွေဦးကျက်သရေ ရသစာတမ်းကို ထားရှိပါသည်။ မောင်ခင်မင်(ဓနုဖြူ)၏ စာတမ်းငယ်ဟူသည်ကို အခြေခံကာ စာတမ်းငယ်ကို ပုံပေါ်စေသည့်နည်းစနစ်ဖြင့် လေ့လာတင်ပြထားပါသည်။ စာရေးသူ၏ ကိုယ်ရည်ကိုယ်သွေး၊ အတွေးအမြင်၊ စာဖတ်သူကို ဆွဲဆောင်နိုင်ပုံ၊ တိုတိုကျဉ်းကျဉ်းရေးပုံနှင့် ရသများကို တွေ့ရှိရပါသည်။ ရသစာတမ်းကို လေ့လာလိုသူများအတွက် အထောက်အကူပြုနိုင်ပါသည်။.

သော့ချက်ဝေါဟာရများ—ကိုယ်ရည်ကိုယ်သွေး၊ အတွေးအမြင်၊ ရသ၊ ဘဝအသိအမြင်။

၁။ နိဒါန်း

မြန်မာစာပေလောကတွင် စာတမ်းဟူသော အမည်ကို ‘ကံ့ကော်မြိုင် စာတမ်း’တွင် စတင်တွေ့ရပါသည်။ ကံ့ကော်မြိုင် စာတမ်းတွင် စာရေးသူ (၁၀)ဦး ပါဝင်ရေးသားထားပါသည်။ ထို(၁၀)ဦးထဲမှ ဆရာဇော်ဂျီ၏ စာပေလက်ရာဖြစ်သည့် “နွေဦးကျက်သရေ” ရသစာတမ်းတွင် ရေကုသိုလ်၊ ရေချမ်းစင်၊ နွားဘေးမဲ့လွတ်ပွဲစသည့် မြန်မာမှုဓလေ့များမှ မြန်မာလူမျိုးတို့၏ ကုသိုလ်ပြုပုံ၊ သဒ္ဓါတရား ကိုယ်ချင်းစာစိတ်တို့ကို တွေ့မြင်နိုင်သည့်အပြင် မြန်မာလူမျိုးတို့၏ စိတ်၊ စေတနာနှင့် ဝမ်းမြောက်ကြည်နူးဖွယ်၊ ရဲရင့်တက်ကြွဖွယ် ခံစားမှုရသ၊ ဘဝအသိအမြင်တို့ကိုပါ ပေးစွမ်းနိုင်ပါသည်။ ထို့ပြင် ကြည်နူးမှုရသ၊ ဘဝအသိအမြင်တို့ကို ပေါ်လွင်ထင်ရှားလာအောင် ရေးသားနိုင်သော ဆရာဇော်ဂျီ၏ စာပေအရေးအသားစွမ်းရည်၊ စာဖတ်သူအပေါ် ထားရှိသောစိတ်စေတနာ၊ မြန်မာမှုဓလေ့များကို မြတ်နိုးသည့်စိတ်ဓာတ်တို့ကို မြင်တွေ့နိုင်သော စာတမ်းကောင်း တစ်စောင်ဖြစ်ပါသည်။

၂။ စာရေးသူ၏အတ္ထုပ္ပတ္တိအကျဉ်း

ဆရာဇော်ဂျီကို၁၉၀၇ခုတွင်အဖဦးယော၊အမိဒေါ်စိန်ညွန့်တို့က ဖျာပုံမြို့၌ ဖွားမြင်ခဲ့သည်။ အမည်ရင်းမှာ ဦးသိန်းဟန်ဖြစ်သည်။ ငယ်စဉ်က ဖျာပုံမြို့အမျိုးသားအထက်တန်းကျောင်းနှင့် ရန်ကုန်မြို့၊ မြို့မ အထက်တန်းကျောင်းတို့၌ ပညာသင်ကြားခဲ့သည်။

၁၉၃၀-ပြည့်နှစ်တွင် ရန်ကုန်တက္ကသိုလ်မှ ဝိဇ္ဇာဘွဲ့၊ ၁၉၃၆-ခုနှစ်တွင် လန်ဒန်တက္ကသိုလ်နှင့် ဒဗ္ဗလင်တက္ကသိုလ်တို့မှ စာကြည့်တိုက်ပညာ ဒီပလိုမာဘွဲ့တို့ ရရှိခဲ့သည်။

၁၉၃၁မှ ၁၉၃၄ထိ မြို့မအထက်တန်းကျောင်းတွင် အထက်တန်းပြဆရာ၊ ၁၉၃၄-မှ ၁၉၃၈-ထိ ရန်ကုန်တက္ကသိုလ်နှင့် မန္တလေးဥပစာကောလိပ်တို့၌ မြန်မာစာနည်းပြဆရာ၊ ၁၉၄၀-ပြည့်နှစ်တွင် ရန်ကုန်တက္ကသိုလ်ကျောင်းစာကြည့်တိုက်၌ ပိဋကတ်တိုက်မှူး၊ ဂျပန်ခေတ်၌ ပညာရေးဌာနတွင် ဒုတိယညွှန်ကြားရေးဝန်၊ စစ်ပြီးချိန်တွင် ရန်ကုန်တက္ကသိုလ်စာကြည့်တိုက်မှူး၊ ရန်ကုန်တက္ကသိုလ်၊ မြန်မာစာဌာနတွင် ဂုဏ်ထူးဆောင်ပါမောက္ခ စသည်ဖြင့် တာဝန်ထမ်းဆောင်ခဲ့ပါသည်။

၁၉၂၃-ခုနှစ်၊ ကျောင်းသားဘဝမှစ၍ ကဗျာများရေးဖွဲ့ခဲ့သည်။ ၁၉၂၈-ခုနှစ် ရန်ကုန်တက္ကသိုလ်၌ ဟံသာကြေးမုံစာစောင် ထုတ်ဝေခဲ့သည်။ ထိုစာစောင်တွင်ပါရှိသော “ပိတောက်ပန်း” ကဗျာမှာ ခေတ်စမ်းစာပေလှုပ်ရှားမှု၏ ပထမဆုံးကဗျာ ဖြစ်သည်။

ဆရာဇော်ဂျီသည် ကဗျာ၊ စကားပြေများစွာ ပြုစုခဲ့ရာ ၁၉၅၅-ခုနှစ်တွင် “သခင်ကိုယ်တော်မှိုင်းဦးကာ”ဖြင့် စာပေဗိမာန်ဆု (စာပဒေသာ)၊ ၁၉၇၉-ခုနှစ်တွင် “နင်လားဟဲ့ချစ်ဒုက္ခနှင့် အခြားဝတ္ထုတိုများ”ဖြင့် အမျိုးသားစာပေဆု(ဘာသာပြန်ရသ)၊ ၁၉၈၇-ခုနှစ်တွင် “ရွေးခေတ် ပုဂံကဗျာများနှင့် အခြားကဗျာများ”ဖြင့် အမျိုးသားစာပေဆု (ကဗျာပေါင်းချုပ်)တို့ ရရှိခဲ့သည်။

မြန်မာ့ယဉ်ကျေးမှုကို တန်ဖိုးထားသူ၊ ခေတ်စမ်းစာပေ ခေါင်းဆောင်၊ ရသစာပေပညာရှင်၊ မျိုးချစ်စာဆို ဆရာဇော်ဂျီသည် “၁၉၉၀-ပြည့်နှစ်၊ စက်တင်ဘာလ ၂၆-ရက်နေ့တွင် ကွယ်လွန်အနိစ္စ ရောက်ခဲ့ပါသည်။” **(၂၀၀၂၊ ၃၉၇)**

၃။ ရသစာတမ်းဝေါဟာရနှင့် သွင်ပြင်လက္ခဏာများ

ရသစာတမ်းဟူသော စာပေအမျိုးအစားသည် ၁၆-ရာစုတွင် ပြင်သစ်နိုင်ငံမှ စတင်ပေါ်ပေါက်လာခဲ့သည်။ ပြင်သစ်ဘာသာဖြင့် “essai”၊ အင်္ဂလိပ်ဘာသာဖြင့် “essay” အမည်တွင်သည်။ မြန်မာစာပေလောကတွင် ၂၀-ရာစုလောက်မှသာ စတင်ပေါ်ပေါက် လာခဲ့သည်။ အက်ဆေး ၊အစမ်းစာ၊ စာတမ်း၊ စာမွန်၊ စာတန်း၊ ရသစာတမ်းငယ်၊ ရသစာတမ်း စသည်ဖြင့် အမည်အမျိုးမျိုး ခေါ်ဝေါ်ခဲ့ကြသည်။

စာတမ်းငယ်ခေါ် ရသစာတမ်းနှင့်ပတ်သက်၍ မောင်ခင်မင် (ဓနုဖြူ)က -

> “စာတမ်းငယ်ဟူသည် အကြောင်းအရာတစ်ခုခုကို စာရေးသူကိုယ်တိုင် တွေးခေါ်ခံစားရသည့် အနေအထားဖြင့် ရသပါအောင် ရေးဖွဲ့ထားသော မတိုမရှည် စကားပြေအဖွဲ့မျိုးဖြစ်သည်”[1](၁၉၈၇၊ ၂၆)

ဟူ၍ ဖွင့်ဆိုထားပါသည်။ ထို့ကြောင့် ရသစာတမ်းဟူသည် စာရေးသူက မိမိခံစားမှု အတွေးအမြင်များကို ရသသဘောပါအောင် တိုတိုနှင့်ထိထိမိမိ ရေးထားသောစကားပြေမျိုးဖြစ်ပါသည်။

ထို့ပြင် ရသစာတမ်း၏ သွင်ပြင်လက္ခဏာများနှင့် ပတ်သက်၍ မောင်ခင်မင် (ခနုဖြူ)က-

> "(၁) စာရေးသူ၏ ကိုယ်ရည်ကိုယ်သွေးပေါ်နေခြင်း၊ (၂) အကြောင်းအရာထက် အတွေးအမြင်ခံစားမှုတို့ကို အားပြုခြင်း ဟူသော 'စာရေးသူ'ဆိုင်ရာ သွင်ပြင်လက္ခဏာများကို လည်းကောင်း (၃) စာဖတ်သူကို ဆွဲဆောင်နိုင်သော စကားပြေ အရေးအဖွဲ့မျိုးဖြစ်ခြင်း (၄) တိုတိုကျဉ်းကျဉ်းရေးဖွဲ့ထားသော အရေးအဖွဲ့မျိုးဖြစ်ခြင်းဟူသော 'စာ' ဆိုင်ရာ သွင်ပြင်လက္ခဏာ များကိုလည်းကောင်း (၅) စာဖတ်သူကို နှစ်သက်မှု ရသပေးခြင်း ဟူသော 'စာဖတ်သူ' ဆိုင်ရာ သွင်ပြင် လက္ခဏာများ"[2] (၁၉၈၇၊ ၃၉)

ဟူ၍ ရှင်းပြထားပါသည်။ ရသစာတမ်း၏သွင်ပြင်လက္ခဏာမှာ အဓိကအားဖြင့် (၅)ချက်ရှိကြောင်း ညွှန်ပြထားသည်ကို တွေ့ရှိရ ပါသည်။

၄။ ကံ့ကော်မြိုင်စာတမ်းလာ ဆရာဇော်ဂျီ၏စာပေလက်ရာ

ဆရာဇော်ဂျီ၏ စာပေလက်ရာဖြစ်သည့် **"နွေဦးကျက်သရေ"** စာတမ်းသည် နွေရာသီတွင် တွေ့ရသော မြန်မာလူမျိုးတို့၏ ကျက်သရေများဖြစ်သည့် ရေအလှူဒါနပြုပုံ၊ ရေချမ်းစင်တည်ပုံ များနှင့် သင်္ကြန်အခါ နွားလွှတ်ပွဲကျင်းပပုံများကို ဖတ်ချင်စဖွယ် ကောင်းအောင်၊ ရသမြောက်အောင်၊ ဘဝအသိရအောင် ရေးသားထားသည့် စာတမ်း ဖြစ်ပါသည်။

ဤစာတမ်းကို စာတမ်းငယ်၏ သွင်ပြင်လက္ခဏာ(၅)ရပ်နှင့် ချိန်ထိုးကာ လေ့လာတင်ပြသွားပါမည်။

၄၊ ၁။ စာရေးသူ၏ကိုယ်ရည်ကိုယ်သွေးပေါ်နေခြင်း

ရသစာတမ်းများတွင် မိမိပတ်ဝန်းကျင်၌ တွေ့ကြုံခံစားရသော ခံစားမှု၊ ဘဝအသိမြင်တို့ကို စာဖတ်သူများပါ ထိတွေ့ခံစား လာရအောင် ကိုယ်တိုင်ပါဝင်ပြောပြနေဟန် ရေးသား လေ့ရှိပါသည်။ ထို့ကြောင့် ရသစာတမ်းများတွင် စာရေးသူ၏ ကိုယ်ရည်ကိုယ်သွေး စရိုက်များ ပေါ်လွင်နေကြပေသည်။

ဆရာဇော်ဂျီ၏ "နွေဦးကျက်သရေ" စာတမ်းတွင် ရေတံနေ သော မိမိတို့ကို စေတနာအပြည့်ဖြင့် ရေကုသိုလ်ပြုလာသော ကျေးလက်သူ တို့ကို ကြည်ညိုစရာကောင်းကြောင်း ချီးကျူးသည်။ နွေဦးတွင် သစ်ပင်ရိပ်ရှိ ရေချမ်းအိုးများ၊ ရေချမ်းစင်များကို **"နွေဦးကျက်သရေ"**ဟု တန်ဖိုးထားသုံးနှုန်းသည်။ သူတစ်ပါး၏ အသက်ကို ကယ်တင်လိုသော မြန်မာတို့၏ စိတ်ထားစရိုက်ကို နွားလွှတ်ပွဲဖြင့် သရုပ်ဖော်ဂုဏ်ပြုကာ အနုစိတ်ခြယ်မှုန်းထားသောကြောင့် စာရေးသူ၏ ကိုယ်ရည်ကိုယ်သွေး ပေါ်လွင်နေပါသည်။

ဆရာဇော်ဂျီတို့ ကျောင်းသားတစ်သိုက် မီးရထားဖြင့် လေ့လာရေး ခရီးထွက်လာရာ ရေတူးပါမလာသောကြောင့် ရေတံရပုံ၊ ဘူတာ တစ်ခုတွင် ရေအလှူရှင် ကျေးလက်သူတစ်စုနှင့် ကြုံရပုံ၊ ဆင်းရဲသည့် ကျေးလက်သူများဖြစ်သော်လည်း စိတ်စေတနာလှကြပုံ၊ ကြည်ညိုစရာ ကောင်းပုံကိုတင်ပြရာတွင်-

> **"**သူတို့၏ ရေအလှူစေတနာ၊ ရေဝေအမှုအရာတို့ကြောင့်လား မသိ သူတို့၏ရုပ်ရည်သည် ဝမ်းသာစရာကောင်း၍ ကျေးဇူးတင် စရာကောင်း၍ ကြည်ညိုစရာကောင်းသည်ဟု ထင်မိသည်။**"** **(၂၀၁၂၊ ၁၅)**

ဟူ၍ ရေးသားထားပါသည်။ စာရေးသူ၏ ကျေးဇူးတရား သိတတ်သော သဘောစရိုက်ကို တိုက်ရိုက်ဖော်ပြနေခြင်း ဖြစ်သည်။ ထို့ကြောင့် ရသစာတမ်းသွင်ပြင်လက္ခဏာနှင့် ပြည့်စုံမှု ရှိပါသည်။

ဤရသစာတမ်းတွင် ဆရာဇော်ဂျီသည် နွားဘေးမဲ့လွှတ်ပွဲ အကြောင်းကိုလည်း တင်ပြထားသည်။ နွေဦးကာလရောက်တိုင်း ကိုဖေသည် နွားများကို တတ်နိုင်သမျှ ဘေးမဲ့လွှတ်ပေးလေ့ရှိသည်။ ထိုကိုဖေကို စာရေးသူက တစ်ခါနှစ်ခါလွှတ်ရုံဖြင့် နွားများအားလုံး မချမ်းသာနိုင်၍ နေတိုင်း၊ နာရီတိုင်း၊ မိနစ်တိုင်း လွှတ်နိုင်မှဟန်မည်ဟု ခနဲ့သောအမူအရာဖြင့် ပြောသည်။ ထိုအခါ ကိုဖေက နွားလွှတ်ပွဲ ကျင်းပတိုင်း ဘေးသင့်နေသော သတ္တဝါမှန်သမျှ၊ ဒုက္ခိတသတ္တဝါမှန်သမျှ ကယ်အပ်၊ စောင့်ရှောက်အပ်သော သတ္တဝါတွေပါလားဟု အသိတရား ရနိုင်ကြောင်း၊ ထိုအသိတရား သည် ကျုပ်တို့ ခင်ဗျားတို့ကို နှစ်စဉ်နှစ်တိုင်း၊ နွေဦးပေါက်တိုင်း နှိုးဆော်နေသည်နှင့်တူကြောင်း၊ ကျင်းပသောပွဲက အရေးမဟုတ်၊ ကျင်းပသောပွဲ၏သဘောကသာ အရေးပါကြောင်း ရှင်းပြသည်။ ထိုအခါ ဆရာဇော်ဂျီမှာ မိမိမှားသွားကြောင်း နောင်တရပြီး ခေါင်းမဖော်နိုင်ဖြစ်ခဲ့ရကြောင်းကို-

> **"**ဟုတ်သည်။ ကိုဖေ့အပေါ်မှာ ကျွန်တော် လူလည်လုပ်မိပြီ။ ကျွန်တော် ခေါင်းငုံ့နေလိုက်ရပါသည်။**"** **(၂၀၁၂၊ ၁၉)**

ဟူ၍ ရိုးသားစွာ ရေးသားဖော်ပြထားသည်မှာ စာရေးသူ၏ အမှားကို ဝန်ခံတတ်သောကိုယ်ရည်ကိုယ်သွေးကို ပေါ်လွင်စေပါသည်။

တစ်ဖန် ကိုဖေတို့သည် အလှူခံရသောငွေဖြင့် နွားသတ်ရုံမှ အသတ်ခံရတော့မည့်ဆဲဆဲနွားကြီးကို ဝယ်ကာ ချိုကို ပိတောက်ပန်း စည်းသည်။ နွားတစ်ကိုယ်လုံးကို နံ့သာရေပက်ဖျန်းသည်။ နွား၏ ကိုယ်ပေါ်ကို ကောဇောခင်းကာ အလှဆင်သည်။ ထို့နောက်အတီးအမှုတ်၊ အကအခုန်တို့ဖြင့် ကုသိုလ်ရှင်များ ဝမ်းမြောက်ရအောင် ရပ်ရွာကို လှည့်ပြသည်။ ဤသို့သော မေတ္တာ၊ ကရုဏာ၊ မုဒိတာတို့လွှမ်းခြုံနေသောပွဲကို ဆရာဇော်ဂျီက-

> "အိုးစည်ဝိုင်းအရှေ့တွင် ဘေးမဲ့နွားကြီး။ ပိတောက်ပန်းနှင့်၊ သနပ်ခါးနှင့်၊ ကတ္တီပါနှင့်၊ ကော်ဇောနှင့်၊ ဣန္ဒြေကြီးနှင့်၊ သိင်္ခာနှင့် တစ်လှမ်းခြင်း လှမ်း၍ ပါလာသည်။ နွားကြီး၏ရှေ့တွင် ကိုဖေ၏အက၊ ကွေး၍၊ ကော့၍၊ ယိမ်း၍၊ ယိုင်၍၊ ရှေ့ဆုံးက သွားသည်။**"** **(၂၀၁၂၊ ၂၀)**

ဟူ၍ ရေးသားထားပေသည်။ ပေါင်းစည်းပြသမှုန္ဓ "နှင့်"၊ တစ်ခုပြီးတစ်ခု ဆောင်ရွက်ကြောင်းကိုပြသည့်သမ္မုန္ဓ "၍"တို့ကို ထပ်ထပ်ကာကာသုံး၍ သွက်သွက်လက်လက်ပြောနေဟန်သည် ဆရာကြီး၏ အားရကျေနပ်သည့် ဟန်ကို ပေါ်လွင်နေပါသည်။ ဇီဝိတဒါနပြုခြင်းကို အားပေးသော၊ ကျေနပ်သော၊ မြတ်နိုးသော ဆရာကြီး၏ ကိုယ်ရည်ကိုယ်သွေးကိုလည်း တွေ့ရပေသည်။

၄၊ ၂။ အကြောင်းအရာထက် အတွေးအမြင်ခံစားမှုတို့ကို အားပြုခြင်း

အကြောင်းအရာထက် အတွေးအမြင်ခံစားမှုကို အားပြုခြင်းသည် ရသစာတမ်းတို့၏ ဒုတိယသွင်ပြင်လက္ခဏာတစ်ရပ် ဖြစ်ပါသည်။ ရသ စာတမ်းတွင် အသေးအဖွဲမှ အကြီးအကျယ်အထိ ရေးလိုရာရာ

အကြောင်းအရာအမျိုးမျိုးကို ရေးလေ့ရှိပါသည်။ သို့သော် အကြောင်းအရာက ပဓာနမဟုတ်ပါ။ ထိုအကြောင်းအရာကို ရေးပြနေသော စာရေးသူ၏ အတွေးအမြင်ခံစားမှုတို့က ပို၍ အရေးပါပါသည်။

ဆရာဇော်ဂျီ၏ "နွေဦးကျက်သရေ"မှာ နွေဦးတွင် ရေကုသိုလ်၊ ဇီတိတကုသိုလ်ပြုကြသည်ကို အကြောင်းပြု၍ ပေါ်ပေါက်ခံစား ရသော စာရေးသူ၏ ခံစားချက်၊ အတွေးအမြင်များကို ရေးသားထားသောစာ ဖြစ်သည်။

ရေဝေ၊ ရေဒါနပြုကြသော ကျေးလက်သူတို့သည် လူဆင်းရဲ ချို့တဲ့သော်လည်း စိတ်စေတနာတို့ကား လှပနေကြသည်။ မိမိတို့မှာ ပညာတတ်၊ မြို့ကြီးသား ဝတ်ကောင်းစားလှများ ဝတ်ဆင်ထား သော်လည်း ထိုကျေးလက်သူတို့ကဲ့သို့ စိတ်စေတနာအလှကို မပြသနိုင်ကြပေ။ ထိုမှတစ်ဆင့် ယဉ်ကျေးမှုနှင့်ပတ်သက်၍ အတွေးအမြင် တန်းမိပုံကို-

> "သူတို့ ဝတ်စားထားသည်မှာ ချည်ထည်တစ်ပတ်နွမ်းများသာ ဖြစ်သည်။ အလုပ်ကြမ်း လုပ်ကြသူများဖြစ်သဖြင့် ကိုယ်လုံး ကိုယ်ပေါက် တောင့်တင်းသည်။ ရုပ်ရည်မှာ ချောသည် လှသည်ဟု မဆိုသာ။ သို့ရာတွင် သူတို့၏ ရေအလှူစေတနာ၊ ရေဝေအမူအရာ တို့ကြောင့်လားမသိ သူတို့၏ရုပ်ရည်သည် ဝမ်းသာစရာကောင်း၍ ကျေးဇူးတင်စရာကောင်း၍ ကြည်ညိုစရာ ကောင်းသည်ဟု ထင်မိသည်။ ထိုအခါ ကျွန်တော့်ကိုယ်ကို ကျွန်တော် ပြန်ကြည့် မိသည်။ ရုပ်အကျီဖြူဖြူစင်စင်နှင့်၊ ပိုးလုံချည်နှင့်၊ လက်ပတ်နာရီ နှင့်၊ ဆီမွှေးလိမ်းဘိုကေနှင့် ဖြစ်သည်။ ဤအခြင်းအရာတို့သည် ယဉ်ကျေးမှုလော၊ ဤသို့ မေးကြည့်သည်။ ဤအခြင်းအရာတို့ကို ယဉ်ကျေးမှုဟုဆိုလျှင် ထိုမိန်းမပျိုတစ်စု၏ အမူအရာသည် အဘယ်နည်း" **(၂၀၁၂၊ ၁၅)**

မတူညီသော နှိုင်းယှဉ်အဖွဲ့နှစ်မျိုးဖြင့် ရေးသားထားသည်။ ထို့ပြင် မေးခွန်းဖြင့်လမ်းခင်းကာ စာရေးသူ၏အတွေးနောက်ကို စာဖတ်သူ ပါလာအောင် ဆွဲဆောင် ရေးသားထားပေသည်။ ဝတ်ကောင်းစားလှ၊ ဂုဏ်ဒြပ်တို့ထက် အစာလိုသူကို အစာ၊ ရေလိုသူကို ရေပေးလှူသည့် အပြုအမူတို့သည်သာ စစ်မှန်သော ယဉ်ကျေးမှုဖြစ်ကြောင်း တွေးပြ၊ ရေးပြထားသည်ဟု ဆိုနိုင်ပါသည်။

တစ်ဖန် နွေဦးတွင်ကျင်းပသော နွားလွှတ်ပွဲတစ်ပွဲကို ကြည့်၍ ဖြစ်ပေါ် လာသော မလွတ်လပ်သေးသည့် အမိမြန်မာပြည်နှင့် ပတ်သက်သော အတွေးကိုလည်း-

> "မြန်မာပြည် မလွတ်လပ်ခင်တုန်းက နွားလွှတ်ပွဲတစ်ပွဲကို မြင်သဖြင့် အနောင်အဖွဲ့နှင့် နေရတုန်းဖြစ်သော ကိုယ့်တိုင်းပြည်ကို နွားကြီးကဲ့သို့ လွတ်မြောက်စေချင်သော စိတ်ကူး ကျွန်တော့်မှာ ပေါက်ဖူးသည်။ လွတ်မြောက်ပါစေ ဟုလည်း ဆုတောင်းဖူး သည်။" **(၂၀၁၂၊ ၂၀)**

ဟူ၍ ရေးသားပြထားသည်။ မိမိတိုင်းပြည်ကို ကျွန်သားပေါက်ဘဝမှ လွတ်မြောက်စေလိုသည့် စာရေးသူ၏ နက်ရှိုင်းလှသောခံစားမှု အတွေးအမြင်တို့ကို ထင်ထင်ရှားရှားတွေ့မြင်ရပေသည်။

၄၊ ၃။ စာဖတ်သူကို ဆွဲဆောင်နိုင်သောစကားပြေ အရေး အဖွဲ့မျိုး ဖြစ်ခြင်း

ရသစာတမ်းတွင် စာရေးသူ၏အတွေးအမြင်၊ ခံစားမှုအသိသည် ပဓာန တစ်ခုဖြစ်သကဲ့သို့ ထိုအတွေးအမြင်၊ ထိုခံစားမှုအသိကို စာဖတ် ပရိသတ်သို့ ကူးစက်အောင် ဆွဲဆောင်ရေးသားနိုင်ခြင်းသည်လည်း ပဓာန တစ်ခုဖြစ်ကြောင်း ဆိုမိန့်ကြပါသည်။

"နွေဦးကျက်သရေ"ရသစာတမ်းတွင် ဆရာဇော်ဂျီက မြန်မာလူမျိုး တို့၏ ယဉ်ကျေးမှုအမူအရာတစ်ခုဖြစ်သည့် ရေချမ်းစင်တည်ကာ ကုသိုလ် ပြုကြပုံကို တင်ပြရာတွင်-

> "ညောင်ပင်ရိပ် ကောင်းကောင်းရှိလျှင် သူရှိတတ်သည်။ ပိတောက်ရိပ် ကောင်းကောင်းရှိလျှင် သူရှိတတ်သည်။ ကုက္ကိုရိပ် ကောင်းကောင်းရှိလျှင် သူရှိတတ်သည်။ ထိုသူကား အခြားမဟုတ်။ သစ်ကိုင်းမှ ဆိုင်းကြိုးဖြင့် တွဲလွဲခိုနေတတ်သော ရေချမ်းအိုး ဖြစ်သည်။ မိန်းမချော မိန်းမလှ ဒန်းစီးနေသည်ဟုပင် တူလေသည်။" **(၂၀၁၂၊ ၁၆)**

ဟူ၍ တိုက်ရိုက်မတင်ပြဘဲ တစ်ဆင့်ပြီးတစ်ဆင့် စိတ်ဝင်စားဖွယ် ကောင်းအောင် တင်ပြသည်။ 'သူ'ဟူသော အညွှန်းနာမ်စားဖြင့် သက်ရှိအသွင်တင်စားကာ ရေးသည်။ ပုံစံတူဟန်ချက်ညီ ဝါကျတို့တို့ကို သုံး၍ ပြေပြေပြစ်ပြစ်ဖြစ်အောင်၊ ချောမောအောင် ရေးသည်။ 'မိန်းမချော မိန်းမလှ ဒန်းစီးနေသည်ဟုပင်တူ' ဟူသော ဥပမာအလင်္ကာဖြင့် နှစ်သက်ဖွယ်ဖြစ်အောင် ရေးသည်။ ထို့ကြောင့် စာရေးသူ ပြောလိုသော ရေချမ်းအိုး၏တည်နေပုံသည် စာဖတ်သူ၏ စိတ်မျက်စိတွင် စွဲထင်စွာ မြင်ယောင်လာရပါသည်။

ဆက်လက်၍ ဆရာဇော်ဂျီက-

> "ထိုရေချမ်းစင်၌ လူတို့၏ စိတ်သစ်စိတ်နှ၊ စေတနာသစ် စေတနာနှတို့လည်း ပေါ်ပေါက်နေကြလေပြီဟု တွေးမိခြင်း ဖြစ်လေသည်" **(၂၀၁၂၊ ၁၃)**

ဟူ၍ တင်ပြထားသည်။ ဤတွင် စိတ်၊ စေတနာတို့သည် ယေဘုယျ စကားလုံးများ ဖြစ်ကြသည်။ ထိုစကားလုံးတို့ကို 'သစ်၊ နှ'တို့နှင့် ပေါင်းစပ်၍ "စိတ်သစ်စိတ်နှ၊ စေတနာသစ် စေတနာနှ" ဝိသေသ စကားလုံးအဖြစ် ဖန်တီးရေးသည်။ ထို့ကြောင့်လည်း နွေဦးပေါက် တိုင်း ရေချမ်းစင်ကို တည်ဆောက်ပေးသော မြန်မာတို့၏စိတ်၊ မြန်မာတို့၏ စေတနာအလှသည် နုပျိုလန်းဆန်းသစ်လွင်နေပုံကို နှစ်သက်ဖွယ် သိမြင်လာစေသည်။

၄၊ ၄။ တိုတိုကျဉ်းကျဉ်းရေးဖွဲ့ထားသော အရေးအဖွဲ့မျိုး ဖြစ်ခြင်း

ရသစာတမ်းသည် တစ်ထိုင်တည်းနှင့် အပြီးဖတ်နိုင်ရုံမျှ ရှိရန် လိုပါသည်။ ထို့ကြောင့် တိုတိုကျဉ်းကျဉ်းရေးဖွဲ့သော အရေးအဖွဲ့မျိုးဖြစ်ရန် လိုအပ် ပါသည်။ တစ်ကွက်ကောင်း နှစ်ကွက်ကောင်း ပြရသည့်အတွက် ပြရသူ၏ ကျွမ်းကျင်မှု၊ ပြသူ၏ အတတ်ပညာသည် အလွန်အရေးပါပါသည်။

"နွေဦးကျက်သရေ"ရသစာတမ်းတွင် ဆရာဇော်ဂျီသည် နွေဦး၏ ကျက်သရေနှစ်ခုဖြစ်သော ရေချမ်းအိုးတည်ခြင်းနှင့် နွားဘေးမဲ့လွှတ်ခြင်း အကြောင်းကို အစ၊ အလယ်၊ အဆုံး အဆက်အစပ် မိမိဖြင့် အံဝင်ခွင်ကျ တိုတိုကျဉ်းကျဉ်းရေးထားပေသည်။ နွေဦးတွင် တွေ့ရ၊ မြင်ရလေ့ရှိသည့် ရေချမ်းစင် အလှူဒါနကို စာရေးသူ မြတ်နိုးသည်။ တန်ဖိုးထားသည်။ ကျက်သရေရှိသည်ဟု ခံယူသည်။ ထိုသို့မြတ်နိုးတန်ဖိုးထားခံယူမှုကို-

> "ထိုအမူအရာမျိုးသည် နွေဦးကျက်သရေ"တစ်ခု ဖြစ်လေသည်။ ထိုအမူအရာမျိုးကို မြန်မာနိုင်ငံသားတို့၏ ရေချမ်းစင်ယဉ်ကျေးမှုဟု ခေါ်ထိုက်လေသည်။ တစ်ဖန်လူထုအတွက် လူထုက ပြုနိုင်သော အမူအရာမျိုးဖြစ်သဖြင့် လူထုယဉ်ကျေးမှုဟူ၍လည်း ဆိုနိုင်လေသည်။" **(၂၀၁၂၊ ၁၇)**

ဟူ၍ ရေးသားထားသည်။ ထိုစာတစ်ကွက်တည်းဖြင့် ရေချမ်းစင် အလှူဒါန အပေါ်ထားရှိသော ဆရာဇော်ဂျီ၏စိတ်သဘောထား၊ စိတ်စေတနာကို ကွက်ကွက်ကွင်းကွင်း တွေ့ရပေသည်။

ထို့အတူ နွားလွှတ်ပွဲကျင်းပခြင်းသည်လည်း အပျော် သက်သက် ကျင်းပသည့်ပွဲမဟုတ်ကြောင်း သဒ္ဓါစေတနာဖြင့် ပြုလုပ်သည့်ပွဲ ဖြစ်ကြောင်း ဆရာကြီးခံယူသည်။ ထိုနွားလွှတ်ပွဲကိုလည်း ကျက်သရေ ရှိသည့်ပွဲပဟု မြင်သည်။ ထိုသဘောကို ဆရာကြီးက-

> "..နွားလွှတ်ပွဲကျင်းပခြင်းသည် သဒ္ဓါစေတနာနှင့် ပြုသည်ဟု ဆိုလျှင်လည်း ဟုတ်သည်။ ကချင် ခုန်ချင်၍ ပြုသည်ဟု ဆိုလျှင်လည်း ဟုတ်သည်။ မြန်မာပီသပါပေသည်။ ထိုအမူအရာမျိုး နွေဦးပေါက်တိုင်း နှစ် သစ်၌ ပေါ်လာတတ်သည်။ ထိုအမူအရာမျိုးသည် နွေဦးကျက်သရေတစ်ခု ဖြစ်လေသည်။ ထိုအမူအရာ မျိုးကို မြန်မာနိုင်ငံသားတို့၏ နွားလွှတ်ပွဲယဉ်ကျေးမှုဟုလည်း ခေါ်ထိုက်လေသည်။ တစ်ဖန် လူထုအတွက် လူထုကပြုနိုင်သော အမူအရာမျိုးဖြစ်သဖြင့် လူထုယဉ်ကျေးမှုဟု၍လည်း ဆိုနိုင်ပါ သတည်း" **(၂၀၁၂၊ ၂၀)**

ဟူ၍ ရေးသားထားပါသည်။ ဤတွင် **"နှ၊ သစ်"**ဟူသော လုံးချင်းကြိယာ အသုံးတို့က နွေဦးပေါက်တိုင်း မရိုးနိုင်သည့် စိတ်စေတနာနှ၊ စိတ်စေတနာသစ်တို့ဖြင့် နွားလွှတ်ပွဲကို ပြုလုပ်ပေးသော မြန်မာတို့၏ စိတ်စေတနာသည် လန်းဆန်းသစ်လွင် လာသည်။

ထို့ပြင် **"ရေချမ်းစင် ယဉ်ကျေးမှု"၊ "နွားလွှတ်ပွဲယဉ်ကျေးမှု"၊ "လူထုယဉ်ကျေးမှု"**ဟူသော ဝိသေသအသုံးတို့ကြောင့်လည်း သာမန် အနေဖြင့် အမှုမဲ့အမှတ်မဲ့ သဘောထားကြသည့်အရာများ၊ အပြုအမူများ အပေါ်တွင် အလေးအနက်တန်ဖိုးထားစေလိုသော ဆရာဇော်ဂျီ၏ စေတနာကို ထင်ထင်ရှားရှား သိမြင်နားလည်လာစေပါသည်။ တိုတိုကျဉ်းကျဉ်းနှင့် စာဖတ်သူများ ထိတွေ့ခံစားမိနိုင်စေရန် ရေးသား နိုင်သည်ဟု ဆိုရပါမည်။

ထို့ကြောင့်လည်း ဆရာမကြီး မမိုးမြေက-

> **"**ဆရာကြီးကမူ မြန်မာ့ပတ်ဝန်းကျင်၌ မြင်တွေ့နေရသော အသေးအဖွဲ၊ အညတရအရာများကို အလေးအနက်ထား၍ ခံစားရှုမြင်သည်။ မြန်မာတို့၏ မြင့်မြတ်သော နှလုံးသားမှ ပေါက်ပွားလာသည့် အလှဆုံး၊ အယဉ်ကျေးဆုံး အရာများဟု ခံစားရှုမြင်သည်။ ထိုသဘော၊ ထိုခံစားမှုဖြင့် "ရေချမ်းစင် ယဉ်ကျေးမှု၊ နွားလွှတ်ပွဲယဉ်ကျေးမှု၊ လူထု ယဉ်ကျေးမှု"ဟု ခံ့ညားထည်ဝါသော စကားသုံးများအဖြစ် ချီးမြှင့်ဖန်တီး ခဲ့ပါသည်။**" (၂၀၀၈၊ ၆၈)**

ဟူ၍ သုံးသပ်ချီးကျူးခဲ့ခြင်း ဖြစ်ပါသည်။

တစ်ဖန် ဆရာကြီးသည် နွားလွှတ်ပွဲကို ကြည့်၍ ဖြစ်ပေါ်လာသော အမိမြန်မာနိုင်ငံတော်အပေါ် ထားရှိသော စိတ်စေတနာကိုလည်း တိုတိုကျဉ်းကျဉ်းနှင့် လိုရင်းရောက်အောင် ရေးသည်။ အမိမြန်မာပြည် အပေါ်ထားရှိသော ဆရာကြီး၏စေတနာကို-

> "မတော်လောဘအနှောင်အဖွဲ့မှ၊ မတော်ဒေါသအနှောင်အဖွဲ့မှ၊ မတော်မာနအနှောင်အဖွဲ့မှ ခပ်သိမ်းကုန်သော အဓမ္မအနှောင်အဖွဲ့တို့မှ မြန်မာပြည်သည် ဘေးမဲ့နွားကြီးကဲ့သို့ လွတ်မြောက်ပါစေဟု ဆုတောင်းဖြစ်အောင် သတိလစ်၍ မနေချင်သောကြောင့် ဖြစ်ပါသည်။" **(၂၀၁၂၊ ၂၀)**

ဟူ၍ ရေးသားထားပါသည်။ လွတ်လပ်ရေးမရမီကလည်း နွားလွှတ်ပွဲကို ကြည့်၍ သူကျွန်ဘဝရောက်နေသော မြန်မာပြည်အတွက် ဆုတောင်း သည်။ လွတ်လပ်ရေးရပြီးနောက်လည်း မလွတ်လပ်သေးသော မြန်မာ ပြည်သူပြည်သားတို့အတွက် ဆုတောင်းသည်။ ကျယ်ပြန့်လှသော အကြောင်းတရားတို့ကို သိမြင်လာအောင် "မတော်လောဘ အနှောင်အဖွဲ့မှ၊ မတော်ဒေါသအနှောင်အဖွဲ့မှ၊ မတော်မာနအနှောင်အဖွဲ့မှ ခပ်သိမ်းကုန်သော အဓမ္မအနှောင်အဖွဲ့တို့မှ" ဟူသော အပြိုင်ဖွဲ့ကာ ဟန်ချက်ညီညီဖြင့် ရေးသည်။ ထွက်ခွာရာပြစကားလုံး "မှ"ကို ထပ်ကာထပ်ကာ သုံးထားသောကြောင့်လည်း မြန်မာပြည်သူ၊ ပြည်သား တို့ကို အနှောင်အဖွဲ့အားလုံးမှ လွတ်မြောက်စေလိုသည့် ဆရာကြီး၏ စေတနာလေသံကို ကြားယောင်လာရသည်။

၄၊ ၅။ စာဖတ်သူကို နှစ်သက်မှုရသပေးခြင်း

ရသစာတမ်းတွင် စာရေးသူက မိမိ၏အတွေ့အကြုံကို မိမိမြင်ရ ကြားရ ခံစားရသကဲ့သို့ စာဖတ်သူလည်း မြင်ရ၊ ကြားရ၊ ခံစား ရလာအောင်ဖွဲ့သည်။ စာဖတ်သူသည် ရသစာတမ်းကို ဖတ်ပြီးနောက် အနည်းနှင့်အများ နှစ်သက်မှုရသကို ခံစားရ စေပါသည်။

"နွေဦးကျက်သရေ"ရသစာတမ်းတွင် ရေဝေသူတို့၏ အမှုအရာ၊ ကိုဖေတို့၏အမှုအရာတို့ကို မြင်ယောင်ကြားယောင် ခံစားလာရအောင် သရုပ်ဖော်ရေးသားထားပါသည်။ စာရေးသူတို့ ကျောင်းသားသူငယ်ချင်း တစ်သိုက် ရေတံနေစဉ် ကျေးလက်လုံမပျိုတစ်စုက ရေကူသိုလ် ပြုလာသည်။ ဤသည်ကို စာရေးသူက-

> "လားလား မိန်းမပျိုတစ်စုသည် ရေအိုးကိုယ်စီရွက်၍၊ မီးရထား ပြတင်းပေါက်များဆီသို့ လာ၍ ရေအလိုရှိရင် ယူကြပါရှင်။ ရေလှူပါတယ်ရှင်"ဟုဆို၍ ရေအိုးများကို ကမ်းပေးကြပါသည်။" **(၂၀၁၂၊ ၁၄)**

ဟူ၍လည်းကောင်း။

> **"**မီးရထားသည် ကြာရှည်ရပ်လေ့မရှိသဖြင့် ထိုမိန်းမတစ်စုသည် ရေလိုသောမီးရထားခရီးသည်များ ရေအစေ့အငရအောင် အားထုတ်ကြသည်။ နေပူစပ်ခါးကို သူတို့မသိ ရေလိုချင်သူ ရေမရလိုက်မည်ကိုသာ သူတို့သိကြဟန်တူသည်။ ထို့ကြောင့် မိန်းမသားတန်မဲ့ အပြေးအလွှား ရေလိုက်ပေးကြခြင်း ဖြစ်သည်။**"**

(၂၀၁၂၊ ၁၅)

ဟူ၍လည်းကောင်း သရုပ်ဖော်ထားပါသည်။ ဤတွင် ကျေးလက် မိန်းမပျိုတစ်စု၏ ယဉ်ကျေးစွာပြောပုံ၊ နေပူစပ်ခါးကို အမှုမထားဘဲ အပြေးအလွှား ရေလိုက်ပေးကာ ကုသိုလ်ပြုပုံတို့သည် ကြည်နူး နှစ်သက်ဖွယ်ကောင်းပါပေသည်။ ဒါနဝိရရသကို ခံစားရပါသည်။

ကိုဖေသည် နွားလွှတ်ပွဲကို ဦးဆောင်သူဖြစ်သည်။ အဖော် သုံးလေးယောက်နှင့် ရပ်ရွာလှည့်ကာ ဇီဝတဒါနအတွက် အလှူခံသည်။ ရသမျှတို့ကိုစုကာ နွားသတ်ရုံမှ နွားကိုဝယ်သည်။ ထို့နောက် အလှူရှင်တို့ ဝမ်းမြောက်ရလေအောင် အတီးအမှုတ်၊ အကအခုန်တို့ဖြင့် ရပ်ရွာ လှည့်ကာပြသည်။ ဤသည်ကိုလည်း ဆရာဇော်ဂျီက-

> ". . .ထက်လှစွာသော ဓားအောက် လည်ပင်းရောက်နေသော နွားကို အရပ်က လှူလိုက်သော တစ်ပဲစု နှစ်ပြားစုနှင့် သူဝယ်သည်။ ထို့နောက် ချိုဖျားတွင် ပိတောက်ပန်းဆင်သည်။ နွားတစ်ကိုယ်လုံးကို သနပ်ခါးအမွှေးအကြိုင် လိမ်းကျံ ပက်ဖျန်းသည်။ နွားကျောပေါ်တွင် အလှအပကော်ဇော လွှားတင်သည်။ ထို့နောက် ပလွေသမား၊ အိုးစည်သမားများနှင့် ဒုတိယမွှဲ ရပ်ရွာကို လှည့်သည်" (၂၀၁၂၊ ၁၈)

ဟူ၍လည်းကောင်း၊

> "နောက်ဆုံးက အိုးစည်ပိုင်း။ အိုးစည်သံ၊ ပလွေသံ၊ လင်းကွင်းသံ၊ လက်ခုပ်သံ၊ သံချပ်ထိုးသံတို့သည် မြည်၍လိုက်လာကြသည်။ အိုးစည်ပိုင်း အရှေ့တွင် ဘေးမဲ့နွားကြီး၊ ပိတောက်ပန်းနှင့်၊ သနပ်ခါးနှင့်၊ ကတ္တီပါနှင့်၊ ကော်ဇောနှင့်၊ ဣန္ဒြေကြိုးနှင့်၊ သိင်္ခာနှင့်၊

တစ်လှမ်းခြင်း လှမ်း၍ပါလာသည်။ နွားကြီး၏ရှေ့တွင် ကိုဖေ၏အက၊ ကွေး၍၊ ကော့၍၊ ယိမ်း၍၊ ယိုင်၍၊ ရှေ့ဆုံးက သွားသည်။" (၂၀၁၂၊ ၂၀)

ဟူ၍လည်းကောင်း မြင်ယောင်၊ ကြားယောင် ခံစားလာရအောင် ရေးသား ထားပါသည်။ အသုံးပြစကားလုံးဖြစ်သည့် "နှင့်"ကို ဆက်တိုက်သုံး ထားသောကြောင့် နွားကြီး၏အဆင်တန်ဆာ အားလုံးတို့သည် တစ်စုတစ်စည်းတည်းဖြစ်လာပြီး တင့်တယ်သော၊ ကျက်သရေရှိသော၊ နွားကြီးအသွင်မှာ ပုံပေါ်လာသည်။ ထို့အတူ "၍"ကို ဆက်တိုက် သုံးထားသည်မှာလည်း ကွေးလိုက်၊ ကော့လိုက်၊ ယိမ်းလိုက်၊ ယိုက်လိုက်ဖြင့် လျင်မြန်စွာကနေသော ကိုဖေ၏ဟန်ကို မြင်ယောင်လာ စေသည်။ ဇီဝိတဒါနပြုလိုက်ရ၍ ကျေနပ်ပျော်ရွှင်နေသော ကိုဖေတို့ကို ကြည့်၍ ကြည်နူးခြင်း၊ ကျေနပ်ခြင်း၊ ကြည်ညိုခြင်းဖြစ်ရသည်။ သန္တရသခံစားရသည့် အဖွဲ့ကောင်းပင် ဖြစ်ပါသည်။

ဆရာဇော်ဂျီ၏ "နွေဦးကျက်သရေ" စာတမ်းသည် စာဖတ်သူတို့နှင့် ခံစားမှု တစ်ထပ်တည်းကျသဖြင့် နှစ်သက်မှု ရသကို ပေးစွမ်းနိုင်သည်ဟု ဆိုရမည်ဖြစ်ပါသည်။

၅။ ခြုံငုံသုံးသပ်ချက်

"ဆရာဇော်ဂျီ"၏စာပေလက်ရာ 'နွေဦးကျက်သရေ' ရသစာတမ်း သည် ရသစာတမ်း၏ သွင်ပြင်လက္ခဏာများနှင့် ကိုက်ညီမှု ရှိသည်ကို တွေ့ရှိရပါသည်။ ကိုယ်ရည်ကိုယ်သွေးပေါ်နေခြင်းတွင် စာရေးသူ၏ ကျေးဇူးရှိသူကို ကြည်ညိုတတ်သောစရိုက်၊ အမှားကို ဝန်ခံတတ်သော စရိုက်၊ မြန်မာမှုဓလေ့တို့ကို မြတ်နိုးသော၊ အားပေးသောစရိုက်တို့ ပေါ်လွင်နေကြောင်း တွေ့ရပါသည်။

အကြောင်းအရာထက် အတွေးအမြင်ခံစားမှုကို အားပြုခြင်းတွင် ဝတ်ကောင်းစားလှ၊ ဂုဏ်ဒြပ်တို့ထက် အစာလိုသူကို အစာ၊ ရေလိုသူကိုရေ ပေးလှူသည့် အပြုအမူတို့သည်လည်း စစ်မှန်သော ယဉ်ကျေးမှု တစ်ခုဖြစ်ကြောင်း တွေးပြ၊ ရေးပြထားသည်။ နွားလွှတ်ပွဲကို ကြည့်၍ မိမိတိုင်းပြည်ကို ကျွန်ဘဝမှ လွတ်မြောက်စေလိုသော အတွေးခံစားမှု ကိုလည်း တွေ့ရသည်။

စာဖတ်သူကို ဆွဲဆောင်နိုင်သောစကားပြေ အရေးအဖွဲ့မျိုး ဖြစ်ခြင်းတွင် နွေဦးပေါက်တိုင်း ရေချမ်းစင်ကို တည်ဆောက်ပေးသော မြန်မာတို့၏စိတ်၊ မြန်မာတို့၏ စေတနာအလှသည် နုပျိုလန်းဆန်း သစ်လွင်နေပုံကို တင်စားမှု၊ ပုံစံတူဟန်ချက်ညီဝါကျ၊ ဥပမာအလင်္ကာ၊ ဝိသေသစကားလုံး တို့ဖြင့် စာဖတ်သူကို ဆွဲဆောင်ရေးသားထားကြောင်း တွေ့ရပါသည်။

တိုတိုကျဉ်းကျဉ်းရေးဖွဲ့ထားသော အရေးအဖွဲ့မျိုးဖြစ်ခြင်းတွင် ရေချမ်းအိုးတည်ခြင်းနှင့် နွားဘေးမဲ့လွှတ်ခြင်းအကြောင်းကို အံဝင်ခွင်ကျ တိုတိုကျဉ်းကျဉ်း ရေးထားပေသည်။ "ရေချမ်းစင်ယဉ်ကျေးမှု"၊ "နွားလွှတ်ပွဲယဉ်ကျေးမှု"၊ "လူထုယဉ်ကျေးမှု" ဟူသော၀ိသေသ စကားလုံး အနည်းငယ်ဖြင့် ထိုယဉ်ကျေးမှုတို့အပေါ်ထားရှိသော ဆရာကြီး၏ သဘောထားကို လှစ်ပြနိုင်သည်မှာ ဆရာကြီး၏ အရေးအသား ကျွမ်းကျင်မှုပင် ဖြစ်သည်။

စာဖတ်သူကို နှစ်သက်မှုရသပေးခြင်းတွင် မိန်းမပျိုတစ်စု၏ နေပူစပ်ခါးကို အမှုမထားဘဲ အပြေးအလွှား ရေကုသိုလ်ပြုပုံကို ကြည်နူးနှစ်သက်ဖွယ် ဒါနဝီရရသ၊ ကိုဖေတို့၏ နွားလွှတ်ပွဲလှည့်ပုံကို ကြည်နူးခြင်း သန္တရသတို့ ခံစားရအောင် ရေးသားနိုင်စွမ်းရှိပါပေသည်။

ထို့ကြောင့် ဆရာဇော်ဂျီ၏ စာပေလက်ရာဖြစ်သည့် 'နွေဦး ကျက်သရေ' ရသစာတမ်းသည် ရသစာတမ်း၏ သွင်ပြင်လက္ခဏာများ ဖြစ်သည့် အချက်(၅)ချက်နှင့် ကိုက်ညီသည့် စာတမ်းကောင်းတစ်စောင် ဖြစ်သည်ဟု ဆိုနိုင်ပါသည်။

နိဂုံး

ဤစာတမ်းသည် "နွေဦးကျက်သရေ"ရသစာတမ်းမှ "ဆရာဇော်ဂျီ၏ စာပေလက်ရာကို ရသစာတမ်းအင်္ဂါရုပ်များဖြင့် လေ့လာတင်ပြထားသည့် စာတမ်းတစ်စောင်သာဖြစ်ပါသည်။ ကျန်စာရေးဆရာ(၉)ဦး၏ စာတမ်း များကိုလည်း ရသ စာတမ်း၏ အင်္ဂါရုပ်များဖြင့် လေ့လာသုတေသနပြုနိုင် ပါသေးသည်။ ဤ စာတမ်းကို ဖတ်ရှုလေ့လာခြင်းဖြင့် ဘဝအသိ၊ ဘဝအမြင်တစ်ခုခု ရလိမ့်မည်ဟု ယုံကြည်မိပါသည်။

ကျေးဇူးတင်လွှာ

ဤစာတမ်းကို ပြုစုခွင့်ရအောင် လမ်းပြခဲ့ကြသော သင်ဆရာ၊ မြင်ဆရာ၊ ကြားဆရာအပေါင်းတို့အား ဦးခိုက်ပူဇော်ကာ ကျေးဇူးတင်ကြောင်း မှတ်တမ်းတင်အပ်ပါသည်။

ကျမ်းကိုးစာရင်း

ခင်မင်၊ မောင်(ဓနုဖြူ)။ (၁၉၈၇)။ ***စာတမ်းဃ်စာပေ စာတမ်းများ၊ ပထမတွဲ***။ ရန်ကုန်၊ စာပေဗိမာန်ပုံနှိပ်တိုက်။

ဇော်ဂျီနှင့်အများနှင့်အများ။ (၂၀၁၂)။ ***ကံ့ကော်မြို့ငြိစာတမ်း***။ ရန်ကုန်၊ ရာပြည့်စာအုပ်တိုက်။

ဘသောင်း (ဗိုလ်မှူး)။ (၂၀၀၂)။ ***စာဆိုတော်များအတ္ထုပ္ပတ္တိ*** (ပဉ္စကြိမ်)။ ရန်ကုန်၊ ရာပြည့်စာအုပ်တိုက်။

မိုးမြေ၊ မ။ (၂၀၀၈)။ ***ဆရာဇော်ဂျီနှင့် ရသစာတမ်းရှင်တို့၏ တွေးဟန်နှင့်ရေးဟန်များ***။ ရန်ကုန်၊ ရွှေကံ့ကော်စာပေ။

ပြည်နဝဒေးနှင့် နတ်ရှင်နောင်တို့၏ မိုးတောရတုများမှ ရသမြောက်အဖွဲ့များ နှိုင်းယှဉ်လေ့လာချက်

ဒေါက်တာအေးအေးထွန်း[၁]

မြန်မာစာဌာန[၁], နည်းပညာတက္ကသိုလ် (မန္တလေး)[၁]

Email: drayeayehtun11@gmail.com[1]

စာတမ်းအကျဉ်း

ဤစာတမ်းသည် တောင်ငူခေတ်စာဆို ပြည်နဝဒေးနှင့် နတ်ရှင်နောင်တို့၏ မိုးတောရတုများမှ ရသမြောက်အဖွဲ့များကို နှိုင်းယှဉ်လေ့လာတင်ပြထားသော သုတေသနစာတမ်း ဖြစ်ပါသည်။ သော့ချက် ဝေါဟာရမှာ ရသဖြစ်သည်။ ရသသည် ရှေးဟောင်းဂန္ထဝင် မြန်မာစာပေနယ်ပယ်ရှိ ရတုကဗျာများ၏ အသက်သွေးကြောပမာ အရေးပါပုံကို သိရှိစေလိုသော ရည်ရွယ်ချက်ဖြင့် ရေးသားပြုစုခြင်း ဖြစ်ပါသည်။ စာပေနယ်ပယ်မှာ ရသစာပေနယ်ပယ် ဖြစ်သည်။ နဝဒေးရတု ပေါင်းချုပ်နှင့် နတ်ရှင်နောင်ဆိုရတုများ စာအုပ်တို့ကို အလေ့လာခံအဖြစ် သတ်မှတ်ပါသည်။ ဤစာတမ်းကို လေ့လာတင်ပြရာတွင် အခန်း(၁) ရတုဝေါဟာရနှင့် သဘောသဘာဝ၊ အခန်း(၂) ရသသဘောဖွင့်ဆိုချက်၊ အခန်း(၃) ပြည်နဝဒေးနှင့် နတ်ရှင်နောင်တို့၏ မိုးတောရတုများမှ ရသမြောက် အဖွဲ့များ နှိုင်းယှဉ်လေ့လာချက်ဟူ၍ အခန်း(၃)ခန်း ခွဲကာ လေ့လာတင်ပြထားပါသည်။ စာဆိုတို့၏ အတွေးစိတ်ကူး နှင့် အရေးအဖွဲ့စွမ်း ထက်မြက်ပုံတို့ကို လေးစားအတုယူဖွယ်တွေ့မြင်ရပါသည်။ ဤစာတမ်းသည် ရှေးမြန်မာစာပေနယ်ပယ်မှ ရတုကဗျာကို စိတ်ဝင်စားလေ့လာလိုသူများ၊ မြန်မာစာအထူးပြု ဆရာ၊ဆရာမများ၊ ကျောင်းသား ကျောင်းသူများ၏ ရတုကဗျာ သင်ကြားရေးအတွက် တစ်စုံတစ်ခုသော အကျိုးကျေးဇူး ပြုနိုင်မည်ဟု မျှော်လင့်မိပါသည်။

အထူးပြုသုတေသနနယ်ပယ် - ရသစာပေ၊ ရတု၊ ပြည်နဝဒေး၊ နတ်ရှင်နောင်

၁။ နိဒါန်း

ပြည်နဝဒေးနှင့် နတ်ရှင်နောင်တို့သည် တောင်ငူခေတ် ရတုကဗျာလောကကို ဦးဆောင်ခဲ့ကြသူများ ဖြစ်သည်။ ပြည်နဝဒေးကြီးသည် မင်းမူထမ်းစာဆိုဖြစ်၍ နတ်ရှင်နောင်သည် မင်းပျိုမင်းလွင် စာဆို ဖြစ်သည်။ ဤစာတမ်းသည် ရာသီဘွဲ့ ပိုဒ်စုံရတုများ ဖြစ်သည့် မိုးတောရတုများကို နှိုင်းယှဉ်တင်ပြထားခြင်း ဖြစ်ပါသည်။ ရာသီဘွဲ့ပိုဒ်စုံရတုများ ဖြစ်သည့် အလျှောက်ပထမပိုဒ်တွင် ရာသီသဘာဝအခြေအနေ၊ ဒုတိယပိုဒ်တွင် မောင်မယ်ဝေးကွာရသည့်အကြောင်းအရင်းနှင့် တတိယပိုဒ်တွင် မောင်မယ်တို့၏ အချစ်အလွမ်း အတွေးခံစားချက်တို့ဖြင့် ရေးဖွဲ့လေ့ရှိပါသည်။

ပြည်နဝဒေးနှင့် နတ်ရှင်နောင်တို့၏ မိုးတောရတုများမှ ရသမြောက်အဖွဲ့များက နှိုင်းယှဉ်လေ့လာရာတွင် ရတုကဗျာ လမ်းကြောင်းကို စတင်ခဲ့သော နဝဒေးကြီး၏ အတွေးစိတ်ကူးနှင့် အရေးအဖွဲ့စွမ်းရည်တို့ကို အဆို နတ်ရှင်နောင်က နည်းမှီးကာဖွဲ့ဆို ထားပုံ၊ အကြံတူ နောက်လူကောင်းစမြဲ ဆိုသည့်အတိုင်း နဝဒေးထက် နတ်ရှင်နောင်က မင်းပျိုမင်းလွင်ပီပီ အတွေးစိတ်ကူး ကောင်းပုံ၊ အရေးအဖွဲ့စွမ်းရည်သာလွန်ပုံတို့ကို နှိုင်းယှဉ် တင်ပြထားပါသည်။ ဤသုတေသနစာတမ်းတွင် ဂန္ထဝင် ရတု စာဆိုကြီးနှစ်ဦး၏ ရသမြောက်အဖွဲ့များကို နှိုင်းယှဉ်လေ့လာ တင်ပြထားပါသည်။

၂။ အခန်း(၁) ရတုဝေါဟာရနှင့် သဘောသဘာဝ

ရတုဟူသော ဝေါဟာရသည် မြန်မာဘာသာ စကားရတု လည်းရှိသည်။ ပါဠိ၊ သက္ကတဘာသာမှ ဆင်းသက်လာသည်လည်းရှိသည်ဟု ပညာရှင်များက အမျိုးမျိုး ကြံဆကြပါသည်။

ရတုဟူသော ဝေါဟာရနှင့်ပတ်သက်၍ ဝေါဟာရလီနတ္ထပကာသနီကျမ်းတွင် -

"ရတုဟူသည်ကား သက္ကတဘာသာ၌ ရိအက္ခရာ တွင်တုစပ်လျက် (ရိတု)ဖြစ်သည်။ ထိုရိတု သဒ္ဒါကို မြန်မာလို ရတုဟု ခေါ်သည်။" [၇]

ဟူ၍ ဖွင့်ဆိုထားပါသည်။ ကဗျာဗန္ဓသာရကျမ်းတွင် -

"ရတုဆိုသည်မှာ မြန်မာဘာသာ ပေါရာဏ သက်သက် ရတုလည်း ရှိသည်။ သက္ကတ ဘာသာ(ရိတု)မှ ပျက်ပြယ်ရွေ့လျားလာသော မြန်မာဘာသာ ရတုလည်း ရှိသည်။" [၂]

ဟု ဖွင့်ဆိုထားပါသည်။ ကဗျာသာရတ္ထသင်္ဂြိဟ်တွင် -

"ရတုဟူသောစကား၏ အနက်အဓိပ္ပါယ် အကျဉ်းမှာ ဂိမှန္တဥတု၊ ဝသန္တဥတု၊ ဟေမန္တဥတုဟူသော နွေ၊မိုး၊ဆောင်း ကာလ အချိန်များကို ပါဠိဘာသာ၌ ဥတု၊သင်္ဝစ္ဆရိ၌ ဘာသာ၌ ရိတုဟု ခေါ်သဖြင့် ဆယ့်နှစ်ရာသီဘွဲ့ ကဗျာတို့ကို ရတုဟု ခေါ်သည်။" [၉]

ဟု ဖွင့်ဆိုထားပါသည်။ မြန်မာစာပေသမိုင်းတွင် -

"ရတုဟူသည် သက္ကတဘာသာရိတုမှ ပျက်လာ သော ရတုလည်း ရှိသည်။ ပေါရာဏသက်သက် ရတုလည်း ရှိသည်။ သက္ကတဘာသာရိတုမှာ အခါရာသီ အနက်ရ၍ မြန်မာဘာသာ ရတုမှာ အခြေအနေဟူသောအနက်၊ အချိန်အခါ ဟူသော အနက်၊ အခမ်းအနားဟူသောအနက် သုံးမျိုး ရသည်။" [၅]

ဟု ဖွင့်ဆိုထားပါသည်။ မြန်မာအဘိဓာန်တွင် -

"ရတု/ယဒု/န - လေးလုံးတစ်ပိုဒ် ရေးဖွဲ့သော ကဗျာတစ်မျိုး" (သ၊ရိတု) [၈]

ဟူ၍ ဖွင့်ဆိုထားပါသည်။

ဤသို့ပညာရှင်အသီးသီး၏ အဓိပ္ပါယ်ဖွင့်ဆိုချက်များအရ ရတုဟူသောဝေါဟာရမှာ သက္ကတဘာသာရိတု၊ ပါဠိဘာသာ ဥတုတို့မှလာ၍ အခါရာသီအနက်ရကြောင်း၊ ထိုမှအခါရာသီတို့၏ တင့်တယ်မှုနှင့် မွေ့လျော်ပျော်ပိုက်ဖွယ်တို့ကို ဖွဲ့သီထားသော ကဗျာလင်္ကာဟု ဆိုနိုင်ပါသည်။

တစ်ဖန် ရတုကဗျာဖွဲ့ဆိုသည့် အကြောင်းအရာနှင့် ပတ်သက်၍ ဘုရားတိုင်၊ ကျေးစေ၊ စစ်ချီ၊ မြို့ဘွဲ့၊ မယ်ဘွဲ့၊ မောင်ဘွဲ့၊ ရာသီဘွဲ့၊ ပန်းဘွဲ့ စသည်ဖြင့် အမျိုးစုံ ဖွဲ့ဆိုခဲ့ကြပါသည်။ တစ်ပိုဒ်စပ်လျှင် ဧကပိုဒ်၊ နှစ်ပိုဒ်စပ်လျှင် အဖြည့်ခံ၊ သုံးပိုဒ်စပ်လျှင် ပိုဒ်စုံရတု ဟူ၍လည်း တွေ့ရပါသည်။ စပ်ဆိုရာတွင် အချီ၊ အချ၊ ကာရန်၊ အသတ် ညီရပါသည်။

ထို့ကြောင့် ရတုကဗျာသည် စာဆို၏ အာရုံ(ဖ)ပါးတွင် တွေ့ကြုံထင်ဟပ်နေသည်များကို အခြေခံ၍ စိတ်ကူးဉာဏ် ကွန့်မြူးကာ နှစ်သက်ဖွယ် ဖြစ်အောင် ရေးဖွဲ့ထားသောကဗျာ ဖြစ်သည်။ ထိုသို့ ရေးဖွဲ့ရာတွင် ပိုဒ်ရေအရလည်းကောင်း၊ ပဒအရေအတွက် အရလည်းကောင်း ကန့်သတ်ချက် ရှိကြောင်း လေ့လာ တွေ့မြင်ရပါသည်။

၃။ အခန်း(၂) ရသသဘောဖွင့်ဆိုချက်

ရသ ဟူသောဝေါဟာရ၏ အနက်အဓိပ္ပါယ်ကို ပညာရှင် များက အမျိုးမျိုးဖွင့်ဆိုခဲ့ကြပါသည်။

အလင်္ကာနိသျကျမ်းတွင် -

"သာမဒ္ဓိကာနံ၊ ပွဲကြည့်သောသူတို့၏၊ ဗန္ဓထ္ထာနုသ္သရိနံ၊ သီချင်း၊ ရတု၊ ကဗျာ အစရှိကုန်သောအဖွဲ့၏အနက်ကို အောက်မေ့ဆင်ခြင်ကုန်သောသူတို့၏၊ ယောအာနန္ဒေါ၊ အကြင်နှစ်သက်အပ်သော သဘောကို၊ ရသီယတိ၊ ပျားထောပတ် အစရှိသော အရသာတို့ကို စားရာ သာယာဘိသက္ခဲသို့၊ သာယာအပ်၏၊ ဣတိ၊ ထို့ကြောင့်၊ အယံ၊ ဤသာယာအပ်၊ နှစ်သက်အပ်သောသဘောကို၊ တညူဟိ၊ ထိုရသကို သိသောပညာရှိတို့သည် ရသောနာမ၊ ရသမည်၏၊" [၆]

ဟူ၍ ဖွင့်ဆိုထားပါသည်။ မြန်မာအလင်္ကာကျမ်းတွင် -

"သူတော်ကောင်းတရားကို နှစ်သက်သာယာခြင်း၊ ပွဲလမ်းသဘင်၊ အကအခုန်၊ အပြောအဟော၊ ကဗျာလင်္ကာ အသိအကုံး အရေးအသားတို့၌ နှစ်သက်သာယာမက်မောခြင်းကို ရသဟု ခေါ်သည်။" [၄]

ဟု နှစ်သက်ခြင်းနှင့် ပတ်သက်၍ ရသကို ရှင်းပြ ထားပါသည်။ ထို့ကြောင့် ရသဟူသည် နှစ်သက်ခြင်းနှင့် ယှဉ်သော စာပေ၊ အနုပညာအရသာပင် ဖြစ်ပါသည်။

၄။ အခန်း(၃) ပြည်နဝဒေးနှင့် နတ်ရှင်နောင်တို့၏ မိုးတောရတု များမှ ရသမြောက်အဖွဲ့များ နှိုင်းယှဉ်လေ့လာချက်

ဤသုတေသနစာတမ်းသည် တောင်ငူခေတ်တွင် ထင်ရှားကျော်ကြားခဲ့သော ဂန္ဓဝင်စာဆိုကြီးနှစ်ဦး၏ မိုးတောရတု များမှ ရသမြောက်အဖွဲ့များကို နှိုင်းယှဉ်လေ့လာတင်ပြထားသော စာတမ်း ဖြစ်ပါသည်။ သိဂီရရသ၊ ကရုဏာရသနှင့် ဘယာနက ရသတို့ကို စာဆိုတစ်ဦးချင်းစီမှ အတွေးစိတ်ကူးခံစားချက်တို့ဖြင့် ရသမြောက်အဖွဲ့များအဖြစ် ဖန်ဆင်းဖွဲ့နွဲ့ခဲ့သည်ကို နှိုင်းယှဉ် တင်ပြသွားမည် ဖြစ်ပါသည်။

၄၊၁။ သိဂီရရသ

သိဂီရရသကို မြန်မာအလင်္ကာကျမ်းတွင် -

> “သူတော်ကောင်းတရား၌မွေ့လျော်ခြင်း၊
> ချစ်ကြိုက်ခြင်း” [၄]

ဟု ဖွင့်ဆိုထားပါသည်။ မြန်မာအဘိဓာန်တွင် -

> “ချစ်ခင်နှစ်သက်မှုရသ” [၈]

ဟု ဖွင့်ဆိုထားပါသည်။ထို့ကြောင့် သိဂီရရသတွင် တရားမမှ၌ မွေ့လျော်ခြင်း ဓမ္မသိဂီရရသနှင့် မောင်မယ် တို့၏ အချစ်၊အလွမ်း အဖွဲ့တို့ကြောင့် ခံစားလာရသော နှစ်သက်မှုနှင့်ယှဉ်သည့် ကာမသိဂီရရသ ဟူ၍ ရှိပါသည်။ ဓမ္မသိဂီရရသကို မြန်မာအလင်္ကာ ကျမ်းတွင် -

> “သူတော်ကောင်းတရား၌ မွေ့လျော်ပျော်ပိုက်ခြင်း ဟူသော သမထ၊ ဝိပဿနာ၊ ဘာဝနာသည် ဓမ္မသိဂီရရသ မည်၏” [၄]

ဟူ၍လည်းကောင်း၊ ကာမသိဂီရ ရသကို -

> “(က) ကိုယ်လက်ထိပါးခြင်းမရှိသေးဘဲ မြင်ရုံ၊ စကား ကမ်းလှမ်းရုံမျှလောက်သာ ချစ်ခင်ရသော အယောဂ သိဂီရရသ၊
>
> (ခ) ကိုယ်လက်နှီးနှောထိပါးခြင်းသို့ ရောက်အောင် ချစ်ခင်ရသော သမ္ဘောဂသိဂီရရသ၊
>
> (ဂ) ပေါင်းသင်းပြီးမှသော်လည်းကောင်း၊ မပေါင်းသင်းရသေးမီသော်လည်းကောင်း၊ သေကွဲ၊ ရှင်ကွဲ နှစ်မျိုးမျိုးဖြင့် ကွဲကွာ ရသော ဝိယောဂသိဂီရရသ” [၄]

ဟူ၍လည်းကောင်း ခွဲခြားဖွင့်ဆိုထားပါသည်။

တောင်ငူခေတ်တွင် ထင်ရှားကျော်ကြားခဲ့သော စာဆို နဝဒေးကြီး၏ မိုးတောရတုများတွင် အယောဂသိဂီရရသမြောက် အဖွဲ့များကို တွေ့နိုင်ပါသည်။ "တနေကသည်”ချီ မိုးတောရတု တွင်-

> “နောင့်တွင်ကြောင်းခ၊ ခြည်မယတည့်၊ စိတ်ကဖျော်ဖြေ၊ တိမ်မြှပ်နေလည်း၊ ထွေထွေကြံရေး၊ မှာမှာသေးမူ၊ ဝေးသည်အပ၊ ဝမ်းကထွေပြား၊ တပါးအမှတ်၊ တိမ်းညွတ်ထားဖီ၊ မရှိပြီတည့်၊ စိတ်ညီဘောက်ပြန်၊ ကျွန်လည်းမအား၊ သူတခြားဝယ်၊ ပါးလိုက်ဆင့်မှာ။ ။ လျှောက်စေလှာသည် ကြာလှ၏” [၃]

ဟု ဖွဲ့ဆိုထားပါသည်။ ဤအဖွဲ့တွင် ချစ်သူမောင်က မယ်လေးအပေါ် မေတ္တာသက်ဝင်ကြောင်း ပြောကြား ခဲ့ပါသည်။ မယ်လေးသည် မောင်၏မေတ္တာကို မတုံ့ပြန် သေးသော်လည်း အခြားတစ်ပါးသူအပေါ် စိတ်တိမ်းညွတ် ခြင်းလည်း မရှိပေ။ ထို့ကြောင့် ချစ်သူမောင်အနေဖြင့် မယ်လေးထံမှ တုံ့ပြန်စကားကို မျှော်လင့်စောင့်စား နေရသည်မှာ ကြာညောင်းနေပြီ ဖြစ်ကြောင်း ဖွဲ့ဆို ထားပါသည်။ ချစ်သူမောင်၏ တစ်ဖက်သတ်အချစ်ကို ပေါ်လွင်လာအောင် ဖွဲ့ဆိုထားသောကြောင့် အယောဂ သိဂီရရသမြောက်ပါသည်။

မင်းပျိုမင်းလွင်စာဆိုဖြစ်သော နတ်ရှင်နောင်၏ မိုးတောရတုများတွင် တစ်ဖက်သတ်အချစ်ကို ဖွဲ့ဆို ထားသော အယောဂသိဂီရရသမြောက် အဖွဲ့များကို မတွေ့ရပေ။ နဝဒေးကြီး ၏ မိုးတောရတုများတွင်သာ အယောဂသိဂီရရသမြောက်အဖွဲ့များကို တွေ့ရပါသည်။ သမ္ဘောဂသိဂီရ ရသမြောက်အဖွဲ့ကိုမူ စာဆိုနှစ်ပါးစလုံး၏ မိုးတောရတုများတွင် မတွေ့ရပေ။

ရတုကဗျာတို့မည်သည် ဇာတ်လမ်း၊ ဇာတ်ကွက် ဆင်၍ စိတ်ကူးယဉ်ရေးဖွဲ့ထားခြင်းမျိုး မဟုတ်ပေ။ စာဆိုတို့၏ အတွေ့အကြုံနှင့် စိတ်ခံစားချက်ကို ဖွဲ့ဆိုသော ကဗျာမျိုးဖြစ်သည်။ ထို့ပြင် စာဆိုတို့သည်လည်း စစ်သည်စာဆိုများ ဖြစ်ကြသောကြောင့် စစ်ချီထွက် ရသည်။ မောင်မယ်နှစ်ဦး ကွဲကွာနေရသည့်အချိန်က များသည်။ ထို့ကြောင့် မောင်မယ်နှစ်ဦး ကြည်နူးရွှင်မြူး နေသော အကြောင်းအရာတို့ကို ဖွဲ့ဆိုသော သမ္မောဂ သိဂီရရသမြောက်အဖွဲ့များကို မတွေ့ရခြင်း ဖြစ်ပါသည်။

စာဆို နဝဒေးနှင့်နတ်ရှင်နောင်တို့၏ မိုးတောရတုများတွင် ဝိယောဂသိဂီရ ရသမြောက်အဖွဲ့ များစွာကို တွေ့မြင်နိုင်ပါသည်။ နဝဒေး၏ “တစိတ်စိတ်လျှင်”ချီ မိုးတောရတုတွင် -

“ရှုအီဘွယ်တည့်၊ ဖြိုးအင်ပြည့်သား၊ သို့သည့်ခါတွင်၊ မွေ့ရာခွင်ဝယ်၊ မရွှင်ယောင်းနွမ်း၊ နေကြောင့် သမ်းသည့်၊ ရေချမ်းကားဝေး၊ ပန်းကြာမွှေးသို့၊ ငြိမ့်လေးစလှ၊ ဆင်းမြမြသည်။ ။ပျောင်းပျ

စက်ရာ ခွေလိမ့်မည်” [၃]

ဟု ဖွဲ့ဆိုထားပါသည်။ ဤအဖွဲ့တွင် ကောင်းခြင်းငါးဖြာနှင့် ပြည့်စုံ၍ ရှုမငြီးအောင်လှပသော မယ်လေးသည် မိမိကို လွမ်းသည့်စိတ်ကြောင့် ရေဝေးသော ကြာပမာ နွမ်းလျကာ စက်ရာခွေလျော့နေလိမ့်မည်ဟု စစ်မြေပြင်ရောက် ချစ်သူမောင် က တွေးတောပူပန်ကြောင့်ကြစိတ် ဖြစ်ပေါ်ရပုံကို ဖွဲ့ဆိုထား ပါသည်။ တစ်ဖက်မှလည်း မယ်လေး၏ အလွမ်းခံစားချက်ကိုပါ ပေါ်လွင်အောင် ဖွဲ့ဆိုထားသောကြောင့် ဝိယောဂသိဂီရရသ မြောက်ပါသည်။

တစ်ဖန် စာဆိုနတ်ရှင်နောင်၏ မိုးတောရတုများတွင် လည်း ဝိယောဂသိဂီရရသမြောက်အဖွဲ့များကို တွေ့နိုင်ပါသည်။

“ခက်ခြည်လျှံဝေ”ချီ မိုးတောရတုတွင် -

“သိဂ်ရည်လေး၊ ပြစ်မျိုးဝေးနှင့်၊ ပိုက်ထွေးတူစုံ၊ ပျော်ရတုံမူ၊ မခြံသော်လည်း၊ လုံလှတော့မည်၊ မှတ်သည်ကိုသာ၊ ဘော်ကွာနှောင့်နှေး၊ ချစ်သူဝေးခဲ့” [၁]

ဟု ဖွဲ့ဆိုထားပါသည်။ ဤအဖွဲ့တွင် သိဂီရွှေစင်၏ အရောင်ကဲ့သို့ အသားအရေဝင်းဝါစိုပြည်၍ အပြစ်ဟူသမျှကင်းဝေးသော ချစ်သူ မယ်လေးနှင့် အတူတကွယုယပိုက်ထွေးကာ ပျော်ရွှင်စွာနေရပါ က၊ မထွေးသော်လည်းနွေး၊ မခြံသော်လည်းလုံမည်ဟု တွေးထင် ခံစားနေမိပါသည်။ သို့သော် မောင်မယ်နှစ်ဦးဆုံစည်းရန် နှောင့်နှေးကြန့်ကြာ နေကြောင်း ဖွဲ့ဆိုထားသောကြောင့် ဝိယောဂ သိဂီရရသမြောက်ကြောင်း တွေ့ရပါသည်။

စာဆို၏ “တာရက်လကို”ချီ မိုးတောရတုတွင် -

“စစ်တပ်မြေတာ၊ ရုပ်ရာထူးခြား၊ ဝေးလေ ငြားလည်း၊ စက်ပါးတွင်ပင်၊ ထင်တုံရေးရေး၊ ချစ်စိတ်ပြေးသည်။ ။ မဝေး ရှုမြော်မိ၏သို့” [၁]

ဟု ဖွဲ့ဆိုထားပါသည်။ ဤအဖွဲ့တွင် ချစ်သူမောင်သည် အလွန် ဝေးလံသီခေါင်သော စစ်မြေစခန်းတွင် ရောက်နေပါသော်လည်း မောင်မယ်နှစ်ဦး၏ ကူးလူး ယှက်နွယ်နေသော မေတ္တာစိတ် ကြောင့် အနီးအပါးတွင် ရှိနေသကဲ့သို့ မှတ်ထင်ယုံကြည်နေမိသည့်စာဆို၏ အတွေးစိတ်ကူးကို ပေါ်လွင်အောင် ရေးဖွဲ့ထားသော ကြောင့် ဝိယောဂသိဂီရရသကို ခံစားလာစေပါသည်။

နဝဒေးနှင့် နတ်ရှင်နောင်တို့၏ မိုးတောရတု များမှ ဝိယောဂသိဂီရရသမြောက်အဖွဲ့များကို နှိုင်းယှဉ် လေ့လာရာတွင် နဝဒေးကြီးသည် စစ်ထွက်ချစ်သူမောင် အား မျှော်လင့်စောင့်စား ကာလွမ်းနေသောမယ်လေး၏ အလွမ်းခံစားချက်များ၊ မိမိအား လွမ်းနေမည့် မယ်လေး အပေါ် တွေးတောပူပန်နေသည့် မောင်၏ ခံစားချက် များကို ပေါ်လွင်အောင် ဖွဲ့ဆိုထားသော ဝိယောဂ သိဂီရ ရသမြောက်အဖွဲ့ကို တွေ့ရပါသည်။ စာဆိုနတ်ရှင်နောင် ကမူ စစ်မြေပြင်ရောက် ချစ်သူမောင်က အနေဝေး သော်လည်း မောင်မယ်နှစ်ဦး၏ ကူးလူးယှက်နွယ်နေသော မေတ္တာစိတ်ကြောင့် အနီးအပါးတွင် ရှိနေသည်ဟု ထင်မှတ်နေမိပုံ၊ ချစ်သူမယ်လေးနှင့် အတူတကွ ယုယပိုက်ထွေးကာ ပျော်ရွှင်စွာနေရပါက နွေးထွေးလုံခြုံမှု ရှိသည်ဟု ခံစားမှတ်ထင်မိပုံတို့ဖြင့် ဝိယောဂသိဂီရ ရသမြောက်အောင် ဖွဲ့ဆိုထားကြောင်း တွေ့ရပါသည်။

မင်းမူထမ်းစာဆို၊ စစ်သည်စာဆိုများ ဖြစ်သည့် အားလျော်စွာ မင်းရေးတာဝန်ဖြင့်ဖြစ်စေ၊ စစ်ရေး

တာဝန်ဖြင့် ဖြစ်စေ၊ ချစ်သူနှင့်ခွဲခွာ၍ အဝေးတစ်နေရာ၌ ရှိနေစဉ် ချစ်သူကို လွမ်းဆွတ်တမ်းတကြောင်း၊ ချစ်သူ မယ်လေးကလည်း မိမိကို လွမ်းဆွတ်တမ်းတနေမည် ဖြစ်ကြောင်းတို့ဖြင့် အချစ်၊အလွမ်း ခံစားချက်တို့ကို ဖွဲ့ဆိုထားသည့် ဝိယောဂသိင်္ဂီရရသမြောက်အဖွဲ့ များကိုမူ စာဆိုနှစ်ဦးလုံး၏ မိုးတောရတုများတွင် အများဆုံး တွေ့ရခြင်းဖြစ်ပါသည်။

၄၊၁၊၁။ ကရုဏာရသ

ကရုဏာရသကို မြန်မာအလင်္ကာကျမ်းတွင် -

“စိုးရိမ်ကြောင့်ကြ၊ သနားကြင်နာခြင်း"[၄]

ဟု ဖွင့်ဆိုထားပါသည်။ မြန်မာအဘိဓာန်တွင် -

“သနားကြင်နာမှုရသ” [၈]

ဟု ဖွင့်ဆိုထားပါသည်။ ထို့ကြောင့် ကရုဏာရသဟူသည် ခံစားရသော ဒုက္ခဝေဒနာ၊ စိုးရိမ်သောက ဗျာပါရစိတ်တို့ကြောင့် ဆောက်တည်ရာမရသော သောက ကရုဏာတရားတို့ကို မြင်ယောင်လာအောင်၊ ကူးစက် ခံစားလာရအောင် ဖွဲ့ဆိုထားခြင်း မျိုးဖြစ်သည်။ စာဖတ်သူ၌ သနားကရုဏာသက်လာစေလျှင် ထိုအဖွဲ့ သည် ကရုဏာရသမြောက်အဖွဲ့ ဖြစ်ပါသည်။

တောင်ငူခေတ်တွင် ထင်ရှားကျော်ကြား ခဲ့ကြသော စာဆိုနဝဒေးနှင့် နတ်ရှင်နောင်တို့၏ မိုးတော ရတုများတွင် ကရုဏာရသမြောက်အဖွဲ့များကို တွေ့နိုင်ပါ သည်။ စာဆို နဝဒေးကြီး၏ “မွန်းချက်ပ-ရှောင်”ချီ ရတုတွင် -

“ရာဇူသဘ၊ ဘူမစိုးရန်၊ ထွတ်ဘုန်းသန်မူ၊ သွေလှန် ယောင်ယောင်၊ ခွာရှောင်လိုလို၊ ဆိုဖြွက်ဘိလေ၊ ရက်သောထွေကို၊ ကုဋ္ဌေထောင်ရာ၊ နှစ်ရှည် ကြာလည်း၊ ဘယ်မှာမေ့ကျန်၊ ကြင်ဆလွန်ခဲ့၊ ထွတ်စွန် ဘုံနေ၊ သူဇာ့ဆွေလည်း၊ ညွတ်ခွေဝမ်းနည်း၊ မယ်ချည်း ဘော်ကွာ၊ စက်ဘုံသာဝယ်၊ ဗျာပါညှိုးသမ်း၊ လွမ်းသည် တချက်၊ ရှက်သည်တကြောင်း၊ လျောင်းလည်းမသာ၊ နေလှည့်ရာကို၊ အာကာဝန်းကျင်၊ ရွာရုပ်ဆင်သည်။ ။ နတ်ရှင်မြူးချိန်လွဲသောကြောင့်” [၃]

ဟူ၍ ဖွဲ့ဆိုထားပါသည်။ ဤအဖွဲ့တွင် တစ်ရာသော ထီးဆောင်းမင်းတို့၏ အရှင်သခင် ဘုန်းတန်ခိုး ကြီးမြတ်သော ချစ်သူမောင်သည် မယ်လေးအား ချစ်မြတ်နိုးခဲ့ပါသည်။ သို့သော် ယခုအခါတွင် မယ်လေးအား သွေဖည်လိုဟန်၊ ရှောင်လွဲလိုဟန်များဖြင့် ရက်စက်သောစကားများ ပြောဆိုခဲ့ပါသည်။ ထိုသို့သော စိမ်းကားသည့်စကားများကို နှစ်၊လ၊မည်မျှ ကြာမြင့် သော်လည်း မယ်လေးက မမေ့နိုင်ပါ။ စိတ်မနာနိုင်ဘဲ ချစ်ခင်ကြင်နာမှုများ တိုးပွားလာခဲ့ပါသည်။ ချစ်သူ၏ စွန့်ပစ်ခြင်းခံရသော မိမိအဖြစ်ကို တွေး၍လည်း ရှက်မိသည်။ စိမ်းကားရက်စက်သော ချစ်သူမောင် ကိုလည်း လွမ်းနေမိပါသည်။ မယ်လေး၏ ခံစားချက်ကို သနားကရုဏာသက်လာအောင် ဖွဲ့ဆိုထားသောကြောင့် ကရုဏာ ရသမြောက်ပါသည်။ စာဆိုနတ်ရှင်နောင်၏ မိုးတောရတုတွင် လည်း ကရုဏာရသမြောက်အဖွဲ့များကို တွေ့နိုင်ပါသည်။ "တပေါင်းကစင်”ချီ မိုးတောရတုတွင် -

“နေ့ညရောက်လာ၊ ကြားကားကြားပြန်၊ မမှန် တို့ဘူး၊ နွေဦးကိုမျှ၊ နေ့ညမပြည့်၊ ထင်တုံလှည့်ရှင့်၊ ဘယ်သည့်ရေးရာ၊ စစ်မြေတာဝယ်၊ ကြောင်းချာရှိထွေ၊ မြင့်မောလေဟု၊ မင်းနေမှာသက်၊ မမေးရက်တည့်” [၁]

ဟု ဖွဲ့ဆိုထားပါသည်။

ဤအဖွဲ့တွင် စစ်ထွက်သွားသော ချစ်သူမောင်သည် မည်သည့်အချိန်ရောက်လိမ့်မည် ဟူသည့် သတင်းများမှာ သတင်းမှားများသာဖြစ်နေသည်။ ချစ်သူမောင်ရောက်မည် ဆိုသောနေ့၊ ရောက်မည်ဆိုသော ညတို့မှာ မျှော်လင့်စောင့်စားရသူ မယ်လေးအဖို့ ကုန်လွယ်လွန်းလှပါသည်။ မယ်လေးအနေဖြင့် ချစ်သူမောင်ပြန်ရောက်မည့်ရက်ကို မျှော်ရဖန် များလာသောအခါ နွေဦးရာသီဖြစ်ပါလျက် နေ့တာရော ညတာပါ အချိန်ပြည့်ပြည့်ဝဝ ရှိပါလေစဟု တွေးထင် မိပါသည်။ စစ်မြေပြင်တွင် အကြောင်းဘယ်သို့ရှိ၍ ကြာမြင့်နေကြောင်းကို သိလိုသော်လည်း ချစ်သူ မောင်အား မမေးရက်သော မယ်လေး၏အဖြစ်ကို စာနာ သနားဖွယ် ဖွဲ့ဆိုထားသောကြောင့် ကရုဏာရသ မြောက်ပါသည်။ တစ်ဖန် စာဆို၏ “နွေနှောင်းရက်လျှင်”ချီ ရတုတွင် -

“မည်းမိုက်အုံ့ပျ၊ မြောက်ရပ်ကလည်း၊ အစရိုက်ဆင့်၊ ကျူးလာရင့်၍၊ လေနှင့်မိုးပါ၊ ရွာလှာထပ်လောင်း၊

မှီလျောင်းအုံးဝန်း၊ ခြူးပန်းပုလဲ၊ မစဲပြိုက်ကျ၊ ပျောင်းပျသည်းဆူး၊ စိတ်ကိုနှူးသည်။ ။
ကိုယ်ထူးမတည်နွမ်းဘိသည်” [၁]

ဟူ၍ ဖွဲ့ဆိုထားပါသည်။ မြောက်အရပ်ဆီမှ မိုးရောလေပါ ရွာသွန်းတိုက်ခတ်လာသဖြင့် မှီအုံးထက်တွင် တစ်ကိုယ်တည်း ဖြေမဆည်နိုင်အောင် နွမ်းလျနေပုံ အလွမ်းသရုပ်ကို ဖွဲ့ဆိုထားပါသည်။ အလွမ်းဓာတ်ခံရှိသူ မယ်လေးအား မိုးနှင့်လေကပါ ဝိုင်းကူ၍ အလွမ်းစိတ်ကို နှူးပေးသကဲ့သို့ ဖြစ်တည်နေပုံတို့ကို ဖွဲ့ဆိုထားသောကြောင့် ကရုဏာရသမြောက်ပါသည်။

နဝဒေးနှင့်နတ်ရှင်နောင်တို့၏ မိုးတောရတုများမှ ကရုဏာရသမြောက်အဖွဲ့များကို နှိုင်းယှဉ်လေ့လာခဲ့ပါသည်။ ထိုသို့လေ့လာရာတွင် နဝဒေးကြီးသည် ချစ်သူမောင်၏ သစ္စာပျက်ယွင်းမှုကြောင့် ခံစားနေရရှာသော မယ်လေး၏ အလွမ်း၊ စစ်ချီသွားသော ချစ်သူမောင် ပြန်ရောက်ချိန်တွင် ရောက်မလာသောကြောင့် စိုးရိမ်သောကရောက်နေရှာသော မယ်လေး၏အလွမ်းတို့ဖြင့် ကရုဏာရသမြောက်အောင် ရေးဖွဲ့ထားကြောင်း တွေ့ရပါသည်။ စာဆိုနတ်ရှင်နောင်ကမူ စစ်ထွက် ချစ်သူမောင် ပြန်လာမည့်သတင်းကို မျှော်လင့်စောင့်စားကာ လွမ်းနေသောမယ်လေး၏ စိုးရိမ်ကြောင့်ကြစိတ်နှင့်ယှဉ်သည့် အလွမ်း၊ လေနှင့်အတူ ရွာသွန်းလာသောမိုးကြောင့် မယ့်တစ်ကိုယ်တည်း ဆောက်တည်ရာမရအောင် အထူးတလည် လွမ်းဆွတ် တမ်းတကာ နွမ်းလျနေရှာတော့မည် ဖြစ်ကြောင်း ကရုဏာမြောက်စွာ ရေးဖွဲ့နိုင်စွမ်းရှိကြောင်း တွေ့ရပါသည်။

၄၊၁၊၂။ ဘယာနက ရသ

ဘယာနကရသကို အလင်္ကာနိသျကျမ်းတွင် -

“ဘောက်ပြန်သော၊ ကြောက်မက်ဖွယ်ရှိသော အသံ၊ ဘီလူးအစရှိသော သတ္တဝါတို့ကြောင့် ကြောက်လန့်ခြင်းသည်။ ဘယာနကော၊ ဘယာနကရသမည်၏” [၆]

ဟူ၍လည်းကောင်း၊ မြန်မာအလင်္ကာကျမ်းတွင် -

“ဆိုးဝါးနက်ကျယ်သော အသံမျိုးကို ကြားရ၍ ကြောက်လန့်ခြင်းမျိုးသည် ဘယာနကရသမည်၏” [၄]

ဟူ၍လည်းကောင်း ဖွင့်ဆိုထားပါသည်။ ထို့ကြောင့် ကြောက်မက်ဖွယ်၊ ထိတ်လန့်ဖွယ် ခံစားရပုံများကို ဖွဲ့ဆိုထား၍ ဖတ်ရှုကြားနာသူတို့အား ကြောက်ရွံ့သော ခံစားချက်မျိုးကို ကူးစက်ခံစားလာစေနိုင်သောအဖွဲ့သည် ဘယာနကရသ ဖြစ်ပါသည်။

တောင်ငူခေတ်တွင် ထင်ရှားကျော်ကြားခဲ့ကြသော နဝဒေးနှင့်နတ်ရှင်နောင်တို့၏ မိုးတောရတုများတွင် ဘယာနက ရသမြောက်အဖွဲ့များကိုမူ အနည်းငယ်မျှသာ တွေ့ရပါသည်။ စာဆိုနဝဒေးကြီး၏ “မည်းလေစွလေ”ချီ မိုးတောရတုတွင် -

“ထစ်ရင့်ကြွေးဟစ်၊ လောင်မီးပစ်သို့၊ မြရစ်သီတာ၊ သွန်းချရွာသော်၊ မြောက်မှာလေမူ၊ မိုးကကူ၍၊ တိမ်ဖြူမထင်၊ မှောင်တိပင်လျှင်” [၃]

ဟု ဖွဲ့ဆိုထားပါသည်။ ဤအဖွဲ့တွင် ကောင်းကင်တစ်ခွင်လုံး မည်မှောင်၍ မိုးခြိမ်းသံများကလည်း ကျယ်လောင်စွာထစ်ချုန်း မြည်ဟည်းလျက် ရှိပါသည်။ လျှပ်ရောင်များကလည်း လောင်မီး ကျသကဲ့သို့ အဆက်မပြတ် ပြက်သန်းလျက်ရှိပါသည်။ မိုးကလည်း ပတ်ဝန်းကျင်တစ်ခွင်လုံး စိမ်းညိုမည်းမှောင်နေအောင် ရွာသွန်းလျက်ရှိပါသည်။ ဖော်ကွာဝေးနေသော ချစ်သူ မယ်လေးအား ထိတ်လန့်စိုးရွံ့အောင် ဖန်တီးနေသည့် ရာသီ သဘာဝအခြေအနေကို ကြောက်မက်ဖွယ် ဖွဲ့ဆိုထားသောကြောင့် ဘယာနက ရသမြောက်ပါသည်။

တစ်ဖန် တောင်ငူခေတ်စာဆိုနတ်ရှင်နောင်၏ မိုးတော ရတုတွင်လည်း ဘယာနကရသမြောက်အဖွဲ့ကို တွေ့ရပါသည်။ စာဆို၏ “အာကာတသွန်”ချီ မိုးတော ရတုတွင် -

“အုံ့ပျိမှိုင်းဆန်း၊ လျှပ်ပန်းပြကာ၊ မလာမရိပ်၊ ချိပ်ချိပ်မည်းမည်း၊ ရိုက်ကြည်းအုံးအင်း၊ ခြင်းခြင်းညီးညီး၊ လောင်မီးပွင့်ဝါ၊ ဆင်တိုင်းပါ၍” [၁]

ဟူ၍ ဖွဲ့ဆိုထားပါသည်။ ဤအဖွဲ့တွင် ပတ်ဝန်းကျင်တစ်ခွင်လုံး အဆန်းတကြယ် မည်မှောင်အုံ့မှိုင်းကာ မိုးခြိမ်းသံများကလည်း ကျယ်လောင်စွာ ထစ်ချုန်းမြည်ဟည်းလျက် ရှိပါသည်။ လျှပ်စီးများက မိုးသားတိမ်ရိပ်များ ရွှေ့လျားရာသို့ လိုက်ပါနေပုံ၊ လောင်မီးကျသကဲ့သို့ အဆက်မပြတ် ပြက်သန်းနေပုံနှင့် ကျယ်လောင်

ပြင်းထန်စွာ ထစ်ချုန်းနေသော မိုးခြိမ်းသံတို့ဖြင့် စာဆို၏ ကြောက်ရွံ့ထိတ်လန့်စွာ ခံစားနေရသောအဖြစ်ကို ပေါ်လွင်လာအောင် ဖွဲ့ဆိုနိုင်သောကြောင့် ဘယာနကရသ မြောက်ပါသည်။

နဝဒေးနှင့်နတ်ရှင်နောင်တို့၏ မိုးတောရတု များမှ ဘယာနကရသအဖွဲ့များကို နှိုင်းယှဉ်လေ့လာ ခဲ့ပါသည်။ ထိုသို့ လေ့လာရာတွင် စာဆိုနှစ်ဦးစလုံးသည် မိုးခြိမ်းသံများ၊ လျှပ်ပြက်ဟန်များနှင့် အာကာတစ်ခွင်လုံး မည်းမှောင်အုံ့မိုင်းကာ မိုးရိပ်ဆင်နေပုံတို့ဖြင့် ကြောက်မက်ဖွယ် ရာသီသဘာဝတို့ကို ဘယာနက ရသမြောက်အောင် ဖန်တီးဖွဲ့ဆိုနိုင်ကြောင်း လေ့လာ တွေ့မြင်ရပါသည်။ ရတုစာဆိုတို့သည် အများအားဖြင့် မောင်မယ်တို့၏အချစ်၊ အလွမ်းခံစားချက်များ၊ ဆွတ်ပျံ့လွမ်းမောဖွယ်ရာ အကြောင်းအရာများကိုသာ ရတုကဗျာ အဖြစ် သီကုံး ဖွဲ့နွဲ့လေ့ရှိကြပါသည်။ ထို့ကြောင့် မိုးတောရတုများတွင် ဘယာနက ရသမြောက်သော အဖွဲ့ကို အနည်းငယ်မျှသာ တွေ့နိုင်ပါသည်။

၅။ ခြုံငုံသုံးသပ်ချက်

. ပြည်နဝဒေးနှင့်နတ်ရှင်နောင်တို့၏ မိုးတောရတု များမှ ရသမြောက်အဖွဲ့များကို နှိုင်းယှဉ်လေ့လာရာတွင် စာဆိုနှစ်ဦး လုံး၏ မိုးတောရတုများတွင် မိုး၏အင်္ဂါရုပ်များကို ထည့်သွင်းရေးဖွဲ့လေ့ရှိကြောင်း တွေ့ရပါသည်။ ရာသီဘွဲ့ ကဗျာဖြစ်သည့် အားလျော်စွာ မိုးရာသီသဘာဝ အခြေအနေများက ဖော်ကွာဝေးနေသော မောင်မယ်တို့၏ အချစ်၊ အလွမ်း ခံစားချက်တို့ကို ရုပ်လုံးကြွလာအောင် ပံ့ပိုး ပေးနေ ကြောင်းလည်း တွေ့ရပါသည်။ ထိုသို့ အလွမ်း ခံစားချက်များ ပိုမို ရုပ်လုံးကြွလာလေ ရသမှာလည်း ပီပြင် ပေါ်လွင်လာလေ ဖြစ်ကြောင်းတွေ့ရပါသည်။ မိုးတော ရတုများမှ ရသများကို ဖန်တီးရာတွင် စာဆိုနဝဒေးကြီး၏ အတွေးစိတ်ကူးကို အခြေခံ၍ နတ်ရှင်နောင်က ဆန်းသစ်သော စိတ်ကူးဉာဏ် ကွန့်မြူးကာ ထူးခြားကောင်းမွန်သော ရသမြောက် အဖွဲ့များအဖြစ် ဖန်တီးဖွဲ့ ဆိုထားကြောင်း တွေ့ရပါသည်။

သင်္ဂီရရသ ဖန်တီးရာတွင် စာဆိုနဝဒေးကြီး၏ မိုးတော ရတုတွင်သာ အယောဂသင်္ဂီရရသအဖွဲ့ကို တွေ့ရပါသည်။ မင်းပျို မင်းလွင်ဖြစ်သော နတ်ရှင်နောင်၏ မိုးတောရတုတွင်မူ အယောဂ ရသမြောက်အဖွဲ့ကို မတွေ့ရပေ။ သို့သော် တောင်ငူခေတ်တွင် ဂန္ဓဝင်စာဆိုကြီးများအဖြစ် ကျော်ကြားခဲ့ကြသော နဝဒေးနှင့် နတ်ရှင်နောင်တို့၏ မိုးတောရတုများတွင် ဝိယောဂသင်္ဂီရ ရသမြောက်အဖွဲ့များစွာကို လေ့လာတွေ့ရှိရပါသည်။

တစ်ဖန် နဝဒေးကြီးသည် မိုးတောရတုများမှ ကရုဏာရသမြောက်အဖွဲ့ကို ဖန်တီးရာတွင် ချစ်သူ မယ်လေးဘက်မှ မည်သို့မည်ပုံ ခံစားနေရရှာ တော့မည်ဆိုသော အတွေးမျိုးဖြင့် ရသကို ဖန်တီးဖွဲ့ဆိုလေ့ရှိကြောင်း တွေ့ရပါသည်။ စာဆို နတ်ရှင်နောင်ကမူ မိမိခံစားရသကဲ့သို့ ချစ်သူမယ်လေး သည်လည်း တစ်ကိုယ်တည်း ဆောက်တည်ရာ မရ ခံစားနေရတော့မည်ဟု သောကနှင့်ယှဉ်ကာ ရသကို ဖန်တီးသောကြောင့် နဝဒေးကြီးထက် နတ်ရှင်နောင်၏ ရသဖန်တီးမှုမှာ ပိုမိုကောင်းမွန်ကြောင်း လေ့လာတွေ့ မြင်နိုင်ပါသည်။ ဘယာနက ရသဖန်တီးမှုကို နှိုင်းယှဉ် လေ့လာရာတွင် စာဆိုနှစ်ဦးစလုံးသည် မိုးတောရတု ပီသစွာ မိုးခြိမ်းပုံ၊ လျှပ်ပြက်ပုံ၊ ကောင်းကင်တစ်ခွင်လုံး အုံ့မှိုင်းကာ မိုးရိပ်ဆင်နေပုံတို့ဖြင့် ကြောက်မက်ဖွယ် ရာသီသဘာဝ အခြေအနေတို့ကို ဘယာနက ရသမြောက်အောင် ဖွဲ့ဆိုထားနိုင်ကြောင်း လေ့လာ တွေ့မြင်နိုင်ပါသည်။

ရတုစာဆိုတို့သည် အများအားဖြင့် မောင်မယ် တို့၏ အချစ်အလွမ်းခံစားချက်များ၊ ဆွတ်ပျံ့လွမ်းမော ဖွယ်ရာ အကြောင်းအရာများကိုသာ ရတုကဗျာအဖြစ် သီကုံးဖွဲ့နွဲ့လေ့ ရှိကြပါသည်။ သင်္ဂီရရသသည် ရတုကဗျာ တို့၏ ပန်းတိုင်ရသ ဖြစ်ပါသည်။ ထို့ကြောင့် ဘယာနက ရသမြောက်အဖွဲ့များကို အနည်းငယ်မျှသာ ဖွဲ့ဆိုလေ့ ရှိသည်ဟု ထင်မြင်ယူဆမိပါသည်။

၄။ နိဂုံး

ဤသုတေသနစာတမ်းသည် ပြည်နဝဒေးနှင့် နတ်ရှင်နောင်တို့၏ မိုးတောရတုများမှ ရသမြောက်

အဖွဲ့များကို နှိုင်းယှဉ်လေ့လာတင်ပြထားသော စာတမ်းတစ်စောင် ဖြစ်ပါသည်။ နောက်နှောင်းစာပေ လေ့လာသူတို့အတွက် သုတေသန နယ်ပယ်များစွာ ကျန်ရှိနေပါသေးသည်။ ရှေးဟောင်းဂန္ထဝင်မြန်မာကဗျာ လေ့လာလိုက်စားလိုသူများနှင့် သင်ကြားရေး ဆရာ၊ဆရာမများအတွက် အကျိုးကျေးဇူး တစ်စုံတစ်ရာ ဖြစ်ထွန်းမည်ဟု မျှော်လင့်မိပါသည်။

ကျမ်းကိုးစာရင်း

[၁] ချမ်းမြေ၁ဦး၊(တည်းဖြတ်)။ (၁၉၆၃)။ ***နတ်ရှင်နောင်ဆိုရတုများ***။ မန္တလေးမြို့။ တက်နေလင်းပုံနှိပ်တိုက်။

[၂] တင်၊ဦး၊(ပုဂံဝန်ထောက်မင်း)။ (၁၉၆၉)။ ***ကဗျာဗန္ဓသာရကျမ်း နှင့်နောက်ဆက်တွဲသုံးပိုင်း***။ ရန်ကုန်မြို့။ လယ်တီမဏ္ဍိုင် ပုံနှိပ်တိုက်။

[၃] နဝဒေး။ (၁၉၆၄)။ နဝဒေးရတုပေါင်းချုပ်။ ရန်ကုန်မြို့။ ဟံသာဝတီ ပုံနှိပ်တိုက်။

[၄] ပဏ္ဍိတထေရ်၊အရှင်၊(ရွှေဟင်္သာဆရာတော်)။(၁၉၇၅)။ မြန်မာ အလင်္ကာကျမ်း၊(ဒု-ကြိမ်)။ရန်ကုန်မြို့။သင့်ဘဝ ပုံနှိပ်တိုက်။

[၅] ဖေမောင်တင်၊ဦး။ (၁၉၅၈)။ ***မြန်မာစာပေသမိုင်း***။ ရန်ကုန်မြို့။ တက္ကသိုလ်များ ပုံနှိပ်တိုက်။

[၆] ဘိုးလှိုင်၊ဦး၊(ယောအတွင်းဝန်)။(၁၉၃၈)။***အလင်္ကာနှိ သျှက***။ ရန်ကုန်မြို့။ ဇမ္ဗူမိတ်ဆွေပိဋကတ်စာပေနှင့် ပုံနှိပ်တိုက်။

[၇] မဟာဇေယျသခ်ိဳယာ။ (၁၉၆၃)။ ***ဝေါဟာရလီနတ္ထပကာသနီ ကျမ်း***။ ရန်ကုန်မြို့။ ရန်ကုန်၊ဟံသာဝတီ ပုံနှိပ်တိုက်။

[၈] မြန်မာစာအဖွဲ့။ (၂၀၀၈)။ ***မြန်မာအဘိဓာန်၊(ဒု-ကြိမ်)***။ ရန်ကုန်မြို့။ တက္ကသိုလ်များ ပုံနှိပ်တိုက်။

[၉] လွန်း၊ဆရာ၊(သခင်ကိုယ်တော်မှိုင်း)။ (၁၉၅၅)။ ***ကဗျာသာရတ္ထသင်္ဂြိဟ်***။ ရန်ကုန်မြို့။ ရန်အောင်မင်္ဂလာ ပုံနှိပ်တိုက်။

လောကနီတိကျမ်းလာ လူမှုရေးလမ်းညွှန်ချက်အဖွဲ့များ

ဒေါက်တာခင်မျိုးထွန်း

ပါမောက္ခ၊ ဌာနမှူး

မြန်မာစာဌာန, ရန်ကုန်နည်းပညာတက္ကသိုလ်

khinmyotun370@gmail.com

စာတမ်းအကျဉ်း

ဤစာတမ်းသည် မြန်မာစာပေနယ်ပယ် စကားပြေကဏ္ဍလာ လောကနီတိကျမ်းတွင် တွေ့ရသော လူမှုရေးလမ်းညွှန်ချက်အဖွဲ့များကို လေ့လာသုံးသပ်ထားသုတေသနပြုထားသည့် စာတမ်းဖြစ်ပါသည်။ ရည်ရွယ်ချက်မှာ လောကရှိ လူသားတို့အနေဖြင့် လိုက်နာကျင့်သုံးသင့်သည့် လူမှုရေးလမ်းညွှန်ချက်များကို သိရှိစေလိုခြင်းဖြစ်သည်။ စံကျောင်းဆရာတော်၏ လောကနီတိဖွင့် အကျယ်လင်စွဲကျမ်းကို အလေ့လာခံအဖြစ် ထားရှိပါသည်။ ထိုသို့လေ့လာတင်ပြရာတွင် ဦးအုန်းသော်၏ စာရေးနည်း ၄ မျိုးကို အခြေခံကာ လူမှုရေးလမ်းညွှန်ချက်များကို ပုံပေါ်စေသောရေးသားနည်း စနစ်ဖြင့် တင်ပြထားပါသည်။ အပိုင်းကဏ္ဍ (၇)ခုကို တွေ့ရှိရပြီး လောကနီတိကျမ်းအကြောင်းကို လေ့လာနေသူများအတွက် များစွာအထောက်အကူ ပြုနိုင်ပါသည်။

သော့ချက်ဝေါဟာရ - ပဏ္ဍိတ၊ သုဇန၊ ဗာလဒဇ္ဈန၊ မိတ္တ၊ ဣတ္ထိ၊ ရာဇ၊ ပကိဏ္ဏတ

၁။ နိဒါန်း

"နီတိ" ဟူသည်မှာ ပါဠိစကားဖြစ်ပြီး ဆောင်ခြင်း၊ နည်းညွှန်လမ်းပြခြင်းဟူ၍ အနက်ဆောင်ပါသည်။ လောကနီတိသည် လောကအတွက် လိုက်နာဆောင်ရွက်ရန် နည်းညွှန်လမ်းပြခြင်း ဆိုင်ရာ စာစုများဖြစ်သည်။ **လောကနီတိကျမ်းကို အဦးအစပြုစုခဲ့သူမှာ ပင်းယခေတ်စာဆို အမတ်ကြီးစတုရင်္ဂဗလ(၆၇၅ခန့်-၇၂၅ခန့်) [၅] (စာ-၄၁)** ဖြစ်သည်။ လောကနီတိကျမ်းလာ လူမှုရေးလမ်းညွှန်ချက်အဖွဲ့များကို လေ့လာတင်ပြရာတွင် အခန်း(၇)ခန်းဖြစ်သည့် ပညာရှိကို ဖွဲ့ဆိုသောအခန်း၊ သူတော်ကောင်းကို ဖွဲ့ဆိုသောအခန်း၊ သူယုတ်မာကို ဖွဲ့ဆိုသောအခန်း၊ မိတ်ဆွေကို ဖွဲ့ဆိုသောအခန်း၊ မိန်းမကို ဖွဲ့ဆိုသောအခန်း၊ မင်းကို ဖွဲ့ဆိုသော အခန်းနှင့် အထွေထွေကို ဖွဲ့ဆိုသောအခန်းဟူ၍ အခန်းကဏ္ဍများ ခွဲခြားကာ လေ့လာတင်ပြထားပါသည်။

၁.၁။ ဆရာတော်၏ထေရုပ္ပတ္တိအကျဉ်း

ညောင်တုန်းရွှေဟာသံတောရ စံကျောင်းဆရာတော် အရှင်ဝါယမကို ပဲခူးမြို့နယ်၊ ကျောက်တန်းကြီးရွာ၌ ခမည်းတော် လှေသူကြီးဦးအောင်လု၊ မယ်တော်ဒေါ်အောင်တို့က ၁၂၃၅ ခု တပေါင်းလဆန်း ၁၀ ရက် (၂၅ ဖေဖော်ဝါရီ ၁၈၇၄) ဗုဒ္ဓဟူးနေ့တွင် ဖွားမြင်ခဲ့ပြီး မွေးချင်း ၈ ယောက်တွင် ၇ ယောက်မြောက် ဖြစ်သည်။ ငယ်မည်မှာ မောင် ဉာဏ်ဖြစ်သည်။ ဆရာတော်သည် ၇ နှစ်သားအရွယ်၌ ကျောက် တန်းရွာ ရွာလယ်ကျောင်း ဆရာတော်ထံ ပညာသင်ယူခဲ့သည်။ မင်္ဂလသုတ်ပရိတ်ကြီး၊ နမက္ကာရ၊ လောကနီတိ၊ ဇာတ်အဋ္ဌကထာ၊ ကစ္စည်းသဒ္ဒါ၊ ကိုးကြောင်း မကာရန္တဖေဒင်တို့ကို သင်ယူတတ် မြောက်ခဲ့သည်။ ၁၈ ဝါရလာသောအခါ "စံကျောင်းဆရာတော်" အဖြစ် ချီးမြှောက် ခြင်းခံရသည်။ ဆရာတော် ပြုစုခဲ့သောကျမ်း များမှာ လောက နီတိဖွင့်အကျယ်ကျမ်း၊ အတွင်းအောင်ခြင်း၊ အပြင်အောင်ခြင်း အဖွင့်ကျမ်း၊ မေတ္တာအဖွင့်ကျမ်း၊ ယထာဘူတ ဝိနိစ္ဆယကျမ်း၊ အလင်္ကာနိသျကျမ်း အစရှိသည်တို့ဖြစ်သည်။ **သက်တော် ၇၃-နှစ်၊ သိက္ခာတော် ၅၄ ဝါအရ ၁၃၀၉ ခု ဝါခေါင် လပြည့်ကျော် ၁ ရက်(၂ ဩဂုတ် ၁၉၄၇) စနေနေ့ နံနက် ၄ နာရီ ၂၀ မိနစ်တွင် ဇီဝိတိန္ဒြေချုပ်ငြိမ်းတော်မူသည်။ [၂] (စာ-၁၃)**

၁.၃။ နီတိ ဟူသောဝေါဟာရအဖွင့်

နီတိဟူသော အနက်အဓိပ္ပာယ်ကို ဦးဟုတ်စိန်၏ ပါဠိ-မြန်မာအဘိဓာန်တွင် **"နီတိ (ပါဠိ)= ဆောင်ခြင်း၊ နည်းပြသော ကျမ်း၊ နီတိကျမ်း" [၈] (စာ-၅၄၉)** ဟူ၍ ဖွင့်ဆိုထားသည်။ နီတိကို ပင် ဦးထွန်းမြင့်က ပါဠိသက်ဝေါဟာရအဘိဓာန်တွင် **"နီတိ = ကြီးပွားတိုးတက်ခြင်းသို့ ပို့ဆောင်သောလမ်းညွှန်။ ယင်းတို့ကို ဖော်ပြ သောကျမ်း" [၄] (စာ-၁၃၇)** ဟူ၍ ဖွင့်ဆိုထားပြီး **"လောက" ကို "လောက= ၁။ သက်ရှိသတ္တဝါများ။ အထူးသဖြင့် လူအားလုံး။ သတ္တလောက။ ၂။ သတ္တဝါတို့တည်နေရာဘုံ။ ဩကာသလောက။ ၃။ မျက်မှောက်။ တမလွန်ဘဝ" [၄] (စာ-၂၇၈)** ဟူ၍ ဖွင့်ဆိုထားသည်ကို တွေ့ရပါသည်။

တင်စိုး၏ ပြည်သူ့နီတိနှင့် လက်တွေ့ဘဝစာအုပ်တွင် လောကနီတိနှင့်ပတ်သက်၍ **"လောကနီတိ ဟူသော ပါဠိစကား လုံး၏ "လောက" ဆိုသည်မှာ မိမိတို့ နေထိုင်ကြီးပြင်းရာ လူ့ဘောင်လောကကို ရည်ညွှန်း၍ "နီတိ" ဆိုသည်မှာ ဆောင်ရန်/ရှောင်ရန် လမ်းညွှန်ချက်များဟု ဆိုလိုသည်။ ထို့ကြောင့် "လောကနီတိ" ကျမ်းဟူသည် လူ့ဘောင်လောကအတွင်း သွားလာနေထိုင်ကြသော လူတို့၏ နေနည်း၊ ထိုင်နည်းနှင့် ပြုမူ**

ဆောင်ရွက်ဖွယ်ရာ အဖြာဖြာကို နည်းပေးလမ်းပြ ဆိုဆုံးမထားသော ကျမ်းဖြစ်သည်။ ထိုကျမ်းကို လေ့လာမှတ်သား လိုက်နာကျင့်သုံးလျှင် ကောင်းကျိုးချမ်းသာ အမျိုးမျိုးရရှိနိုင်သည်။" [၃] (စာ-၅၇) ဟု ဆိုထားသည်။ ထို့ကြောင့် လောကနီတိကျမ်းဟူသည် သက်ရှိ သတ္တဝါလူအားလုံးကို ကြီးပွားတိုးတက်အောင် နည်းလမ်းပြလမ်းညွှန်သောကျမ်းဟု ဆိုရမည်ဖြစ်ပါသည်။

၂။ စာပေလေ့လာဆန်းစစ်ချက်

လူမှုရေးလမ်းညွှန်ချက်အဖွဲ့များနှင့် ပတ်သက်၍ ညောင်တုန်းမြို့၊ ရွှေဟင်္သာတောရ အဂ္ဂမဟာပဏ္ဍိတ စံကျောင်းဆရာတော်ဘုရားကြီး ပြုစုစီမံရေးသားဖွင့်ဆိုခဲ့သော "လောကနီတိဖွင့် အကျယ်လက်စွဲကျမ်း"၊ လောကနီတိနှင့်ပတ်သက်၍ ဦးဟုတ်စိန်၏ ပါဠို-မြန်မာအဘိဓာန်၊ ဦးထွန်းမြင့်၏ ပါဠိသက်ဝေါဟာရ အဘိဓာန်၊ အမှာတော်ရေးဦးရှင်ကလေး၏ လောကနီတိပျို့ဆုံးမစာ၊ ဦးသုခ၏ လောကနီတိ၊ တင်စိုး၏ ပြည်သူ့နီတိနှင့် လက်တွေ့ဘဝအစရှိသည့် စာအုပ်များကို ဖတ်ရှုလေ့လာခဲ့ပါသည်။

၃။ သုတေသနမေးခွန်းနှင့် ပြဿနာ

. လောကနီတိကျမ်းလာ လူမှုရေးလမ်းညွှန်ချက်အဖွဲ့များ လေ့လာချက်စာတမ်းကိုပြုစုရာတွင် အောက်ဖော်ပြပါသုတေသနမေးခွန်းများ ထွက်ပေါ်လာနိုင်ပါသည်။

၁။ လောကနီတိကျမ်းကို အဘယ့်ကြောင့် လူမှုရေးလမ်းညွှန်ချက်ရှုထောင့်မှ လေ့လာရသနည်း။

၂။ ထိုသို့လေ့လာရာတွင် လူမှုရေးလမ်းညွှန်ချက်များ ပေါ်လွင်မှုရှိပါသလား။

အဆိုပါမေးခွန်းများအတွက် စိစစ်လေ့လာချက်အနေဖြင့် အလေ့လာခံ လောကနီတိဖွင့် အကျယ်လက်စွဲကျမ်းကို လည်းကောင်း၊ လူမှုရေးလမ်းညွှန်ချက်အဖွဲ့များကို ပေါ်လွင်စေသည့် နည်းနာများကို လည်းကောင်း သုတေသနအစီအစဉ်ဖြင့် ဤစာတမ်းတွင် သုံးသပ်သုတေသနပြု တင်ပြထားပါသည်။

၄။ လောကနီတိကျမ်းလာ လူမှုရေးလမ်းညွှန်ချက်အဖွဲ့များ

လောနီတိကျမ်းလာ လူမှုရေးလမ်းညွှန်ချက်အဖွဲ့များကို အပိုင်း (၇) ပိုင်းခွဲ၍ လေ့လာတင်ပြသွားပါမည်။

၄၊၁။ ပဏ္ဍိတကဏ္ဍလာ လူမှုရေးလမ်းညွှန်အဖွဲ့များ

ပဏ္ဍိတကဏ္ဍ(ပညာရှိကို ဖွဲ့ဆိုသော) လာ လမ်းညွှန်ချက်များကို ဆရာတော်က အကျယ်ဖွင့်ဆိုရာ၌ နီတိသင်ရခြင်း၏ အကျိုးပြဆိုကြောင်းမှ ပညာရှိနှင့်ပေါင်းမိမှ ပညာရှိဖြစ်နိုင်ကြောင်းထိ အချက်(၄၀)ပြဆိုထားသည်။ ယင်းကို အကျဉ်းမျှ ထုတ်နုတ်တင်ပြပါမည်။ ပညာရှိအကြောင်းရေးသားရာတွင်-

"အလဿ ကုတော သိပ္ပံ၊ အသိပ္ပဿ ကုတော ဓနံ၊ အဓနဿ ကုတော မိတ္တံ၊ အမိတ္တဿ ကုတော သုခံ၊ အသုခဿ ကုတော ပုညံ၊ အပုညဿ ကုတော ဝဏ္ဏံ" [၇] (စာ-၂၁) ဟူ၍ ပျင်းရိသောသူကား အတတ်ပညာ မတတ်နိုင်ပုံ၊ အတတ်ပညာမရှိသူကား ဥစ္စာမရနိုင်ပုံ၊ ဥစ္စာမရှိသူကား အဆွေခင်ပွန်းမရနိုင်ပုံ၊ အဆွေခင်ပွန်းမရှိသူကား ချမ်းသာခြင်း မရှိနိုင်ပုံ၊ မချမ်းသာသူကား ကုသိုလ်ကောင်းမှု မပြုလုပ်နိုင်ပုံ၊ ကုသိုလ်ကောင်းမှု မပြုနိုင်သူကား ဗုဒ္ဓဘာသာဝင်များကို အကျိုးသင့် အကြောင်းသင့် ပြဆိုထားသည်ကို တွေ့ရပါသည်။

အမှာတော်ရေး ဦးရှင်ကလေး၏ လောကနီတိပျို့ဆုံးမစာတွင်လည်း **"နိတုံရွှေနှယ်၊ ကျေးဇူးကြွယ်သား၊ မှတ်ဖွယ်သုတ၊ ဆည်းပူးကြလေ့၊ ပျင်းလှသည်သူ၊ ဘယ်မှုအတတ်၊ ရတုံလတ်အံ့၊ အတတ်ကင်းလျှင်၊ ဘယ်တွင်ဥစ္စာ၊ ရတို့ပါလိမ့်၊ ဥစ္စာမရ၊ ရှိလတ်ကမူ၊ ကြည်ဖြူချစ်ခင်၊ မိတ်မမြင်တည့်၊ မိတ်လျှင်မရ၊ သုခဘယ်မှာ၊ ပွားတို့ရှာလိမ့်၊ ချမ်းသာတစ်၊ မရှိလတ်မူ၊ အလှူကောင်းမှု၊ ဘယ်ကိုပြုအံ့၊ ကောင်းမှုမသန်၊ နိဗ္ဗာန်ဘယ်မှာ၊ ရတို့ပါအံ့၊ မြဲစွာမှတ်လေ၊ တတ်မြောက်ချေက၊ ရွှေငွေမတူ၊ ခိုးယူမရ၊ ဤလောကခွ်၊ ပညာ့အရာ၊ မိတ်ကြီးသာတည့်၊ ခန္ဓာပြောင်းကြွ၊ နောင်ဘဝလည်း၊ သုခမြားမြောင်၊ ချမ်းသာဆောင်သည်၊ လူ့ဘောင်မှတ်လေ့-တသင်းတည်း" [၆] (စာ-၃၂၁)** ဟူ၍ ပိုဒ်ရေ(၁၅)ပိုဒ်ဖြင့် ပညာကို အပတ်တကုတ်ရှာဖွေသင့်ကြောင်း၊ ပျင်းရိသောသူသည် အတတ်ပညာမရနိုင်ဘဲ အဆုံးတွင် နိဗ္ဗာန်မရနိုင်ကြောင်း ဖွဲ့ဆိုထားသည်။ ထို့ပြင် နှုတ်မှုပညာကိုလည်းကောင်း၊ လက်မှုပညာကိုလည်းကောင်း ငယ်၏ဟူ၍ မအောက်မေ့ဘဲ ကုန်စင်အောင် တတ်မြောက်သင့်ကြောင်း၊ အိုးလုပ်သောသူသည် မိမိအိုးကို ကွဲစိမ့်ငှာ ပုတ်ခတ်သည်မဟုတ်ဘဲ တင့်တယ်စေသောငှာ ပုတ်ခတ်သကဲ့သို့ ဆရာကောင်းတို့သည် တပည့်တို့ကို အတတ်ပညာတတ်မြောက်စေလိုခြင်းငှာ ရိုက်နှက်ပေးခြင်းဖြစ်ကြောင်းတို့ကို အပြည့်အစုံဖွဲ့ဆိုထားသည်ကို တွေ့ရပါသည်။ ဤ လမ်းညွှန်ချက်များသည် လူ့လောကတွင် လိုက်နာကျင့်ကြံလုပ်ဆောင်သင့်သည့် လူမှုရေးလမ်းညွှန်ချက်အဖွဲ့များဟု ဆိုရပါမည်။

၄၊၂။ သုဇနကဏ္ဍလာ လူမှုရေးလမ်းညွှန်ချက်အဖွဲ့များ

သုဇနကဏ္ဍ(သူတော်ကောင်းကို ဖွဲ့ဆိုသော) လာ လမ်းညွှန်ချက်အဖွဲ့များကို ဆရာတော်က အကျယ်ဖွင့်ဆိုရာ၌ သူတော်ကောင်းတို့နှင့်သာ ပေါင်းဖော်သင့်ကြောင်းမှ သူယုတ်ကို နှစ်သက်က အကျိုးပျက်စီးကြောင်းထိ အချက်(၂၆)ချက်တိုင်ဖွဲ့ဆိုထားသည်။ သူတော်ကောင်းတရားနှင့်ပတ်သက်၍ သူတော်ကောင်းတို့ကိုသာ ပေါင်းသင်းဆက်ဆံသင့်ကြောင်း၊ သူတော်ကောင်းတို့၏ စိတ်နှလုံးဖြူစင်မှုနှင့် သူတော်ကောင်းတရား လက်ကိုင်ထားသင့်ကြောင်းကို ဆရာတော်က **"ယထာပိ, ပနသ, ပဏ္ဍာ၊ ဗဟိ, ကဏ္ဍာ ကမေဝစ။ အန္တာအမတာ သမွန္နာ၊ ဧဝံ သုဇန ဟဒ္ဒဟာ"[၁](စာ-**

၇၁) ဟူ၍ ပိန္နဲသီးမှည့်တို့သည်ကား အပြင်အပဒ္ဒ ဆူးတို့သာရှိကုန်သော်လည်း အတွင်းပိုင်းတွင်မူ အမြိန်အရသာ ရှိသည်ဖြစ်သကဲ့သို့ သူတော်ကောင်းတို့၏ စိတ်နှလုံးသည်လည်း ထပ်တူဖြစ်ကြောင်း ကျိုးကြောင်းပြရှင်းလင်းထားပါသည်။ ထို့အတူ လောကတွင် စန္ဒကူးပင်တို့သည် ခြောက်သွေ့သော်လည်း အနံ့ကို မစွန့်ကြောင်း၊ ဆင်ပြောင်သည် စစ်မြေပြင်သို့ရောက်သော်လည်း လူတို့၏ရှေ့တွင် တင့်တယ်ခြင်းကို မစွန့်ကြောင်း၊ ကြံပင်သည် ယန္တရားစက်၏ ရှေ့ကိုရောက်သော်လည်း ချိုသောအရသာကို မစွန့်သကဲ့သို့ပင် သူတော်ကောင်းတို့သည် မည်သို့ပင်ဆင်းရဲခြင်းသို့ရောက်စေကာမူ သူတော်ကောင်းတရားကို မစွန့်ကြကြောင်း ပြဆိုထားသည်ကို တွေ့ရပါသည်။

အမှာတော်ရေး ဦးရှင်ကလေး၏ လောကနီတိပျို့ဆုံးမစာတွင်လည်း **"ပိန္နဲသီးမှာ၊ ဆူးသာပြင်ပ၊ အတွင်းကျသော်၊ ချိုမြိန်အံ့ချီး၊ စားမငြီးသို့၊ မိတ်ကြီးသူတော်၊ ပေါင်းစသော်မူ၊ အပေါ်လောကွတ်၊ ကျင့်မြဲဝတ်ဖြင့်၊ မချွတ်သေခွေ၊ ကြာလေလေပင်၊ ကောင်းအင်လွန်ပြီး၊ ကျေးဇူးကြီး၏၊ သစ်သီးနှစ်ပါး၊ ပမာထားသည်၊ ထင်ရှားယုတ်မြတ် နှစ်ဖြာတည်း" [၆] (စာ-၃၂၆)** ဟူ၍ သူတော်ကောင်းနှင့် ပေါင်းဖော်လျှင် အကျိုးကြီးမားကြောင်းလမ်းညွှန်ထားသည်ကို တွေ့ရပါသည်။ အပိုဒ်(၆)ပိုဒ်ဖြင့် ပိန္နဲသီး၏ ချိုမြိန်ပုံ၊ အပြင်ပန်းတွင် ဆူးများဖြင့် ပြည့်နှက်နေသော်လည်း အတွင်းပိုင်းတွင် ချိုမြသောအရသာများဖြင့် စောင့်မျှော်နေပုံကို လေးလုံးစပ်ပုံစံအဖွဲ့ဖြင့် ဖွဲ့ဆိုထားသည်။

သူတော်ကောင်းနှင့်ပေါင်းဖော်ရာတွင် တောင်ဇလပ်ပန်းကို ပေါက်ဖက်နှင့်ထုပ်ထားလျှင် ပေါက်ဖက်ကိုလည်း အမွှေးရနံ့သင်းကြိုင်သကဲ့သို့ ပညာရှိသူတော်ကောင်းနှင့် ပေါင်းဖော်လျှင် ကောင်းမြတ်သော ဂုဏ်သတင်းကို ရရှိနိုင်ကြောင်း ပြဆိုထားသည်။ လောကတွင် အပေါင်းအသင်းကြောင့် ဂုဏ်တက်ရသည်ရှိသကဲ့သို့ ဂုဏ်ပျက်ရသည်လည်းရှိသည်။ ယင်းကြောင့် ပေါင်းသင်းဆက်ဆံရေးသည်လည်း အရေးကြီးကြောင်း နီတိကျမ်းက ပြဆိုလျက်ရှိတော့သည်။

ထို့ပြင် မြင့်မြတ်သော၊ မျိုးရိုးဂုဏ်ကိုစောင့်ထိန်းသော အမျိုးကောင်းသား သူတော်ကောင်းတို့သည် ဆင်းရဲခြင်းသို့ရောက်သည့်တိုင် ယုတ်မာသောအမှုကို မပြုကြောင်း၊ ခြင်္သေ့တို့ မည်သည် မည်မျှပင်ဆာလောင်မွတ်သိပ်သော်လည်း သစ်ရွက်တို့ကို မစားကြောင်း၊ ထို့အတူ မည်မျှပင် ကြံလှီနေစေကာမူ ဆင်၏အသားကို စားလေ့မရှိကြောင်း၊ ထို့ကြောင့် အမြဲအစဉ် သူတော်ကောင်းများကို ပေါင်းဖော်သင့်ကြောင်း လူမှုရေးလမ်းညွှန်ချက်အဖွဲ့များအဖြစ် တွေ့ရှိရပါသည်။

၄၊၃။ ဗာလဒုဇ္ဇနကဏ္ဍလာ လူမှုရေးလမ်းညွှန်ချက်အဖွဲ့များ

ဗာလဒုဇ္ဇနကဏ္ဍ(သူယုတ်မာကို ဖွဲ့ဆိုသော) လာ လမ်းညွှန်ချက်များကို ဆရာတော်က အကျယ်ဖွင့်ဆိုရာ၌ သူယုတ်မာကို မချစ်မခင်အပ်ကြောင်းမှ ရန်ဖက်မပြိုင် အနိုင်ယူအပ်သောသူလေးမျိုးအကြောင်းထိ အချက်(၁၁)ချက် ရှင်းလင်းပြဆိုထား၏။ ယုတ်မာသောသဘောရှိသောသူသည် သူတစ်ပါးတို့၏နှမ်းစေ့မျှသောအပြစ်တို့ကို မြင်တတ်ပြီး အုန်းသီးတမျှကြီးမားသော မိမိအပြစ်ကိုကား မမြင်တတ်ကြောင်းကို **"တိလမတ္တံ ပရေဿံဝ၊ အတ္တ ဒေါသဉ္စ ပဿတိ။ နာဠိတေရမ္ပိ သ,ဒေါသံ၊ ခလဇာတော် နံ ပဿတိ။" [၇](စာ-၁၁၅)** ဟူ၍ ပြဆိုထားသည်။ ဤမည်သောသူတို့သည် မိမိအတွက်သာသိပြီး သူတစ်ပါးအတွက် မသိတတ်သော၊ လုပ် ဆောင်မပေးတတ်သောသူများဖြစ်ခြင်းကြောင့် မပေါင်းသင်းအပ်သောသူများ စာရင်းတွင် ထည့်သွင်းရမည်ဖြစ်သည်။ ယင်းကြောင့် ဤလမ်းညွှန်ချက်များသည် လူမှုဆက်ဆံရာတွင် မည်သူကို ပေါင်းဖော်၍ မည်သူကို မပေါင်းဖော်သင့်ကြောင်း ပြဆိုထားသည့် လမ်းညွှန်ကောင်းအဖွဲ့တစ်ခုဟု ဆိုရပါမည်။

အမှာတော်ရေး ဦးရှင်ကလေးဖွဲ့ဆိုသည့် လောကနီတိပျို့ဆုံးမစာတွင်လည်း **"သူယုတ်တို့ကား၊ တပါးသူဝယ်၊ နှမ်းငယ်ခန့်မျှ၊ အပြစ်ရသော်၊ ကြီးလှထင်ယောင်၊ မြားမြောင်အပြစ်၊ ကိုယ်မမြင်တည့်"[၆](စာ-၃၃၀)** ဟူ၍ တိုတိုရှင်းရှင်းနှင့် နားလည်လွယ်ကူအောင် ရေးဖွဲ့ထားသည်ကို တွေ့ရပါသည်။ ထို့ပြင် သူယုတ်မာများအပေါ်ကို လွန်မင်းစွာ ချစ်ခင်ကြင်နာမှု မပြုကြရန်၊ အဘယ်ကြောင့်ဆိုသော် သူယုတ်မာတို့သည် ခေါင်းဖြင့် ရွက်ထားသော်လည်း ရေ မပြည့်သည့်အိုးဖြစ်နေခြင်း ကြောင့် မိမိကိုပြန်၍ အကျိုးမပြုနိုင်ကြောင်း မြင်သာအောင် ဖွဲ့ဆိုထားသည်။ သူမိုက်၊ သူယုတ်တို့သည် မိမိပြုလုပ်သော မကောင်းမှုအတွက် ပြန်လည်မခံစားရသေးခင် ပျားရည်တမျှ ချိုမြိန်လှသည်ဟု အားရကျေနပ်တတ်ကြသည်။ ထို့ကြောင့် သူမိုက်၊ သူယုတ်တို့ အင်အားရှိနေပါက မကောင်းပေ။ ထိုအင်အားဖြင့် သူတစ်ပါး၏ စည်းစိမ်တို့အား အနိုင်အထက်လုယူတတ်ကြသောကြောင့် အင်အားရှိအောင် အားမပေးသင့်ကြောင်း လမ်းညွှန်ထားသည်ကို တွေ့ရသည်။

၄၊၄။ မိတ္တကဏ္ဍလာ လူမှုရေးလမ်းညွှန်ချက်အဖွဲ့များ

မိတ္တကဏ္ဍ(မိတ်ဆွေကို ဖွဲ့ဆိုသော) လာ လမ်းညွှန်ချက်များကို ဆရာတော်က အကျယ်ဖွင့်ဆိုရာ၌ ဆွေမျိုးနှင့် သူစိမ်းကို ခွဲခြား၍ပြကြောင်းမှ မိတ်ဆွေများပြား၊ နည်းပါးတစ်ဖုံ၊ တွေ့ကြုံအထိ အချက်(၁၅)ချက်ပြဆိုထားသည်။ မိတ်ဆွေနှင့်ပတ်သက်၍ အဆွေခင်ပွန်းကောင်းတို့သည် အနာရောဂါ နှိပ်စက်သောကာလ၌လည်းကောင်း၊ ငတ်မွတ်ခေါင်းပါးသောကာလ၌လည်းကောင်း၊ စည်းစိမ်ပျက်စီးသောကာလ၌လည်းကောင်း၊ ရန်သူမှဖမ်းမိသောကာလ၌လည်းကောင်း၊ မင်းအိမ်တံခါး၌လည်းကောင်း၊ သုသာန်တစပြင်၌လည်းကောင်း အနားမှမခွာဘဲ ရပ်တည်ပေးကြသည်။ ထိုခင်ပွန်းတို့သာလျှင် အဆွေခင်ပွန်းကောင်းဖြစ်ကြောင်းကို **"ရောဂါ-တုရေစ ဒု-ဇ္ဈိကွေ၊ ဗျသနေ သတြု-ဝိဂ္ဂဟေ။ ရာဇ- ဒ္ဒါရ**

သုသာနေ စ၊ ယေ တိဋ္ဌန္တိသု-မိတ္တ်ကာ။" [၇](စာ-၁၄၉) ဟူ၍ ဖွင့်ဆိုထားသည်။ မိမိအပေါ်ကောင်းမွန်သော မိတ်ဆွေကောင်း တို့ကို ဆက်လက်ပေါင်းဖော်သင့်ကြောင်း လမ်းညွှန်ထားသည့် လူမှုရေး လမ်းညွှန်ချက်အဖွဲ့ကောင်းတစ်ခုဖြစ်ပါသည်။

အမှာတော်ရေး ဦးရှင်ကလေး ဖွဲ့ဆိုသည့် လောကနီတိ ပျို့ဆုံးမစာတွင်လည်း **"မမြတ်ရန်သူ၊ အတူမကွေ၊ ပေါင်းရလေသော်၊ စိတ်နေမြဲမြံ၊ အကြံချိန်ထောက်၊ မမြောက်သေးမူ၊ ရန်သူကိုလျှင်၊ ပခုံးတင်၍၊ ငြိုငြင်လျက်သာ၊ ရွှက်ဆောင်ရာ၏။ အခါရောက်သော်၊ ကျောက်ဖျာပြင်၌၊ ရိုက်၍အိုးကို၊ ခွဲလိုက်ဆိုသို့၊ ထိုရန်သူအား၊ ခွဲဖျက်ငြားလော့"[၆](စာ-၃၃၁)** ဟူ၍ ဖွဲ့ဆိုထားသည်ကိုတွေ့ရသည်။ မိတ်ဆွေစစ် မိတ်ဆွေမှန်တို့သည် မိမိတွင် မည်သို့သော အခက်အခဲရှိစေကာမူ ဖဲခွာမသွားကြဘဲ "အေးအတူပူအမျှ" ဖြစ်လာသမျှ ဒုက္ခကို အတူခံယူကြသည်။ ရန်သူကို ရင်ဆိုင်ရာတွင်လည်း အတူတကွပူးပေါင်းဖြေရှင်းကြသည်။ ယင်းကြောင့် မိတ်ဆွေစစ်ကို အထူးပေါင်းသင်းဆက်ဆံရန်လိုအပ်ကြောင်း လူမှုရေးလမ်းညွှန်ချက်အဖွဲ့ကောင်းတစ်ခုအဖြစ် တွေ့ရပါသည်။ ထို့ပြင် မိတ်ဆွေအတုအယောင်တို့သည် မိမိရှေ့တွင် တစ်မျိုး၊ မိမိကွယ်ရာတွင်တစ်မျိုး ပြောဆိုတတ်ကြသည်။ ထိုသူမျိုးကို ပျားက အဆိပ်အိုးကို ရှောင်သကဲ့သို့ ရှောင်ကြဉ်ရမည်ဖြစ်ကြောင်းလည်း သိမှတ်ရပါသည်။

၄၊၅။ ဣတ္ထိကဏ္ဏလာ လူမှုရေးလမ်းညွှန်ချက်အဖွဲ့များ

ဣတ္ထိကဏ္ဏ(မိန်းမကို ဖွဲ့ဆိုသော) လာ လမ်းညွှန်ချက်များကို ဆရာတော်က အကျယ်ဖွင့်ဆိုရာ၌ သတ္တဝါအလိုက် အဆင်းလေးမျိုးအကြောင်းမှ အဘိုးအို မိန်းမငယ်ကိုယူလျှင် ပျက်စီးကြောင်းအထိ အချက်(၂၅) ချက်ပြဆိုထားသည်။ မိန်းမကိုဖွဲ့ဆိုရာတွင် မိန်းမတို့၏ ဥစ္စာကား အဆင်းဖြစ်ကြောင်း၊ အကြင်မိန်းမသည် ငြင်းခုံတတ်သောအလေ့ရှိလျှင်၊ ငြူစူစောင်းမြောင်းပြောဆိုတတ်သောအလေ့ရှိလျှင်၊ မြင်သည့်အရာအားလုံးကို ပိုင်ဆိုင်တပ်မက်တတ်လျှင်၊ အများအပြား ချက်ပြုတ် စားသောက်တတ်လျှင်၊ လင်ယောကျ်ား၏ အဦးအဖျားကို စားသောက်တတ်သော အလေ့ရှိလျှင်၊ သူတစ်ပါးအိမ်သို့ လှည့်ပတ်သွားလာတတ်သော အလေ့ရှိလျှင် ထိုမိန်းမသည် သားတစ်ရာပင် ဖွားမြင်သော်လည်း လင်ယောကျ်ားက စွန့်ပစ်အပ်ကြောင်း မိန်းမတို့လိုက်နာကျင့်ဆောင်အပ်သည့် အကြောင်းတရားတို့ကို လမ်းညွှန်ချက်ပေးကာ ရှင်းလင်းထားပါသည်။ ယင်းမှာ **"ဝိဒါသီလိ ဥဿူယဘာဏိနိ၊ သမ္မသတဏိ ဗဟုပါကဘုတ္တိနိ အဂ္ဂန္ဓဘုတ္တိ ပရဂေဟဝါသိနိ၊ နာရိစဇေ ပုတ္တေသတမ္ပိ ပုမာ" [၁](စာ-၂၂၅)** ဟူ၍ ပြဆိုထားသည်။

အမှာတော်ရေး ဦးရှင်ကလေး ဖွဲ့ဆိုသည့် လောကနီတိ ပျို့ဆုံးမစာတွင်လည်း **" အကြင်မိန်းမ၊ ဒေါသမကင်း၊ ငြင်းခုံတတ်ရှောင်း၊ စောင်းမြောင်းငြူစူ၊ ပြောထူများစွာ၊ မြင်တိုင်းမှာပင် လိုချင်တပ်မက်၊ များစွာချက်တည့်၊ စားတုံလှည့်လျက်၊ လင်၏ရှေးဦး၊ ခူးခပ်စားသောက်၊ ရောက်ရက်မငြိမ်၊ သူ့အိမ်သွားလာ၊ ပြစ်ခြောက်ဖြာတည့်၊ ကယ်၍ရှိမူ၊ သူနှင့်မွေးဘွား၊ သားတရာစင်၊ ရှိတုံကျင်လည်း၊ ချစ်ခင်မသာ၊ စွန့်လိုက်ခွာလော့။ ။ ကျမ်းလာသည်တိုင်း-အမှန်တည်း" [၆](စာ-၃၃၄)** ဟူ၍ ဖွဲ့ဆိုထားပါသည်။ လောကတွင် မိန်းမတို့အတွက် လင်ယောကျ်ားသည်သာ အင်အားဖြစ်သောကြောင့် မိမိတို့အိမ်ဦးနတ် စိတ်ရွှင်လန်းကျေနပ်စေရန် မည်သို့နေထိုင်စားသောက်ရမည်ကို လမ်းညွှန်ထားသည့် လူမှုရေးလမ်းညွှန်ချက်အဖွဲ့တစ်ခုဖြစ်သည်။ ဥဩဇာက်တို့၏ အဆင်းသည် အသံဖြစ်၍ မိန်းမတို့၏အဆင်းသည် လင်ကိုမြတ်နိုးခြင်းဖြစ်ကြောင်း၊ ယင်းကြောင့် မိမိ၏ခင်ပွန်းလင်ကို ချစ်မြတ်စွာနေထိုင်ရမည်ဖြစ်ကြောင်းလည်း ပြဆိုထားသည့် လူမှုရေးလမ်းညွှန်တစ်ခုဖြစ်သည်။ ထို့ပြင် မိန်းကလေးများ မည်သို့နေထိုင်ရမည်ကိုလည်း ဥပမာပေး လမ်းညွှန်ထားသည်။ မြစ်သည် ကွေ့ကောက်တတ်သည်။ တောတို့တွင် ထင်းများဖြင့်ပြည့်တတ်သည်။ ထို့အတူ မိန်းမတို့သည် ဆိတ်ငြိမ်သောအရပ်တွင် နေထိုင်ရသည်ရှိသော် ကြီးစွာသောမကောင်းမှုကို ပြုတတ်ကြောင်း၊ ထို့ကြောင့် ဆိတ်ငြိမ်သောအရပ်တွင် မနေထိုင်သင့်ကြောင်း ညွှန်ဆိုထားသည်ကို လည်းတွေ့ရသည်။

၄၊၆။ ရာဇကဏ္ဏလာ လူမှုရေးလမ်းညွှန်ချက်အဖွဲ့များ

ရာဇကဏ္ဏ(မင်း၊ ရှင်ဘုရင်ကို ဖွဲ့ဆိုသော) လာ လမ်းညွှန်ချက်များကို ဆရာတော်က အကျယ်ဖွင့်ဆိုရာ၌ ညဉ့်လေးယာမ်၌ ဆင်ခြင်၍ အိပ်သင့်ကြောင်းမှ မှီရာမရှိသော် မတင့်တယ်အထိ အချက်(၂၆)ချက်ပြဆိုထားသည်။ မင်းနှင့်ပတ်သက်၍ မင်းနှင့်အပြိုင် ကာမစည်းစိမ်ကို မခံစားသင့်ကြောင်း၊ အသွင်ဟန်ပန်ပုံသဏ္ဌာန်မှာလည်း မင်းနှင့်တူအောင် မပြုသင့်ကြောင်း၊ အရသာစားရာတွင်လည်း မင်းနှင့်အတူအပြိုင် မစားရကြောင်း၊ ပန်းပန်ခြင်း၊ နံ့သာလိမ်းကျံခြင်းတို့လည်း မင်းနှင့်အပြိုင် မပြုရကြောင်း၊ အဝတ်အထည်ဝတ်ရာတွင်လည်း မင်းနှင့်အပြိုင် မင်းထက်လွန်ကဲကာ မဝတ်ဆင်ရကြောင်း၊ တန်ဆာဆင်ရာတွင်လည်း မင်းနှင့်အပြိုင် မပြုလုပ်ရကြောင်း၊ အရာအားလုံးအလုံးစုံကို မင်းနှင့်မပြိုင်ရကြောင်း လမ်းညွှန်ချက်ပေးထားသည်ကို တွေ့ရသည်။ ယင်းကို **"နာ ရညော သမကံ ဘုဉ္ဇေ၊ ကာမဘောဂံ ကုဒါစနံ။ အာကပ္ပံ ရဿ ဘုတ္တိဝါ၊ မာလာ ဂန္ဓ ဝိလေပနံ။ ဝတ္ထံ သဗ္ဗအလင်္ကာရံ၊ နာ ရညော သဒိသံ ကရေ" [၁](စာ-၃၃၇)** ဟူ၍ ပြဆိုထားသည်။

အမှာတော်ရေး ဦးရှင်ကလေး ဖွဲ့ဆိုသည့် လောကနီတိ ပျို့ဆုံးမစာတွင်လည်း **"တတည်မှတ်ကြ၊ မင်းနှင့်မျှအောင်၊ ကာမချမ်းသာ၊ မခံရာတည့်၊ နံ့သာပန်းပေါင်း၊ ဝတ်ကောင်းပုဆိုး၊ မင်းစိုး တန်ဆာ၊ မင်းမှာဟန်လို၊ မိန့်ဆိုမူယူ၊ မင်းနှင့်တူအောင်၊ ပုံမဆောင်နှင့်၊ ရှောင်ကြဉ်သင့်၏" [၇](စာ-၃၄၀)** ဟူ၍ ဖွဲ့ဆိုထားသည်။ ရေမြေအရှင်မင်းကြီးနှင့် တုပ၍ ကာမစည်းစိမ်ချမ်းသာကို

မခံစားသင့်ကြောင်း၊ နံ့သာ၊ ဝတ်ကောင်းပုဆိုးတို့ကို တုပ မဝတ်ဆင်သင့်ကြောင်း၊ မင်းနှင့်တူအောင် မနေသင့်ကြောင်း၊ အလိုက်တသိ ရှောင်ကြဉ်သင့်ကြောင်းတို့ကို လောကသိမှတ်ဖွယ်ရာများအဖြစ် ပုံဆောင်ရေးဖွဲ့ထားသည်ကို တွေ့ရသည်။ ဤသည်တို့မှာ လောကနီတိကျမ်းက ပေးသော လူမှုရေးလမ်းညွှန်ချက်တစ်ခုဟု ဆိုနိုင်ပါသည်။

၄၊၇။ ပကိဏ္ဏတကဏ္ဍလာ လူမှုရေးလမ်းညွှန်ချက်အဖွဲ့များ

ပကိဏ္ဏတကဏ္ဍ(အထွေထွေကို ဖွဲ့ဆိုသော) လာ လမ်းညွှန်ချက်များကို ဆရာတော်က အကျယ်ဖွင့်ဆိုရာ၌ သီလ စသည် မရှိနိုင်ခြင်းအကြောင်းမှ ဆုတ်ကပ်ကာလ၌ ဥစ္စာကိုသာ ပဓာနပြုခြင်းအထိ အချက်(၃၀)ပြဆိုထားသည်။ အထွေထွေကို ဖွဲ့ဆိုသော အခန်းကဏ္ဍတွင် လောက၌ ခြင်္သေ့သည်လည်းကောင်း၊ သူတော်ကောင်းသည်လည်းကောင်း၊ ဆင်သည်လည်းကောင်း၊ ဤသူတို့သည် အကျိုးမရှိသောအရပ်ကိုစွန့်၍ သွားကြကုန်သည်။ ကျီးသည်လည်းကောင်း၊ ယုတ်မာသောယောကျ်ားသည် လည်းကောင်း၊ သမင်သည်လည်းကောင်း၊ ဤသတ္တဝါတို့သည် မိမိဖြစ်ရှိကျင်လည်ရာအရပ်၌သာလျှင် ပျက်စီးခြင်းသို့ရောက်ကုန်ကြောင်းကို **“ဒေသံ ဩသဇ္ဇ ဂစ္ဆန္တိ၊ သီဟော သပ္ပုရိသော ဂဇော။ တတ္ထေ - ဝ နိမနံ ယန္တိ၊ ကာကော ကာ-ပုရိသော မိဂေါ။” [၁](စာ-၃၉၆)** ဟူ၍ ပြဆိုထားသည်။ လောကရှိလူသားတို့သည် မိမိတို့အတွက် အကျိုးမရှိသည့်နေရာတွင် နေထိုင်၍မသင့်ကြောင်း “တစ်ရွာမပြောင်း သူကောင်းမဖြစ်” ဟူသည့်အတိုင်းပင် မိမိနေထိုင်ရာအရပ်ကို စွန့်ခွာသင့်ကြောင်း လမ်းညွှန်ချက်ပေးထားသည်။

အမှာတော်ရေး ဦးရှင်ကလေး ဖွဲ့ဆိုသည့် လောကနီတိပျို့ဆုံးမတွင်လည်း **“ဆင်နှင့်ခြင်္သေ့၊ မြတ်မွေ့သူတော်၊ ဤသုံးဘော်ကား၊ မတော်ရပ်ရွာ၊ ရှောင်လေပါ၏။ ယုတ်မာသူပျက်၊ ကျီးနက်သမင်၊ ထို ၃-အင်ကား၊ အကြင်ရပ်မှာ၊ မကောင်းပါလည်း၊ ရှောင်ခွာမသွား၊ လွန်ပျော်ပါး။” [၇](စာ-၃၄၃)** ဟူ၍ ဖွဲ့ဆိုထားသည်။ လောကရှိလူသားတို့သည် ကြီးပွားတိုးတက်ချမ်းသာလိုလျှင် မိမိနှင့် အကျိုးမပေးသော နေရပ်ဌာနီကို စွန့်ခွာရမည်ဟူသောအသိကို ပေးစွမ်းထားသည်။ သိရှိလိုက်နာဖွယ်ရာကောင်းသော လူမှုရေးလမ်းညွှန်မှုတစ်ခုဟု မှတ်ယူနိုင်သည်။

၅။ ခြုံငုံသုံးသပ်ချက်

လောကနီတိကျမ်းလာ လမ်းညွှန်ချက်များမှာ မှတ်သား၍ပင် မကုန်နိုင်အောင် များပြားလှပါသည်။ ပညာရှိကိုဖွဲ့သော အဖွဲ့တွင် ပျင်းရိသောသူများသည် အတတ်ပညာမရနိုင်သည့် အပြင် အဆုံးတွင် နိဗ္ဗာန်မရနိုင်ပုံထိ ပညာတတ်ခြင်း၏အရေးပါပုံကို ရှင်းလင်းပြဆိုထားသည်ကို တွေ့ရပါသည်။ သူတော်ကောင်းအကြောင်းကို ဖွဲ့ဆိုရာတွင် ဝိန္ဓသီးတို့၏ ချိုမြမှုကို အပြင်ပန်းတွင် မမြင်တွေ့နိုင်ကြောင်းနှင့် သူတော်ကောင်းတို့ကိုသာ ပေါင်းဖော်ဆက်ဆံသင့်ကြောင်း စာဖတ်သူများ နားလည်လက်ခံလာစေရန် တစ်ချက်ချင်း ရှင်းလင်း လမ်းညွှန်ထားသည်ကို တွေ့ရပါသည်။ သူယုတ်(သူမိုက်)အကြောင်းကို ဖွဲ့ဆိုရာတွင် ယုတ်ညံ့သောစိတ်ထားရှိသောသူများသည် မိမိပြုလုပ်ထားသည့် မကောင်းမှု အပြစ်များကို အုန်းသီးလုံးလောက်ပင်ရှိသော်လည်း မမြင်တတ်ကြကြောင်း၊ သူတစ်ပါး၏အပြစ်ကို နှမ်းစေ့တစ်စေ့သာသာရှိသည်ကိုပင် မြင်တတ်ကြကြောင်း လူမှုဆက်ဆံရေးနှင့်ပတ်သက်၍ လူများကို အကောင်းမြင် မြင်တတ်ကြစေရန် လမ်းညွှန်ထားသည်ကို တွေ့ရပါသည်။ မိတ်ဆွေအကြောင်းကို ရေးသားရာတွင် မိတ်ဆွေစစ် မိတ်ဆွေမှန်လျှင် မည်မျှပင် အခက်အခဲရှိနေစေကာမူ မိမိကို စွန့်ပစ်မသွားကြကြောင်း၊ မိမိအနားတွင် ဒုက္ခမှန်သမျှ ခံယူပြီး သေသည်အထိ အတူရှိနေပေးတတ်ကြောင်းနှင့် လောကတွင် မိတ်ဆွေစစ်များသာလျှင် တန်ဖိုးအရှိဆုံးအရာဖြစ်ကြောင်း လမ်းညွှန်ပြဆိုထားသည်ကို တွေ့ရပါသည်။ အမျိုးသမီး (မိန်းမ) အကြောင်းကို ရေးသားရာတွင် မိန်းမများ မပြုလုပ်အပ်သည့် အရာများကို တစ်ချက်ချင်း ရှင်းရှင်းလင်းလင်းပြဆိုလမ်းညွှန်ထားသည်ကို တွေ့ရပါသည်။ မင်း(ရှင်ဘုရင်) အကြောင်းကို ရေးသားရာတွင် တိုင်းပြည်အုပ်ချုပ်သည့် အာဏာအရှိဆုံးဖြစ်သည့်ရှင်ဘုရင်နှင့် တုပြိုင်၍ မည်သည့်အရာမှ မပြုလုပ်သည့်ကြောင်း ပြဆိုထားသည်ကို တွေ့ရပါသည်။ အထွေထွေအကြောင်းကို ရေးသားရာတွင် လောက၌ လူအများလုပ်သင့်လုပ်ထိုက်သည့်အရာများကို ပြဆိုလမ်းညွှန်ထားသည်။ မိမိတို့နှင့် အကျိုးဆက်စပ်သည့်နေရာတွင်သာ နေထိုင်ရမည်ဖြစ်ကြောင်းနှင့် မိမိတို့နှင့် မအပ်စပ်သည့်နေရာတွင် နေထိုင်ရန် မသင့်လျော်ကြောင်း လမ်းညွှန်ထားသည်ကို တွေ့ရပါသည်။ အချုပ်အားဖြင့် ဆိုရပါမူ လောကနီတိကျမ်းသည် လောကရှိလူသားတို့ မည်သို့နေထိုင်ပြုမူ ဆက်ဆံသင့်ကြောင်း လမ်းညွှန်ပြသထားသည့် ကျမ်းကောင်းတစ်စောင်ဟု ဆိုရပေတော့မည်။

နိဂုံး

ဤစာတမ်းသည် ညောင်တုန်းရွှေဟင်္သာတောရ စံကျောင်းဆရာတော်ဘုရားကြီး ရေးသားစီမံခဲ့သော “လောကနီတိဖွင့် အကျယ်လက်စွဲကျမ်း” ကို ကိုးကား၍ ပြုစု ထားသည့် လောကနီတိကျမ်းလာ ဆုံးမဩဝါဒများအကြောင်း သိကောင်းစရာများကို လေ့လာတင်ပြထားသော စာတမ်း တစ်စောင် ဖြစ်ပါသည်။ လောကနီတိနှင့်ပတ်သက်၍ ပညာရှင် အများစုက ရေးသားဖွင့်ဆိုခဲ့ကြသောကြောင့် မိမိနှစ်သက်ရာ လောကနီတိကျမ်းအဖွင့်များကို ဆက်လက်လေ့လာ သုတေသန ပြုကြပါရန် တိုက်တွန်းအပ်ပါသည်။

ကျမ်းကိုးစာရင်း

[၁] စံကျောင်း၊ ဆရာတော်။ (၂၀၁၈)။ ***လောကနီတိဖွင့်အကျယ်လက်စွဲကျမ်း***။ ရန်ကုန်၊ စိတ်ကူးချိုချိုပုံနှိပ်တိုက်။

[၂] စိုးညွန့်၊ ဦး(ရာပြည့်)။ (၂၀၁၄)။ ***၂၀ ရာစု မြန်မာစာရေးဆရာ ၁၀၀ အတ္ထုပ္ပတ္တိအကျဉ်း ၊ တတိယအုပ်။*** ရန်ကုန်၊ ရာပြည့်စာအုပ်တိုက်။

[၃] တင်စိုး။ (၂၀၂၃) ။ ***ပြည်သူ့နီတိနှင့် လက်တွေ့ဘဝ*** ။ ရန်ကုန်၊ ကြည်ဖြူနိုင်စာအုပ်တိုက်။

[၄] ထွန်းမြင့်၊ ဦး။ (၂၀၁၆)။ ***ပါဠိသက်ဝေါဟာရအဘိဓာန်***။ ရန်ကုန်၊ စိတ်ကူးချိုချိုပုံနှိပ်တိုက်။

[၅] ဘသောင်း၊ ဗိုလ်မှူး။ (၂၀၀၂)။ ***စာဆိုတော်များအတ္ထုပ္ပတ္တိ***။ ရန်ကုန်၊ ရာပြည့်စာအုပ်တိုက်။

[၆] ရှင်ကလေး၊ ဦး။ (၁၉၆၂)။ ***လောကနီတိပျို့-ဆုံးမစာ***။ ရန်ကုန်၊ ဟံသာဝတီပုံနှိပ်တိုက်။

[၇] သုခ၊ ဦး။ (၂၀၀၇)။ ***လောကနီတိ***။ ရန်ကုန်၊ အောင်ပါရမီပုံနှိပ်တိုက်။

[၈] ဟုတ်စိန်၊ ဦး။ (၁၉၅၄) ***ပါဠိ-မြန်မာ အဘိဓာန်***။ ရန်ကုန်၊ ပြည်ထောင်စုမြန်မာနိုင်ငံတော်အစိုးရစာပုံနှိပ်ရေးနှင့် စာရေးကိရိယာဌာန။

ကိုးခန်းပျို့မှ လောကုတ္တရာဆိုင်ရာလေ့လာချက်

သီတာနှင်း [၁], အေးအေးထွန်း [၂]
တွဲဖက်ပါမောက္ခ, မြန်မာစာဌာန[၁], နည်းပညာတက္ကသိုလ် (မန္တလေး)[၁]
ပါမောက္ခ မြန်မာစာဌာန[၂], နည်းပညာတက္ကသိုလ် (မန္တလေး)[၂]
Email: thidahnin249@gmail.com[1], drayeayehtun11@gmail.com[2]

စာတမ်းအကျဉ်း

အင်းဝခေတ် စာဆိုရှင်မဟာရဋ္ဌသာရ၏ ကိုးခန်းပျို့မှ ရရှိသော လောကုတ္တရာဇဟုသုတများကို လေ့လာတင်ပြပါမည်။ အခန်း(၁)တွင် ရှင်မဟာရဋ္ဌသာရ၏ ထေဂုပ္ပတ္တိအကျဉ်း၊ အခန်း(၂)တွင် ပျို့ဝေါဟာရနှင့် သဘောသဘာဝသမိုင်းအကျဉ်း၊ အခန်း(၃)တွင် ကိုးခန်းပျို့မှ လောကုတ္တရာသုတများကို လေ့လာတင်ပြပါမည်။ ကိုးခန်းပျို့တွင် လူငယ်လူရွယ်များကို ဆုံးမထားသည်ကို တွေ့ရပါသည်။ အဆုံးအမများကို လိုက်နာကျင့်ကြံခြင်းဖြင့် တိုင်ပြည်အကျိုး၊ နိုင်ငံအကျိုးကို သယ်ပိုနိုင်သော သားကောင်းရတနာများဖြစ်လာနိုင်သော အကျိုးကျေးဇူးများကို ရရှိနိုင်ပါသည်။ ဤစာတမ်းမှ စာဆိုရှင်မဟာရဋ္ဌသာရ၏ လောကုတ္တရာဇဟုသုတများကို လေ့လာတင်ပြသော သုတေသနစာတမ်း ဖြစ်ပါသည်။

သော့ချက်ဝေါဟာရ။ ။ လောကုတ္တရာ သုတ၊

နိဒါန်း

မြန်မာစာပေရေစီးကြောင်းကို လေ့လာကြည့်လျှင် မြစ်ဖျားခံရာဖြစ်သော ပုဂံခေတ်မှစ၍ စကားပြေနှင့် ကဗျာဟူသည့် ရသစာပေများ စတင်ထွန်းကားခဲ့ကြောင်း တွေ့ရသည်။ ပုဂံခေတ်တွင် ရေးထိုးခဲ့သော အလှူမှတ်တမ်းတင်ကျောက်စာ၊ မင်စာများမှတစ်ဆင့် မြန်မာစာပေအရေးအသား စတင်ထွန်းကားခဲ့ပါသည်။ အင်းဝခေတ်သို့ ရောက်သောအခါ စကားပြေအရေးအသားများထက် ကဗျာအဖွဲ့အနွဲ့ဖြစ်သော ပျို့ကဗျာများ အင်တိုက်အားတိုက် ထွန်းကားလာကြောင်း တွေ့ရပါသည်။ စာဆိုများသည် ရဟန်းစာဆို များဖြစ်သည့်အားလျှော်စွာ ဗုဒ္ဓစာပေကို အခြေခံ၍ရေးဖွဲ့သော ပျို့ကဗျာများစွာ ပေါ်ထွန်းခဲ့ပါသည်။

ထိုပျို့ကဗျာများတွင် အများအားဖြင့် လောကီလောကုတ္တရာဆိုင်ရာများ၊ ဓမ္မရေး၊ ရာဇရေးဆိုင်ရာများကို အခြေခံ၍ ရေးဖွဲ့လေ့ရှိကြောင်း တွေ့ရပါသည်။ စာဆိုရှင်မဟာရဋ္ဌသာရရေးဖွဲ့ခဲ့သည့် ပျို့ကဗျာများအနက် ကိုးခန်းပျို့သည်လည်း ထင်ရှားသော ပျို့ကဗျာအဖြစ် မြန်မာစာပေလောကတွင် မှတ်တိုင်စိုက်ထူနိုင်ခဲ့ပါသည်။ ကိုးခန်းပျို့တွင် ဇာတ်လမ်း၊ ဇာတ်ဆောင်၊ ကာလဒေသနောက်ခံဝန်းကျင်၊ ဘုရားဟော ဇာတ်နိပါတ်ကို အခြေခံ၍ နှစ်သက်ဖွယ်ကောင်းအောင် ရေးဖွဲ့ထားကြောင်း တွေ့ရပါသည်။

ဖခင်ပုဏ္ဏားကြီးမှ သားဟတ္ထိပါလတောထွက်မည်ကို စိုးရိမ်၍ တားမြစ်သောအခန်းသည် တရား အဆီအနှစ်၊ လောကီပညာရပ်ဆိုင်ရာ သုတများကိုပို၍ ဖန်တီးရေးဖွဲ့ထားနိုင်သော အခန်းအဖြစ် တွေ့ရသည်။ အဓိကအားဖြင့် သားလေးဦးအား ပုဏ္ဏားနှင့်မင်းကြီးတို့က ငယ်ရွယ်စဉ်တရားမရှာဖွေမီ လောကီပညာရပ်များကို လေ့လာလိုက်စားစေလိုသည့် ဖခင်ပုဏ္ဏားကြီး၏ အယူအဆသဘောများကို သားဟတ္ထိပါလနှင့် ညီနောင်လေးဦးက လောကုတ္တရာတရားအသိနှင့် နှိုင်းယှဉ်ပြကာရေးဖွဲ့ထားခဲ့သည်။ နောက်ဆုံးတွင် တရားအဆီအနှစ်သည် လောကီလူသားများ အပေါ် လွှမ်းမိုးအနိုင်ယူခဲ့ပုံဖြင့် ရေးဖွဲ့ထားသောကြောင့် ကိုးခန်းပျို့သည် တန်ဖိုးမဖြတ်နိုင်သော ပျို့တစ်စောင်ဖြစ်ကြောင်းသိရှိစေရန် လောကုတ္တရာသုတများကို ထုတ်နှုတ်လေ့လာတင်ပြ သွားမည်ဖြစ်ပါသည်။

အခန်း(၁)
ရှင်မဟာရဋ္ဌသာရ၏ထေဂုပ္ပတ္တိအကျဉ်း

ရှင်မဟာရဋ္ဌသာရသည် သက္ကရာဇ်(၈၃၀)ပြည့်နှစ်တွင် အင်းဝနေပြည်တော်၌ ဖွားမြင်ခဲ့သည်။ ဖခင်မှာ ဓမ္မပါလ အမတ်ဖြစ်ပြီး၊ မိခင်မှာအင်းဝမြို့တည် သတိုးမင်းဖျား၏ သမီးတော် စောနန်း၏ မြစ်ဖြစ်သည်။ ရှင်မဟာရဋ္ဌသာရ၏ ငယ်အမည်မှာ မောင်မောက်ဖြစ်သည်။ အဖမျိုးရိုး၊ အမိမျိုးရိုး ဘက်မှသော်လည်းကောင်း ရာဇသွေးပါသော မျိုးရိုးဖြစ်ပါသည်။ ငယ်စဉ်မှစ၍ နန်းတော်တွင်း၌ ကြီးပြင်းလာသူဟုဆိုနိုင်သည်။ နန်းတော်တွင်း ကြီးပြင်းခဲ့ရသူပီပီ စိတ်ခက်ထန်သည်။

မာန်မာနကြီးသည်။ ငယ်စဉ်ကပင် ကဗျာ၊ လင်္ကာအဖွဲ့အနွဲ့၌ ကျွမ်းကျင်ပိုင်နိုင်သည်။ ကျမ်းကြီးကျမ်းငယ်အစောင်စောင်တို့ကို လေ့လာဆည်းပူးခြင်း၊ နန်းတွင်းပညာရှိ ပုဂ္ဂိုလ်များ၊ ကျမ်းတတ်မထေရ်ဆရာမြတ်တို့ထံမှ လေ့လာဆည်းပူးခြင်း၊ ဖခင်ဓမ္မပါလအမတ်ထံမှ စာပေအရပ်ရပ်တို့ကို သင်ကြားတတ်မြောက်ခဲ့သည်။ အရှင်ဝရစက္ကပါလဆရာထံ သင်ရိုးကျမ်းဂန်များကို ဂရုတစိုက်လေ့လာ သင်ကြားခဲ့ပါသည်။

တစ်ခါက မောင်မောက်(၁၀)နှစ်သားအရွယ်တွင် ဖခင်ဖြစ်သူဓမ္မပါလအမတ်သည် သားငယ် မောင်မောက်ကို လက်ကဆွဲ၍ နန်းတော်တွင်းသို့ ဝင်ခဲ့သည်။ ထိုအချိန်တွင် နန်းတော်တွင်း အိမ်ရှေမင်းမဟာသီဟသူ၏ တောင်ဆောင်စံမြောက်သားတော်သမီး "ရှင်မင်းစိုး၊ မြောက်ဆောင်စံမြောက်သားတော်သမီး မင်းလှမြတ်နှင့် မင်းဘုန်ထွတ်တို့ နားထွင်းမင်္ဂလာသဘင် ဆင်ယင်ကျင်းပခိုက်ဖြစ်သည်။ အိမ်ရှေ့မင်းက ဓမ္မပါလာအမတ်ကြီးအား သမီးတော်သုံးပါးနှင့် စပ်ဆိုင်ရာ ပျို့၊ ကဗျာလင်္ကာ၊ ရတုများ ဖွဲ့ဆိုလျှောက်ထားရမည်ဟု အမိန့်တော်မှတ်ရာ သားမောင်မောက်က ဖခင်အစားဖွဲ့ဆိုလျှောက်ထားကာ ရုတ်ခြည်းမင်းသမီးတော်သုံးပါးကို -

"အိုဘဲ့ဘယ်၊ အိုဘဲ့သမီးတော်၊ ထင်ပေါ်ဖုန်းပျံသင်း"

"အိုဘဲ့ဘယ်၊ အိုဘဲ့သမီးတော်၊ နတ်သော်ပုံမယွင်း

"အိုဘဲ့ဘယ်၊ အိုဘဲ့သမီးတော်၊ စန္ဒာလသွယ်ဝင်း" ဟူ၍ အရွယ်နှင့်မလိုက်အောင် ကာရန်၊ ဝါကျညီညွတ်စွာဖြင့် ဖွဲ့စပ်လျှောက်ထားခဲ့သည်။ ပညာရှိအမတ်ကြီး၏ သားမြတ်ဖြစ်သည့်အပြင် ကိုယ်တိုင်နန်းတွင်း၊ နန်းပြင်ဗဟုသုတကျွမ်းဝင်မှု၊ ထိုးထွင်းဉာဏ်ထက်သန်မှုတို့ကြောင့် စာပေအရာတွင် ထူးချွန်ခဲ့ခြင်းဖြစ်ပါသည်။ မောင်မောက်သည် ဘူရိဒတ်လင်္ကာကြီးကို သက္ကရာဇ် ၈၄ဖခုနှစ် သက်တော်၁၆နှစ်အရွယ် ရှင်သာမဏေဘောင်သို့ မရောက်ခင်ဖွဲ့နွဲ့စပ်ဆိုခဲ့ပါသည်။ ရှေးအကျဆုံး အဟောင်ဆုံးလင်္ကာဖြစ်သော ဘူရိဒတ်လင်္ကာကြီးကို အလင်္ကာအမျိုးမျိုးဖြင့် တန်ဆာဆင်၍ မြန်မာပြန်ဆိုရေးသားခဲ့သည်။ နန်းတွင်းမြို့တွင်၌ ကြီးပြင်းခဲ့ရသူဖြစ်သောကြောင့် လူမှုရေးရာ၊ လောကရေးရာများကို ကျွမ်းကျင်ပိုင်နိုင်စွာ စပ်ခဲ့ပါသည်။ ရှင်မဟာရဋ္ဌသာရ ရဟန္တာဝသို့ ရောက်ပြီးနောက် ဘူရိဒတ်ဇာတ် ပေါင်းခန်းပျို့ကို သက္ကရာဇ် ၈၅ဖခု သက်တော်၂၆နှစ်တွင် ရေးသားပြုစုခဲ့သည်။ ၈၆ဝခုနှစ်တွင် ဂန္ဓိသာရပျို့၊ ၈၉၁ခုနှစ်တွင် သံဝရပျို့၊ တံဋီးတည်မော်ကွန်းသုံးစောင်နှင့် အခြားသော တောလား၊ လင်္ကာ၊ ကဗျာ၊ ရတုများကို ရေးသားခဲ့ပါသည်။ ရှင်မဟာရဋ္ဌသာရသည် သက္ကရာဇ် ၈၉၂ခုနှစ် သက်တော် ၆၂နှစ်တွင် ပြည်မြို့၌ ပျံလွန်တော်မူခဲ့လေသည်။ ၁(၂၀၀၂၊ ၆၃၊၆၄)

၁၊၁။ ပျို့ဝေါဟာရ၊ သဘောသဘာဝနှင့် သမိုင်းကြောင်း

မြန်မာစာပေအရေးအသားသည် ဗုဒ္ဓစာပေပေါ်ထွန်းလာသည့် ပုဂံခေတ်မှစ၍ ထွန်းကားလာခဲ့ပါသည်။ စကားပြေ၊ ကဗျာဟူသည့် ပင်စည်မှ ပေါက်ပွားလာသော စာပေများသည် အမျိုးအစားစုံလင်စွာဖြင့် ခေတ်အလိုက် ပေါ်ထွန်းခဲ့ပါသည်။ ဗုဒ္ဓစာပေတို့ကို ပါဠိဘာသာမှ မြန်မာဘာသာပြန်ဆိုခြင်းဖြင့် မြန်မာစာပေလမ်းကြောင်းသည် ပုဂံခေတ် ကျောက်စာ၊ မင်စာ ကဗျာများမှ တဖြည်းဖြည်းစတင်၍ တိုးတက်လာခဲ့ပါသည်။ အင်းဝခေတ်ရောက်သောအခါ ကျောက်စာ၊ မင်စာများအပြင် ပျို့ကဗျာအလင်္ကာ၊ ရတု၊ တောလားစသည်ဖြင့် မြန်မာစာပေသည် အရှိန်အဟုန်ဖြင့် တိုးတက်လာခဲ့ပါသည်။ အင်းဝခေတ်၏ မှတ်တိုင်ဟုဆိုရမည်ဖြစ်သော ပျို့ကဗျာ လမ်းကြောင်းသည် ပို၍ထင်ရှားခဲ့ပါသည်။

ပျို့ကဗျာများဟူသည် **"တရားအဆိအနှစ်များနှင့် ပြည့်လျှမ်း၍နေသော ကဗျာသည် 'ပို့'မည်၏ဟု ဆိုရမည်သာတည်း"**ဟူ၍ လည်းကောင်း

"သဒ္ဒါလင်္ကာရ၊ အတ္ထာလင်္ကာရ တို့နှင့် ပြည့်စုံအောင် ဖွဲ့နွဲ့ထား၍ နှစ်သက်ဖွယ်ကောင်း သောကြောင့်လည်း ပျို့မည်၏" "ပျို့သည် တရားသဘောနွယ် သောလင်္ကာ ဖြစ်၏" ဟူ၍ မြန်မာစာပေးသမိုင်းတွင် ဦးဖေမောင်တင်က ဖွင့်ဆိုခဲ့ကြသည်။ ၂ (၂၀၀၃၊ ၉၂) ထိုပြင်ပျို့နှင့်ပတ်သက်၍ မြန်မာအဘိဓာန် တွင်-

"ပျို့-နာ-ပိုဒ်ရေပေါင်းများစွာ ဖွဲ့ဆိုသော

လေးလုံးစပ်အလင်္ကာရုဏ်တစ်မျိုး" ဟူ၍ အဓိပ္ပာယ်ဖွင့်ဆိုခဲ့သည်။ ၃ (၂၀၀၈၊ ၂၃၁)

ပျို့ဝေါဟာရနှင့်ပတ်သက်၍ ပညာရှင်အသီးသီးက အနက်အဓိပ္ပာယ် အမျိုးမျိုးတို့ကို ကြံဆ ပြသခဲ့ကြသည်။

"ပျို့သည် ပုဒ်ရေပေါင်းများစွာပါဝင်သော လေးလုံးစပ် ကဗျာဖြစ်သည်။ ရေးဖွဲ့သည့် အကြောင်းအရင်းကို စကားတန်ဆာ၊ အနက်တန်ဆာများဖြင့် နှစ်သက်ဖွယ်ကောင်းအောင် ဝေဝေဆာဆာ ရေးဖွဲ့သည့်အတွက် ထိုကဗျာမျိုးကိုနှစ်သက်ဖွယ်

ဟု အဓိပ္ပာယ်ရသောပျို့ဟူ၍ ဝေါဟာရဖြင့် အမည်သညာပြုထားခြင်းဖြစ်သည်။" ဟူ၍ ဖွင့်ဆိုထားသည်။ ၁ (၂၀၁၈၊ ၉)

ထို့ကြောင့်ပျို့ကဗျာကို လေ့လာရာတွင် ပျို့သည် လေးလုံးစပ်လင်္ကာ တစ်မျိုးပင်ဖြစ်သည်။ ဘုရားဟော ကျမ်းဂန်လာ ဗုဒ္ဓဝင်ဇာတ်နိပါတ်တော်ကြီးများမှ ကောင်းနိုးရာရာ ဝတ္ထုကြောင်းကို ထုတ်နှုတ်၍ ကဗျာလင်္ကာဖြင့် တန်ဆာဆင် ရေးဖွဲ့ထားခြင်းဖြစ်သည်။ အင်းဝခေတ်သည် ပျို့ကဗျာများစွာ ပေါ်ပေါက်သော အချိန်ဖြစ်၍ ရေးဖွဲ့သောပုဂ္ဂိုလ်များမှာ ရဟန်းစာဆို ကျမ်းတတ်ပုဂ္ဂိုလ်တို့ ဖြစ်ကြသည်။ ရေးဖွဲ့သော အကြောင်း အရာများမှာ လောက၊ ဓမ္မ၊ ရာဇရေး အကြောင်းများကို ထည့်သွင်းရေးဖွဲ့ခဲ့ကြပါသည်။ အများစုမှာ ဓမ္မအကြောင်းနွယ်သော စာများဖြစ်ကြသည်။ ပျို့ကဗျာများ အနက် ဆရာတော်ရှင်မဟာရဋ္ဌသာရ၏ ကိုးခန်းပျို့ခေါ် စတုဓမ္မသာရပျို့သည် အင်းဝခေတ်၏ထင်ရှားဆုံး ပျို့တစ်စောင်အဖြစ်ရပ် တည်နိုင်ခဲ့ကြောင်းတွေ့ရပါသည်။

အခန်း(၂)
ကိုးခန်းပျို့မှ လောကုတ္တရာဆိုင်ရာလေ့လာချက်

၂.၁။ လောကုတ္တရာဆိုင်လေ့လာချက်များ

မြတ်စွာဘုရားသခင်သည် နိဗ္ဗာန်မပါရမီကို အကြောင်းပြု၍ ဟတ္ထိပါလဇာတ်ကို ဟောတော်မူခဲ့သည်၊ ဟတ္ထိပါလဇာတ်ကို စာဆိုရှင်မဟာရဋ္ဌသာရက ပျို့ကဗျာအဖြစ် ရေးဖွဲ့ခဲ့ခြင်းဖြစ်ပါသည်။ ပျို့ကဗျာတွင် လောကီစည်းစိမ်ကို ဖယ်စွန့်၍ ချမ်းသာရာအမှန်မြတ်နိဗ္ဗာန်ကို ရည်မှန်းကာ ရဟန်းပြုနိုင်ကြရန် ရည်ရွယ်ထားသော ပျို့ဖြစ်ပါသည်။ ထို့အကြောင့် စာဆိုသည်ကိုးခန်းပျို့တွင် လောကုတ္တရာရေးရာနှင့် လောကီရေးရာတို့ကို အားပြိုင်ကာတည့်သွင်းရေးဖွဲ့ထားပါသည်။ စာဆိုကိုယ်တိုင်သည် ရဟန်းစာဆိုဖြစ်သောကြောင့် ဓမ္မကြောင်းနှင့် ဆိုင်သည့်တရားအဆိအနှစ်များကို ပျို့တွင် ကျွမ်းကျင်ပိုင်နိုင်စွာ ရေးဖွဲ့တင်ပြထားနိုင်သည်ကို လေ့လာတွေ့ရှိ ရပါသည်။

ဟတ္ထိပါလသည် ပုဏ္ဏာကြီးနှင့်မင်းကြီးတို့ ရသေ့ယောင်ဆောင်၍ ကြွလာသောအခါ ဆွမ်းစားပင့်ဖိတ် ကျွေးမွေးခဲ့သည်။ သဒ္ဓါတရားနှင့် အလှူဒါနမျိုးစေ့ကို တစ်ကြိမ်တစ်ခါမျှ ပြုခဲ့ဖူးပါသော်လည်း သဒ္ဓါစိတ်သည် မိမိပြုခဲ့ဖူးသော အလှူဒါနအပေါ်၌ အကြိမ်ကြိမ်ကြည်နူးပွားများနေလျှင် ကုသိုလ်ဒါနအကျိုးဆက်သည် အသင်္ချေအနန္တ မရေမတွက်နိုင်အောင် ပွားများစေနိုင်ကြောင်း ကို -

"သဒ္ဓါလှူမျိုး၊ တစ်ကြိမ်ပျိုးက၊

ကောင်းကျိုးသင်္ချေ၊ ပွားတက်စေသည်"ဟု ဖွဲ့ဆိုထားရာ ဗုဒ္ဓဘာသာဝင်တို့၏ ယုံကြည်မှုအဖြစ် လေ့လာတွေ့မြင်လာရပါသည်။

ဗေဒင်ပညာမတတ်သော်လည်း ရဟန်းကျင့်ဝတ် တစ်ပါးပါးကိုသာ တတ်မြောက်ပါက လူနတ်တို့၏ ချီးကျူးပူဇော်ခံရကြောင်း၊ ကမ္မဋ္ဌာန်းတရားကို ကျင့်ကြံအားထုတ်ပါက ဘုရားတို့ကပင် ချီးမွမ်းကြကြောင်း ဖော်ပြထားပါသည်။ ထိုသဘောကို စာဆိုက-

"ကံသုံးပါးဖြင့်၊ ပြစ်မှားမရှိ၊ သမာဓိနှင့်၊ သတိသမ္ဗဇ္ဈင်၊

ယှဉ်သားကမ္မဋ္ဌာန်း၊ စီးဖြန်းတုံးတုံး၊ နှလုံးသိပ်သိပ်၊

မလိပ်မလည်း၊ ကုသိုလ်ချည်းလျှင်၊ ဆည်းသည်သူအား၊

ဘုရားပစ္စေကဗုဒ္ဓါ၊ ရဟန္တာတို့၊ လိမ္မာမှတ်ပိုက်၊

နှစ်အင်ခြိုက်၏" ဟူ၍ ရေးဖွဲ့ထားပါသည်။ ရဟန်းတို့သည် ကံသုံးပါးပြစ်မှားမှုမရှိဘဲ သမာဓိကို တရားအသိဖြင့်ယှဉ်၍ ကမ္မဋ္ဌာန်းတရားစီးဖြန်းသင့်ကြောင်းတို့ဖြင့် ရေးဖွဲ့ထားရာ လောကုတ္တရာဆိုင်ရာ ဗဟုသုတကို ရရှိစေသောအဖွဲ့ကောင်းတစ်ခု အဖြစ် တွေ့မြင်လာရပါသည်။

တစ်ဖန်ဟတ္ထိပါလက လောကီပစ္စည်းဥစ္စာတို့သည် ရန်သူမျိုးငါးပါးကြောင့်ပျက်စီးစေတတ်သည်။ ပစ္စည်းဥစ္စာမည်မျှရှိစေကာမူ၊ ကြာလာသောအခါ ဥစ္စာပစ္စည်းက လူကိုစွန့်ခွာသွားတတ်သကဲ့သို့ လူကလည်း ပစ္စည်းဥစ္စာများကို စွန့်ခွာသွားရတတ်ကြောင်းစာဆိုက-

" ပစ္စည်းပုံယင်၊ ဥစ္စာရှင်တို့၊ ကြည်းငင်ဖမ်းဆွဲ၊

သေမင်းမဲသော်၊ အထဲအပ၊

ထိုမျှဥစ္စာ၊ အိမ်ခန်းဝါကို၊

စွန့်ကာလည်းကောင်း၊ သွားရရှောင်ခဲ့" ဟူ၍ ဖွဲ့ဆိုထားပါသည်။ ၂ (၁၉၇၀၊ ၂၂-၃၂)

ထို့ပြင်ပစ္စည်းဥစ္စာများကို တပ်မက်စွဲလမ်းစိတ်ဖြင့် သေလွန်သောအခါ အစွဲအလမ်းကြောင့် ပြိတ္တာဘဝ ရောက်နိုင်ပါသည်။ လောကီပစ္စည်းဥစ္စာများကို ခင်တွယ်ခြင်းသည် ပစ္စုပ္ပန်၊ သံသရာနှစ်ဘဝစလုံး ဆုံးရှုံးနိုင်ကြောင်းကို စာဆိုက-

" ကံကတ္တားကား၊ တစ်ပါးမလာ၊

ကိုယ်သာလည်းကောင်း၊ တပ်ဟောင်းမပြယ်၊

ခန္ဓာကွယ်လည်း၊ မပါယ်တို့ရွာ၊

မွတ်သိပ်စွာသား၊ ပြိတ္တာတို့ဘောင်၊

ဥစ္စာဆောင်၏၊ နောင်တမလွန်၊

ပစ္စုပ္ပန်ဟု၊ နှစ်တန်ကာလ၊

နှစ်ဘဝလုံး၊ နှစ်ပါးရှုံးကြီး၊

အချည်းနှီးကို”ဟူ၍ ဖွဲ့ဆိုထားပါသည်။

ထို့ကြောင့်ဆရာတော်က တစ်ပါးသူပိုင်ဆိုင်ချင်၍မရ၊ လုယက်ခိုးယူခြင်းလည်းမရ၊ ပေးကမ်းဝေခြမ်း၍ လျော့နည်းသွားခြင်းမရှိ၊ အစဉ်အမြဲအဖိုးထိုက်သော လောကုတ္တရာအမြိုက်ဥစ္စာကိုသာ ရှာဖွေရန် တိုက်တွန်းထား ပါသည်။ တရားရှာသူတို့အတွက် လောကုတ္တရာဗဟုသုတကို ရရှိစေသောစာဆို၏ အရေးအဖွဲ့ စွမ်းရည်ကို ဂုဏ်ယူဖွယ်ရာ တွေ့မြင်နိုင်ပါသည်။

ပုရောဟိတ်ပုဏ္ဏားကြီးက မိမိ၏သား ဟတ္ထိပါလအား အသက်အရွယ်ကြီးမှ တောထွက်ခြင်းပြုရန် တားမြစ်ခဲ့သည်။ သို့ရာတွင် ဟတ္ထိပါလက ဖခင်ကို အသက်အရွယ်ကြီး၍ ဇရာထောင်းချိန်မှ တရားအားထုတ်လျှင် စိတ်သွားတိုင်းကိုယ်မပါနိုင်တော့ကြောင်း၊ ခွန်အားကုန်ခမ်းနေပြီဖြစ်၍ တရားကိုကောင်းစွာအားမထုတ်နိုင်ကြောင်း ပြန်လည်ချေပ၍ ပြောဆိုထားပါသည်။ တရားအားထုတ်ရမည့်အရွယ်သည်-

“တောင်ညွန့်ကုန်းထက်၊ ကမ်းရိုးသက်ဝယ်၊

အနှက်အဖြိုး၊ ရေပြည့်အိုးကို၊

ကြိုးကြိုးပမ်းပမ်း၊ မဖိတ်ထမ်းသည်၊

လူစွမ်းသဖွယ်၊ ပျိုနုနယ်က၊

စင်ကြယ်သိမ်မွေ့၊ ရသေ့ရဟန်း၊

ဖြစ်ထွန်းလေငြား”ဟူ၍ တောင်ဆင်းတောင်တက် ကျန်းမာသန်စွမ်းသည့် အရွယ်မှ တရားအားထုတ်လျှင် တရားရနိုင်သည့်အပြင် နိဗ္ဗာန်ချမ်းသာကို တက်လှမ်းနိုင်မည်ဖြစ်ကြောင်း၊ ဆရာတော်၏ လောကုတ္တရာအမြင်ကို ဟတ္ထိပါလတောထွက်ခန်းတွင် ရေးဖွဲ့တင်ပြထားပါသည်။

ဆရာတော်သည် ဟတ္ထိပါလမှ ဖခင်ပုဏ္ဏားကြီးအား တောထွက်ခြင်းနှင့် ပတ်သက်၍ ပြန်လည်ချေပပြောဆိုခန်းတွင် လောကုတ္တရာအဆီအနှစ်များကို ထည့်သွင်းဖွဲ့ဆိုထားသည်ကို တွေ့ရပါသည်။ မိဘတို့ကို အသက်ထက်ဆုံးပြုစုစောင့်ရှောက်၍ ကျေးဇူးဆပ်သော်လည်း မကျေနိုင်ပေ။ မိဘတို့အား မင်ဖိုလ်သို့ ရောက်စေနိုင်သော ကုသိုလ်တရားကို ကျင့်ကြံပြောကြားနိုင်မှ မိဘကျေးဇူးကို ဆပ်နိုင်ရာ ရောက်ကြောင်းကို ဆရာတော်က-

“ရောက်တိုင်မင်ဖိုလ်၊ ကုသိုလ်တရား၊

ကြားစပေလှ၊ တို့ရချေဟု၊

လောကတံခွန်၊ ပုဂ္ဂိုလ်မွန်တို့၊

ဟောညွှန်နည်းမှီး၊ တောထွက်ပြီးသော်၊

ပွားစီးပညာ၊ ဒေသနာဖြင့်၊

မာတာပိတု၊ သဂြိုဟ်မှုကို၊

ပြုအံ့မရွံ့၊ ကောင်းအားသံသည်” ၁ (၁၉၇၀၊ ၃၃-၄၈)ဟူ၍ ရေးဖွဲ့တင်ပြ ထားသည်။ တရားဘာဝနာကို ကိုယ်တိုင်ကျင့်ကြံခြင်း၊ မိဘဆွေမျိုးများကို တရားအားထုတ်ရန် စွမ်းဆောင်ပေးခြင်း သည်၊ ကျေးဇူးဆပ်ရာတွင်ပို၍ ထိရောက်စေကြောင်း လောကုတ္တရာဗဟုသုတကို ရရှိစေပါသည်။

လူတို့သည် သေခြင်းတရားနှင့် မည်သူမျှမယှဉ်ပြိုင်နိုင်ကြပေ။ သေခြင်းတရားမလာမီကာလကြားတွင် တရားဘာဝနာစီးဖြန်းမှသာ သေခြင်းကင်းသော မြတ်နိဗ္ဗာန်သို့ တက်လှမ်းနိုင်မည် ဖြစ်ပါသည်။ ဆရာတော်က သေခြင်းတရားသည် လူတိုင်းထံသို့ အသက်အရွယ်မရွေး အချိန်အခါမရွေး ဝင်ရောက်လာနိုင်ကြောင်းကို-

“အနိစ္စကား၊ တကာဘိုးဘွား၊

မြေးသားမကွေ၊ နေပစေဟု၊

ရှောင်ထွေကြိုးကြား၊ ဘယ်သူ့အားလျှင်၊

ဆွေဝါးမှတ်ပေတုံအံ့နည်း”[၅]ဟူ၍လည်းကောင်း

“ဤရပ်ဤရွာ၊ဤခန်းဝါ၌၊

ဣရိယာပထ၊ ဤကိစ္စဖြင့်၊

နှစ်လရက်နေ့၊ ဤရွှေ့ဝယ်သာ၊

သေကိန်းလာ၏၊ ဤခါမရောက်၊

သက်မပျောက်ဟု၊ မဖောက်မလှဲ၊

မြဲသားအယူ၊ ဝိုင်းခြားမူ၍၊

ဘယ်သူသိချေ၊ တုံအံ့နည်း”ဟူ၍လည်းကောင်း ရေးဖွဲ့ထားသည်။ ဆရာတော်သည် လောကတွင် ကျင်လည်နေသည့် လူသားတို့အား သေခြင်းကင်းသော မြတ်နိဗ္ဗာန်ကို ရောက်စေရန် လောကုတ္တရာတရားကို ကျင့်ကြံစေလိုဟန် တူပါသည်။

ထို့ပြင်ဆရာတော်သည် ဂေါပါလတောထွက်ခန်းတွင် ဂေါပါလသတိုးသားထံ ပုဏ္ဏားကြီးနှင့် မင်းကြီးတို့သည် ရဟန်းအသွင်ဆောင်၍ မင်းစည်းစိမ်ကို အပ်နှင်းရန်သွားရောက်ခဲ့ပါသည်။ ဂေါပါလက နောင်တော်များနည်းတူ မင်းစည်းစိမ်ကို ငြင်းပယ်ကာ လောကုတ္တရာတရားဖြင့် ဖခင်တို့အား ဟောပြောညွှန်ပြခဲ့သည်။ လူ့လောကတွင် ကျင်လည်နေကြသော လူတို့သည် ဝမ်းစာရရှိရန်အတွက်၊ အစားပျက်၊ အအိပ်ပျက်ကာ စစ်မှုထမ်းရခြင်း၊ သူတစ်ပါးထံအစေအပါးလုပ်ရခြင်း၊ လယ်လုပ်၊ ကုန်သွယ်ရောင်းဝယ်ခြင်းဖြင့် ရှာဖွေစားသောက်ရသည်မှာ ပင်ပန်းဆင်းရဲလှပေသည်။ ရသေ့တို့မှာ-

“ပညာထွန်းတုံး၊ ကြည်လုံးထမ်းပိုး၊

ထွန်ညင်းပိုးလျက်၊ စွဲကြိုးကိုင်ပဲ့၊

ပန်းဘွဲ့အဟန်၊ မြဲစိတ်မွန်ဖြင့်၊

ထွန်သန်ထွန်ကိုင်း၊ တုန္နိုင်းဟီရိ၊

သတိတရား၊ ထွန်သွားလှင်ကန်၊

သင့်ကြန်စုံပြီး၊ တက်စီးကမ္မဋ္ဌာန်း၊

ဆော်သံမွန်းလျက်၊ ရဟန်းဝိရိယ၊

ထွန်နွားက၍၊ သီလပဓိန်၊

မိုးရွာဟုန်ဝယ်၊ မအုန်မအောက်၊

သွေ့ခြောက်လမ်းမာ၊ သဒ္ဓါမျိုးစေ့၊

ကြဲထွန်ပျိုးမှ၊ ဖြိုးဖြိုးပြည့်ဝန်၊

မြတ်နိဗ္ဗာန်” ၁(၁၉၇၀၊ ၄၉၊ ၆၇)သို့ ရောက်နိုင်ကြောင်း တင်ပြထား ပါသည်။ ဆရာတော်က ရဟန်းတို့ လုပ်ဆောင်ရမည့်ကိစ္စကို သာဓကပြု၍ လမ်းညွှန်းထားပါသည်။ ပညာတည်းဟူသော ထွန်တုံး၊ သမာဓိဟူသောကြိုး၊ ထွန်သံကိုင်းနှင့်တူသော ဟီရိတရား၊ နှင်တံနှင့်တူသော သုတတရားတို့ဖြင့် ကမ္မဋ္ဌာန်း စီးဖြန်းခြင်းကိုပြုကာ သဒ္ဓါတရားတည်းဟူသော မျိုးစေ့ကို စိုက်ပျိုး၍ နိဗ္ဗာန်ပြည်ကြီးနှင့်တူသော သီးနှံတို့ကို ထွက်စေ ကြောင်း၊ လောကီဥပမာနှင့် လောကုတ္တရာတရားတို့ကို ယှဉ်တွဲ၍ လမ်းညွှန်ပြခဲ့ပါသည်။ ဆရာတော်ရှင်မဟာရဋ္ဌသာရသည် အမျိုးလေးပါးတို့အား သဒ္ဓါတရားမျိုးစေ့များချ၍ နိဗ္ဗာန်ပြည်ကြီးသို့ တက်လှမ်းစေနိုင်ရန် တိုက်တွန်းပြောဆိုထားခြင်းဖြစ်ပါသည်။

ကောင်းမူကုသိုလ်ပြုသူသည် သဒ္ဓါမျိုးစေ့ကို ချရန် ရည်ရွယ်လျှင် ယနေ့နက်ဖြန်စသည်ဖြင့် အချိန်ကာလမရွေးသင့်ကြောင်းကို ဆရာတော်က-

“ဖိန်းနွဲ့ဖိန်းခါ၊ ကြာခဲ့ရွှေ့ရွှေ့၊

တစ်နေ့တစ်ပါး၊ ရွှေ့စများသော်”၃ဟူ၍လည်းကောင်း

“ကုသိုလ်မှာကား၊ ကြာကြာနေးနေး၊

အခါမေးလျက်၊ တွေးတွေးဆဆ၊

ထိုင်းပျဉ်လှသည်” ၂(၁၉၇၀၊ ၇၂) ဟူ၍လည်းကောင်း အမျိုးလေးပါး တို့ လိုက်နာစေရန် လမ်းညွှန်ထားသော ဆရာတော်၏ လောကုတ္တရာရာကျွမ်းကျင်နှံ့စပ်မှုကို သိရှိရပါသည်။

ကိုးခန်းပျို့တွင် ညီနောင်လေးဦးဟောကြားသော တရားအဆိအနှစ်များသည် ဖခင်ပုဏ္ဏားကြီးနှင့် မင်းကြီးတို့အတွက်သာမက လောကရှိအမျိုးလေးပါးတို့ပါ လိုက်နာကျင့်ကြံစေရန် ဆရာတော်ရှင်မဟာရဋ္ဌသာရက ညွှန်ပြဆုံးမထားခြင်းဖြစ်ပါသည်။ တရားအားထုတ်ခြင်း အမှုသည် အသက်အရွယ်ကြီးမှသာ မဟုတ်ဘဲ ငယ်ရွယ်စဉ်ကပင် တရားအားထုတ်သင့်ကြောင်း၊ လူ့ဘဝခဏတာတွင် သေခြင်းတရားသည် အလျှင်အမြန်ဝင်ရောက်လာနိုင်သဖြင့် ဆင်းရဲခပ်သိမ်းခြင်းကင်းသော မြတ်နိဗ္ဗာန်သို့ တက်လှမ်းနိုင်ရန် ဒါနမျိုးစေ့များ ချ၍ တရားအားထုတ်နိုင်ရန် အရေးကြီးကြောင်းဆရာတော်၏ ဆန္ဒကို ပျို့ကဗျာတွင် ထုတ်ဖော်ပြခဲ့ပါသည်။

ခြုံငုံသုံးသပ်ချက်

စာဆိုရှင်မဟာရဋ္ဌသာရသည် ကိုးခန်းပျို့တွင် လောကုတ္တရာ တရားအဆိအနှစ်များသာမက၊ လောကီဆိုင်ရာ အကြောင်းအရာများကို ကျွမ်းကျင်ပိုင်နိုင်စွာ ဖွဲ့စပ်နိုင်သော ပုဂ္ဂိုလ် ဖြစ်ပါသည်။ လောကုတ္တရာရေးနှင့် ပတ်သက်၍ ရဟန်းတို့၏ နေထိုင်ကြံမှု၊ တရားဘဝနာကို အားထုတ်ရာတွင် **“ဖြူကျားဆံရောက်၊ အိုရုပ်ပေါက်မှ”** တရားကို အားမထုတ်

သင့်ကြောင်း၊ ပျိုရွယ်နုငယ်သောအရွယ်တွင် တရားအထုတ်ခြင်းသည် ဉာဏ်ပညာအရပါပို၍ ထက်မြက်နိုင်သည့်အပြင် လူနတ်ကစ ချီးမွမ်းကြကြောင်း တင်ပြထားသည်။ အသက်ကြီးမှ တရားအားထုတ်လျှင် **“ညစ်ကြိတ်ယန္တရား၊ ကြံဖက်လား”** သက့ဲသို့ဖြစ်တတ်ကြောင်း၊ ထိမိခြင်သာသော ဥပမာများဖြင့် တရားအဆီအနှစ်ကို ပေးစွမ်းခဲ့သည်။ မင်းစည်းစိမ်ပစ္စည်းဥစ္စာတို့သည် မမြဲသောတရားများဖြစ်ကြသည်။ မိဘမောင်နှမ သားသမီးတို့သည်လည်း တရားကို မှေလျော့နေပါက သေခြင်းတရားသည် ယနေ့နက်ဖြန် တားဆီး၍ မရနိုင် သောကြောင်း တရားကို လူတိုင်းမသေမီစပ်ကြားတွင် အားထုတ် သင့်ကြောင့် တင်ပြထားသည်။ သေခြင်းတရားသည်

“သားကိုလွှတ်ငြား၊ သာကိုယ်စားလျှင်၊

သား၏မိဘ၊ သေချင်စွဟု၊

ဂူတလှည့်ကာ၊ ဖွေရှာမခြင်” နိုင်ကာ သားကို သေမင်းကခေါ်လျှင် မိဘတို့က သားကိုယ်စား သေချင်၍ မရနိုင်။ မိခင်ဖခင်တို့ကိုယ်စား သားသမီးတို့ကလဲ သေပေး၍ မရသော သေခြင်တရားသည် မည်သူမျှ မလွတ်ကင်းနိုင်ကြပေ။ ထို့ကြောင့် သေခြင်းကင်းသော မြတ်နိဗ္ဗာန်သို့ရောက်အောင် ကြီးငယ်မရွေးတရား အားထုတ်နေထိုင်သင့်ကြောင့် ဆရာတော်က အမျိုးလေးပါးတို့အား တရားဆီအနှစ်များ ပြည့်ဝသည့် လောကုတ္တရာဗဟုသုတတို့ဖြင့် ဆုံးမခဲ့သည်။ ကိုးခန်းပျို့သည် စာဆိုအသက်အရွယ်ကြီးမှ ပြုစုထားသောကြောင့် ဗဟုသုတ ပြည့်စုံသော၊ လောကုတ္တရာ ဓမ္မအရသာတို့နှင့်လည်း ပြည့်စုံသော ကျမ်းကြီးတစ်စောင်ပင် ဖြစ်ပါတော့သည်။

နိဂုံး

ကိုးခန်းပျို့သည် စာဆိုရှင်မဟာရဋ္ဌသာရရေးသားသော ပျို့များထဲတွင် ထင်ရှားသောပျို့တစ်စောင် ဖြစ်ခဲ့ပါသည်။ ၅၅၀ဇာတ်မှ ဟတ္ထိပါလဇာတ်ကို အခြေခံဖွဲ့ဆိုထားသော ပျို့ဖြစ်ပါသည်။ ဆရာတော်သည် ပုဏ္ဏားကြီး၊ သေကာရီမင်းကြီးနှင့် ဟတ္ထိပါလတို့ အပြန်အလှန်ပြောဆိုကြသည့်အခန်းတွင် လောကီဆိုင်ရာများကို ငယ်စဉ်အရွယ်မှ သင်ယူလေ့လာ၍ အသက်အရွယ်ကြီးမှသာ လောကုတ္တရာတရားကို အားထုတ်သင့်ကြောင်း တင်ပြထားပါသည်။ ဆရာတော်ကိုယ်တိုင် ရဟန်းဖြစ်သောကြောင့် တရားနှင့်ဆိုင်သော ဆောင်ရန်ရှောင်ရန်၊ ကျင့်ဝတ်၊ သွားလာနေထိုင်မှု၊ တရားဖြင့် နိဗ္ဗာန်တည်းဟူသော အေးချမ်းသည့် အမြိုက်ခွင်ကို လျှောက်လှမ်းကြစေရန်၊ ဟတ္ထိပါလ ညီနောင်လေးပါးတို့၏ တရားအပေါ်ထားရှိသော ခံယူချက်၊ တရားသဘောကို အမျိုးလေးပါးတို့ သိရှိလိုက်နာကျင့်ကြံစေရန် ရေးဖွဲ့တင်ပြထားသော ပျို့တစ်စောင်ဖြစ်ပါသည်။ ထိုပျို့ထဲမှ လောကုတ္တရာဆိုင်ရာ သုတများကို ဖော်ပြခြင်းဖြင့် ကောင်းနိုးရာရာ အကျင့်သီလများကို တုပ ဆင်ခြင်တတ်စေရန် ရည်ရွယ်လေ့လာ တင်ပြသော စာတမ်းတစ်စောင်ဖြစ်ပါသည်။

ကျေးဇူးတင်လွှာ

ဤစာတမ်းရေးသားရန် တိုက်တွန်းပေးပါသော ဒုတိယပါမောက္ခချုပ်(တာဝန်ခံ) Dr.စုယဉ်ဝင်း၊ စာတမ်းကို ကြီးကြပ်ပေးပါသော မြန်မာစာဌာနမှ ဌာနမှူး Dr.အေးအေးထွန်း အား အထူး ကျေးဇူးတင်ရှိပါသည်။

ကျမ်းကိုးစာရင်း

ဖေမောင်တင်၊ ဦး။ (၂၀၁၃)။ မြန်မာစာပေသမိုင်း၊ (၎ကဒသမအကြိမ်)။ ရန်ကုန်၊ ဝင်းတိုးအောင်အော့ဖ်ဆက်။

မင်းကျော်၊ ၂၀၀၈။ မလိခ၏ပျို့အညွှန်း၊ (ဒုတိယအကြိမ်)၊ ရန်ကုန်၊ သီရိမေရောင်ပုံနှိပ်တိုက်။ မြန်မာစာအဖွဲ့။ (၂၀၁၈)။ မြန်မာအဘိဓာန်။ ဒုတိယအကြိမ်၊ ရန်ကုန်၊ နေလင်းပုံနှိပ်တိုက်

ရဋ္ဌသာရ၊ မဟာ၊ ရှင်။ ၁၉၇၀။ ကိုးခန်းပျို့၊ ရန်ကုန်၊ စိတ်ကူးချိုချိုစာပေ။

သုတ၊ မောင်(ဗိုလ်မှူးဘသောင်း)။ (၂၀၀၂)။ စာဆိုတော်များအတ္ထုပ္ပတ္တိ။ ပဉ္စမကြိမ်။ ရန်ကုန်၊ ရာပြည့်စာအုပ်တိုက်။

Selection of Pumping Mode for Sucker Rod Pumping Well in Mann Oil Field

Ye Tun[1], Ah Kah Htun,Dr[2]

[1]*Department of Petroleum Engineering, Technological University (Mandalay)*

[2] *Department of Petroleum Engineering, Yangon Technological University*

Email: [1]yetun2447@gmail.com, [2]akhtun80@gmail.com

***Abstract*— Within the limitations set by the designated well and reservoir, the goal of artificial lift design is to optimise the production process and guarantee the most cost-effective method of fluid production. Sucker rod pumped well production testing is a crucial diagnostic technique for identifying possible production issues and tracking reservoir performance. Furthermore, the production system is integrated with the well test data and the inflow performance relationship (IPR). A sucker rod pumping system's whole design is the result of extensive trial and error. The engineer must select the pump type and size, the sucker rod string size, taper, and material, the surface unit type and size, the gear box rating, the beam rating, the stroke length, and the prime mover type and size in order to create a "optimum" design. A fundamental responsibility in the design of a rod pumping system is to balance the downhole pump's capacity with the well's inflow rate. Checking for overload situations on the pumping unit is the next stage. Additional operating characteristics, including lifting efficiency, Economic Index (EI), Performance Index (PIX), and polished rod horse power (PRHP), are calculated. From the pumping modes, the optimal one is selected by comparing the various performance rating concepts. Using the geological configuration and the historical production data from the Mann Oil Field in Myanmar, detailed computations are finished while taking into account the actual well conditions. The majority of wells in the Mann Oil Field use artificial lift techniques to create fluid, with sucker rod pumping systems being the most popular kind.**

Keywords—artificial lift, sucker rod pumping system, IPR, performance rating concepts

I. Introduction

To select the appropriate equipment and determine the operating parameters of a sucker rod pumping system in order to meet the operator's objectives and guarantee economical liquid production, all significant calculation methods for determining operating conditions in sucker rod pumping are examined. Accurate information of the maximum fluid flow that the specified well can produce is necessary for the proper design of the sucker rod pumping system. The design and selection of the sucker rod pumping installation require a thorough understanding of both surface and subsurface equipment.

Sucker rod pumping systems are mechanically straightforward and have a long history of being economically viable when used, but designing an effective system requires careful consideration of a number of variables. An optimal rod pumping installation from a technical and financial standpoint is the goal of good design. Complex rating systems, including as EI, PIX, and lifting efficiency, which should incorporate a number of crucial sucker rod pumping operating factors, are necessary to get optimal performance. Using the well data of MF-1 in the Mann Oil Field of Myanmar, the problem can be addressed to illustrate the design technique proposed in this study.

II. History Background of Mann Oil Field

The central Myanmar Basin's Salin basin is home to Mann Oil Field. Approximately 330 kilometres north of Yangon, in Minbu Township, on the west bank of the Ayeyarwaddy River, is where you may find this oil field. The Burma Oil Company first surveyed the field in the late 1960s while conducting seismic and gravity operations. The total area of Mann Field is 5623 acres. Drilled more than 650 wells since the production began in 1970. In the early stages of the field's growth, the operational mandate was to maximise primary output, with little regard for long-term developmental techniques. As a result, tracking production from the various producing intervals was not done, nor was optimal well spacing a consideration. The location of the deposits that remain is uncertain, and the effects of these practices are poorly understood in terms of the depletion of the various layers. Main production formations are Kyaukkok, Pywaebwe, Okhmintaung and Padaung. Total net pay thickness is 664 ft. [5]

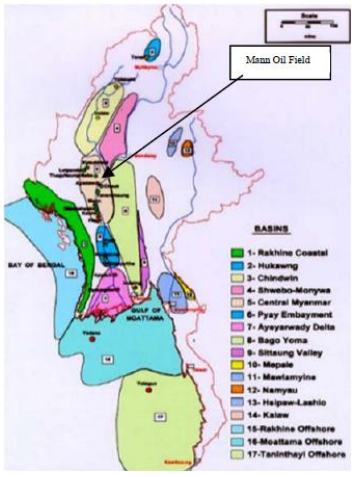

Fig. 1. Myanmar Basin Map. [5]

III. Inflow Performance of Pumping Wells

A production engineer needs to be well-versed in the factors that control the flow of fluid into a well. Establishing a link between bottomhole pressure and related production rates is necessary to accurately describe the behaviour of wells. The Inflow Performance Relationship (IPR) for a well is the function that is produced, and it is often acquired by conducting well testing. The producing bottomhole pressure must to be lower than the reservoir pressure or static

bottomhole pressure in order to achieve maximum withdrawal. [4]

The productivity index is;

$$PI = \frac{q}{P_{ws} - P_{wf}} \quad (1)$$

Vogel's idea of IPR is used as follows:

$$\frac{q_o}{(q_o)_{max}} = 1 - 0.2\left(\frac{P_{wf}}{p_r}\right) - 0.8\left(\frac{P_{wf}}{p_r}\right)^2 \quad (2)$$

wherein

PI is the productivity index, expressed as bpd/psi, and q is the observed liquid production rate, expressed as bpd.

The variables P_{ws} and P_{wf} represent the static and production bottomhole pressures in pounds per squared, while $(q_o)_{max}$ represents the theoretical maximum production rate, respectively. [3]

IV. Determining Producing and Static Bottomhole Pressure

The producing rate efficiency of a well can be determined using the IPR curve, although doing so necessitates understanding both the producing and static bottomhole pressures. in wells with minimal gas production. The pressure resulting from the annulus's fluid column and the surface casing pressure add up to the producing bottomhole pressure. The gas gradient adjustment factor is used to adjust the surface casinghead pressure to depth. [4]

$$C_g = 1 / e^{0.0000347GL} \quad (3)$$

The producing bottomhole pressure will be;

$$P_{wf} = P_c / C_g + 0.433 \times SG \times H \times F_x \quad (4)$$

It is possible to calculate static bottomhole pressure using the following formula:

P_s is equal to P_{sc} / C_g plus the pressure in the oil and liquid columns (5)

wherein

Gas gradient correction factor, or C_g

e is the natural logarithm base.

G is the gas's specific gravity.

L is the gas column length, in feet

P_c is the casing head pressure, in psig

SG is the liquid's specific gravity.

H is the gaseous liquid column's height, in feet.

F_x is the gradient correction factor for a column of gaseous liquid.

P_{sc} stands for shut-in casing pressure, in psg [4]

V. Sucker Rod Pumping System

There are two main categories into which the parts of a sucker rod pumping system can be separated: downhole and surface. The polished rod, wellhead assembly, gear reducer, and prime mover are examples of surface equipment. The working barrel, pump plunger, and rod string are all part of the downhole apparatus. [3]

A. Pumping Unit

Speed reducers, also known as gear reducers, are designed to reduce the high spinning speed of the prime mover to the required pumping speed. As a result, peak net torque (PT) is within the speed reducer's rating. [1]

B. Speed Reducer

The purpose of speed reducers, also known as gear reducers, is to lower the prime mover's high spinning speed to the necessary pumping speed. Peak net torque (PT) as a result is within the speed reducer's rating. [4]

C. Prime Mover

Since PRHP directly affects the system's overall energy need, the pumping mode requires the least amount of prime mover power. One of the more crucial elements is choosing a prime mover correctly so that the required amount of energy is minimised. Commonly utilised prime movers are of two types: (i) internal combustion engines; (ii) electronic motors. The rated mechanical power needed at the shaft of the electric motor can be computed using the formula below:

$$P_{np} = \frac{PRHP}{n_{mech}} \times CLF \quad (6)$$

where;

P_{np} is the necessary horsepower for the nameplate, in hp

PRHP stands for polished rod power, in hp

n_{mech} represents the pumping unit's mechanical efficiency.

Mechanical cyclic load factor is CLF. [4]

D. Subsurface Pump

The pump's duties include lifting the fluid that is admitted to the surface and admitting fluid from the formation into the producing string. Four components are required for a pump: a working barrel, a plunger, a stationary valve, and a travelling valve. The fluid is displaced from the tubing at the surface during the upstroke. The plunger's motion lowers the pressure above the standing valve, allowing fluid from the formation to be admitted. The plunger starts to fall through the fluid in the tubing at the start of the downstroke. As a result, the fluid load is moved from the plunger to the tubing, the travelling valves open, and the standing valve closes. [2]

E. Pump Size Selection

The optimum pump design cannot be overestimated the minimum energy requirements. The main factor in selecting the right pump size is the amount of fluid the pump displaces every inch of stroke. It may be necessary to calculate the required pumping speed by using the following approached formula;

$$PD = 0.1166 D_p^2 S_p N \quad (7)$$

where;

PD stands for total pump displacement, in bpd

D_p denotes the plunger diameter, in inches

S_p represents the effective plunger stroke, in inches

N is the plunger speed in number of stroke per minute. [1]

F. Sucker Rod String

Since it connects the subsurface pump to the surface pumping unit, the sucker rod string is the most crucial

component of the pumping system. Individual sucker rods that are attached to one another until the necessary pumping depth is reached make up the rod string. [4]

G. Design of Sucker Rod String

The decision of (a) the rod sizes to be utilised in the string, (b) the lengths of the separate taper sections, and (c) the rod material to be used are the three main goals of rod string design. [6]

I. DATA ON SUCKER ROD [4]

Dimensions of the Rod (in)	Area of Metal (sq.in)	Weight in Air (pound per feet)	Elastic Constant (inch per pound-feet)
½	0.196	0.726	1.99×10^6
5/8	0.307	1.135	1.27×10^6
¾	0.442	1.634	0.883×10^6
7/8	0.601	2.224	0.649×10^6
1	0.785	2.904	0.497×10^6

VI. SELECTION IN PUMPING MODE

The real combination of pump size, polished rod stroke length, pumping speed, and rod string design is known as the sucker rod system's pumping mode. Additionally, there are a variety of typical API pump sizes and stroke lengths available. [4]

A. Performance Rating Concepts

The intended production rate and fluid lift are the two main design parameters taken into account while creating a sucker rod pump. The lifting efficiency, PT, PRHP, and PPRL values are all included in the economic index. [4]

$$EI = 10^{-7} \times \frac{PPRL \times PT \times PRHP}{\eta_{lift}} \quad (8)$$

In order to assess a pumping system's overall economy, the Performance Index (PIX), which is defined as:

$$PIX = 10^{-9} \times \frac{PPRL \times PT \times P_{np} \times CLF}{ITE \times \eta_{lift}} \quad (9)$$

where;

EI stands for economic index

η_{lift} is the lifting efficiency, in %

PPRL represents the peak polished rod load, in pound

PT denotes the peak net torque on speed reducer, in inch-pound, PIX is the performance index and ITE (index of torsional effectiveness) is equal $6.3 \times 10^6 \times \frac{PRHP}{N \times PT}$

As before, optimal rod pumping economy is ensured by the lowest EI and PIX value. [4]

B. Optimising the Efficiency of Lifting

Every technique places a strong value on lifting efficiency and works to maximise it. It has the following definition:

$$\eta_{lift} = \frac{P_{hydr}}{PRHP} \quad (11)$$

where;

P_{hydr} is the hydraulic horsepower needed to raise fluid, in hp. [4]

C. Reduction in Operating Costs

It is impossible to overstate how crucial it is to choose a pump design that minimises energy consumption. Polished rod horsepower (PRHP) and the pumping system's overall energy are intimately correlated. [4]

VII. DESIGN PROCEDURE FOR PUMPING WELL

The step (I) is determined the producing bottomhole pressure.

$$P_x = \frac{P_c + 14.7}{C_g} + 0.433 \times SG \times (D_x - FL) \times F_x \quad (12)$$

Determining the shut-in bottomhole pressure is the step (II).

$$P_r = \frac{P_c + 14.7}{C_g} + \text{oil column pressure} + \text{mixed column pressure} \quad (13)$$

Step (III) uses Vogel's equation for the generalised IPR curve to determine the necessary rate and pump setting depth. The design of the sucker rod string and the determination of the operational characteristics are steps (IV) and (V).

$$PPRL = W_{rb} + \left(\frac{F_1}{SlK_r} \times SlK_r\right) \quad (14)$$

$$MPRL = W_{rb} + \left(\frac{F_2}{SlK_r} \times SlK_r\right) \quad (15)$$

$$PRHP = 2.35 \times 10^{-6} \times \frac{F_3}{SlK_r} \times Sl^2NK_r \quad (16)$$

$$PT = \frac{2T}{Sl^2K_r} \times \frac{S^2}{2} \times K_r\{1 + (\frac{W_{rb}}{SlK_r} - 0.3)\frac{T_a}{10}\} \quad (17)$$

$$P_{hydr} = 7.36 \times 10^{-6} \times Q \times \gamma_g \times L_{hydr} \quad (18)$$

where;

MPRL denotes the minimum polished rod load, in pound

Sl represents the polished rod stroke length, in inches

K_r is the spring constant of the rod string, in pound per inch

W_{rb} stands for buoyant rod string weight, in pound

γ_g is the specific gravity of the produced fluid

T_a is the torque adjustment factor

Performance rating concepts is the step (VI). These steps are the design procedure for sucker rod pumping wells. [6]

VIII. RESULTS AND FINDING

In this paper, by using the well data from MF-1 in Mann Oil Field are shown in table 2. It is being produced with a conventional sucker rod pumping unit. To determine the desired rate and pump setting depth, by using Vogel's equation for generalized IPR curve, $(q_o)_{max}$ is 356 bpd at 7200 ft. This pressure is the first point for the well's performance curve. Bottomhole pressure is divided into the reservoir pressure by 0.5 psi/ft is 4946 ft and by subtracting 4946 ft from the depth of the well to obtain the height of the liquid column at zero production rate is 2254 ft. Then, zero

rate at 2254 ft becomes the second point. According to the behavior of Vogel's curve, 70 percent of maximum production at the one-half of the static column, 70% of $(q_o)_{max}$ is 249 bpd at 4727 ft. This pressure is the third point. These three points are plotted on the same graph the "Fig. 2", together with the pump capacity available from various pumps setting depth of API units. From the intersection points it can be obtained one possible rates and pump setting depth for the well. The results of 315 bpd with a pump setting depth of 6050 ft are presented in the "Fig. 2".

From optimum design, pump plunger sizes recommended for this result can be determined by the API and it is found that 1.75 inches pump size can be selected. To obtain the desired production rate of 315 bpd from the pump setting depth of 6050 ft, the pumping unit with the structural capacity of 21300 lb, reducer rating of 320000 in-lb and maximum stroke length of 84 inches must be used from pumping unit size ratings of API units. From preciously described procedure, the similar calculations with the variable value of stroke length, pumping speed and rod strings are made. The output results are presented in the table 3. From output results, the optimum pumping mode with the higher lifting efficiency of 93%.; lower Economic Index of 5696 and lower Performance Index (PIX) of 6.5 will be selected.

II. WELL DATA FROM MANN OIL FILED

Production data	Well # MF-1
Well Depth	7200 ft
Pump Setting Depth	6550 ft
Pumping Fluid Level	4700 ft
ID of 5 ½ in Casing	4.95 in
OD of Tubing	2.875 in
Sucker Rod String	5/8 in, 3/4 in, 7/8 in
Pumping Speed	18 spm
Stroke Length	74 in
Pumping Unit Installed	Salzgitter (226-246-86)
Pump Size	1.5 in
Production	219 bpd
Bottomhole Pressure	2473 psi
P_{wf}	1435 psi

III. CALCULATED RESULTS OF PUMPING MODE DESIGN ON WELL MF-1 (MANN OIL FIELD)

Well No.	Pump Depth (ft)	Liquid Rate (bpd)	Pump Size (in)	Rod No.	Stroke Length (in)	Pumping Speed (spm)	Rod Size (in)	Rod Length (ft)	PPRL (lb)	MPRL (lb)	PT (in-lb)	PRHP (HP)	Lift η%	EI	PIX
MF-1	6050	315	1.75	75	74	15	5/8 3/4 7/8	1250 2575 2225	18577.00	58839.64	221397.58	15.26	73%	8595.7	8.50
					84	12.5	5/8 3/4 7/8	950 2350 2750	18694.73	6623.27	236455.59	11.98	93%	5696	6.50
				76	74	15	3/4 7/8	3725 2325	19653.37	6098.65	239364.17	16.38	68%	11331	11.29
					84	12.5	3/4 7/8	3600 2450	19181.29	6693.90	236202.50	12.75	87%	6614.8	7.10
				86	64	10	3/4 7/8 1	2700 1775 1575	23244.28	6520.70	261214.40	26.86	41%	39397	30.13
					74	15	3/4 7/8 1	2475 1900 1675	21879.91	7252.42	254060.49	17.59	63%	15448	14.63
					84	12.5	3/4 7/8 1	2325 1975 1750	21358.43	7951.41	291765.50	13.80	81%	10616	12.78

Finally, the selection of optimum pumping mode can be accomplished by the pump size is 1.75 inches, stroke length is 84 inches, pumping speed is 13 spm (12.5 spm), API rod number is 75 and rod sizes and lengths are (5/8 inch and 950 ft), (3/4 inch and 2350 ft) and (7/8 inch and 2750 ft). By studying the selection of pumping mode for sucker rod pumping well, not only the pumping unit would be choosing the optimum mode and most safety unit for well but also the oil production would economic and profitable.

IX. CONCLUSION

The sucker rod pumping design depends on the best choice of pumping mode in order to enhance production methods and guarantee the most cost-effective way to produce liquids. Among the several pumping modes, the selection of optimum pumping mode will not only assure minimal operating cost. To selected the optimum pumping mode, it must be necessary to calculate the lifting efficiency and performance rating concepts such as Economic Index (EI) and Performance Index (PIX). In this paper, several

pumping modes are calculated by using the well data of MF-1 in Mann oil field. If one pumping mode has the highest value of lifting efficiency and higher value of EI and PIX, it cannot be selected as optimum condition. Because, these value of EI and PIX are high compare to the other pumping mode and consequently the investment cost and the operating cost will not be minimum and the pumping system will not be economy. These optimum pumping modes are the lower EI, PIX and higher efficiency in each well. These pumping modes are the most cost-effective and energy-efficient ones.

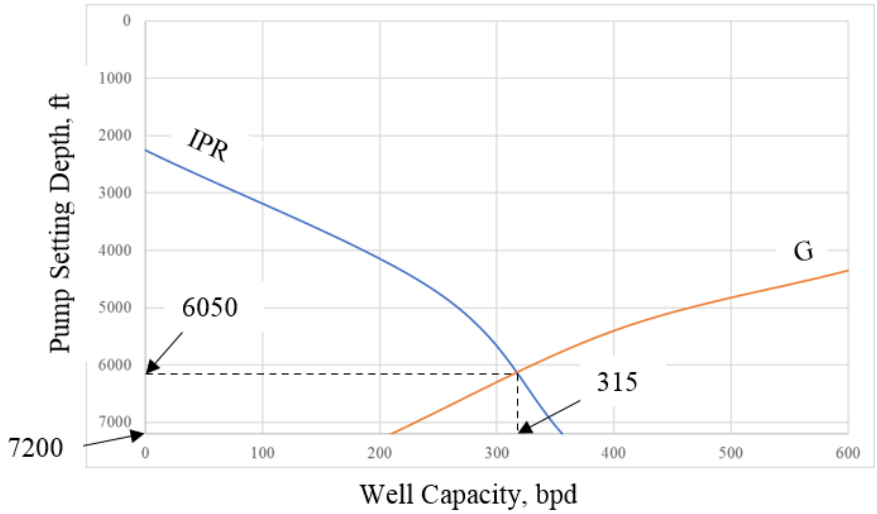

Fig. 2. Well Producing Capacity and Equivalent Capacity and Depth for Producing MF-1 Well.

ACKNOWLEDGMENT

The author would like to express gratitude to Engr. Prof. Dr. Aung Myo, Professor and Head of the Petroleum and Mining Engineering Department at Technological University (Mandalay), and Prof. Dr. Ah Kah Htun, Professor and Head of the Petroleum Engineering Department at Yangon Technological University, for their invaluable suggestions, supports and editing this paper. The author also wishes to thank to U Pyay Zaw Htet (MPRL E&P Pte Ltd.) valuable data and giving advice and suggestion. Finally, the author is greatly indebted to his parents and relatives for their kind encouragement, moral and financial support throughout his entire life.

REFERENCES

[1] Brown., K., E., "The Technology of Artificial Lift Methods:" Volume 2a, Penn Well Books, PPC, Tulsa, Oklahoma, 1980.

[2] Craft., B.C., Hold en., W.R. and Gra,ves, E. P. .Jr., "Well Design; Drilling and Production," Prentice - Hall, Inc., Englewood Cliffs, New Jersey, 1962.

[3] Gabor, Tkacs, Ph.D, "Sucker Rod Pumping Manual," Penn Well Corporation, Tulsa, Oklahoma, 2003.

[4] Taka'cs, G:., "Modern Sucker Rod Pumping," Penn Well Publishing Company Tulsa, 1992.

[5] THAN TUN (Petrol), "OIL Field OF MYANMAR," 2018.

[6] U Win Myint, unpublished M.E. Thesis., "Optimization of Operation Criteria for Beam Pumping Design," Yangon Technological University, Department of Petroleum Engineering, June, 1997.

The Relationship between Geology and Rock Weathering on the Rock Instability along Myogyi-Ywangan Car Road, Ywangan Township, Southern Shan State

Zaw Win Htut[1], Sai Hlaing Sang[2]

[1]*Department of Petroleum Engineering, Technological University Mandalay*

[2]*Department of Engineering Geology, Technological University Lashio*

Email: [1]zawwinhtutofficer@gmail.com, [2]hlaingsang20796@gmail.com

***Abstract*— The Myogyi-Ywangan car road ran alongside the study area. The main rock types found in the research area are metagreywacke, slate, phyllite, quartzite, limestone, dolomite, siltstone, and mudstone. A relationship between field observations and microscopic investigations has been attempted to be understood, given the significant influence of geology and rock weathering on instabilities. The two primary techniques utilized to assess the weathering of the rocks in the study area were laboratory testing and field surveys. Large and complicated landslides have been found to be related to slope features, rock weathering, and the intervention of geological structures such as faults, joints, and fractures. The research as a whole led to this result. Most of the rock units in the study area are highly jointed, and brecciated. Debris flow occurred in the Lebyin Group. In the microscopic study, the rock of weathering grade may be ranged from moderate to high, and engineering behavior of rock strength is decreased.**

Keywords—weathering, fault, joint, fracture, geological structure, rock strength

I. INTRODUCTION

The study area is located in western part of the Southern Shan State, tracing a path along about 49.6 kilometer mountainous route stretching from Myogyi to Ywangan. This road spans from 21° 27' 42.28" N to 21° 28' 17.74" N in longitude and 96° 19' 48.43" E to 96° 21' 08.09" E in latitude, encompassing a rugged terrain within the Shan Plateau. Originating 46 miles southeast of Kyaukse, the road winds through the undulating slopes and valleys of the Shan Plateau. The research area is readily accessible by cars and motorbikes using this road the whole year. The location map of the study area is shown in (Fig. 1).

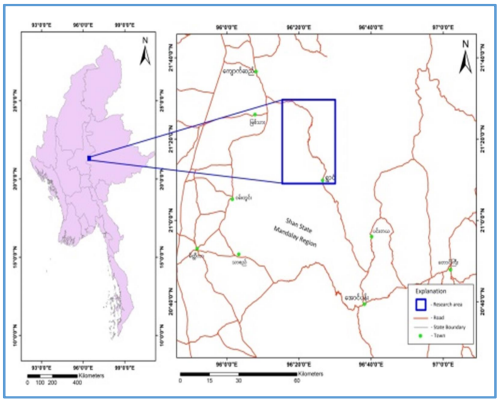

Fig. 1. Location map of the study are.

In general, the study area is a rugged terrain made up of NNW-SSE trending ranges with a maximum elevation of over 1360 meters above sea-level. The northwestern and western parts of the area are generally low in relief, occupying around 100 meters above sea-level. The rugged terrain in the area is mainly due to the predominance of limestone formation. Physiolgraphically, the Ywangan area may be subdivided into four main provinces. The eastern province is characterized by the abundant knolls separated by valleys and gullies which are deep and steep. It is a result of long-term denudation on fairly resistant metasedimentary rocks. The individual hillocks gain in height towards north and west of the study area, attaining more than 1666 meters above sea-level (Fig. 2).

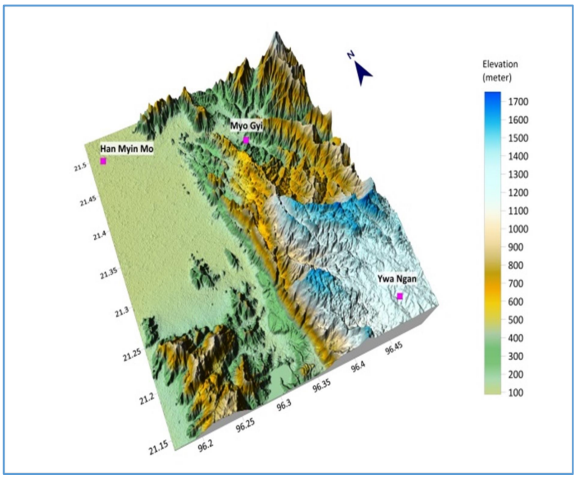

Fig. 2. Three dimensional terrain map showing physiographic features of the study area.

Over the course of 24 years (2000-2023) climatic observations recorded in Ywangan Township, the mean monthly temperature ranged from 18° to 25° C with a mean annual temperature of 22.5°C. The mean annual rainfall was 2048 mm, ranging from 2800 to 4900 mm. August and September are the most rain falling months in the annual year. The rock units of the study area are increased in pore water pressure during these months. In the study area, the Zawgi river is a perennial stream, but its tributaries are of ephemeral streams. In the eastern province, fairly spaced tributaries join the major stream at various angles, assuming a medium dendritic pattern. The areas of limestone units with prominent joint sets have given rise to fine rectangular and trellis patterns. Some sink holes are present in the western part (Fig. 3).

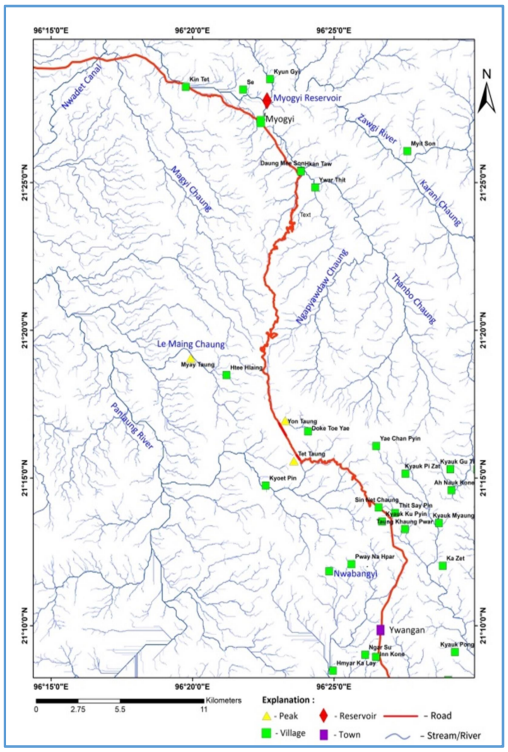

Fig. 3. Drainage pattern of the study area.

A. *Purposes of Study*

The aim of the present study is to assessment the weathering grade of the rocks and to identify the rock strength in the study area.

B. *Methods of Study*

There are two kinds of methods: field method includes systematic collection of soil and rocks samples for laboratory tests and collecting of the joints, and laboratory method includes thin section for microscopic study to determine the mineral composition of the rocks, cementation, dolomitization and other diagenetic features.

.

II. Regional Reology

Regionally, the study area is located along Myogyi and Ywangan car road which consists of the Chaung Magyi Group, Lokepyin Formation, Wunbye Formation and Nan-on Formation of Pindaya Group, Lebyin Group, Nwabangyi Formation of Plateau Limestone Group, and recent younger alluvium. The Precambrian Chaung Magyi Group widely observed the inner part of a major anticline (Yechanzin Anticline), lied in the North of Ye-U, Ywangan Township. There, the Permian-Triassic sequence of the Plateau Limestone Group unconformably had overlain the Lower Paleozoic rocks. [7]

A. *Rock Units of the Study Area*

The study area and its environ can be mainly cropped out into four types of rock units such as (1) Upper Chaungmagyi Group consists of phyllites, slate, metagreywacke, and low-grade schist, (2) Pindaya Group consists of Lokepyin Formation and Wunbye Formation, (3) Lebyin Group consists of mudstone and greywacke, (4) Plateau Limestone Group consists of Nwabangyi Formation, and recent younger alluvium. These rock units are NNW-SSE trending. Their brief descriptions are as shown in Table (I). [6]

I. Rock Units Of The Study Area

Rock Unit		Lithology	Age
Alluvium		Reddish-brown color, massive soil with gravels	Quaternary
Plateau Limeston Group	Nwabangyi Formation	Reddish-grey to dark-grey color, massive, brecciated dolomite	Permian to Middle Triassic
Lebyin Group	Indurated Mudstone and Greywacke	Brown color, medium- to-very thick - bedded, greywacke intercalated with mudstone	Carboniferous to Middle Permian
Pindaya Group	Wunbye Formation	Bluish-grey color, medium- to - very thick - bedded, limestone with silt patches	Middle Ordovician
	Lokepyin Formation	Bluish-grey color,medium bedded to massive limestione and yellow color massive siltstione	Early Ordovician
Upper Chaung Magyi Group	Thin-bedded silty limestone	Light-grey color, medium-to-thick bedded limestone	Precambrian
	Phyllites and slate	Brown color, medium-to-thick-bedded phyllite, metagreywacke, slate, quartizite	

B. *Geological Structures of the Study area and its Environ*

Generally, it is a south plunging anticline, however the range of the northern half is very complicated, having overturned and recumbent folds, and faults systems at diagonal directions. At the northwestern part of the range, the whole sequence from the Pindaya Group to the Plateau Limestone Group, extending over the distance of five miles in width, had been overturned, and dips eastwards instead of westwards. The Pindaya plain is located between the Pindaya Anticline and the Bawsaing Anticline apparently as syncline, which in detail appears to be complex. The collision between the Indian Plate and the Eurasian Plate is resulting from complex tectonic activity in Shan State. The geological structures of the study area are complex. The Paulaung Fault is a major fault in the southwestern part of the study area which passed through the nearly N-S trending. Mae Pin Fault passed through the southwest part

of the Ywangan area. Minor faults and folds were observed in the study area. Minor faulted are traced by slickenslides. Minor faults occurs in the meatgreywacke of the Upper Chaung Magyi Group (Fig. 4), minor folds occurs in the quartzite of the Upper Chaung Magyi Group (Fig. 5) and joints are well-observed in the study area. Most of the rock units are highly jointed and brecciated. [5]

Fig. 4. Minor fault occured in metagreywacke of Upper Chaung Magyi Group.

Fig. 5. Minor fold structure occurred in quartzite of Upper Chaung Magyi Group.

III. Petrography

Based on the constituent mineral assemblages and textures, the major rock types of the study area are metasedimentary rocks and sedimentary rocks. For the petrographic criteria of the mineral assemblages, more than 32 thin sections were cut from various representative rock samples.

Petrographic techniques have been used to evaluate successive stages in mineralogical and textural changes brought about by weathering. The rock mass rating can be assessment from the amount of discoloration, decomposition and disintegration. In a microscopic study, the mineral composition, degree of alteration and frequency of microfractures can be used to identify the strength of rocks.

A. Implication of Petrography on the Engineering Properties of Metamorphic Rocks along Myogyi-Ywangan Road

Metamorphic rocks of the quartzite, phyllite, and slates along the Myogyi-Ywangan road are collected and made the thin section on microscopic study. Quartzite is poorly compaction due to their grain boundaries. Cement is detrital quartz and mica, sometimes mica altered to clay. Some quartz grains are deformed due to the high strain and pressure solution occurs between the grains.There are many microfractures between the grain boundaries and iron minerals are well-observed. The poorly compaction, alteration, high strain, and microfractures caused to the strength of rock in decrease. Iron minerals may be oxidized that effect rapidly weathered the rocks. Weathered the rock increased, the strength of rock decrease. [3]

Biotites in the metagreywacke altered to chlorite or vermiculite are clearly noted. Most of the grains are deformed due to high strain occurred in quartz grain in len-shape. Mineral grains are foliated and the cleavage plane is the weakness of the rocks. Mica and other clay minerals are occurred along the cleavage plane and affected the strain and weathered these minerals easily slip in its. Thus, opaque minerals are well-observed and caused the easily weathering and may decrease its strength. Phyllite includes the quartz; feldspar and mica are the major constituents. These are foliation and biotite has inclusions. Recrystallization also occurred and changes the bulk volume of the rock. Opaque minerals are clearly observed. These factors may be caused to the instability to the slope and strength of rock in decreased. [1]

B. Implication of Petrography on the Engineering Properties of Sedimentary Rocks along Myogyi-Ywangan Road

Mineral grains in the mudstone are folded due to strain. In mudstone contains high clay mineral which may possess the weak strength and their durability may be suspect. The mudstone becomes physically more stable which decrease in the percentage of expandable clay minerals. Clay minerals have swelling effect to the absorption of free water by certain clay minerals and fraction which extremely detrimental to the integrity of many engineering structures. The mudstone is rich in iron minerals; it rises to reduce stability on weathering. Greywacke in the Lebyin Group is poorly sorting; many pore spaces laminated in varieties and are invariably jointed. Greywacke is indicated to immediate surface deterioration on out corps. Especially, the amount of rock fragments occupying the pores influenced the porosity of greywacke. Its porosity, amount and type of cement and/or matrix material, as well as the composition of the individual grains controlled the compressive strength of greywacke. If cement binds the grains together a stronger rock is produced. However, the amount of cementing material is more important than the type of cement; siliceous cementation is stronger than calcareous cementation. The compressive strength and deformation characteristics of a greywacke are very significant role by pore water. The grain size, porosity, and density play a major role for the degree of induration and strength in the engineering properties of carbonate rocks. The grain size and those post-depositional changes in carbonate rocks that bring about induration and it can sustain high overburden pressures. High overburden pressures creep and recrystallization produces crystalline limestone with very low porosity. The age related with increased in density and porosity is decreased. Older limestones are lower porosities due to the diagenetic processes. When limestones are dolomitized in the Nwabangyi Formation, it takes place high porosity and possesses a lower compressive strength than limestone. The significant effect of dissolution in limestone is increased in the pores, which make water circulation thereby encouraging further solution and increase in stress within the remaining rock framework that leads to increasing stress corrosion and the rock instability.

Furthermore, rain water is susceptible to solution the carbonate rocks, which commonly dissolved out the shell fragments in the Lokepyin Formation, and ooids in the Wunbye Formation. [2]

C. Results and Discussion

Metamorphic rocks of the Upper Chaung Magyi Group in the study area, alteration intensity moderate to high as the result of microscopic characteristics. In microstructural -ly, increased in microfractures or microcracks in the mineral grains and between the grains, decreased in strength. Quartzite of the Upper Chaung Magyi Group is clearly observed in numerous microfractrures. The mineral composition, grain size, and packing (amount and type of cement/matrix), degree of grain interlock are influenced by rock strength and fracture. Carbonate rock is perhaps more prone to pre- and post-consolidation changes than any other rock type. Carbonate rocks take place many changes during transformation from soft and generally porous carbonate sediment to a dense, hard limestone with a low porosity. The limestone of Lokepyin Formation is contained fossil fragments. These fragments are reacted with the acid in the rainwater and may be dissolved. Siltstone of the Lokepyin Formation is iron-staining, and may be oxidized which leads to readily weathering. The limestone of the Wunbye Formation is well-observed in ooid grains and porosity is 50% of the total volume between the grains. The porosity is higher, the strength is lower. The greywacke of the Lebyin Group composed of ununiformed grains lead to poor compaction and increase in porosity. The mudstone of the Lebyin Group is composed of the clay mineral predominantly. Clay minerals have swelling in saturated condition. The type of cement/matrix is important, not only influencing strength and elasticity, but also density, porosity and permeability. Neomorphism and dolomitization are observed in dolomites of the Nwabangyi Formation. The original calcite forms the newly dolomites and bulk density decreased. It is significant to identify the mode of preservation from complete solution of fragments leading to mould formation and consequence infilling with cement to occur a classic casts. The weathering of the rocks in the study area may range from moderate to high. Not only the chemical or mineralogical composition but also the texture and bonding depend on the engineering properties of the rocks.

IV. Conclusion

The rock units of the study area are highly jointed and brecciated in the field investigation. In the microscopic study, the metagreywacke and phyllite are foliation, minerals alteration, grain size changing, porosity, ore minerals including, and numerous microfractures within and between the grains limestone contains shell fragments, siltstones are iron-staining, and dolomites are neomorphism and dolomitization. The geology of the study area is complex in tectonically. These factors that lead to the easily weathering of the rocks and rock strength in decreased. The weathering grade of the rock units in the study area may range from moderate to high as result of the field and laboratory methods.

Acknowledgment

I would like to express my sincere gratitude to Engr. Prof. Dr. Aung Myo, Head of Department, for providing the necessary facilities and kind peremission to publish the work. Furthermore, I am deeply grateful to Sai Hlaing Sang, Demostrator, Department of Engineering Geology Technological University (Lashio) for helping the fieldwork.

References

[1] F. G. Bell. "Engineering Properties of Soils and Rocks", 4th ed., Blackwell Science Limited, UK, 2000, pp. 332-442.

[2] F. G. Bell. "Basic Enviromental and Engineering Geology",Whittles Publishing Limited, Dunbeath, Caithness, KW6 6EY,Scotland, UK, 2008, pp. 248-250.

[3] John D. Winter "Principles of Igneous and Metamorphic Petrology", 2nd ed., Pearson Education Limited, UK, 2014, pp. 465-583.

[4] Maurice E. Tucker "Sedimentary Rocks in the F", 3rd ed., John Wiley and Sons Limited, UK, 2003, pp. 248-250.

[5] Myint Lwin Thein."The lower Paleozoic Stratigraphy of Western Part of the Southern Shan State, Burma." Bulletin of the Geological Society of Malaysia, vol. 6, pp. 143-163, July 1973.

[6] Khin Khin Lin. "Cambro-Ordovician Sequence Stratigraphy and Sedimentology of the Myogyi-Pindaya area, Southern Shan State." Ph.D thesis, University of Mandalay, 2004.

[7] Ko Ko Myint."Geology of the Myogyi area,Ye-ngan township." M.Sc. thesis, University of Mandalay, 1989.

VOLUME 1
August 2024
esej2024 @gmail.com